Live Long and Phosphor: Extending Absorptive Cross-Sections and Excited-State Lifetimes Through Benzannulation

by

Issiah Byen Mandia Lozada

A Thesis submitted to the Faculty of Graduate Studies of
The University of Manitoba
in partial fulfilment of the requirements of the degree of

Doctor of Philosophy

Department of Chemistry
University of Manitoba
Winnipeg, MB, Canada

To my mom

Abstract

There are several strategies in modifying the electronic structure of molecules. Functional group modification is perhaps the most used approach. In this thesis, I explore a different approach through the expansion of ligand π-systems by fusing benzene rings (benzannulation). Benzannulation introduces physicochemical and photophysical changes in molecules without significant changes in the parent framework. In this work, I use computational analysis to investigate the impact of benzo-fused pyridines, quinoline and phenanthridine. Phenanthridine introduces a lower-lying unoccupied molecular orbital (LUMO) compared with quinoline, red-shifting the absorption spectra of complexes. Combining phenanthridines with π-donor ligands enabled the isolation of iron complexes with panchromatic absorption. In addition, benzannulation enables more efficient mixing between the excited singlet and triplet states facilitating the direct $T_n \leftarrow S_0$ transition. Interestingly, the luminescent properties of the complexes supported by phenanthridine exhibit blue-shifted emission compared with the quinoline-supported analogues. The enhanced rigidity provided by phenanthridine contributes to the observed higher energy shift.

Building on these findings, a series of new phenanthridine-containing ligands and their boron, zinc and platinum complexes were then pursued. Some of these complexes exhibit long-live emissive excited states originating from triplet states. In addition, new phenanthridine precursors bearing water-soluble and surface-anchoring groups were introduced. Finally, the antineoplastic activity of Pt(II) complexes supported by *N^N^O* ligands was explored, leading to the discovery of complexes with enhanced cytotoxicity compared with cisplatin both in dark and upon exposure to light.

Acknowledgments

Table of Contents

List of Figures

List of Schemes

List of Tables

List of Abbreviations and Terms

Py: pyridine or pyridyl

Bpy: 2,2'-bipyridine or 2,2'-bipyridyl

Tpy: terpyridine or terpyridyl

OTf: triflate or trifluoromethanesulfonate

FcH: ferrocene

$FcH^{0/+}$: ferrocene/ferrocenium redox event

PAH: polyaromatic hydrocarbon

GS: ground state

Eq: equilibrium geometry

CT: charge transfer

MLCT: Metal-to-ligand charge transfer

LLCT: ligand-to-ligand charge tranfer

ILCT: intraligand charge transfer

PALCT: π-antibonding-to-ligand charge transfer

PBLCT: π-bonding-to-ligand charge transfer

SBCT: symmetry breaking charge transfer

PES: potential energy surface

IC: internal conversion

ISC: intersystem crossing

SOC: spin orbit coupling

ZORA: zeroth order regular approximation

HS: high spin

BS: broken-symmetry

PhOLED: phosphorescent organic light emitting diode

TADF: thermally activated delayed fluorescence

MO: molecular orbital

HOMO: highest occupied molecular orbital

LUMO: lowest unoccupied molecular orbital

WFT: wavefunction theory

DFT: density functional theory

TDDFT: time-dependent density functional theory

BOA: Born-Oppenheimer Approximation

SCE: standard calomel electrode

CV: cyclic voltammetry

DPV: differential pulse voltammetry

XRD: X-ray diffraction

PDT: photodynamic therapy

DSSC: dye-sensitized solar cells

FWHM: full-width at half maximum

NMR: nuclear magnetic resonance

NOE: nuclear overhauser effect

ATR-IR: attenuated total reflectance infrared

GFAAS: graphite furnace atomic absorption spectroscopy

MTT: 3-(4,5-dimethylthiazol-2-yl)-2,5-diphenyltetrazolium bromide

MET5A: mesothelial cells

HEK-293: human embryonic kidney cells

A2780: cisplatin sensitive ovarian cancer

A2780-cis: cisplatin resistant ovarian cancer

SKOV-3: ovarian cancer

MDA-MB-231: breast cancer

A549: lung cancer

IC_{50}: half maximal inhibitory concentration

ds-DNA: double stranded deoxyribonucleic acid

ss-DNA: single stranded deoxyribonucleic acid

BSA: bovine serum albumin

RHAU: RNA Helicase associated with AU-rich element

MRI: magnetic resonance imaging

1 Introduction

1.1 Benzannulation: From Benzene and Beyond

Benzene holds a special place in chemistry. It has a rich and contentious history, owing to its highly polyunsaturated structure (ratio of hydrogen to carbon is 1:1) which made the assignment of its structure challenging to determine before the advent of advanced instrumentation. While it was first isolated and identified in 1825 by Michael Faraday[1], it was Kekulé who was credited for solving the long-standing question of its structure—a ring of six carbon atoms each with one hydrogen and with alternating single and double bonds. The emergence of X-ray crystallography in the late 19th and early 20th centuries made possible the confirmation of benzene's structure. The initial work of Kathleen Lonsdale on hexamethylbenzene and hexachlorobenzene confirmed the cyclic nature of benzene and revealed the planar structure of benzene. Even to this day, advanced instrumentations reveal subtle information about its structure.[2,3]

Benzene's importance in chemistry cannot be overstated. It is present in natural products, pharmaceuticals, agrochemicals, a primary building block in synthetic organic chemistry, ligand scaffolds in coordination chemistry and continues to serve as a reference molecule in computational chemistry thanks to its chemical stability and properties arising from its aromatic nature.[4–7] Moreover, the development of various synthetic methodologies has enabled the incorporation of benzene rings as substituents or fused into other ring systems[8] enabling the expansion of the conjugated π-system. The latter example is often called benzannulation in the literature, and it is the main theme of this thesis—benzannulation in ligand design and coordination chemistry.

Fusion of additional benzene rings has a profound impact on the physicochemical properties of aromatic, organic scaffolds such as in polyaromatic hydrocarbons (PAHs). For example, benzene exists as a liquid at room temperature (m.p. 5.5 °C) compared with naphthalene (m.p. 80 °C). Fusion of another benzene ring leads to a further increase in the melting point of PAHs (anthracene, m.p. 215 °C; phenanthrene, m.p. 101 °C). Aromatic systems are known to form noncovalent π-stacking interaction between neighbours. The differences in the melting point of the PAHs may be attributed to the increased π-stacking interactions in the solid state with increasing number of fused aromatic rings. Benzannulation also impacts the electronic properties of PAHs as evidenced by the differences in their reduction potentials [$E°_{red}$/V (vs standard calomel electrode or SCE): benzene, -3.42; naphthalene, -2.60; anthracene, -1.96; phenanthrene, -2.46; pentacene, -1.35]. This implies that the lowest unoccupied molecular orbital (LUMO) of PAHs are stabilized by benzannulation.

It becomes evident in the anthracene and phenanthrene examples, structural isomers of each other, that the effect of benzannulation is not always linear. The site-selective impact of benzannulation in anthracene and phenanthrene is also reflected by the difference in their lowest energy absorption [$λ_{max}$(abs): anthracene, 374 nm; phenanthrene, 293 nm]. These subtle modifications introduced by benzannulation are expanded further in the following sections of this chapter. In Chapters 2 to 5, the impact of benzannulated phenanthridine (3,4-benzoquinoline) on the properties of molecular complexes are described and discussed.

1.2 Structure and Reactivity of Benzannulated Metal Complexes

Benzannulation has also profound impact on the properties and reactivity of coordination complexes. This is exemplified by the indenyl effect[9–12] observed in indenyl sandwich complexes. Indenyl can be thought of as benzannulated cyclopentadienyl (Figure 1.1). η^5-Indenyl complexes exhibit enhanced substitution rates compared with the η^5-cyclopentadienyl analogues. The kinetics can be further enhanced by further benzannulation as in η^5-fluorenyl complexes. Electrochemical studies on iron(II) sandwich complexes demonstrate the increasing ease of oxidation on going from $\eta^{5\text{-cyclopentadienide}}$ to η^5-indenide complexes.[13] Previous electrochemical studies on ruthenium(II) , η^5-indenide and η^5-cyclopentadienide sandwich complexes reveal the same trend with the oxidation potentials shifting cathodically with benzannulation. This shift is mirrored in the first ionization potentials of the same complexes revealed by photoelectron spectroscopy (lower ionization potential in the η^5-indenide complex.[14] These observations indicate that η^5-indenide is overall a stronger donor than η^5-cyclopentadienide. Apart from the changes in the donor strength to cyclopentadienide, benzannulation can also introduce asymmetry in the system leading to further changes in bonding and electronic structure. For example, the asymmetry of the indenide ligand has been leveraged to alter the spin-states of bis(indenyl)chromium(II) complexes.[15]

Cyclopentadienide   Indenide   Fluorenide
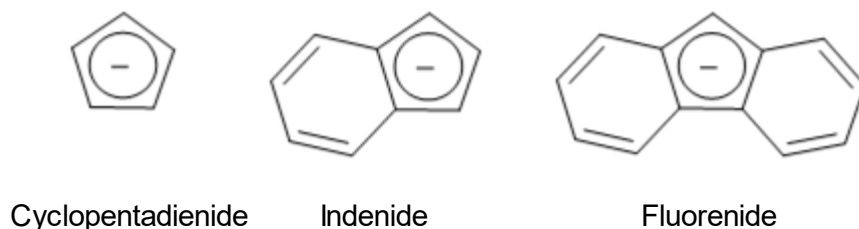
Figure 1.1 Molecular structures of cyclopentadiene anion and its benzannulated congeners.

1.3 Impact on Photophysics

Perhaps a more obvious impact of benzannulation is on the photophysical properties of molecules. In general, benzannulation leads to a smaller HOMO-LUMO gap (HOMO is defined as the highest occupied molecular orbital), shifting the energy of the HOMO→LUMO excitation to lower energies. For example, benzannulation in a series of zwitterionic pyridinium-*N*-phenoxide betain dyes[16] led to a red-shift in the lowest energy absorption band (attributed to HOMO→LUMO transition) into the near-infrared region of the electromagnetic spectrum. A simple model is shown in Figure 1.2 that describes the narrowing effect to the ΔE_{H-L} by extending the conjugation of π-systems.
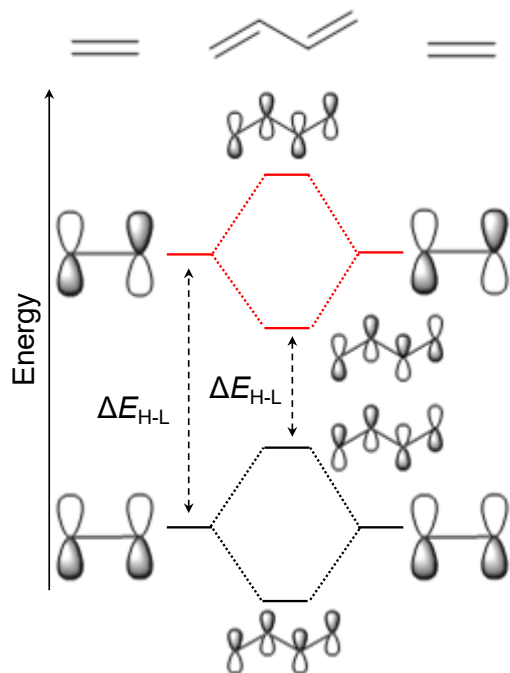
Figure 1.2. Impact of extending the conjugation on the HOMO-LUMO gap (ΔE_{H-L}). Horizonal, black and red solid lines denote filled and vacant frontier molecular orbitals, respectively.

4

However, from the earlier discussion on anthracene and its structural isomer phenanthrene, narrowing the $\Delta E_{\text{H-L}}$ by extending the π-system is not always linear. In the context of coordination complexes, Thompson *et al.*rs studied the site-selective benzannulation of bis(2-pyridylimino)isoindolate platinum chloride, [Pt(BPI)Cl] shown in Figure 1.3. In their work, Thompson *et al.* revealed benzannulation only has significant effect on the LUMO energy as evidenced by the electrochemical properties of the complexes (Table 1.1). Benzannulation either at the C_3/C_4 and C_5/C_6 sites led to a smaller $\Delta E_{\text{H-L}}$, and consequently a bathochromic shift in the $\lambda_{\text{max,abs}}$ and $\lambda_{\text{max,em}}$ of **3** and **4**. In contrast, benzannulation at C_6/C_7 (**2**) surprisingly produced the opposite effect, blue shifting not only the $\Delta E_{1/2}$ but also the $\lambda_{\text{max,abs}}$ and $\lambda_{\text{max,em}}$. Computational analysis on the Pt(BPI)Cl complexes indicates that the blue shift on going from **1** to **2** is due to destabilization of LUMO with the expansion of the central isoindole fragment. In contrast, benzannulation in complexes **3** and **4** led to stabilization of the LUMO in both complexes. The HOMO of all complexes remained unperturbed with respect to the parent complex (**1**) leading to invariant $E_{1/2}^{\text{ox}}$.
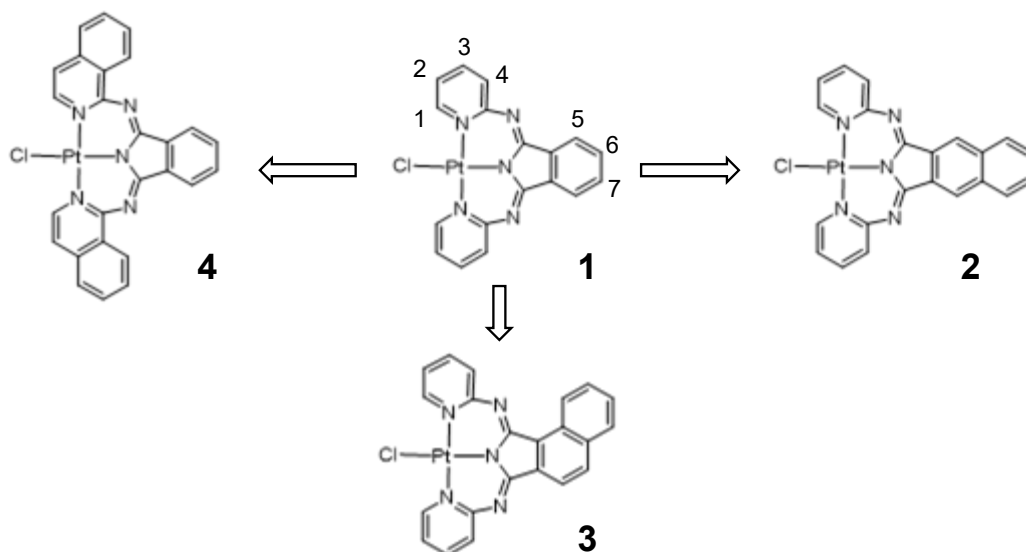
Figure 1.3. Site-selective benzannulation in Pt(BPI)Cl[17] complexes.

Table 1.1. Selected electrochemical and photophysical properties of Pt(BPI)Cl complexes. [17]

Complex	$E_{1/2}^{red1}$ / V	$E_{1/2}^{ox}$ / V	$\Delta E_{1/2}$ / V	$\lambda_{max,abs}$ / nm	$\lambda_{max,em}$ / nm	ΔE_{H-L} / eV
1	-1.44	-0.79	2.22	487	641	2.99
2	-1.53	-0.80	2.33	477	611	3.07
3	-1.32	-0.77	2.09	529	682	2.83
4	-1.23	-0.79	2.07	511	711	2.75

Another example wherein benzannulation can be employed to selectively tune either the HOMO or LUMO energies has been demonstrated in a series of cationic Ir(III) cyclometallated complexes (Figure 1.4). The HOMO energies can be tuned by ring expansion of the phenylpyridine ligands.[18] Computational modelling indicated that the HOMO orbital density is delocalized between the two phenylpyridine ligands. In contrast, localization of the LUMO on the bipyridyl ligand in the same family of complexes enabled the selective modification of the LUMO energies by site-selective ring expansion.[19] Interestingly, the same group has shown that benzannulation

could also enhance or turn-on direct $T_n \leftarrow S_0$ transitions in a series of cationic Ru(II) complexes ligated by benzannulated bipyridine ligands (Figure 1.5).[20] These complexes were examined for their photodynamic therapeutic (PDT) properties. In the series, complexes **8** and **9** exhibit a broad, weak absorption (ε / $M^{-1} \cdot cm^{-1}$: < 800) between 550-900 nm. This suggests that benzannulation enhances S_n-T_n mixing, permitting direct $T_n \leftarrow S_0$ transitions which are considered forbidden transitions. This phenomenon is a desirable component for the development of broadband reverse-saturable absorbers and PDT agents and could open new avenues in photochemistry by directly accessing triplet states.
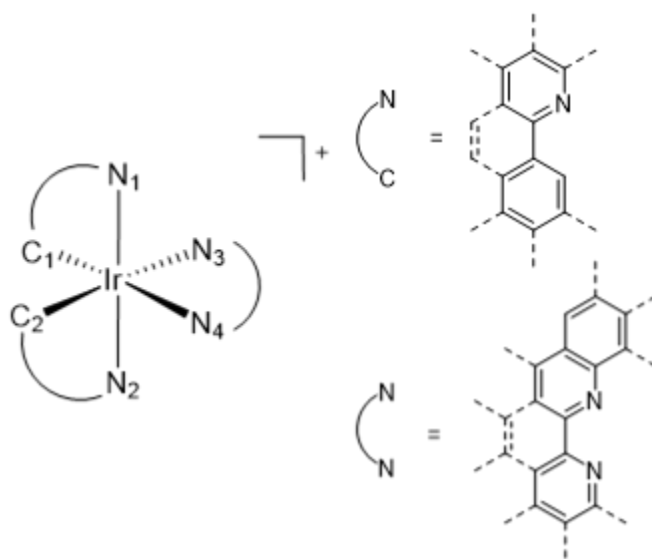
Figure 1.4. Benzannulated cyclometallated cationic Ir(III) complexes. Dashed lines indicate sites of benzannulation.

These examples provided demonstrate the utility of benzannulation in ligand design to modify the optoelectronic properties of complexes without significant modification to the parent ligand framework. This allows flexibility in designing new emissive molecules and molecular photosensitizers. Combining the benzannulation strategy with advanced computational

methodologies could guide the development of such materials. The efficiency of modern computers, algorithms and programs could be used to screen a library of complexes and pinpoint potential candidates for synthesis and further experiments. In this thesis, Chapters 3 and 4 describe the impact of π-expansion of quinoline to phenanthridine to the photophysical properties of various complexes as revealed by combined experimental and computational efforts. Two common themes emerge, namely, (i) phenanthridine introduces lower-lying vacant acceptor π^* orbitals red shifting the absorption, and (ii) the extended π-system of phenanthridine further rigidifies the system leading to unexpected blue-shifts in the emission of some complexes and prolonged excited state lifetimes.
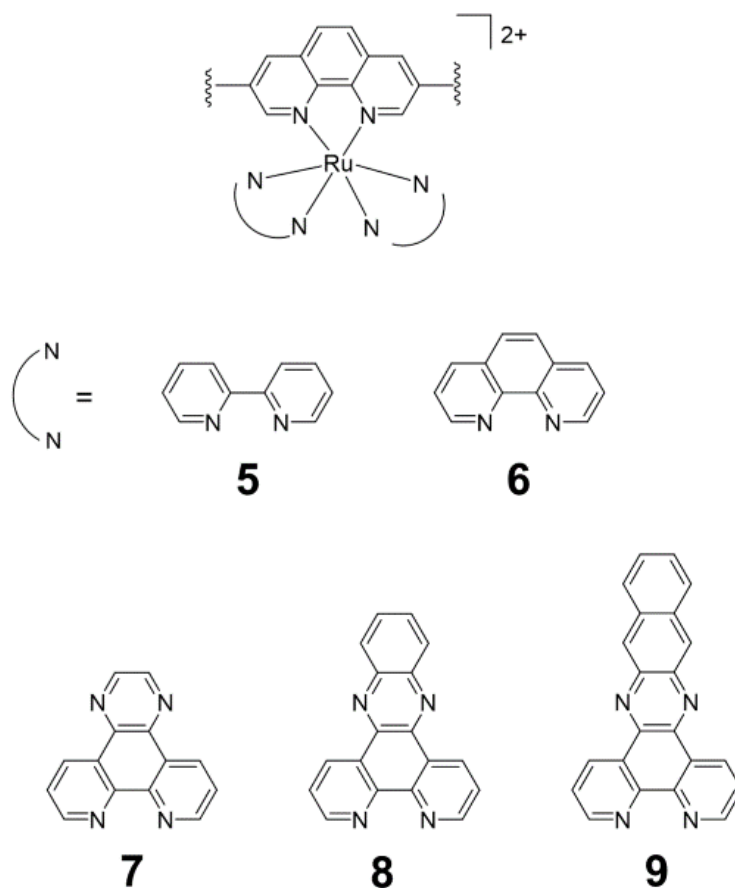
Figure 1.5. Benzannulated bipyridyl ligands to access direct $T_n \leftarrow S_0$ transitions in Ru(II) complexes.

1.4 Benzannulation and Noncovalent π-Stacking Interactions

Due to the highly polarizable π-system of conjugated aromatic systems, weak noncovalent intermolecular π-stacking interactions can emerge. There are three known conformations of π-stacking phenomena (Figure 1.6). Most encountered conformations are the T-shaped and staggered. While it was initially a curiosity, π-stacking has become one of the most important noncovalent interactions aside from hydrogen bonding.[21] The stabilization energy from this intermolecular interaction in a benzene dimer is estimated to be between 1.8-2.8 kcal/mol,[22] and is dependent on the relative position of the benzene rings with respect to each other with the

sandwich conformer being the least stable. As with dispersion interactions, which increase with molecular size, stabilization from π-stacking also increases with increasing number of fused benzene rings. As mentioned earlier, benzannulation of benzene to naphthalene leads to a melting point increase from 5.5 °C to 81 °C, and further expansion leads to insoluble materials.

sandwich   T-shaped   staggered
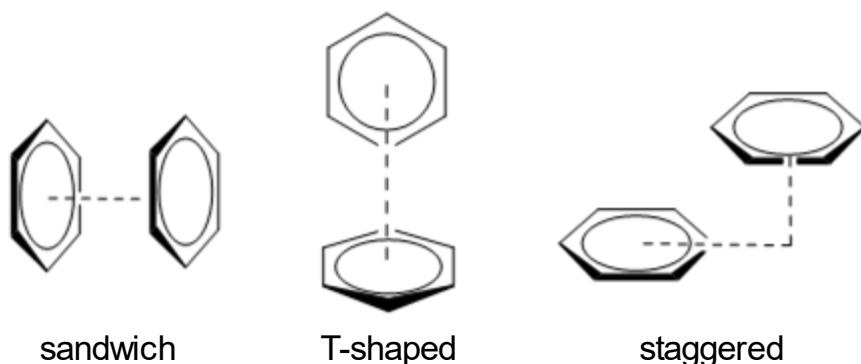
Figure 1.6. Three most encountered π-stacking conformations.

Phosphorescent organic light emitting diodes (PhOLEDs) and thermally activated delayed fluorescent (TADF) organic/organometallic light emitting diodes are efficient replacements for conventional light sources. However, their efficiency decreases at high brightness levels (efficiency roll-off). Efficiency roll-off is detrimental in these materials as it leads to increased power consumption and decreased device lifetimes. Often PhOLED/TADF materials are diluted into hosts to suppress efficiency roll-off. Duan and co-workers[23] have shown that π-stacking between highly benzannulated bipolar hosts (molecules that serve as both the electron and hole charge carriers) can be leveraged to improve hole/electron mobilities in these materials leading to a decreased efficiency roll-off in PhOLED/TADF materials. Noncovalent π-stacking interactions are also often responsible for emission enhancement through aggregation induced/enhanced emission or similarly could lead to aggregation induced quenching through the formation of

excimers.[24] As discussed in Chapter 4, this behaviour plays a key role in the enhancement of phosphorescence in Zn(II) complexes.

Apart from materials chemistry, π-stacking interactions are also present in biological systems. In proteins, π-stacking interactions have been observed between aromatic side chains of the amino acids: phenylalanine, tyrosine, histidine, and tryptophan. Stabilization of ~0.5-1 kcal/mol for the staggered conformation compared with the T-shaped has been estimated, explaining the predominance of the staggered conformation in these systems.[25] The role of π-stacking in proteins has long been recognized as an important strategy in the drug development.[26] In addition, π-stacking interactions between nucleobases also contribute to the structure of the DNA double helix apart from hydrogen-bond. The propensity of DNA nucleobases to form π-stacks has been exploited to study the DNA. For example, ethidium bromide or **EthBr** (Figure 1.7) is widely used as a DNA fluorescent tag in molecular biology. While **EthBr** is weakly fluorescent in water, titration with DNA leads to the intercalation of the tag to DNA grooves leading to fluorescent enhancement. An emerging class of anticancer Pt(II) complexes is based on polyaromatic ligands (Figure 1.7) and operates similarly to **EthBr**. While the exact mechanism of action is still unclear, these complexes intercalate with DNA with high binding constants and are extremely cytotoxic toward cancerous cells.[27] The ability of phenanthridine, molecular core of **EthBr**, to intercalate with DNA is incorporated in some Pt(II) complexes presented in Chapter 5 of this thesis.
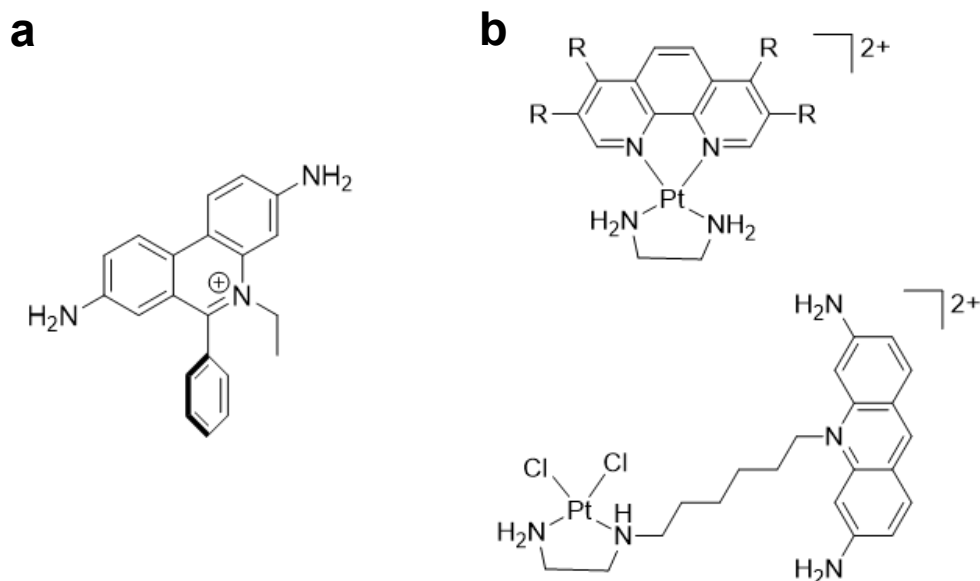
Figure 1.7. Molecular structure of (a) ethidium bromide and (b) examples of intercalating Pt(II) complexes.

1.5 Description of Thesis

This thesis aims to describe the synthesis, coordination chemistry, photophysics, and applications of benzannulated ligands based on phenanthridine. Chapter 2 delves into the motivation behind the incorporation of phenanthridine in multidentate ligand scaffolds. I first introduce the impact of benzannulation (comparing quinoline with phenanthridine) on the optical properties of complexes ligated by bidentate P^N and N^N, and tridentate diarylamido ligands. This chapter also describes the synthesis and characterization of N^N(H)^O ligands. The last aspect of this chapter introduces new phenanthridine precursors incorporating water soluble and surface anchoring functional groups. Chapter 3 describes the coordination chemistry of N^N(H)^O with main group (boron) and transition metal (zinc and platinum) elements. This chapter also

reveals interesting photophysical properties of the complexes. Moving to Chapter 4, the photophysical properties of complexes are explained using density functional (DFT) and time-dependent functional theories (TDDFT). I first present my contributions to previously studied complexes in our group, and part of collaborative effort in our group. I investigated the impact of benzannulation to the optical properties establishing common themes between different complexes. I also present my contributions on iron complexes bearing diarylamido ligands, which exhibit panchromatic absorption and long-lived excited states. This work is extended to other metal complexes supported by the same diarylamido ligands. I end this chapter with a discussion on complexes of *N^N^O* ligands. Chapter 5 explores the cytotoxic properties of Pt(NNO)Cl complexes. Attempts to understand its mechanism of action is presented uncovering an interesting turn-on phosphorescence phenomenon in the presence of DNA. Lastly, the potential of the Pt(II) complexes as PDT agents are discussed. Chapter 6 summarizes the findings reported throughout the chapters and includes ongoing work and outlook for projects.

The format of this thesis is a classic Ph.D. thesis decided upon by myself, my supervisor, and my committee, with the main theme of benzannulation as ligand design strategy to tune the properties of complexes. Each chapter is written similar to manuscripts published in peer-reviewed scientific journals with some additions and modifications. Each draft was written by I with input from the principal investigator.

1.6 Acknowledgements

The syntheses of P^N and N^N and diarylamido ligands and their complexes are credited to Drs. Rajarshi Mondal, Jason Braun, and Pavan Mandapati. Some X-ray crystallography experiments were performed by Dr. Jason Braun (zinc complexes) and my supervisor (*N^N*(H)*^O*

ligand). Most of the UV-Vis and emission studies were carried out by Prof. J.A. Gareth Williams from Durham University, UK. The resonant inelastic X-ray scattering data were collected at SLAC National Accelerator Laboratory, USA, in collaboration with the group of Profs. Kelly Gaffney and Dr. Amy Cordones-Hahn including Dr. Christopher Larsen. All mass spectrometry experiments were performed by Emy Komatsu from the Manitoba Chemical Analysis Lab at the University of Manitoba. The syntheses and characterization of *N^N*(H)*^O* ligands and their complexes, and new phenanthridine precursors were done by I including all NMR experiments, all cyclic and differential pulse voltammetry experiments, some UV-Vis and emission experiments, IR, and some X-ray crystallography. Some computational contributions from Dr. Rebecca Davis (iron and copper complexes) and Robert John Ortiz (rhenium and boron complexes) are recognized. Most calculations were performed by I.

Chapter 1: Introduces benzannulation and its impact on the physicochemical and photophysical properties of molecules.

Chapter 2: This chapter first discusses the ligand design behind the incorporation of phenanthridine in ligand scaffolds. Furthermore, I present some preliminary results on the impact of benzannulation on the optical properties of some complexes by merging selections from two manuscripts {Mondal, R.; Braun, J.D.; Lozada, I.B.; Nickel, R.; van Lierop, J.; Herbert, D.E. *New J. Chem.* **2021**, 45, 4427; Gaire, S.; Ortiz, R.J.; Schrage, B.R.; Lozada, I.B.; Mandapati, P.; Osinski, A.J.; Herbert, D.E.; Ziegler, C. *J. Organomet. Chem.* **2020**, 121338.}. The impact of incorporating phenanthrdinyl moieties with amido π-donors on the emission of Pt(II) is subsequently presented from Mandapati, P.; Braun, J.D.; Lozada, I.B.; Williams, J.A.G.; Herbert, D.E. *Inorg. Chem.* **2020**, 59, 12504. These ligands are then extended to 3*d* transition metals from

Larsen, C.B.; Braun, J.D.; Lozada, I.B., *et al. J. Am. Chem Soc.* **2021**, 143, 20645; Braun, J.D.; Lozada, I.B.; Shepit, M.; van Lierop, J.; Herbert, D.E. **2021**, 11, 3547; Braun, J.D.; Lozada, I.B.; Herbert, D.E. *Inorg. Chem.* **2020**, 59, 17746. This is followed by the introduction of new phenanthridine-based *N^N*H^*O* ligands that were reported in Lozada, I.B.; Huang, B.; Stilgenbauer, M.; Beach, T.; Qiu, Z.; Zheng, Y.; Herbert, D.E. *Dalton Trans.*, **2020**, 49, 6557 and Lozada, I.B.; Ortiz, R.J.; Williams, J.A.G.; Herbert, D.E. *J. Org. Chem.*, **2022**, 87, 184. Finally, some unpublished work is disclosed.

Chapter 3: This chapter delves into the syntheses and photophysics of complexes supported by *N^N*(H)^*O* ligands featuring works from Lozada, I.B.; Ortiz, R.J.; Williams, J.A.G.; Herbert, D.E. *J. Org. Chem.*, **2022**, 87, 184; Lozada, I.B.; Williams, J.A.G.; Herbert, D.E. *Inorg. Chem. Front.*, **2022**, 9, 10. Most of the syntheses and characterization are performed by I with some of the X-ray crystallography experiments done by Dr. Jason Braun and synthesis of the boron complexes performed by Robert Ortiz. Most of the photophysical studies were conducted by Prof. J.A. Gareth Williams. All drafts of the manuscript were written as part of a collaborative effort by all authors.

Chapter 4: Chapter 4 probes the electronic structures, photophysics and excited state dynamics of molecular complexes. Most of the work was carried out by I, with a few preliminary studies done by Prof. Rebecca Davis.

Chapter 5: This extends the Pt complexes presented in Chapter 3 to investigate their antineoplastic properties. This is part of a collaborative effort with the syntheses, characterization and computations carried out by I while all biological work done by Prof. Yaorong Zheng's group. This features the following publication: Lozada, I.B.; Huang, B.; Stilgenbauer, M.; Beach, T.; Qiu, Z.; Zheng, Y.; Herbert, D.E. *Dalton Trans.*, **2020**, 49, 6557.

References

(1) Faraday, M. On New Compounds of Carbon and Hydrogen, and on Certain Other Products Obtained during the Decomposition of Oil by Heatrstl.1825.Pdf. *Philos. Trans. R. Soc.* **1825**, *115*, 440–466.

(2) Heo, I.; Lee, J. C.; Özer, B. R.; Schultz, T. Mass-Correlated High-Resolution Spectra and the Structure of Benzene. *J. Phys. Chem. Lett.* **2022**, *13* (35), 8278–8283. https://doi.org/10.1021/acs.jpclett.2c02035.

(3) Kunishige, S.; Katori, T.; Baba, M.; Nakajima, M.; Endo, Y. Spectroscopic Study on Deuterated Benzenes. I. Microwave Spectra and Molecular Structure in the Ground State. *J. Chem. Phys.* **2015**, *143* (24), 244302. https://doi.org/10.1063/1.4937949.

(4) Watson, M. D.; Fechtenkötter, A.; Müllen, K. Big Is Beautiful−"Aromaticity" Revisited from the Viewpoint of Macromolecular and Supramolecular Benzene Chemistry. *Chem. Rev.* **2001**, *101* (5), 1267–1300. https://doi.org/10.1021/cr990322p.

(5) Vij, V.; Bhalla, V.; Kumar, M. Hexaarylbenzene: Evolution of Properties and Applications of Multitalented Scaffold. *Chem. Rev.* **2016**, *116* (16), 9565–9627. https://doi.org/10.1021/acs.chemrev.6b00144.

(6) Price, C. C. Substitution and Orientation in the Benzene Ring. *Chem. Rev.* **1941**, *29* (1), 37–67. https://doi.org/10.1021/cr60092a002.

(7) Papadakis, R.; Ottosson, H. The Excited State Antiaromatic Benzene Ring: A Molecular Mr Hyde? *Chem. Soc. Rev.* **2015**, *44* (18), 6472–6493. https://doi.org/10.1039/C5CS00057B.

(8) Swami, B.; Yadav, D.; Menon, R. S. Benzannulation Reactions: A Case for Perspective Change From Arene Decoration to Arene Construction. *Chem. Rec.* **2022**, *22* (1), e202100249. https://doi.org/10.1002/tcr.202100249.

(9) Hart-Davis, A. J.; White, C.; Mawby, F. J. Reactions Of-WIndeny Complexes of Transition Metals. III.' Kinetics and Mechanisms of Substitution Reactions of Tricarbonyl-Mindenylhalomolybdenum(II) Complexes. 6.

(10) Rerek, M. E.; Basolo, F. Kinetics and Mechanism of Substitution Reactions of .Eta.5-Cyclopentadienyldicarbonylrhodium(I) Derivatives. Rate Enhancement of Associative Substitution in Cyclopentadienylmetal Compounds. *J. Am. Chem. Soc.* **1984**, *106* (20), 5908–5912. https://doi.org/10.1021/ja00332a026.

(11) Rerek, M. E.; Ji, L.-N.; Basolo, F. The Lndenyl Ligand Effect on the Rate of Substitution Reactions of Rh(Rl-C9H7)C(O), and Mn(Rl -CgH7)C(O)a. 2.

(12) Okada, Y.; Miyamoto, N.; Hishimoto, M.; Hayashi, T. Studies on Ferrocene Derivatives. Part XIII. Ligand Exchange Reactions of Benzoferrocenes. *Transit. Met Chem* **1999**, 5.

(13) Treichel, P. M.; Johnson, J. W.; Wagner, K. P. OXIDATIONS OF VARIOUS INDENYL-IRON. 4.

(14) Crossley, N. S.; Green, J. C.; Nagy, A.; Stringer, G. Electronic Structure of Transition-Metal Lndenyl Compounds: A He I and He I I Photoelectron Spectroscopic Study of [Mn(Q5-C,H7)(CO),], [Fe(Q5-CgH7),]. Ru(Q5-C9H7)21 and Ru(T5-C9H7)(q-C5Me5) I t. *J CHEM SOC DALTON TRANS* **1989**, 9.

(15) Brady, E. D.; Overby, J. S.; Meredith, M. B.; Mussman, A. B.; Cohn, M. A.; Hanusa, T. P.; Yee, G. T.; Pink, M. Spin-State Alteration from Sterically Enforced Ligand Rotation in

Bis(Indenyl)Chromium(II) Complexes [1]. *J. Am. Chem. Soc.* **2002**, *124* (32), 9556–9566. https://doi.org/10.1021/ja012390a.

(16)   Shimizu, A.; Ishizaki, Y.; Horiuchi, S.; Hirose, T.; Matsuda, K.; Sato, H.; Yoshida, J. HOMO–LUMO Energy-Gap Tuning of π-Conjugated Zwitterions Composed of Electron-Donating Anion and Electron-Accepting Cation. *J. Org. Chem.* **2021**, *86* (1), 770–781. https://doi.org/10.1021/acs.joc.0c02343.

(17)   Hanson, K.; Roskop, L.; Djurovich, P. I.; Zahariev, F.; Gordon, M. S.; Thompson, M. E. A Paradigm for Blue- or Red-Shifted Absorption of Small Molecules Depending on the Site of π-Extension. *J. Am. Chem. Soc.* **2010**, *132* (45), 16247–16255. https://doi.org/10.1021/ja1075162.

(18)   Liu, B.; Lystrom, L.; Kilina, S.; Sun, W. Effects of Varying the Benzannulation Site and π Conjugation of the Cyclometalating Ligand on the Photophysics and Reverse Saturable Absorption of Monocationic Iridium(III) Complexes. *Inorg. Chem.* **2019**, *58* (1), 476–488. https://doi.org/10.1021/acs.inorgchem.8b02714.

(19)   Liu, B.; Lystrom, L.; Brown, S. L.; Hobbie, E. K.; Kilina, S.; Sun, W. Impact of Benzannulation Site at the Diimine (N^N) Ligand on the Excited-State Properties and Reverse Saturable Absorption of Biscyclometallated Iridium(III) Complexes. *Inorg. Chem.* **2019**, *58* (9), 5483–5493. https://doi.org/10.1021/acs.inorgchem.8b03162.

(20)   Wang, L.; Yin, H.; Jabed, M. A.; Hetu, M.; Wang, C.; Monro, S.; Zhu, X.; Kilina, S.; McFarland, S. A.; Sun, W. π-Expansive Heteroleptic Ruthenium(II) Complexes as Reverse Saturable Absorbers and Photosensitizers for Photodynamic Therapy. *Inorg. Chem.* **2017**, *56* (6), 3245–3259. https://doi.org/10.1021/acs.inorgchem.6b02624.

(21)   Chen, T.; Li, M.; Liu, J. π–π Stacking Interaction: A Nondestructive and Facile Means in Material Engineering for Bioapplications. *Cryst. Growth Des.* **2018**, *18* (5), 2765–2783. https://doi.org/10.1021/acs.cgd.7b01503.

(22)   Sinnokrot, M. O.; Valeev, E. F.; Sherrill, C. D. Estimates of the Ab Initio Limit for Π−π Interactions: The Benzene Dimer. *J. Am. Chem. Soc.* **2002**, *124* (36), 10887–10893. https://doi.org/10.1021/ja025896h.

(23)   Cai, M.; Song, X.; Zhang, D.; Qiao, J.; Duan, L. π–π Stacking: A Strategy to Improve the Electron Mobilities of Bipolar Hosts for TADF and Phosphorescent Devices with Low Efficiency Roll-Off. *J. Mater. Chem. C* **2017**, *5* (13), 3372–3381. https://doi.org/10.1039/C7TC00733G.

(24)   Hong, Y.; Lam, J. W. Y.; Tang, B. Z. Aggregation-Induced Emission: Phenomenon, Mechanism and Applications. *Chem. Commun.* **2009**, No. 29, 4332. https://doi.org/10.1039/b904665h.

(25)   McGaughey, G. B.; Gagné, M.; Rappé, A. K. π-Stacking Interactions. *J. Biol. Chem.* **1998**, *273* (25), 15458–15463. https://doi.org/10.1074/jbc.273.25.15458.

(26)   Babine, R. E.; Bender, S. L. Molecular Recognition of Protein−Ligand Complexes: Applications to Drug Design. *Chem. Rev.* **1997**, *97* (5), 1359–1472. https://doi.org/10.1021/cr960370z.

(27)   Pages, B. J.; Garbutcheon-Singh, K. B.; Aldrich-Wright, J. R. Platinum Intercalators of DNA as Anticancer Agents. *Eur. J. Inorg. Chem.* **2017**, *2017* (12), 1613–1624. https://doi.org/10.1002/ejic.201601204.

(28)   Hayashi, K.; Nakatani, M.; Hayashi, A.; Takano, M.; Okazaki, M.; Toyota, K.; Yoshifuji, M.; Ozawa, F. Synthesis and Structures of Platinum(0) Alkyne Complexes with Extended

π-Conjugated Systems. *Organometallics* **2008**, *27* (9), 1970–1972. https://doi.org/10.1021/om800163p.

(29) Flamigni, L.; Encinas, S.; Barigelletti, F.; MacDonnell, F. M.; Kim, K.-J.; Puntoriero, F.; Campagna, S. Excited-State Interconversion between Emissive MLCT Levels in a Dinuclear Ru(Ii) Complex Containing a Bridging Ligand with an Extended π System. *Chem. Commun.* **2000**, No. 13, 1185–1186. https://doi.org/10.1039/b004109m.

(30) Roznyatovskiy, V. V.; Lee, C.-H.; Sessler, J. L. π-Extended Isomeric and Expanded Porphyrins. *Chem Soc Rev* **2013**, *42* (5), 1921–1933. https://doi.org/10.1039/C2CS35418G.

(31) Barbon, S. M.; Staroverov, V. N.; Gilroy, J. B. Effect of Extended π Conjugation on the Spectroscopic and Electrochemical Properties of Boron Difluoride Formazanate Complexes. *J. Org. Chem.* **2015**, *80* (10), 5226–5235. https://doi.org/10.1021/acs.joc.5b00620.

(32) Kappaun, S.; Rentenberger, S.; Pogantsch, A.; Zojer, E.; Mereiter, K.; Trimmel, G.; Saf, R.; Möller, K. C.; Stelzer, F.; Slugovc, C. Organoboron Quinolinolates with Extended Conjugated Chromophores: Synthesis, Structure, and Electronic and Electroluminescent Properties. *Chem. Mater.* **2006**, *18* (15), 3539–3547. https://doi.org/10.1021/cm060720q.

(33) Kiprof, P.; Carlson, J. C.; Anderson, D. R.; Nemykin, V. N. Systematic Color Tuning of a Family of Luminescent Azole-Based Organoboron Compounds Suitable for OLED Applications. *Dalton Trans.* **2013**, *42* (42), 15120. https://doi.org/10.1039/c3dt51853a.

(34) Bossi, A.; Rausch, A. F.; Leitl, M. J.; Czerwieniec, R.; Whited, M. T.; Djurovich, P. I.; Yersin, H.; Thompson, M. E. Photophysical Properties of Cyclometallated Pt(II) Complexes: Counterintuitive Blue Shift in Emission with an Expanded Ligand π System. *Inorg. Chem.* **2013**, *52* (21), 12403–12415. https://doi.org/10.1021/ic4011532.

(35) Gunanathan, C.; Gnanaprakasam, B.; Iron, M. A.; Shimon, L. J. W.; Milstein, D. "Long-Range" Metal−Ligand Cooperation in H_2 Activation and Ammonia-Promoted Hydride Transfer with a Ruthenium−Acridine Pincer Complex. *J. Am. Chem. Soc.* **2010**, *132* (42), 14763–14765. https://doi.org/10.1021/ja107770y.

(36) Neufeldt, S. R.; Sanford, M. S. Controlling Site Selectivity in Palladium-Catalyzed C–H Bond Functionalization. *Acc. Chem. Res.* **2012**, *45* (6), 936–946. https://doi.org/10.1021/ar300014f.

(37) Krichevsky, O.; Bonnet, Gregoire. Fluorescence Correlation Spectroscopy: The Technique and Its Applications. *Rep. Prog. Phys.* **2002**, *65* (2), 251–297. https://doi.org/10.1088/0034-4885/65/2/203.

(38) Tumir, L.-M.; Stojkovic, M. R.; Piantanida, I. Come-Back of Phenanthridine and Phenanthridinium Derivatives in the 21st Century. *Beilstein J Org Chem* **2014**, *10*, 2930–2954.

(39) Park, G. Y.; Wilson, J. J.; Song, Y.; Lippard, S. J. Phenanthriplatin, a Monofunctional DNA-Binding Platinum Anticancer Drug Candidate with Unusual Potency and Cellular Activity Profile. *Proc Natl Acad Sci* **2012**, *109*, 11987–11992.

(40) Lu, L.-Q.; Li, Y.; Junge, K.; Beller, Matthias. Iron-Catalyzed Hydrogenation for the In Situ Regeneration of an NAD(P)H Model: Biomimetic Reduction of α-Keto-/α-Iminoesters. *Angew. Chem. Int. Ed.* **2013**, *52* (32), 8382–8386. https://doi.org/10.1002/anie.201301972.

(41) Chen, Q.-A.; Gao, K.; Duan, Y.; Ye, Z.-S.; Shi, L.; Yang, Y.; Zhou, Y.-Gui. Dihydrophenanthridine: A New and Easily Regenerable NAD(P)H Model for Biomimetic

Asymmetric Hydrogenation. *J. Am. Chem. Soc.* **2012**, *134* (4), 2442–2448. https://doi.org/10.1021/ja211684v.

(42)   Jensen, K. A.; Nielsen, P. Halfdan. Chelates with Heterocyclic Ligands. I. Chelates Derived from e N,N'-Bis(8-Quinolyl)Ethylenediamine and Analogous Compounds. *Acta Chem. Scand. 1947-1973* **1964**, *18* (1), 1–10. https://doi.org/10.3891/acta.chem.scand.18-0001.

(43)   Puzas, J. P.; Nakon, R.; Petersen, J. L. Direct Evidence for an SN1CB Mechanism. 4. Crystal and Molecular Structure of Chloro(Bis(8-Quinolinyl)Amido-N1,N2,N3)Copper(II), a Metal Chelate Containing an Sp2-Hybridized Deprotonated Amine. *Inorg. Chem.* **1986**, *25* (21), 3837–3840. https://doi.org/10.1021/ic00241a026.

(44)   Peters, J. C.; Harkins, S. B.; Brown, S. D.; Day, M. W. Pincer-like Amido Complexes of Platinum, Palladium, and Nickel. *Inorg. Chem.* **2001**, *40* (20), 5083–5091. https://doi.org/10.1021/ic010336p.

(45)   Maiti, D.; Paul, H.; Chanda, N.; Chakraborty, S.; Mondal, B.; Puranik, V. G.; Lahiri, G. Kumar. Synthesis, Structure, Spectral and Electron-Transfer Properties of Octahedral-[CoIII(L)2]+/[ZnII(L)2] and Square Planar-[CuII(L){OC(=O)CH3}] Complexes Incorporating Anionic Form of Tridentate Bis(8-Quinolinyl)Amine [N1C9H6-N2-C9H6N3, L-] Ligand. *Polyhedron* **2004**, *23* (5), 831–840. https://doi.org/10.1016/j.poly.2003.11.053.

(46)   Valk, J.-M.; Claridge, T. D. W.; Brown, J. M.; Hibbs, D.; Hursthouse, M. B. Synthesis and Chemistry of a New P-N Chelating Ligand; (R)- and (S)-6-(2'-Diphenylphosphino-1'-Naphthyl)Phenanthridine. *Tetrahedron Asymmetry* **1995**, *6* (Copyright (C) 2017 American Chemical Society (ACS). All Rights Reserved.), 2597–2610. https://doi.org/10.1016/0957-4166(95)00341-L.

(47)   Raszeja, L.; Maghnouj, A.; Hahn, S.; Metzler-Nolte, Nils. A Novel Organometallic ReI Complex with Favourable Properties for Bioimaging and Applicability in Solid-Phase Peptide Synthesis. *ChemBioChem* **2011**, *12* (3), 371–376. https://doi.org/10.1002/cbic.201000576.

(48)   Sicilia, V.; Fuertes, S.; Martin, A.; Palacios, Adrian. N-Assisted CPh-H Activation in 3,8-Dinitro-6-Phenylphenanthridine. New C,N-Cyclometallated Compounds of Platinum(II): Synthesis, Structure, and Luminescence Studies. *Organometallics* **2013**, *32* (15), 4092–4102. https://doi.org/10.1021/om400159g.

(49)   Jiang, B.; Gu, Y.; Qin, J.; Ning, X.; Gong, S.; Xie, G.; Yang, Chuluo. Deep-Red Iridium(III) Complexes Cyclometallated by Phenanthridine Derivatives for Highly Efficient Solution-Processed Organic Light-Emitting Diodes. *J. Mater. Chem. C Mater. Opt. Electron. Devices* **2016**, *4* (16), 3492–3498. https://doi.org/10.1039/C6TC00148C.

(50)   Theobald, R. S.; Schofield, K. The Chemistry of Phenanthridine and Its Derivatives. *Chem. Rev.* **1950**, *46* (1), 170–189. https://doi.org/10.1021/cr60143a004.

(51)   Crystal and molecular structure of phenanthridine. Roychowdhury1973.Pdf. *Acta. Cryst., Sect. B* **1973**, *29*, 1362–1364.

(52)   Brett, W. A.; Rademacher, P.; Boese, R. Redetermination of the Structure of Phenanthridine. *Acta Crystallogr. C* **1993**, *49* (9), 1564–1566. https://doi.org/10.1107/S0108270193005062.

(53)   Katritzky, A. R. *Handbook of Heterocyclic Chemistry*, 3rd ed.; Elsevier, 2010.

(54)   Benmachiche, A.; Zendaoui, S.-M.; Bouaoud, S.-E.; Zouchoune, B. Electronic Structure and Coordination Chemistry of Phenanthridine Ligand in First-Row Transition Metal

Complexes: A DFT Study. *Int. J. Quantum Chem.* **2013**, *113* (7), 985–996. https://doi.org/10.1002/qua.24071.

(55) Giesbrecht, P. K.; Nemez, D. B.; Herbert, D. E. Electrochemical Hydrogenation of a Benzannulated Pyridine to a Dihydropyridine in Acidic Solution. *Chem. Commun.* **2018**, *54* (4), 338–341. https://doi.org/10.1039/C7CC07907A.

(56) Mondal, R.; Giesbrecht, P. K.; Herbert, D. E. Nickel(II), Copper(I) and Zinc(II) Complexes Supported by a (4-Diphenylphosphino)Phenanthridine Ligand. *Polyhedron* **2016**, *108*, 156–162.

(57) Mandapati, P.; Giesbrecht, P. K.; Davis, R. L.; Herbert, D. E. Phenanthridine-Containing Pincer-like Amido Complexes of Nickel, Palladium, and Platinum. *Inorg Chem* **2017**, *56*, 3674–3685.

(58) Mandapati, P.; Braun, J. D.; Killeen, C.; Davis, R. L.; Williams, J. A. G.; Herbert, D. E. Luminescent Platinum(II) Complexes of N^N⁻^N Amido Ligands with Benzannulated N-Heterocyclic Donor Arms: Quinolines Offer Unexpectedly Deeper Red Phosphorescence than Phenanthridines. *Inorg Chem* **2019**, *58*, 14808–14817.

(59) Mandapati, P.; Braun, J. D.; Lozada, I. B.; Williams, J. A. G.; Herbert, D. E. Deep-Red Luminescence from Platinum(II) Complexes of N^N⁻^N-Amido Ligands with Benzannulated N-Heterocyclic Donor Arms. *Inorg. Chem.* **2020**, *59*, 12504–12517.

(60) Mondal, R.; Lozada, I. B.; Davis, R. L.; Williams, J. A. G.; Herbert, D. E. Site-Selective Benzannulation of N-Heterocycles in Bidentate Ligands Leads to Blue-Shifted Emission from [(P^N)Cu]$_2$(μ-X)$_2$ Dimers. *Inorg Chem* **2018**, *57*, 4966–4978.

(61) Mondal, R.; Lozada, I. B.; Davis, R. L.; Williams, J. A. G.; Herbert, D. E. Exploiting Synergy between Ligand Design and Counterion Interactions to Boost Room Temperature Phosphorescence from Cu(I) Compounds. *J. Mater. Chem. C* **2019**, *7*, 3772–3778.

(62) Lozada, I. B.; Murray, T.; Herbert, D. E. Monomeric Zinc(II) Amide Complexes Supported by Bidentate, Benzannulated Phenanthridine Amido Ligands. *Polyhedron* **2019**, *161*, 261–267.

(63) Mondal, R.; Lozada, I. B.; Davis, R. L.; Williams, J. A. G.; Herbert, D. E. Site-Selective Benzannulation of N-Heterocycles in Bidentate Ligands Leads to Blue-Shifted Emission from [(P^N)Cu]2(μ-X)2 Dimers. *Inorg Chem* **2018**, *57*, 4966–4978.

(64) Mandapati, P.; Giesbrecht, P. K.; Davis, R. L.; Herbert, D. E. Phenanthridine-Containing Pincer-like Amido Complexes of Nickel, Palladium, and Platinum. *Inorg Chem* **2017**, *56*, 3674–3685.

(65) Gaire, S.; Ortiz, R. J.; Schrage, B. R.; Lozada, I. B.; Mandapati, P.; Osinski, A. J.; Herbert, D. E.; Ziegler, C. J. (8-Amino)Quinoline and (4-Amino)Phenanthridine Complexes of Re(CO)3 Halides. *J. Organomet. Chem.* **2020**, *921*, 121338.

(66) Nemez, D. B.; Lozada, I. B.; Braun, J. D.; Williams, J. A. G.; Herbert, D. E. Synthesis and Coordination Chemistry of a Benzannulated Bipyridine: 6,6′-Biphenanthridine. *Inorg. Chem.* **2022**, *61* (34), 13386–13398. https://doi.org/10.1021/acs.inorgchem.2c01514.

(67) Hanson, K.; Roskop, L.; Djurovich, P. I.; Zahariev, F.; Gordon, M. S.; Thompson, M. E. A Paradigm for Blue- or Red-Shifted Absorption of Small Molecules Depending on the Site of π-Extension. *J. Am. Chem. Soc.* **2010**, *132*, 16247–16255.

(68) Barbon, S. M.; Staroverov, V. N.; Gilroy, J. B. Effect of Extended π Conjugation on the Spectroscopic and Electrochemical Properties of Boron Difluoride Formazanate Complexes. *J. Org. Chem.* **2015**, *80*, 5226–5235.

(69) Liu, B.; Lystrom, L.; Kilina, S.; Sun, W. Tuning the Ground State and Excited State Properties of Monocationic Iridium(III) Complexes by Varying the Site of Benzannulation on Diimine Ligand. *Inorg. Chem.* **2017**, *56*, 5361–5370.

(70) Westcott, B. L.; Gruhn, N. E.; Michelsen, L. J.; Lichtenberger, D. L. Experimental Observation of Non-Aufbau Behavior: Photoelectron Spectra of Vanadyloctaethylporphyrinate and Vanadylphthalocyanine. *J. Am. Chem. Soc.* **2000**, *122*, 8083–8084.

(71) Hewage, J. S.; Wanniarachchi, S.; Morin, T. J.; Liddle, B. J.; Banaszynski, M.; Lindeman, S. V.; Bennett, B.; Gardinier, J. R. Homoleptic Nickel(II) Complexes of Redox-Tunable Pincer-Type Ligands. *Inorg. Chem.* **2014**, *53* (19), 10070–10084. https://doi.org/10.1021/ic500657e.

(72) Lozada, I. B.; Ortiz, R. J.; Braun, J. D.; Williams, J. A. G.; Herbert, D. E. Donor–Acceptor Boron-Ketoiminate Complexes with Pendent *N*-Heterocyclic Arms: Switched-on Luminescence through *N*-Heterocycle Methylation. *J. Org. Chem.* **2022**, *87* (1), 184–196. https://doi.org/10.1021/acs.joc.1c02138.

(73) Braun, J. D.; Lozada, I. B.; Kolodziej, C.; Burda, C.; Newman, K. M. E.; van Lierop, J.; Davis, R. L.; Herbert, D. E. Iron(II) Coordination Complexes with Panchromatic Absorption and Nanosecond Charge-Transfer Excited State Lifetimes. *Nat. Chem.* **2019**, *11*, 1144–1150.

(74) Bruker-AXS. APEX3 V2016.1-0, 2016.

(75) Dolomanov, O. V.; Bourhis, L. J.; Gildea, R. J.; Howard, J. A. K.; Puschmann, H. OLEX2: A Complete Structure Solution, Refinement and Analysis Program. *J. Appl. Crystallogr.* **2009**, *42*, 339–341.

(76) Spek, A. L. Structure Validation in Chemical Crystallography. *Acta Cryst* **2009**, *D65*, 148–155.

(77) Fan, C.; Yang, C. Yellow/Orange Emissive Heavy-Metal Complexes as Phosphors in Monochromatic and White Organic Light-Emitting Devices. *Chem Soc Rev* **2014**, *43* (17), 6439–6469. https://doi.org/10.1039/C4CS00110A.

(78) Vreshch, V. D.; Yang, J.-H.; Zhang, H.; Filatov, A. S.; Dikarev, E. V. Monomeric Square-Planar Cobalt(II) Acetylacetonate: Mystery or Mistake? *Inorg. Chem.* **2010**, *49* (18), 8430–8434. https://doi.org/10.1021/ic100963r.

(79) Sokolow, J. D.; Trzop, E.; Chen, Y.; Tang, J.; Allen, L. J.; Crabtree, R. H.; Benedict, J. B.; Coppens, P. Binding Modes of Carboxylate- and Acetylacetonate-Linked Chromophores to Homodisperse Polyoxotitanate Nanoclusters. *J. Am. Chem. Soc.* **2012**, *134* (28), 11695–11700. https://doi.org/10.1021/ja303692r.

(80) Muñoz-García, A. B.; Sannino, F.; Vitiello, G.; Pirozzi, D.; Minieri, L.; Aronne, A.; Pernice, P.; Pavone, M.; D'Errico, G. Origin and Electronic Features of Reactive Oxygen Species at Hybrid Zirconia-Acetylacetonate Interfaces. *ACS Appl. Mater. Interfaces* **2015**, *7* (39), 21662–21667. https://doi.org/10.1021/acsami.5b06988.

(81) Seco, M. Acetylacetone: A Versatile Ligand. *J. Chem. Educ.* **1989**, *66* (9), 779. https://doi.org/10.1021/ed066p779.

(82) Allen, G.; Lewis, J.; Long, R. F.; Oldham, C. A Novel Form of Co-Ordination of Acetylacetone to Platinum(LI). *Nature* **1964**, *202*, 589–590. https://doi.org/10.1038/202589a0.

(83) Patra, S.; Mondal, B.; Sarkar, B.; Niemeyer, M.; Lahiri, G. K. First Example of μ_3-Sulfido Bridged Mixed-Valent Triruthenium Complex Triangle Ru$^{III}_2$ Ru^{II} (O , O -Acetylacetonate) $_3$ (μ - O , O ,γ- C -Acetylacetonate) $_3$ (μ_3 -S) (**1**) Incorporating Simultaneous O,O- and γ-C-Bonded Bridging Acetylacetonate Units. Synthesis, Crystal Structure, and Spectral and Redox Properties. *Inorg. Chem.* **2003**, *42* (4), 1322–1327. https://doi.org/10.1021/ic026221i.

(84) Zhu, D.; Budzelaar, P. H. M. N-Aryl β-Diiminate Complexes of the Platinum Metals. *Dalton Trans.* **2013**, *42* (32), 11343. https://doi.org/10.1039/c3dt50715g.

(85) Bernskoetter, W. H.; Lobkovsky, E.; Chirik, P. J. Ancillary Ligand Effects on C−H Bond Activation Reactions Promoted by β-Diiminate Iridium Complexes. *Organometallics* **2005**, *24* (25), 6250–6259. https://doi.org/10.1021/om050705f.

(86) Roesky, H. W. The Renaissance of Aluminum Chemistry. *Inorg. Chem.* **2004**, *43* (23), 7284–7293. https://doi.org/10.1021/ic0400641.

(87) Mears, K. L.; Stennett, C. R.; Taskinen, E. K.; Knapp, C. E.; Carmalt, C. J.; Tuononen, H. M.; Power, P. P. Molecular Complexes Featuring Unsupported Dispersion-Enhanced Aluminum–Copper and Gallium–Copper Bonds. *J. Am. Chem. Soc.* **2020**, *142* (47), 19874–19878. https://doi.org/10.1021/jacs.0c10099.

(88) Mondal, R.; Lozada, I. B.; Davis, R. L.; Williams, J. A. G.; Herbert, D. E. Exploiting Synergy between Ligand Design and Counterion Interactions to Boost Room Temperature Phosphorescence from Cu(I) Compounds. *J. Mater. Chem. C* **2019**, *7*, 3772–3778.

(89) Mandapati, P.; Braun, J. D.; Lozada, I. B.; Williams, J. A. G.; Herbert, D. E. Deep-Red Luminescence from Platinum(II) Complexes of N^N⁻^N-Amido Ligands with Benzannulated N-Heterocyclic Donor Arms. *Inorg. Chem.* **2020**, *59*, 12504–12517.

(90) Ortiz, R. J.; Braun, J. D.; Williams, J. A. G.; Herbert, D. E. Brightly Luminescent Platinum Complexes of *N^C⁻^N* Ligands Forming Six-Membered Chelate Rings: Offsetting Deleterious Ring Size Effects Using Site-Selective Benzannulation. *Inorg. Chem.* **2021**, *60*, 16881–16894.

(91) Lozada, I. B.; Huang, B.; Stilgenbauer, M.; Beach, T.; Qiu, Z.; Zheng, Y.; Herbert, D. E. Monofunctional Platinum(II) Anticancer Complexes Based on Multidentate Phenanthridine-Containing Ligand Frameworks. *Dalton Trans.* **2020**, *49*, 6557–6560.

(92) Myers, E. L.; Butts, C. P.; Aggarwal, V. K. BF3·OEt2 and TMSOTf: A Synergistic Combination of Lewis Acids. *Chem. Commun.* **2006**, No. 42, 4434–4436.

(93) Macedo, F. P.; Gwengo, C.; Lindeman, S. V.; Smith, M. D.; Gardinier, J. R. β-Diketonate, β-Ketoiminate, and β-Diiminate Complexes of Difluoroboron. *Eur. J. Inorg. Chem.* **2008**, *2008*, 3200–3211.

(94) Dohe, J.; Kossmann, J.; Mueller, T. J. J. Diversity-Oriented Four-Component Synthesis of Solid State Luminescent Difluoro Oxazaborinines. *Dyes Pigments* **2018**, *157*, 198–217.

(95) Köhling, J.; Kozel, V.; Jovanov, V.; Pajkert, R.; Tverdomed, S. N.; Gridenco, O.; Fugel, M.; Grabowsky, S.; Röschenthaler, G.-V.; Wagner, V. Synthesis and Characterization of Oxazaborinin Phosphonate for Blue OLED Emitter Applications. *ChemPhysChem* **2019**, *20*, 665–671.

(96) Mtiraoui, H.; Gharbi, R.; Msaddek, M.; Bretonnière, Y.; Andraud, C.; Renard, P.-Y.; Sabot, C. Solution and Solid-State Fluorescence of 2-(2′-Hydroxyphenyl)-1,5-Benzodiazepin-2-One (HBD) Borate Complexes. *RSC Adv.* **2016**, *6*, 86352–86360.

(97) Chęcińska, L.; Mebs, S.; Ośmiałowski, B.; Zakrzewska, A.; Ejsmont, K.; Kohout, M. Tuning the Electronic Properties of the Dative N−B Bond with Associated O−B Interaction: Electron Localizability Indicator from X-Ray Wavefunction Refinement. *ChemPhysChem* **2016**, *17*, 2395–2406.

(98) Itoh, K.; Okazaki, K.; Fujimoto, M. The Structure of 1,3-Enaminoketonatoboron Difluorides in Solution and in the Solid State. *Aust. J. Chem.* **2003**, *56*, 1209–1214.

(99) Grepioni, F.; Cojazzi, G.; Draper, S. M.; Scully, N.; Braga, D. Crystal Forms of Hexafluorophosphate Organometallic Salts and the Importance of Charge-Assisted C−H---F Hydrogen Bonds. *Organometallics* **1998**, *17*, 296–307.

(100) Mandapati, P.; Braun, J. D.; Killeen, C.; Davis, R. L.; Williams, J. A. G.; Herbert, D. E. Luminescent Platinum(II) Complexes of N^N⁻^N Amido Ligands with Benzannulated N-Heterocyclic Donor Arms: Quinolines Offer Unexpectedly Deeper Red Phosphorescence than Phenanthridines. *Inorg. Chem.* **2019**, *58*, 14808–14817.

(101) Lozada, I. B.; Williams, J. A. G.; Herbert, D. E. Platinum(II) Complexes of Benzannulated N^N⁻^O-Amido Ligands: Bright Orange Phosphors with Long-Lived Excited States. *Inorg. Chem. Front.* **2022**, *9*, 10–22.

(102) Donckt, E. V.; Dramaix, R.; Nasielski, J.; Vogels, C. Photochemistry of Aromatic Compounds. Part 1.—Acid-Base Properties of Singlet and Triplet Excited States of Pyrene Derivatives and Aza-Aromatic Compounds. *Trans. Faraday Soc.* **1969**, *65*, 3258–3262.

(103) Zander, M. The Significance of Donor-Acceptor Interactions in the External Heavy Atom Effect of Silver Nitrate on the Luminescence Behavior of Aza-Aromatic Systems and Carbazoles. *Z Naturforsch A* **1978**, *33*, 998–1000.

(104) Norek, M.; Dresner, J.; Prochorow, J. Spectroscopy and Photophysics of Monoazaphenanthrenes. I. Absorption and Fluorescence Spectra of Phenanthridine and 7,8-Benzoquinoline. *Acta Phys. Pol. A* **2003**, *104*, 425–439.

(105) Marzzacco, C. J.; Deckey, G.; Colarulli, R.; Siuzdak, G.; Halpern, A. M. Excited-State Protonation and Photophysical Properties of Azaphenanthrenes. *J. Phys. Chem.* **1989**, *93*, 2935–2939.

(106) Parker, D.; Senanayake, P. K.; Williams, J. A. G. Luminescent Sensors for PH, PO2, Halide and Hydroxide Ions Using Phenanthridine as a Photosensitiser in Macrocyclic Europium and Terbium Complexes. *J. Chem. Soc. Perkin Trans. 2* **1998**, 2129–2140.

(107) Norek, M.; Kozankiewicz, B.; Prochorow, J. Spectroscopy and Photophysics of Monoazaphenanthrenes. III. Luminescence of Phenanthridine and 7,8-Benzoquinoline in Crystalline State. *Acta Phys Pol A* **2004**, *106*, 77–94.

(108) Lozada, I. B.; Murray, T.; Herbert, D. E. Monomeric Zinc(II) Amide Complexes Supported by Bidentate, Benzannulated Phenanthridine Amido Ligands. *Polyhedron* **2019**, *161*, 261–267.

(109) Lozada, I. B.; Ortiz, R. J.; Braun, J. D.; Williams, J. A. G.; Herbert, D. E. Donor–Acceptor Boron-Ketoiminate Complexes with Pendent N-Heterocyclic Arms: Switched-on Luminescence through N-Heterocycle Methylation. *J. Org. Chem.* **2022**, *87*, 184–196.

(110) Bridgeman, A. J.; Cavigliasso, G.; Ireland, L. R.; Rothery, J. The Mayer Bond Order as a Tool in Inorganic Chemistry. *J. Chem. Soc. Dalton Trans.* **2001**, 2095–2108.

(111) Lu, T.; Chen, F. Atomic Dipole Moment Corrected Hirshfeld Population Method. *J. Theor. Comput. Chem.* **2012**, *11*, 163–183.

(112) Montalti, M.; Credi, A.; Prodi, L.; Gandolfi, M. *Handbook of Photochemistry. 3rd Ed.*; CRC Press: Boca Raton, 2006.

(113) Oyler, K. D.; Coughlin, F. J.; Bernhard, S. Controlling the Helicity of 2,2'-Bipyridyl Ruthenium(II) and Zinc(II) Hemicage Complexes. *J. Am. Chem. Soc.* **2007**, *129*, 210–217.

(114) Martinez, S.; Igoa, F.; Carrera, I.; Seoane, G.; Veiga, N.; De Camargo, A. S. S.; Kremer, C.; Torres, J. A Zn(II) Luminescent Complex with a Schiff Base Ligand: Solution, Computational and Solid State Studies. *J. Coord. Chem.* **2018**, *71*, 874–889.

(115) Mei, J.; Leung, N. L. C.; Kwok, R. T. K.; Lam, J. W. Y.; Tang, B. Z. Aggregation-Induced Emission: Together We Shine, United We Soar! *Chem. Rev.* **2015**, *115*, 11718–11940.

(116) Singh, K.; Siddiqui, I.; Sridharan, V.; Kumar Yadav, R. A.; Jou, J.-H.; Adhikari, D. Aggregation-Induced Enhanced Emission-Active Zinc(II) β-Diketiminate Complexes Enabling High-Performance Solution-Processable OLEDs. *Inorg. Chem.* **2021**, *60*, 19128–19135.

(117) Singh, K.; S., V.; Adhikari, D. Visible Light Photoredox by a (Ph,ArNacNac)2Zn Photocatalyst: Photophysical Properties and Mechanistic Understanding. *Inorg. Chem. Front.* **2021**, *8*, 2078–2087.

(118) Lozada, I. B.; Huang, B.; Stilgenbauer, M.; Beach, T.; Qiu, Z.; Zheng, Y.; Herbert, D. E. Monofunctional Platinum(II) Anticancer Complexes Based on Multidentate Phenanthridine-Containing Ligand Frameworks. *Dalton Trans.* **2020**, *49*, 6557–6560.

(119) Mandapati, P.; Giesbrecht, P. K.; Davis, R. L.; Herbert, D. E. Phenanthridine-Containing Pincer-like Amido Complexes of Nickel, Palladium, and Platinum. *Inorg. Chem.* **2017**, *56*, 3674–3685.

(120) Mandapati, P.; Braun, J. D.; Killeen, C.; Davis, R. L.; Williams, J. A. G.; Herbert, D. E. Luminescent Platinum(II) Complexes of N^N-^N Amido Ligands with Benzannulated N-Heterocyclic Donor Arms: Quinolines Offer Unexpectedly Deeper Red Phosphorescence than Phenanthridines. *Inorg Chem* **2019**, *58*, 14808–14817.

(121) Mandapati, P.; Braun, J. D.; Lozada, I. B.; Williams, J. A. G.; Herbert, D. E. Deep-Red Luminescence from Platinum(II) Complexes of N^N−^N-Amido Ligands with Benzannulated N-Heterocyclic Donor Arms. *Inorg. Chem.* **2020**, *59*, 12504–12517.

(122) Reineke, M. H.; Sampson, M. D.; Rheingold, A. L.; Kubiak, C. P. Synthesis and Structural Studies of Nickel(0) Tetracarbene Complexes with the Introduction of a New Four-Coordinate Geometric Index, Tδ. *Inorg. Chem.* **2015**, *54*, 3211–3217.

(123) Puttock, E. V.; Fradgley, J. D.; Yufit, D. S.; Williams, J. A. G. A Family of Readily Synthesised Phosphorescent Platinum(II) Complexes Based on Tridentate *N^N^O* -Coordinating Schiff-Base Ligands. *Dalton Trans.* **2019**, *48*, 15012–15028.

(124) Davidson, J. J.; DeMott, J. C.; Douvris, C.; Fafard, C. M.; Bhuvanesh, N.; Chen, C.-H.; Herbert, D. E.; Lee, C.-I.; McCulloch, B. J.; Foxman, B. M.; Ozerov, O. V. Comparison of the Electronic Properties of Diarylamido-Based PNZ Pincer Ligands: Redox Activity at the Ligand and Donor Ability Toward the Metal. *Inorg. Chem.* **2015**, *54*, 2916–2935.

(125) Giesbrecht, P. K.; Nemez, D. B.; Herbert, D. E. Electrochemical Hydrogenation of a Benzannulated Pyridine to a Dihydropyridine in Acidic Solution. *Chem. Commun.* **2018**, *54*, 338–341.

(126) Reichardt, C. Solvatochromic Dyes as Solvent Polarity Indicators. *Chem. Rev.* **1994**, *94*, 2319–2358.

(127) Catalán, J. Toward a Generalized Treatment of the Solvent Effect Based on Four Empirical Scales: Dipolarity (SdP, a New Scale), Polarizability (SP), Acidity (SA), and Basicity (SB) of the Medium. *J. Phys. Chem. B* **2009**, *113*, 5951–5960.

(128) Van der Zwan, G.; Hynes, J. T. Time-Dependent Fluorescence Solvent Shifts, Dielectric Friction, and Nonequilibrium Solvation in Polar Solvents. *J. Phys. Chem.* **1985**, *89*, 4181–4188.

(129) Caspar, J. V.; Meyer, T. J. Photochemistry of Tris(2,2'-Bipyridine)Ruthenium(2+) Ion $(Ru(Bpy)_3^{2+})$. Solvent Effects. *J. Am. Chem. Soc.* **1983**, *105*, 5583–5590.

(130) Kwok, C.-C.; Ngai, H. M. Y.; Chan, S.-C.; Sham, I. H. T.; Che, C.-M.; Zhu, N. [(O∧N∧N)PtX] Complexes as a New Class of Light-Emitting Materials for Electrophosphorescent Devices. *Inorg. Chem.* **2005**, *44*, 4442–4444.

(131) Garner, K. L.; Parkes, L. F.; Piper, J. D.; Williams, J. A. G. Luminescent Platinum Complexes with Terdentate Ligands Forming 6-Membered Chelate Rings: Advantageous and Deleterious Effects in N ∧ N ∧ N and N ∧ C ∧ N-Coordinated Complexes. *Inorg. Chem.* **2010**, *49*, 476–487.

(132) Williams, J. A. G. The Coordination Chemistry of Dipyridylbenzene: N-Deficient Terpyridine or Panacea for Brightly Luminescent Metal Complexes? *Chem. Soc. Rev.* **2009**, *38*, 1783–1801.

(133) Meech, S. R.; Phillips, D. Photophysics of Some Common Fluorescence Standards. *J. Photochem.* **1983**, *23*, 193–217.

(134) Suzuki, K.; Kobayashi, A.; Kaneko, S.; Takehira, K.; Yoshihara, T.; Ishida, H.; Shiina, Y.; Oishi, S.; Tobita, S. Reevaluation of Absolute Luminescence Quantum Yields of Standard Solutions Using a Spectrometer with an Integrating Sphere and a Back-Thinned CCD Detector. *Phys. Chem. Chem. Phys.* **2009**, *11*, 9850–9860.

(135) Murov, S. L.; Carmichael, I.; Hug, G. L. *Handbook of Photochemistry, 2nd Ed.*; Marcel Dekker: New York, 1993.

(136) Hohenberg, P.; Kohn, W. Inhomogeneous Electron Gas. *Phys. Rev.* **1964**, *136* (3B), B864–B871. https://doi.org/10.1103/PhysRev.136.B864.

(137) Kohn, W.; Sham, L. J. Self-Consistent Equations Including Exchange and Correlation Effects. *Phys. Rev.* **1965**, *140* (4A), A1133–A1138. https://doi.org/10.1103/PhysRev.140.A1133.

(138) Bühl, M.; Kabrede, H. Geometries of Transition-Metal Complexes from Density-Functional Theory. *J. Chem. Theory Comput.* **2006**, *2* (5), 1282–1290. https://doi.org/10.1021/ct6001187.

(139) Waller, M. P.; Braun, H.; Hojdis, N.; Bühl, M. Geometries of Second-Row Transition-Metal Complexes from Density-Functional Theory. *J. Chem. Theory Comput.* **2007**, *3* (6), 2234–2242. https://doi.org/10.1021/ct700178y.

(140) Bühl, M.; Reimann, C.; Pantazis, D. A.; Bredow, T.; Neese, F. Geometries of Third-Row Transition-Metal Complexes from Density-Functional Theory. *J. Chem. Theory Comput.* **2008**, *4* (9), 1449–1459. https://doi.org/10.1021/ct800172j.

(141) de Souza, B.; Farias, G.; Neese, F.; Izsák, R. Predicting Phosphorescence Rates of Light Organic Molecules Using Time-Dependent Density Functional Theory and the Path Integral Approach to Dynamics. *J. Chem. Theory Comput.* **2019**, *15* (3), 1896–1904. https://doi.org/10.1021/acs.jctc.8b00841.

(142) de Souza, B.; Neese, F.; Izsák, R. On the Theoretical Prediction of Fluorescence Rates from First Principles Using the Path Integral Approach. *J. Chem. Phys.* **2018**, *148* (3), 034104. https://doi.org/10.1063/1.5010895.

(143) Petrenko, T.; Neese, F. Analysis and Prediction of Absorption Band Shapes, Fluorescence Band Shapes, Resonance Raman Intensities, and Excitation Profiles Using the Time-Dependent Theory of Electronic Spectroscopy. *J. Chem. Phys.* **2007**, *127* (16), 164319. https://doi.org/10.1063/1.2770706.

(144) Wenger, O. S. Is Iron the New Ruthenium? *Chem. – Eur. J.* **2020**, *25*, 6043–6052.

(145) Baková, R.; Chergui, M.; Daniel, C.; Vlček Jr., A.; Záliš, S. Relativistic Effects in Spectroscopy and Photophysics of Heavy-Metal Complexes Illustrated by Spin–Orbit Calculations of [Re(Imidazole)(CO)3(Phen)]+. *Coord. Chem. Rev.* **2011**, *255* (7–8), 975–989. https://doi.org/10.1016/j.ccr.2010.12.027.

(146) Giesbrecht, P. K.; Nemez, D. B.; Herbert, D. E. Electrochemical Hydrogenation of a Benzannulated Pyridine to a Dihydropyridine in Acidic Solution. *Chem. Commun.* **2018**, *54* (4), 338–341. https://doi.org/10.1039/c7cc07907a.

(147) Mandapati, P.; Giesbrecht, P. K.; Davis, R. L.; Herbert, D. E. Phenanthridine-Containing Pincer-like Amido Complexes of Nickel, Palladium, and Platinum. *Inorg. Chem.* **2017**, *56* (6), 3674–3685. https://doi.org/10.1021/acs.inorgchem.7b00075.

(148) Mondal, R.; Lozada, I. B.; Davis, R. L.; Williams, J. A. G.; Herbert, D. E. Exploiting Synergy between Ligand Design and Counterion Interactions to Boost Room Temperature Phosphorescence from Cu(i) Compounds. *J. Mater. Chem. C* **2019**, *7* (13), 3772–3778. https://doi.org/10.1039/C9TC00040B.

(149) Mandapati, P.; Braun, J. D.; Killeen, C.; Davis, R. L.; Williams, J. A. G.; Herbert, D. E. Luminescent Platinum(II) Complexes of N^ N-^ N Amido Ligands with Benzannulated N-Heterocyclic Donor Arms: Quinolines Offer Unexpectedly Deeper Red Phosphorescence than Phenanthridines. *Inorg. Chem.* **2019**, *58* (21), 14808–14817. https://doi.org/10.1021/acs.inorgchem.9b02480.

(150) Lozada, I. B.; Murray, T.; Herbert, D. E. Monomeric Zinc(II) Amide Complexes Supported by Bidentate, Benzannulated Phenanthridine Amido Ligands. *Polyhedron* **2019**, *161*, 261–267. https://doi.org/10.1016/j.poly.2019.01.023.

(151) Braun, J. D.; Lozada, I. B.; Kolodziej, C.; Burda, C.; Newman, K. M. E.; van Lierop, J.; Davis, R. L.; Herbert, D. E. Iron(Ii) Coordination Complexes with Panchromatic Absorption and Nanosecond Charge-Transfer Excited State Lifetimes. *Nat. Chem.* **2019**, *11* (12), 1144–1150. https://doi.org/10.1038/s41557-019-0357-z.

(152) Mondal, R.; Lozada, I. B.; Davis, R. L.; Williams, J. A. G.; Herbert, D. E. Site-Selective Benzannulation of N-Heterocycles in Bidentate Ligands Leads to Blue-Shifted Emission from [(P^N)Cu]2(μ-X)2 Dimers. *Inorg. Chem.* **2018**, *57* (9), 4966–4978. https://doi.org/10.1021/acs.inorgchem.7b03223.

(153) Mondal, R.; Giesbrecht, P. K.; Herbert, D. E. Nickel(II), Copper(I) and Zinc(II) Complexes Supported by a (4-Diphenylphosphino)Phenanthridine Ligand. *Polyhedron* **2016**, *108*, 156–162. https://doi.org/10.1016/j.poly.2015.10.051.

(154) Stufkens, D. J.; Vlček, A. Ligand-Dependent Excited State Behaviour of Re(I) and Ru(II) Carbonyl-Diimine Complexes. *Coord. Chem. Rev.* **1998**, *177* (1), 127–179. https://doi.org/10.1016/s0010-8545(98)00132-5.

(155) Vlček, A. Ultrafast Excited-State Processes in Re(I) Carbonyl-Diimine Complexes: From Excitation to Photochemistry. *Top Organomet Chem* **2010**, *29* (May 2009), 73–114. https://doi.org/10.1007/3418.

(156) Mandapati, P.; Braun, J. D.; Killeen, C.; Davis, R. L.; Williams, J. A. G.; Herbert, D. E. Luminescent Platinum(II) Complexes of N⁀N-⁀N Amido Ligands with Benzannulated N-Heterocyclic Donor Arms: Quinolines Offer Unexpectedly Deeper Red Phosphorescence than Phenanthridines. *Inorg Chem* **2019**, *58*, 14808–14817.

(157) Dixon, I. M.; Khan, S.; Alary, F.; Boggio-Pasqua, M.; Heully, J.-L. Probing the Photophysical Capability of Mono and Bis(Cyclometallated) Fe(II) Polypyridine Complexes Using Inexpensive Ground State DFT. *Dalton Trans.* **2014**, *43*, 15898–15905.

(158) Zhang, K.; Ash, R.; Girolami, G. S.; Vura-Weis, J. Tracking the Metal-Centered Triplet in Photoinduced Spin Crossover of Fe(Phen)32+ with Tabletop Femtosecond M-Edge X-Ray Absorption Near-Edge Structure Spectroscopy. *J. Am. Chem. Soc.* **2019**, *141*, 17180–17188.

(159) Juban, E. A.; Smeigh, A. L.; Monat, J. E.; McCusker, J. K. Ultrafast Dynamics of Ligand-Field Excited States. *Coord Chem Rev* **2006**, *250*, 1783–1791.

(160) Gryn'ova, G.; Coote, M. L.; Corminboeuf, C. Theory and Practice of Uncommon Molecular Electronic Configurations. *WIREs Comput. Mol. Sci.* **2015**, *5* (6), 440–459. https://doi.org/10.1002/wcms.1233.

(161) Kaim, W. Manifestations of Noninnocent Ligand Behavior. *Inorg Chem* **2011**, *50* (20), 9752–9765.

(162) Bowman, D. N.; Jakubikova, E. Low-Spin versus High-Spin Ground State in Pseudo-Octahedral Iron Complexes. *Inorg. Chem.* **2012**, *51*, 6011–6019.

(163) Ashley, D. C.; Jakubikova, E. Ironing out the Photochemical and Spin-Crossover Behavior of Fe(II) Coordination Compounds with Computational Chemistry. *Coord. Chem. Rev.* **2017**, *337*, 97–111.

(164) Reiher, M.; Salomon, O.; Artur Hess, B. Reparameterization of Hybrid Functionals Based on Energy Differences of States of Different Multiplicity. *Theor. Chem. Acc.* **2001**, *107*, 48–55.

(165) Jakubikova, E.; Bowman, D. N. Fe(II)-Polypyridines as Chromophores in Dye-Sensitized Solar Cells: A Computational Perspective. *Acc. Chem. Res.* **2015**, *48*, 1441–1449.

(166) Nemykin, V. N.; Hadt, R. G. Influence of Hartree−Fock Exchange on the Calculated Mössbauer Isomer Shifts and Quadrupole Splittings in Ferrocene Derivatives Using Density Functional Theory. *Inorg. Chem.* **2006**, *45*, 8297–8307.

(167) Zhao, Y.; Truhlar, D. G. A New Local Density Functional for Main-Group Thermochemistry, Transition Metal Bonding, Thermochemical Kinetics, and Noncovalent Interactions. *J. Chem. Phys.* **2006**, *125*, 194101.

(168) Cohen, A. J.; Handy, N. C. Dynamic Correlation. *Mol. Phys.* **2001**, *99*, 607–615.

(169) Zhao, Y.; Truhlar, D. G. The M06 Suite of Density Functionals for Main Group Thermochemistry, Thermochemical Kinetics, Noncovalent Interactions, Excited States, and Transition Elements: Two New Functionals and Systematic Testing of Four M06-Class Functionals and 12 Other Functionals. *Theor. Chem. Acc.* **2008**, *120*, 215–241.

(170) Ditchfield, R.; Hehre, W. J.; Pople, J. A. Self-Consistent Molecular-Orbital Methods. IX. Extended Gaussian-Type Basis for Molecular-Orbital Studies of Organic Molecules. *J. Chem. Phys.* **1971**, *54*, 724–728. https://doi.org/10.1063/1.1674902.

(171) Hehre, W. J.; Ditchfield, R.; Pople, J. A. Self-Consistent Molecular Orbital Methods. XII. Further Extensions of Gaussian-Type Basis Sets for Use in Molecular Orbital Studies of Organic Molecules. *J. Chem. Phys.* **1972**, *56*, 2257–2261.

(172) Hariharan, P. C.; Pople, J. A. Influence of Polarization Functions on MO Hydrogenation Energies. *Theor. Chim. Acta* **1973**, *28*, 213–222.

(173) Clark, T.; Chandrasekhar, J.; Spitznagel, G. W.; Schleyer, P. v R. Efficient Diffuse Function-Augmented Basis Sets for Anion Calculations. III. The 3-21 + G Basis Set for First-Row Elements, Lithium to Fluorine. *J. Comput. Chem.* **1983**, *4*, 294–301.

(174) Rassolov, V. A.; Pople, J. A.; Ratner, M. A.; Windus, T. L. 6-31G* Basis Set for Atoms K through Zn. *J. Chem. Phys.* **1998**, *109*, 1223–1229.

(175) Zhao, Y.; Truhlar, D. G. A New Local Density Functional for Main-Group Thermochemistry, Transition Metal Bonding, Thermochemical Kinetics, and Noncovalent Interactions. *J. Chem. Phys.* **2006**, *125* (19), 194101. https://doi.org/10.1063/1.2370993.

(176) Krishnan, R.; Binkley, J. S.; Seeger, R.; Pople, J. A. Self-consistent Molecular Orbital Methods. XX. A Basis Set for Correlated Wave Functions. *J. Chem. Phys.* **1980**, *72* (1), 650–654. https://doi.org/10.1063/1.438955.

(177) Clark, T.; Chandrasekhar, J.; Spitznagel, G. W.; Schleyer, P. V. R. Efficient Diffuse Function-Augmented Basis Sets for Anion Calculations. III. The 3-21+G Basis Set for First-Row Elements, Li-F. *J. Comput. Chem.* **1983**, *4* (3), 294–301. https://doi.org/10.1002/jcc.540040303.

(178) Dennington, Roy; Keith, Todd A.; Millam, John M. *GaussView, Version 6*; Semichem Inc.: Shawnee Mission, KS, 2016.

(179) Soda, T.; Kitagawa, Y.; Onishi, T.; Takano, Y.; Shigeta, Y.; Nagao, H.; Yoshioka, Y.; Yamaguchi, K. Ab Initio Computations of Effective Exchange Integrals for H–H, H–He–H and Mn2O2 Complex: Comparison of Broken-Symmetry Approaches. *Chem. Phys. Lett.* **2000**, *319* (3–4), 223–230. https://doi.org/10.1016/S0009-2614(00)00166-4.

(180) Yamaguchi, K.; Takahara, Y.; Fueno, T. Ab-Initio Molecular Orbital Studies of Structure and Reactivity of Transition Metal-OXO Compounds. In *Applied Quantum Chemistry*; Smith, V. H., Schaefer, H. F., Morokuma, K., Eds.; Springer Netherlands: Dordrecht, 1986; pp 155–184. https://doi.org/10.1007/978-94-009-4746-7_11.

(181) Heydová, R.; Gindensperger, E.; Romano, R.; Sýkora, J.; Vlček, A.; Záliš, S.; Daniel, C. Spin-Orbit Treatment of UV-Vis Absorption Spectra and Photophysics of Rhenium(I) Carbonyl-Bipyridine Complexes: MS-CASPT2 and TD-DFT Analysis. *J. Phys. Chem. A* **2012**, *116* (46), 11319–11329. https://doi.org/10.1021/jp305461z.

(182) Ronca, E.; De Angelis, F.; Fantacci, S. Time-Dependent Density Functional Theory Modeling of Spin-Orbit Coupling in Ruthenium and Osmium Solar Cell Sensitizers. *J. Phys. Chem. C* **2014**, *118* (30), 17067–17078. https://doi.org/10.1021/jp500869r.

(183) Mai, S.; Gattuso, H.; Fumanal, M.; Muñoz-Losa, A.; Monari, A.; Daniel, C.; González, L. Excited-States of a Rhenium Carbonyl Diimine Complex: Solvation Models, Spin-Orbit Coupling, and Vibrational Sampling Effects. *Phys. Chem. Chem. Phys.* **2017**, *19* (40), 27240–27250. https://doi.org/10.1039/c7cp05126c.

(184) Shi, L. L.; Liao, Y.; Zhao, L.; Su, Z. M.; Kan, Y. H.; Yang, G. C.; Yang, S. Y. Theoretical Studies on the Electronic Structure and Spectral Properties of Versatile Diarylethene-Containing 1,10-Phenanthroline Ligands and Their Rhenium(I) Complexes. *J. Organomet. Chem.* **2007**, *692* (24), 5368–5374. https://doi.org/10.1016/j.jorganchem.2007.08.031.

(185) Silva-Junior, M. R.; Schreiber, M.; Sauer, S. P. A.; Thiel, W. Benchmarks for Electronically Excited States: Time-Dependent Density Functional Theory and Density Functional Theory Based Multireference Configuration Interaction. *J. Chem. Phys.* **2008**, *129* (10). https://doi.org/10.1063/1.2973541.

(186) Jacquemin, D.; Perpète, E. A.; Ciofini, I.; Adamo, C. Assessment of Functionals for TD-DFT Calculations of Singlet-Triplet Transitions. *J. Chem. Theory Comput.* **2010**, *6* (5), 1532–1537. https://doi.org/10.1021/ct100005d.

(187) Santoro, F.; Lami, A.; Improta, R.; Barone, V. Effective Method to Compute Vibrationally Resolved Optical Spectra of Large Molecules at Finite Temperature in the Gas Phase and in Solution. *J. Chem. Phys.* **2007**, *126* (18). https://doi.org/10.1063/1.2721539.

(188) Tozer, D. J.; Handy, N. C. On the Determination of Excitation Energies Using Density Functional Theory. *Phys. Chem. Chem. Phys.* **2000**, *2* (10), 2117–2121. https://doi.org/10.1039/a910321j.

(189) Chibani, S.; Charaf-Eddin, A.; Le Guennic, B.; Jacquemin, D. Boranil and Related NBO Dyes: Insights From Theory. *J. Chem. Theory Comput.* **2013**, *9*, 3127–3135.

(190) Mondal, R.; Giesbrecht, P. K.; Herbert, D. E. Nickel(II), Copper(I) and Zinc(II) Complexes Supported by a (4-Diphenylphosphino)Phenanthridine Ligand. *Polyhedron* **2016**, *108*, 156–162.

(191) Mondal, R.; Lozada, I. B.; Davis, R. L.; Williams, J. A. G.; Herbert, D. E. Site-Selective Benzannulation of N-Heterocycles in Bidentate Ligands Leads to Blue-Shifted Emission from [(*P^N*)Cu]$_2$(μ-X)$_2$ Dimers. *Inorg Chem* **2018**, *57*, 4966–4978.

(192) Gaire, S.; Ortiz, R. J.; Schrage, B. R.; Lozada, I. B.; Mandapati, P.; Osinski, A. J.; Herbert, D. E.; Ziegler, C. J. (8-Amino)Quinoline and (4-Amino)Phenanthridine Complexes of Re(CO)3 Halides. *J. Organomet. Chem.* **2020**, *921*, 121338.

(193) Tomasi, J.; Mennucci, B.; Cammi, R. Quantum Mechanical Continuum Solvation Models. *Chem Rev* **2005**, *105*, 2999–3094.

(194) Melenbacher, A.; Dhindsa, J. S.; Gilroy, J. B.; Stillman, M. J. Unveiling the Hidden, Dark, and Short Life of a Vibronic State in a Boron Difluoride Formazanate Dye. *Angew. Chem. Int. Ed.* **2019**, *58* (43), 15339–15343.

(195) El-Sayed, M. A. Spin—Orbit Coupling and the Radiationless Processes in Nitrogen Heterocyclics. *J. Chem. Phys.* **1963**, *38* (12), 2834–2838.

(196) Braun, J. D.; Lozada, I. B.; Kolodziej, C.; Burda, C.; Newman, K. M. E.; van Lierop, J.; Davis, R. L.; Herbert, D. E. Iron(II) Coordination Complexes with Panchromatic Absorption and Nanosecond Charge-Transfer Excited State Lifetimes. *Nat. Chem.* **2019**, *11*, 1144–1150.

(197) Larsen, C. B.; Braun, J. D.; Lozada, I. B.; Kunnus, K.; Biasin, E.; Kolodziej, C.; Burda, C.; Cordones, A. A.; Gaffney, K. J.; Herbert, D. E. Reduction of Electron Repulsion in Highly Covalent Fe-Amido Complexes Counteracts the Impact of a Weak Ligand Field on Excited-State Ordering. *J. Am. Chem. Soc.* **2021**, *143*, 20645–20656.

(198) Das, S.; Thornbury, W. G.; Bartynski, A. N.; Thompson, M. E.; Bradforth, S. E. Manipulating Triplet Yield through Control of Symmetry-Breaking Charge Transfer. *J. Phys. Chem. Lett.* **2018**, *9*, 3264–3270.

(199) Trinh, C.; Kirlikovali, K.; Das, S.; Ener, M. E.; Gray, H. B.; Djurovich, P.; Bradforth, S. E.; Thompson, M. E. Symmetry-Breaking Charge Transfer of Visible Light Absorbing Systems: Zinc Dipyrrins. *J. Phys. Chem. C* **2014**, *118*, 21834–21845.

(200) Kellogg, M.; Akil, A.; Muthiah Ravinson, D. S.; Estergreen, L.; Bradforth, S. E.; Thompson, M. E. Symmetry Breaking Charge Transfer as a Means to Study Electron Transfer with No Driving Force. *Faraday Discuss.* **2019**, *216*, 379–394.

(201) Mahmood, Z.; Rehmat, N.; Ji, S.; Zhao, J.; Sun, S.; Di Donato, M.; Li, M.; Teddei, M.; Huo, Y. Tuning the Triplet Excited State of Bis(Dipyrrin) Zinc(II) Complexes: Symmetry Breaking Charge Transfer Architecture with Exceptionally Long Lived Triplet State for Upconversion. *Chem. – Eur. J.* **2020**, *26*, 14912–14918.

(202) Weller, A. Photoinduced Electron Transfer in Solution: Exciplex and Radical Ion Pair Formation Free Enthalpies and Their Solvent Dependence By. *Zeitshcrift Phys. Chem. N. F.* **1982**, *133*, 93–98.

(203) Rehm, D.; Weller, A. Kinetics of Fluorescence Quenching by Electron and H-Atom Transfer. *Isr. J. Chem.* **1970**, *8*, 259–271.

(204) Vauthey, E. Photoinduced Symmetry-Breaking Charge Separation. *ChemPhysChem* **2012**, *13*, 2001–2011.

(205) Smith, A. R. G.; Burn, P. L.; Powell, B. J. Spin–Orbit Coupling in Phosphorescent Iridium(III) Complexes. *ChemPhysChem* **2011**, *12*, 2429–2438.

(206) Ronca, E.; De Angelis, F.; Fantacci, S. Time-Dependent Density Functional Theory Modeling of Spin–Orbit Coupling in Ruthenium and Osmium Solar Cell Sensitizers. *J. Phys. Chem. C* **2014**, *118*, 17067–17078.

(207) Gourlaouen, C.; Daniel, C. Spin–Orbit Effects in Square-Planar Pt(II) Complexes with Bidentate and Terdentate Ligands: Theoretical Absorption/Emission Spectroscopy. *Dalton Trans* **2014**, *43*, 17806–17819.

(208) Braun, J. D.; Lozada, I. B.; Herbert, D. E. In Pursuit of Panchromatic Absorption in Metal Coordination Complexes: Experimental Delineation of the HOMO Inversion Model Using Pseudo-Octahedral Complexes of Diarylamido Ligands. *Inorg. Chem.* **2020**, *59*, 17746–17757.

(209) Hayashi, M.; Takahashi, Y.; Yoshida, Y.; Sugimoto, K.; Kitagawa, H. Role of D-Elements in a Proton–Electron Coupling of d–π Hybridized Electron Systems. *J. Am. Chem. Soc.* **2019**, *141*, 11686–11693.

(210) Spencer, M.; Santoro, A.; Freeman, G. R.; Díez, Á.; Murray, P. R.; Torroba, J.; Whitwood, A. C.; Yellowlees, L. J.; Williams, J. A. G.; Bruce, D. W. Phosphorescent, Liquid-Crystalline Complexes of Platinum(II): Influence of the β-Diketonate Co-Ligand on Mesomorphism and Emission Properties. *Dalton Trans.* **2012**, *41*, 14244–14256.

(211) Neese, F. The ORCA Program System. *WIREs Comput. Mol. Sci.* **2012**, *2*, 73–78.

(212) Neese, F. Software Update: The ORCA Program System, Version 4.0. *WIREs Comput. Mol. Sci.* **2018**, *8*, e1327.

(213) Frisch, M. J.; Trucks, G. W.; Schlegel, H. B.; Scuseria, G. E.; Robb, M. A.; Cheeseman, J. R.; Scalmani, G.; Barone, V.; Petersson, G. A.; Nakatsuji, H.; Li, X.; Caricato, M.; Marenich, A. V.; Bloino, J.; Janesko, B. G.; Gomperts, R.; Mennucci, B.; Hratchian, H. P.; Ortiz, J. V.; Izmaylov, A. F.; Sonnenberg, J. L.; Williams; Ding, F.; Lipparini, F.; Egidi, F.; Goings, J.; Peng, B.; Petrone, A.; Henderson, T.; Ranasinghe, D.; Zakrzewski, V. G.; Gao, J.; Rega, N.; Zheng, G.; Liang, W.; Hada, M.; Ehara, M.; Toyota, K.; Fukuda, R.; Hasegawa, J.; Ishida, M.; Nakajima, T.; Honda, Y.; Kitao, O.; Nakai, H.; Vreven, T.; Throssell, K.; Montgomery Jr., J. A.; Peralta, J. E.; Ogliaro, F.; Bearpark, M. J.; Heyd, J. J.; Brothers, E. N.; Kudin, K. N.; Staroverov, V. N.; Keith, T. A.; Kobayashi, R.; Normand, J.;

Raghavachari, K.; Rendell, A. P.; Burant, J. C.; Iyengar, S. S.; Tomasi, J.; Cossi, M.; Millam, J. M.; Klene, M.; Adamo, C.; Cammi, R.; Ochterski, J. W.; Martin, R. L.; Morokuma, K.; Farkas, O.; Foresman, J. B.; Fox, D. J. *Gaussian 16 Rev. C.01*; Wallingford, CT, 2016.

(214) Marenich, A. V.; Cramer, C. J.; Truhlar, D. G. Universal Solvation Model Based on Solute Electron Density and on a Continuum Model of the Solvent Defined by the Bulk Dielectric Constant and Atomic Surface Tensions. *J Phys Chem B* **2009**, *113*, 6378–6396.

(215) Grimme, S.; Ehrlich, S.; Goerigk, L. Effect of the Damping Function in Dispersion Corrected Density Functional Theory. *J. Comput. Chem.* **2011**, *32*, 1456–1465.

(216) Becke, A. D. Density-Functional Thermochemistry. III. The Role of Exact Exchange. *J Chem Phys* **1993**, *98*, 5648–5652.

(217) Lee, C.; Yang, W.; Parr, R.G. Development of the Colle-Salvetti Correlation-Energy Formula into a Functional of the Electron Density. *Phys. Rev. B Condens. Matter* **1988**, *37*, 785–789.

(218) Vosko, S. H.; Wilk, L.; Nusair, M. Accurate Spin-Dependent Electron Liquid Correlation Energies for Local Spin Density Calculations: A Critical Analysis. *Can. J. Phys.* **1980**, *58*, 1200–1211.

(219) Stephens, P. J.; Devlin, F. J.; Chabalowski, C. F.; Frisch, M. J. Ab Initio Calculation of Vibrational Absorption and Circular Dichroism Spectra Using Density Functional Force Fields. *J Phys Chem* **1994**, *98*, 11623–11627.

(220) Weigend, F.; Ahlrichs, R. Balanced Basis Sets of Split Valence, Triple Zeta Valence and Quadruple Zeta Valence Quality for H to Rn: Design and Assessment of Accuracy. *Phys Chem Chem Phys* **2005**, *7*, 3297–3305.

(221) Tao, J.; Perdew, J. P.; Staroverov, V. N.; Scuseria, G. E. Climbing the Density Functional Ladder: Nonempirical Meta--Generalized Gradient Approximation Designed for Molecules and Solids. *Phys. Rev. Lett.* **2003**, *91*, 146401.

(222) Staroverov, V. N.; Scuseria, G. E.; Tao, J.; Perdew, J. P. Comparative Assessment of a New Nonempirical Density Functional: Molecules and Hydrogen-Bonded Complexes. *J. Chem. Phys.* **2003**, *119*, 12129–12137.

(223) O'Boyle, N. M.; Tenderholt, A. L.; Langner, K. M. Software News and Updates Cclib: A Library for Package-Independent Computational Chemistry Algorithms. *J Comput Chem* **2008**, *29*, 839–845.

(224) Lu, T.; Chen, F. Multiwfn: A Multifunctional Wavefunction Analyzer. *J Comput Chem* **2012**, *33*, 580–592.

(225) Xiao, M; Lu, T. Generalized Charge Decomposition Analysis (GCDA) Method. *J. Adv. Phys. Chem.* **2015**, *4*, 111–124.

(226) Frisch, M. J.; Trucks, G. W.; Schlegel, H. B.; Scuseria, G. E.; Robb, M. A.; Cheeseman, J. R.; Scalmani, G.; Barone, V.; Petersson, G. A.; Nakatsuji, H.; Li, X.; Caricato, M.; Marenich, A. V.; Bloino, J.; Janesko, B. G.; Gomperts, R.; Mennucci, B.; Hratchian, H. P.; Ortiz, J. V.; Izmaylov, A. F.; Sonnenberg, J. L.; Williams-Young, D.; Ding, F.; Lipparini, F.; Egidi, F.; Goings, J.; Peng, B.; Petrone, A.; Henderson, T.; Ranasinghe, D.; Zakrzewski, V. G.; Gao, J.; Rega, N.; Zheng, G.; Liang, W.; Hada, M.; Ehara, M.; Toyota, K.; Fukuda, R.; Hasegawa, J.; Ishida, M.; Nakajima, T.; Honda, Y.; Kitao, O.; Nakai, H.; Vreven, T.; Throssell, K.; Montgomery, J. A.; Peralta, J. E.; Ogliaro, F.; Bearpark, M. J.; Heyd, J. J.; Brothers, E. N.; Kudin, K. N.; Staroverov, V. N.; Keith, T. A.; Kobayashi, R.; Normand, J.;

Raghavachari, K.; Rendell, A. P.; Burant, J. C.; Iyengar, S. S.; Tomasi, J.; Cossi, M.; Millam, J. M.; Klene, M.; Adamo, C.; Cammi, R.; Ochterski, J. W.; Martin, R. L.; Morokuma, K.; Farkas, O.; Foresman, J. B.; Fox, D. J. *Gaussian 16, Revision B.01*; Gaussian 16, Revision B.01, Gaussian, Inc., Wallingford CT; Gaussian, Inc.: Wallingford CT, 2016.

(227) Adamo, C.; Barone, V. Toward Reliable Density Functional Methods without Adjustable Parameters: The PBE0 Model. *J. Chem. Phys.* **1999**, *110* (13), 6158–6170.

(228) Andrae, D.; Huermann, U.; Dolg, M.; Stoll, H.; Preu, H. Energy-Adjustedab Initio Pseudopotentials for the Second and Third Row Transition Elements. *Theor. Chim. Acta* **1990**, *77*, 123–141.

(229) Yanai, T.; Tew, D. P.; Handy, N. C. A New Hybrid Exchange–Correlation Functional Using the Coulomb-Attenuating Method (CAM-B3LYP). *Chem. Phys. Lett.* **2004**, *393*, 51–57.

(230) Neese, F.; Wennmohs, F.; Hansen, A.; Becker, U. Efficient, Approximate and Parallel Hartree–Fock and Hybrid DFT Calculations. A 'Chain-of-Spheres' Algorithm for the Hartree–Fock Exchange. *Chem. Phys.* **2009**, *356*, 98–109.

(231) Lenthe, E. van; Baerends, E. J.; Snijders, J. G. Relativistic Regular Two-component Hamiltonians. *J. Chem. Phys.* **1993**, *99*, 4597–4610.

(232) Weigend, F. Accurate Coulomb-Fitting Basis Sets for H to Rn. *Phys. Chem. Chem. Phys.* **2006**, *8*, 1057.

(233) Pantazis, D. A.; Neese, F. All-Electron Scalar Relativistic Basis Sets for the Lanthanides. *J. Chem. Theory Comput.* **2009**, *5*, 2229–2238.

(234) Pantazis, D. A.; Neese, F. All-Electron Scalar Relativistic Basis Sets for the Actinides. *J. Chem. Theory Comput.* **2011**, *7*, 677–684.

(235) Pantazis, D. A.; Chen, X.-Y.; Landis, C. R.; Neese, F. All-Electron Scalar Relativistic Basis Sets for Third-Row Transition Metal Atoms. *J. Chem. Theory Comput.* **2008**, *4*, 908–919.

(236) Hirshfeld, F. L. Bonded-Atom Fragments for Describing Molecular Charge Densities. *Theor. Chim. Acta* **1977**, *44*, 129–138.

(237) Hanwell, M. D.; Curtis, D. E.; Lonie, D. C.; Vandermeersch, T.; Zurek, E.; Hutchison, G. R. Avogadro: An Advanced Semantic Chemical Editor, Visualization, and Analysis Platform. *J Cheminf* **2012**, *4*, 17.

(238) Frisch, M. J.; Trucks, G. W.; Schlegel, H. B.; Scuseria, G. E.; Robb, M. A.; Cheeseman, J. R.; Scalmani, G.; Barone, V.; Petersson, G. A.; Nakatsuji, H.; Li, X.; Caricato, M.; Marenich, A. V.; Bloino, J.; Janesko, B. G.; Gomperts, R.; Mennucci, B.; Hratchian, H. P.; Ortiz, J. V.; Izmaylov, A. F.; Sonnenberg, J. L.; Williams; Ding, F.; Lipparini, F.; Egidi, F.; Goings, J.; Peng, B.; Petrone, A.; Henderson, T.; Ranasinghe, D.; Zakrzewski, V. G.; Gao, J.; Rega, N.; Zheng, G.; Liang, W.; Hada, M.; Ehara, M.; Toyota, K.; Fukuda, R.; Hasegawa, J.; Ishida, M.; Nakajima, T.; Honda, Y.; Kitao, O.; Nakai, H.; Vreven, T.; Throssell, K.; Montgomery Jr., J. A.; Peralta, J. E.; Ogliaro, F.; Bearpark, M. J.; Heyd, J. J.; Brothers, E. N.; Kudin, K. N.; Staroverov, V. N.; Keith, T. A.; Kobayashi, R.; Normand, J.; Raghavachari, K.; Rendell, A. P.; Burant, J. C.; Iyengar, S. S.; Tomasi, J.; Cossi, M.; Millam, J. M.; Klene, M.; Adamo, C.; Cammi, R.; Ochterski, J. W.; Martin, R. L.; Morokuma, K.; Farkas, O.; Foresman, J. B.; Fox, D. J. Gaussian 16 Rev. C.01, 2016.

(239) Marenich, A. V.; Cramer, C. J.; Truhlar, D. G. Universal Solvation Model Based on Solute Electron Density and on a Continuum Model of the Solvent Defined by the Bulk Dielectric Constant and Atomic Surface Tensions. *J Phys Chem B* **2009**, *113*, 6378–6396.

(240) Dennington, Roy; Keith, Todd A.; Millam, John M. GaussView, Version 6, 2016.

(241) O'Boyle, N. M.; Tenderholt, A. L.; Langner, K. M. Software News and Updates Cclib: A Library for Package-Independent Computational Chemistry Algorithms. *J Comput Chem* **2008**, *29*, 839–845.

(242) Lu, T.; Chen, F. Multiwfn: A Multifunctional Wavefunction Analyzer. *J Comput Chem* **2012**, *33*, 580–592.

(243) Tian, L. U.; Fei-Wu, C. Calculation of Molecular Orbital Composition. *Acta Chim. Sin.* **2011**, *69*, 2393.

(244) Frisch, M. J.; Trucks, G. W.; Schlegel, H. B.; Scuseria, G. E.; Robb, M. A.; Cheeseman, J. R.; Scalmani, G.; Barone, V.; Petersson, G. A.; Nakatsuji, H.; Li, X.; Caricato, M.; Marenich, A. V.; Bloino, J.; Janesko, B. G.; Gomperts, R.; Mennucci, B.; Hratchian, H. P.; Ortiz, J. V.; Izmaylov, A. F.; Sonnenberg, J. L.; Williams-Young, D.; Ding, F.; Lipparini, F.; Egidi, F.; Goings, J.; Peng, B.; Petrone, A.; Henderson, T.; Ranasinghe, D.; Zakrzewski, V. G.; Gao, J.; Rega, N.; Zheng, G.; Liang, W.; Hada, M.; Ehara, M.; Toyota, K.; Fukuda, R.; Hasegawa, J.; Ishida, M.; Nakajima, T.; Honda, Y.; Kitao, O.; Nakai, H.; Vreven, T.; Throssell, K.; Montgomery Jr., J. A.; Peralta, J. E.; Ogliaro, F.; Bearpark, M. J.; Heyd, J. J.; Brothers, E. N.; Kudin, K. N.; Staroverov, V. N.; Keith, T. A.; Kobayashi, R.; Normand, J.; Raghavachari, K.; Rendell, A. P.; Burant, J. C.; Iyengar, S. S.; Tomasi, J.; Cossi, M.; Millam, J. M.; Klene, M.; Adamo, C.; Cammi, R.; Ochterski, J. W.; Martin, R. L.; Morokuma, K.; Farkas, O.; Foresman, J. B.; Fox, D. J. Gaussian 16 Rev. C.01, 2016.

(245) Marenich, A. V.; Cramer, C. J.; Truhlar, D. G. Universal Solvation Model Based on Solute Electron Density and on a Continuum Model of the Solvent Defined by the Bulk Dielectric Constant and Atomic Surface Tensions. *J Phys Chem B* **2009**, *113*, 6378–6396.

(246) Grimme, S.; Ehrlich, S.; Goerigk, L. Effect of the Damping Function in Dispersion Corrected Density Functional Theory. *J. Comput. Chem.* **2011**, *32*, 1456–1465.

(247) Weigend, F.; Ahlrichs, R. Balanced Basis Sets of Split Valence, Triple Zeta Valence and Quadruple Zeta Valence Quality for H to Rn: Design and Assessment of Accuracy. *Phys. Chem. Chem. Phys.* **2005**, *7*, 3297.

(248) Allouche, A.-R. Gabedit—A Graphical User Interface for Computational Chemistry Softwares. *J. Comput. Chem.* **2011**, *32*, 174–182.

(249) Liu, Z.; Lu, T.; Chen, Q. An Sp-Hybridized All-Carboatomic Ring, Cyclo[18]Carbon: Electronic Structure, Electronic Spectrum, and Optical Nonlinearity. *Carbon* **2020**, *165*, 461–467.

(250) Lu, T.; Chen, F. Multiwfn: A Multifunctional Wavefunction Analyzer. *J Comput Chem* **2012**, *33*, 580–592.

(251) Dennington, Roy; Keith, Todd A.; Millam, John M. GaussView, Version 6, 2016.

(252) Becke, A. D. Density-functional Thermochemistry. III. The Role of Exact Exchange. *J. Chem. Phys.* **1998**, *98*, 5648.

(253) Lee, C.; Yang, W.; Parr, R. G. Development of the Colle-Salvetti Correlation-Energy Formula into a Functional of the Electron Density. *Phys. Rev. B* **1988**, *37*, 785–789.

(254) Vosko, S. H.; Wilk, L.; Nusair, M. Accurate Spin-Dependent Electron Liquid Correlation Energies for Local Spin Density Calculations: A Critical Analysis. *Can. J. Phys.* **1980**, *58*, 1200–1211.

(255) Amin, E. A.; Truhlar, D. G. Zn Coordination Chemistry: Development of Benchmark Suites for Geometries, Dipole Moments, and Bond Dissociation Energies and Their Use To Test

and Validate Density Functionals and Molecular Orbital Theory. *J. Chem. Theory Comput.* **2008**, *4*, 75–85.

(256) Otto, S.; Moll, J.; Förster, C.; Geißler, D.; Wang, C.; Resch-Genger, U.; Heinze, K. Three-in-One Crystal: The Coordination Diversity of Zinc Polypyridine Complexes. *Eur. J. Inorg. Chem.* **2017**, *2017*, 5033–5040.

(257) Grimme, S.; Antony, J.; Ehrlich, S.; Krieg, H. A Consistent and Accurate *Ab Initio* Parametrization of Density Functional Dispersion Correction (DFT-D) for the 94 Elements H-Pu. *J. Chem. Phys.* **2010**, *132*, 154104.

(258) Ernzerhof, M.; Scuseria, G. E. Assessment of the Perdew–Burke–Ernzerhof Exchange-Correlation Functional. *J. Chem. Phys.* **1999**, *110*, 5029–5036.

(259) Perdew, J. P.; Burke, K.; Ernzerhof, M. Generalized Gradient Approximation Made Simple. *Phys. Rev. Lett.* **1996**, *77*, 3865–3868.

(260) van Wüllen, C. Molecular Density Functional Calculations in the Regular Relativistic Approximation: Method, Application to Coinage Metal Diatomics, Hydrides, Fluorides and Chlorides, and Comparison with First-Order Relativistic Calculations. *J. Chem. Phys.* **1998**, *109* (2), 392–399.

(261) Rosenberg, B.; Van Camp, L.; Krigas, Thomas. Inhibition of Cell Division in Escherichia Coli by Electrolysis Products from a Platinum Electrode. *Nature* **1965**, *205* (4972), 698–699. https://doi.org/10.1038/205698a0.

(262) Wang, D.; Lippard, S. J. Cellular Processing of Platinum Anticancer Drugs. *Nat. Rev. Drug Discov.* **2005**, *4* (4), 307–320. https://doi.org/10.1038/nrd1691.

(263) Englinger, B.; Pirker, C.; Heffeter, P.; Terenzi, A.; Kowol, C. R.; Keppler, B. K.; Berger, W. Metal Drugs and the Anticancer Immune Response. *Chem. Rev.* **2019**, *119* (2), 1519–1624. https://doi.org/10.1021/acs.chemrev.8b00396.

(264) Wheate, N. Multi-Nuclear Platinum Complexes as Anti-Cancer Drugs. *Coord. Chem. Rev.* **2003**, *241* (1–2), 133–145. https://doi.org/10.1016/S0010-8545(03)00050-X.

(265) Johnstone, T. C.; Park, G. Y.; Lippard, S. J. Understanding and Improving Platinum Anticancer Drugs - Phenanthriplatin. *Anticancer Res.* **2014**, *34*, 471–476.

(266) Johnstone, T. C.; Wilson, J. J.; Lippard, S. J. Monofunctional and Higher-Valent Platinum Anticancer Agents. *Inorg. Chem.* **2013**, *52* (21), 12234–12249. https://doi.org/10.1021/ic400538c.

(267) Todd, R. C.; Lippard, S. J. Structure of Duplex DNA Containing the Cisplatin 1,2-{Pt(NH3)2}2+-d(GpG) Cross-Link at 1.77 Å Resolution. *J. Inorg. Biochem.* **2010**, *104*, 902–908.

(268) Park, G. Y.; Wilson, J. J.; Song, Y.; Lippard, S. J. Phenanthriplatin, a Monofunctional DNA-Binding Platinum Anticancer Drug Candidate with Unusual Potency and Cellular Activity Profile. *Proc Natl Acad Sci* **2012**, *109*, 11987–11992.

(269) Lovejoy, K. S.; Serova, M.; Bieche, I.; Emami, S.; D'Incalci, M.; Broggini, M.; Erba, E.; Gespach, C.; Cvitkovic, E.; Faivre, S.; Raymond, E.; Lippard, S. J. Spectrum of Cellular Responses to Pyriplatin, a Monofunctional Cationic Antineoplastic Platinum(II) Compound, in Human Cancer Cells. *Mol. Cancer Ther.* **2011**, *10* (9), 1709–1719. https://doi.org/10.1158/1535-7163.MCT-11-0250.

(270) Almaqwashi, A. A.; Zhou, W.; Naufer, M. N.; Riddell, I. A.; Yilmaz, Ö. H.; Lippard, S. J.; Williams, M. C. DNA Intercalation Facilitates Efficient DNA-Targeted Covalent Binding

of Phenanthriplatin. *J. Am. Chem. Soc.* **2019**, *141* (4), 1537–1545. https://doi.org/10.1021/jacs.8b10252.

(271) Tullius, T. D.; Lippard, S. J. Ethidium Bromide Changes the Nuclease-Sensitive DNA Binding Sites of the Antitumor Drug Cis-Diamminedichloroplatinum(II). *Proc. Natl. Acad. Sci.* **1982**, *79* (11), 3489–3492. https://doi.org/10.1073/pnas.79.11.3489.

(272) Boulikas, T.; Vougiouka, M. Cisplatin and Platinum Drugs at the Molecular Level (Review). *Oncol. Rep.* **2003**. https://doi.org/10.3892/or.10.6.1663.

(273) Dasari, S.; Bernard Tchounwou, P. Cisplatin in Cancer Therapy: Molecular Mechanisms of Action. *Eur. J. Pharmacol.* **2014**, *740*, 364–378. https://doi.org/10.1016/j.ejphar.2014.07.025.

(274) Lozada, I. B.; Williams, J. A. G.; Herbert, D. E. Platinum(II) Complexes of Benzannulated N ^ N ⁻^ O-Amido Ligands: Bright Orange Phosphors with Long-Lived Excited States. *Inorg. Chem. Front.* **2022**, *9* (1), 10–22. https://doi.org/10.1039/D1QI01120K.

(275) Che, C.-M.; Yang, M.; Wong, K.-H.; Chan, H.-L.; Lam, W. Platinum(II) Complexes of Dipyridophenazine as Metallointercalators for DNA and Potent Cytotoxic Agents against Carcinoma Cell Lines. *Chem. – Eur. J.* **1999**, *5*, 3350–3356.

(276) Kieltyka, R.; Fakhoury, J.; Moitessier, N.; Sleiman, H. F. Platinum Phenanthroimidazole Complexes as G-Quadruplex DNA Selective Binders. *Chem. – Eur. J.* **2008**, *14* (4), 1145–1154. https://doi.org/10.1002/chem.200700783.

(277) Cusumano, M.; Di Pietro, M. L.; Giannetto, A.; Nicolò, F.; Rotondo, E. Noncovalent Interactions of Platinum(II) Square Planar Complexes Containing Ligands Out-of-Plane with DNA. *Inorg. Chem.* **1998**, *37* (3), 563–568. https://doi.org/10.1021/ic9705406.

(278) Suntharalingam, K.; Mendoza, O.; Duarte, A. A.; Mann, D. J.; Vilar, R. A Platinum Complex That Binds Non-Covalently to DNA and Induces Cell Death via a Different Mechanism than Cisplatin. *Metallomics* **2013**, *5* (5), 514. https://doi.org/10.1039/c3mt20252f.

(279) Luedtke, N. W.; Liu, Q.; Tor, Y. Synthesis, Photophysical Properties, and Nucleic Acid Binding of Phenanthridinium Derivatives Based on Ethidium. *Bioorg. Med. Chem.* **2003**, *11*, 5235–5247.

(280) Nandi, R.; Chaudhuri, K.; Maiti, M. EFFECTS OF IONIC STRENGTH and PH ON THE BINDING OF SANGUINARINE TO DEOXYRIBONUCLEIC ACID. *Photochem. Photobiol.* **1985**, *42* (5), 497–503. https://doi.org/10.1111/j.1751-1097.1985.tb01600.x.

(281) Howe-Grant, M.; Lippard, S. J. Binding of Platinum(II) Intercalation Reagents to Deoxyribonucleic Acid. Dependence on Base-Pair Composition, Nature of the Intercalator, and Ionic Strength. *Biochemistry* **1979**, *18* (26), 5762–5769. https://doi.org/10.1021/bi00593a003.

(282) Murphy, M. P. How Mitochondria Produce Reactive Oxygen Species. *Biochem. J.* **2009**, *417* (1), 1–13. https://doi.org/10.1042/BJ20081386.

(283) Ivashkevich, A.; Redon, C. E.; Nakamura, A. J.; Martin, R. F.; Martin, O. A. Use of the γ-H2AX Assay to Monitor DNA Damage and Repair in Translational Cancer Research. *Cancer Lett.* **2012**, *327* (1–2), 123–133. https://doi.org/10.1016/j.canlet.2011.12.025.

(284) Mah, L.-J.; El-Osta, A.; Karagiannis, T. C. ΓH2AX: A Sensitive Molecular Marker of DNA Damage and Repair. *Leukemia* **2010**, *24* (4), 679–686. https://doi.org/10.1038/leu.2010.6.

(285) Chargaff, E.; Lipshitz, R. Composition of Mammalian Desoxyribonucleic Acids [1]. *J. Am. Chem. Soc.* **1953**, *75* (15), 3658–3661. https://doi.org/10.1021/ja01111a016.

(286) Kaim, W.; Schwederski, B.; Klein, A. Manganese-Catalyzed Oxidation of Water to O2. In *Bioinorganic Chemistry: Inorganic Elements in the Chemistry of Life*; Wiley: Chichester, 2013; pp 67–74.

(287) Pan, D.; Schmieder, A. H.; Wickline, S. A.; Lanza, G. M. Manganese-Based MRI Contrast Agents: Past, Present, and Future. *Tetrahedron* **2011**, *67* (44), 8431–8444. https://doi.org/10.1016/j.tet.2011.07.076.

(288) East, N. R.; Förster, C.; Carrella, L. M.; Rentschler, E.; Heinze, K. The Full d^3–d^5 Redox Series of Mononuclear Manganese Complexes: Geometries and Electronic Structures of $[Mn(Dgpy)_2]^{n+}$. *Inorg. Chem.* **2022**, *61* (37), 14616–14625. https://doi.org/10.1021/acs.inorgchem.2c01680.

(289) Herr, P.; Kerzig, C.; Larsen, C. B.; Häussinger, D.; Wenger, O. S. Manganese(i) Complexes with Metal-to-Ligand Charge Transfer Luminescence and Photoreactivity. *Nat. Chem.* **2021**, *13* (10), 956–962. https://doi.org/10.1038/s41557-021-00744-9.

(290) Betley, T. A.; Qian, B. A.; Peters, J. C. Group VIII Coordination Chemistry of a Pincer-Type Bis(8-Quinolinyl)Amido Ligand. *Inorg. Chem.* **2008**, *47* (24), 11570–11582. https://doi.org/10.1021/ic801047s.

(291) Huynh, M. T.; Anson, C. W.; Cavell, A. C.; Stahl, S. S.; Hammes-Schiffer, S. Quinone 1 e$^-$ and 2 e$^-$/2 H$^+$ Reduction Potentials: Identification and Analysis of Deviations from Systematic Scaling Relationships. *J. Am. Chem. Soc.* **2016**, *138* (49), 15903–15910. https://doi.org/10.1021/jacs.6b05797.

(292) Michaelis, L.; Hill, E. S. THE VIOLOGEN INDICATORS. *J. Gen. Physiol.* **1933**, *16* (6), 859–873. https://doi.org/10.1085/jgp.16.6.859.

(293) Woodhouse, M. D.; McCusker, J. K. Mechanistic Origin of Photoredox Catalysis Involving Iron(II) Polypyridyl Chromophores. *J. Am. Chem. Soc.* **2020**, *142* (38), 16229–16233. https://doi.org/10.1021/jacs.0c08389.

2 Benzannulation in Ligand Design

2.1 Abstract

Benzannulation is a ligand design strategy that can provide low-lying vacant acceptor orbitals stabilizing metal-to-ligand charge transfer (MLCT) states in metal complexes. A counterintuitive trend is observed from the emission spectra of the complexes, blue shifting the emission, and to some degree prolonging the excited state lifetimes, with increasing benzannulation. Computational studies reveal the enhanced rigidification conferred by benzannulation contributing to this counterintuitive effect. These key aspects are combined with π-donor ligands, such as in diarylamidos, to extend the absorptive cross-section of metal complexes below the visible region achieving panchromatic absorption. For these analogs, computational studies reveal some degree of mixing between the nominally metal t_{2g} and ligand $N_{\mathrm{amido}}(\pi)$ manifolds increasing the covalency of the M–L bond. This lends some ligand character to the highest filled orbitals increasing the intensity of the nominally MLCT transitions, here assigned as π-antibonding-toligand charge transfer (PALCT). These results are desirable for dye-senstitized solar cells(DSSCs) as these allow for the capture for more photons. Detailed analyses of the lowest-lying excited states (^{3}PALCT, ^{3}MC, and ^{5}MC; MC states are defined as metal-centred states) suggest that increased covalency in these diarylamido complexes tempers the effect of the weak field induced by π-donor ligands leading to a significant stabilization of the ^{3}CT states compared with those found in [Fe(tpy)$_2$]$^{2+}$. Expanding all the desirable aspects of the tridentate diarylamido ligands to other ligand scaffolds, new tridentate ligands based on the β-ketoimine $N^{\wedge}N$(H)$^{\wedge}O$ motif and tetradentate malonamide are presented. In addition, new phenanthridine

precursors that incorporate carboxylate and nitrile functional groups that are targets in surface functionalization and water-soluble complexes are disclosed.

2.2   Introduction

Fusion of benzene rings to aromatic systems enables the expansion of the conjugated π-system. This modifies the electronic structure of the compounds impacting the aromaticity, the physicochemical properties, and intermolecular interactions of the system. Similarly in coordination chemistry, extending the π-system of conjugated ligands is widely used to tune electronic transitions in transition metal[28–30] and main-group[31–33] complexes without significantly altering the parent ligand framework. This can provide important flexibility in the design of new emissive molecules and photosensitizers, as photophysical properties can be adjusted without wholesale changes to the core molecular shape. Furthermore, as exemplified by a published series of (BPI)PtCl (BPI = *bis*(2-pyridylimino)isoindolate) complexes mentioned in Chapter 1, red or blue shifts are both possible with increasing π-extension. The direction of the shift was rationalized by establishing how the site of benzannulation impacts the energies of the frontier orbitals (HOMO/LUMO).[34] The same site-selective benzannulation design is applied to a series of cationic Ru(II) complexes supported by benzannulated bipyridines (see Chapter 1, Figure X). Here, benzannulation not only shifts the energies of the MLCT transitions but also enhances the mixing of the excited S_n and T_n manifolds facilitating the direct $T_n \leftarrow S_0$.

The benzannulated aromatic *N*-heterocycle phenanthridine (3,4-benzoquinoline) is much less well-known as a ligand than its more symmetric isomer acridine (2,3-benzoquinoline),[35] the readily cyclometallated benzo[h]quinoline (7,8-benzoquinoline)[36] and quinoline itself (2,3-benzopyridine). This is despite phenanthridine's utility in fluorescent DNA intercalators such as

ethidium bromide[37] as noted in the introduction chapter and related emissive organic materials,[38] in platin drug candidates (phenathriplatin: *cis*-[Pt(NH$_3$)$_2$(phenanthridine)Cl]NO$_3$),[39] and as a co-catalyst in hydrogenation reactions.[40,41] To our knowledge, only a handful of multi-dentate ligands that bring phenanthridinyl units into the coordination sphere of metals are known. Emissive *tris*(4-phenanthridinolato)lithium and aluminum complexes have been used in electroluminescent devices.[42–45] (*R*)- and (*S*)-6-(2'-diphenylphosphino-l'-naphthyl)phenanthridines were applied as atropisomeric ligands in Pd-catalyzed allylic alkylations.[46] *Fac*-binding, tridentate *bis*(phenanthridinylmethyl)amines bound to Re(I) carbonyls have been used for live-cell fluorescence imaging.[47] Chelate-assisted C-H activation of substituted 6-arylphenanthridines has been used to generate luminescent C,N-cyclometallated phenanthridine-containing platinum(II)[48] and deep-red emitting iridium(III) complexes.[49]

2.3   Results and Discussion

2.3.1 Incorporating Phenanthridines in Ligand Scaffolds

Phenanthridine is an *N*-heterocyclic polycyclic aromatic hydrocarbon with a long history.[50] It is structurally analogous to phenanthrene (ethylene-bridged biphenyl), and can be described as an imine-bridged biphenyl. Moreover, phenanthridine can be thought of as a benzo-fused pyridine and is a structural isomer of the more symmetric acridine (Figure 2.1).
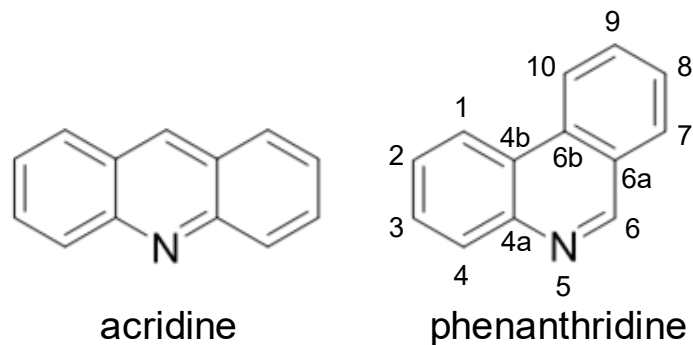
Figure 2.1. Molecular structure of acridine and phenanthridine. The IUPAC numbering scheme for phenanthridine is also shown.

The advancement of analytical instrumentations such as X-ray crystallography and NMR enabled the elucidation of the electronic structure of phenanthridine. The solid state structure of phenanthridine[51,52] revealed insights not only to its molecular structure but also some of its physicochemical properties. For example, its insolubility has been attributed to the extended π-stacking interaction in the solid state.[52] But perhaps the more interesting information that can be extracted from the solid state structure are some key bond angles and distances. Most notable, the C=N bond length is much shorter than in pyridine, quinoline, and acridine (Figure 2.2) indicating an imine-like character to the bonding. ^{1}H NMR spectra of phenanthridine in CDCl$_3$ exhibit a singlet C-*H* resonance at 9.32 ppm, which is attributed to the C-*H* moiety adjacent to the nitrogen heteroatom (labeled as C$_6$-*H*; see Figure 2.1). Comparing the same C-*H* moiety of pyridine and quinoline, phenanthridine appears at higher chemical shift (Figure 2.2), which supports the imine-like character of the C=N fragment of phenanthridine. Our group has exploited this property of phenanthridine as a diagnostic tool in assigning the success of ligand and complex syntheses. The C-*H* [1]H chemical shift is sensitive to the chemical environment around the nitrogen. This becomes evident in Chapter 3 with the discussion of the complexes of *N^NH^O* ligands.
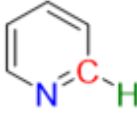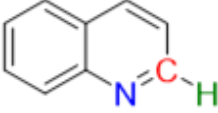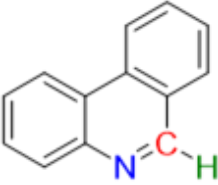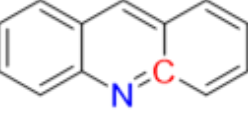
d(C=N)/Å	1.34	1.34	1.29	1.35
δ(C–^1H)/ppm (CDCl$_3$)	8.61	8.95	9.32	–
LUMO/eV	-0.14	-0.47	-0.60	-1.04

Figure 2.2. Imine bond lengths, CH ^{1}H NMR resonances (CDCl$_3$) and LUMO energies of pyridine, quinoline, phenanthridine and acridine.

Previous computational studies[53,54] indicate that benzannulation has a general stabilization effect on the LUMO (Figure 2.2). It is worth noting that impact of benzannulation can be site-dependent as exemplified by phenanthridine (3,4-benzoquinoline) and its structural isomer acridine (2,3-benzoquinoline). This difference is manifested in the $\lambda_{max,abs}$ of phenanthridine and acridine (λ_{max}(abs): anthracene, 374 nm; phenanthrene, 293 nm). Interestingly, the asymmetry intoduced by benzannulation at the C$_3$ and C$_4$ positions of quinoline leads to a localization of the orbital density at the C=N fragment of phenanthridine leading to reactivity similar to aldehydes and other imines[55] further supporting the imine-bridged biphenyl description of phenanthridine.[55] This description is consistent with Clar's rule, as the imine-bridged biphenyl resonance contributor maximizes the number of aromatic sextets in the polycyclic aromatic system. These observations indicate that phenanthridine can provide ligands with low-lying vacant acceptor orbitals that are anticipated to stabilize metal-to-ligand charge-transfer excited states (MLCT).
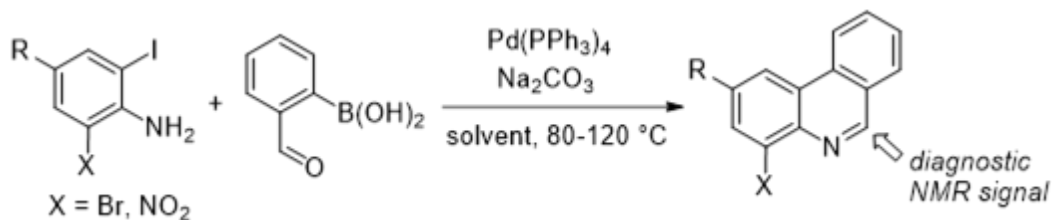
Scheme 2.1. General synthetic scheme for phenanthridine precursors.

Our group has devised various synthetic protocols that incorporate phenanthridine in different ligand scaffolds. A general strategy employed is the one-pot Suzuki coupling/condensation of 2-haloanilines and 2-formylphenylboronic acid (Scheme 2.1) affording 4-bromo and 4-nitrophenanthridine precursors. Further functionalization enabled us to isolate ligands with different denticity with particular focus on bidentate and tridentate ligands. Increasing the ligand denticity is known to confer stability to molecular complexes thanks to the chelate effect, an important aspect to consider in materials chemistry and drug design. I investigated the impact of benzannulation on the optical and luminescent properties of a variety of transition metal complexes as part of a collaborative effort within the Herbert group. The syntheses of the ligands and their properties have been published and will not be described here further.[56–62] Some of the ligands studied in this work are shown in Figure 2.3. Benzannulation, as revealed by these works, has an opposite effect on the optical and luminescent properties of the complexes.
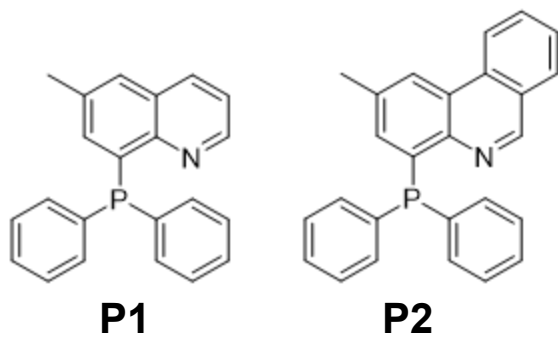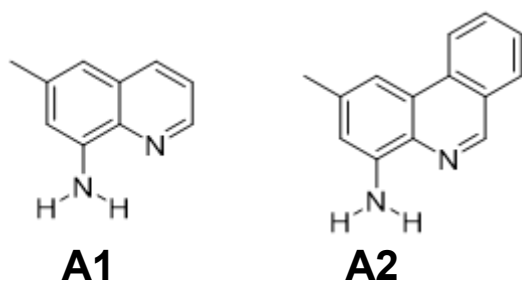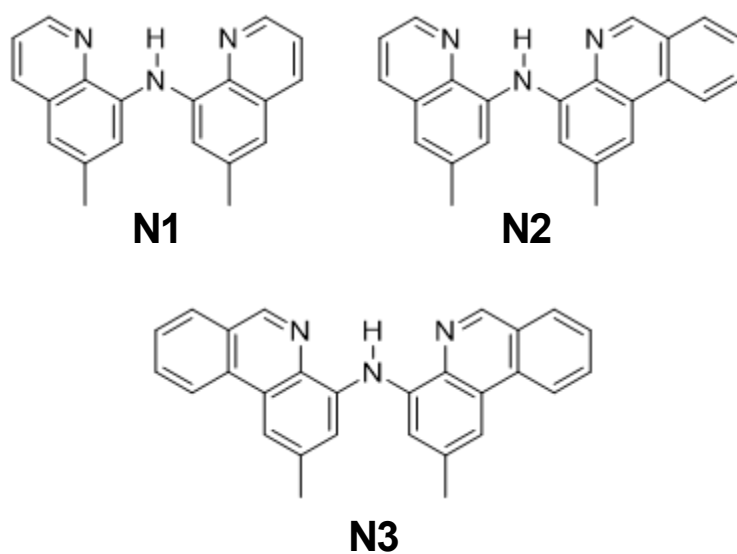
Figure 2.3. Representative ligands used to probe the impact of benzannulation in the optoelectronic and photophysical properties of transition metal complexes: (a) neutral bidentate *P^N* ligands, (b) neutral bidentate *N^N* ligands and (c) symmetric and asymmetric diarylamido *N^N*H*^N* ligands.

2.3.2 Stranger Things: Unexpected Results with Benzannulation

While some of the examples shown in Chapter 1 demonstrate stabilization of vacant π*-MOs with benzannulation, this effect is not always transferrable or generalizable. Thus, predicting the impact of benzannulation *a priori* is not always straightforward. Here, I present three representative examples of transition metal complexes of the ligands in Figure 2.3 that display unexpected results from benzannulation. Firstly, in collaboration with a colleague (Dr. Rajarshi Mondal), we investigated the impact of benzannulation in a series of *P^N* ligated Fe(II) complexes (Figure 2.4). The electrochemical response observed for **FP1** and **FP2** in acetonitrile solution was reversible. Both complexes show a reversible $Fe^{2+/3+}$ couple at comparable potentials (**FP2**: $E_{1/2} =$ 0.82 V vs $FcH^{0/+}$; **FP1**: $E_{1/2} =$ 0.83 V vs $FcH^{0/+}$; FcH = ferrocene). A reversible reduction event can be also seen, again at comparable potentials (**FP2**: $E_{1/2} =$ -1.61 V vs $FcH^{0/+}$; **FP1**: $E_{1/2} =$ -1.55 V vs $FcH^{0/+}$). The slight cathodic shift to the reduction event for the more π-extended phenanthridine ligand suggests a higher energy LUMO, consistent with the blue-shifted λ_{max} for **FP2** observed by UV-Vis absorption spectroscopy.[33] With the counter-intuitive shift of the lowest energy absorption to higher energy for the complex comprised of a ligand with a larger π-system, **FP2**, stands in contrast to trends observed for Cu(I) complexes of related quinoline/phenanthridine-based *P^N* ligands.[63] There, a bathochromic shift of the lowest energy MLCT absorptions is observed for dimeric $(P\textasciicircum N)_2Cu_2X_2$ complexes of **P2** compared with those of **P1**. In comparison, Group 10 complexes of pincer-like tridentate *N^N^N* ligands bearing either quinolinyl or phenanthridinyl arms show nearly identical λ_{max} values that were invariant in the face of increasing π-extension.[64] Isoenergetic lowest energy absorptions were also observed for pseudo-octahedral $Re(CO)_3X$ (X = Br, Cl) complexes of bidentate (4-amino)phenanthridine and

(8-amino)quinoline ligands.[65] In $[Ru(L)_3]^{2+}$ complexes,[66] the usual trend expected from benzannulation is retained with cathodic shift in the reduction potentials (L $E_{1/2(red)}$: bpy -1.71 V, bq -1.11 V, biq -1.89, biphe -1.14 V) and red-shifting of the optical spectra (L $\lambda_{max,abs}$: bpy 452 nm, bq 524 nm, biq 392 nm, biphe 549 nm). In each of these scenarios the different impacts of ligand benzannulation cannot be solely connected to the (de)stabilization of the frontier orbitals, as suggested by some other studies.[67–69] It is in Chapter 4 that the origin of this unusual behaviour of *tris*-ligated homoleptic pseudo-octahedral Fe(II) complexes with benzannulation is revealed through extensive computational analysis.
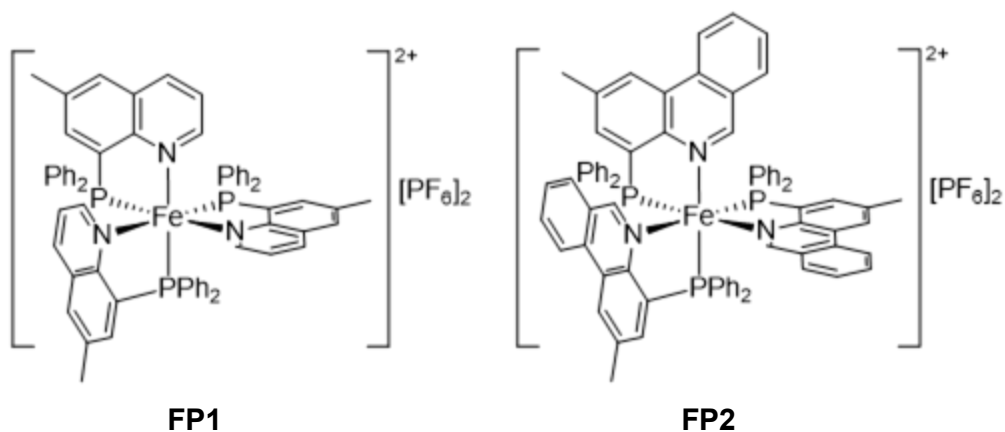
Figure 2.4. Fe(II) complexes studied to investigate the impact of benzannulation on the optoelectronic properties of complexes.

As mentioned above, Re(I) complexes (Figure 2.5, **Re1** and **Re2**) ligated by bidentate, neutral aminoaryls (Figure 2.3b) exhibit isoenergetic lower energy absorptions. This was a collaborative project between the Ziegler and Herbert groups. I led the computational investigation for this project with significant contribution from Robert John Ortiz. While no red shift is observed, there are still some notable differences between the spectra of **Re1** and **Re2**. The UV-Vis spectrum

45

of **Re2** has a wider absorptive cross-section and more intense transitions compared with **Re1**. It is notable that the absorption greater than 400 nm in **Re1** and **Re2** is below $\varepsilon < 250\ M^{-1} \cdot cm^{-1}$ indicating that direct $T_n \leftarrow S_0$ is operative in Re(I) complexes, particularly for benzannulated phenanthridinyl analogs. This suggests that benzannulation enhances mixing of S_n and T_n excited state manifolds. These results have significant implications on the photophysics of complexes containing heavy elements in this thesis.
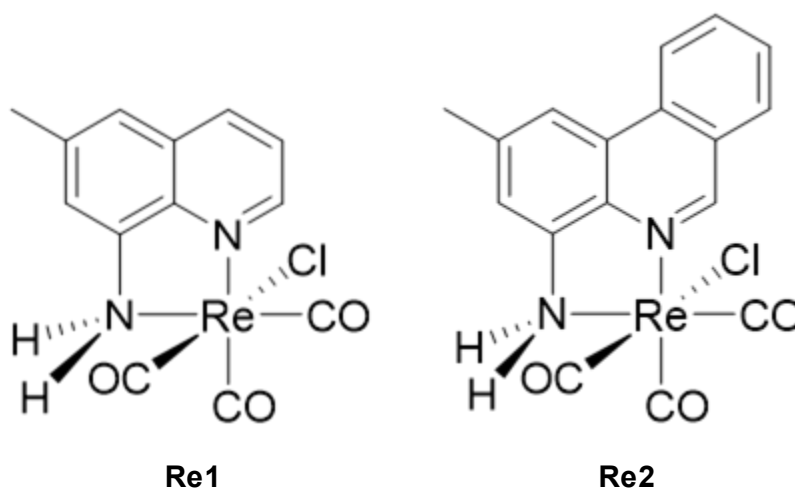
Figure 2.5. Re(I) complexes studied to investigate the impact of benzannulation on the optoelectronic properties of complexes.

Another unexpected result from benzannulation is exemplified by a collaborative project with Dr. Pavan Mandapati (Herbert Group). There, Pt(II) complexes supported by symmetric and asymmetric diarylamido ligands (Figure 2.3c) are presented. Two ligand designs are incorporated in the ligand scaffolds, namely, low-lying π^*-MOs introduced by phenanthridine and π-donor amido ligands that increases metal d-orbital energies leading to smaller HOMO-LUMO gap. The

π-donor properties of the amido donors lead to $d\pi$-$p\pi$ orbital mixing imparting increased covalency to the Pt–N$_{amide}$ bond. This is a collective effort within the group.

Our group has previously investigated a series of Pt(II) complexes that to date present some of the most red-shifted phosphorescence for non-porphyrinic Pt(II) complexes emitting from monomolecular excited states.[58] These complexes are based on anionic, tridentate pincer-like ligands, with the form ($N^\wedge N^-{}^\wedge N$)PtCl. We further extend our synthetic strategy and demonstrate how ligand substitution can be used to further tune the emission properties of a rare class of mononuclear Pt(II) deep red emitters (Figure 2.6).

Pt1 (R = CH$_3$)   **Pt2** (R^1 = CH$_3$, R^2 = CH$_3$)   **Pt3** (R^1 = CH$_3$, R^2 = CH$_3$)
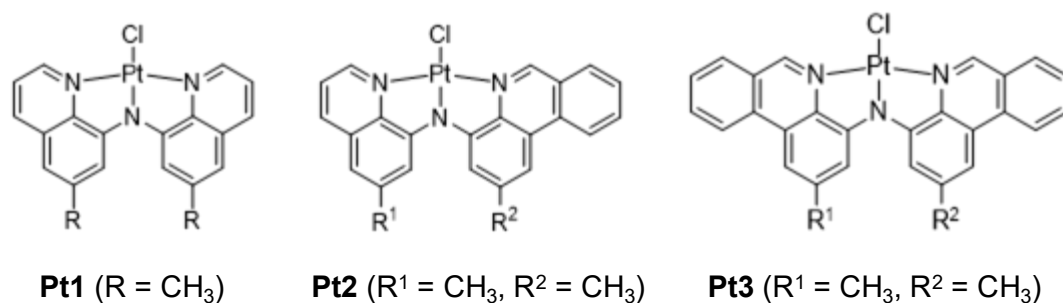
Figure 2.6. Pt(II) complexes supported by symmetric and asymmetric diarylamido ligands.

The Pt complexes are all dark red in colour. Accordingly, a broad and intense absorption band can be observed in each case, with a maximum at ~500 nm. Deprotonation of the amine N–H and chelation to a Lewis acidic Pt(II) centre thus increases the energy of the highest occupied orbitals and concomitantly stabilizes the heterocycle-based π* orbitals, displacing the lowest energy absorption band by ~5000 cm^{-1} compared with the proligands. The major difference between the phenanthridine-containing complexes (**Pt2** and **Pt3)** and the *bis*(quinoline) analogs

(**Pt1**) is the higher absorption of the former in the 300–350 nm region, as observed for the proligands. The identity of the substituents in the 2-position of the phenanthridine (or the 6-position of the quinoline) is seen to have minimal effect on the lowest-energy absorption band. As demonstrated for the methyl substituted analogs **Pt1**-**Pt2**, the main contributor to the lowest energy absorption is from the HOMO→LUMO+1 transition.[58] Population analysis of both these orbitals revealed only small contributions of the carbon at the site of substitution. Only a small shift to lower energy is observed for the lowest energy absorption in **Pt3** compared with **Pt2**.

The platinum complexes are emissive at room temperature in deoxygenated solution, with luminescence in the deep red/NIR that tails to 800–1000 nm. Each spectrum contains a relatively narrow, unstructured band (FWHM ~ 2300 cm^{-1}; FWHM = full-width at half maximum). In our initial study of the parent dimethyl complexes, we noted how emission from the *bis*(phenanthridine) complex **Pt3** is unequivocally higher in energy compared to that of the quinoline-containing complexes **Pt1** and **Pt2**, in spite of the greater conjugation of the phenanthridinyl-containing ligands.[58] We traced this to enhanced rigidity within the benzannulated phenanthridinyl systems, which results in a higher energy emissive triplet state.[60] The "mixed" system **Pt2** behaves like the *bis*(quinoline) **Pt1**, implying the emissive state in both primarily involves the quinoline. Extensive and detailed computational analyses are presented in Chapter 4.

2.3.3 More Pie! Fusing Benzannulated Acceptors and π-Donors in Ligands

As part of a collaborative effort between Dr. Jason Braun and I, we sought to understand the synergy in incorporating benzannulated phenanthridinyl moieties and the amido π-donors in

the diarylamido ligand scaffolds (Figure 2.7). Together with field experts at the Stanford Linear Accelerator Centre led by Prof. Kelly Gaffney, we provided experimental support to the initial computational studies in [Fe(N^N^N)$_2$]$^{0/+}$ (Figure 2.8) showing the mixing of the $N_{amido}(\pi)$ and Fe(II) d-orbitals with appropriate symmetry on the highest filled MOs of the complexes. This implies that the Fe–N_{amido} bond has increased covalent character in these complexes. The increased ligand contribution in the highest filled (dπ-pπ)* MOs or covalency contributes to the intense absorptions in the red region of the visible spectrum lending transitions in this region with π-antibonding-to-ligand charge-transfer character (PALCT). Covalency also tempers the weak field induced by π-donors leading to an overall destabilization of metal-centred states in these complexes.
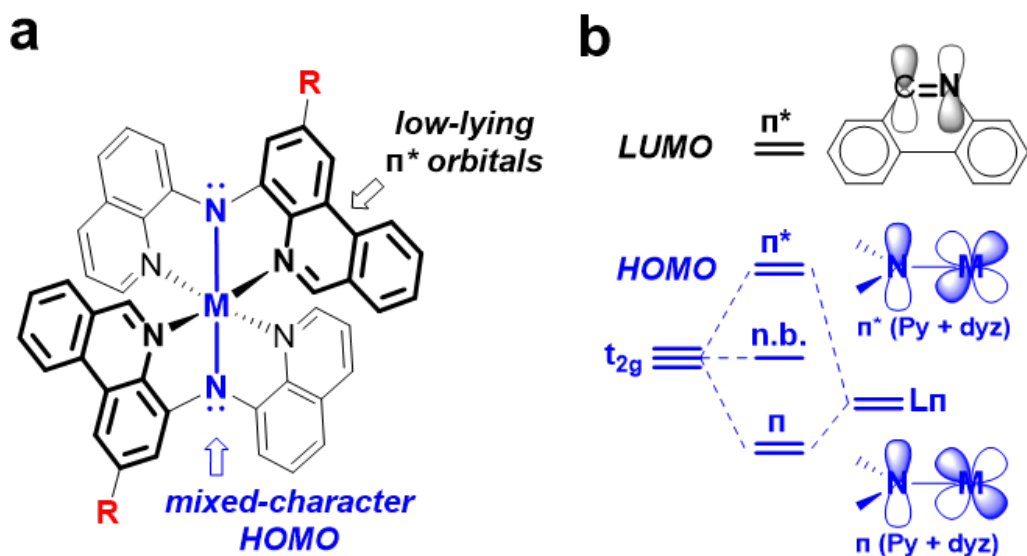
Figure 2.7. (a) Combining phenanthridine with amido π-donors in asymmetric diarylamido ligands and (b) illustration of the dπ-pπ mixing.

Fe1 (R = *t*Bu)
Fe2 (R = CF$_3$)
Fe3 (R = Cl)

Fe4 (R = *t*Bu)
Fe5 (R = CF$_3$)
Fe6 (R = Cl)
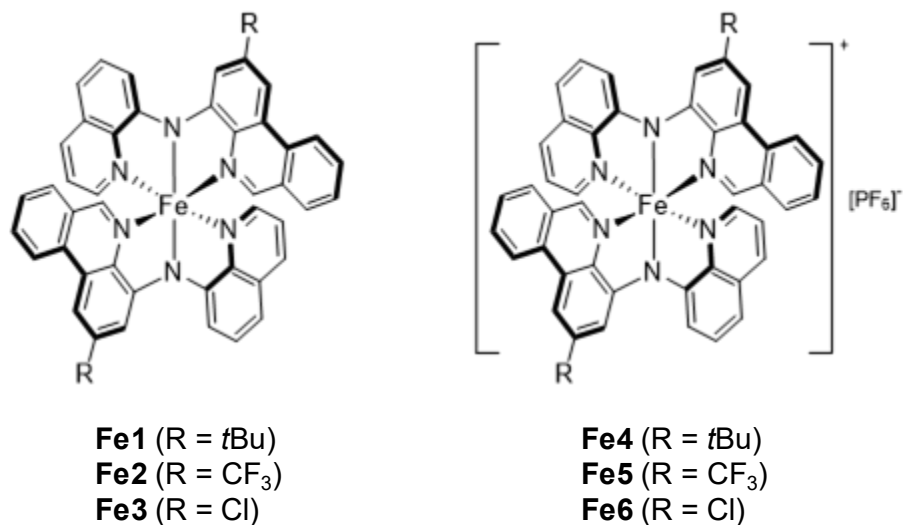
Figure 2.8. Asymmetric, homoleptic diarylamidoiron(II) complexes exhibiting panchromatic absorption.

To better understand the covalency in these complexes homoleptic pseudo-octahedral Co(III), d^6 electron count; Ni(II), d^8 electron count; Zn(II), d^{10} electron count; and Ga(III), d^{10} electron count, diarylamido complexes (Figure 2.9) were prepared. In this series, the complexes show interesting differences in their colors and therefore in their electronic absorption spectra. All are deeply colored thanks to the benzannulated ligand framework, but the metal identity strongly influences each absorption profile. When the central metal is Co(III), Ni(II) or Zn(II), the resultant complexes are dark red both as amorphous powders and crystalline solids. In acetonitrile solution, the compounds all show high molar absorptivities (ε ~20 000-30 000 M^{-1} cm^{-1}) for transitions in the visible range (~480-540 nm). The lowest energy absorptions for **Co1**, **Ni1** and **Zn1** are all relatively narrow bands (FWHM = ~3290 cm^{-1}), with maxima at ~500 nm. The λ_{max} for **Ga2** is blue-shifted (λ_{max} = 472 nm, ε = 17 220 M^{-1} cm^{-1}) and the complex is accordingly a lighter orange to the eye. The proligand is a yellow solid, with a narrow λ_{max} of 388 nm (ε value of ~ 12 270 M^{-1}

cm^{-1}). In contrast, **Fe1** is deep green, showing true panchromatic absorption with a broad and large absorptive cross-section spanning across the visible. Extending absorption of the solar spectra to 900 nm represents a doubling in both the number of harvestable photons and the theoretical incident photon-to-current efficiency when compared to dyes with absorption that attenuates at ~650 nm, underscoring the motivation to design such complexes.
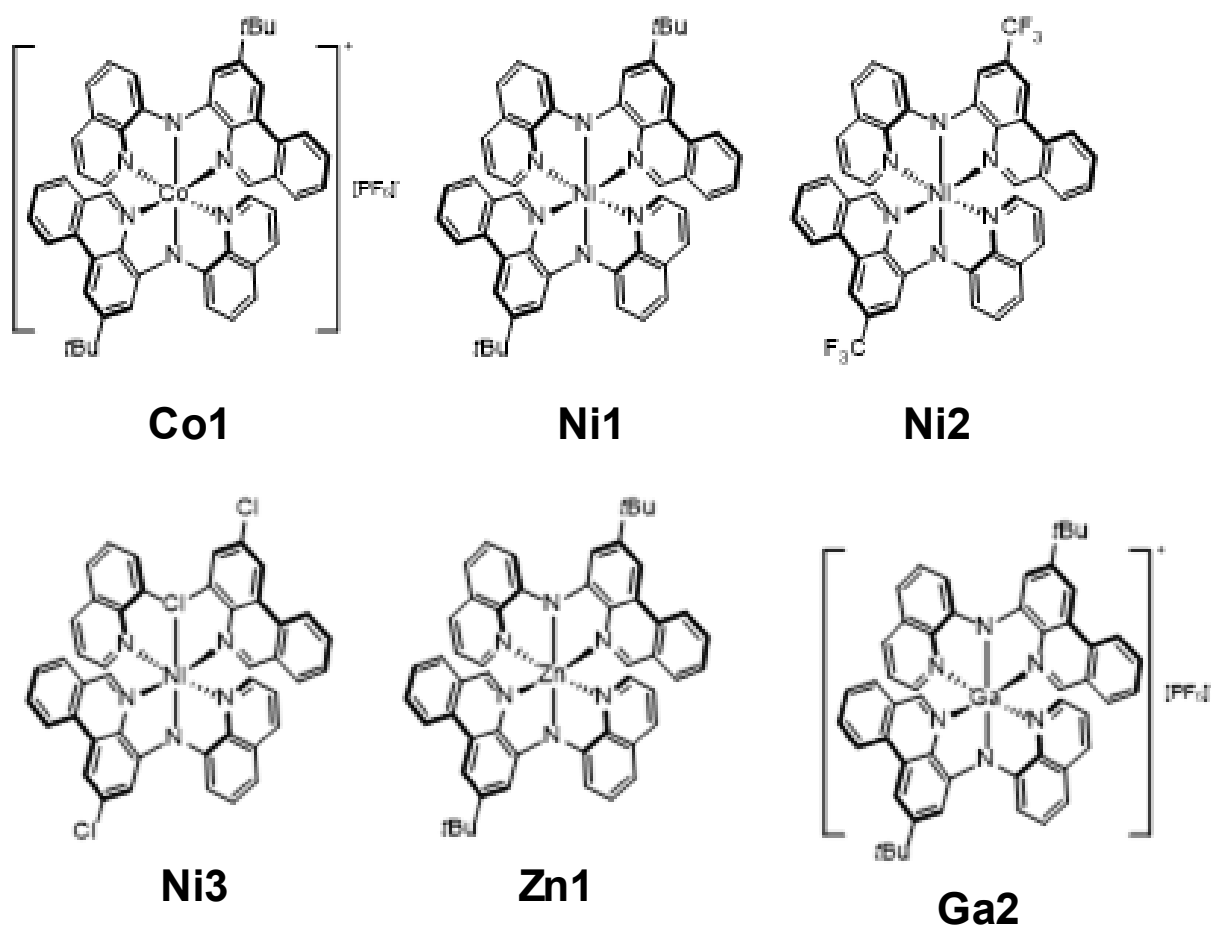
Figure 2.9. Molecular structures of Co(III), Ni(II), Zn(II) and Ga(III) diarylamido complexes.

Complexes **Co1**, **Ni1**, **Zn1** and **Ga1** show similar anodic redox behavior, with two closely spaced quasi-reversible or irreversible oxidation events observed at ~ -0.05 V vs FcH$^{0/+}$ for the neutral parent species and between 0.3-0.6 V for the monocations. In the context of the ligand

51

design, metal-N_{amido} dπ-pπ mixing stabilizes the radicals formed by these oxidations, and the events observed for [(^{tBu}L)$_2$Co][PF$_6$] (and (^{tBu}L)$_2$Fe[28]) are the most reversible within the series, consistent with the smallest amount of 'naked' aminyl radical character.[55] For the Co(III) species, an electrochemically reversible reduction is observed at -1.30 V. Ligand-based reduction events are also observed for all complexes close to the edge of the solvent window (CH$_3$CN, ~ -2.5 V), suggesting similar LUMO energies and implying that the metal-centre does not induce significant perturbations. The similarities in the electrochemical and optical properties of these complexes indicate that the dπ-pπ mixing on going to the right of iron diminishes owing to the increasing energy mismatch between the nominally metal t_{2g} orbitals relative to the $N_{amido}(\pi)$ MOs.

In our investigation, we additionally uncovered unusual behaviour in **Ni1-Ni3** complexes. All three complexes contain nickel in its +2-oxidation state implying a d^8 electron count. In an octahedral d^8 complex, the t_{2g} orbitals are fully occupied while each of the d-orbitals in the e_g manifold is singly occupied (SOMO) making the complexes paramagnetic. In contrast to the t_{2g} orbitals, the e_g set cannot form π-bonds owing to the symmetry mismatch between the interacting orbitals and thus is not expected to be perturbed by π-bonding. This electronic configuration implies that the nickel complexes have accessible d-electrons that should be readily removed upon oxidation, instead of the observed ligand-based oxidation. In addition, MLCT is anticipated to be the lowest energy transition in the optical spectra of nickel complexes, and thus is expected to have a different spectrum when compared with other complexes in Figure 2.9. Instead the nickel complexes exhibit ligand-centred $N_{amido}(\pi)$ oxidations and interligand CT (ILCT) transitions mirroring those found in **Zn1** and **Ga2**. This suggests a *non-Aufbau* behaviour in the nickel complexes. Similar non-Aufbau behaviour has been reported for vanadium porphyrinate and

phthalocyanines,[70] as well as for closely related pseudo-octahedral Ni complexes,[71] where the minimization of the spin-pairing energy favours removal of an electron from a lower-lying N_{amido} lone-pair orbital rather than from a higher energy metal-based SOMO.

2.3.4 Even More Pie: Switching Quinoline with More π-Donors

With encouraging results from our studies with diarylamido ligands, our group sought to expand our ligand set with different donor atoms. An interesting question arises by replacing the quinolinyl donor arm with a different donor atom, in particular with another donor atom that has π-donor abilities. According to ligand field theory, ligands with π-donor properties are considered weak field ligands owing to the smaller ligand field stabilization (10 Dq) it imparts to molecules. However, as seen in section 2.3.3, π-donors impart ligand character to the metal t_{2g} orbitals leading to increased M–L covalency. It is envisaged that by increasing the number of π-donors in a ligand scaffold the M–L covalency can be enhanced but at the same time will decrease 10 Dq. In this regard, I synthesized a series of 4-(4-enaminophenanthridinyl)-3-penten-2-ones incorporating both $N_{amido}(\pi)$ and $O(\pi)$ in β-ketoiminate scaffolds. The 4-aminophenanthridines are synthesised according to previously published protocols in our group.[58,72] Once in hand, the proligands were prepared via acid-catalyzed condensation of 4-aminophenanthridines with acetylacetone (Scheme 2.2). The electronic influence of the substituent in the 2 and/or 6-positions did not significantly influence the progress of the reaction as all proligands were isolated in similar yields (64-72%). All proligands were isolated with sufficient purity to be used without further purification.
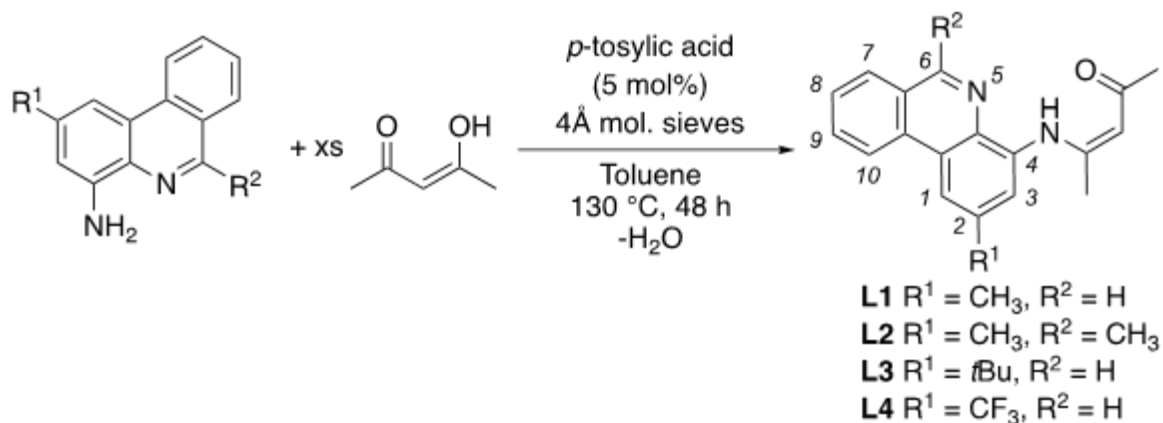
Scheme 2.2. Synthesis of *N*^*N*H^O ligands.

Single crystals of **L3** suitable for X-ray crystallography were grown from mixtures of diethylether and chloroform (Figure 2.10a). The structural metrics are consistent with a ketoenamine tautomer (Figure 2.10b, top). In particular, the solid-state structure revealed a short C(21)-O(1) bond distance of 1.244(3) Å. This assignment was corroborated by comparing solution NMR and IR parameters with related compounds.[21] Density functional theory (DFT; RIJCOSX-PBE0/def2-TZVP) predicted IR spectra of the optimized structures of **L3** and **L4** accordingly reproduce the two notable peaks observed experimentally between 1600-1550 cm^{-1}. The medium-strength, narrow peak at 1617 cm^{-1} (**L1**) and 1634 cm^{-1} (**L2**) is consistent with a C=O stretching mode, while the stronger absorption at 1570 cm^{-1} (**L1**) and 1579 cm^{-1} (**L2**) is attributed to an N-H bend. The presence of electron-releasing substituents in the 2-position (CH$_3$, **L1**; *t*Bu, **L3**) shifts the C=O stretching and N−H bending modes to lower energy in **L1** and **L3** compared with the electron-withdrawing CF$_3$ substituent in **L4** ($\nu_{C=O}$: 1617, 1617 and 1634 cm^{-1} and ν_{N-H}: 1569, 1570, and 1579 cm^{-1} for **L1**, **L3** and **L4** respectively).
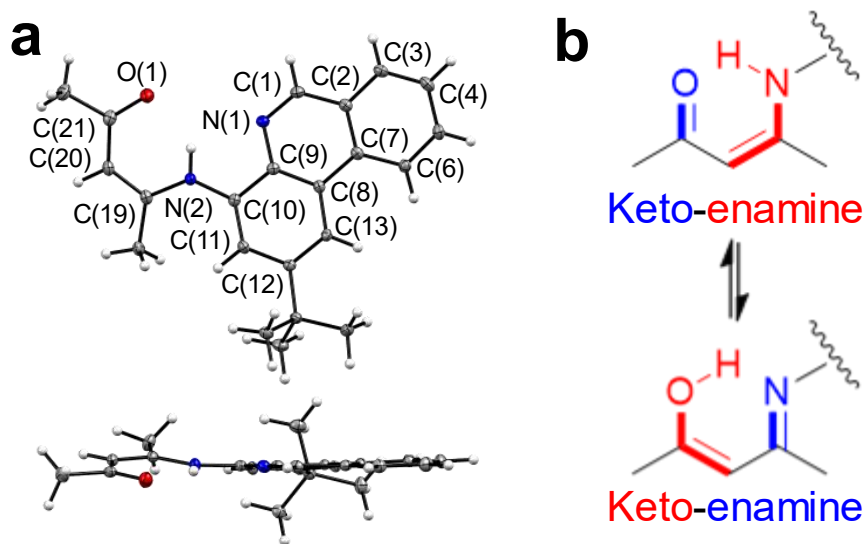
Figure 2.10. Two views of the solid-state structure of L3 with thermal ellipsoid shown at 30% probability levels. Selected bond distances (Å): C(1)-N(1) 1.303(3), C(9)-N(1) 1.380(3), C(8)-C(9) 1.410(3), C(7)-C(8) 1.451(3), C(1)-C(2) 1.423(3), C(2)-C(7) 1.411(3), C(10)-N(2) 1.396(3), C(19)-N(2) 1.363(3), C(19)-C(20) 1.370(3), C(20)-C(21) 1.433(3), C(21)-O(1) 1.244(3). (b) Canonical forms of the tautomers possible for L1-L4.

To probe the electronic structures of the new ligands, cyclic voltammetry (CV) and differential pulse voltammetry (DPV) were performed. Two irreversible oxidation events are apparent from the CV of the ligands and confirmed by DPV (Figure 2.11). The first oxidation event displays an apparent sensitivity of the ligand substitution, shifting cathodically with electron-releasing substituent. This event is ascribed to the removal of one electron in the $N_{amido}(\pi)$ orbital. In comparison to previously reported *N*-phenyl-4-amino-2-(*tert*-butyl)phenanthridine,[62] the first oxidation event in **L3**, appear at a much higher potential. This suggests that a greater delocalization of the $N_{amido}(\pi)$ orbitals is achieved by incorporation of 4-aminophenanthridines in β-ketoimines than in the *N*-phenyl derivatives. This stabilizes the $N_{amido}(\pi)$ orbitals and concomitantly shifting

the oxidation event to higher potentials. An opposite effect is observed in the single irreversible reduction event occurring at E vs FcH$^{0/+}$ < -2.2 V which is anodically shifted in **L4** compared with **L1-3** containing electron-releasing substituents. This implies that the CF$_3$ modestly stabilizes the phenanthridinyl vacant π^*-MO leading to the anodic shift. The separation of oxidation and reduction events, an experimental estimate to the HOMO-LUMO gap, remains relatively invariant in the series.
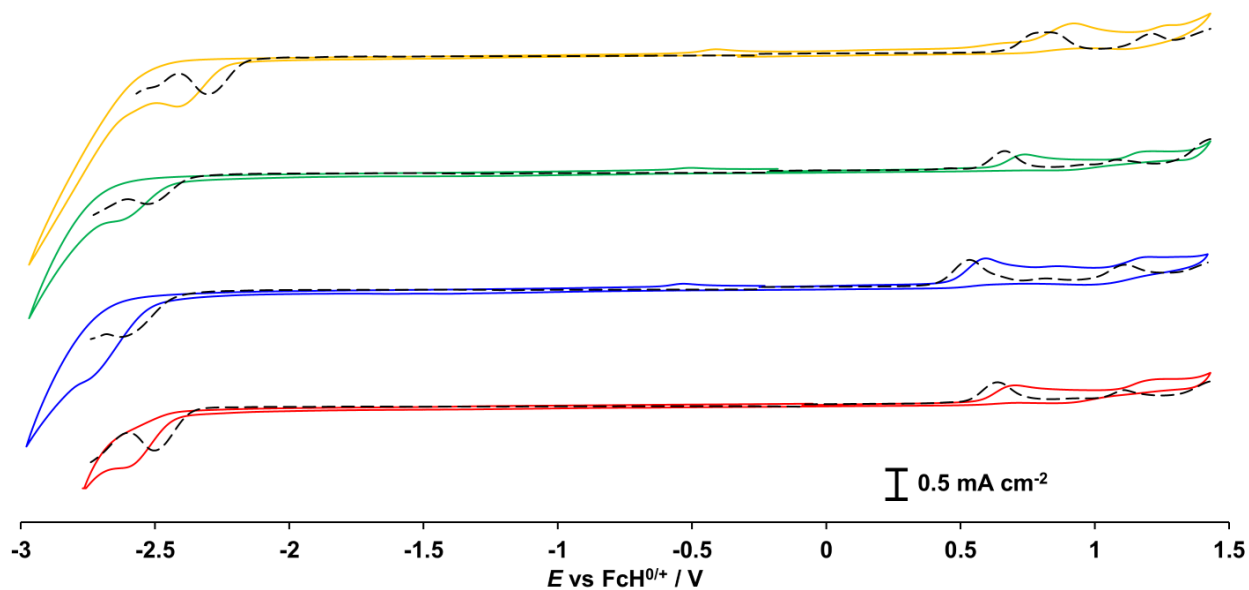
Figure 2.11. Cyclic voltammograms (—) and differential pulse voltammograms (---) of **L1**, **L2**, **L3** and **L4** in CH$_2$Cl$_2$ with 0.1 mM of [NBu$_4$][PF$_6$] as the supporting electrolyte, glassy carbon as the working electrode, and Pt wire as the counter electrodes. CV scan rates were 100 mV/s. Potentials are listed vs. FcH$^{0/+}$ redox couple (FcH = ferrocene).

A similar trend is observed in the absorption spectra of the ligands (Figure 2.12) wherein only a minor blue shift is observed on going from electron-releasing to electron-withdrawing substituents. All four ligands emit in the blue region of the visible spectrum and are weakly emissive in CH_2Cl_2 and EPA at 295 K and 77 K (Table 2.1), respectively. Additional long-lived (millisecond regime) components emerge at 77 K, and are assigned to originate from a triplet state.
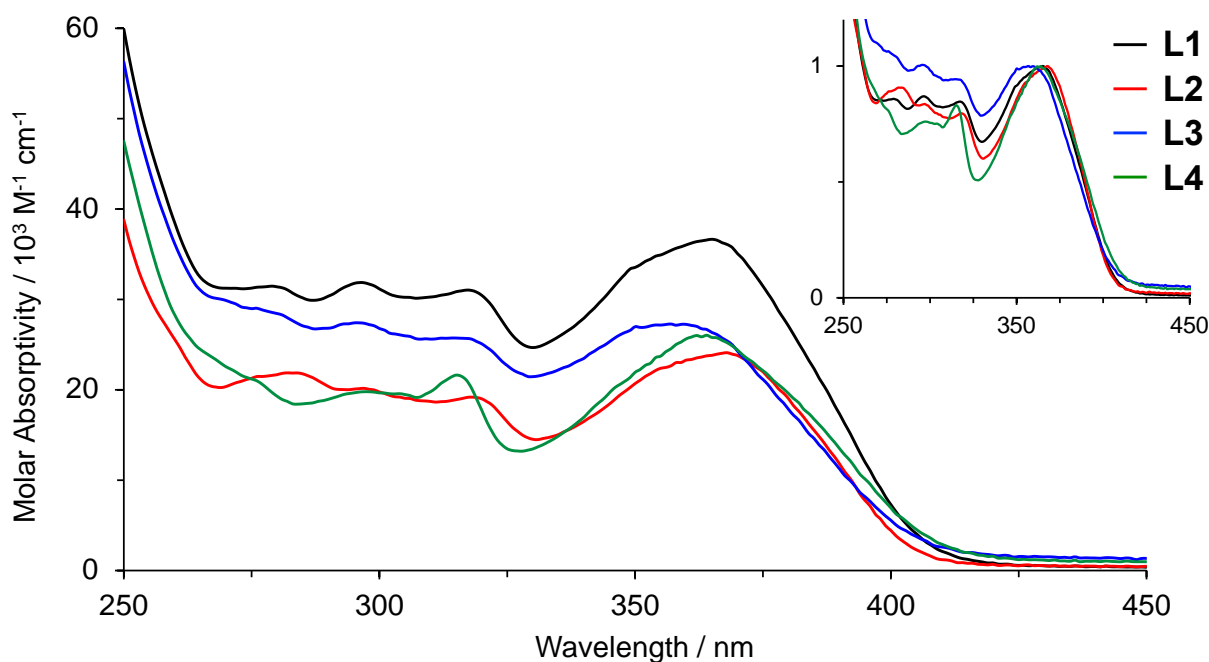
Figure 2.12. UV-Vis spectra of **L1-L4** in CH2Cl2 at 298 K. Inset shows normalized spectra.

Table 2.1. Emission data for the proligands.

Ligands	Emission in CH_2Cl_2 at 295 K			Emission in EPA at 77K[a]	
	λ_{max} / nm	Φ_F	τ / ns	λ_{max} / nm	τ
L1	480	0.008	1.9	402, 425 (F)	1.4 ns
				512, 555, 599 (P)	190 ms
L3	470	0.006	3.9	410, 419 (F)	1.3 ns
				498, 532 (P)	190 ms
L4	456	0.004	4.3, 1.0[b]	401, 421 (F)	1.2 ns
			(55:45)	507, 549 (P)	250 ms, 70 ms[b] (60:40)

[a] EPA = diethyl ether / isopentane / ethanol (2:2:1 v/v)
[b] The emission decay kinetics of this proligand did not fit well to a single exponential.

2.4 Experimental Details

2.4.1 Synthesis of 4-(4-Enamino-2-substitutedphenanthridinyl)-3-penten-2-one, L1-L4

General Considerations

Air-sensitive manipulations were carried out in an N_2-filled glove box or using standard Schlenk techniques under Ar. 4-Amino-2-methylphenanthrdine,[64] 4-amino-2,6-dimethylphenanthridine,[72] 4-amino-2-(*tert*-butyl)phenanthridine[73] and 4-amino-2-(trifluoromethyl)phenanthridine[73] were synthesized according to literature procedures. *P*-toluenesulfonic acid monohydrate (Sigma-Aldrich) and other common reagents were purchased from commercial suppliers and used without further purification. Organic solvents were dried and distilled using appropriate drying agents. 1- and 2D NMR spectra were recorded on a Bruker Avance 300 MHz spectrometer or a Bruker Avance 500 MHz spectrometer. ^1H and $^{13}C\{^1H\}$ NMR spectra were referenced to residual solvent peaks. High resolution mass spectra were recorded using a Bruker microOTOF-QIII. Attenuated total reflectance infrared spectroscopy (ATR-IR) was collected using a Bruker Invenio R FTIR or a Perkin Elmer Spectrum Two FTIR spectrometer. X-ray crystal structure data was using collected on a Bruker D8 QUEST ECO diffractometer from multi-faceted crystals of suitable size and quality selected from a representative sample of crystals of the same habit using an optical microscope. In each case, crystals were mounted on MiTiGen loops and data collection carried out in a cold stream of nitrogen (150 K; Mo Kα radiation). All diffractometer manipulations were carried out using Bruker APEX3 software.[74] Structure solution and refinement was carried out using XS, XT and XL software, embedded within OLEX2.[75] For each structure, the absence of

additional symmetry was confirmed using ADDSYM incorporated in the PLATON program.[76]

For electrochemical analysis, 5-10 mg of each compound was dissolved in 15 mL of 0.1 M

[nBu$_4$N][PF$_6$] in CH$_2$Cl$_2$. The measurements were performed on the solutions in an N$_2$-filled

glovebox using a CHI 760c bipotentiostat, a 3 mm diameter glassy carbon working electrode, a

Ag$^+$|Ag quasi-non-aqueous reference electrode separated by a Vycor tip, and a Pt wire counter

electrode. Cyclic voltammetry was conducted using a scan rate of 100 mV/s. Upon completion,

ferrocene (FcH) was added to the solution as an internal standard, and all potentials are reported

versus the FcH$^+$|FcH redox couple.

4-(4-Enamino-2-methylphenanthridinyl)-3-penten-2-one (L1): A
Teflon-stoppered flask was charged with (4-amino-2-
methyl)phenanthridine (1.00 g, 4.80 mmol), acetylacetone (1.5 mL, 15
mmol), 4-toluenesulfonic acid monohydrate (0.0459 g, 0.241 mmol)
and 4 Å molecular sieves (7 g). The mixture was sealed and stirred at
reflux for 48 h in an oil bath set to 130 °C. The reaction mixture was
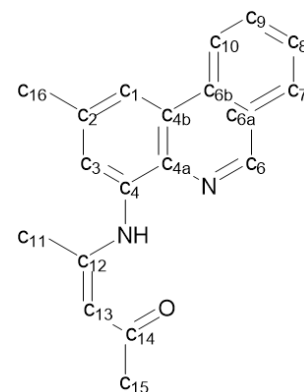
cooled and filtered, and the filtrate concentrated to give a dark brown viscous oil. The product was

precipitated as a brown solid by addition of diisopropylether (20 mL) and isolated by filtration,

giving a spectroscopically pure product which could be used without further purification. Isolated

yield = 1.00 g (72 %). ^{1}H NMR (CDCl$_3$, 300 MHz, 25 °C): δ 13.53 (b s, 1H; NH), 9.29 (s, 1H;

C$_6H$), 8.55 (d, $^3J_{HH}$ = 8.2 Hz, 1H; C$_{10}H$), 8.06 (s, 1H; C$_1H$), 8.04 (dd, $^3J_{HH}$ = 8.1 Hz, $^4J_{HH}$ = 0.6 Hz,

1H; C$_7H$), 7.69 (m, 1H; C$_8H$), 7.83 (m, 1H; C$_9H$), 7.34 (d, $^4J_{HH}$ = 1.1 Hz, 1H; C$_3H$), 5.33 (s, 1H;

C$_{13}H$), 2.59 (s, 3H; C$_{16}H$), 2.26 (s, 3H; C$_{11}H$), 1.18 ppm (s, 9H; C$_{15}H$). ^{13}C{^{1}H} NMR (CDCl$_3$, 75

MHz, 25 °C): δ 196.4 (C_{14}), 158.2 (C_{12}), 151.9 (C_6), 137.2 (C_4), 136.7 (C_{4a}), 135.7 (C_2), 132.2

(C_{4b}), 130.9 (C_9), 128.9 (C_7), 127.7 (C_8), 126.8 (C_{6a}), 124.8 (C_{6b}), 122.2 (C_{10}), 121.6 (C_3), 117.5

(C_1), 100.1 (C_{13}), 29.6 (C_{15}), 22.6 (C_{16}), 21.4 ppm (C_{11}). IR (ATR): ν_{max} 3100-2800 (C-H stretch,

broad, w), 1617 (C=O stretch, sharp, m), 1569 cm^{-1} (N-H bend, sharp, s). HRMS (APCI-TOF)

m/z: [M + H]$^+$ calcd for [$C_{19}H_{18}N_2O$]$^+$ 291.1942; Found 291.1493.

4-(2,6-Dimethyl-4-enaminophenanthridinyl)-3-penten-2-one

(**L2**): The above procedure was followed using 2,6-dimethyl-4-
aminophenanthridine (1.00 g, 4.50 mmol), acetylacetone (1.4 mL,
14 mmol), 4-toluenesulfonic acid monohydrate (0.0470 g, 0.247
mmol), and 4 Å molecular sieves (7 g) in toluene (10 mL). Brown
solid. Isolated yield = 0.929 g (68 %). ^{1}H NMR (CDCl$_3$, 300 MHz,
25 °C): δ 13.59 (b s, 1H; NH), 8.50 (d, $^3J_{HH}$ = 8.2Hz, 1H; C$_{10}H$),
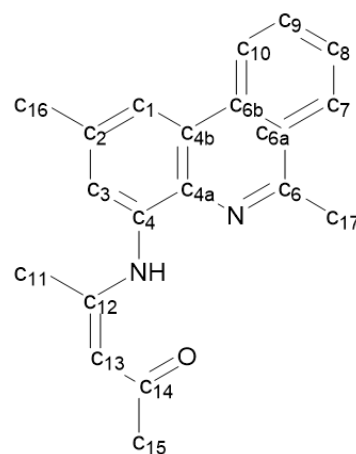
8.15 (dd, $^3J_{HH}$ = 8.3Hz, $^4J_{HH}$ = 0.8 Hz, 1H; C$_7H$), 7.92 (s, 1H; C$_1H$), 7.75 (m, 1H; C$_9H$), 7.63 (m,

1H; C$_8H$), 7.329 (d, $^4J_{HH}$ = 1.1Hz, 1H; C$_3H$), 5.33 (s, 1H; C$_{13}H$), 3.08 (s, 3H; C$_{17}H$), 2.52 (s, 3H;

C$_{16}H$), 2.29 (s, 3H; C$_{11}H$), 2.17 ppm (s, 3H; C$_{15}H$). ^{13}C{^{1}H} NMR (CDCl$_3$, 75 MHz, 25 °C): 196.0

(C_{14}), 157.4 (C_{12}), 157.0 (C_6), 136.7 (C_2), 135.6 (C_{4b}), 133.6 (C_4), 132.1 (C_{6a}), 130.3 (C_8), 127.4

(C_9), 126.6 (C_7), 126.2 (C_{6b}), 124.2 (C_{4a}), 122.6 (C_{10}), 119.9 (C_3), 116.6 (C_1), 100.4 (C_{13}), 29.7

(C_{15}), 23.9 (C_{17}), 22.6 (C_{16}), 21.8 (C_{11}). IR (ATR): ν_{max} 3100-2800 (C-H stretch, broad, w), 1615

(C=O stretch, narrow, m), 1569 cm^{-1} (N-H bend, narrow, s). HRMS (APCI-TOF) m/z: [M + H]$^+$

calcd for [$C_{20}H_{20}N_2O$]$^+$ 305.1648; Found 305.1644.

Synthesis of *t*Bu-phenanthridine-nacac proligand (L3): A Teflon-stoppered flask was charged with 4-amino-(2-*tert*-butyl)phenanthridine (1.01 g, 3.03 mmol), acetylacetone (1.30 mL, 12.7 mmol), *p*-tosic acid (0.050 g, 0.27 mmol), toluene (10 mL) and 4 Å molecular sieves. The reaction was heated to reflux for 48 h, then cooled to room temperature and filtered over Celite. The solvent was then evaporated to leave an oily dark brown residue, which was redissolved in a minimal amount of CH_2Cl_2 and passed through a short plug of silica. The solvent was evaporated to isolate a beige solid. Yield = 0.858 g (64%). ^{1}H NMR (CDCl$_3$, 300 MHz, 22 °C): δ 13.44 (s, 1H; N*H*), 9.31 (s, 1H; C$_6$-*H*), 8.63 (d, J_{HH} = 8.3 Hz, 1H; C$_{10}$-*H*), 8.32 (d, J_{HH} = 1.9 Hz, 1H; C$_1$-*H*), 8.06 (d, J_{HH} = 7.3 Hz, 1H; C$_7$-*H*), 7.86 (ddd, J_{HH} = 1.3 Hz, 7.7 Hz, 8.5 Hz, 1H; C$_8$-*H*), 7.71 (ddd overlapped, J_{HH} = 0.9 Hz, 7.5 Hz, 8.5 Hz, 1H; C$_9$-*H*), 7.60 (d, J_{HH} = 1.9 Hz, 1H; C$_3$-*H*), 5.35 (s, 1H; C$_{13}$-*H*), 2.23 (s, 3H; C$_{11}$-*H*), 2.18 (s, 3H; C$_{15}$-*H*), 1.49 ppm (s, 9H; C$_{17}$-*H*). ^{13}C{^{1}H} NMR (CDCl$_3$, 75 MHz, 22 °C): δ 196.33 (C$_{14}$), 158.65 (C$_{12}$), 152.42 (C$_6$), 149.74 (C$_2$), 136.91 (C$_4$), 136.12 (C$_{4a}$), 132.74 (C$_{4b}$), 130.97 (C$_8$), 129.06 (C$_7$), 127.65 (C$_9$), 126.83 (C$_{6a}$), 124.39 (C$_{6b}$), 122.16 (C$_{10}$), 119.68 (C$_3$), 113.88 (C$_1$), 99.74 (C$_{13}$), 35.46 (C$_{16}$), 31.57 (C$_{17}$), 29.54 (C$_{15}$), 21.09 ppm (C$_{13}$). IR (ATR): ν_{max} 3100-2800 (C-H stretch, b, w), 1617 (C=O stretch, n, m), 1570 cm^{-1} (N-H bend, n, s).
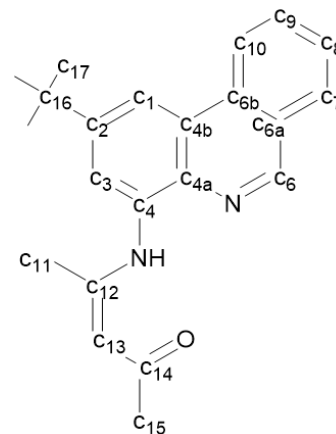
Synthesis of CF₃-phenanthridine-nacac proligand (L4): An identical procedure to the synthesis of **L1** was followed using 4-amino-(2-trifluoromethyl)phenanthridine (1.09 g, 3.15 mmol), acetylacetone (1.30 mL, 12.7 mmol), *p*-tosic acid (0.040 g, 0.23 mmol), toluene (10 mL), and 4 Å molecular sieves. **L4** was isolated as an off-white solid. Yield = 0.911 g (64%). ^{1}H NMR (CDCl₃, 300 MHz, 22 °C): δ 13.72 (s, 1H; N*H*), 9.44 (s, 1H; C_6-*H*), 8.60 (d, J_{HH} = 8.3 Hz, 1H; C_{10}-*H*), 8.49 (s, 1H; C_1-*H*), 8.12 (d, J_{HH} = 7.9 H, 1H; C_7-*H*), 7.93 (ddd, J_{HH} = 1.2 Hz, 7.7 Hz, 8.7 Hz, 1H; C_8-*H*), 7.79 (ddd overlapped, J_{HH} = 0.8 Hz, 7.5 Hz, 8.7 Hz, 1H; C_9-*H*), 7.68 (d, J_{HH} = 1.4 Hz, 1H; C_3-*H*), 5.41 (s, 1H; C_{13}-*H*), 2.36 (s, 3H; C_{11}-*H*), 2.21 ppm (s, 3H; C_{15}-*H*). ^{13}C{^{1}H} NMR (CDCl₃, 75 MHz, 22 °C): δ 197.22 (C_{14}), 156.59 (C_{12}), 154.58 (C_6), 138.73 (C_4), 137.90 (C_2), 132.34 (C_{6a}), 131.90 (C_8), 129.32 (C_7), 128.73 (C_9), 126.91 (C_{6b}), 124.71 (C_{4a}), 122.47 (C_{4b}), 122.34 (C_{10}), 114.08 (q overlapped, C_1), 113.94 (q overlapped, C_3), 101.79 (C_{13}), 29.84 (C_{15}), 21.59 ppm (C_{11}), C_{11} - not observed. ^{19}F NMR (CDCl₃, 470 MHz, 22 °C): δ -62.25 ppm. IR (ATR): ν_{max} 3100-2800 (C-H stretch, b, w), 1634 (C=O stretch, n, s), 1579 cm^{-1} (N-H bend, n, s).
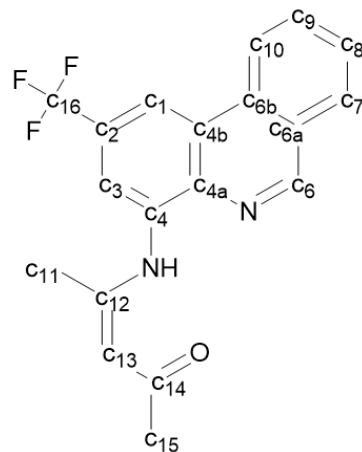
2.4.2 UV-Vis Absorption and Luminescence Experiments

Absorption spectra were measured on a Biotek Instruments XS spectrometer, using quartz cuvettes of 1 cm pathlength. Steady-state luminescence spectra were measured using a Jobin Yvon FluoroMax-2 spectrofluorimeter, fitted with a red-sensitive Hamamatsu R928 photomultiplier tube; the spectra shown are corrected for the wavelength dependence of the detector, and the quoted emission maxima refer to the values after correction. Degassed samples for emission

measurements were contained within quartz cuvettes of 1 cm pathlength modified with appropriate glassware to allow connection to a high-vacuum line. Degassing was achieved via a minimum of three freeze-pump-thaw cycles whilst connected to the vacuum manifold.

2.4.3 Computational Details

DFT calculations were performed using ORCA version 4.1.2.[28] Tight convergence criteria (TightSCF and TightOpt) were used and the SCF and energy integration grids were set to 4 and 5, respectively (Grid4 Finalgrid5). The ligands were optimized in the gas phase using the PBE0 functional[29, 30] and the def2-TZVP basis set[31] on all atoms using the crystal structure coordinates of **L1** as starting input. The resolution of identity (split-RI-J) with chain-of-spheres approximation (RIJCOSX) was employed to speed up the calculation (Intaccx: 4.01, 4.01, 4.34; Gridx: 1, 1, 2). Frequency analyses were subsequently performed to confirm all structures were at a minimum on the ground state potential energy surface, and to interpret experimental IR spectra.

Conclusions

This chapter presents the principles behind the design and synthesis of various multidentate, phenanthridine-based ligands. Some unexpected results emerged from the optical and photophysical properties of Fe(II), Re(I) and Ru(II) complexes with quinoline- and phenanthridine-based ligands.

Combining lower energy vacant MOs with amido π-donors in ligand scaffolds led to the panchromatic absorption in iron(II) complexes and increases the covalency. The increased in covalency tempers the weak field induced by the amido π-donors stabilizing the PALCT state. In addition, the d_π-p_π mixing can be controlled by varying the metal centre; here, the mixing decreases

on going to the right of iron, as the energy mismatch of the participating metal d- and ligand N_{amido} lone pair orbitals becomes more pronounced.

Encouraged bythe results in the pincert-type diarylamido ligands, new tridentate ligands based on the $N^\wedge N$(H)$^\wedge O$ motif were synthesized and characterized. Spectroscopic analyses of the ligands reveal the keto-enamine tautomer as the predominant tautomer both in solid state and in solution.

References

(1)   Faraday, M. On New Compounds of Carbon and Hydrogen, and on Certain Other Products Obtained during the Decomposition of Oil by Heatrstl.1825.Pdf. *Philos. Trans. R. Soc.* **1825**, *115*, 440–466.

(2)   Heo, I.; Lee, J. C.; Özer, B. R.; Schultz, T. Mass-Correlated High-Resolution Spectra and the Structure of Benzene. *J. Phys. Chem. Lett.* **2022**, *13* (35), 8278–8283. https://doi.org/10.1021/acs.jpclett.2c02035.

(3)   Kunishige, S.; Katori, T.; Baba, M.; Nakajima, M.; Endo, Y. Spectroscopic Study on Deuterated Benzenes. I. Microwave Spectra and Molecular Structure in the Ground State. *J. Chem. Phys.* **2015**, *143* (24), 244302. https://doi.org/10.1063/1.4937949.

(4)   Watson, M. D.; Fechtenkötter, A.; Müllen, K. Big Is Beautiful−"Aromaticity" Revisited from the Viewpoint of Macromolecular and Supramolecular Benzene Chemistry. *Chem. Rev.* **2001**, *101* (5), 1267–1300. https://doi.org/10.1021/cr990322p.

(5)   Vij, V.; Bhalla, V.; Kumar, M. Hexaarylbenzene: Evolution of Properties and Applications of Multitalented Scaffold. *Chem. Rev.* **2016**, *116* (16), 9565–9627. https://doi.org/10.1021/acs.chemrev.6b00144.

(6)   Price, C. C. Substitution and Orientation in the Benzene Ring. *Chem. Rev.* **1941**, *29* (1), 37–67. https://doi.org/10.1021/cr60092a002.

(7)   Papadakis, R.; Ottosson, H. The Excited State Antiaromatic Benzene Ring: A Molecular Mr Hyde? *Chem. Soc. Rev.* **2015**, *44* (18), 6472–6493. https://doi.org/10.1039/C5CS00057B.

(8)   Swami, B.; Yadav, D.; Menon, R. S. Benzannulation Reactions: A Case for Perspective Change From Arene Decoration to Arene Construction. *Chem. Rec.* **2022**, *22* (1), e202100249. https://doi.org/10.1002/tcr.202100249.

(9)   Hart-Davis, A. J.; White, C.; Mawby, F. J. Reactions Of-WIndeny Complexes of Transition Metals. III.' Kinetics and Mechanisms of Substitution Reactions of Tricarbonyl-Mindenylhalomolybdenum(II) Complexes. 6.

(10)   Rerek, M. E.; Basolo, F. Kinetics and Mechanism of Substitution Reactions of .Eta.5-Cyclopentadienyldicarbonylrhodium(I) Derivatives. Rate Enhancement of Associative Substitution in Cyclopentadienylmetal Compounds. *J. Am. Chem. Soc.* **1984**, *106* (20), 5908–5912. https://doi.org/10.1021/ja00332a026.

(11) Rerek, M. E.; Ji, L.-N.; Basolo, F. The Lndenyl Ligand Effect on the Rate of Substitution Reactions of Rh(Rl-C9H7)C(O), and Mn(Rl -CgH7)C(O)a. 2.

(12) Okada, Y.; Miyamoto, N.; Hishimoto, M.; Hayashi, T. Studies on Ferrocene Derivatives. Part XIII. Ligand Exchange Reactions of Benzoferrocenes. *Transit. Met Chem* **1999**, 5.

(13) Treichel, P. M.; Johnson, J. W.; Wagner, K. P. OXIDATIONS OF VARIOUS INDENYL-IRON. 4.

(14) Crossley, N. S.; Green, J. C.; Nagy, A.; Stringer, G. Electronic Structure of Transition-Metal Lndenyl Compounds: A He I and He I I Photoelectron Spectroscopic Study of [Mn(Q5-C,H7)(CO),], [Fe(Q5-CgH7),]. Ru(Q5-C9H7)21 and Ru(T5-C9H7)(q-C5Me5) I t. *J CHEM SOC DALTON TRANS* **1989**, 9.

(15) Brady, E. D.; Overby, J. S.; Meredith, M. B.; Mussman, A. B.; Cohn, M. A.; Hanusa, T. P.; Yee, G. T.; Pink, M. Spin-State Alteration from Sterically Enforced Ligand Rotation in Bis(Indenyl)Chromium(II) Complexes [1]. *J. Am. Chem. Soc.* **2002**, *124* (32), 9556–9566. https://doi.org/10.1021/ja012390a.

(16) Shimizu, A.; Ishizaki, Y.; Horiuchi, S.; Hirose, T.; Matsuda, K.; Sato, H.; Yoshida, J. HOMO–LUMO Energy-Gap Tuning of π-Conjugated Zwitterions Composed of Electron-Donating Anion and Electron-Accepting Cation. *J. Org. Chem.* **2021**, *86* (1), 770–781. https://doi.org/10.1021/acs.joc.0c02343.

(17) Hanson, K.; Roskop, L.; Djurovich, P. I.; Zahariev, F.; Gordon, M. S.; Thompson, M. E. A Paradigm for Blue- or Red-Shifted Absorption of Small Molecules Depending on the Site of π-Extension. *J. Am. Chem. Soc.* **2010**, *132* (45), 16247–16255. https://doi.org/10.1021/ja1075162.

(18) Liu, B.; Lystrom, L.; Kilina, S.; Sun, W. Effects of Varying the Benzannulation Site and π Conjugation of the Cyclometalating Ligand on the Photophysics and Reverse Saturable Absorption of Monocationic Iridium(III) Complexes. *Inorg. Chem.* **2019**, *58* (1), 476–488. https://doi.org/10.1021/acs.inorgchem.8b02714.

(19) Liu, B.; Lystrom, L.; Brown, S. L.; Hobbie, E. K.; Kilina, S.; Sun, W. Impact of Benzannulation Site at the Diimine (N^N) Ligand on the Excited-State Properties and Reverse Saturable Absorption of Biscyclometallated Iridium(III) Complexes. *Inorg. Chem.* **2019**, *58* (9), 5483–5493. https://doi.org/10.1021/acs.inorgchem.8b03162.

(20) Wang, L.; Yin, H.; Jabed, M. A.; Hetu, M.; Wang, C.; Monro, S.; Zhu, X.; Kilina, S.; McFarland, S. A.; Sun, W. π-Expansive Heteroleptic Ruthenium(II) Complexes as Reverse Saturable Absorbers and Photosensitizers for Photodynamic Therapy. *Inorg. Chem.* **2017**, *56* (6), 3245–3259. https://doi.org/10.1021/acs.inorgchem.6b02624.

(21) Chen, T.; Li, M.; Liu, J. π–π Stacking Interaction: A Nondestructive and Facile Means in Material Engineering for Bioapplications. *Cryst. Growth Des.* **2018**, *18* (5), 2765–2783. https://doi.org/10.1021/acs.cgd.7b01503.

(22) Sinnokrot, M. O.; Valeev, E. F.; Sherrill, C. D. Estimates of the Ab Initio Limit for Π−π Interactions: The Benzene Dimer. *J. Am. Chem. Soc.* **2002**, *124* (36), 10887–10893. https://doi.org/10.1021/ja025896h.

(23) Cai, M.; Song, X.; Zhang, D.; Qiao, J.; Duan, L. π–π Stacking: A Strategy to Improve the Electron Mobilities of Bipolar Hosts for TADF and Phosphorescent Devices with Low Efficiency Roll-Off. *J. Mater. Chem. C* **2017**, *5* (13), 3372–3381. https://doi.org/10.1039/C7TC00733G.

(24) Hong, Y.; Lam, J. W. Y.; Tang, B. Z. Aggregation-Induced Emission: Phenomenon, Mechanism and Applications. *Chem. Commun.* **2009**, No. 29, 4332. https://doi.org/10.1039/b904665h.

(25) McGaughey, G. B.; Gagné, M.; Rappé, A. K. π-Stacking Interactions. *J. Biol. Chem.* **1998**, *273* (25), 15458–15463. https://doi.org/10.1074/jbc.273.25.15458.

(26) Babine, R. E.; Bender, S. L. Molecular Recognition of Protein−Ligand Complexes: Applications to Drug Design. *Chem. Rev.* **1997**, *97* (5), 1359–1472. https://doi.org/10.1021/cr960370z.

(27) Pages, B. J.; Garbutcheon-Singh, K. B.; Aldrich-Wright, J. R. Platinum Intercalators of DNA as Anticancer Agents. *Eur. J. Inorg. Chem.* **2017**, *2017* (12), 1613–1624. https://doi.org/10.1002/ejic.201601204.

(28) Hayashi, K.; Nakatani, M.; Hayashi, A.; Takano, M.; Okazaki, M.; Toyota, K.; Yoshifuji, M.; Ozawa, F. Synthesis and Structures of Platinum(0) Alkyne Complexes with Extended π-Conjugated Systems. *Organometallics* **2008**, *27* (9), 1970–1972. https://doi.org/10.1021/om800163p.

(29) Flamigni, L.; Encinas, S.; Barigelletti, F.; MacDonnell, F. M.; Kim, K.-J.; Puntoriero, F.; Campagna, S. Excited-State Interconversion between Emissive MLCT Levels in a Dinuclear Ru(Ii) Complex Containing a Bridging Ligand with an Extended π System. *Chem. Commun.* **2000**, No. 13, 1185–1186. https://doi.org/10.1039/b004109m.

(30) Roznyatovskiy, V. V.; Lee, C.-H.; Sessler, J. L. π-Extended Isomeric and Expanded Porphyrins. *Chem Soc Rev* **2013**, *42* (5), 1921–1933. https://doi.org/10.1039/C2CS35418G.

(31) Barbon, S. M.; Staroverov, V. N.; Gilroy, J. B. Effect of Extended π Conjugation on the Spectroscopic and Electrochemical Properties of Boron Difluoride Formazanate Complexes. *J. Org. Chem.* **2015**, *80* (10), 5226–5235. https://doi.org/10.1021/acs.joc.5b00620.

(32) Kappaun, S.; Rentenberger, S.; Pogantsch, A.; Zojer, E.; Mereiter, K.; Trimmel, G.; Saf, R.; Möller, K. C.; Stelzer, F.; Slugovc, C. Organoboron Quinolinolates with Extended Conjugated Chromophores: Synthesis, Structure, and Electronic and Electroluminescent Properties. *Chem. Mater.* **2006**, *18* (15), 3539–3547. https://doi.org/10.1021/cm060720q.

(33) Kiprof, P.; Carlson, J. C.; Anderson, D. R.; Nemykin, V. N. Systematic Color Tuning of a Family of Luminescent Azole-Based Organoboron Compounds Suitable for OLED Applications. *Dalton Trans.* **2013**, *42* (42), 15120. https://doi.org/10.1039/c3dt51853a.

(34) Bossi, A.; Rausch, A. F.; Leitl, M. J.; Czerwieniec, R.; Whited, M. T.; Djurovich, P. I.; Yersin, H.; Thompson, M. E. Photophysical Properties of Cyclometallated Pt(II) Complexes: Counterintuitive Blue Shift in Emission with an Expanded Ligand π System. *Inorg. Chem.* **2013**, *52* (21), 12403–12415. https://doi.org/10.1021/ic4011532.

(35) Gunanathan, C.; Gnanaprakasam, B.; Iron, M. A.; Shimon, L. J. W.; Milstein, D. "Long-Range" Metal−Ligand Cooperation in H_2 Activation and Ammonia-Promoted Hydride Transfer with a Ruthenium−Acridine Pincer Complex. *J. Am. Chem. Soc.* **2010**, *132* (42), 14763–14765. https://doi.org/10.1021/ja107770y.

(36) Neufeldt, S. R.; Sanford, M. S. Controlling Site Selectivity in Palladium-Catalyzed C–H Bond Functionalization. *Acc. Chem. Res.* **2012**, *45* (6), 936–946. https://doi.org/10.1021/ar300014f.

(37) Krichevsky, O.; Bonnet, Gregoire. Fluorescence Correlation Spectroscopy: The Technique and Its Applications. *Rep. Prog. Phys.* **2002**, *65* (2), 251–297. https://doi.org/10.1088/0034-4885/65/2/203.

(38) Tumir, L.-M.; Stojkovic, M. R.; Piantanida, I. Come-Back of Phenanthridine and Phenanthridinium Derivatives in the 21st Century. *Beilstein J Org Chem* **2014**, *10*, 2930–2954.

(39) Park, G. Y.; Wilson, J. J.; Song, Y.; Lippard, S. J. Phenanthriplatin, a Monofunctional DNA-Binding Platinum Anticancer Drug Candidate with Unusual Potency and Cellular Activity Profile. *Proc Natl Acad Sci* **2012**, *109*, 11987–11992.

(40) Lu, L.-Q.; Li, Y.; Junge, K.; Beller, Matthias. Iron-Catalyzed Hydrogenation for the In Situ Regeneration of an NAD(P)H Model: Biomimetic Reduction of α-Keto-/α-Iminoesters. *Angew. Chem. Int. Ed.* **2013**, *52* (32), 8382–8386. https://doi.org/10.1002/anie.201301972.

(41) Chen, Q.-A.; Gao, K.; Duan, Y.; Ye, Z.-S.; Shi, L.; Yang, Y.; Zhou, Y.-Gui. Dihydrophenanthridine: A New and Easily Regenerable NAD(P)H Model for Biomimetic Asymmetric Hydrogenation. *J. Am. Chem. Soc.* **2012**, *134* (4), 2442–2448. https://doi.org/10.1021/ja211684v.

(42) Jensen, K. A.; Nielsen, P. Halfdan. Chelates with Heterocyclic Ligands. I. Chelates Derived from e N,N'-Bis(8-Quinolyl)Ethylenediamine and Analogous Compounds. *Acta Chem. Scand. 1947-1973* **1964**, *18* (1), 1–10. https://doi.org/10.3891/acta.chem.scand.18-0001.

(43) Puzas, J. P.; Nakon, R.; Petersen, J. L. Direct Evidence for an SN1CB Mechanism. 4. Crystal and Molecular Structure of Chloro(Bis(8-Quinolinyl)Amido-N1,N2,N3)Copper(II), a Metal Chelate Containing an Sp2-Hybridized Deprotonated Amine. *Inorg. Chem.* **1986**, *25* (21), 3837–3840. https://doi.org/10.1021/ic00241a026.

(44) Peters, J. C.; Harkins, S. B.; Brown, S. D.; Day, M. W. Pincer-like Amido Complexes of Platinum, Palladium, and Nickel. *Inorg. Chem.* **2001**, *40* (20), 5083–5091. https://doi.org/10.1021/ic010336p.

(45) Maiti, D.; Paul, H.; Chanda, N.; Chakraborty, S.; Mondal, B.; Puranik, V. G.; Lahiri, G. Kumar. Synthesis, Structure, Spectral and Electron-Transfer Properties of Octahedral-[CoIII(L)2]+/[ZnII(L)2] and Square Planar-[CuII(L){OC(=O)CH3}] Complexes Incorporating Anionic Form of Tridentate Bis(8-Quinolinyl)Amine [N1C9H6-N2-C9H6N3, L-] Ligand. *Polyhedron* **2004**, *23* (5), 831–840. https://doi.org/10.1016/j.poly.2003.11.053.

(46) Valk, J.-M.; Claridge, T. D. W.; Brown, J. M.; Hibbs, D.; Hursthouse, M. B. Synthesis and Chemistry of a New P-N Chelating Ligand; (R)- and (S)-6-(2'-Diphenylphosphino-1'-Naphthyl)Phenanthridine. *Tetrahedron Asymmetry* **1995**, *6* (Copyright (C) 2017 American Chemical Society (ACS). All Rights Reserved.), 2597–2610. https://doi.org/10.1016/0957-4166(95)00341-L.

(47) Raszeja, L.; Maghnouj, A.; Hahn, S.; Metzler-Nolte, Nils. A Novel Organometallic ReI Complex with Favourable Properties for Bioimaging and Applicability in Solid-Phase Peptide Synthesis. *ChemBioChem* **2011**, *12* (3), 371–376. https://doi.org/10.1002/cbic.201000576.

(48) Sicilia, V.; Fuertes, S.; Martin, A.; Palacios, Adrian. N-Assisted CPh-H Activation in 3,8-Dinitro-6-Phenylphenanthridine. New C,N-Cyclometallated Compounds of Platinum(II): Synthesis, Structure, and Luminescence Studies. *Organometallics* **2013**, *32* (15), 4092–4102. https://doi.org/10.1021/om400159g.

(49)   Jiang, B.; Gu, Y.; Qin, J.; Ning, X.; Gong, S.; Xie, G.; Yang, Chuluo. Deep-Red Iridium(III) Complexes Cyclometallated by Phenanthridine Derivatives for Highly Efficient Solution-Processed Organic Light-Emitting Diodes. *J. Mater. Chem. C Mater. Opt. Electron. Devices* **2016**, *4* (16), 3492–3498. https://doi.org/10.1039/C6TC00148C.

(50)   Theobald, R. S.; Schofield, K. The Chemistry of Phenanthridine and Its Derivatives. *Chem. Rev.* **1950**, *46* (1), 170–189. https://doi.org/10.1021/cr60143a004.

(51)   Crystal and molecular structure of phenanthridine. Roychowdhury1973.Pdf. *Acta. Cryst., Sect. B* **1973**, *29*, 1362–1364.

(52)   Brett, W. A.; Rademacher, P.; Boese, R. Redetermination of the Structure of Phenanthridine. *Acta Crystallogr. C* **1993**, *49* (9), 1564–1566. https://doi.org/10.1107/S0108270193005062.

(53)   Katritzky, A. R. *Handbook of Heterocyclic Chemistry*, 3rd ed.; Elsevier, 2010.

(54)   Benmachiche, A.; Zendaoui, S.-M.; Bouaoud, S.-E.; Zouchoune, B. Electronic Structure and Coordination Chemistry of Phenanthridine Ligand in First-Row Transition Metal Complexes: A DFT Study. *Int. J. Quantum Chem.* **2013**, *113* (7), 985–996. https://doi.org/10.1002/qua.24071.

(55)   Giesbrecht, P. K.; Nemez, D. B.; Herbert, D. E. Electrochemical Hydrogenation of a Benzannulated Pyridine to a Dihydropyridine in Acidic Solution. *Chem. Commun.* **2018**, *54* (4), 338–341. https://doi.org/10.1039/C7CC07907A.

(56)   Mondal, R.; Giesbrecht, P. K.; Herbert, D. E. Nickel(II), Copper(I) and Zinc(II) Complexes Supported by a (4-Diphenylphosphino)Phenanthridine Ligand. *Polyhedron* **2016**, *108*, 156–162.

(57)   Mandapati, P.; Giesbrecht, P. K.; Davis, R. L.; Herbert, D. E. Phenanthridine-Containing Pincer-like Amido Complexes of Nickel, Palladium, and Platinum. *Inorg Chem* **2017**, *56*, 3674–3685.

(58)   Mandapati, P.; Braun, J. D.; Killeen, C.; Davis, R. L.; Williams, J. A. G.; Herbert, D. E. Luminescent Platinum(II) Complexes of N^N⁻^N Amido Ligands with Benzannulated N-Heterocyclic Donor Arms: Quinolines Offer Unexpectedly Deeper Red Phosphorescence than Phenanthridines. *Inorg Chem* **2019**, *58*, 14808–14817.

(59)   Mandapati, P.; Braun, J. D.; Lozada, I. B.; Williams, J. A. G.; Herbert, D. E. Deep-Red Luminescence from Platinum(II) Complexes of N^N⁻^N-Amido Ligands with Benzannulated N-Heterocyclic Donor Arms. *Inorg. Chem.* **2020**, *59*, 12504–12517.

(60)   Mondal, R.; Lozada, I. B.; Davis, R. L.; Williams, J. A. G.; Herbert, D. E. Site-Selective Benzannulation of N-Heterocycles in Bidentate Ligands Leads to Blue-Shifted Emission from [(P^N)Cu]₂(μ-X)₂ Dimers. *Inorg Chem* **2018**, *57*, 4966–4978.

(61)   Mondal, R.; Lozada, I. B.; Davis, R. L.; Williams, J. A. G.; Herbert, D. E. Exploiting Synergy between Ligand Design and Counterion Interactions to Boost Room Temperature Phosphorescence from Cu(I) Compounds. *J. Mater. Chem. C* **2019**, *7*, 3772–3778.

(62)   Lozada, I. B.; Murray, T.; Herbert, D. E. Monomeric Zinc(II) Amide Complexes Supported by Bidentate, Benzannulated Phenanthridine Amido Ligands. *Polyhedron* **2019**, *161*, 261–267.

(63)   Mondal, R.; Lozada, I. B.; Davis, R. L.; Williams, J. A. G.; Herbert, D. E. Site-Selective Benzannulation of N-Heterocycles in Bidentate Ligands Leads to Blue-Shifted Emission from [(P^N)Cu]2(μ-X)2 Dimers. *Inorg Chem* **2018**, *57*, 4966–4978.

(64) Mandapati, P.; Giesbrecht, P. K.; Davis, R. L.; Herbert, D. E. Phenanthridine-Containing Pincer-like Amido Complexes of Nickel, Palladium, and Platinum. *Inorg Chem* **2017**, *56*, 3674–3685.

(65) Gaire, S.; Ortiz, R. J.; Schrage, B. R.; Lozada, I. B.; Mandapati, P.; Osinski, A. J.; Herbert, D. E.; Ziegler, C. J. (8-Amino)Quinoline and (4-Amino)Phenanthridine Complexes of Re(CO)3 Halides. *J. Organomet. Chem.* **2020**, *921*, 121338.

(66) Nemez, D. B.; Lozada, I. B.; Braun, J. D.; Williams, J. A. G.; Herbert, D. E. Synthesis and Coordination Chemistry of a Benzannulated Bipyridine: 6,6′-Biphenanthridine. *Inorg. Chem.* **2022**, *61* (34), 13386–13398. https://doi.org/10.1021/acs.inorgchem.2c01514.

(67) Hanson, K.; Roskop, L.; Djurovich, P. I.; Zahariev, F.; Gordon, M. S.; Thompson, M. E. A Paradigm for Blue- or Red-Shifted Absorption of Small Molecules Depending on the Site of π-Extension. *J. Am. Chem. Soc.* **2010**, *132*, 16247–16255.

(68) Barbon, S. M.; Staroverov, V. N.; Gilroy, J. B. Effect of Extended π Conjugation on the Spectroscopic and Electrochemical Properties of Boron Difluoride Formazanate Complexes. *J. Org. Chem.* **2015**, *80*, 5226–5235.

(69) Liu, B.; Lystrom, L.; Kilina, S.; Sun, W. Tuning the Ground State and Excited State Properties of Monocationic Iridium(III) Complexes by Varying the Site of Benzannulation on Diimine Ligand. *Inorg. Chem.* **2017**, *56*, 5361–5370.

(70) Westcott, B. L.; Gruhn, N. E.; Michelsen, L. J.; Lichtenberger, D. L. Experimental Observation of Non-Aufbau Behavior: Photoelectron Spectra of Vanadyloctaethylporphyrinate and Vanadylphthalocyanine. *J. Am. Chem. Soc.* **2000**, *122*, 8083–8084.

(71) Hewage, J. S.; Wanniarachchi, S.; Morin, T. J.; Liddle, B. J.; Banaszynski, M.; Lindeman, S. V.; Bennett, B.; Gardinier, J. R. Homoleptic Nickel(II) Complexes of Redox-Tunable Pincer-Type Ligands. *Inorg. Chem.* **2014**, *53* (19), 10070–10084. https://doi.org/10.1021/ic500657e.

(72) Lozada, I. B.; Ortiz, R. J.; Braun, J. D.; Williams, J. A. G.; Herbert, D. E. Donor–Acceptor Boron-Ketoiminate Complexes with Pendent *N*-Heterocyclic Arms: Switched-on Luminescence through *N*-Heterocycle Methylation. *J. Org. Chem.* **2022**, *87* (1), 184–196. https://doi.org/10.1021/acs.joc.1c02138.

(73) Braun, J. D.; Lozada, I. B.; Kolodziej, C.; Burda, C.; Newman, K. M. E.; van Lierop, J.; Davis, R. L.; Herbert, D. E. Iron(II) Coordination Complexes with Panchromatic Absorption and Nanosecond Charge-Transfer Excited State Lifetimes. *Nat. Chem.* **2019**, *11*, 1144–1150.

(74) Bruker-AXS. APEX3 V2016.1-0, 2016.

(75) Dolomanov, O. V.; Bourhis, L. J.; Gildea, R. J.; Howard, J. A. K.; Puschmann, H. OLEX2: A Complete Structure Solution, Refinement and Analysis Program. *J. Appl. Crystallogr.* **2009**, *42*, 339–341.

(76) Spek, A. L. Structure Validation in Chemical Crystallography. *Acta Cryst* **2009**, *D65*, 148–155.

(77) Fan, C.; Yang, C. Yellow/Orange Emissive Heavy-Metal Complexes as Phosphors in Monochromatic and White Organic Light-Emitting Devices. *Chem Soc Rev* **2014**, *43* (17), 6439–6469. https://doi.org/10.1039/C4CS00110A.

(78) Vreshch, V. D.; Yang, J.-H.; Zhang, H.; Filatov, A. S.; Dikarev, E. V. Monomeric Square-Planar Cobalt(II) Acetylacetonate: Mystery or Mistake? *Inorg. Chem.* **2010**, *49* (18), 8430–8434. https://doi.org/10.1021/ic100963r.

(79) Sokolow, J. D.; Trzop, E.; Chen, Y.; Tang, J.; Allen, L. J.; Crabtree, R. H.; Benedict, J. B.; Coppens, P. Binding Modes of Carboxylate- and Acetylacetonate-Linked Chromophores to Homodisperse Polyoxotitanate Nanoclusters. *J. Am. Chem. Soc.* **2012**, *134* (28), 11695–11700. https://doi.org/10.1021/ja303692r.

(80) Muñoz-García, A. B.; Sannino, F.; Vitiello, G.; Pirozzi, D.; Minieri, L.; Aronne, A.; Pernice, P.; Pavone, M.; D'Errico, G. Origin and Electronic Features of Reactive Oxygen Species at Hybrid Zirconia-Acetylacetonate Interfaces. *ACS Appl. Mater. Interfaces* **2015**, *7* (39), 21662–21667. https://doi.org/10.1021/acsami.5b06988.

(81) Seco, M. Acetylacetone: A Versatile Ligand. *J. Chem. Educ.* **1989**, *66* (9), 779. https://doi.org/10.1021/ed066p779.

(82) Allen, G.; Lewis, J.; Long, R. F.; Oldham, C. A Novel Form of Co-Ordination of Acetylacetone to Platinum(LI). *Nature* **1964**, *202*, 589–590. https://doi.org/10.1038/202589a0.

(83) Patra, S.; Mondal, B.; Sarkar, B.; Niemeyer, M.; Lahiri, G. K. First Example of μ_3-Sulfido Bridged Mixed-Valent Triruthenium Complex Triangle Ru$^{III}_2$ Ru^{II} (O , O -Acetylacetonate) $_3$ (μ - O , O ,γ- C -Acetylacetonate) $_3$ (μ_3 -S) (**1**) Incorporating Simultaneous O,O- and γ-C-Bonded Bridging Acetylacetonate Units. Synthesis, Crystal Structure, and Spectral and Redox Properties. *Inorg. Chem.* **2003**, *42* (4), 1322–1327. https://doi.org/10.1021/ic026221i.

(84) Zhu, D.; Budzelaar, P. H. M. N-Aryl β-Diiminate Complexes of the Platinum Metals. *Dalton Trans.* **2013**, *42* (32), 11343. https://doi.org/10.1039/c3dt50715g.

(85) Bernskoetter, W. H.; Lobkovsky, E.; Chirik, P. J. Ancillary Ligand Effects on C−H Bond Activation Reactions Promoted by β-Diiminate Iridium Complexes. *Organometallics* **2005**, *24* (25), 6250–6259. https://doi.org/10.1021/om050705f.

(86) Roesky, H. W. The Renaissance of Aluminum Chemistry. *Inorg. Chem.* **2004**, *43* (23), 7284–7293. https://doi.org/10.1021/ic0400641.

(87) Mears, K. L.; Stennett, C. R.; Taskinen, E. K.; Knapp, C. E.; Carmalt, C. J.; Tuononen, H. M.; Power, P. P. Molecular Complexes Featuring Unsupported Dispersion-Enhanced Aluminum–Copper and Gallium–Copper Bonds. *J. Am. Chem. Soc.* **2020**, *142* (47), 19874–19878. https://doi.org/10.1021/jacs.0c10099.

(88) Mondal, R.; Lozada, I. B.; Davis, R. L.; Williams, J. A. G.; Herbert, D. E. Exploiting Synergy between Ligand Design and Counterion Interactions to Boost Room Temperature Phosphorescence from Cu(I) Compounds. *J. Mater. Chem. C* **2019**, *7*, 3772–3778.

(89) Mandapati, P.; Braun, J. D.; Lozada, I. B.; Williams, J. A. G.; Herbert, D. E. Deep-Red Luminescence from Platinum(II) Complexes of N^N⁻^N-Amido Ligands with Benzannulated N-Heterocyclic Donor Arms. *Inorg. Chem.* **2020**, *59*, 12504–12517.

(90) Ortiz, R. J.; Braun, J. D.; Williams, J. A. G.; Herbert, D. E. Brightly Luminescent Platinum Complexes of *N^C⁻^N* Ligands Forming Six-Membered Chelate Rings: Offsetting Deleterious Ring Size Effects Using Site-Selective Benzannulation. *Inorg. Chem.* **2021**, *60*, 16881–16894.

(91) Lozada, I. B.; Huang, B.; Stilgenbauer, M.; Beach, T.; Qiu, Z.; Zheng, Y.; Herbert, D. E. Monofunctional Platinum(II) Anticancer Complexes Based on Multidentate Phenanthridine-Containing Ligand Frameworks. *Dalton Trans.* **2020**, *49*, 6557–6560.

(92) Myers, E. L.; Butts, C. P.; Aggarwal, V. K. BF3·OEt2 and TMSOTf: A Synergistic Combination of Lewis Acids. *Chem. Commun.* **2006**, No. 42, 4434–4436.

(93) Macedo, F. P.; Gwengo, C.; Lindeman, S. V.; Smith, M. D.; Gardinier, J. R. β-Diketonate, β-Ketoiminate, and β-Diiminate Complexes of Difluoroboron. *Eur. J. Inorg. Chem.* **2008**, *2008*, 3200–3211.

(94) Dohe, J.; Kossmann, J.; Mueller, T. J. J. Diversity-Oriented Four-Component Synthesis of Solid State Luminescent Difluoro Oxazaborinines. *Dyes Pigments* **2018**, *157*, 198–217.

(95) Köhling, J.; Kozel, V.; Jovanov, V.; Pajkert, R.; Tverdomed, S. N.; Gridenco, O.; Fugel, M.; Grabowsky, S.; Röschenthaler, G.-V.; Wagner, V. Synthesis and Characterization of Oxazaborinin Phosphonate for Blue OLED Emitter Applications. *ChemPhysChem* **2019**, *20*, 665–671.

(96) Mtiraoui, H.; Gharbi, R.; Msaddek, M.; Bretonnière, Y.; Andraud, C.; Renard, P.-Y.; Sabot, C. Solution and Solid-State Fluorescence of 2-(2′-Hydroxyphenyl)-1,5-Benzodiazepin-2-One (HBD) Borate Complexes. *RSC Adv.* **2016**, *6*, 86352–86360.

(97) Chęcińska, L.; Mebs, S.; Ośmiałowski, B.; Zakrzewska, A.; Ejsmont, K.; Kohout, M. Tuning the Electronic Properties of the Dative N−B Bond with Associated O−B Interaction: Electron Localizability Indicator from X-Ray Wavefunction Refinement. *ChemPhysChem* **2016**, *17*, 2395–2406.

(98) Itoh, K.; Okazaki, K.; Fujimoto, M. The Structure of 1,3-Enaminoketonatoboron Difluorides in Solution and in the Solid State. *Aust. J. Chem.* **2003**, *56*, 1209–1214.

(99) Grepioni, F.; Cojazzi, G.; Draper, S. M.; Scully, N.; Braga, D. Crystal Forms of Hexafluorophosphate Organometallic Salts and the Importance of Charge-Assisted C−H---F Hydrogen Bonds. *Organometallics* **1998**, *17*, 296–307.

(100) Mandapati, P.; Braun, J. D.; Killeen, C.; Davis, R. L.; Williams, J. A. G.; Herbert, D. E. Luminescent Platinum(II) Complexes of N^N⁻^N Amido Ligands with Benzannulated N-Heterocyclic Donor Arms: Quinolines Offer Unexpectedly Deeper Red Phosphorescence than Phenanthridines. *Inorg. Chem.* **2019**, *58*, 14808–14817.

(101) Lozada, I. B.; Williams, J. A. G.; Herbert, D. E. Platinum(II) Complexes of Benzannulated N^N⁻^O-Amido Ligands: Bright Orange Phosphors with Long-Lived Excited States. *Inorg. Chem. Front.* **2022**, *9*, 10–22.

(102) Donckt, E. V.; Dramaix, R.; Nasielski, J.; Vogels, C. Photochemistry of Aromatic Compounds. Part 1.—Acid-Base Properties of Singlet and Triplet Excited States of Pyrene Derivatives and Aza-Aromatic Compounds. *Trans. Faraday Soc.* **1969**, *65*, 3258–3262.

(103) Zander, M. The Significance of Donor-Acceptor Interactions in the External Heavy Atom Effect of Silver Nitrate on the Luminescence Behavior of Aza-Aromatic Systems and Carbazoles. *Z Naturforsch A* **1978**, *33*, 998–1000.

(104) Norek, M.; Dresner, J.; Prochorow, J. Spectroscopy and Photophysics of Monoazaphenanthrenes. I. Absorption and Fluorescence Spectra of Phenanthridine and 7,8-Benzoquinoline. *Acta Phys. Pol. A* **2003**, *104*, 425–439.

(105) Marzzacco, C. J.; Deckey, G.; Colarulli, R.; Siuzdak, G.; Halpern, A. M. Excited-State Protonation and Photophysical Properties of Azaphenanthrenes. *J. Phys. Chem.* **1989**, *93*, 2935–2939.

(106) Parker, D.; Senanayake, P. K.; Williams, J. A. G. Luminescent Sensors for PH, PO2, Halide and Hydroxide Ions Using Phenanthridine as a Photosensitiser in Macrocyclic Europium and Terbium Complexes. *J. Chem. Soc. Perkin Trans. 2* **1998**, 2129–2140.

(107) Norek, M.; Kozankiewicz, B.; Prochorow, J. Spectroscopy and Photophysics of Monoazaphenanthrenes. III. Luminescence of Phenanthridine and 7,8-Benzoquinoline in Crystalline State. *Acta Phys Pol A* **2004**, *106*, 77–94.

(108) Lozada, I. B.; Murray, T.; Herbert, D. E. Monomeric Zinc(II) Amide Complexes Supported by Bidentate, Benzannulated Phenanthridine Amido Ligands. *Polyhedron* **2019**, *161*, 261–267.

(109) Lozada, I. B.; Ortiz, R. J.; Braun, J. D.; Williams, J. A. G.; Herbert, D. E. Donor–Acceptor Boron-Ketoiminate Complexes with Pendent N-Heterocyclic Arms: Switched-on Luminescence through N-Heterocycle Methylation. *J. Org. Chem.* **2022**, *87*, 184–196.

(110) Bridgeman, A. J.; Cavigliasso, G.; Ireland, L. R.; Rothery, J. The Mayer Bond Order as a Tool in Inorganic Chemistry. *J. Chem. Soc. Dalton Trans.* **2001**, 2095–2108.

(111) Lu, T.; Chen, F. Atomic Dipole Moment Corrected Hirshfeld Population Method. *J. Theor. Comput. Chem.* **2012**, *11*, 163–183.

(112) Montalti, M.; Credi, A.; Prodi, L.; Gandolfi, M. *Handbook of Photochemistry. 3rd Ed.*; CRC Press: Boca Raton, 2006.

(113) Oyler, K. D.; Coughlin, F. J.; Bernhard, S. Controlling the Helicity of 2,2'-Bipyridyl Ruthenium(II) and Zinc(II) Hemicage Complexes. *J. Am. Chem. Soc.* **2007**, *129*, 210–217.

(114) Martinez, S.; Igoa, F.; Carrera, I.; Seoane, G.; Veiga, N.; De Camargo, A. S. S.; Kremer, C.; Torres, J. A Zn(II) Luminescent Complex with a Schiff Base Ligand: Solution, Computational and Solid State Studies. *J. Coord. Chem.* **2018**, *71*, 874–889.

(115) Mei, J.; Leung, N. L. C.; Kwok, R. T. K.; Lam, J. W. Y.; Tang, B. Z. Aggregation-Induced Emission: Together We Shine, United We Soar! *Chem. Rev.* **2015**, *115*, 11718–11940.

(116) Singh, K.; Siddiqui, I.; Sridharan, V.; Kumar Yadav, R. A.; Jou, J.-H.; Adhikari, D. Aggregation-Induced Enhanced Emission-Active Zinc(II) β-Diketiminate Complexes Enabling High-Performance Solution-Processable OLEDs. *Inorg. Chem.* **2021**, *60*, 19128–19135.

(117) Singh, K.; S., V.; Adhikari, D. Visible Light Photoredox by a (Ph,ArNacNac)2Zn Photocatalyst: Photophysical Properties and Mechanistic Understanding. *Inorg. Chem. Front.* **2021**, *8*, 2078–2087.

(118) Lozada, I. B.; Huang, B.; Stilgenbauer, M.; Beach, T.; Qiu, Z.; Zheng, Y.; Herbert, D. E. Monofunctional Platinum(II) Anticancer Complexes Based on Multidentate Phenanthridine-Containing Ligand Frameworks. *Dalton Trans.* **2020**, *49*, 6557–6560.

(119) Mandapati, P.; Giesbrecht, P. K.; Davis, R. L.; Herbert, D. E. Phenanthridine-Containing Pincer-like Amido Complexes of Nickel, Palladium, and Platinum. *Inorg. Chem.* **2017**, *56*, 3674–3685.

(120) Mandapati, P.; Braun, J. D.; Killeen, C.; Davis, R. L.; Williams, J. A. G.; Herbert, D. E. Luminescent Platinum(II) Complexes of N^N-^N Amido Ligands with Benzannulated N-Heterocyclic Donor Arms: Quinolines Offer Unexpectedly Deeper Red Phosphorescence than Phenanthridines. *Inorg Chem* **2019**, *58*, 14808–14817.

(121) Mandapati, P.; Braun, J. D.; Lozada, I. B.; Williams, J. A. G.; Herbert, D. E. Deep-Red Luminescence from Platinum(II) Complexes of N^N−^N-Amido Ligands with Benzannulated N-Heterocyclic Donor Arms. *Inorg. Chem.* **2020**, *59*, 12504–12517.

(122) Reineke, M. H.; Sampson, M. D.; Rheingold, A. L.; Kubiak, C. P. Synthesis and Structural Studies of Nickel(0) Tetracarbene Complexes with the Introduction of a New Four-Coordinate Geometric Index, Tδ. *Inorg. Chem.* **2015**, *54*, 3211–3217.

(123) Puttock, E. V.; Fradgley, J. D.; Yufit, D. S.; Williams, J. A. G. A Family of Readily Synthesised Phosphorescent Platinum(II) Complexes Based on Tridentate *N^N^O* -Coordinating Schiff-Base Ligands. *Dalton Trans.* **2019**, *48*, 15012–15028.

(124) Davidson, J. J.; DeMott, J. C.; Douvris, C.; Fafard, C. M.; Bhuvanesh, N.; Chen, C.-H.; Herbert, D. E.; Lee, C.-I.; McCulloch, B. J.; Foxman, B. M.; Ozerov, O. V. Comparison of the Electronic Properties of Diarylamido-Based PNZ Pincer Ligands: Redox Activity at the Ligand and Donor Ability Toward the Metal. *Inorg. Chem.* **2015**, *54*, 2916–2935.

(125) Giesbrecht, P. K.; Nemez, D. B.; Herbert, D. E. Electrochemical Hydrogenation of a Benzannulated Pyridine to a Dihydropyridine in Acidic Solution. *Chem. Commun.* **2018**, *54*, 338–341.

(126) Reichardt, C. Solvatochromic Dyes as Solvent Polarity Indicators. *Chem. Rev.* **1994**, *94*, 2319–2358.

(127) Catalán, J. Toward a Generalized Treatment of the Solvent Effect Based on Four Empirical Scales: Dipolarity (SdP, a New Scale), Polarizability (SP), Acidity (SA), and Basicity (SB) of the Medium. *J. Phys. Chem. B* **2009**, *113*, 5951–5960.

(128) Van der Zwan, G.; Hynes, J. T. Time-Dependent Fluorescence Solvent Shifts, Dielectric Friction, and Nonequilibrium Solvation in Polar Solvents. *J. Phys. Chem.* **1985**, *89*, 4181–4188.

(129) Caspar, J. V.; Meyer, T. J. Photochemistry of Tris(2,2'-Bipyridine)Ruthenium(2+) Ion (Ru(Bpy)$_3{}^{2+}$). Solvent Effects. *J. Am. Chem. Soc.* **1983**, *105*, 5583–5590.

(130) Kwok, C.-C.; Ngai, H. M. Y.; Chan, S.-C.; Sham, I. H. T.; Che, C.-M.; Zhu, N. [(O∧N∧N)PtX] Complexes as a New Class of Light-Emitting Materials for Electrophosphorescent Devices. *Inorg. Chem.* **2005**, *44*, 4442–4444.

(131) Garner, K. L.; Parkes, L. F.; Piper, J. D.; Williams, J. A. G. Luminescent Platinum Complexes with Terdentate Ligands Forming 6-Membered Chelate Rings: Advantageous and Deleterious Effects in N ^ N ^ N and N ^ C ^ N-Coordinated Complexes. *Inorg. Chem.* **2010**, *49*, 476–487.

(132) Williams, J. A. G. The Coordination Chemistry of Dipyridylbenzene: N-Deficient Terpyridine or Panacea for Brightly Luminescent Metal Complexes? *Chem. Soc. Rev.* **2009**, *38*, 1783–1801.

(133) Meech, S. R.; Phillips, D. Photophysics of Some Common Fluorescence Standards. *J. Photochem.* **1983**, *23*, 193–217.

(134) Suzuki, K.; Kobayashi, A.; Kaneko, S.; Takehira, K.; Yoshihara, T.; Ishida, H.; Shiina, Y.; Oishi, S.; Tobita, S. Reevaluation of Absolute Luminescence Quantum Yields of Standard Solutions Using a Spectrometer with an Integrating Sphere and a Back-Thinned CCD Detector. *Phys. Chem. Chem. Phys.* **2009**, *11*, 9850–9860.

(135) Murov, S. L.; Carmichael, I.; Hug, G. L. *Handbook of Photochemistry, 2nd Ed.*; Marcel Dekker: New York, 1993.

(136) Hohenberg, P.; Kohn, W. Inhomogeneous Electron Gas. *Phys. Rev.* **1964**, *136* (3B), B864–B871. https://doi.org/10.1103/PhysRev.136.B864.

(137) Kohn, W.; Sham, L. J. Self-Consistent Equations Including Exchange and Correlation Effects. *Phys. Rev.* **1965**, *140* (4A), A1133–A1138. https://doi.org/10.1103/PhysRev.140.A1133.

(138) Bühl, M.; Kabrede, H. Geometries of Transition-Metal Complexes from Density-Functional Theory. *J. Chem. Theory Comput.* **2006**, *2* (5), 1282–1290. https://doi.org/10.1021/ct6001187.

(139) Waller, M. P.; Braun, H.; Hojdis, N.; Bühl, M. Geometries of Second-Row Transition-Metal Complexes from Density-Functional Theory. *J. Chem. Theory Comput.* **2007**, *3* (6), 2234–2242. https://doi.org/10.1021/ct700178y.

(140) Bühl, M.; Reimann, C.; Pantazis, D. A.; Bredow, T.; Neese, F. Geometries of Third-Row Transition-Metal Complexes from Density-Functional Theory. *J. Chem. Theory Comput.* **2008**, *4* (9), 1449–1459. https://doi.org/10.1021/ct800172j.

(141) de Souza, B.; Farias, G.; Neese, F.; Izsák, R. Predicting Phosphorescence Rates of Light Organic Molecules Using Time-Dependent Density Functional Theory and the Path Integral Approach to Dynamics. *J. Chem. Theory Comput.* **2019**, *15* (3), 1896–1904. https://doi.org/10.1021/acs.jctc.8b00841.

(142) de Souza, B.; Neese, F.; Izsák, R. On the Theoretical Prediction of Fluorescence Rates from First Principles Using the Path Integral Approach. *J. Chem. Phys.* **2018**, *148* (3), 034104. https://doi.org/10.1063/1.5010895.

(143) Petrenko, T.; Neese, F. Analysis and Prediction of Absorption Band Shapes, Fluorescence Band Shapes, Resonance Raman Intensities, and Excitation Profiles Using the Time-Dependent Theory of Electronic Spectroscopy. *J. Chem. Phys.* **2007**, *127* (16), 164319. https://doi.org/10.1063/1.2770706.

(144) Wenger, O. S. Is Iron the New Ruthenium? *Chem. – Eur. J.* **2020**, *25*, 6043–6052.

(145) Baková, R.; Chergui, M.; Daniel, C.; Vlček Jr., A.; Záliš, S. Relativistic Effects in Spectroscopy and Photophysics of Heavy-Metal Complexes Illustrated by Spin–Orbit Calculations of [Re(Imidazole)(CO)3(Phen)]+. *Coord. Chem. Rev.* **2011**, *255* (7–8), 975–989. https://doi.org/10.1016/j.ccr.2010.12.027.

(146) Giesbrecht, P. K.; Nemez, D. B.; Herbert, D. E. Electrochemical Hydrogenation of a Benzannulated Pyridine to a Dihydropyridine in Acidic Solution. *Chem. Commun.* **2018**, *54* (4), 338–341. https://doi.org/10.1039/c7cc07907a.

(147) Mandapati, P.; Giesbrecht, P. K.; Davis, R. L.; Herbert, D. E. Phenanthridine-Containing Pincer-like Amido Complexes of Nickel, Palladium, and Platinum. *Inorg. Chem.* **2017**, *56* (6), 3674–3685. https://doi.org/10.1021/acs.inorgchem.7b00075.

(148) Mondal, R.; Lozada, I. B.; Davis, R. L.; Williams, J. A. G.; Herbert, D. E. Exploiting Synergy between Ligand Design and Counterion Interactions to Boost Room Temperature Phosphorescence from Cu(i) Compounds. *J. Mater. Chem. C* **2019**, *7* (13), 3772–3778. https://doi.org/10.1039/C9TC00040B.

(149) Mandapati, P.; Braun, J. D.; Killeen, C.; Davis, R. L.; Williams, J. A. G.; Herbert, D. E. Luminescent Platinum(II) Complexes of N^ N-^ N Amido Ligands with Benzannulated N-Heterocyclic Donor Arms: Quinolines Offer Unexpectedly Deeper Red Phosphorescence than Phenanthridines. *Inorg. Chem.* **2019**, *58* (21), 14808–14817. https://doi.org/10.1021/acs.inorgchem.9b02480.

(150) Lozada, I. B.; Murray, T.; Herbert, D. E. Monomeric Zinc(II) Amide Complexes Supported by Bidentate, Benzannulated Phenanthridine Amido Ligands. *Polyhedron* **2019**, *161*, 261–267. https://doi.org/10.1016/j.poly.2019.01.023.

(151) Braun, J. D.; Lozada, I. B.; Kolodziej, C.; Burda, C.; Newman, K. M. E.; van Lierop, J.; Davis, R. L.; Herbert, D. E. Iron(Ii) Coordination Complexes with Panchromatic Absorption and Nanosecond Charge-Transfer Excited State Lifetimes. *Nat. Chem.* **2019**, *11* (12), 1144–1150. https://doi.org/10.1038/s41557-019-0357-z.

(152) Mondal, R.; Lozada, I. B.; Davis, R. L.; Williams, J. A. G.; Herbert, D. E. Site-Selective Benzannulation of N-Heterocycles in Bidentate Ligands Leads to Blue-Shifted Emission from [(P^N)Cu]2(μ-X)2 Dimers. *Inorg. Chem.* **2018**, *57* (9), 4966–4978. https://doi.org/10.1021/acs.inorgchem.7b03223.

(153) Mondal, R.; Giesbrecht, P. K.; Herbert, D. E. Nickel(II), Copper(I) and Zinc(II) Complexes Supported by a (4-Diphenylphosphino)Phenanthridine Ligand. *Polyhedron* **2016**, *108*, 156–162. https://doi.org/10.1016/j.poly.2015.10.051.

(154) Stufkens, D. J.; Vlček, A. Ligand-Dependent Excited State Behaviour of Re(I) and Ru(II) Carbonyl-Diimine Complexes. *Coord. Chem. Rev.* **1998**, *177* (1), 127–179. https://doi.org/10.1016/s0010-8545(98)00132-5.

(155) Vlček, A. Ultrafast Excited-State Processes in Re(I) Carbonyl-Diimine Complexes: From Excitation to Photochemistry. *Top Organomet Chem* **2010**, *29* (May 2009), 73–114. https://doi.org/10.1007/3418.

(156) Mandapati, P.; Braun, J. D.; Killeen, C.; Davis, R. L.; Williams, J. A. G.; Herbert, D. E. Luminescent Platinum(II) Complexes of N^N-^N Amido Ligands with Benzannulated N-Heterocyclic Donor Arms: Quinolines Offer Unexpectedly Deeper Red Phosphorescence than Phenanthridines. *Inorg Chem* **2019**, *58*, 14808–14817.

(157) Dixon, I. M.; Khan, S.; Alary, F.; Boggio-Pasqua, M.; Heully, J.-L. Probing the Photophysical Capability of Mono and Bis(Cyclometallated) Fe(II) Polypyridine Complexes Using Inexpensive Ground State DFT. *Dalton Trans.* **2014**, *43*, 15898–15905.

(158) Zhang, K.; Ash, R.; Girolami, G. S.; Vura-Weis, J. Tracking the Metal-Centered Triplet in Photoinduced Spin Crossover of Fe(Phen)32+ with Tabletop Femtosecond M-Edge X-Ray Absorption Near-Edge Structure Spectroscopy. *J. Am. Chem. Soc.* **2019**, *141*, 17180–17188.

(159) Juban, E. A.; Smeigh, A. L.; Monat, J. E.; McCusker, J. K. Ultrafast Dynamics of Ligand-Field Excited States. *Coord Chem Rev* **2006**, *250*, 1783–1791.

(160) Gryn'ova, G.; Coote, M. L.; Corminboeuf, C. Theory and Practice of Uncommon Molecular Electronic Configurations. *WIREs Comput. Mol. Sci.* **2015**, *5* (6), 440–459. https://doi.org/10.1002/wcms.1233.

(161) Kaim, W. Manifestations of Noninnocent Ligand Behavior. *Inorg Chem* **2011**, *50* (20), 9752–9765.

(162) Bowman, D. N.; Jakubikova, E. Low-Spin versus High-Spin Ground State in Pseudo-Octahedral Iron Complexes. *Inorg. Chem.* **2012**, *51*, 6011–6019.

(163) Ashley, D. C.; Jakubikova, E. Ironing out the Photochemical and Spin-Crossover Behavior of Fe(II) Coordination Compounds with Computational Chemistry. *Coord. Chem. Rev.* **2017**, *337*, 97–111.

(164) Reiher, M.; Salomon, O.; Artur Hess, B. Reparameterization of Hybrid Functionals Based on Energy Differences of States of Different Multiplicity. *Theor. Chem. Acc.* **2001**, *107*, 48–55.

(165) Jakubikova, E.; Bowman, D. N. Fe(II)-Polypyridines as Chromophores in Dye-Sensitized Solar Cells: A Computational Perspective. *Acc. Chem. Res.* **2015**, *48*, 1441–1449.

(166) Nemykin, V. N.; Hadt, R. G. Influence of Hartree−Fock Exchange on the Calculated Mössbauer Isomer Shifts and Quadrupole Splittings in Ferrocene Derivatives Using Density Functional Theory. *Inorg. Chem.* **2006**, *45*, 8297–8307.

(167) Zhao, Y.; Truhlar, D. G. A New Local Density Functional for Main-Group Thermochemistry, Transition Metal Bonding, Thermochemical Kinetics, and Noncovalent Interactions. *J. Chem. Phys.* **2006**, *125*, 194101.

(168) Cohen, A. J.; Handy, N. C. Dynamic Correlation. *Mol. Phys.* **2001**, *99*, 607–615.

(169) Zhao, Y.; Truhlar, D. G. The M06 Suite of Density Functionals for Main Group Thermochemistry, Thermochemical Kinetics, Noncovalent Interactions, Excited States, and Transition Elements: Two New Functionals and Systematic Testing of Four M06-Class Functionals and 12 Other Functionals. *Theor. Chem. Acc.* **2008**, *120*, 215–241.

(170) Ditchfield, R.; Hehre, W. J.; Pople, J. A. Self-Consistent Molecular-Orbital Methods. IX. Extended Gaussian-Type Basis for Molecular-Orbital Studies of Organic Molecules. *J. Chem. Phys.* **1971**, *54*, 724–728. https://doi.org/10.1063/1.1674902.

(171) Hehre, W. J.; Ditchfield, R.; Pople, J. A. Self-Consistent Molecular Orbital Methods. XII. Further Extensions of Gaussian-Type Basis Sets for Use in Molecular Orbital Studies of Organic Molecules. *J. Chem. Phys.* **1972**, *56*, 2257–2261.

(172) Hariharan, P. C.; Pople, J. A. Influence of Polarization Functions on MO Hydrogenation Energies. *Theor. Chim. Acta* **1973**, *28*, 213–222.

(173) Clark, T.; Chandrasekhar, J.; Spitznagel, G. W.; Schleyer, P. v R. Efficient Diffuse Function-Augmented Basis Sets for Anion Calculations. III. The 3-21 + G Basis Set for First-Row Elements, Lithium to Fluorine. *J. Comput. Chem.* **1983**, *4*, 294–301.

(174) Rassolov, V. A.; Pople, J. A.; Ratner, M. A.; Windus, T. L. 6-31G* Basis Set for Atoms K through Zn. *J. Chem. Phys.* **1998**, *109*, 1223–1229.

(175) Zhao, Y.; Truhlar, D. G. A New Local Density Functional for Main-Group Thermochemistry, Transition Metal Bonding, Thermochemical Kinetics, and Noncovalent Interactions. *J. Chem. Phys.* **2006**, *125* (19), 194101. https://doi.org/10.1063/1.2370993.

(176) Krishnan, R.; Binkley, J. S.; Seeger, R.; Pople, J. A. Self-consistent Molecular Orbital Methods. XX. A Basis Set for Correlated Wave Functions. *J. Chem. Phys.* **1980**, *72* (1), 650–654. https://doi.org/10.1063/1.438955.

(177) Clark, T.; Chandrasekhar, J.; Spitznagel, G. W.; Schleyer, P. V. R. Efficient Diffuse Function-Augmented Basis Sets for Anion Calculations. III. The 3-21+G Basis Set for First-Row Elements, Li-F. *J. Comput. Chem.* **1983**, *4* (3), 294–301. https://doi.org/10.1002/jcc.540040303.

(178) Dennington, Roy; Keith, Todd A.; Millam, John M. *GaussView, Version 6*; Semichem Inc.: Shawnee Mission, KS, 2016.

(179) Soda, T.; Kitagawa, Y.; Onishi, T.; Takano, Y.; Shigeta, Y.; Nagao, H.; Yoshioka, Y.; Yamaguchi, K. Ab Initio Computations of Effective Exchange Integrals for H–H, H–He–H and Mn2O2 Complex: Comparison of Broken-Symmetry Approaches. *Chem. Phys. Lett.* **2000**, *319* (3–4), 223–230. https://doi.org/10.1016/S0009-2614(00)00166-4.

(180) Yamaguchi, K.; Takahara, Y.; Fueno, T. Ab-Initio Molecular Orbital Studies of Structure and Reactivity of Transition Metal-OXO Compounds. In *Applied Quantum Chemistry*;

Smith, V. H., Schaefer, H. F., Morokuma, K., Eds.; Springer Netherlands: Dordrecht, 1986; pp 155–184. https://doi.org/10.1007/978-94-009-4746-7_11.

(181) Heydová, R.; Gindensperger, E.; Romano, R.; Sýkora, J.; Vlček, A.; Záliš, S.; Daniel, C. Spin-Orbit Treatment of UV-Vis Absorption Spectra and Photophysics of Rhenium(I) Carbonyl-Bipyridine Complexes: MS-CASPT2 and TD-DFT Analysis. *J. Phys. Chem. A* **2012**, *116* (46), 11319–11329. https://doi.org/10.1021/jp305461z.

(182) Ronca, E.; De Angelis, F.; Fantacci, S. Time-Dependent Density Functional Theory Modeling of Spin-Orbit Coupling in Ruthenium and Osmium Solar Cell Sensitizers. *J. Phys. Chem. C* **2014**, *118* (30), 17067–17078. https://doi.org/10.1021/jp500869r.

(183) Mai, S.; Gattuso, H.; Fumanal, M.; Muñoz-Losa, A.; Monari, A.; Daniel, C.; González, L. Excited-States of a Rhenium Carbonyl Diimine Complex: Solvation Models, Spin-Orbit Coupling, and Vibrational Sampling Effects. *Phys. Chem. Chem. Phys.* **2017**, *19* (40), 27240–27250. https://doi.org/10.1039/c7cp05126c.

(184) Shi, L. L.; Liao, Y.; Zhao, L.; Su, Z. M.; Kan, Y. H.; Yang, G. C.; Yang, S. Y. Theoretical Studies on the Electronic Structure and Spectral Properties of Versatile Diarylethene-Containing 1,10-Phenanthroline Ligands and Their Rhenium(I) Complexes. *J. Organomet. Chem.* **2007**, *692* (24), 5368–5374. https://doi.org/10.1016/j.jorganchem.2007.08.031.

(185) Silva-Junior, M. R.; Schreiber, M.; Sauer, S. P. A.; Thiel, W. Benchmarks for Electronically Excited States: Time-Dependent Density Functional Theory and Density Functional Theory Based Multireference Configuration Interaction. *J. Chem. Phys.* **2008**, *129* (10). https://doi.org/10.1063/1.2973541.

(186) Jacquemin, D.; Perpète, E. A.; Ciofini, I.; Adamo, C. Assessment of Functionals for TD-DFT Calculations of Singlet-Triplet Transitions. *J. Chem. Theory Comput.* **2010**, *6* (5), 1532–1537. https://doi.org/10.1021/ct100005d.

(187) Santoro, F.; Lami, A.; Improta, R.; Barone, V. Effective Method to Compute Vibrationally Resolved Optical Spectra of Large Molecules at Finite Temperature in the Gas Phase and in Solution. *J. Chem. Phys.* **2007**, *126* (18). https://doi.org/10.1063/1.2721539.

(188) Tozer, D. J.; Handy, N. C. On the Determination of Excitation Energies Using Density Functional Theory. *Phys. Chem. Chem. Phys.* **2000**, *2* (10), 2117–2121. https://doi.org/10.1039/a910321j.

(189) Chibani, S.; Charaf-Eddin, A.; Le Guennic, B.; Jacquemin, D. Boranil and Related NBO Dyes: Insights From Theory. *J. Chem. Theory Comput.* **2013**, *9*, 3127–3135.

(190) Mondal, R.; Giesbrecht, P. K.; Herbert, D. E. Nickel(II), Copper(I) and Zinc(II) Complexes Supported by a (4-Diphenylphosphino)Phenanthridine Ligand. *Polyhedron* **2016**, *108*, 156–162.

(191) Mondal, R.; Lozada, I. B.; Davis, R. L.; Williams, J. A. G.; Herbert, D. E. Site-Selective Benzannulation of N-Heterocycles in Bidentate Ligands Leads to Blue-Shifted Emission from [(*P^N*)Cu]$_2$(μ-X)$_2$ Dimers. *Inorg Chem* **2018**, *57*, 4966–4978.

(192) Gaire, S.; Ortiz, R. J.; Schrage, B. R.; Lozada, I. B.; Mandapati, P.; Osinski, A. J.; Herbert, D. E.; Ziegler, C. J. (8-Amino)Quinoline and (4-Amino)Phenanthridine Complexes of Re(CO)3 Halides. *J. Organomet. Chem.* **2020**, *921*, 121338.

(193) Tomasi, J.; Mennucci, B.; Cammi, R. Quantum Mechanical Continuum Solvation Models. *Chem Rev* **2005**, *105*, 2999–3094.

(194) Melenbacher, A.; Dhindsa, J. S.; Gilroy, J. B.; Stillman, M. J. Unveiling the Hidden, Dark, and Short Life of a Vibronic State in a Boron Difluoride Formazanate Dye. *Angew. Chem. Int. Ed.* **2019**, *58* (43), 15339–15343.

(195) El-Sayed, M. A. Spin—Orbit Coupling and the Radiationless Processes in Nitrogen Heterocyclics. *J. Chem. Phys.* **1963**, *38* (12), 2834–2838.

(196) Braun, J. D.; Lozada, I. B.; Kolodziej, C.; Burda, C.; Newman, K. M. E.; van Lierop, J.; Davis, R. L.; Herbert, D. E. Iron(II) Coordination Complexes with Panchromatic Absorption and Nanosecond Charge-Transfer Excited State Lifetimes. *Nat. Chem.* **2019**, *11*, 1144–1150.

(197) Larsen, C. B.; Braun, J. D.; Lozada, I. B.; Kunnus, K.; Biasin, E.; Kolodziej, C.; Burda, C.; Cordones, A. A.; Gaffney, K. J.; Herbert, D. E. Reduction of Electron Repulsion in Highly Covalent Fe-Amido Complexes Counteracts the Impact of a Weak Ligand Field on Excited-State Ordering. *J. Am. Chem. Soc.* **2021**, *143*, 20645–20656.

(198) Das, S.; Thornbury, W. G.; Bartynski, A. N.; Thompson, M. E.; Bradforth, S. E. Manipulating Triplet Yield through Control of Symmetry-Breaking Charge Transfer. *J. Phys. Chem. Lett.* **2018**, *9*, 3264–3270.

(199) Trinh, C.; Kirlikovali, K.; Das, S.; Ener, M. E.; Gray, H. B.; Djurovich, P.; Bradforth, S. E.; Thompson, M. E. Symmetry-Breaking Charge Transfer of Visible Light Absorbing Systems: Zinc Dipyrrins. *J. Phys. Chem. C* **2014**, *118*, 21834–21845.

(200) Kellogg, M.; Akil, A.; Muthiah Ravinson, D. S.; Estergreen, L.; Bradforth, S. E.; Thompson, M. E. Symmetry Breaking Charge Transfer as a Means to Study Electron Transfer with No Driving Force. *Faraday Discuss.* **2019**, *216*, 379–394.

(201) Mahmood, Z.; Rehmat, N.; Ji, S.; Zhao, J.; Sun, S.; Di Donato, M.; Li, M.; Teddei, M.; Huo, Y. Tuning the Triplet Excited State of Bis(Dipyrrin) Zinc(II) Complexes: Symmetry Breaking Charge Transfer Architecture with Exceptionally Long Lived Triplet State for Upconversion. *Chem. – Eur. J.* **2020**, *26*, 14912–14918.

(202) Weller, A. Photoinduced Electron Transfer in Solution: Exciplex and Radical Ion Pair Formation Free Enthalpies and Their Solvent Dependence By. *Zeitshcrift Phys. Chem. N. F.* **1982**, *133*, 93–98.

(203) Rehm, D.; Weller, A. Kinetics of Fluorescence Quenching by Electron and H-Atom Transfer. *Isr. J. Chem.* **1970**, *8*, 259–271.

(204) Vauthey, E. Photoinduced Symmetry-Breaking Charge Separation. *ChemPhysChem* **2012**, *13*, 2001–2011.

(205) Smith, A. R. G.; Burn, P. L.; Powell, B. J. Spin–Orbit Coupling in Phosphorescent Iridium(III) Complexes. *ChemPhysChem* **2011**, *12*, 2429–2438.

(206) Ronca, E.; De Angelis, F.; Fantacci, S. Time-Dependent Density Functional Theory Modeling of Spin–Orbit Coupling in Ruthenium and Osmium Solar Cell Sensitizers. *J. Phys. Chem. C* **2014**, *118*, 17067–17078.

(207) Gourlaouen, C.; Daniel, C. Spin–Orbit Effects in Square-Planar Pt(II) Complexes with Bidentate and Terdentate Ligands: Theoretical Absorption/Emission Spectroscopy. *Dalton Trans* **2014**, *43*, 17806–17819.

(208) Braun, J. D.; Lozada, I. B.; Herbert, D. E. In Pursuit of Panchromatic Absorption in Metal Coordination Complexes: Experimental Delineation of the HOMO Inversion Model Using Pseudo-Octahedral Complexes of Diarylamido Ligands. *Inorg. Chem.* **2020**, *59*, 17746–17757.

(209) Hayashi, M.; Takahashi, Y.; Yoshida, Y.; Sugimoto, K.; Kitagawa, H. Role of D-Elements in a Proton–Electron Coupling of d–π Hybridized Electron Systems. *J. Am. Chem. Soc.* **2019**, *141*, 11686–11693.

(210) Spencer, M.; Santoro, A.; Freeman, G. R.; Díez, Á.; Murray, P. R.; Torroba, J.; Whitwood, A. C.; Yellowlees, L. J.; Williams, J. A. G.; Bruce, D. W. Phosphorescent, Liquid-Crystalline Complexes of Platinum(II): Influence of the β-Diketonate Co-Ligand on Mesomorphism and Emission Properties. *Dalton Trans.* **2012**, *41*, 14244–14256.

(211) Neese, F. The ORCA Program System. *WIREs Comput. Mol. Sci.* **2012**, *2*, 73–78.

(212) Neese, F. Software Update: The ORCA Program System, Version 4.0. *WIREs Comput. Mol. Sci.* **2018**, *8*, e1327.

(213) Frisch, M. J.; Trucks, G. W.; Schlegel, H. B.; Scuseria, G. E.; Robb, M. A.; Cheeseman, J. R.; Scalmani, G.; Barone, V.; Petersson, G. A.; Nakatsuji, H.; Li, X.; Caricato, M.; Marenich, A. V.; Bloino, J.; Janesko, B. G.; Gomperts, R.; Mennucci, B.; Hratchian, H. P.; Ortiz, J. V.; Izmaylov, A. F.; Sonnenberg, J. L.; Williams; Ding, F.; Lipparini, F.; Egidi, F.; Goings, J.; Peng, B.; Petrone, A.; Henderson, T.; Ranasinghe, D.; Zakrzewski, V. G.; Gao, J.; Rega, N.; Zheng, G.; Liang, W.; Hada, M.; Ehara, M.; Toyota, K.; Fukuda, R.; Hasegawa, J.; Ishida, M.; Nakajima, T.; Honda, Y.; Kitao, O.; Nakai, H.; Vreven, T.; Throssell, K.; Montgomery Jr., J. A.; Peralta, J. E.; Ogliaro, F.; Bearpark, M. J.; Heyd, J. J.; Brothers, E. N.; Kudin, K. N.; Staroverov, V. N.; Keith, T. A.; Kobayashi, R.; Normand, J.; Raghavachari, K.; Rendell, A. P.; Burant, J. C.; Iyengar, S. S.; Tomasi, J.; Cossi, M.; Millam, J. M.; Klene, M.; Adamo, C.; Cammi, R.; Ochterski, J. W.; Martin, R. L.; Morokuma, K.; Farkas, O.; Foresman, J. B.; Fox, D. J. *Gaussian 16 Rev. C.01*; Wallingford, CT, 2016.

(214) Marenich, A. V.; Cramer, C. J.; Truhlar, D. G. Universal Solvation Model Based on Solute Electron Density and on a Continuum Model of the Solvent Defined by the Bulk Dielectric Constant and Atomic Surface Tensions. *J Phys Chem B* **2009**, *113*, 6378–6396.

(215) Grimme, S.; Ehrlich, S.; Goerigk, L. Effect of the Damping Function in Dispersion Corrected Density Functional Theory. *J. Comput. Chem.* **2011**, *32*, 1456–1465.

(216) Becke, A. D. Density-Functional Thermochemistry. III. The Role of Exact Exchange. *J Chem Phys* **1993**, *98*, 5648–5652.

(217) Lee, C.; Yang, W.; Parr, R.G. Development of the Colle-Salvetti Correlation-Energy Formula into a Functional of the Electron Density. *Phys. Rev. B Condens. Matter* **1988**, *37*, 785–789.

(218) Vosko, S. H.; Wilk, L.; Nusair, M. Accurate Spin-Dependent Electron Liquid Correlation Energies for Local Spin Density Calculations: A Critical Analysis. *Can. J. Phys.* **1980**, *58*, 1200–1211.

(219) Stephens, P. J.; Devlin, F. J.; Chabalowski, C. F.; Frisch, M. J. Ab Initio Calculation of Vibrational Absorption and Circular Dichroism Spectra Using Density Functional Force Fields. *J Phys Chem* **1994**, *98*, 11623–11627.

(220) Weigend, F.; Ahlrichs, R. Balanced Basis Sets of Split Valence, Triple Zeta Valence and Quadruple Zeta Valence Quality for H to Rn: Design and Assessment of Accuracy. *Phys Chem Chem Phys* **2005**, *7*, 3297–3305.

(221) Tao, J.; Perdew, J. P.; Staroverov, V. N.; Scuseria, G. E. Climbing the Density Functional Ladder: Nonempirical Meta--Generalized Gradient Approximation Designed for Molecules and Solids. *Phys. Rev. Lett.* **2003**, *91*, 146401.

(222) Staroverov, V. N.; Scuseria, G. E.; Tao, J.; Perdew, J. P. Comparative Assessment of a New Nonempirical Density Functional: Molecules and Hydrogen-Bonded Complexes. *J. Chem. Phys.* **2003**, *119*, 12129–12137.

(223) O'Boyle, N. M.; Tenderholt, A. L.; Langner, K. M. Software News and Updates Cclib: A Library for Package-Independent Computational Chemistry Algorithms. *J Comput Chem* **2008**, *29*, 839–845.

(224) Lu, T.; Chen, F. Multiwfn: A Multifunctional Wavefunction Analyzer. *J Comput Chem* **2012**, *33*, 580–592.

(225) Xiao, M; Lu, T. Generalized Charge Decomposition Analysis (GCDA) Method. *J. Adv. Phys. Chem.* **2015**, *4*, 111–124.

(226) Frisch, M. J.; Trucks, G. W.; Schlegel, H. B.; Scuseria, G. E.; Robb, M. A.; Cheeseman, J. R.; Scalmani, G.; Barone, V.; Petersson, G. A.; Nakatsuji, H.; Li, X.; Caricato, M.; Marenich, A. V.; Bloino, J.; Janesko, B. G.; Gomperts, R.; Mennucci, B.; Hratchian, H. P.; Ortiz, J. V.; Izmaylov, A. F.; Sonnenberg, J. L.; Williams-Young, D.; Ding, F.; Lipparini, F.; Egidi, F.; Goings, J.; Peng, B.; Petrone, A.; Henderson, T.; Ranasinghe, D.; Zakrzewski, V. G.; Gao, J.; Rega, N.; Zheng, G.; Liang, W.; Hada, M.; Ehara, M.; Toyota, K.; Fukuda, R.; Hasegawa, J.; Ishida, M.; Nakajima, T.; Honda, Y.; Kitao, O.; Nakai, H.; Vreven, T.; Throssell, K.; Montgomery, J. A.; Peralta, J. E.; Ogliaro, F.; Bearpark, M. J.; Heyd, J. J.; Brothers, E. N.; Kudin, K. N.; Staroverov, V. N.; Keith, T. A.; Kobayashi, R.; Normand, J.; Raghavachari, K.; Rendell, A. P.; Burant, J. C.; Iyengar, S. S.; Tomasi, J.; Cossi, M.; Millam, J. M.; Klene, M.; Adamo, C.; Cammi, R.; Ochterski, J. W.; Martin, R. L.; Morokuma, K.; Farkas, O.; Foresman, J. B.; Fox, D. J. *Gaussian 16, Revision B.01*; Gaussian 16, Revision B.01, Gaussian, Inc., Wallingford CT; Gaussian, Inc.: Wallingford CT, 2016.

(227) Adamo, C.; Barone, V. Toward Reliable Density Functional Methods without Adjustable Parameters: The PBE0 Model. *J. Chem. Phys.* **1999**, *110* (13), 6158–6170.

(228) Andrae, D.; Huermann, U.; Dolg, M.; Stoll, H.; Preu, H. Energy-Adjustedab Initio Pseudopotentials for the Second and Third Row Transition Elements. *Theor. Chim. Acta* **1990**, *77*, 123–141.

(229) Yanai, T.; Tew, D. P.; Handy, N. C. A New Hybrid Exchange–Correlation Functional Using the Coulomb-Attenuating Method (CAM-B3LYP). *Chem. Phys. Lett.* **2004**, *393*, 51–57.

(230) Neese, F.; Wennmohs, F.; Hansen, A.; Becker, U. Efficient, Approximate and Parallel Hartree–Fock and Hybrid DFT Calculations. A 'Chain-of-Spheres' Algorithm for the Hartree–Fock Exchange. *Chem. Phys.* **2009**, *356*, 98–109.

(231) Lenthe, E. van; Baerends, E. J.; Snijders, J. G. Relativistic Regular Two-component Hamiltonians. *J. Chem. Phys.* **1993**, *99*, 4597–4610.

(232) Weigend, F. Accurate Coulomb-Fitting Basis Sets for H to Rn. *Phys. Chem. Chem. Phys.* **2006**, *8*, 1057.

(233) Pantazis, D. A.; Neese, F. All-Electron Scalar Relativistic Basis Sets for the Lanthanides. *J. Chem. Theory Comput.* **2009**, *5*, 2229–2238.

(234) Pantazis, D. A.; Neese, F. All-Electron Scalar Relativistic Basis Sets for the Actinides. *J. Chem. Theory Comput.* **2011**, *7*, 677–684.

(235) Pantazis, D. A.; Chen, X.-Y.; Landis, C. R.; Neese, F. All-Electron Scalar Relativistic Basis Sets for Third-Row Transition Metal Atoms. *J. Chem. Theory Comput.* **2008**, *4*, 908–919.

(236) Hirshfeld, F. L. Bonded-Atom Fragments for Describing Molecular Charge Densities. *Theor. Chim. Acta* **1977**, *44*, 129–138.

(237) Hanwell, M. D.; Curtis, D. E.; Lonie, D. C.; Vandermeersch, T.; Zurek, E.; Hutchison, G. R. Avogadro: An Advanced Semantic Chemical Editor, Visualization, and Analysis Platform. *J Cheminf* **2012**, *4*, 17.

(238) Frisch, M. J.; Trucks, G. W.; Schlegel, H. B.; Scuseria, G. E.; Robb, M. A.; Cheeseman, J. R.; Scalmani, G.; Barone, V.; Petersson, G. A.; Nakatsuji, H.; Li, X.; Caricato, M.; Marenich, A. V.; Bloino, J.; Janesko, B. G.; Gomperts, R.; Mennucci, B.; Hratchian, H. P.; Ortiz, J. V.; Izmaylov, A. F.; Sonnenberg, J. L.; Williams; Ding, F.; Lipparini, F.; Egidi, F.; Goings, J.; Peng, B.; Petrone, A.; Henderson, T.; Ranasinghe, D.; Zakrzewski, V. G.; Gao, J.; Rega, N.; Zheng, G.; Liang, W.; Hada, M.; Ehara, M.; Toyota, K.; Fukuda, R.; Hasegawa, J.; Ishida, M.; Nakajima, T.; Honda, Y.; Kitao, O.; Nakai, H.; Vreven, T.; Throssell, K.; Montgomery Jr., J. A.; Peralta, J. E.; Ogliaro, F.; Bearpark, M. J.; Heyd, J. J.; Brothers, E. N.; Kudin, K. N.; Staroverov, V. N.; Keith, T. A.; Kobayashi, R.; Normand, J.; Raghavachari, K.; Rendell, A. P.; Burant, J. C.; Iyengar, S. S.; Tomasi, J.; Cossi, M.; Millam, J. M.; Klene, M.; Adamo, C.; Cammi, R.; Ochterski, J. W.; Martin, R. L.; Morokuma, K.; Farkas, O.; Foresman, J. B.; Fox, D. J. Gaussian 16 Rev. C.01, 2016.

(239) Marenich, A. V.; Cramer, C. J.; Truhlar, D. G. Universal Solvation Model Based on Solute Electron Density and on a Continuum Model of the Solvent Defined by the Bulk Dielectric Constant and Atomic Surface Tensions. *J Phys Chem B* **2009**, *113*, 6378–6396.

(240) Dennington, Roy; Keith, Todd A.; Millam, John M. GaussView, Version 6, 2016.

(241) O'Boyle, N. M.; Tenderholt, A. L.; Langner, K. M. Software News and Updates Cclib: A Library for Package-Independent Computational Chemistry Algorithms. *J Comput Chem* **2008**, *29*, 839–845.

(242) Lu, T.; Chen, F. Multiwfn: A Multifunctional Wavefunction Analyzer. *J Comput Chem* **2012**, *33*, 580–592.

(243) Tian, L. U.; Fei-Wu, C. Calculation of Molecular Orbital Composition. *Acta Chim. Sin.* **2011**, *69*, 2393.

(244) Frisch, M. J.; Trucks, G. W.; Schlegel, H. B.; Scuseria, G. E.; Robb, M. A.; Cheeseman, J. R.; Scalmani, G.; Barone, V.; Petersson, G. A.; Nakatsuji, H.; Li, X.; Caricato, M.; Marenich, A. V.; Bloino, J.; Janesko, B. G.; Gomperts, R.; Mennucci, B.; Hratchian, H. P.; Ortiz, J. V.; Izmaylov, A. F.; Sonnenberg, J. L.; Williams-Young, D.; Ding, F.; Lipparini, F.; Egidi, F.; Goings, J.; Peng, B.; Petrone, A.; Henderson, T.; Ranasinghe, D.; Zakrzewski, V. G.; Gao, J.; Rega, N.; Zheng, G.; Liang, W.; Hada, M.; Ehara, M.; Toyota, K.; Fukuda, R.; Hasegawa, J.; Ishida, M.; Nakajima, T.; Honda, Y.; Kitao, O.; Nakai, H.; Vreven, T.; Throssell, K.; Montgomery Jr., J. A.; Peralta, J. E.; Ogliaro, F.; Bearpark, M. J.; Heyd, J. J.; Brothers, E. N.; Kudin, K. N.; Staroverov, V. N.; Keith, T. A.; Kobayashi, R.; Normand, J.; Raghavachari, K.; Rendell, A. P.; Burant, J. C.; Iyengar, S. S.; Tomasi, J.; Cossi, M.; Millam, J. M.; Klene, M.; Adamo, C.; Cammi, R.; Ochterski, J. W.; Martin, R. L.; Morokuma, K.; Farkas, O.; Foresman, J. B.; Fox, D. J. Gaussian 16 Rev. C.01, 2016.

(245) Marenich, A. V.; Cramer, C. J.; Truhlar, D. G. Universal Solvation Model Based on Solute Electron Density and on a Continuum Model of the Solvent Defined by the Bulk Dielectric Constant and Atomic Surface Tensions. *J Phys Chem B* **2009**, *113*, 6378–6396.

(246) Grimme, S.; Ehrlich, S.; Goerigk, L. Effect of the Damping Function in Dispersion Corrected Density Functional Theory. *J. Comput. Chem.* **2011**, *32*, 1456–1465.

(247) Weigend, F.; Ahlrichs, R. Balanced Basis Sets of Split Valence, Triple Zeta Valence and Quadruple Zeta Valence Quality for H to Rn: Design and Assessment of Accuracy. *Phys. Chem. Chem. Phys.* **2005**, *7*, 3297.

(248) Allouche, A.-R. Gabedit—A Graphical User Interface for Computational Chemistry Softwares. *J. Comput. Chem.* **2011**, *32*, 174–182.

(249) Liu, Z.; Lu, T.; Chen, Q. An Sp-Hybridized All-Carboatomic Ring, Cyclo[18]Carbon: Electronic Structure, Electronic Spectrum, and Optical Nonlinearity. *Carbon* **2020**, *165*, 461–467.

(250) Lu, T.; Chen, F. Multiwfn: A Multifunctional Wavefunction Analyzer. *J Comput Chem* **2012**, *33*, 580–592.

(251) Dennington, Roy; Keith, Todd A.; Millam, John M. GaussView, Version 6, 2016.

(252) Becke, A. D. Density-functional Thermochemistry. III. The Role of Exact Exchange. *J. Chem. Phys.* **1998**, *98*, 5648.

(253) Lee, C.; Yang, W.; Parr, R. G. Development of the Colle-Salvetti Correlation-Energy Formula into a Functional of the Electron Density. *Phys. Rev. B* **1988**, *37*, 785–789.

(254) Vosko, S. H.; Wilk, L.; Nusair, M. Accurate Spin-Dependent Electron Liquid Correlation Energies for Local Spin Density Calculations: A Critical Analysis. *Can. J. Phys.* **1980**, *58*, 1200–1211.

(255) Amin, E. A.; Truhlar, D. G. Zn Coordination Chemistry: Development of Benchmark Suites for Geometries, Dipole Moments, and Bond Dissociation Energies and Their Use To Test and Validate Density Functionals and Molecular Orbital Theory. *J. Chem. Theory Comput.* **2008**, *4*, 75–85.

(256) Otto, S.; Moll, J.; Förster, C.; Geißler, D.; Wang, C.; Resch-Genger, U.; Heinze, K. Three-in-One Crystal: The Coordination Diversity of Zinc Polypyridine Complexes. *Eur. J. Inorg. Chem.* **2017**, *2017*, 5033–5040.

(257) Grimme, S.; Antony, J.; Ehrlich, S.; Krieg, H. A Consistent and Accurate *Ab Initio* Parametrization of Density Functional Dispersion Correction (DFT-D) for the 94 Elements H-Pu. *J. Chem. Phys.* **2010**, *132*, 154104.

(258) Ernzerhof, M.; Scuseria, G. E. Assessment of the Perdew–Burke–Ernzerhof Exchange-Correlation Functional. *J. Chem. Phys.* **1999**, *110*, 5029–5036.

(259) Perdew, J. P.; Burke, K.; Ernzerhof, M. Generalized Gradient Approximation Made Simple. *Phys. Rev. Lett.* **1996**, *77*, 3865–3868.

(260) van Wüllen, C. Molecular Density Functional Calculations in the Regular Relativistic Approximation: Method, Application to Coinage Metal Diatomics, Hydrides, Fluorides and Chlorides, and Comparison with First-Order Relativistic Calculations. *J. Chem. Phys.* **1998**, *109* (2), 392–399.

(261) Rosenberg, B.; Van Camp, L.; Krigas, Thomas. Inhibition of Cell Division in Escherichia Coli by Electrolysis Products from a Platinum Electrode. *Nature* **1965**, *205* (4972), 698–699. https://doi.org/10.1038/205698a0.

(262) Wang, D.; Lippard, S. J. Cellular Processing of Platinum Anticancer Drugs. *Nat. Rev. Drug Discov.* **2005**, *4* (4), 307–320. https://doi.org/10.1038/nrd1691.

(263) Englinger, B.; Pirker, C.; Heffeter, P.; Terenzi, A.; Kowol, C. R.; Keppler, B. K.; Berger, W. Metal Drugs and the Anticancer Immune Response. *Chem. Rev.* **2019**, *119* (2), 1519–1624. https://doi.org/10.1021/acs.chemrev.8b00396.

(264) Wheate, N. Multi-Nuclear Platinum Complexes as Anti-Cancer Drugs. *Coord. Chem. Rev.* **2003**, *241* (1–2), 133–145. https://doi.org/10.1016/S0010-8545(03)00050-X.

(265) Johnstone, T. C.; Park, G. Y.; Lippard, S. J. Understanding and Improving Platinum Anticancer Drugs - Phenanthriplatin. *Anticancer Res.* **2014**, *34*, 471–476.

(266) Johnstone, T. C.; Wilson, J. J.; Lippard, S. J. Monofunctional and Higher-Valent Platinum Anticancer Agents. *Inorg. Chem.* **2013**, *52* (21), 12234–12249. https://doi.org/10.1021/ic400538c.

(267) Todd, R. C.; Lippard, S. J. Structure of Duplex DNA Containing the Cisplatin 1,2-{Pt(NH3)2}2+-d(GpG) Cross-Link at 1.77 Å Resolution. *J. Inorg. Biochem.* **2010**, *104*, 902–908.

(268) Park, G. Y.; Wilson, J. J.; Song, Y.; Lippard, S. J. Phenanthriplatin, a Monofunctional DNA-Binding Platinum Anticancer Drug Candidate with Unusual Potency and Cellular Activity Profile. *Proc Natl Acad Sci* **2012**, *109*, 11987–11992.

(269) Lovejoy, K. S.; Serova, M.; Bieche, I.; Emami, S.; D'Incalci, M.; Broggini, M.; Erba, E.; Gespach, C.; Cvitkovic, E.; Faivre, S.; Raymond, E.; Lippard, S. J. Spectrum of Cellular Responses to Pyriplatin, a Monofunctional Cationic Antineoplastic Platinum(II) Compound, in Human Cancer Cells. *Mol. Cancer Ther.* **2011**, *10* (9), 1709–1719. https://doi.org/10.1158/1535-7163.MCT-11-0250.

(270) Almaqwashi, A. A.; Zhou, W.; Naufer, M. N.; Riddell, I. A.; Yilmaz, Ö. H.; Lippard, S. J.; Williams, M. C. DNA Intercalation Facilitates Efficient DNA-Targeted Covalent Binding of Phenanthriplatin. *J. Am. Chem. Soc.* **2019**, *141* (4), 1537–1545. https://doi.org/10.1021/jacs.8b10252.

(271) Tullius, T. D.; Lippard, S. J. Ethidium Bromide Changes the Nuclease-Sensitive DNA Binding Sites of the Antitumor Drug Cis-Diamminedichloroplatinum(II). *Proc. Natl. Acad. Sci.* **1982**, *79* (11), 3489–3492. https://doi.org/10.1073/pnas.79.11.3489.

(272) Boulikas, T.; Vougiouka, M. Cisplatin and Platinum Drugs at the Molecular Level (Review). *Oncol. Rep.* **2003**. https://doi.org/10.3892/or.10.6.1663.

(273) Dasari, S.; Bernard Tchounwou, P. Cisplatin in Cancer Therapy: Molecular Mechanisms of Action. *Eur. J. Pharmacol.* **2014**, *740*, 364–378. https://doi.org/10.1016/j.ejphar.2014.07.025.

(274) Lozada, I. B.; Williams, J. A. G.; Herbert, D. E. Platinum(II) Complexes of Benzannulated N ^ N ⁻^ O-Amido Ligands: Bright Orange Phosphors with Long-Lived Excited States. *Inorg. Chem. Front.* **2022**, *9* (1), 10–22. https://doi.org/10.1039/D1QI01120K.

(275) Che, C.-M.; Yang, M.; Wong, K.-H.; Chan, H.-L.; Lam, W. Platinum(II) Complexes of Dipyridophenazine as Metallointercalators for DNA and Potent Cytotoxic Agents against Carcinoma Cell Lines. *Chem. – Eur. J.* **1999**, *5*, 3350–3356.

(276) Kieltyka, R.; Fakhoury, J.; Moitessier, N.; Sleiman, H. F. Platinum Phenanthroimidazole Complexes as G-Quadruplex DNA Selective Binders. *Chem. – Eur. J.* **2008**, *14* (4), 1145–1154. https://doi.org/10.1002/chem.200700783.

(277) Cusumano, M.; Di Pietro, M. L.; Giannetto, A.; Nicolò, F.; Rotondo, E. Noncovalent Interactions of Platinum(II) Square Planar Complexes Containing Ligands Out-of-Plane with DNA. *Inorg. Chem.* **1998**, *37* (3), 563–568. https://doi.org/10.1021/ic9705406.

(278) Suntharalingam, K.; Mendoza, O.; Duarte, A. A.; Mann, D. J.; Vilar, R. A Platinum Complex That Binds Non-Covalently to DNA and Induces Cell Death via a Different

Mechanism than Cisplatin. *Metallomics* **2013**, *5* (5), 514. https://doi.org/10.1039/c3mt20252f.

(279) Luedtke, N. W.; Liu, Q.; Tor, Y. Synthesis, Photophysical Properties, and Nucleic Acid Binding of Phenanthridinium Derivatives Based on Ethidium. *Bioorg. Med. Chem.* **2003**, *11*, 5235–5247.

(280) Nandi, R.; Chaudhuri, K.; Maiti, M. EFFECTS OF IONIC STRENGTH and PH ON THE BINDING OF SANGUINARINE TO DEOXYRIBONUCLEIC ACID. *Photochem. Photobiol.* **1985**, *42* (5), 497–503. https://doi.org/10.1111/j.1751-1097.1985.tb01600.x.

(281) Howe-Grant, M.; Lippard, S. J. Binding of Platinum(II) Intercalation Reagents to Deoxyribonucleic Acid. Dependence on Base-Pair Composition, Nature of the Intercalator, and Ionic Strength. *Biochemistry* **1979**, *18* (26), 5762–5769. https://doi.org/10.1021/bi00593a003.

(282) Murphy, M. P. How Mitochondria Produce Reactive Oxygen Species. *Biochem. J.* **2009**, *417* (1), 1–13. https://doi.org/10.1042/BJ20081386.

(283) Ivashkevich, A.; Redon, C. E.; Nakamura, A. J.; Martin, R. F.; Martin, O. A. Use of the γ-H2AX Assay to Monitor DNA Damage and Repair in Translational Cancer Research. *Cancer Lett.* **2012**, *327* (1–2), 123–133. https://doi.org/10.1016/j.canlet.2011.12.025.

(284) Mah, L.-J.; El-Osta, A.; Karagiannis, T. C. ΓH2AX: A Sensitive Molecular Marker of DNA Damage and Repair. *Leukemia* **2010**, *24* (4), 679–686. https://doi.org/10.1038/leu.2010.6.

(285) Chargaff, E.; Lipshitz, R. Composition of Mammalian Desoxyribonucleic Acids [1]. *J. Am. Chem. Soc.* **1953**, *75* (15), 3658–3661. https://doi.org/10.1021/ja01111a016.

(286) Kaim, W.; Schwederski, B.; Klein, A. Manganese-Catalyzed Oxidation of Water to O2. In *Bioinorganic Chemistry: Inorganic Elements in the Chemistry of Life*; Wiley: Chichester, 2013; pp 67–74.

(287) Pan, D.; Schmieder, A. H.; Wickline, S. A.; Lanza, G. M. Manganese-Based MRI Contrast Agents: Past, Present, and Future. *Tetrahedron* **2011**, *67* (44), 8431–8444. https://doi.org/10.1016/j.tet.2011.07.076.

(288) East, N. R.; Förster, C.; Carrella, L. M.; Rentschler, E.; Heinze, K. The Full d^3–d^5 Redox Series of Mononuclear Manganese Complexes: Geometries and Electronic Structures of $[Mn(Dgpy)_2]^{n+}$. *Inorg. Chem.* **2022**, *61* (37), 14616–14625. https://doi.org/10.1021/acs.inorgchem.2c01680.

(289) Herr, P.; Kerzig, C.; Larsen, C. B.; Häussinger, D.; Wenger, O. S. Manganese(i) Complexes with Metal-to-Ligand Charge Transfer Luminescence and Photoreactivity. *Nat. Chem.* **2021**, *13* (10), 956–962. https://doi.org/10.1038/s41557-021-00744-9.

(290) Betley, T. A.; Qian, B. A.; Peters, J. C. Group VIII Coordination Chemistry of a Pincer-Type Bis(8-Quinolinyl)Amido Ligand. *Inorg. Chem.* **2008**, *47* (24), 11570–11582. https://doi.org/10.1021/ic801047s.

(291) Huynh, M. T.; Anson, C. W.; Cavell, A. C.; Stahl, S. S.; Hammes-Schiffer, S. Quinone $1 e^-$ and $2 e^-/2 H^+$ Reduction Potentials: Identification and Analysis of Deviations from Systematic Scaling Relationships. *J. Am. Chem. Soc.* **2016**, *138* (49), 15903–15910. https://doi.org/10.1021/jacs.6b05797.

(292) Michaelis, L.; Hill, E. S. THE VIOLOGEN INDICATORS. *J. Gen. Physiol.* **1933**, *16* (6), 859–873. https://doi.org/10.1085/jgp.16.6.859.

(293) Woodhouse, M. D.; McCusker, J. K. Mechanistic Origin of Photoredox Catalysis Involving Iron(II) Polypyridyl Chromophores. *J. Am. Chem. Soc.* **2020**, *142* (38), 16229–16233. https://doi.org/10.1021/jacs.0c08389.

3 Coordination Chemistry and Photophysics of $N\wedge N^-\wedge O$ Ligated Complexes

3.1 Abstract

A series of complexes supported by phenanthridine-based $N\wedge NH\wedge O$ ligands are presented and discussed. A variety of different coordination numbers and geometries are obtained depending on the metal centre. A switch from the keto-enaminate to the enolato-imine tautomer is observed when the proton is replaced by a nonhydrogen atom (boron, zinc, and platinum) as evident from the solution nuclear magnetic resonance (NMRs) and attenuated total reflectance infrared (ATR-IR) spectra, and crystal structures of the ligands and the complexes. The complexes exhibit some CT character on the lower energy absorption manifold. The phosphorescence radiative decay channel becomes prominent with increasing metal centre size.

3.2 Introduction

The β-diketonate ligands (Figure 3.1) are monovalent bifunctional ligands that have become some of the most popular ligands used in coordination chemistry.[77–80] These ligands have strong chelating tendencies forming stable complexes. Two tautomers exist at equilibrium in solution, the diketone and the keto-enol tautomers. The most prominent binding mode is through the oxygen donor atoms. However, two novel binding modes have also been observed, (i) in K[Pt(acac)$_2$Cl] wherein the $\pi_{\text{C-C}}$ binds to Pt in an η^2 fashion,[81,82] and (ii) ligation of the central C$_3$ carbon to metal centres.[83] The steric and electronic properties of these ligands can be tuned by replacing the oxygen donor atoms with nitrogen as in β-diiminates. This enables installment of bulky alkyl or aryl substituents on the nitrogen allowing for the isolation of coordinatively

unsaturated metal centres[84] and has profound impact on the reactivity of the complexes.[85] The same strategy has also been employed to isolate unusual oxidation states in main group elements.[86,87] Intermediate between the β-diketonates and β-diiminates are the β-ketoiminates combining some of the properties that have been found desirable in the β-diketonates and β-diiminates congeners.
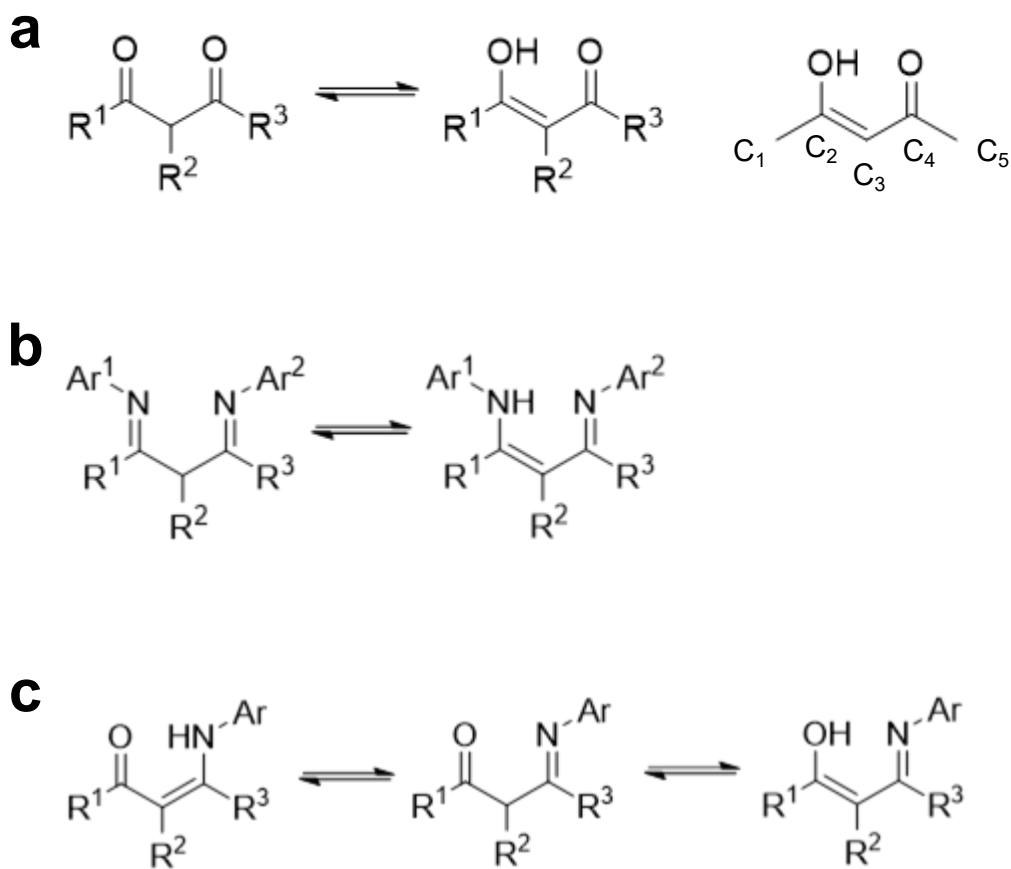
Figure 3.1. Bidentate (a) β-diketonate, (b) β-diiminate, (c) β-ketoiminate ligands and the different tautomers. Also shown is acetylacetone and numbering scheme.

Our group has constructed a monoanionic 4-(4-amino-2-R-phenanthridinyl)-3-penten-2-ones ligand scaffolds (Figure 3.2) bearing benzannulated phenanthridine (3,4-benzoquinoline)

87

units. Main group (boron) and transition metal (zinc and platinum) complexes have been successfully synthesized and characterized. While these ligands are expected to bind in tridentate fashion forming 5,6-ring chelates around the metal centre, the small size of boron preferentially allows only for the 6-ring chelate with the phenanthridinyl moiety acting as a pendent. This chapter discusses the synthesis, structure, and photophysical properties of the complexes.
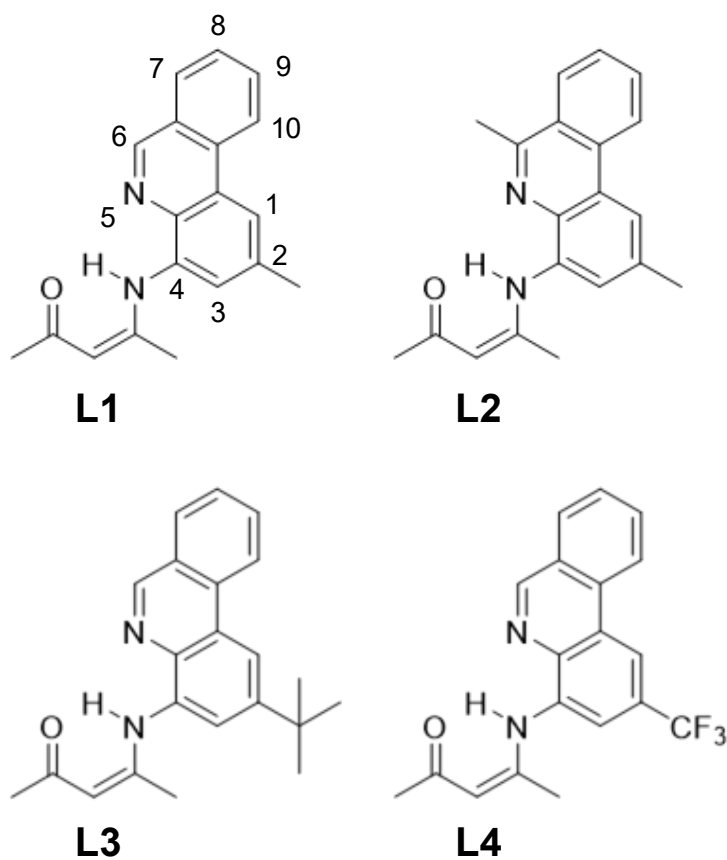
Figure 3.2. 4-(4-Amino-2-R-phenanthridinyl)-3-penten-2-ones (N^NH^O), Ln (n = 1-4), ligand scaffolds. The IUPAC numbering system for phenanthridines is illustrated for the proligands.

3.3 Turning on Emission in Donor-Acceptor Boron-Ketoiminates

3.3.1 Synthesis and Structure

L1-**L4** presented in Chapter 2 were reacted with boron trifluoride diethyl etherate in the presence of excess base (NEt$_3$) to install a BF$_2$ unit (Scheme 3.1). Substitution in the 2-position of phenanthridine (R^1) had no significant influence on the overall progress of the reaction, and compounds **1**, **3** and **4** were isolable as brown or orange solids in high yields (72-86%). A lower yield was observed for **2** (38%), possibly attributable to the presence of a more sterically demanding CH$_3$ at the 6-position of the phenanthridinyl arm (R^2).[88] The isolated compounds were found to be stable to air and ambient moisture, in solution and the solid state, and to protic solvents such as alcohols. Both solution (NMR) and solid state (ATR-IR) spectra of the complexes are consistent with ligand deprotonation and binding to boron. For example, the resonance attributed to the enamine proton in the ^{1}H NMR spectra (δ_{NH}/ppm: **L1**, 13.53; **L2**, 13.61; **L3**, 13.44; **L4**, 13.72) and the N–H bending mode in the IR ($\nu_{\text{N-H, bend}}$/cm^{-1}: **L1**, 1569; **L2**, 1569; **L3**, 1570; **L4**, 1579) are both absent in the spectra of the complexes. In addition, the CH resonance of the methine group of the ketoenamine subunit is shifted downfield by ~0.3 ppm. A comparably more minor shift is observed for the ^{1}H resonance attributed to the CH unit in the 6-position of phenanthridine, with an average upfield shift of ~0.09 ppm. Our previous studies on coordination complexes supported by phenanthridine-based ligands typically saw larger shifts in the ^{1}H resonance of the C$_6H$ (using the IUPAC numbering highlighted in Scheme 1) upon binding to Lewis acids such as transition metals, with the shift being dependent on the metal.[89,90] Indeed, Pt(II) complexes of **L3** and **L4** exhibit a more pronounced downfield shift on the C$_6H$ resonance of ~0.7 ppm.[91] The ^{1}H NMR spectroscopy therefore implies that the phenanthridinyl unit does not associate significantly

with the boron centre in solution. High-resolution mass spectrometry of **1**-**4** supports their

formulation as 1:1 ligand-BF_2 complexes.
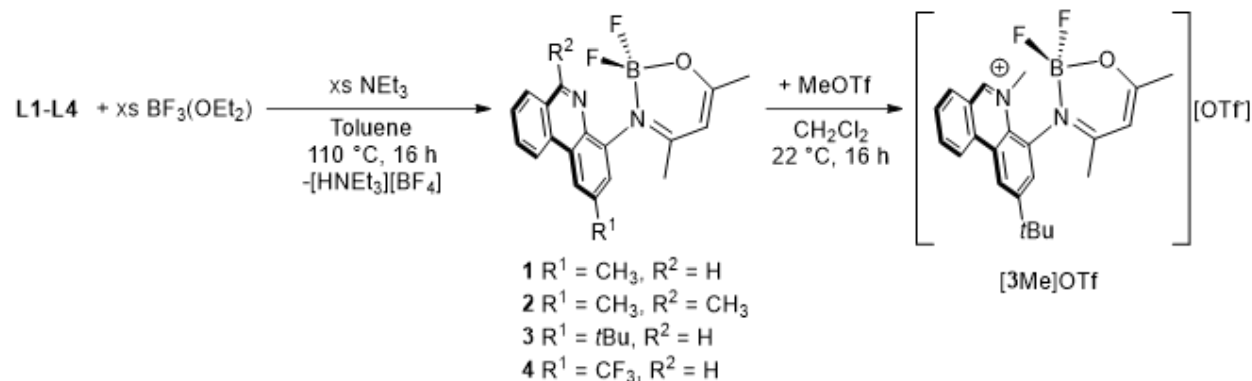
Scheme 3.1. Synthesis of N^N−^O-ligated boron difluoride complexes (**1-4**), and the methylated complex

[**3**Me]OTf.

Despite the lack of phenanthridine coordination, no dynamic processes associated, for

example, with rotation about the C_4–N bond axis are observed at room temperature by solution

NMR spectroscopy. ^{19}F NMR spectra of **1-4** exhibit two distinct doublet-of-quartet resonances due

to the inequivalence of the fluorine nuclei (Figure 3.3). A doublet-of-doublets is accordingly

observed in by ^{11}B NMR spectroscopy, consistent with a rigid BF_2 unit. These signals are quite

sharp and well-resolved compared to the broad resonances for $BF_3(OEt_2)$.[92] Most *N*-aryl-

substituted difluoroboron ketoiminates, in comparison, exhibit a more symmetric boron

environment with a single quartet resonance in the ^{19}F NMR and a triplet resonance in the ^{11}B

NMR appearing at ~0 ppm.[93] Increasing the steric congestion close to boron through inclusion of

substituents *ortho* to the nitrogen donor, however, or any introduction of asymmetry at the *N*-aryl

substituent does lead to similar patterns in the ^{19}F and ^{11}B NMR spectra to those observed for **1-
4**.[94] The inequivalence of the fluorine nuclei in closely related systems[93] has been attributed to the

magnetic anisotropy associated with the ring-current of the chelate π-system, with F^2 experiencing greater shielding (average ^{19}F δ = -139 ppm) than F^1 (average ^{19}F δ = -130 ppm). Here, the rigid, near-orthogonal arrangement of the phenanthridinyl unit relative to the azaoxaborinine chelate enables close contact between the hydrogen in the 3-position of the phenanthridinyl ring and one of the two fluorine nuclei (F^1), which can be observed by ^{19}F-^1H Nuclear Overhauser Effect (NOE) NMR spectroscopy (Figure 3.3b). This interaction likely contributes to the less shielded ^{19}F chemical shift of F^1. This is highlighted by the strong linear correlation between the B$-$F$^1\cdots$C$_3H^{phenanthridinyl}$ distance (obtained from the solid-state structures, *vide infra*) and the ^{19}F chemical shift of F^1, with the shortest B$-$F$^1\cdots$C$_3H^{phenanthridinyl}$ separation of the neutral complexes (**2**) exhibiting the greatest deshielding in the $^{19}F(F^1)$ resonance.

Complex	δ_{F1} / ppm ($^2J_{FF}$ / Hz, $^1J_{BF}$ / Hz)	δ_{F2} / ppm ($^2J_{FF}$ / Hz, $^1J_{BF}$ / Hz)	δ_B / ppm
1	-129.9 (96, 20)	-139.4 (95, 11)	1.0
2	-129.0 (95, 21)	-141.4 (95, 10)	1.0
3	-130.7 (96, 18)	-138.4 (96, 11)	1.0
4	-129.8 (94, 19)	-138.1 (95, 11)	1.0
[**3**Me]OTf	-128.5 (94, 22)	-141.8 (93, 10)	0.9
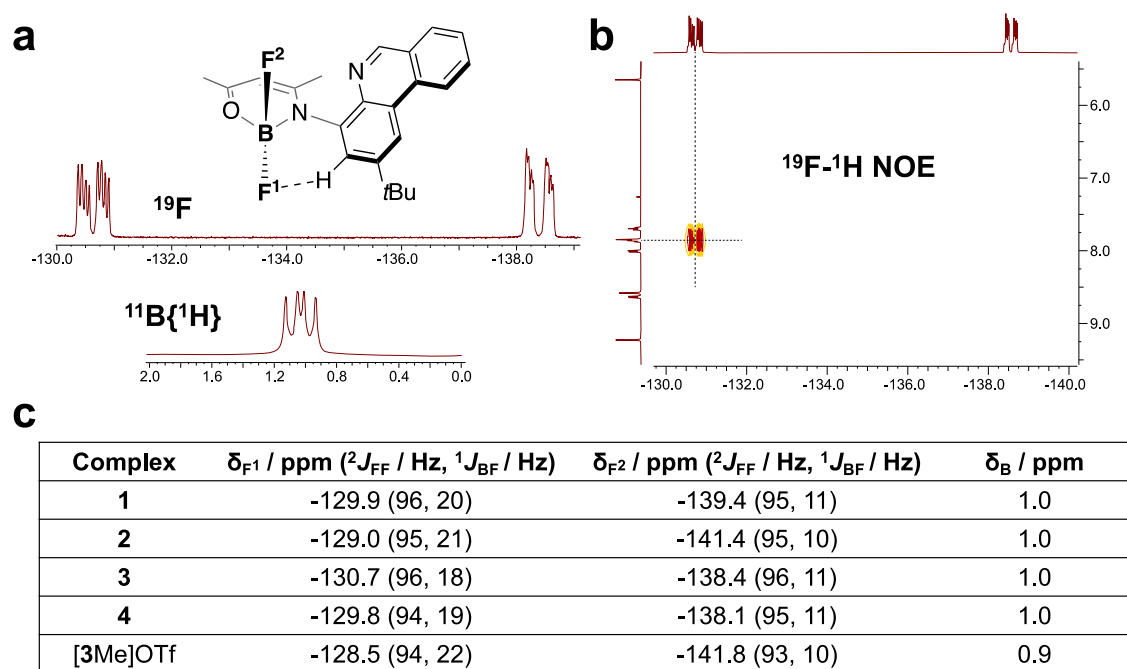
Figure 3.3. (a) 19F, 11B and (b) 19F-1H NOE NMR spectra and (c) assignments for **1-4** and [**3**Me]OTf.

Reacting **3** with methyl trifluoromethanesulfonate (OTf⁻, triflate) resulted in the selective methylation of the phenanthridinyl nitrogen, generating the *N*-methylated phenanthridinium salt [**3Me**]OTf. A pronounced downfield shift in the C_6H resonance of 0.8 ppm is observed, accompanied by a downfield shift of the methine $C_{13}H$ resonance by 0.2 ppm compared with **3**. In addition, a new methyl ¹H resonance appears at 4.63 ppm ($C_{18}H$), which is far more downfield than the ¹H resonances of the $C_{11}H$ (2.35 ppm) and $C_{15}H$ (2.03 ppm) methyl substituents of the azaoxaborinine chelate ring. The appearance of a new ¹⁹F resonance with the correct integration for OTf⁻ further supports the structural assignment, as does the high-resolution mass spectrum.

Methylation also induces steric repulsion between the *N*-methyl substituent and the BF_2 unit, leading to a greater difference between the magnetic environments of the two F atoms, as indicated by a downfield shift of the signal for F^1 (δ_F: -128.5 ppm, [**3Me**]OTf; *cf.* -130.7 ppm, **3**) and an upfield shift of that of F^2 (δ_F: -141.8 ppm, [**3Me**]OTf; -138.4 ppm, **3**). The more imposing N-Me unit increases the interaction between F^1 and the phenanthridinyl C_3H in two ways. First, the phenanthridinyl moiety tilts to move the N-Me unit away from the (N^O)BF_2 unit, in turn pushing the H atom in the 3-position closer as illustrated in Figure 3.4. Second, the boron centre unit drops slightly more out of the plane formed by the ligand, evidenced by changes to the angle between the plane comprised of the N-C-C-C-O ligand backbone and that formed by the N-B-O unit (20.0°, [**3Me**]⁺; 13.2°, **3**; ground state equilibrium geometries in CH_2Cl_2 at the SMD-CAM-B3LYP-D3(BJ)/def2-SVP level of theory). This is accompanied by a slight upfield shift of the ¹¹B resonance (δ(¹¹B): 0.9 ppm, [**3Me**]OTf; 1.0 ppm, **3**). A further consequence is a weaker interaction between F^2 and the boron centre in solution, as evidenced by a less well-resolved $^1J_{BF}$ coupling constant and a broader signal in both ¹⁹F and ¹¹B spectra compared to **3**, suggesting elongation of

the B−F bond. The $^2J_{FF}$ coupling constant is also slightly reduced in [**3**Me]OTf (**3**: $^2J_{FF}$ = 96 Hz; [**3**Me]OTf: $^2J_{FF}$ = 94 Hz).
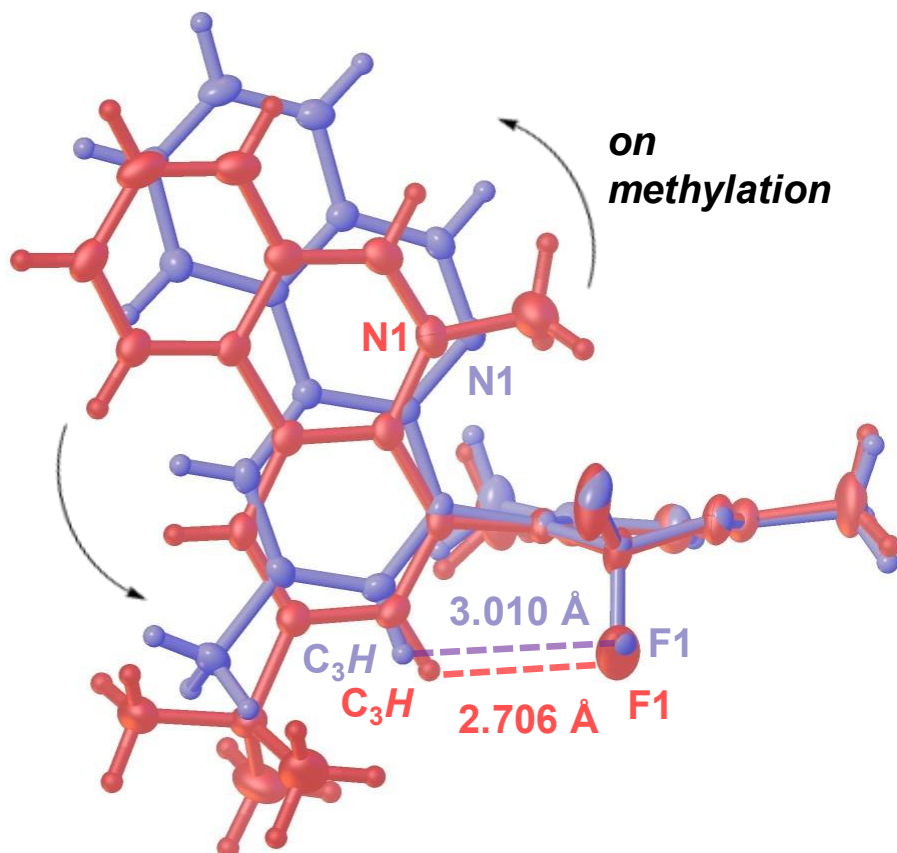
Figure 3.4. Overlay of the crystal structures highlighting the change in H_{11} F^1 distance between **1** and [**3**Me][OTf].

The nuclearity and binding modes of the complexes in the solid state were confirmed using single crystal X-ray diffraction (Figure 3.5a-e). Suitable crystals of **1**, **2**, **4** and [**3**Me]OTf were grown by the slow diffusion of hexanes or pentane vapors into chloroform solutions. In each structure, the boron centre is monomeric and four-coordinate. Consistent with literature boron complexes supported by ketoiminate ligands,[93,95–97] the B−N bonds (1.562 Å average) are ~0.09 Å longer than the B−O bonds (1.469 Å; Table 3.1). Compared with symmetric boron diketonates,

diketoiminates and diiminates,[93] the BF_2 unit is displaced further away from the plane of the chelate ring and the F−B−F angle more acute. Compared with the solid-state structure of the proligand **L3**,[91] the C−N and C−O bonds of the chelating ligand backbone are shorter and longer, respectively, across the series of BF_2 complexes. This suggests a switch from keto-enamine to an enolato-imine tautomeric structure upon deprotonation and binding to boron (Figure 3.5e). The solid-state IR spectra support this assignment, which is also corroborated by DFT simulations of the IR spectra [CAM-B3LYP-D3(BJ)/def2-SVP; gas-phase]. For example, the vibrational mode attributable to the C-O stretch shifts to lower energy in the BF_2 complexes compared with the free ligands ($v_{C=O, stretch}$ / cm^{-1}: **L1** 1617 vs **1** 1397; **L2** 1615 vs **2** 1404; **L3** 1617 vs **3** 1403; **L4** 1634 vs **4** 1524). A similar shift to lower frequency of the C-O stretch was observed for a series of (*N*-methyl-1,3-enaminoketonato)boron difluorides.[98]
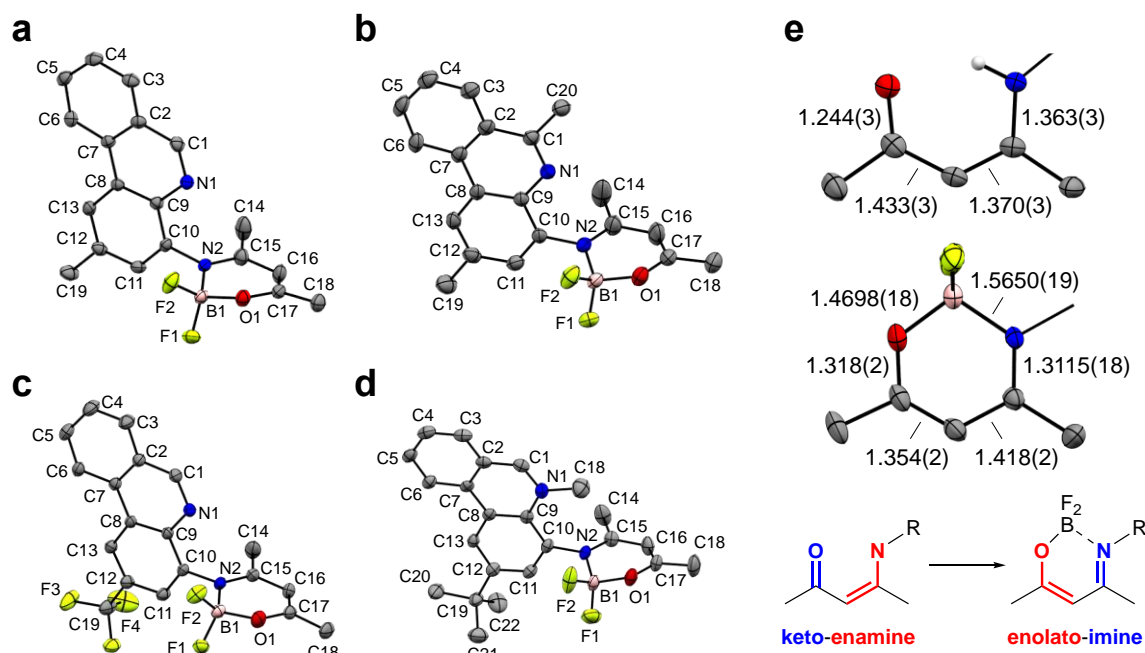
Figure 3.5. Solid-state X-ray structures of (a) **1**, (b) **2**, (c) **4**, and (d) [**3**Me]OTf, with thermal ellipsoids shown at 50% probability level. Hydrogen atoms, counterion, and co-crystallized solvents are omitted for clarity. (e) Bonding description highlighting keto-enamine tautomer in proligand **L3** and enolato-imine tautomer in **4**.

Table 3.1. Selected bond lengths (Å), bond angles (°), and dihedral angles (°) between the boron difluoride chelate and phenanthridine planes.

Complex	1	2	4	[**3**Me]$^+$
B1−O1	1.467(3)	1.471(4)	1.4698(18)	1.472(5)
B1−N2	1.563(4)	1.558(4)	1.5650(19)	1.558(5)
B1−F1	1.374(3)	1.379(3)	1.3751(19)	1.358(5)
B1−F2	1.376(3)	1.380(3)	1.3841(19)	1.375(5)
O1−B1−N2	108.6(2)	109.4(2)	109.48(12)	108.5(3)
F1−B1−F2	110.7(2)	110.1(2)	109.86(13)	111.4(3)
O1−B1−F1	109.5(2)	108.3(2)	109.84(12)	109.3(3)
O1−B1−F2	108.9(2)	109.8(2)	108.99(12)	109.3(3)
N2−B1−F1	109.3(2)	110.3(2)	109.78(11)	109.5(3)
N2−B1−F2	109.8(2)	109.0(2)	108.87(12)	108.7(3)
Interplanar angle^a	86.4	81.2	87.4	88.7
BF$_2$ "pucker"^{b}	25.1	20.6	12.1	27.7

As concluded in solution, the phenanthridinyl arms are not associated with the boron centres in the solid state. In each structure, the phenanthridinyl ring is nearly orthogonal to the plane formed by the B-N-C-C-C-O backbone of the (N^O)BF_2 unit (**1**, 86.4°; **2**, 81.2°; **4**, 87.4°; [**3**Me]$^+$: 88.7°; Figure 3.6a and Table 3.1). The small variation between the complexes is likely ascribable to packing effects rather than to any electronic influence of the substituents, as values for the optimized ground-state geometries of the neutral boron complexes in the gas phase are predicted to lie within an even narrower range (69-71°), while the cationic analogue displays a slight decrease relative to the solid-state structure (81.7°). As discussed above, the (N^O)BF_2 rings are not completely planar, thanks to the preference of the four-coordinate boron for tetrahedral geometry, and the boron nucleus lies to one side of the plane formed by the N-C-C-C-O atoms of the ligand backbone, distinguishing the two B−F bonds, consistent with the solution-phase assignment described above (Figure 3.6b). Analysis of extended interactions in the solid state suggests that this deviation from planarity is not only influenced by crystal packing, but also by weak intermolecular CH⋯F non-covalent interactions[99] and intramolecular steric repulsion between the phenanthridinyl moiety and (N^O)BF_2 unit (Figures 3.7a-d). As discussed above, the BF_2 unit in each structure leans toward the C11-*H* unit and away from the C=N subunit, with B1−F1⋯C11-*H* and B1−F2⋯N1=C1 separations of 2.9 Å and 3.4 Å, respectively. The solid-state structure of [**3**Me]$^+$ shows that both the out-of-plane positioning of the boron relative to the plane of the N^O ligand backbone ([**3**Me]$^+$: 27.7°; *cf.* **1**, 25.1°; **2**, 20.6°; **4**, 12.1°; the BF_2 "pucker" angle in Table 3.1) and the tilting of the phenanthridinyl plane relative to the chelate plane increase upon

N-methylation, resulting from the mutual repulsion between the methyl and the BF_2 units, as predicted by the solution NMR data. The B1–F2 bond distance is also elongated by 0.017 Å compared with B1–F1. This is consistent with the smaller $^1J_{BF}$ and $^2J_{FF}$ coupling constants measured for [**3**Me]$^+$ compared to **3**.

a

Interplanar angle
1   86.4°
2   81.2°
4   87.4°
[**3**Me]$^+$ 88.7°

b

"Pucker" angle
1   25.1°
2   20.6°
4   12.1°
[**3**Me]$^+$ 27.7°
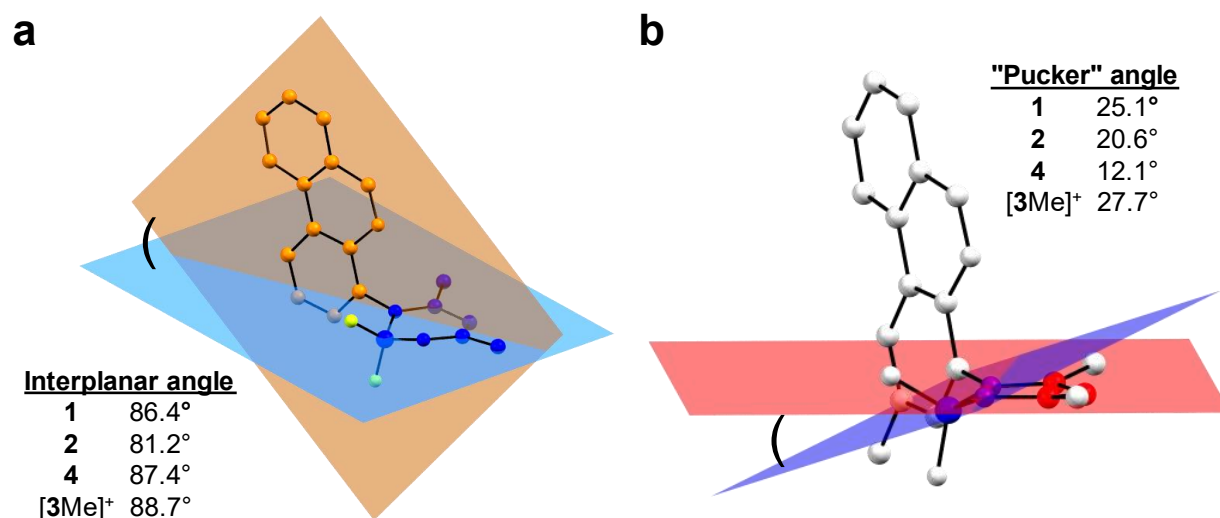
Figure 3.6. Visualization of interplanar and BF_2 "pucker" angles in Table 3.1.
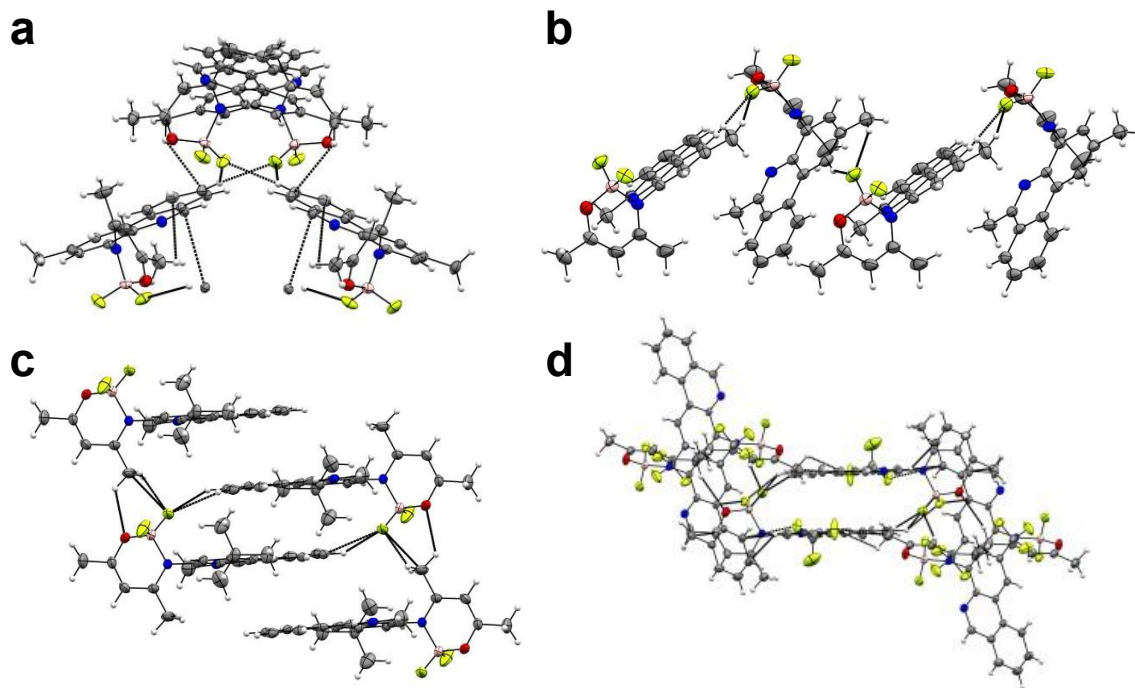
Figure **3.7.** Packing diagrams of (a) **1**, (b) **2**, (c) [**3**Me][OTf] and (d) **4** illustrating the different intermolecular interactions in the solids state.

3.3.2 Photophysical Properties

Compounds **1**-**3** are pale brown or orange (**4**) as powders and light yellow in solution. Solution optical absorption spectra accordingly lack significant absorptive cross-section in the visible region of the spectrum but contain three notable features in the UV: two intense absorptions at ~225 and 300 nm, and a weak but sharp peak on the low-energy edge of these bands at ~350 nm (Figure 3.8). Such features have been observed in Pt(II) complexes with phenanthridinyl-based ligands related to those here.[100,101] Indeed, a series of relatively weak but well-resolved bands around 350 nm is typical of the ^1L_b π-π* transitions of azaphenanthrenes including phenanthridine.[102–104] The lowest-energy singlet excited state of the heterocycles remains similar

to that of phenanthrene itself, despite the introduction of the heteroatom, and its energy is largely insensitive to the local environment. In the present instance, no significant solvatochromism was observed in the spectrum, consistent with this assignment. *N*-Methylation to generate [**3**Me]OTf results in a red-shift and the absorption then tails to ~400 nm, consistent with the effect of protonation or *N*-methylation of phenanthridine itself.[105,106]
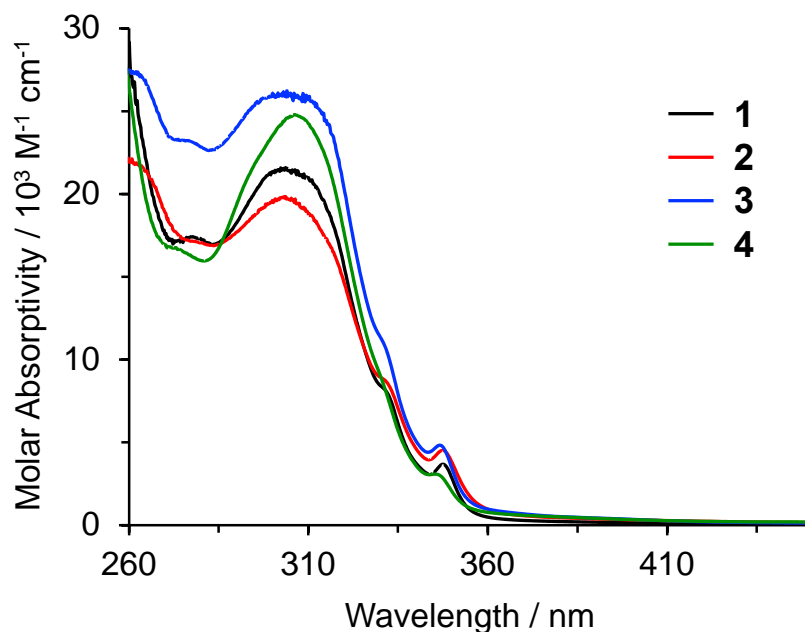
Figure 3.8. UV-Vis absorption spectra of **1**-**4** in CH2Cl2 at 295 K.

For complexes **1**–**4** in deoxygenated dichloromethane, excitation into the lowest energy manifold (~350 nm) produces only very weak, broad emission in the 360–600 nm region. The most convincing data were obtained for compound **3** (Figure 3.9a), with an emission maximum around 370 nm, resembling fluorescence from phenanthridine itself but lacking the expected vibrational structure and with a much lower quantum yield (1% versus 19% for phenanthridine[105]). The excitation spectrum of **3** does show reasonable agreement with the absorption spectrum, but for **1**, **2**, and **4**, the excitation spectra show bands that extend to longer wavelength than the

absorption spectrum. Strikingly, the *N*-methylated compound [**3**Me]OTf is much more brightly emissive, showing broad, unstructured emission centred at 508 nm in deoxygenated CH_2Cl_2 with a quantum yield and emission decay time of 9 ± 2 % and 2.7 ± 0.5 ns (Figure 3.9b), respectively. The absorption and excitation spectra now show a convincing match. There is no significant change in the quantum yield or lifetime in air-equilibrated solution compared to the deoxygenated conditions. The short lifetime and lack of sensitivity to dissolved oxygen point to the emission being spin-allowed fluorescence from a singlet excited state. The emission is, however, significantly red-shifted by about 100 nm compared to *N*-methylated phenanthridines,[41] and thus is unlikely to emanate from a simple phenanthridine-localized excited state. The emission band shows only a small degree of positive solvatochromism, being slightly blue-shifted in THF (λ_{max} = 504 nm) and slightly red-shifted in CH_3CN (λ_{max} = 514 nm; Figure S8). In both cases, the quantum yield is reduced relative to that in CH_2Cl_2 (1.1 and 1.9 %, respectively).
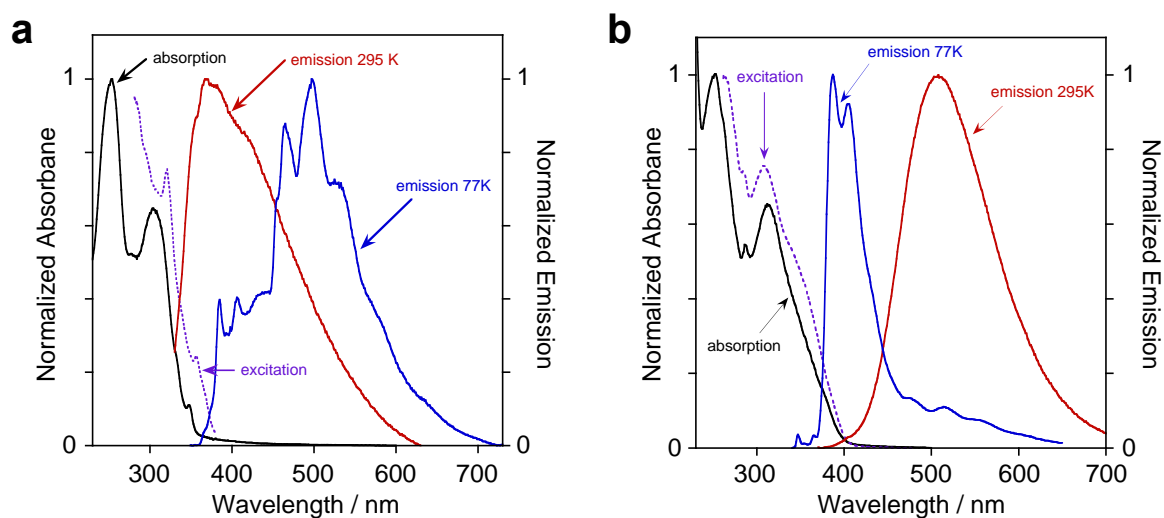
Figure 3.9. Absorption and emission spectra of (a) **3** and (b) [**3**Me]OTf.

At 77 K, all five compounds display two sets of vibrational bands, one in the region 360–420 nm and the other roughly between 460–600 nm. These are consistent with the fluorescence

and phosphorescence bands, respectively, displayed by phenanthridine at low temperature.[107] This assignment is supported by very different emission decay times (τ) of the two sets of bands (9.6 ns and 750 ms, in the case of [**3**Me]OTf) corresponding to spin-allowed and formally spin-forbidden transitions respectively. The lifetimes of the phosphorescence bands of **1**, **3** and **4** were similar ($\tau = 870, 880, 820$ ms; the estimated uncertainty is $\pm 10\%$), while that of **2** was a little longer at 1300 ms. Interestingly, the ratio of the integrated intensities of the fluorescence to phosphorescence bands is much higher for the methylated compound (ratios are approximately 3.5:1 for [**3**Me]OTf and 1:4 for **3**), which might indicate that the rate of intersystem crossing (ISC) has been retarded upon methylation. ISC competes with fluorescence as a deactivation pathway for the singlet state, and thus a reduction in the rate of ISC may lead to an increase in fluorescence. Meanwhile, a reduction in ISC also limits the yield of triplet state upon light absorption, lowering the contribution from phosphorescence. Such an effect might also account, at least in part, for the more intense fluorescence exhibited by [**3**Me]OTf at room temperature. However, the earlier conclusion that the room temperature fluorescence is not solely phenanthridine-based is reinforced by the large bathochromic shift of the fluorescence by around 5000 cm^{-1} on going from 77 K to room temperature, much larger than typical rigidochromic effects for aromatics.

3.4   Enabling Phosphorescence in Zinc(II) Complexes

3.4.1 Synthesis and Structure

As shown in Section 3.3.2. it is possible to control the radiative decay pathways in boron complexes by controlling the orientation of the phenanthrdinyl pendent arm relative the

azaoxaborinine chelate. In summary, orthogonal orientation of the phenanthridinyl moiety relative to the azaoxaborinine chelate imposed by methylation of the phenanthridinyl nitrogen ([**3**Me][PF$_6$]) led to a selective radiative decay from the emissive S$_1$ state. In contrast, in **3** both fluorescence and phosphorescence phenomena are observed owing to the functionality of the molecule in the excited state suggesting that a conformation allows for the decay from the emissive T$_1$ state. A conformation where both the phenanthridinyl and azaoxaborinine chelate planes are nearly coplanar is proposed to facilitate the ISC from S$_n$ to T$_1$ manifolds. To test this hypothesis zinc complexes of ligands **L1**, **L3** and **L4**, complexes **5**-**7**, were prepared in a similar way to homoleptic Zn(II) complexes supported by monoanionic, bidentate *N*-phenyl-4-aminophenanthridines.[108] That is, via the dropwise addition of a solution of diethylzinc in hexanes into a solution of the proligands in 3:1 hexanes/toluene, both pre-cooled to -38 °C, which is then warmed to ambient temperature (Scheme 3.2). Solutions of the proligands in the binary solvent mixture were pale yellow but grew more intensely colored on addition of diethylzinc, and bright yellow precipitates formed after stirring overnight. These solids were isolated by filtration and further purified by repeated washing with cyclohexane or recrystallization from hot cyclohexane. Complexes **5**-**7** were isolated in this way in yields of 54, 84 and 79% for R = *t*Bu, Me and CF$_3$, respectively. The increased solubility of **6** in organic solvents conferred by the *tert*-butyl substituents likely contributes to the reduced isolated yield. In contrast to four-coordinate, homoleptic, *bis*[phenanthridinyl-4-(*N*-phenyl)amido]zinc(II),[108] **5**-**7** are all stable to both air and ambient moisture, as well as to mildly acidic solvents such as chloroform. Only one set of ^{1}H and ^{13}C NMR signals is observed in solution, suggesting that the two ligands have the same magnetic environment in solution, introducing C_2 symmetry to the complexes. In the ^{1}H NMR spectrum, coordination to Zn(II) induces a ~0.7 ppm shift upfield to the N=C$_6$*H* resonance of the phenanthridinyl ligand arms [e.g.,

$\delta(\mathrm{N=C_6}H)$: L1, 9.29 ppm; 5, 8.58 ppm] which likely results from ring-current induced shielding by the (N^O)Zn chelate.[109]
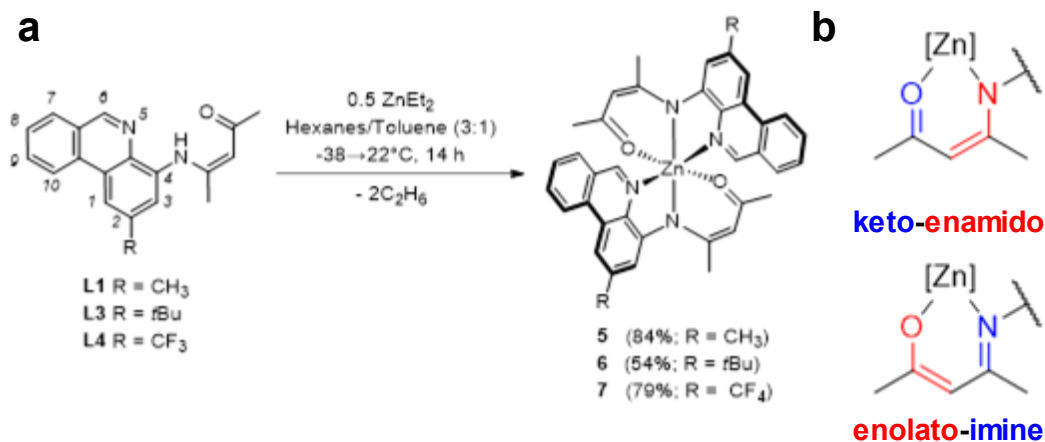
Scheme 3.2. (a) Synthesis of **5-7** with isolated yields indicated in parentheses. (b) Canonical forms of the tautomers possible for **L1**, **L3**, and **L4**.

The solid-state structures of **6** and **7** determined using single-crystal X-ray diffraction confirm the pseudo-octahedral coordination around the metal centre (Figure 3.10). The structure of **6** contains crystallographically distinct ligand environments, while **7** possesses the same approximate C_2 point group symmetry observed in solution by NMR spectroscopy. The asymmetry of **6** in the solid state appears to arise from the presence of short-contact, non-covalent C–H$^{\mathrm{phenanthridinyl}}$...$\pi^{\mathrm{phenanthridinyl}}$ interactions between adjacent Zn(II) complexes, and non-bonding interactions between a CH unit of co-crystallized $\mathrm{CH_2Cl_2}$ and the oxygen donor and $\pi_{\mathrm{C=N}}$ of the ketoiminate chelate ring (Figure 3.11). Indeed, the optimized geometry of **6** in the gas phase presents a quite symmetric environment around the metal. As mentioned in section 3.2, chelating ligands of the β-ketoimine type can exist in tautomeric forms (Figure 3.1) with anionic character

localized at either nitrogen ('amido') or oxygen ('alkoxy'; Scheme 3.2b). The Zn1−O1/2 (2.060-2.075 Å) and Zn1-N2/4 (2.112-2.131 Å) bond distances suggest that a metal-alkoxy descriptor is more appropriate here. In general, in boron (section 3.3) and platinum (section 3.5) complexes of **L1-L4**, the enolato-imine tautomer predominates upon deprotonation or coordination to metal centres,[91,101,109] while structural and spectroscopic data for the proligands (**L1-L4**) are more consistent with the keto-enamine tautomer[91] [C15−N2 / C17−O1: **L3**, 1.363(3) / 1.244(3) Å;[91] **6**, 1.315(11) / 1.255(10) Å; **7**, 1.328(3) / 1.263(3) Å].
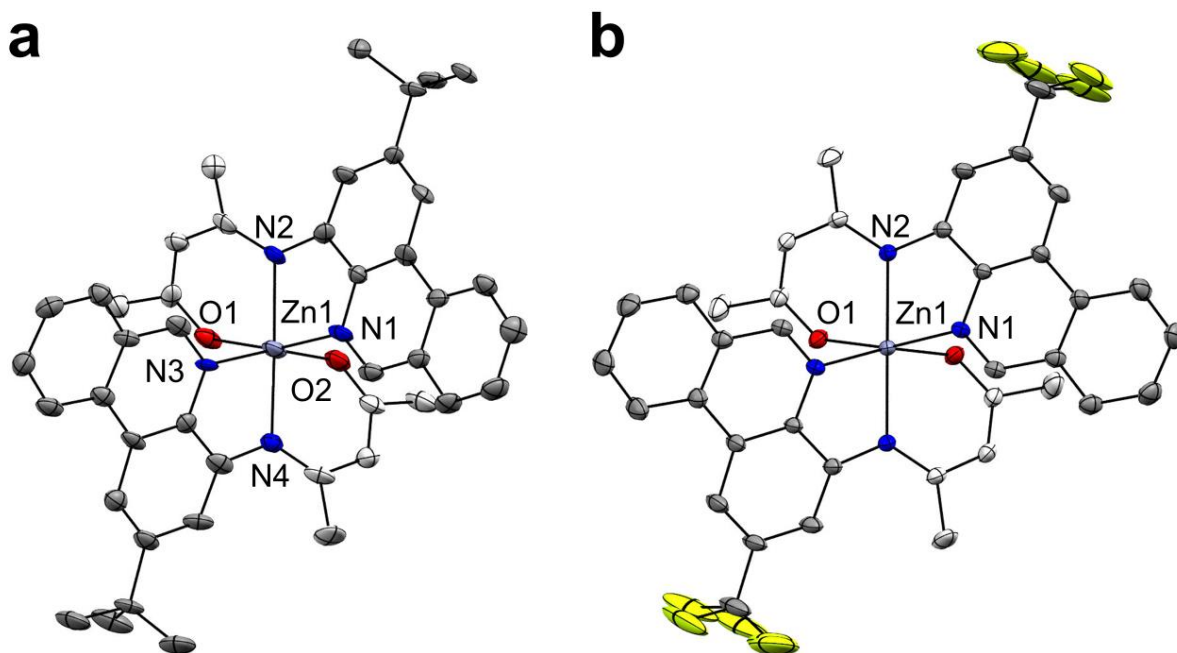
Figure 3.10. Solid-state structures of (a) **6** and (b) **7** with thermal ellipsoids shown at 50% probability levels. Hydrogen and co-crystallized solvents are omitted for clarity. Selected bond lengths (Å) and bond angles (°) for **6**: Zn1−N1 2.201(8), Zn1−N3 2.188(7), Zn1−N2 2.112(6), Zn1−N4 2.131(6), Zn1−O1 2.060(6), Zn1−O2 2.066(6); N1−Zn1−N3 89.8(3), N2−Zn1−N4 168.6(3), O1−Zn1−O2 91.7(2), N1−Zn1−N2 75.7(3), N1−Zn1−N4 95.2(3), N1−Zn1−O1 163.7(2), N1−Zn1−O2 90.1(2), N2−Zn1−N3 96.5(2), N3−Zn1−N4

76.2(3), N3–Zn1–O1 93.0(3), N3–Zn1–O2 163.5(2). **7**: Zn1–N1 2.203(2), Zn1–N2 2.103(2), Zn1–O1 2.075(2); N1–Zn1–N1 97.49(12), N1–Zn1–N2 76.42(8)/98.44(8), O1–Zn1–O1 93.81(12), N1–Zn1–O1 86.51(8)/164.12(8).
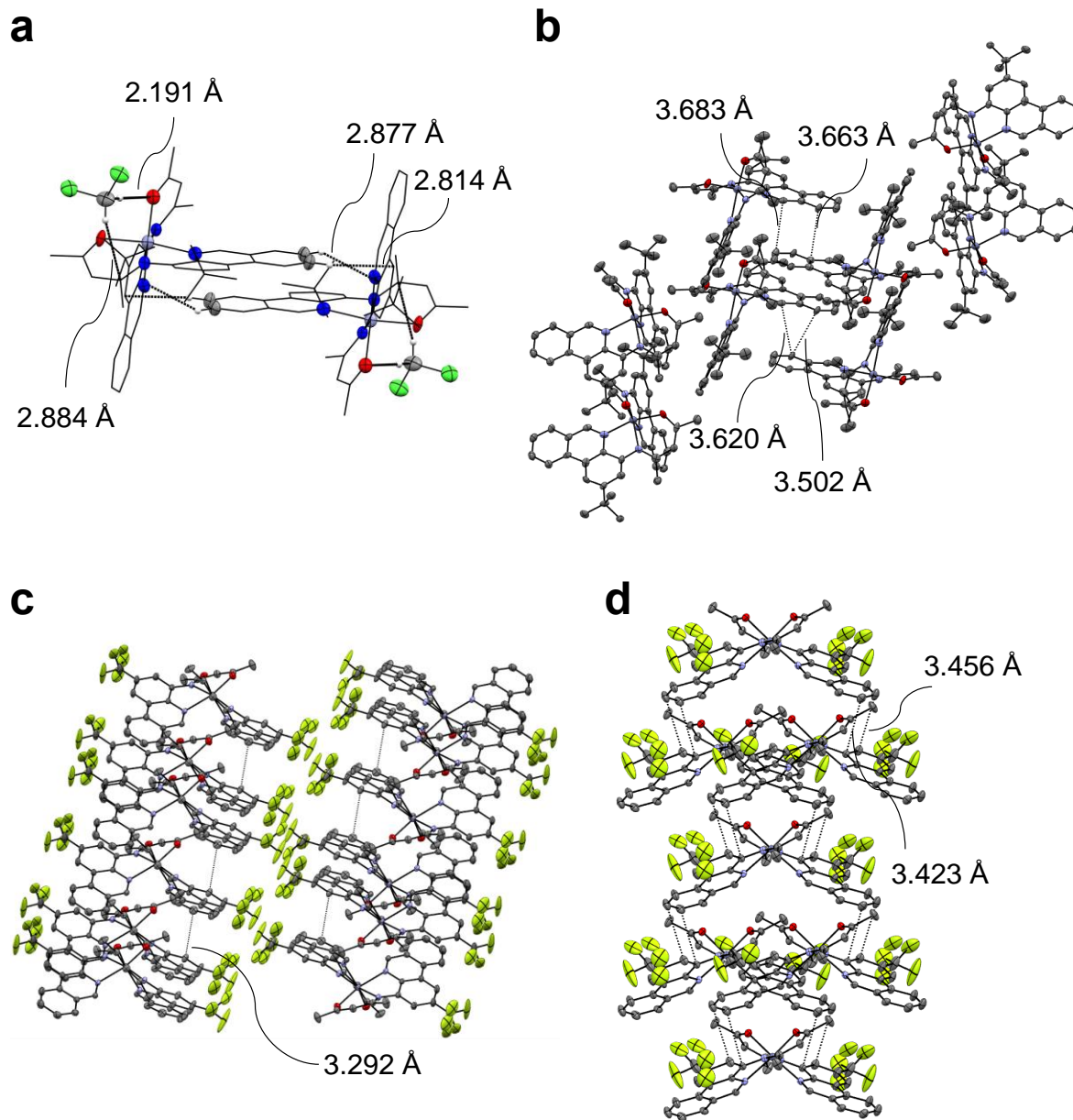
Figure 3.11. View of the solid-state structures of **6** and **7** highlighting (a) non-covalent interactions between co-crystallized CH$_2$Cl$_2$ solvent molecules and **6** interactions; (b) intermolecular interactions between adjacent complexes in **6**; and (c,d) intermolecular interactions between adjacent complexes in **7**.

Infrared (IR) spectra of the complexes in the solid state were collected to examine the tautomerism, and gas-phase IR spectra simulated from their respective optimized geometries (Figure 3.12-3.14). The proligands are generally characterized by two relevant vibrational modes: $\nu_{C=O,stretch}$ (**L1/L3**, 1617 cm^{-1}; **L4**, 1634 cm^{-1}) and $\nu_{N-H,bend}$ (**L1**, 1569 cm^{-1}; **L3**, 1570 cm^{-1}; **L4**, 1579 cm^{-1}). Upon deprotonation and coordination to zinc, the characteristic **L***n* IR frequencies are replaced by new bands which appear between 1400 and 1600 cm^{-1}. DFT suggests that two vibrational modes (insets, Figure 3.12-3.14) dominate this region, in addition to lower intensity vibrational modes of similar character. The more intense, lower energy peak [**5** 1391 cm^{-1}; **6** 1396 cm^{-1}; **7** 1380 cm^{-1}] is characterized by co-stretching of the C–N and C–O subunits of the enolato-imine fragment. The appearance of a higher energy peak [**5** 1449 cm^{-1}; **6** 1453 cm^{-1}; **7** 1433 cm^{-1}] is attributed to a combination of enolato-imine C=C and phenanthridinyl C=N stretches. In contrast, boron complexes of this ligand set[109] show distinct signals for the $\nu_{C–O,stretch}$ of the enolato-imine unit, which suggests that π-bonds of the N^O fragment are more delocalized in the zinc complexes, extending over all five atoms of the chelating unit. Consistent with this description, Mayer bond order analysis[110] of the enolato-imine π-bonds O1–C^{CH3}–CH–C^{CH3}–N2 yields bond orders of 1.48, 1.33, 1.32, 1.49, respectively. Atomic dipole-corrected Hirshfeld charges[111] indicate greater concentration of charge at the oxygen donor atom (-0.34) compared with the nitrogen donor atom (-0.16).
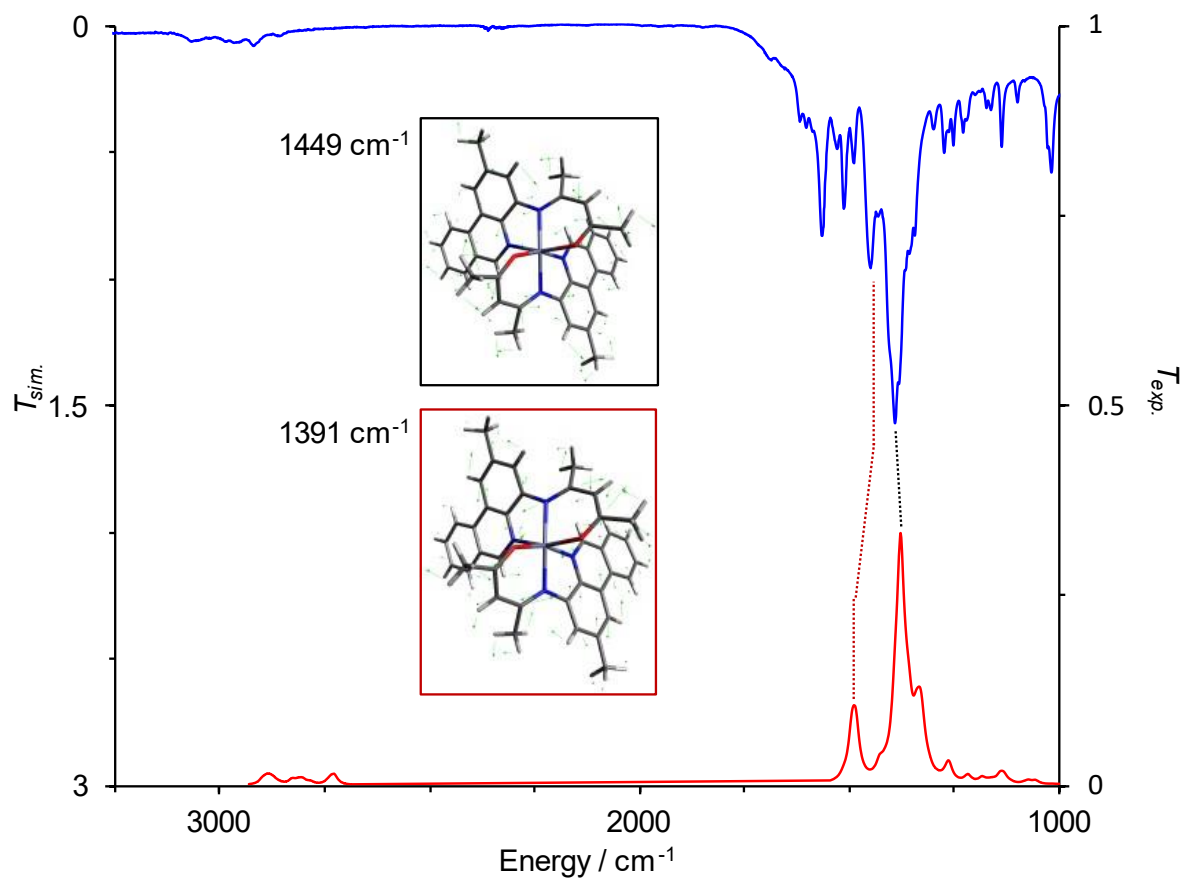
Figure 3.12. Experimental ATR-IR (blue) and simulated (red) gas phase IR (ZORA-B3LYP-D3(BJ)/def2-SV(P); Lorentzian broadening, FWHM = 20 cm^{-1}; scaling factor = 0.9) spectra of **5**. Inset: most intense vibrational modes predicted to appear at the most intense bands.
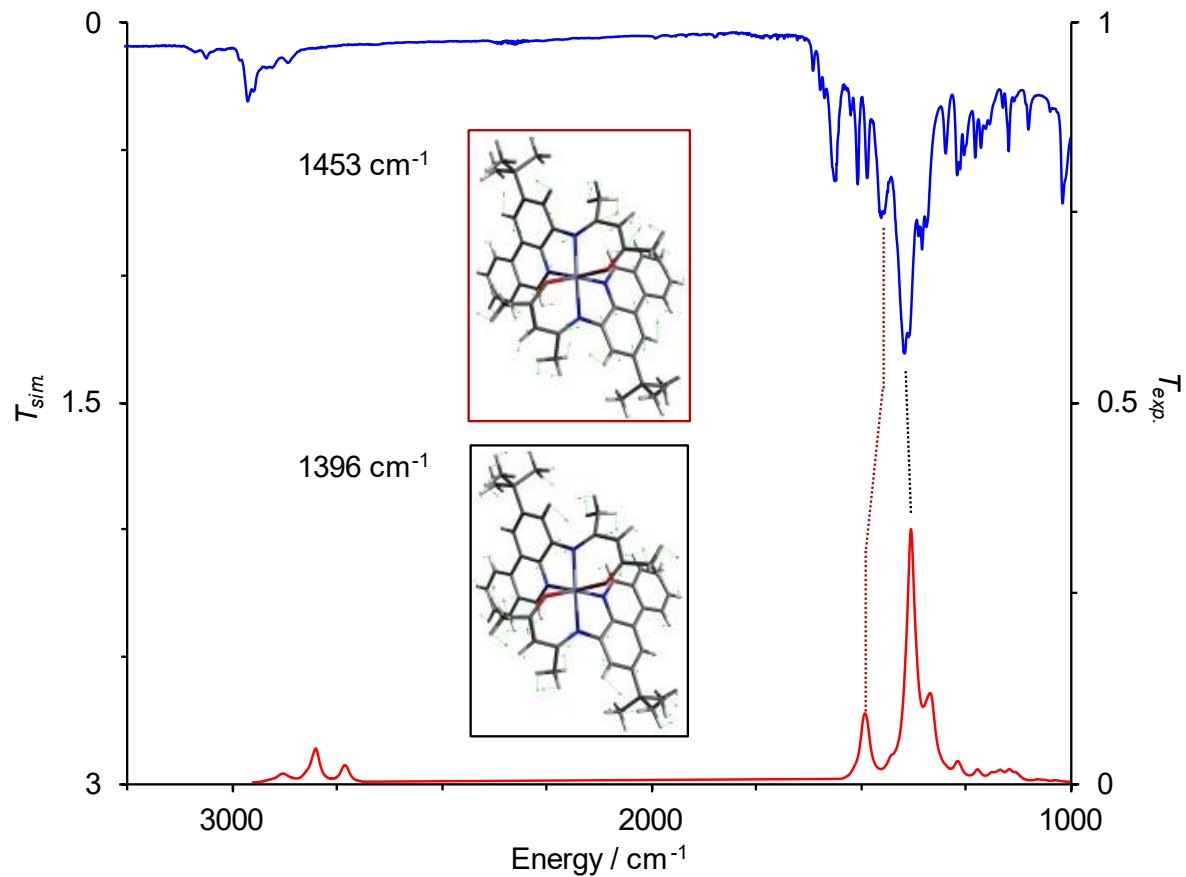
Figure 3.13. Experimental ATR-IR (blue) and simulated (red) gas phase IR (ZORA-B3LYP-D3(BJ)/def2-SV(P); Lorentzian broadening, FWHM = 20 cm^{-1}; scaling factor = 0.9) spectra of **6**. Inset: most intense vibrational modes predicted to appear at the most intense bands.
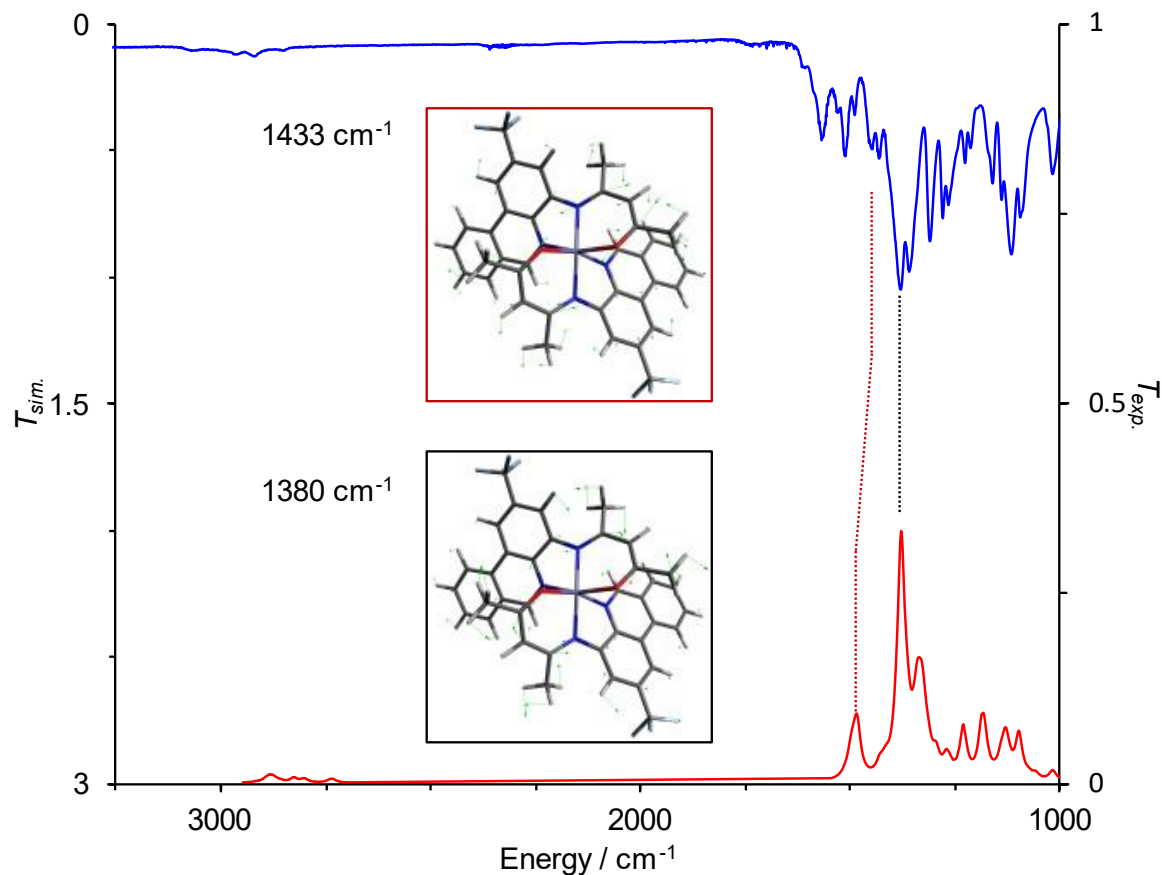
Figure 3.14. Experimental ATR-IR (blue) and simulated (red) gas phase IR (ZORA-B3LYP-D3(BJ)/def2-SV(P); Lorentzian broadening, FWHM = 20 cm^{-1}; scaling factor = 0.9) spectra of **7**. Inset: most intense vibrational modes predicted to appear at the most intense bands.

3.4.2 Photophysical Properties

All three complexes are yellow solids which dissolve in CH$_2$Cl$_2$ to produce intense yellow solutions. Their UV-Vis absorption spectra lack prominent features in the visible region and are reminiscent of the proligands which attenuate at ~400 nm.[101] A low energy tail stretching to ~475 nm accounts for the color of all three complexes. Three notable features are evident in the UV, with relatively well-resolved maxima evident at ~300, ~320 and ~365 nm that are invariant to

109

ligand substitution (Figure 3.15, Table 3.2). Similar features have been observed in the proligands and in Pt(II) complexes with phenanthridinyl-based ligands related to those here.[100,101] A series of weak but well-resolved bands in this region is, in fact, typical of the ^1L_b π-π* transitions of azaphenanthrenes including phenanthridine.[102–104] In general, the lowest-energy singlet excited state of azaphenanthrene heterocycles like phenanthridine is comparable to that of the parent all-hydrocarbon phenanthrene, notwithstanding the inclusion of a heteroatom, and the energy is fairly insensitive to the local environment. Here, only slight solvatochromism was observed (Figure 3.16), consistent with this assignment.
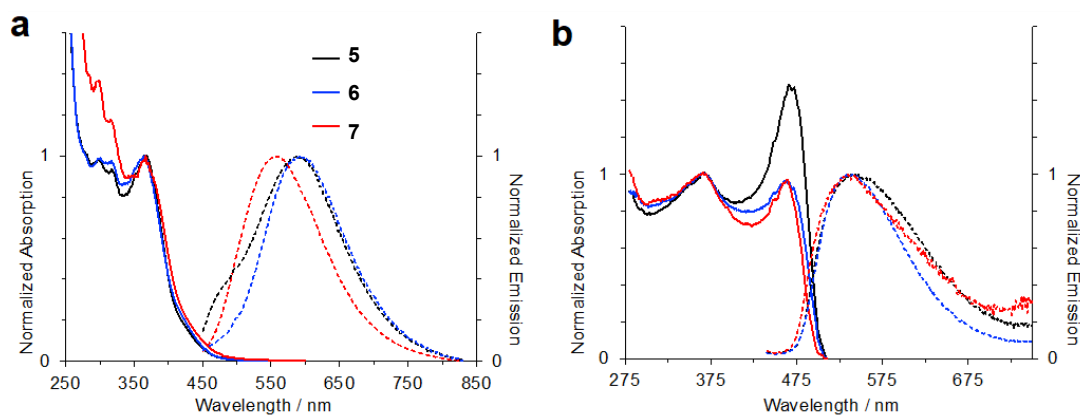
Figure 3.15. Normalized (a) UV-vis absorption (solid) and emission (dashed) spectra of **5-7** in CH₂Cl₂ at 295 K (λ_{ex} = 432 nm) and (b) solid-state emission (dashed) and excitation (solid) spectra at 295 K (λ_{ex} = 400 nm).

Table 3.2. Photophysical and electrochemical data for **5-7**.

Complex	Absorption[a] λ_{max} / nm (ε / M^{-1} cm^{-1})	Emission at 295 K[a] λ_{max} / nm	Emission 77 K[b]		Emission Solid-State 295 K			$E_{1/2}$ / V[d,e]
			λ_{max} / nm	τ / ms	λ_{max} / nm	τ / ms	Φ^{c}	
5	298 (14 430), 317 (14 550), 364 (15 830)	587	510	190	543	25	4.4	0.22, 0.58
6	298 (19 190), 317 (20 020), 366 (21 330)	593	503	120	539	27	6.0	0.22, 0.59
7	288 (14 150), 328 (13 040), 367 (15 450)	557	500	160	536	22	1.0	-2.21[f], 0.39, 0.69

[a] in CH_2Cl_2

[b] in EPA glass [EPA = diethyl ether / isopentane / ethanol (2:2:1 v/v)][112]

[c] Measured using an integrating sphere, with a sample of finely powdered $BaSO_4$ as a non-emissive blank.

[d] vs $FcH^{0/+}$ in CH_2Cl_2 at scan rates of 100 mV s⁻¹.

[e] Irreversible.

[f] Reduction
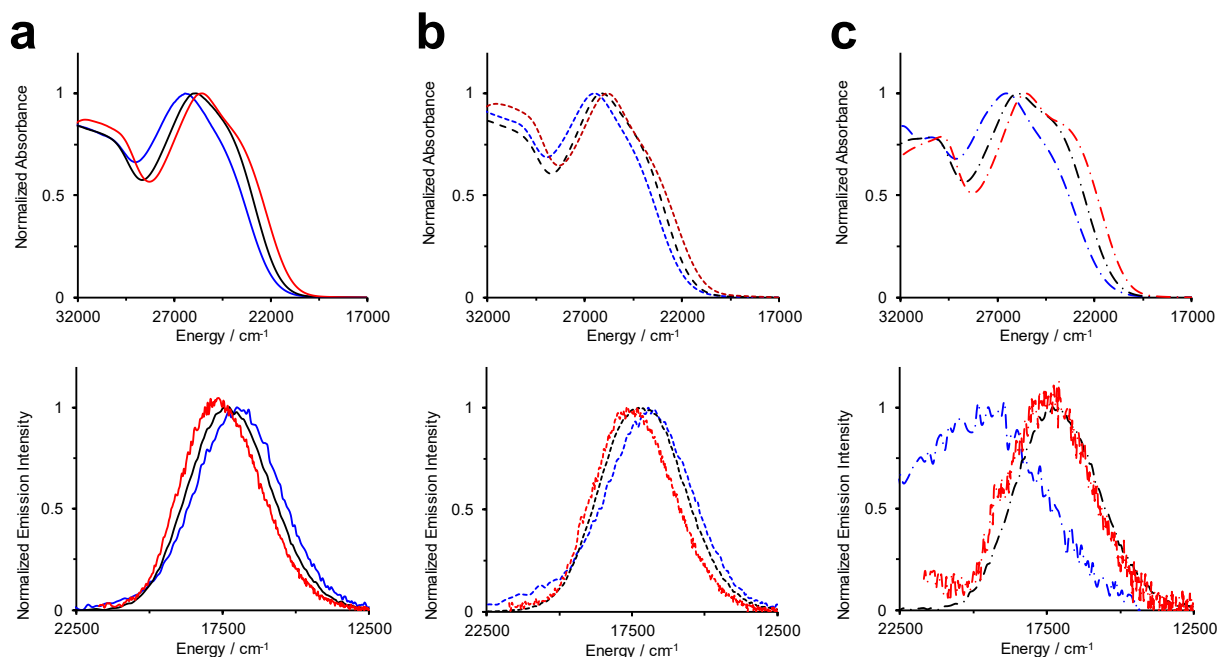
Figure 3.16. Solvent dependence (toluene, red; CH$_2$Cl$_2$, black; CH$_3$CN, blue) of the UV-Vis absorbance (top) and emission (bottom) of (a) **5**, (b) **6** and (c) **7**.

All three complexes display weak, yellow luminescence in degassed dichloromethane solution at room temperature with quantum yields around 1%. The spectra are broad and largely unstructured. The emission maxima of **5** and **6** are very similar, while that of **7** is somewhat blue shifted. It was not possible to reliably determine emission lifetimes under these conditions, but we note that the emission intensity is significantly reduced upon aeration. A similar quenching response was observed for phosphorescent, 'caged' Zn tris-bipyridine complexes, but not for their uncaged, fluorescent congeners.[113] This implies that the excited state responsible for emission from **5-6** is itself relatively long-lived, or that it is being populated from a long-lived excited state. At 77 K in an EPA glass, the spectra are all shifted to higher energy (λ_{max} ~ 500 nm; EPA = diethyl ether / isopentane / ethanol, 2:2:1 v/v). The emission is long-lived under these conditions, with

112

average lifetimes > 100 ms, suggestive of phosphorescence from a triplet state. In comparison, pseudo-octahedral Zn(II) complexes of (*E*)-*N'*-((*E*)-(hydroxyimino)butan-2-ylidene)salicyloylhydrazide ligands have been reported to emit with $\lambda_{max} = 550$ nm as a *N,N*-dimethylformamide solvate and $\lambda_{max} = 590$ nm in their pure form.[114] Solid-state samples at room temperature display quite bright yellow emission, with similar λ_{max} values around 540 nm. The emission is visually brightest for **5** and weakest for **7**. Quantum yields recorded on powdered samples in an integrating sphere confirm this trend and range from 1- 6 % (Table 3.2). The average lifetimes are reduced compared to those in a frozen glass to around 25 ms. Interestingly, the excitation spectra of the solid samples show an extra band at ~460 nm that is not present in dilute solution (Figure 3.15). Indeed, the packing diagrams of the two crystallographically characterized complexes reveal intermolecular distances typical of luminogens exhibiting aggregation or crystallization-induced luminescence[115] [**6** 3.5-3.7 A; **7** 3.2-3.5 Å; Figure 3.11]. A representative powder X-ray diffractogram of **6** is provided as Figure 3.17. Aggregation-induced enhanced emission from non-planar Zn(II) β-diiminate complexes has been reported.[116] In comparison to **5-7**, such nacnac-supported, tetrahedral Zn complexes emit in fluid solution with smaller Stokes' shifts (300 cm^{-1}) and ~12 ns lifetimes consistent with fluorescence; accordingly, no changes to the photophysical properties were observed in the presence of triplet quenchers.[117]
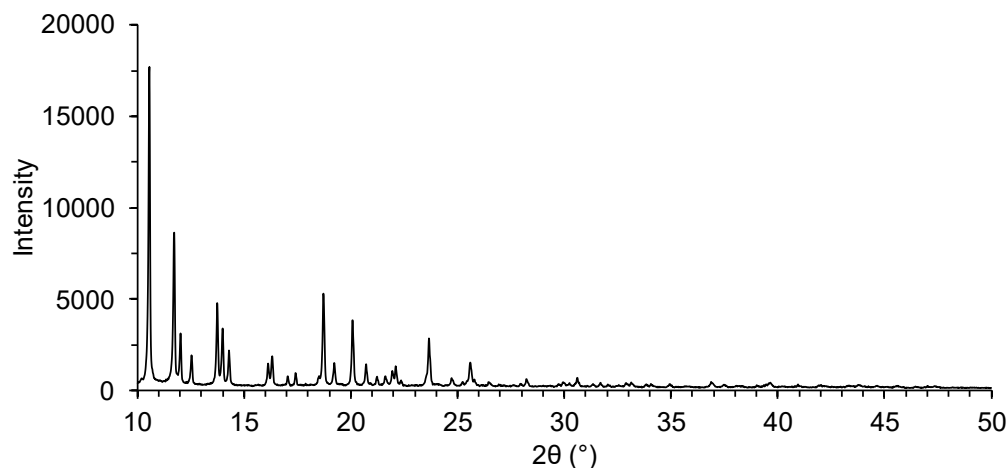
Figure 3.17. Powder X-ray diffractogram of a polycrystalline sample of **6** collected at 295 K.

3.5 Orange Phosphorescent Pt(II) Complexes

3.5.1 Synthesis and structures

Expanding the portfolio and to further understand the coordination chemistry of *N^N*H^*O* ligands, platinum complexes (**8-11**) were obtained by refluxing a mixture of $PtCl_2$ and the respective proligands in THF in the presence of a Brønsted base. Initial investigation into the appropriate synthetic approach[118] found the use of Ag_2O allowed for the highest yields (Scheme 3.3) compared with alkoxide bases (e.g., NaO*t*Bu). Work-up enabled isolation of bright orange solids in moderate (**8**, 34%; **9**, 49%) to high (**10**, 87%; **11**, 86%) yields. The Pt(II) complexes are stable to both air and ambient moisture in solution and as solids. Coordination to Pt(II) induces a downfield shift to the N=C*H* resonance of the phenanthridinyl ligand arm observed by ^{1}H NMR (δ(N=C*H*): **L1**, 9.29 ppm; **7**, 10.04 ppm). Similarly, the ^{1}H resonance of the methyl-substituent at this same carbon in **9** also shifts downfield [δ(N=C(C*H₃*)): **L2**, 3.05 ppm; **9**, 3.53 ppm]. This characteristic shift of the N=C*H* [1]H resonance, and in the case of **9** the N=C(C*H₃*), upon

114

coordination to a Lewis acidic metal ion is also diagnostic in other square-planar Pt(II) complexes supported by phenanthridine-based ligand frameworks.[118–121] Observation of coupling between the N=C*H* and spin-active ^{195}Pt ($^3J_{\text{PtH}} = 40$ Hz in **8**) further supports the binding of the phenanthridinyl donor to the metal centre. High resolution mass spectra (HRMS) of **8** and **9** are consistent with the proposed molecular formulae.

7 $R^1 = CH_3$, $R^2 = H$ (34)
8 $R^1 = CH_3$, $R^2 = CH_3$ (49)
9 $R^1 = t$Bu, $R^2 = H$ (87)
10 $R^1 = CF_3$, $R^2 = H$ (86)
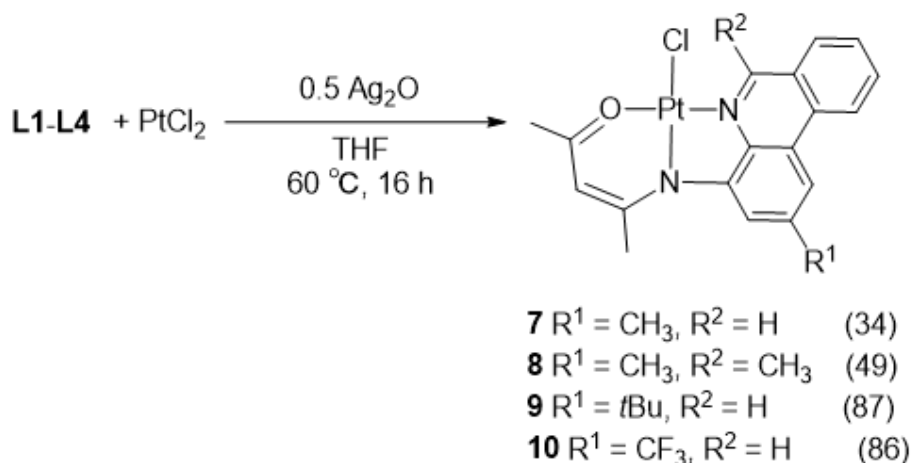
Scheme 3.3. Synthesis of Pt(II) complexes **8-11** with % yields in parentheses.

The solid-state structures of three of the Pt(II) complexes were established using single-crystal X-ray diffraction (Figure 3.18; the structure of **10** has been previously reported[118]). In each complex, the Pt(II) ion is arranged in a pseudo-square planar coordination environment with the chloride ligand *trans* to the amido nitrogen donor, and the fused tricyclic phenanthridinyl unit more or less coplanar with the square coordination plane of Pt(II). Of the series, **9** exhibits a significant distortion as revealed by the angles of 19.5° (θ: Cl2−Pt2−N3−C21) and 30.6° (θ: Cl1−Pt1−N1−C1) between the phenanthridinyl and metal coordination planes due to the increased steric congestion arising from the methyl substituent at the N=*C* carbon of the heterocyclic donor arm. Accordingly, the calculated τ_δ value[122] for **9** is more distorted from an ideal square-planar coordination environment compared with **8**, **10** and **11** (τ_4^δ for **9**: 0.16; **8**: 0.03; **10**: 0.03; **11**: 0.02). Moreover,

115

the N2−Pt1−Cl1 / N4-Pt2-Cl2 angles are smaller in **9** [168.24(10)° and 172.48(9)°, respectively,

for the two molecules in the asymmetric unit] compared with **8** [177.45(17)°], **10** [176.70(11)°][118]

or **11** [177.97(18)°]. These distortions in the ground state of **9** have implications for its

photophysics (*vide infra*). The four proligands present NMR and IR spectra consistent with the

keto-enamine tautomer predominating in solution.[118] In the Pt(II) complexes, the C-O distance is

still quite short but does elongate slightly compared to in the proligand (C17-O1 1.278-1.297 Å,

cf. 1.244(3) in **L3**[118]), while the C16-N2 distance contracts (1.322-1.334 Å, *cf.* 1.363(3) in **L3**[118]).

This implies at least some C−O−Pt/C=N−Pt character. Indeed, the Pt1-N2 distances (1.998-1.987

Å) are not significantly different from unambiguous Pt-N$_{imine}$ distances *trans* to chloro ligands

reported for square-planar Pt(II) complexes with closely related coordination environments.[123]
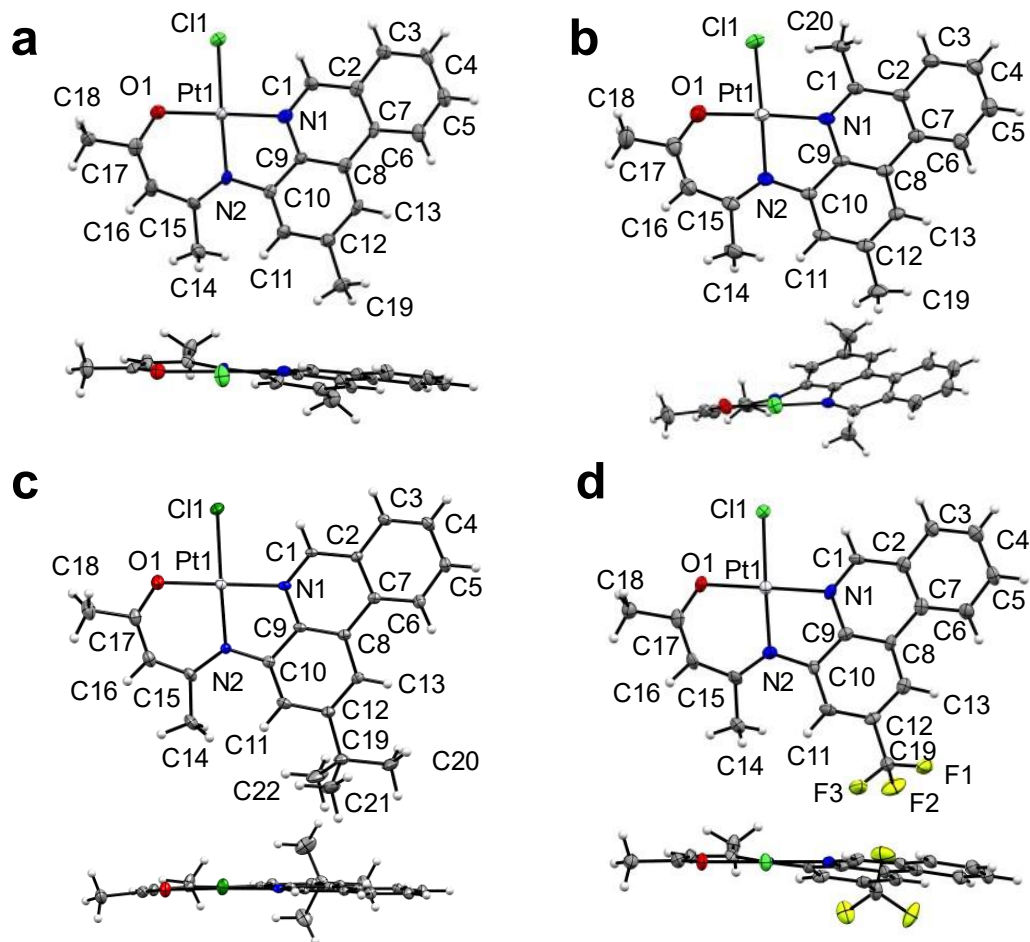
Figure 3.18. Solid-state structures of (a) **8**, (b) **9** (c) **10** and (d) **11**. Thermal ellipsoids are shown at 50% probability levels. Co-crystallized solvent molecules, when present, and a second molecule of the complex in the asymmetric unit of **9** are omitted for clarity. Selected bond lengths (Å) and bond angles (°): **Complex 8:** Pt1−Cl1 2.3166(19); Pt1−O1 1.987(5), Pt1−N1 1.987(6), Pt1−N2 1.997(6), C17-O1 1.288(10); N1−Pt1−Cl1 94.66(18), N1−Pt1−N2 83.1(2), N1−Pt1−O1 179.4(2), N2−Pt1−O1 96.3(2), N2−Pt1−Cl1 177.45(17), O1−Pt1−Cl1 85.91(16). **Complex 9:** Pt1−Cl1 2.3341(10), Pt2−Cl2 2.3308(10), Pt1−O1 1.992(3), Pt2−O2 1.986(3), Pt1−N1 2.016(3), Pt2−N3 2.025(3), Pt1−N2 1.987(3), Pt2−N4 1.998(3), C17-O1, 1.297(5), C37-O2 1.283(5); N1−Pt1−Cl1 99.63(9), N3−Pt2−Cl2 100.60(9), N1−Pt1−N2 81.87(13), N3−Pt2−N4 82.26(13), N1−Pt1−O1 174.83(12), N3−Pt2−O2 177.09(13), N2−Pt1−O1 95.47(13), N4−Pt2−O2 95.03(13),

N2−Pt1−Cl1 168.24(10), N4−Pt2−Cl2 172.48(9), O1−Pt1−Cl1 83.88(9), O2−Pt2−Cl2 81.97(9). **Complex 10:** N1-Pt1 1.978(4), N2-Pt1 1.991(3), O-Pt1 1.979(3), Cl2-Pt1 2.3137(12), C10-N2 1.419(6), C19-N2 1.357(6), C19-C20 1.402(7), C20-C21 1.376(8), C21-O1 1.278(6); N1-Pt1-N2 82.68(14), N1-Pt1-O1 178.49(15), N1-Pt1-Cl2 95.34(10), N2-Pt1-O1 97.61(15), N2-Pt1-Cl1 176.70(11), O1-Pt1-Cl2 84.44(11). **Complex 11:** Pt1−Cl1 2.3305(18); Pt1−O1 1.985(5), Pt1−N1 1.990(6), Pt1−N2 1.995(6), C17-O1 1.278(9); N1−Pt1−Cl1 95.45(18), N1−Pt1−N2 82.6(2), N1−Pt1−O1 179.5(2), N2−Pt1−O1 96.9(2), N2−Pt1−Cl1 177.98(18), O1−Pt1−Cl1 85.07(16).

3.5.2 Photophysical Properties

Deprotonation of **L1**-**L4** and installation on Pt(II) introduces at least partial amido character, which, in the context of pincer-type tridentate ligand scaffolds, should be accessible for electrochemical oxidation.[124] Similarly, low-lying, vacant π^* orbitals in the benzannulated ligand framework are anticipated to be accessible for electrochemical reduction.[125] Electrochemical analysis of **L1**-**L4** (Figure 3.19) and **8**-**11** (Figure 3.20) was therefore undertaken using cyclic voltammetry and differential pulse voltammetry. Largely irreversible anodic and cathodic events are observed, which become more reversible at increased scan rates for **8** and **10**, and to a lesser extent for **9** (Figure 3.19). Related *bis*(quiniolinyl)amido, *bis*(phenanthridinyl)amido and (phenanthridinyl/quinolinyl)amido Pt(II) chloro complexes show closely related redox behavior.[119] Here, however, the oxidation events are shifted to more positive potentials due to the stabilization provided by the imine/enolato character evident in the solid-state structures. The cathodic events are similarly accessible at less negative potentials and are much more reversible, with the exception of **8**, which presents an electron-donating substituent at the (Me)C=N sub-unit

hosting the majority of the orbital density for its LUMO. The results, summarized in Table 3.3, have been used to estimate experimental HOMO-LUMO gaps.
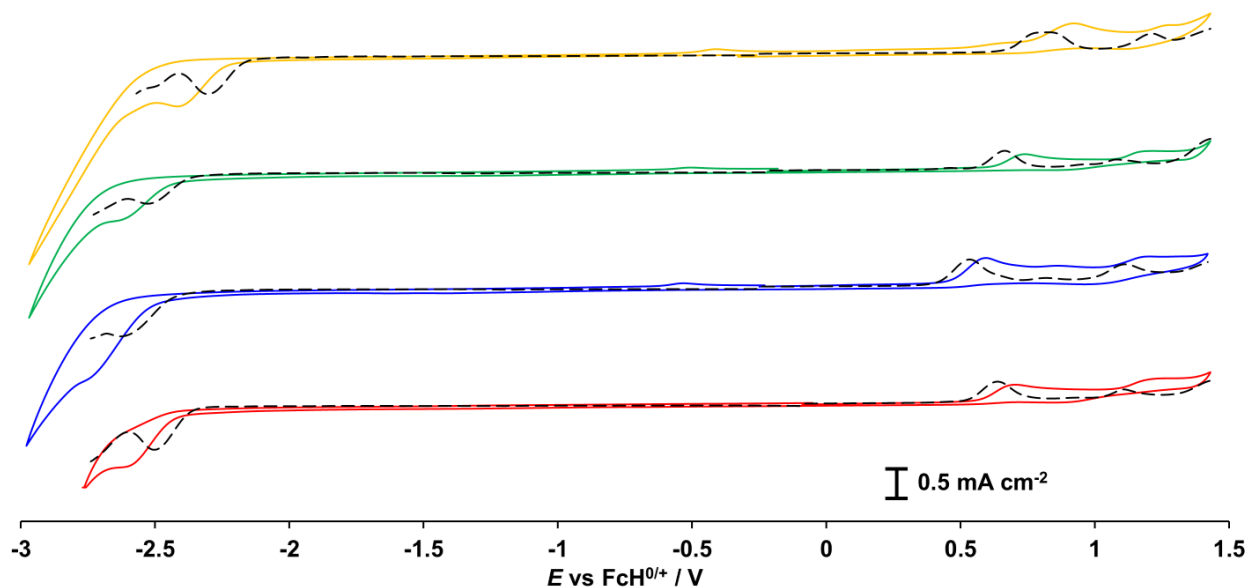
Figure 3.19. Cyclic voltammograms (—) and differential pulse voltammograms (---) of **L1**, **L2**, **L3** and **L4** in CH_2Cl_2 with 0.1 mM of $[NBu_4][PF_6]$ as the supporting electrolyte, glassy carbon as the working electrode, and Pt wire as the counter electrodes. CV scan rates were 100 mV/s. Potentials are listed vs. $FcH^{0/+}$ redox couple (FcH = ferrocene).
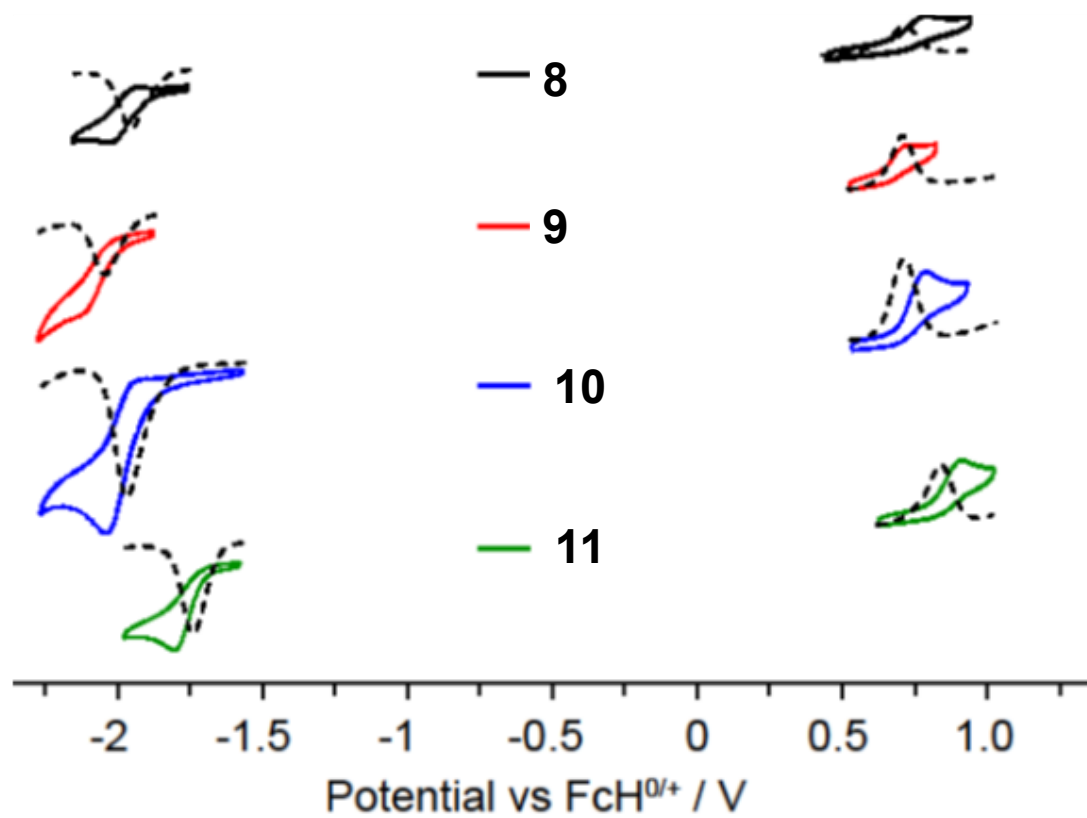
Figure 3.20. Cyclic voltammograms (solid lines; 100 mV s^{-1}) and differential pulse voltammograms (dashed lines) for **8-11** in CH$_2$Cl$_2$ containing 0.1 M [nBu$_4$N][PF$_6$] at 295 K.

Table 3.3. Electrochemistry data and experimental HOMO/LUMO energies and gaps.

Compound	$E_{1/2}$ / V [a]	$E_{HOMO/LUMO}$ / eV [b]	$\Delta E_{HOMO-LUMO}$ / eV	E_g [c]
L1	-2.50, 0.64	-5.44/-2.30	3.14	3.22
L2	-2.63, 0.53	-5.33/-2.17	3.16	3.22
L3	-2.53, 0.66	-5.46/-2.27	3.19	3.24
L4	-2.30, 0.82	-5.62/-2.50	3.12	3.20
8	-1.95, 0.72	-5.52/-2.85	2.67	2.68
9	-2.05, 0.71	-5.51/-2.75	2.76	2.74
10	-1.96, 0.71	-5.51/-2.84	2.67	2.70
11	-1.74, 0.85	-5.65/-3.06	2.59	2.61

[a] vs $FcH^{0/+}$ in CH_2Cl_2 at scan rates of 100 mV s^{-1}.

[b] Estimated using equations 1 and 2 all in eV.

$$E_{HOMO} = -(E_{onset,ox} + 4.8 - E_{FcH}) \qquad (1)$$

$$E_{LUMO} = -(E_{onset,red} + 4.8 - E_{FcH}) \qquad (2)$$

[c] Estimated using equation 3 for **L1-4**, and equation 4 for **8-11**.

$$E_g = \frac{hc}{\lambda_{onset}} \qquad (3)$$

$$E_g = \frac{hc}{\lambda_{max}} \qquad (4)$$

A general destabilization of the HOMO energies of the ligands is expected on going from electron-withdrawing (CF_3) to electron-releasing (CH_3, tBu) substitution in the 2-position of the phenanthridinyl unit. A further destabilization results from introducing an electron-releasing CH_3 substituent into the 6-position as in **L2** (E_{HOMO}/eV: **L2** > **L3** ≈ **L1** > **L4**). Consequently, oxidation

121

events occur at lower potentials for **L1**-**L3**, with the most negative oxidation potential for **L2** and most positive oxidation potential observed for **L4**. A similar trend can be discerned in the irreversible cathodic events associated with reduction of the ligands, with **L2** reduced at the most negative potential. This implies that the LUMO energies of the proligands are in the order E_{LUMO}/eV: **L2** > **L3** ≈ **L1** > **L4**. Overall, however, the HOMO-LUMO gaps estimated from electrochemistry ($\Delta E_{HOMO\text{-}LUMO}$) are quite similar for **L1**-**L4**, indicating that substitution induces similar perturbations to the two frontier molecular orbitals of the ligands. Consistent with this, the UV-Vis spectra of the four proligands are quite similar, except for **L3** which presents a broader and slightly blue-shifted λ_{max} (Figure 3.21).
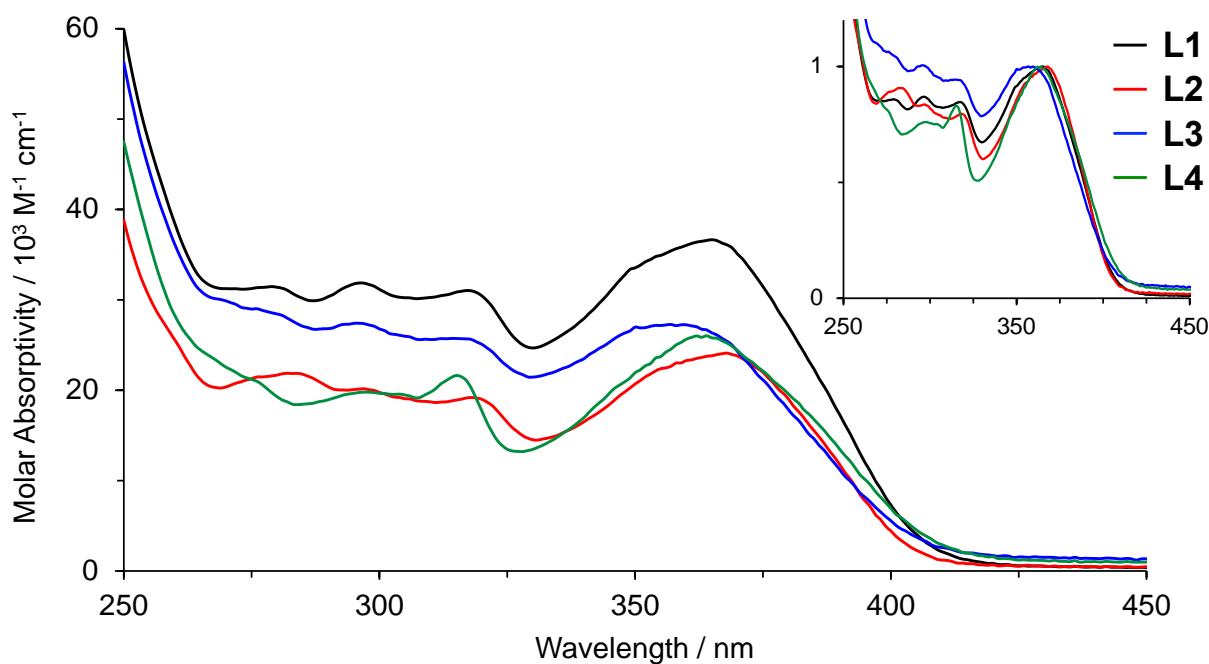
Figure 3.21. UV-Vis spectra of **L1**-**L4** in CH$_2$Cl$_2$ at 298 K. Inset shows normalized spectra.

Upon deprotonation and coordination to Lewis acidic Pt(II), a shift to more positive potentials is observed for both the oxidation and reduction potentials. While it might be expected that the bigger change to the character of the HOMOs of **8**-**11** through introduction of metal/chloride character would more significantly impact oxidation than reduction involving the largely phenanthridine-localized LUMO, the observed shifts suggest a larger stabilization of the LUMO energies (ΔE_{LUMO} / meV: **L1** vs **8**, -550; **L2** vs **9** -580; **L3** vs **10**, -570; **L4** vs **11**, -560; ΔE_{HOMO} / meV: **L1** vs **8**, -180; **L2** vs **9** -190; **L3** vs **10**, -50; **L4** vs **11**, -30). For the series, the electrochemically estimated HOMO energies of **8-11** are comparable, while the HOMO of **11** is further stabilized ($\Delta E_{stab.}$ ~ 140 meV vs **7**). In sharp contrast, the LUMO energies mirror the trend observed for the proligands: E_{LUMO} / eV: **9** > **10** ≈ **8** > **11**, with a larger stabilization energy of 210 meV in **11** relative to **8**. Electronic perturbations by the substituent in the frontier molecular orbital energies are evidently larger for the LUMO than the HOMO in the complexes. We return to these points later.

As noted above, all four complexes are bright orange solids and give rise to similarly coloured solutions. UV-Vis absorption spectra (Figure 3.22) accordingly exhibit broad and strong bands in the visible region of the electromagnetic spectrum (λ_{max} ~ 460 nm, ε > 5 000 M^{-1} cm^{-1}) consistent with transitions of charge-transfer character. In addition, two strong transitions are evident in the UV (λ ~ 260 nm, ε > 24 000 M^{-1} cm^{-1}; λ ~ 350 nm, ε > 11 000 M^{-1} cm^{-1}), ascribable to ligand-based excitations. Comparison with analogous Pt(II) chloride complexes of monoanionic, pincer-type *N*-8-quinolinyl-4-aminophenanthridines[119–121] favours a mixed [M+L]LCT assignment for the lowest energy manifold. Such N_{amido}-Pt-Cl systems can be compartmentalized in terms of the character of the donor (n_{Cl} + d_{Pt} + n_{Namido}) and acceptor (largely

phenanthridine-based π^* orbitals, with significant contribution from the HC=N sub-unit) molecular fragments.
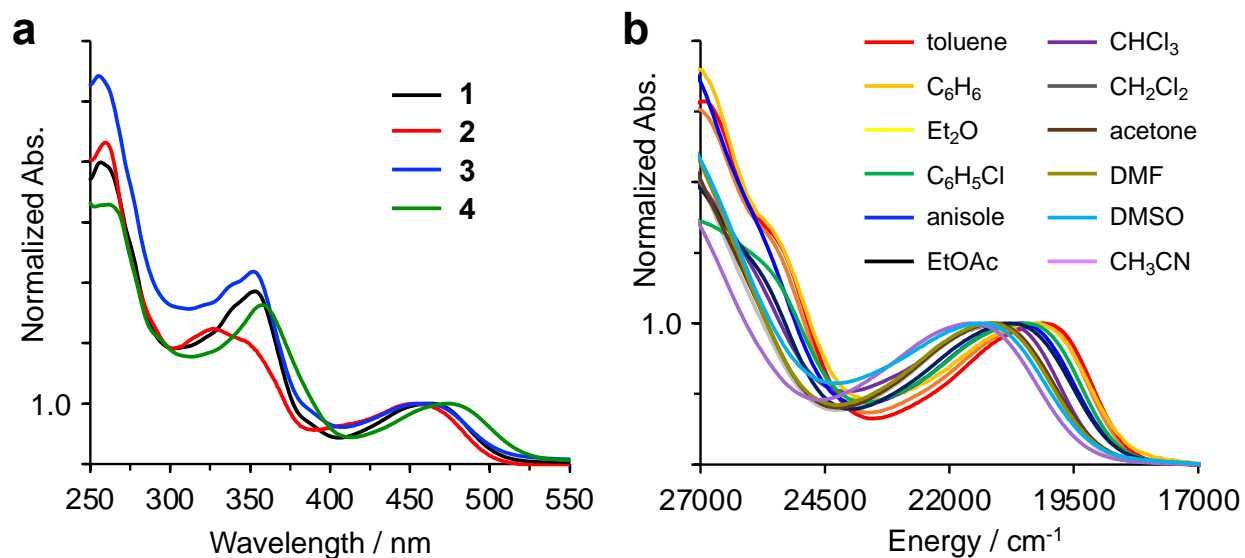
Figure 3.22. (a) UV-Vis absorption spectra of **8-11** in CH_2Cl_2 at 295 K. (b) UV-Vis absorption spectra of **11** in a variety of solvents illustrating the solvatochromism of the lowest energy band.

UV-Vis absorption spectra collected for **11** in a range of solvents support the CT assignment (Figure 3.22b). The lowest energy absorption exhibits negative solvatochromism, suggesting stabilization of the ground-state relative to the excited state of interest with increasing solvent polarity. Fitting the transition energies to Reichardt's E_N^T function[126] leads to a relatively weak correlation ($R^2 = 0.78$; Figure 3.23), which improves when protic and aprotic solvents are treated separately ($R^2 = 0.96, 0.93$) indicating that specific solute-solvent interactions need to be taken into account. Using Catalan's four parameter solvent scale[127] to separate contributions of specific solute-solvent interactions (e.g., solvent acidity/basicity) from non-specific interactions

(solvent polarizability/dipolarity) produces a much better correlation between calculated and experimental transition energies (Figure 3.24). Given solubility constraints on the range of solvents employed, we attribute the hypsochromic shift of λ_{max} in increasingly polar solvents with the most confidence to solvent dipolarity (i.e., solute-solvent dipole interactions) and solvent acidity (i.e., hydrogen bonding; Tables 3.4-3.5). In particular, the large coefficient and positive sign obtained from fitting the solvent dipolarity indicate preferential ground-state stabilization.[126] Increasing solvent dipolarity would be expected to stabilize the larger dipole moment typically associated with an excited state of CT character. However, the [M+L]LCT character of **8**-**11** induces an excited state dipole moment (μ_e) which is not expected to orient in the same direction as the ground state dipole moment (μ_g). The Franck-Condon principle necessitates the solvent to be in a 'frozen' state; that is, the solvent remains in its ground-state equilibrium orientation around the chromophore. This leads to 'orientational strain' on the solvent contributing to the apparent hypsochromic shift in the CT excitation energies with increasing solvent polarity.[128] In contrast, ground state stabilization by solvent acidity is made possible by hydrogen bonding to atom(s) contributing to the HOMO, likely through the chloride. Indeed, incorporation of hydrogen-bonding solvents (e.g., $CHCl_3$) with close contacts to the chloride and oxygen of the ligand is observed in the solid-state structure of **9** (Figure 3.25).
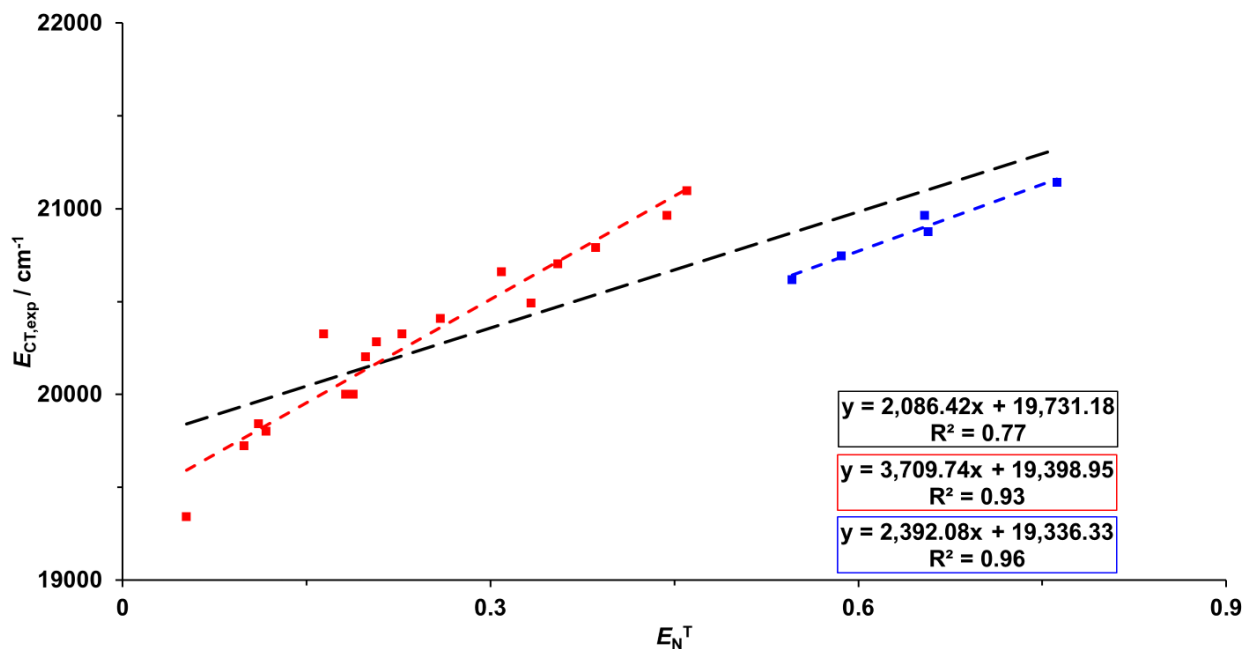
Figure 3.23. Correlation between $E_{CT,exp}$ (cm^{-1}) on Reichardt's solvent E_N^T parameters with aprotic and protic solvents treated together (---), and protic (---) and aprotic (---) solvents treated separately for complex **11**.
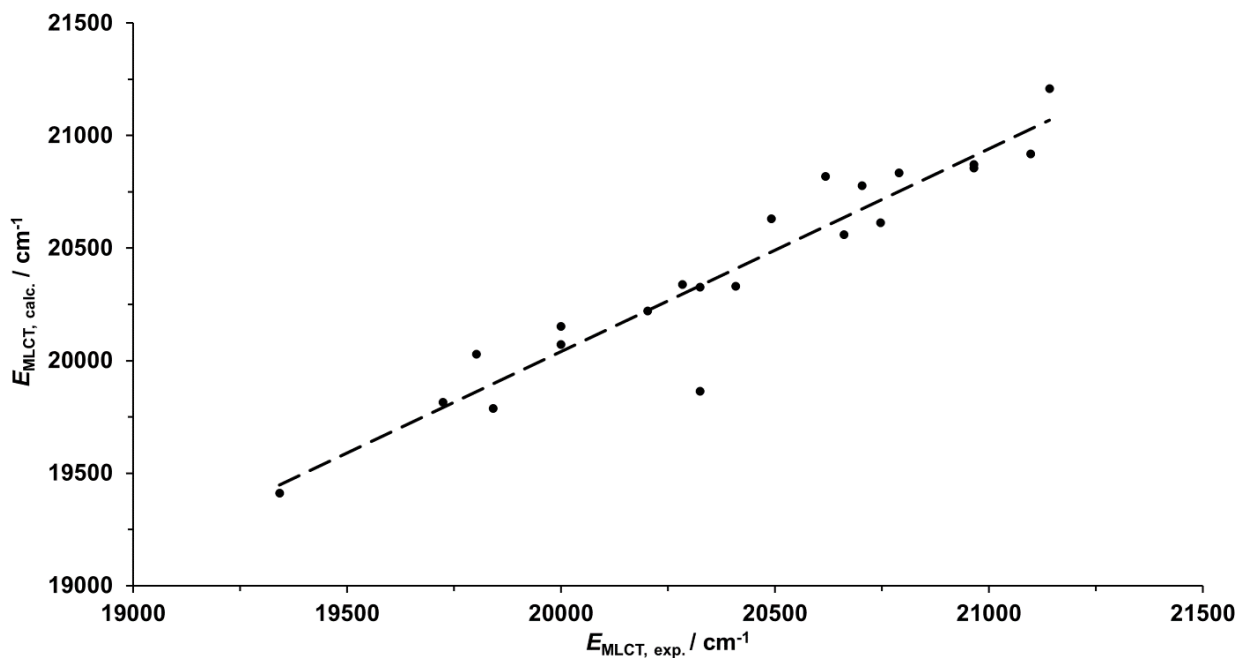
Figure 3.24. Correlation between $E_{CT,exp.}$ (cm^{-1}) and $E_{CT,calc.}$ (cm^{-1}) calculated using Catalan's multiparameter solvent approach for complex **11**.

Table 3.4. Reichardt's E_N^T and Catalan solvent (SP, SdP, SA and SB) parameters for **11**.

Solvent	$\lambda_{abs,CT}$/nm	E_{CT}/cm^{-1}	SP	SdP	SA	SB	E_N^T
CCl$_4$	517	19342	0.768	0	0	0.044	0.052
benzene	504	19841	0.793	0.27	0	0.124	0.111
toluene	507	19724	0.782	0.284	0	0.128	0.099
CHCl$_3$	490	20408	0.783	0.614	0.047	0.071	0.259
Et$_2$O	505	19802	0.617	0.385	0	0.562	0.117
anisole	495	20202	0.82	0.543	0.084	0.299	0.198
CH$_2$Cl$_2$	484	20661	0.761	0.769	0.04	0.178	0.309
ClPh	500	20000	0.833	0.537	0	0.182	0.188
BrPh	500	20000	0.875	0.497	0	0.192	0.182
THF	493	20284	0.714	0.634	0	0.591	0.207
acetone	483	20704	0.651	0.907	0	0.475	0.355
DMF	481	20790	0.759	0.977	0.031	0.613	0.386
CH$_3$CN	474	21097	0.645	0.974	0.044	0.286	0.46
DMSO	474	21097	0.83	1	0.072	0.647	0.444
CNPh	488	20492	0.851	0.852	0.047	0.281	0.333
EtOAc	492	20325	0.656	0.603	0	0.542	0.228
iProH	485	20619	0.633	0.808	0.283	0.83	0.546
1-BuOH	482	20747	0.674	0.655	0.341	0.809	0.586
CH$_3$OH	473	21142	0.608	0.904	0.605	0.545	0.762
EtOH	477	20964	0.633	0.783	0.4	0.658	0.654
2OMeEtOH	479	20877	-	-	-	-	0.657

Table 3.5. Catalan solvent parameter coefficients and statistics obtained from linear regression for **11**.

Regression Statistics			Coefficients	Standard Error	t statistic	P-value
Multiple R	0.974	**Intercept**	19619	368	53.326	0.000
R Square	0.948	**SP**	-402	452	-0.890	0.387
Adjusted R Square	0.935	**SdP**	1649	133	12.382	2.81E-09
Standard Error	130.4	**SA**	774	220	3.517	0.003
Observations	20	**SB**	-151	176	-0.860	0.403
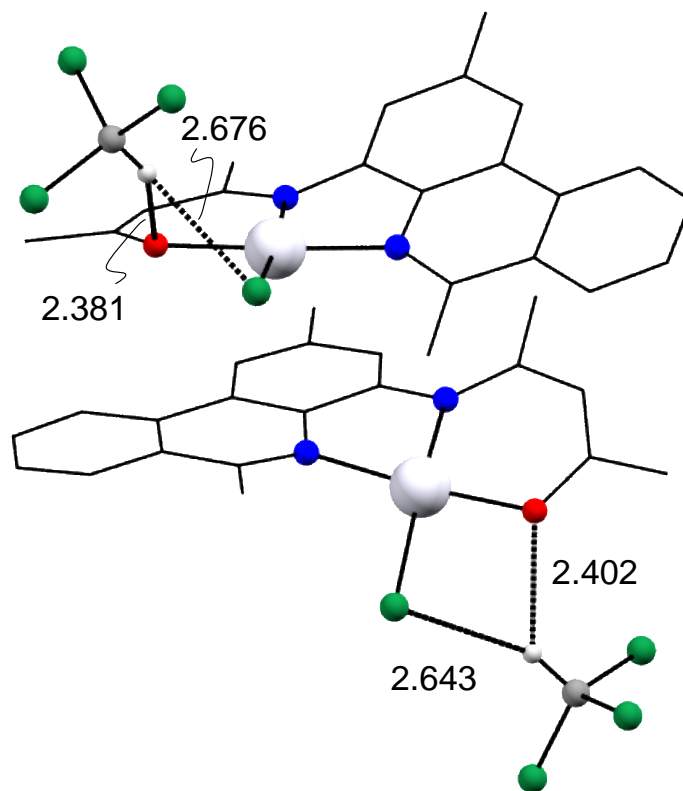
Figure 3.25. Solid-state structure of **11** showing hydrogen bonding interaction with co-crystallized $CHCl_3$ solvent molecules.

As with related Pt(II) complexes chelated by monanionic, tridentate $N^\wedge N^\wedge O$ Schiff-base ligands,[123] the novel Pt(II) complexes presented here emit in the orange region of the visible spectrum ($\lambda_{max} \sim 600$ nm; Figure 3.26). Each of complexes **8**, **10** and **11** are brightly emissive, with quantum yields up to 16% in deoxygenated dichloromethane at room temperature (Table 3.6), superior to those of the archetypal MLCT emitter $[Ru(bpy)_3]^{2+}$ for example,[129] and one to two orders of magnitude larger than those observed for Pt(II) complexes of closely related phenanthridine-based diarylamido ligands.[121] In contrast, the 2,6-dimethyl substituted **9** is only very weakly emissive at room temperature, too weak to reliably record a quantum yield or lifetime. Amongst the other three, complex **11** emits with (marginally) the narrowest band structure (FWHM = 2460 cm^{-1} compared to 2730 cm^{-1} for **10**) and the highest quantum yield. These values far exceed those reported for (N$^\wedge$N$^\wedge$O)PtCl complexes based on dipyridylphenolato frameworks, which emit at λ_{em} 593-606 nm, with Φ ~1-4 % in the solid-state,[130] and those for Pt(II) emitters with Schiff-base ligand frameworks (λ_{em} 686-735 nm; Φ = 0.5-4.6 % in fluid solution for quinoline-based derivatives; λ_{em} 580-636 nm for hydrazone derived analogs, with Φ reaching 11% for acetylide derivatives).[123] The luminescence of **8**, **10** and **11** follows mono-exponential decay kinetics, with a lifetime of around 22 µs in each. Values in the microsecond range are typical of phosphorescence from the triplet state in cyclometallated Pt(II) complexes, although most examples tend to be somewhat shorter-lived, typically < 10 µs. Some insight into the longer lifetimes can be gleaned by estimating the radiative k_r and non-radiative Σk_{nr} rate constants from the quantum yields and lifetimes (Table 3.6). The former are around an order of magnitude lower than found for the brightest Pt(II) emitters (though the brightest tend to be green emitters), but not

dissimilar to values for [Pt(dqpy)Cl]$^+$, for example (dqpy = 1,3-di(8-quinolyl)pyridine).[131] The

Σk_{nr} values, meanwhile, are of a magnitude fairly typical for Pt(II) emitters with tridentate ligands.
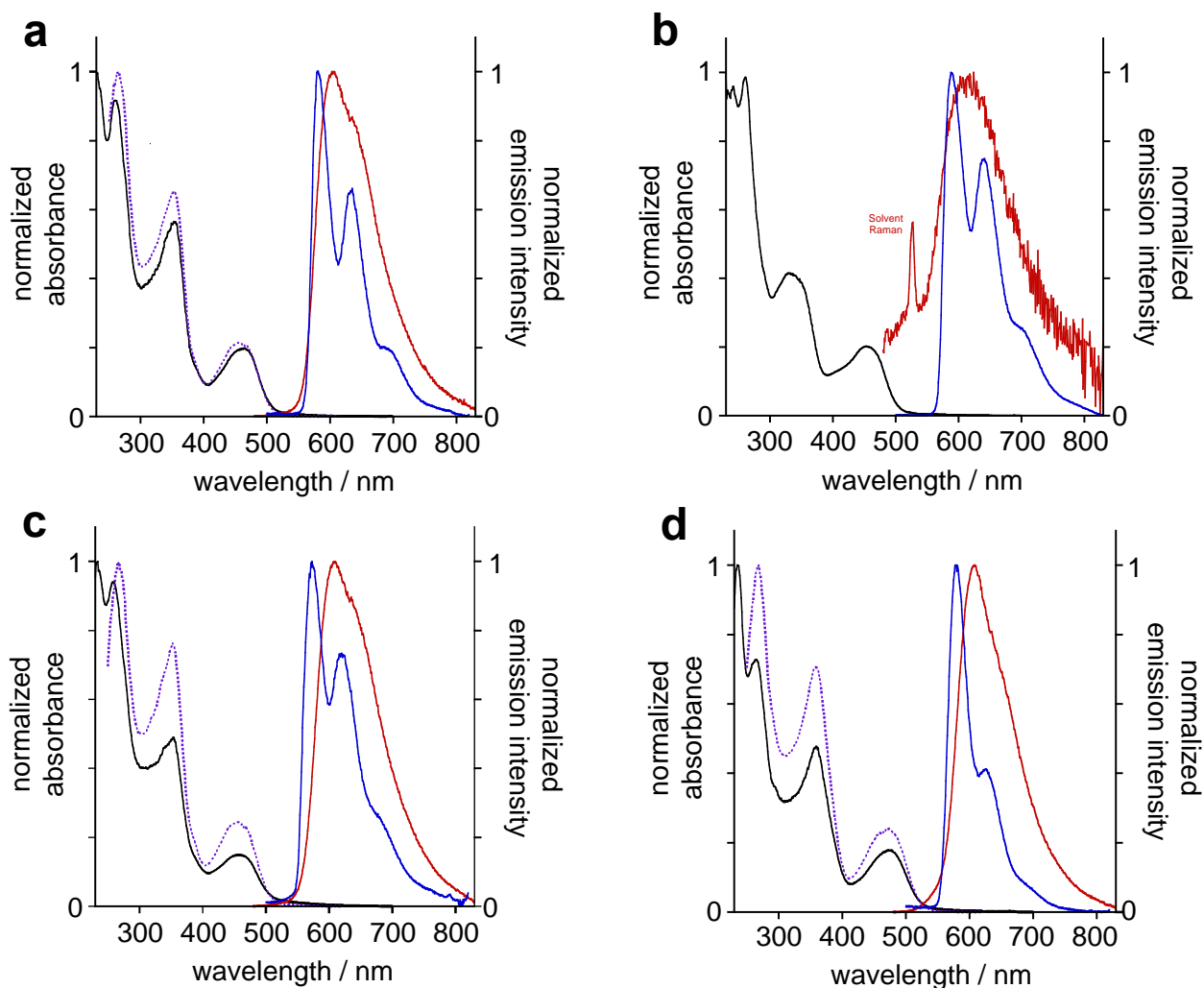
Figure 3.26. UV-Vis absorption (−), excitation (- - -) and emission (− at 295 K, − at 77 K) spectra for Pt

complexes (a) **8**, (b) **9**, (c) **10** and (d) **11**. Note: emission of **9** is too weak at concentrations suitable for an

exciation spectrum for one to be recorded

Given the long lifetimes in fluid solution, it is not surprising to find that the emission is

strongly quenched by dissolved molecular oxygen, with bimolecular quenching constants of the

order of 10^9 M^{-1} s^{-1} at room temperature. A modest degree of self-quenching is also observed in concentrated solutions, though the self-quenching constants of $1–2 \times 10^8$ M^{-1} s^{-1} are much lower than for systems such as Pt($N^\wedge C^\wedge N$-dpyb)Cl and derivatives {dpyb = 1,3-di(2-pyridyl)benzene}.[132] Moreover, there is no evidence of excimer emission to lower energy at elevated concentrations, unlike many of the latter group.

Table 3.6. Absorption and emission data of Pt(II) complexes.

	Absorption λ_{max}/nm $(\varepsilon / M^{-1} cm^{-1})$[a]	Emission λ_{max}/nm[b]	Φ_{lum} / 10^{-2} [c]	τ / μs [d]	k_Q^{SQ} / $10^8 M^{-1} s^{-1}$ [e]	k_Q^{O2} / $10^8 M^{-1} s^{-1}$	k_r / $10^3 s^{-1}$ [f]	Σk_{nr} / $10^3 s^{-1}$ [f]	Emission 77 K[g] λ_{max} / nm	τ / μs
8	261 (27800), 354 (17200), 463 (6030)	604	9.1	23 [0.42]	1.5	11	4.0	40	573, 620, 682sh	64
9	261 (28736), 343 (11241), 453 (5424)	610	--[h]	--	--	--	--	--	587, 640, 700sh	36
10	258 (31800), 354 (16500), 459 (5080)	608	6.8	22 [0.41]	2.0	11	3.1	42	573, 620, 682sh	61
11	265 (24600), 360 (16100), 475 (5980)	608	16	24 [0.48]	1.1	9.3	6.7	35	579, 626, 694sh	52

[a] In CH_2Cl_2 at 295 K.

[b] In deoxygenated CH_2Cl_2 at 295 K.

[c] Measured using [Ru(bpy)$_3$]Cl$_2$ $_{(aq)}$ as the standard.

[d] Values in parenthesis refer to air-equilibrated solution.

[e] Self-quenching rate constant estimated from concentration dependence of lifetime.

[f] Radiative k_r and non-radiative Σk_{nr} rate constants calculated assuming that the emitting state is formed with unit efficiency, under which conditions $k_r = \Phi/\tau$ and $\Sigma k_{nr} = (1-\Phi)/\tau$.

[g] In diethyl ether / isopentane / ethanol (2:2:1 v/v).

[h] The emission intensity of complex **9** is too weak to determine the lifetime or a reliable Φ_{lum}.

3.6 Experimental Details

3.6.1 Syntheses of Complexes

General Considerations

Air-sensitive manipulations were carried out in a N_2-filled glove box or using standard Schlenk techniques under Ar. Organic solvents were dried and distilled using appropriate drying agents. Diethylzinc (1 M in hexanes) was purchased from Sigma-Aldrich. 1- and 2D NMR spectra were recorded on a Bruker Avance 300 MHz spectrometer or a Bruker Avance 500 MHz spectrometer. ^1H and $^{13}C\{^1H\}$ NMR spectra were referenced to residual solvent peaks. High resolution mass spectra were recorded using a Bruker microTOF-QIII. Attenuated total reflectance infrared spectroscopy (ATR-IR) was performed using a Bruker Invenio R FTIR. For electrochemical analysis, 5-10 mg of each compound was dissolved in 15 mL of 0.1 M $[nBu_4N][PF_6]$ in CH_2Cl_2. The measurements were performed on the solutions in an N_2-filled glovebox using a CHI 760c bipotentiostat, a 3 mm diameter glassy carbon working electrode, a $Ag^+|Ag$ quasi-non-aqueous reference electrode separated by a Vycor tip, and a Pt wire counter electrode. Cyclic voltammetry was conducted using a scan rate of 100 mV/s. Upon completion, ferrocene (FcH) was added to the solution as an internal standard, and all potentials are reported versus the $FcH^+|FcH$ redox couple.

Complex 1: In a Teflon-stoppered flask, triethylamine (148 μL, 1.07 mmol) was added to a stirring solution of **L1** (0.100 g, 344 mmol) and boron trifluoride diethyl etherate (217 μL, 1.76 mmol) in toluene (11 mL). The mixture was heated to reflux in an oil bath set to 110°C for 16 h. A precipitate was
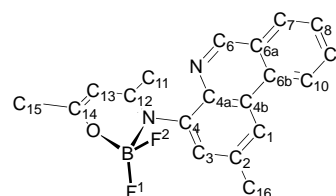
observed to gradually form over this time. The resultant suspension was then cooled to room temperature. Addition of CH_2Cl_2 (approximately 25 mL) re-dissolved the precipitate, and the mixture was then washed with deionized water (2 x 25 mL) and 2 M HCl (2 x 25 mL). The organic layer was separated, filtered over Celite, and dried *in vacuo*. The resulting solid was re-dissolved in minimal CH_2Cl_2 and precipitated by addition of MeOH, followed by ice-cold water. The precipitate was filtered over Celite, then isolated using CH_2Cl_2. The solution was dried over Na_2SO_4 and dried *in vacuo* to isolate a light brown solid. Isolated yield = 84 g (72 %). ^{1}H NMR (CDCl₃, 300 MHz, 25 °C): δ 9.22 (s, 1H; C₆H), 8.59 (d, $^3J_{HH}$ = 8.2 Hz, 1H; C₁₀H), 8.39 (s, 1H; C₁H), 8.02 (d, $^3J_{HH}$ = 7.9 Hz, 1H; C₇H), 7.86 (m, 1 H; C₉H), 7.71 (m, 1H; C₈H), 7.64 (s, 1 H; C₃H), 5.65 (s, 1 H; C₁₃H), 2.65 (s, 3 H; C₁₅H), 2.25 (s, 3 H; C₁₅H), 1.87 ppm (s, 3 H; C₁₁H). ^{13}C{^{1}H} NMR (CDCl₃, 75 MHz, 25 °C): δ 176.9 (C_{14}), 173.1 (C_{12}), 153.4 (C_6), 137.9 (C_4), 137.5 (C_{4a}), 137.2 (C_2), 132.2 (C_{4b}), 131.3 (C_9), 128.9 (C_7), 128.0 (C_8), 127.9 (C_3), 126.6 (C_{6a}), 125.2 (C_{6b}), 122.4 (C_1), 122.2 (C_{10}), 99.0 (C_{13}), 23.2 (C_{15}), 22.1 (C_{15}), 21.8 ppm (C_{11}). ^{19}F NMR (CDCl₃, 282 MHz, 25 °C): δ -129.9 (dq, $^2J_{FF}$ = 96, $^1J_{FB}$ = 20 Hz, 1F; BF^1), -139.4 ppm (dq, $^2J_{FF}$ = 95, $^1J_{FB}$ =11 Hz, 1F; BF^2). ^{11}B NMR (CDCl₃, 160 MHz, 25 °C): δ 1.0 ppm (dd, $^1J_{BF}$ = 11 Hz, 20 Hz). IR (ATR): ν 3100-2800 (C-H stretch, broad, w), 1614 (C_{13}=N stretch, narrow, m), 1534 (C_{14}=C_{15} stretch, narrow, m), 1397 (C_{15}– O stretch, narrow, m), 1325 (C_{12}–H and C_{16}–H bend, narrow, m), 1260 cm^{-1} (B–F stretch, C_6–H and C_3–H bend, narrow, m). HR-MS (APCI-TOF) m/z: [M + Na]$^+$ calcd for [$C_{19}H_{17}N_2OBF_2Na$]$^+$ 361.1298; Found 361.1311.

Complex 2: Following the procedure described above, triethylamine (142 μL, 1.02 mmol) was added to a stirring solution of **L2** (0.100 g, 329 mmol) and boron trifluoride diethyl etherate (207 μL, 1.68 mmol) in toluene (10 mL) and heated to reflux in an oil bath set to 110°C for 16 h. Brown solid. Isolated
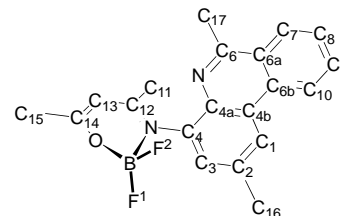
yield = 44 mg (38 %). ^{1}H NMR (CDCl$_3$, 300 MHz, 25 °C): δ 8.61 (d, J_{HH} = 8.2 Hz, 1H; C$_{10}H$),

8.33 (s, 1 H; C$_1H$), 8.18 (d, $^3J_{HH}$ = 8.1 Hz, 1H; C$_7H$), 7.83 (m, 1 H; C$_9H$), 7.69 (m, 1 H; C$_8H$),

7.62 (s, 1 H; C$_3H$), 5.63 (s, 1 H; C$_{13}H$), 2.93 (s, 3 H; C$_{17}H$), 2.63 (s, 3 H; C$_{16}H$), 2.26 (s, 3 H;

C$_{15}H$), 1.88 ppm (s, 3 H; C$_{11}H$). ^{13}C{^{1}H} NMR (CDCl$_3$, 75 MHz, 25 °C): δ 176.2 (C_{14}), 173.1

(C_{12}), 158.5 (C_6), 137.0 (C_4, C_{4a}), 136.1 (C_2), 132.2 (C_{4b}), 130.5 (C_9), 127.7 (C_8), 127.5 (C_3), 126.6

(C_7), 126.1 (C_{6a}), 124.7 (C_{6b}), 122.6 (C_{10}), 122.1 (C_1), 98.9 (C_{13}), 23.9 (C_{17}), 23.1 (C_{15}), 22.1 (C_{16}),

22.0 ppm (C_{11}). ^{19}F NMR (CDCl$_3$, 282 MHz, 25 °C): δ -129.0 (dq, $^2J_{FF}$ = 95, $^1J_{FB}$ = 21 Hz, 1F;

BF^1), -141.4 ppm (dq, $^2J_{FF}$ = 95, J_{FB} = 10 Hz, 1F; BF^2). ^{11}B NMR (CDCl$_3$, 160 MHz, 25 °C): δ

1.0 ppm (dd, $^1J_{BF}$ = 10, 21 Hz). IR (ATR): ν 3100-2800 (C-H stretch, b, w), 1620 (C$_{14}$=N stretch,

n, m), 1540 (C$_{15}$=C$_{16}$ stretch, n, m), 1404 (C$_{16}$–O stretch, n, m), 1326 (C$_{13}$–H and C$_{17}$–H bend, n,

m), 1261 cm^{-1} (B–F stretch, n, m). HRMS (APCI-TOF) m/z: [M + H]$^+$ calcd for [C$_{20}$H$_{20}$N$_2$OBF$_2$]$^+$

353.1635; Found 353.1652.

Complex 3: Triethylamine (130 μL, 0.932 mmol) was added to a

stirring solution of **L3** (0.100 g, 301 mmol) and boron trifluoride

diethyl etherate (189 μL, 1.53 mmol) in toluene (9 mL) and heated to

reflux in an oil bath set to 110°C for 16 h. A spectroscopically pure
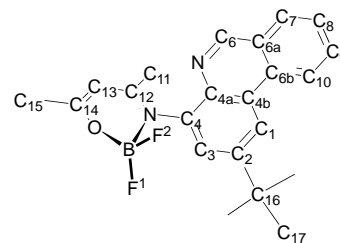
brown solid was isolated. Isolated yield = 88 mg (76 %). ^{1}H NMR (CDCl$_3$, 300 MHz, 25 °C): δ

9.23 (s, 1H; C$_6H$), 8.64 (d, $^3J_{HH}$ = 8.3 Hz, 1H; C$_{10}H$), 8.58 (s, 1 H; C$_1H$), 8.01 (d, $^3J_{HH}$ = 7.9 Hz, 1

H; C$_7H$), 7.87 (overlapped m, 2 H; C$_3H$ and C$_9H$), 7.70 (m, 1 H; C$_8H$), 5.65 (s, 1 H; C$_{13}H$), 2.25

(s, 3 H; C$_{11}H$), 1.87 (s, 3 H; C$_{15}H$), 1.51 ppm (s, 9 H; C$_{17}H$). ^{13}C{^{1}H} NMR (CDCl$_3$, 75 MHz, 25

°C): δ 176.7 (C_{14}), 173.1 (C_{12}), 153.6 (C_6), 150.2 (C_2), 137.9 (C_4), 137.3 (C_{4a}), 132.5 (C_{4b}), 131.3

(C_8), 129.0 (C_7), 127.9 (C_9), 126.5 (C_{6a}), 124.9 (C_3), 124.7 (C_{6b}), 122.0 (C_{10}), 118.3 (C_1), 99.0

(C_{13}), 35.5 (C_{16}), 31.5 (C_{17}), 23.1 (C_{15}), 21.8 ppm (C_{11}). ^{19}F NMR (CDCl$_3$, 282 MHz, 25 °C): δ -

130.7 (dq, $^2J_{FF}$ = 96, $^1J_{FB}$ = 18 Hz, 1F; BF^1), -138.4 ppm (dq, $^2J_{FF}$ = 96, J_{FB} = 11 Hz, 1F; BF^2). ^{11}B

NMR (CDCl$_3$, 160 MHz, 25 °C): δ 1.0 ppm (dd, $^1J_{BF}$ = 12, 19 Hz). IR (ATR): ν 3100-2800 (C-H

stretch, b, w), 1617 (C$_{14}$=N stretch, n, m), 1537 (C$_{15}$=C$_{16}$ stretch, n, m), 1403 (C$_{16}$–O stretch, n,

m), 1328 (C$_{13}$–H and C$_{17}$–H bend, n, m), 1261 cm^{-1} (B–F stretch, C$_6$–H and C$_3$–H bend, n, m).

HRMS (APCI-TOF) m/z: [M + H]$^+$ calcd for [C$_{22}$H$_{24}$N$_2$OBF$_2$]$^+$ 381.1948; Found 381.1969.

Complex 4: Triethylamine (125 μL, 0.900 mmol) was added to a

stirring solution of **L4** (0.100 g, 290 mmol) and boron trifluoride

diethyl etherate (183 μL, 1.48 mmol) in toluene (9 mL) heated to reflux

in an oil bath se t to 110°C for 16 h. A spectroscopically pure orange
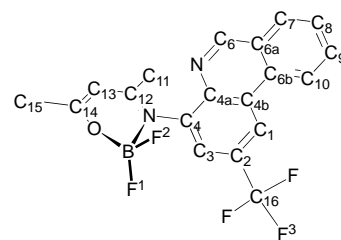
solid was isolated. Isolated yield = 98 mg (86%). ^{1}H NMR (CDCl$_3$, 300 MHz, 25 °C): δ 9.32 (s, 1

H; C$_6$$H$), 8.83 (s, 1 H; C$_1$$H$), 8.56 (d, $^3J_{HH}$ = 8.3 Hz, 1 H; C$_{10}$$H$), 8.03 (overlapped m, 2 H; C$_3$$H$

and C$_7$$H$), 7.89 (m, 1 H; C$_8$$H$), 7.74 (m, 1 H; C$_9$$H$), 5.70 (s, 1 H; C$_{13}$$H$), 2.26 (s, 3 H; C$_{15}$$H$), 1.87

ppm (s, 3 H; C$_{11}$$H$). ^{13}C{^{1}H} NMR (CDCl$_3$, 75 MHz, 25 °C): δ 178.0 (C_{14}), 173.5 (C_{12}), 156.4

(C_6), 141.2 (C_4), 138.7 (C_2), 138.0 (C_{6a}), 132.3 (C_8), 132.0 (C_{4a}), 129.2 (C_7), 129.1 (C_9), 129.1

(C_{4b}) 126.5 (C_{6b}), 122.8 (q, $^4J_{CF}$ = 3.2 Hz; C_3), 122.1 (C_{10}), 120.4 (q, $^4J_{CF}$ = 4.1 Hz; C_1), 99.2 (C_{13}),

23.2 (C_{11}), 21.8 ppm (C_{15}). ^{19}F NMR (CDCl$_3$, 282 MHz, 25 °C): δ -61.7 (s, 3F; C$_{11}$$F^3$), -129.8 (dq,

$^2J_{FF}$ = 94, $^1J_{FB}$ = 19 Hz, 1F; BF^1), -138.1 ppm (dq, $^2J_{FF}$ = 95, $^1J_{FB}$ =11 Hz, 1F; BF^2). ^{11}B NMR

(CDCl$_3$, 160 MHz, 25 °C): δ 1.0 ppm (dd, $^1J_{BF}$ = 12, 19 Hz). ν 3100-2800 (C-H stretch, b, w), 1616

(C$_{14}$=N stretch, n, m), 1538 (C$_{15}$=C$_{16}$ stretch, n, m), 1524 cm^{-1} (C$_{16}$–O stretch, n, m). HRMS

(APCI-TOF) m/z: [M + H]$^+$ calcd for [C$_{19}$H$_{15}$N$_2$OBF$_5$]$^+$ 393.1196; Found 393.1213.

[3Me]OTf: Methyl trifluoromethanesulfonate (10.0 μL, 88.4 μmol) was added to a stirring solution of **3** (0.0305 g, 80.2 μmol) in CH_2Cl_2 (3 mL) at room temperature. After overnight stirring, the solvent was evaporated, and the brown residue was subjected to repeated recrystallization (3x) via vapor diffusion of pentane into a $CHCl_3$ solution to afford a spectroscopically pure product. Beige crystalline solid. Yield = 0.0119 g (27%). ^{1}H NMR (CDCl$_3$, 300 MHz, 25 °C): δ 10.01 (s, 1H; C$_6$*H*), 8.84 (d, $^4J_{HH}$ = 2.3 Hz, 1H; C$_1$*H*), 8.79 (d, $^3J_{HH}$ = 8.4 Hz, 1H; C$_{10}$*H*), 8.60 (d, $^3J_{HH}$ = 8.4 Hz, 1H; C$_7$*H*), 8.31 (ddd, $^3J_{HH}$ = 8.8, 7.6 Hz, $^4J_{HH}$ = 1.4 Hz, 1H; C$_9$*H*), 8.00 (m, 1H; C$_8$*H*), 7.92 (s, 1H; C$_3$*H*), 5.87 (s, 1H; C$_{13}$*H*), 4.63 (s, 3H; C$_{18}$*H*), 2.35 (s, 3H; C$_{11}$*H*), 2.03 (s, 3H; C$_{15}$*H*), 1.53 ppm (s, 9H; C$_{17}$*H*). ^{13}C{^{1}H} NMR (CDCl$_3$, 125 MHz, 25 °C): δ 181.7 (*C*$_{14}$), 175.1 (*C*$_{12}$), 159.1 (*C*$_6$), 154.5 (*C*$_2$), 138.7 (*C*$_9$), 135.1 (*C*$_{4a}$), 133.9 (*C*$_7$), 132.0 (*C*$_3$), 131.7 (*C*$_{4b}$), 131.0 (*C*$_8$), 128.9 (*C*$_4$), 128.3 (*C*$_{6b}$), 124.2 (*C*$_{6a}$), 122.7 (*C*$_{10}$), 120.9(*C*$_1$), 100.8 (*C*$_{13}$), 51.0 (*C*$_{18}$), 31.1 (*C*$_{17}$), 23.6 (*C*$_{15}$), 22.4 (*C*$_{11}$) ppm. ^{19}F NMR (CDCl$_3$, 282 MHz, 25 °C): δ -78.4 (s, 3F; SO$_3$CF$_3$), -128.5 (dq, $^2J_{FF}$ = 94 Hz, $^1J_{FB}$ = 22 Hz; 1F; B*F*^{1}), -141.8 ppm (d, $^2J_{FF}$ = 93 Hz, $^1J_{FB}$ = 10 Hz; 1F; B*F*^{2}). ^{11}B NMR (CDCl$_3$, 160 MHz, 25 °C): δ 0.9 ppm (d, $^1J_{BF}$ = 22, 10 Hz). HRMS (ESI-TOF) m/z: [M]$^+$ calcd for [C$_{23}$H$_{26}$N$_2$OBF$_2$]$^+$ 395.2105; Found 395.2120.

Synthesis of complex 5. To a cooled solution of **L1** (0.105 g, 0.360 mmol) in hexanes/toluene (7.5 mL/2.5 mL, -38 °C), a cooled solution of diethylzinc (1 M in hexanes; 250 μL, 0.25 mmol; -38 °C) was added dropwise and the mixture left stirring overnight at room temperature, over which period the solution color changed from a pale to intense yellow with formation of a yellow precipitate. The solvent was removed *in vacuo* and the resulting residue was

repeatedly washed with cyclohexane, then crystallized by cooling solutions of the product prepared in hot cyclohexane. Yield = 0.0836 g (84%). ^{1}H NMR (CDCl$_3$, 300 MHz, 25 °C): δ 8.58 (s, 1H, C$_1$$H$), 8.40 (d, $^3J_{HH}$ = 8.7 Hz; 1H, C$_6$$H$), 7.65-7.80 (m, 3 H, C$_{3,5,13}$$H$), 7.54 (ddd, $^3J_{HH}$ = 7.5, 8.8 Hz, $^4J_{HH}$ = 0.8 Hz; 1H, C$_4$$H$), 7.16 (d, $^4J_{HH}$ = 1.1 Hz; 1H, C$_{11}$$H$), 5.08 (s, 1H, C$_{16}$$H$), 2.52 (s, 3H, C$_{19}$$H$), 2.27 (s, 3H, C$_{14}$$H$), 1.79 (s, 3H, C$_{18}$$H$). ^{13}C{^{1}H} NMR (CDCl$_3$, 75 MHz, 25 °C): δ 187.5 (C$_{17}$), 168.4 (C$_{15}$), 157.0 (C$_1$), 144.1 (C$_{10}$), 135.4 (C$_{12}$), 134.6 (C$_9$), 132.4 (C$_5$), 130.4 (C$_3$), 126.7 (C$_4$ and C$_8$), 126.0 (C$_7$), 123.4 (C$_2$), 123.1 (C$_{11}$), 122.4 (C$_6$), 114.6 (C$_{13}$), 99.4 (C$_{16}$), 28.1 (C$_{19}$), 23.0 (C$_{18}$), 22.3 (C$_{14}$). HRMS (ESI-TOF) m/z: [M + H]$^+$ Calcd for [C$_{38}$H$_{35}$N$_4$O$_2$Zn]$^+$ 643.2046; Found 643.2066.
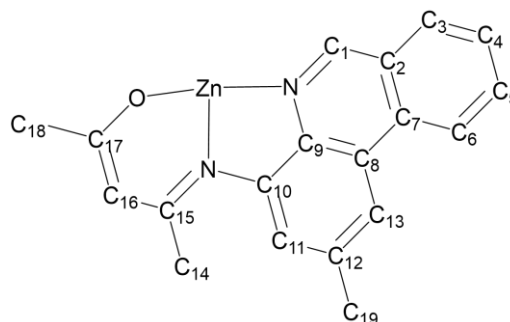
Synthesis of complex 6. The procedure was the same as for **5** starting from **L3** (0.104 g, 0.312 mmol) in hexanes/toluene (7.5 mL/2.5 mL, -38 °C), and diethylzinc (1 M in hexanes; 220 μL, 0.22 mmol; -38 °C). Yield = 0.0607 g (54%), yellow solid. ^{1}H NMR (CDCl$_3$, 300 MHz, 25 °C): δ 8.57 (s, 1H, C$_1$$H$), 8.43

(d, $^3J_{HH}$ = 8.4 Hz; 1H, C$_6$$H$), 7.90 (d, $^4J_{HH}$ = 1.4 Hz; 1H, C$_{13}$$H$), 7.65-7.78 (m, 2H, C$_3$$H$ and C$_5$$H$), 7.52 (ddd, $^3J_{HH}$ = 7.3, 8.5 Hz, $^4J_{HH}$ = 1.0 Hz; 1H, C$_4$$H$), 7.46 (d, $^4J_{HH}$ = 1.5 Hz; 1H, C$_{11}$$H$), 5.13 (s, 1H, C$_{16}$$H$), 2.30 (s, 3H, C$_{14}$$H$), 1.82 (s, 3H, C$_{18}$$H$), 1.44 (s, 9H, C$_{20}$$H$). ^{13}C{^{1}H} NMR (CDCl$_3$, 75 MHz, 25 °C): δ 187.7 (C$_{17}$), 168.4 (C$_{15}$), 149.8 (C$_{12}$), 149.2 (C$_1$), 145.0 (C$_{10}$), 134.7 (C$_9$), 133.2 (C$_5$), 131.1 (C$_8$), 129.2 (C$_3$), 127.0 (C$_4$), 126.2 (C$_2$), 123.7 (C$_7$), 122.2 (C$_6$), 120.3 (C$_{11}$), 110.5 (C$_{13}$), 100.1 (C$_{16}$), 35.4 (C$_{19}$), 31.5 (C$_{20}$), 28.4 (C$_{18}$), 23.0 (C$_{14}$). HRMS (ESI-TOF) m/z: [M + H]$^+$ Calcd for [C$_{44}$H$_{47}$N$_4$O$_2$Zn]$^+$ 727.2985; Found 727.3040.

Synthesis of 7. The procedure was the same as for **5**, starting from **L4** (0.117 g, 0.340 mmol) in hexanes/toluene (7.5 mL/2.5 mL, -38 °C), and diethylzinc (1 M in hexanes; 240 μL, 0.24 mmol; -38 °C). Yield = 0.100 g (79%), yellow solid. ^{1}H NMR (CDCl$_3$, 300 MHz, 25 °C): δ 8.70 (s, 1H, C$_1H$), 8.41 (d,

$^{3}J_{HH}$ = 8.2 Hz; 1H, C$_6H$), 8.13 (s, 1H, C$_{13}H$), 7.77-7.90 (m, 2H, C$_3H$ and C$_5H$), 7.66 (ddd, $^{3}J_{HH}$ = 7.4, 8.5 Hz, $^{4}J_{HH}$ = 0.8 Hz; 1H, C$_4H$), 7.50 (d, $^{4}J_{HH}$ = 1.5 Hz; 1H, C$_{11}H$), 5.20 (s, 1H, C$_{16}H$), 2.30 (s, 3H, C$_{14}H$), 1.84 (s, 3H, C$_{18}H$). ^{19}F NMR (CDCl$_3$, 282 MHz, 25 °C): δ 62.35 (s, C$_{19}F$). ^{13}C{^{1}H} NMR (CDCl$_3$, 75 MHz, 25 °C): δ 189.7 (C$_{17}$), 168.8 (C$_{15}$), 151.9 (C$_1$), 146.5 (C$_{10}$), 137.4 (C$_9$), 132.8 (C$_7$), 132.4 (C$_5$), 129.5 (C$_3$), 128.8 (q, $^{2}J_{CF}$ = 32.1 Hz; C$_{12}$), 128.4 (C$_4$), 126.1 (C$_8$), 124.2 (C$_2$), 122.3 (C$_6$), 117.0 (q, $^{3}J_{CF}$ = 3.3 Hz; C$_{11}$), 111.7 (q, $^{3}J_{CF}$ = 4.4 Hz; C$_{13}$), 101.0 (C$_{16}$), 28.6 (C$_{18}$), 22.9 (C$_{14}$). HRMS (ESI-TOF) m/z: [M + H]$^{+}$ Calcd for [C$_{38}$H$_{29}$N$_4$O$_2$Zn]$^{+}$ 751.1481; Found 751.1552.

Synthesis of [Pt(L1)Cl], 8: A solution of **L1** (0.0587 g, 0.113 mmol) in THF (3.5 mL) was added to a suspension of PtCl$_2$ (0.0618 g, 0.232 mmol), Ag$_2$O (0.0293 g, 0.126 mmol) and 4 Å molecular sieves (0.180 g) in THF (3.5 mL). The mixture was protected from light and heated in an oil bath set to 60 °C for 16 h. The mixture was then filtered over Celite then the solvent was evaporated to isolate an orange solid compound. The product was purified by precipitation from a

CHCl$_3$ solution using petroleum ether. Isolated yield = 0.0362 g (34 %). ^{1}H NMR (CDCl$_3$, 500

MHz, 22 °C): δ 9.97 (s, 1H, $^3J_{PtH}$ = 40 Hz; C$_1$H), 8.46 (d, $^3J_{HH}$ = 8.3 Hz, 1H; C$_6$H), 8.03 (d, $^3J_{HH}$ =

8.0 Hz, 1H; C$_3$H), 7.95 (m, 1H; C$_5$H), 7.81 (s, 1H; C$_{13}$H), 7.72 (m, 1H; C$_4$H), 7.53 (s, 1H; C$_{11}$H),

5.28 (s, 1H; C$_{16}$H), 2.62 (s, 3H; C$_{19}$H), 2.42 (s, 3H; C$_{20}$H), 2.07 ppm (s, 3H; C$_{14}$H). ^{13}C{^{1}H} NMR

(CDCl$_3$, 125 MHz, 22 °C): δ 179.8 (C$_{16}$), 158.1 (C$_{18}$), 154.7 (C$_1$), 148.8 (C$_{10}$), 139.1 (C$_{12}$), 138.9

(C$_9$), 133.5 (C$_5$), 131.9 (C$_2$), 130.0 (C$_3$), 128.9 (C$_4$), 126.3 (C$_8$), 125.5 (C$_7$), 122.6 (C$_6$), 122.6 (C$_{11}$),

117.9 (C$_{13}$), 106.7 (C$_{16}$), 26.2 (C$_{14}$), 25.7 (C$_{18}$), 22.6 ppm (C$_{19}$). HRMS (ESI-TOF) m/z: [M + Na]$^+$

Calcd for [C$_{19}$H$_{17}$ClN$_2$OPt+Na]$^+$ 542.0571; Found 542.0532.

Synthesis of [Pt(L2)Cl], 9: An identical procedure to the preparation

of **1** was followed using a solution of **L2** (0.0612 g, 0.115 mmol) in

THF (3.5 mL), and a suspension of PtCl$_2$ (0.0590 g, 0.222 mmol),

Ag$_2$O (0.0313 g, 0.135 mmol) and 4 Å molecular sieves (0.122 g) in

THF (3.5 mL). After precipitation from CHCl$_3$, the supernatant was further concentrated, and more

product was following diffusion of diethylether vapors into the solution. Isolated yield = 0.0519 g

(49%). ^{1}H NMR (CDCl$_3$, 500 MHz, 22 °C): δ 8.51 (d, $^3J_{HH}$ = 8.4 Hz, 1H; C$_6$H), 8.21 (d, $^3J_{HH}$ = 8.4

Hz, 1H; C$_3$H), 7.92 (ddd, $^3J_{HH}$ = 8.4, 7.6 Hz, $^4J_{HH}$ = 1.0 Hz, 1H; C$_5$H), 7.78 (s; 1H; C$_{13}$H), 7.69

(ddd; $^3J_{HH}$ = 8.7, 7.7 Hz; $^4J_{HH}$ = 0.9 Hz; 1H; C$_4$H), 7.19 (s; 1H; C$_{11}$H), 5.27 (s; 1H; C$_{16}$H), 3.53 (s;

1H; C$_{19}$H), 2.56 (s; 1H; C$_{20}$H), 2.28 (s; 1H; C$_{14}$H), 2.06 (s; 1H; C$_{18}$H). 13C{1H} NMR (CDCl$_3$,

125 MHz, 22 °C): δ 179.9 (C$_{19}$), 167.8 (C$_1$), 158.3 (C$_{17}$), 148.8 (C$_{10}$), 140.1 (C$_9$), 137.7 (C$_{12}$), 133.0

(C$_5$), 131.4 (C$_7$), 128.8 (C$_4$), 127.9 (C$_3$), 127.1 (C$_2$), 124.6 (C$_8$), 122.7 (C$_6$), 121.0 (C$_{11}$), 117.4

(C$_{13}$), 106.5 (C$_{16}$), 26.8 (C$_{19}$), 25.3 (C$_{18}$), 23.7 (C$_{14}$), 22.2 ppm (C$_{20}$). HRMS (ESI-TOF) m/z: [M]$^+$

Calcd for [C$_{20}$H$_{19}$N$_2$OPt]$^+$ 498.1142; Found 498.1130.

Synthesis of [Pt(L3)Cl], 10: An identical procedure to the preparation of **1** was followed using a solution of **L3** (0.501 g, 1.51 mmol) in THF (25 mL) was added to a suspension of $PtCl_2$ (0.407 g, 1.53 mmol), Ag_2O (0.179 g, 0.774 mmol) and 4 Å molecular sieves in THF (25 mL). The mixture was protected from light and heated to reflux at 60 °C for 16 h. The mixture was then cooled and filtered over Celite. The solvent was then evaporated under vacuum to leave an orange solid, which was redissolved in $CHCl_3$ and recrystallized via diffusion of diethylether vapours into the filtered solution. Yield = 0.739 g (87%). ^{1}H NMR (CDCl_3, 500 MHz, 22°C): δ 10.03 (s, 1H, [3]J_{PtH} = 39 Hz; C_6-*H*), 8.57 (d, J_{HH} = 8.3 Hz, 1H; C_{10}- *H*), 8.10 (d, J_{HH} = 1.2 Hz, 1H; C_1-*H*), 8.07 (d, J_{HH} = 7.9 Hz, 1H; C_7-*H*), 7.99 (ddd, J_{HH} = 7.5 H, 9 Hz, 1H; C_8-*H*), 7.78 (d, J_{HH} = 1.3 Hz, 1H; C_3-*H*), 7.74 (ddd, J_{HH} = 7.5 Hz, 8.5 Hz, 1H; C_9-*H*), 5.32 (s, 1H; C_{14}-H), 2.46 (s, 3H; C_{12}-H), 2.07 (s, 3H; C_{16}-H), 1.50 ppm (s, 9H; C_{17}-H). ^{13}C{^{1}H} NMR (CDCl_3, 125 MHz, 22 °C): 179.80 (C_{15}), 157.85 (C_{13}), 155.01 (C_6), 151.96 (C_2), 148.78 (C_4), 139.22 (C_{4a}), 133.54 (C_8), 132.36 (C_{6a}), 130.18 (C_7), 128.83 (C_9), 126.38 (C_{6b}), 125.19 (C_{4b}), 122.48 (C_{10}), 119.57 (C_3), 114.02 (C_1), 106.66 (C_{14}), 35.72 (C_{11}), 31.61 (C_{17}), 25.98 (C_{16}), 25.66 ppm (C_{12}). HRMS (APCI-TOF) m/z: [M + H][+] Calcd for $C_{22}H_{23}ClN_2OPt$ 561.1198; Found 561.1085.

Synthesis of [Pt(L4)Cl], 11: An identical procedure to the synthesis of **1** was followed using **L4** (0.501 g, 1.46 mmol) in THF (25 mL) and a suspension of $PtCl_2$ (0.398 g, 1.50 mmol), Ag_2O (0.174 g, 0.752 mmol) and 4 Å molecular sieves in THF (25 mL). Dark red crystals were obtained by diffusion of diethylether vapours into a $CHCl_3$ solution of **11**. Yield = 0.722 g (86%). ^{1}H NMR (CDCl_3, 500 MHz, 22 °C): δ 10.20 (s, 1H, [3]J_{PtH} = 39 Hz; C_6-*H*), 8.57 (d, J_{HH} =

7.9 Hz, 1H; C_{10}-H), 8.33 (s, 1H; C_1-H), 8.18 (d, J_{HH} = 7.6 Hz, 1H; C_7-H), 8.10 (ddd, J_{HH} = 7.0 H,

9.4 Hz, 1H; C_8-H), 7.88 (s overlapping, 1H; C_3-H), 7.87 (ddd overlapping, 1H; C_9-H), 5.39 (s, 1H;

C_{14}-H), 2.46 (s, 3H; C_{12}-H), 2.09 ppm (s, 3H; C_{16}-H). $^{13}C\{^1H\}$ NMR (CDCl$_3$, 125 MHz, 22 °C): δ

181.84 (C_{15}), 158.39 (C_{13}), 158.01 (C_6), 150.00 (C_4), 142.00 (C_{6b}), 134.70 (C_8), 132.10 (C_{6a}),

130.70 (C_7), 130.06 (C_{4a}), 126.49 (C_2), 125.78 (C_9), 124.74 (C_{6b}), 122.66 (C_{4b}), 122.57 (C_{10}),

116.40 (q, J_{CF} = 3.6 Hz; C_3), 115.13 (q, J_{CF} = 3.6 Hz; C_1), 107.63 (C_{14}), 25.98 (C_{16}), 25.96 ppm

(C_{12}). ^{19}F NMR (CDCl$_3$, 470 MHz, 22°C): δ -62.14 ppm. HRMS (APCI-TOF) m/z: $[M + H]^+$ Calcd

for $C_{19}H_{14}ClF_3N_2OPt$ 573.0446; Found 573.0327. Anal. Calcd for $Pt_1C_{19}H_{14}F_3N_2O_1Cl_1$: C, 39.77;

H, 2.46. Found: C, 39.55; H, 2.79.

3.6.2 X-ray Crystallography Details

X-ray crystal structure data were collected from multi-faceted crystals of suitable size and

quality, selected from a representative sample of crystals of the same habit using an optical

microscope. Crystals were mounted on MiTiGen loops and data collection was carried out in a

cold stream of nitrogen (150 K; Bruker D8 QUEST ECO). Diffractometer manipulations were

carried out using Bruker APEX3 software.[74] Structure solution and refinement were performed

using XS, XT and XL software, embedded within the OLEX2.[75] For each structure, the absence

of additional symmetry was confirmed using ADDSYM incorporated in the PLATON program.[76]

PXRD patterns were acquired in a Bruker D8 Advance diffractometer (Cu Kα) using a

room temperature rotation stage.

Crystal structure data for 1 (CCDC 2097101): X-ray quality crystals were grown from vapour

diffusion of chloroform with hexanes as the non-solvent. Crystal structure parameters: Orange

blocks; $C_{19}H_{17}BF_2N_2O$ 338.15 g mol^{-1}, orthorhombic, space group Fdd2; a = 19.2122(6) Å, b =

42.8928(13) Å, c = 7.8535(3) Å, $\alpha = \beta = \gamma = 90°$, V = 6471.8(4) Å^3; Z = 16, ρ_{calcd} = 1.388 g cm^{-3}; crystal dimensions 0.480 x 0.200 x 0.050 mm; $2\theta_{max}$ = 61.128°; 49800 reflections, 4954 independent (R_{int} = 0.0617), intrinsic phasing; μ = 0.101 mm^{-1}, absorption correction semi-empirical from equivalents (SADABS); refinement (against $F_o{}^2$) with SHELXTL V6.1, 229 parameters, 1 restraints, R_1 = 0.0532 (I > 2σ) and wR_2 = 0.1172 (all data), Goof = 1.094, residual electron density 0.25/−0.26 Å^{-3}.

Crystal structure data for 2 (CCDC 2097102): X-ray quality crystals were grown from vapour diffusion of chloroform and hexanes. Crystal structure parameters: Orange plates; $C_{20}H_{19}BF_2N_2O$ 352.18 g mol^{-1}, orthorhombic, space group Fdd2; a = 20.9666(9) Å, b = 43.2401(18) Å, c = 7.8041(3) Å, $\alpha = \beta = \gamma = 90°$, V = 7075.2(5) Å^3; Z = 16, ρ_{calcd} = 1.323 g cm^{-3}; crystal dimensions 0.440 x 0.110 x 0.030 mm; $2\theta_{max}$ = 55.392°; 48959 reflections, 4144 independent (R_{int} = 0.0728), intrinsic phasing; μ = 0.096 mm^{-1}, absorption correction semi-empirical from equivalents (SADABS); refinement (against $F_o{}^2$) with SHELXTL V6.1, 239 parameters, 1 restraints, R_1 = 0.0431 (I > 2σ) and wR_2 = 0.0929 (all data), Goof = 1.059, residual electron density 0.19/−0.22 Å^{-3}.

Crystal structure data for 4 (CCDC 2097104): X-ray quality crystals were grown from vapour diffusion of chloroform and hexanes. Crystal structure parameters: Orange blocks; $C_{19}H_{14}BF_5N_2O$ 392.13 g mol^{-1}, monoclinic, space group $P2_1/c$; a = 10.3312(3) Å, b = 12.1157(4) Å, c = 13.6022(4) Å, $\alpha = \gamma = 90°$, β = 90.3410(10)°, V = 1702.55(9) Å^3; Z = 4, ρ_{calcd} = 1.530 g cm^{-3}; crystal dimensions 0.470 x 0.410 x 0.250 mm; $2\theta_{max}$ = 72.786°; 74965 reflections, 8277 independent (R_{int} = 0.0578), intrinsic phasing; μ = 0.132 mm^{-1}, absorption correction semi-empirical from equivalents (SADABS); refinement (against $F_o{}^2$) with SHELXTL V6.1, 255 parameters, 0

143

restraints, $R_1 = 0.0696$ ($I > 2\sigma$) and $wR_2 = 0.1786$ (all data), Goof = 1.045, residual electron density $0.51/-0.37$ Å^{-3}.

Crystal structure data for [3Me]OTf (CCDC 2097103): X-ray quality crystals were grown from vapour diffusion of pentane into a chloroform solution. Crystal structure parameters: Colourless needles; $C_{25}H_{27}BCl_3F_5N_2O_4S$ 663.70 g mol^{-1}, monoclinic, space group $P2_1/n$; a = 14.6473(8) Å, b = 7.2455(4) Å, c = 28.3346(15) Å, $\alpha = \gamma = 90°$, $\beta = 97.785(2)°$, V = 2979.4(3) Å^3; Z = 4, $\rho_{calcd} = 1.480$ g cm^{-3}; crystal dimensions 0.80 x 0.20 x 0.07 mm; $2\theta_{max} = 52.730°$; 64607 reflections, 6051 independent ($R_{int} = 0.0598$), intrinsic phasing; $\mu = 0.444$ mm^{-1}, absorption correction semi-empirical from equivalents (SADABS); refinement (against F_o^2) with SHELXTL V6.1, 376 parameters, 0 restraints, R_1 0.0799 ($I > 2\sigma$) and $wR_2 = 0.2174$ (all data), Goof = 1.052, residual electron density $1.919/-0.548$ Å^{-3}.

Crystal structure data of 6 (CCDC 2119917): X-ray quality crystals were grown following layering of hexanes into a CH_2Cl_2 solution at room temperature. Crystal structure parameters: $C_{45}H_{48}Cl_2N_4O_2Zn$ 813.14 g/mol, monoclinic, space group $P2_1/n$; $a = 20.825(3)$ Å, $b = 8.8858(11)$ Å, $c = 22.615(3)$ Å, $\alpha = \gamma = 90°$, $\beta = 102.594(5)°$, V = 4084.2(9) Å^3; Z = 4, $\rho_{calcd} = 1.322$ g cm^{-3}; crystal dimensions 0.32 x 0.13 x 0.05 mm; diffractometer Bruker D8 QUEST ECO CMOS; Mo K_α radiation, 150(2) K, $2\theta_{max} = 2.502$ to 24.415°; 34008 reflections, 7174 independent ($R_{int} = 0.0648$), direct methods; absorption coeff ($\mu = 0.686$ mm^{-1}), absorption correction semi-empirical from equivalents (SADABS); refinement (against F_o^2) with SHELXTL V6.1, 497 parameters, 0 restraints, $R_1 = 0.1147$ ($I > 2\sigma$) and $wR_2 = 0.2041$ (all data), Goof = 1.123, residual electron density $1.190/-1.587$ e Å^{-3}.

Crystal structure data of 7 (CCDC 2119918): X-ray quality crystals were grown following layering of hexanes into a benzene solution. Crystal structure parameters: $C_{44}H_{42}F_6N_4O_2Zn$ 838.18 g/mol, monoclinic, space group $C2/c$; $a = 10.4717(6)$ Å, $b = 12.3015(6)$ Å, $c = 30.9829(16)$ Å, $\alpha = \gamma = 90°$, $\beta = 90.077(2)°$, V = 3991.1(4) Å^3; Z = 4, $\rho_{calcd} = 1.395$ g cm^{-3}; crystal dimensions 0.45 x 0.26 x 0.09 mm; diffractometer Bruker D8 QUEST ECO CMOS; Mo K$_\alpha$ radiation, 150(2) K, $2\theta_{max} = 2.554$ to $30.628°$; 64265 reflections, 6157 independent (R$_{int}$ = 0.0468), direct methods; absorption coeff ($\mu = 6.804$ mm^{-1}), absorption correction semi-empirical from equivalents (SADABS); refinement (against F$_o^2$) with SHELXTL V6.1, 262 parameters, 0 restraints, $R_1 = 0.0684$ ($I > 2\sigma$) and $wR_2 = 0.1897$ (all data), Goof = 1.115, residual electron density 2.577/-1.313 e Å^{-3}.

Crystal structure data for 8 (CCDC 2100576): X-ray quality crystals were grown following diffusion of diethyl ether vapor into CHCl$_3$ at room temperature. Crystal structure parameters: $C_{19}H_{17}ClN_2OPt$ 519.89 g/mol, monoclinic, space group $P2_1/n$; $a = 9.2499(5)$ Å, $b = 11.5853(6)$ Å, $c = 15.3470(8)$ Å, $\alpha = \gamma = 90°$, $\beta = 103.623(2)°$, V = 1598.36(15) Å^3; Z = 4, $\rho_{calcd} = 2.160$ g cm^{-3}; crystal dimensions 0.16 x 0.14 x 0.02 mm; diffractometer Bruker D8 QUEST ECO CMOS; Mo K$_\alpha$ radiation, 150(2) K, $2\theta_{max} = 2.731$ to $24.790°$; 23441 reflections, 2739 independent (R$_{int}$ = 0.0642), direct methods; absorption coeff ($\mu = 8.954$ mm^{-1}), absorption correction semi-empirical from equivalents (SADABS); refinement (against F$_o^2$) with SHELXTL V6.1, 220 parameters, 0 restraints, $R_1 = 0.0351$ ($I > 2\sigma$) and $wR_2 = 0.0754$ (all data), Goof = 1.121, residual electron density 1.745/−1.521 e Å^{-3}.

Crystal structure data for 9 (CCDC 2100577): X-ray quality crystals were grown following diffusion of diethyl ether vapor into CHCl$_3$ at room temperature. Crystal structure parameters:

145

$C_{21}H_{20}Cl_4N_2OPt$ 653.28 g/mol, triclinic, space group $P{-}1$; a = 11.0564(7) Å, b = 14.0350(9) Å, c = 16.4321(10) Å, α = 113.018(2)°, β = 99.705(2)°, γ = 100.551(2)°, V = 2224.4(2) Å^3; Z = 4, ρ_{calcd} = 1.951 g cm^{-3}; crystal dimensions 0.35 x 0.14 x 0.06 mm; diffractometer Bruker D8 QUEST ECO CMOS; Mo K$_\alpha$ radiation, 150(2) K, $2\theta_{max}$ = 2.550 to 30.591°; 61734 reflections, 13610 independent (R_{int} = 0.0468), direct methods; absorption coeff (μ = 6.804 mm^{-1}), absorption correction semi-empirical from equivalents (SADABS); refinement (against F_o^2) with SHELXTL V6.1, 531 parameters, 0 restraints, R_1 = 0.0335 ($I > 2\sigma$) and wR_2 = 0.652 (all data), Goof = 1.044, residual electron density 1.784/-1.569 e Å^{-3}

Crystal structure data for 10 (CCDC 2100578): X-ray quality crystals were grown following diffusion of diethyl ether vapor into CHCl$_3$ at room temperature. Crystal structure parameters: $C_{19}H_{14}ClF_3N_2OPt$ 573.86 g/mol, monoclinic, space group $P2_1/n$; a = 9.5576(6) Å, b = 11.5940(7) Å, c = 15.7469(10) Å, $\alpha = \gamma$ = 90°, β = 105.381(2)°, V = 1682.43(18) Å^3; Z = 4, ρ_{calcd} = 2.266 g cm^{-3}; crystal dimensions 0.1 x 0.08 x 0.05 mm; diffractometer Bruker D8 QUEST ECO CMOS; Mo K$_\alpha$ radiation, 150(2) K, $2\theta_{max}$ = 2.683 to 27.553°; 40565 reflections, 3880 independent (R_{int} = 0.0828), direct methods; absorption coeff (μ = 8.543 mm^{-1}), absorption correction semi-empirical from equivalents (SADABS); refinement (against F_o^2) with SHELXTL V6.1, 231 parameters, 0 restraints, R_1 = 0.0436 ($I > 2\sigma$) and wR_2 = 0.0844 (all data), Goof = 1.115, residual electron density 2.469/-2.433 e Å^{-3}.

Crystal structure data for 11 (CCDC 1959704): X-ray quality crystals were grown following diffusion of diethylether vapor into CHCl$_3$ at room temperature. Crystal structure parameters: $C_{23}H_{24}Cl_4N_2O_1Pt_1$ 681.33 g/mol, monoclinic, space group $P2_1/n$; a = 6.9467(3) Å, b = 18.7502(6) Å, c = 18.4435(6) Å, $\alpha = \gamma$ = 90°, β = 100.0770(10)°, V = 2365.24(15) Å^3; Z = 4, ρ_{calcd} = 1.913 g

cm^{-3}; crystal dimensions 0.150 x 0.059 x 0.047 mm; diffractometer Bruker D8 QUEST ECO CMOS; Mo K$_\alpha$ radiation, 150(2) K, $2\theta_{max}$ = 2.243 to 27.535°; 44379 reflections, 5419 independent (R_{int} = 0.0646), direct methods; absorption coeff (μ = 6.403 mm^{-1}), absorption correction semi-empirical from equivalents (SADABS); refinement (against F$_o^2$) with SHELXTL V6.1, 285 parameters, 0 restraints, R_1 = 0.0326 ($I > 2\sigma$) and wR_2 = 0.0677 (all data), Goof = 1.075, residual electron density 1.442/−1.154 e Å^{-3}.

3.6.3 UV-Vis Absorption and Luminescence Experiments

General Aspects

Absorption spectra were measured on a Biotek Instruments XS spectrometer, using quartz cuvettes of 1 cm pathlength. Steady-state luminescence spectra were measured using a Jobin Yvon FluoroMax-2 spectrofluorimeter, fitted with a red-sensitive Hamamatsu R928 photomultiplier tube; the spectra shown are corrected for the wavelength dependence of the detector, and the quoted emission maxima refer to the values after correction. Degassed samples for emission measurements were contained within quartz cuvettes of 1 cm pathlength modified with appropriate glassware to allow connection to a high-vacuum line. Degassing was achieved via a minimum of three freeze-pump-thaw cycles whilst connected to the vacuum manifold.

Luminescence Experiments for Boron Complexes

Luminescence quantum yields were determined using quinine sulfate in 1M H_2SO_4(aq) as the standard (Φ = 0.546).[133] Fluorescence lifetimes were measured, where possible, by time-correlated single-photon counting following excitation at 374 nm with a pulsed-diode laser. The emitted light was detected at 90° using a Peltier-cooled R928 PMT after passage through a

monochromator. Phosphorescence lifetimes at 77 K were measured following excitation with a microsecond-pulsed xenon lamp and detection using the same PMT operating in multichannel scaling mode.

Luminescence Experiments for Zinc Complexes

The spectra in the solid state were recorded by means of an integrating sphere attached to a Jobin Yvon Fluorolog instrument through optical fibers. Finely powdered samples were contained within Spectralon sample holders of 10 mm diameter. Quantum yields were determined using a sample of finely powdered $BaSO_4$ as a non-emissive blank. Luminescence lifetimes were measured following excitation with a microsecond-pulsed xenon lamp and detection using a Hamamatsu R928 photomultiplier tube operating in multichannel scaling mode. For all measurements, the decays were much longer than the instrument response, and data were analyzed by tail fitting to the following equation (5):

$$I(t) = I(0) \exp(-kt) + c \qquad (5)$$

where $I(t)$ is the intensity of light detected at time t, k is the first-order rate constant for decay ($k = 1/\tau$), and c is a constant reflecting the intrinsic "dark count" during the measurement. The data in solid-state fit well to the above equation, with no significant improvement upon introducing additional components. At 77 K, the data show evidence of an additional short-lived component and the values quoted in Table 3.2 refer to tail-fitting of the long component only.

Luminescence Experiments for Platinum Complexes

Luminescence quantum yields were determined using $[Ru(bpy)_3]Cl_2$ in aqueous solution as the standard ($\Phi = 0.04\pm0.002$).[134] The estimated uncertainty on the quantum yields obtained in this way on the instrumentation employed is up to $\pm20\%$. Luminescence lifetimes of the complexes

148

in air-equilibrated solutions were measured by time-correlated single-photon counting, following excitation at 405 nm with a pulsed-diode laser. The emitted light was detected at 90° using a Peltier-cooled R928 PMT after passage through a monochromator. The estimated uncertainty in the quoted lifetimes is ± 10% or better. Lifetimes in deoxygenated solution and at 77 K were measured following excitation with a microsecond-pulsed xenon lamp and detection using the same PMT operating in multichannel scaling mode. For all measurements, the decays were much longer than the instrument response and data were analyzed by tail fitting to the equation (5) [rather than by deconvolution of the response function]. The estimated uncertainty in the quoted lifetimes is ±10%. Bimolecular rate constants for quenching by molecular oxygen, k_Q, were determined from the lifetimes in degassed and air-equilibrated solution, taking the concentration of oxygen in CH_2Cl_2 at 0.21 atm O_2 to be 2.2 mmol dm^{-3}.[135]

Conclusions

In this chapter, the main group and transition metal complexes of $N^\wedge NH^\wedge O$ ligands, **L1**-**L4**, are presented. The syntheses, electronic structures, and photophysical properties of the different complexes are disclosed. Due to the smaller size of boron, coordination of the phenanthridinyl is restricted compared with the larger zinc and platinum centres. Ligation of the phenanthridinyl on metal centres induces significant perturbation to the chemical shift of the C_6H moiety that is dependent on the metal and coordination number. In contrast, the phenanthridinyl pendent arm in the boron complexes did not exhibit any significant perturbation compared with the ligands or phenanthridine.

The electronic and photophysical properties of the complexes are markedly different from their ligands. The complexes show some CT character to their lowest absorption manifolds as evident from solvatochromic studies. All complexes exhibit luminescence albeit weakly in solution for both boron and zinc complexes. Phosphorescence as the preferential radiative decay pathway can be enabled by increasing the size of the metal centre and noncovalent intermolecular interactions (in zinc complexes).

References

(1)   Faraday, M. On New Compounds of Carbon and Hydrogen, and on Certain Other Products Obtained during the Decomposition of Oil by Heatrstl.1825.Pdf. *Philos. Trans. R. Soc.* **1825**, *115*, 440–466.

(2)   Heo, I.; Lee, J. C.; Özer, B. R.; Schultz, T. Mass-Correlated High-Resolution Spectra and the Structure of Benzene. *J. Phys. Chem. Lett.* **2022**, *13* (35), 8278–8283. https://doi.org/10.1021/acs.jpclett.2c02035.

(3)   Kunishige, S.; Katori, T.; Baba, M.; Nakajima, M.; Endo, Y. Spectroscopic Study on Deuterated Benzenes. I. Microwave Spectra and Molecular Structure in the Ground State. *J. Chem. Phys.* **2015**, *143* (24), 244302. https://doi.org/10.1063/1.4937949.

(4)   Watson, M. D.; Fechtenkötter, A.; Müllen, K. Big Is Beautiful−"Aromaticity" Revisited from the Viewpoint of Macromolecular and Supramolecular Benzene Chemistry. *Chem. Rev.* **2001**, *101* (5), 1267–1300. https://doi.org/10.1021/cr990322p.

(5)   Vij, V.; Bhalla, V.; Kumar, M. Hexaarylbenzene: Evolution of Properties and Applications of Multitalented Scaffold. *Chem. Rev.* **2016**, *116* (16), 9565–9627. https://doi.org/10.1021/acs.chemrev.6b00144.

(6)   Price, C. C. Substitution and Orientation in the Benzene Ring. *Chem. Rev.* **1941**, *29* (1), 37–67. https://doi.org/10.1021/cr60092a002.

(7)   Papadakis, R.; Ottosson, H. The Excited State Antiaromatic Benzene Ring: A Molecular Mr Hyde? *Chem. Soc. Rev.* **2015**, *44* (18), 6472–6493. https://doi.org/10.1039/C5CS00057B.

(8)   Swami, B.; Yadav, D.; Menon, R. S. Benzannulation Reactions: A Case for Perspective Change From Arene Decoration to Arene Construction. *Chem. Rec.* **2022**, *22* (1), e202100249. https://doi.org/10.1002/tcr.202100249.

(9)   Hart-Davis, A. J.; White, C.; Mawby, F. J. Reactions Of-WIndeny Complexes of Transition Metals. III.' Kinetics and Mechanisms of Substitution Reactions of Tricarbonyl-Mindenylhalomolybdenum(II) Complexes. 6.

(10)   Rerek, M. E.; Basolo, F. Kinetics and Mechanism of Substitution Reactions of .Eta.5-Cyclopentadienyldicarbonylrhodium(I) Derivatives. Rate Enhancement of Associative

Substitution in Cyclopentadienylmetal Compounds. *J. Am. Chem. Soc.* **1984**, *106* (20), 5908–5912. https://doi.org/10.1021/ja00332a026.

(11) Rerek, M. E.; Ji, L.-N.; Basolo, F. The Lndenyl Ligand Effect on the Rate of Substitution Reactions of Rh(Rl-C9H7)C(O), and Mn(Rl -CgH7)C(O)a. 2.

(12) Okada, Y.; Miyamoto, N.; Hishimoto, M.; Hayashi, T. Studies on Ferrocene Derivatives. Part XIII. Ligand Exchange Reactions of Benzoferrocenes. *Transit. Met Chem* **1999**, 5.

(13) Treichel, P. M.; Johnson, J. W.; Wagner, K. P. OXIDATIONS OF VARIOUS INDENYL-IRON. 4.

(14) Crossley, N. S.; Green, J. C.; Nagy, A.; Stringer, G. Electronic Structure of Transition-Metal Lndenyl Compounds: A He I and He I I Photoelectron Spectroscopic Study of [Mn(Q5-C,H7)(CO),], [Fe(Q5-CgH7),]. Ru(Q5-C9H7)21 and Ru(T5-C9H7)(q-C5Me5) I t. *J CHEM SOC DALTON TRANS* **1989**, 9.

(15) Brady, E. D.; Overby, J. S.; Meredith, M. B.; Mussman, A. B.; Cohn, M. A.; Hanusa, T. P.; Yee, G. T.; Pink, M. Spin-State Alteration from Sterically Enforced Ligand Rotation in Bis(Indenyl)Chromium(II) Complexes [1]. *J. Am. Chem. Soc.* **2002**, *124* (32), 9556–9566. https://doi.org/10.1021/ja012390a.

(16) Shimizu, A.; Ishizaki, Y.; Horiuchi, S.; Hirose, T.; Matsuda, K.; Sato, H.; Yoshida, J. HOMO–LUMO Energy-Gap Tuning of π-Conjugated Zwitterions Composed of Electron-Donating Anion and Electron-Accepting Cation. *J. Org. Chem.* **2021**, *86* (1), 770–781. https://doi.org/10.1021/acs.joc.0c02343.

(17) Hanson, K.; Roskop, L.; Djurovich, P. I.; Zahariev, F.; Gordon, M. S.; Thompson, M. E. A Paradigm for Blue- or Red-Shifted Absorption of Small Molecules Depending on the Site of π-Extension. *J. Am. Chem. Soc.* **2010**, *132* (45), 16247–16255. https://doi.org/10.1021/ja1075162.

(18) Liu, B.; Lystrom, L.; Kilina, S.; Sun, W. Effects of Varying the Benzannulation Site and π Conjugation of the Cyclometalating Ligand on the Photophysics and Reverse Saturable Absorption of Monocationic Iridium(III) Complexes. *Inorg. Chem.* **2019**, *58* (1), 476–488. https://doi.org/10.1021/acs.inorgchem.8b02714.

(19) Liu, B.; Lystrom, L.; Brown, S. L.; Hobbie, E. K.; Kilina, S.; Sun, W. Impact of Benzannulation Site at the Diimine (N^N) Ligand on the Excited-State Properties and Reverse Saturable Absorption of Biscyclometallated Iridium(III) Complexes. *Inorg. Chem.* **2019**, *58* (9), 5483–5493. https://doi.org/10.1021/acs.inorgchem.8b03162.

(20) Wang, L.; Yin, H.; Jabed, M. A.; Hetu, M.; Wang, C.; Monro, S.; Zhu, X.; Kilina, S.; McFarland, S. A.; Sun, W. π-Expansive Heteroleptic Ruthenium(II) Complexes as Reverse Saturable Absorbers and Photosensitizers for Photodynamic Therapy. *Inorg. Chem.* **2017**, *56* (6), 3245–3259. https://doi.org/10.1021/acs.inorgchem.6b02624.

(21) Chen, T.; Li, M.; Liu, J. π–π Stacking Interaction: A Nondestructive and Facile Means in Material Engineering for Bioapplications. *Cryst. Growth Des.* **2018**, *18* (5), 2765–2783. https://doi.org/10.1021/acs.cgd.7b01503.

(22) Sinnokrot, M. O.; Valeev, E. F.; Sherrill, C. D. Estimates of the Ab Initio Limit for $\Pi-\pi$ Interactions: The Benzene Dimer. *J. Am. Chem. Soc.* **2002**, *124* (36), 10887–10893. https://doi.org/10.1021/ja025896h.

(23) Cai, M.; Song, X.; Zhang, D.; Qiao, J.; Duan, L. π–π Stacking: A Strategy to Improve the Electron Mobilities of Bipolar Hosts for TADF and Phosphorescent Devices with Low

Efficiency Roll-Off. *J. Mater. Chem. C* **2017**, *5* (13), 3372–3381. https://doi.org/10.1039/C7TC00733G.

(24)   Hong, Y.; Lam, J. W. Y.; Tang, B. Z. Aggregation-Induced Emission: Phenomenon, Mechanism and Applications. *Chem. Commun.* **2009**, No. 29, 4332. https://doi.org/10.1039/b904665h.

(25)   McGaughey, G. B.; Gagné, M.; Rappé, A. K. π-Stacking Interactions. *J. Biol. Chem.* **1998**, *273* (25), 15458–15463. https://doi.org/10.1074/jbc.273.25.15458.

(26)   Babine, R. E.; Bender, S. L. Molecular Recognition of Protein−Ligand Complexes: Applications to Drug Design. *Chem. Rev.* **1997**, *97* (5), 1359–1472. https://doi.org/10.1021/cr960370z.

(27)   Pages, B. J.; Garbutcheon-Singh, K. B.; Aldrich-Wright, J. R. Platinum Intercalators of DNA as Anticancer Agents. *Eur. J. Inorg. Chem.* **2017**, *2017* (12), 1613–1624. https://doi.org/10.1002/ejic.201601204.

(28)   Hayashi, K.; Nakatani, M.; Hayashi, A.; Takano, M.; Okazaki, M.; Toyota, K.; Yoshifuji, M.; Ozawa, F. Synthesis and Structures of Platinum(0) Alkyne Complexes with Extended π-Conjugated Systems. *Organometallics* **2008**, *27* (9), 1970–1972. https://doi.org/10.1021/om800163p.

(29)   Flamigni, L.; Encinas, S.; Barigelletti, F.; MacDonnell, F. M.; Kim, K.-J.; Puntoriero, F.; Campagna, S. Excited-State Interconversion between Emissive MLCT Levels in a Dinuclear Ru(Ii) Complex Containing a Bridging Ligand with an Extended π System. *Chem. Commun.* **2000**, No. 13, 1185–1186. https://doi.org/10.1039/b004109m.

(30)   Roznyatovskiy, V. V.; Lee, C.-H.; Sessler, J. L. π-Extended Isomeric and Expanded Porphyrins. *Chem Soc Rev* **2013**, *42* (5), 1921–1933. https://doi.org/10.1039/C2CS35418G.

(31)   Barbon, S. M.; Staroverov, V. N.; Gilroy, J. B. Effect of Extended π Conjugation on the Spectroscopic and Electrochemical Properties of Boron Difluoride Formazanate Complexes. *J. Org. Chem.* **2015**, *80* (10), 5226–5235. https://doi.org/10.1021/acs.joc.5b00620.

(32)   Kappaun, S.; Rentenberger, S.; Pogantsch, A.; Zojer, E.; Mereiter, K.; Trimmel, G.; Saf, R.; Möller, K. C.; Stelzer, F.; Slugovc, C. Organoboron Quinolinolates with Extended Conjugated Chromophores: Synthesis, Structure, and Electronic and Electroluminescent Properties. *Chem. Mater.* **2006**, *18* (15), 3539–3547. https://doi.org/10.1021/cm060720q.

(33)   Kiprof, P.; Carlson, J. C.; Anderson, D. R.; Nemykin, V. N. Systematic Color Tuning of a Family of Luminescent Azole-Based Organoboron Compounds Suitable for OLED Applications. *Dalton Trans.* **2013**, *42* (42), 15120. https://doi.org/10.1039/c3dt51853a.

(34)   Bossi, A.; Rausch, A. F.; Leitl, M. J.; Czerwieniec, R.; Whited, M. T.; Djurovich, P. I.; Yersin, H.; Thompson, M. E. Photophysical Properties of Cyclometallated Pt(II) Complexes: Counterintuitive Blue Shift in Emission with an Expanded Ligand π System. *Inorg. Chem.* **2013**, *52* (21), 12403–12415. https://doi.org/10.1021/ic4011532.

(35)   Gunanathan, C.; Gnanaprakasam, B.; Iron, M. A.; Shimon, L. J. W.; Milstein, D. "Long-Range" Metal−Ligand Cooperation in H_2 Activation and Ammonia-Promoted Hydride Transfer with a Ruthenium−Acridine Pincer Complex. *J. Am. Chem. Soc.* **2010**, *132* (42), 14763–14765. https://doi.org/10.1021/ja107770y.

(36)   Neufeldt, S. R.; Sanford, M. S. Controlling Site Selectivity in Palladium-Catalyzed C–H Bond Functionalization. *Acc. Chem. Res.* **2012**, *45* (6), 936–946. https://doi.org/10.1021/ar300014f.

(37)   Krichevsky, O.; Bonnet, Gregoire. Fluorescence Correlation Spectroscopy: The Technique and Its Applications. *Rep. Prog. Phys.* **2002**, *65* (2), 251–297. https://doi.org/10.1088/0034-4885/65/2/203.

(38)   Tumir, L.-M.; Stojkovic, M. R.; Piantanida, I. Come-Back of Phenanthridine and Phenanthridinium Derivatives in the 21st Century. *Beilstein J Org Chem* **2014**, *10*, 2930–2954.

(39)   Park, G. Y.; Wilson, J. J.; Song, Y.; Lippard, S. J. Phenanthriplatin, a Monofunctional DNA-Binding Platinum Anticancer Drug Candidate with Unusual Potency and Cellular Activity Profile. *Proc Natl Acad Sci* **2012**, *109*, 11987–11992.

(40)   Lu, L.-Q.; Li, Y.; Junge, K.; Beller, Matthias. Iron-Catalyzed Hydrogenation for the In Situ Regeneration of an NAD(P)H Model: Biomimetic Reduction of α-Keto-/α-Iminoesters. *Angew. Chem. Int. Ed.* **2013**, *52* (32), 8382–8386. https://doi.org/10.1002/anie.201301972.

(41)   Chen, Q.-A.; Gao, K.; Duan, Y.; Ye, Z.-S.; Shi, L.; Yang, Y.; Zhou, Y.-Gui. Dihydrophenanthridine: A New and Easily Regenerable NAD(P)H Model for Biomimetic Asymmetric Hydrogenation. *J. Am. Chem. Soc.* **2012**, *134* (4), 2442–2448. https://doi.org/10.1021/ja211684v.

(42)   Jensen, K. A.; Nielsen, P. Halfdan. Chelates with Heterocyclic Ligands. I. Chelates Derived from e N,N'-Bis(8-Quinolyl)Ethylenediamine and Analogous Compounds. *Acta Chem. Scand. 1947-1973* **1964**, *18* (1), 1–10. https://doi.org/10.3891/acta.chem.scand.18-0001.

(43)   Puzas, J. P.; Nakon, R.; Petersen, J. L. Direct Evidence for an SN1CB Mechanism. 4. Crystal and Molecular Structure of Chloro(Bis(8-Quinolinyl)Amido-N1,N2,N3)Copper(II), a Metal Chelate Containing an Sp2-Hybridized Deprotonated Amine. *Inorg. Chem.* **1986**, *25* (21), 3837–3840. https://doi.org/10.1021/ic00241a026.

(44)   Peters, J. C.; Harkins, S. B.; Brown, S. D.; Day, M. W. Pincer-like Amido Complexes of Platinum, Palladium, and Nickel. *Inorg. Chem.* **2001**, *40* (20), 5083–5091. https://doi.org/10.1021/ic010336p.

(45)   Maiti, D.; Paul, H.; Chanda, N.; Chakraborty, S.; Mondal, B.; Puranik, V. G.; Lahiri, G. Kumar. Synthesis, Structure, Spectral and Electron-Transfer Properties of Octahedral-[CoIII(L)2]+/[ZnII(L)2] and Square Planar-[CuII(L){OC(=O)CH3}] Complexes Incorporating Anionic Form of Tridentate Bis(8-Quinolinyl)Amine [N1C9H6-N2-C9H6N3, L-] Ligand. *Polyhedron* **2004**, *23* (5), 831–840. https://doi.org/10.1016/j.poly.2003.11.053.

(46)   Valk, J.-M.; Claridge, T. D. W.; Brown, J. M.; Hibbs, D.; Hursthouse, M. B. Synthesis and Chemistry of a New P-N Chelating Ligand; (R)- and (S)-6-(2'-Diphenylphosphino-1'-Naphthyl)Phenanthridine. *Tetrahedron Asymmetry* **1995**, *6* (Copyright (C) 2017 American Chemical Society (ACS). All Rights Reserved.), 2597–2610. https://doi.org/10.1016/0957-4166(95)00341-L.

(47)   Raszeja, L.; Maghnouj, A.; Hahn, S.; Metzler-Nolte, Nils. A Novel Organometallic ReI Complex with Favourable Properties for Bioimaging and Applicability in Solid-Phase Peptide Synthesis. *ChemBioChem* **2011**, *12* (3), 371–376. https://doi.org/10.1002/cbic.201000576.

(48)   Sicilia, V.; Fuertes, S.; Martin, A.; Palacios, Adrian. N-Assisted CPh-H Activation in 3,8-Dinitro-6-Phenylphenanthridine. New C,N-Cyclometallated Compounds of Platinum(II): Synthesis, Structure, and Luminescence Studies. *Organometallics* **2013**, *32* (15), 4092–4102. https://doi.org/10.1021/om400159g.

(49) Jiang, B.; Gu, Y.; Qin, J.; Ning, X.; Gong, S.; Xie, G.; Yang, Chuluo. Deep-Red Iridium(III) Complexes Cyclometallated by Phenanthridine Derivatives for Highly Efficient Solution-Processed Organic Light-Emitting Diodes. *J. Mater. Chem. C Mater. Opt. Electron. Devices* **2016**, *4* (16), 3492–3498. https://doi.org/10.1039/C6TC00148C.

(50) Theobald, R. S.; Schofield, K. The Chemistry of Phenanthridine and Its Derivatives. *Chem. Rev.* **1950**, *46* (1), 170–189. https://doi.org/10.1021/cr60143a004.

(51) Crystal and molecular structure of phenanthridine. Roychowdhury1973.Pdf. *Acta. Cryst., Sect. B* **1973**, *29*, 1362–1364.

(52) Brett, W. A.; Rademacher, P.; Boese, R. Redetermination of the Structure of Phenanthridine. *Acta Crystallogr. C* **1993**, *49* (9), 1564–1566. https://doi.org/10.1107/S0108270193005062.

(53) Katritzky, A. R. *Handbook of Heterocyclic Chemistry*, 3rd ed.; Elsevier, 2010.

(54) Benmachiche, A.; Zendaoui, S.-M.; Bouaoud, S.-E.; Zouchoune, B. Electronic Structure and Coordination Chemistry of Phenanthridine Ligand in First-Row Transition Metal Complexes: A DFT Study. *Int. J. Quantum Chem.* **2013**, *113* (7), 985–996. https://doi.org/10.1002/qua.24071.

(55) Giesbrecht, P. K.; Nemez, D. B.; Herbert, D. E. Electrochemical Hydrogenation of a Benzannulated Pyridine to a Dihydropyridine in Acidic Solution. *Chem. Commun.* **2018**, *54* (4), 338–341. https://doi.org/10.1039/C7CC07907A.

(56) Mondal, R.; Giesbrecht, P. K.; Herbert, D. E. Nickel(II), Copper(I) and Zinc(II) Complexes Supported by a (4-Diphenylphosphino)Phenanthridine Ligand. *Polyhedron* **2016**, *108*, 156–162.

(57) Mandapati, P.; Giesbrecht, P. K.; Davis, R. L.; Herbert, D. E. Phenanthridine-Containing Pincer-like Amido Complexes of Nickel, Palladium, and Platinum. *Inorg Chem* **2017**, *56*, 3674–3685.

(58) Mandapati, P.; Braun, J. D.; Killeen, C.; Davis, R. L.; Williams, J. A. G.; Herbert, D. E. Luminescent Platinum(II) Complexes of N^N⁻^N Amido Ligands with Benzannulated N-Heterocyclic Donor Arms: Quinolines Offer Unexpectedly Deeper Red Phosphorescence than Phenanthridines. *Inorg Chem* **2019**, *58*, 14808–14817.

(59) Mandapati, P.; Braun, J. D.; Lozada, I. B.; Williams, J. A. G.; Herbert, D. E. Deep-Red Luminescence from Platinum(II) Complexes of N^N⁻^N-Amido Ligands with Benzannulated N-Heterocyclic Donor Arms. *Inorg. Chem.* **2020**, *59*, 12504–12517.

(60) Mondal, R.; Lozada, I. B.; Davis, R. L.; Williams, J. A. G.; Herbert, D. E. Site-Selective Benzannulation of N-Heterocycles in Bidentate Ligands Leads to Blue-Shifted Emission from [(P^N)Cu]₂(μ-X)₂ Dimers. *Inorg Chem* **2018**, *57*, 4966–4978.

(61) Mondal, R.; Lozada, I. B.; Davis, R. L.; Williams, J. A. G.; Herbert, D. E. Exploiting Synergy between Ligand Design and Counterion Interactions to Boost Room Temperature Phosphorescence from Cu(I) Compounds. *J. Mater. Chem. C* **2019**, *7*, 3772–3778.

(62) Lozada, I. B.; Murray, T.; Herbert, D. E. Monomeric Zinc(II) Amide Complexes Supported by Bidentate, Benzannulated Phenanthridine Amido Ligands. *Polyhedron* **2019**, *161*, 261–267.

(63) Mondal, R.; Lozada, I. B.; Davis, R. L.; Williams, J. A. G.; Herbert, D. E. Site-Selective Benzannulation of N-Heterocycles in Bidentate Ligands Leads to Blue-Shifted Emission from [(P^N)Cu]2(μ-X)2 Dimers. *Inorg Chem* **2018**, *57*, 4966–4978.

(64) Mandapati, P.; Giesbrecht, P. K.; Davis, R. L.; Herbert, D. E. Phenanthridine-Containing Pincer-like Amido Complexes of Nickel, Palladium, and Platinum. *Inorg Chem* **2017**, *56*, 3674–3685.

(65) Gaire, S.; Ortiz, R. J.; Schrage, B. R.; Lozada, I. B.; Mandapati, P.; Osinski, A. J.; Herbert, D. E.; Ziegler, C. J. (8-Amino)Quinoline and (4-Amino)Phenanthridine Complexes of Re(CO)3 Halides. *J. Organomet. Chem.* **2020**, *921*, 121338.

(66) Nemez, D. B.; Lozada, I. B.; Braun, J. D.; Williams, J. A. G.; Herbert, D. E. Synthesis and Coordination Chemistry of a Benzannulated Bipyridine: 6,6′-Biphenanthridine. *Inorg. Chem.* **2022**, *61* (34), 13386–13398. https://doi.org/10.1021/acs.inorgchem.2c01514.

(67) Hanson, K.; Roskop, L.; Djurovich, P. I.; Zahariev, F.; Gordon, M. S.; Thompson, M. E. A Paradigm for Blue- or Red-Shifted Absorption of Small Molecules Depending on the Site of π-Extension. *J. Am. Chem. Soc.* **2010**, *132*, 16247–16255.

(68) Barbon, S. M.; Staroverov, V. N.; Gilroy, J. B. Effect of Extended π Conjugation on the Spectroscopic and Electrochemical Properties of Boron Difluoride Formazanate Complexes. *J. Org. Chem.* **2015**, *80*, 5226–5235.

(69) Liu, B.; Lystrom, L.; Kilina, S.; Sun, W. Tuning the Ground State and Excited State Properties of Monocationic Iridium(III) Complexes by Varying the Site of Benzannulation on Diimine Ligand. *Inorg. Chem.* **2017**, *56*, 5361–5370.

(70) Westcott, B. L.; Gruhn, N. E.; Michelsen, L. J.; Lichtenberger, D. L. Experimental Observation of Non-Aufbau Behavior: Photoelectron Spectra of Vanadyloctaethylporphyrinate and Vanadylphthalocyanine. *J. Am. Chem. Soc.* **2000**, *122*, 8083–8084.

(71) Hewage, J. S.; Wanniarachchi, S.; Morin, T. J.; Liddle, B. J.; Banaszynski, M.; Lindeman, S. V.; Bennett, B.; Gardinier, J. R. Homoleptic Nickel(II) Complexes of Redox-Tunable Pincer-Type Ligands. *Inorg. Chem.* **2014**, *53* (19), 10070–10084. https://doi.org/10.1021/ic500657e.

(72) Lozada, I. B.; Ortiz, R. J.; Braun, J. D.; Williams, J. A. G.; Herbert, D. E. Donor–Acceptor Boron-Ketoiminate Complexes with Pendent *N*-Heterocyclic Arms: Switched-on Luminescence through *N*-Heterocycle Methylation. *J. Org. Chem.* **2022**, *87* (1), 184–196. https://doi.org/10.1021/acs.joc.1c02138.

(73) Braun, J. D.; Lozada, I. B.; Kolodziej, C.; Burda, C.; Newman, K. M. E.; van Lierop, J.; Davis, R. L.; Herbert, D. E. Iron(II) Coordination Complexes with Panchromatic Absorption and Nanosecond Charge-Transfer Excited State Lifetimes. *Nat. Chem.* **2019**, *11*, 1144–1150.

(74) Bruker-AXS. APEX3 V2016.1-0, 2016.

(75) Dolomanov, O. V.; Bourhis, L. J.; Gildea, R. J.; Howard, J. A. K.; Puschmann, H. OLEX2: A Complete Structure Solution, Refinement and Analysis Program. *J. Appl. Crystallogr.* **2009**, *42*, 339–341.

(76) Spek, A. L. Structure Validation in Chemical Crystallography. *Acta Cryst* **2009**, *D65*, 148–155.

(77) Fan, C.; Yang, C. Yellow/Orange Emissive Heavy-Metal Complexes as Phosphors in Monochromatic and White Organic Light-Emitting Devices. *Chem Soc Rev* **2014**, *43* (17), 6439–6469. https://doi.org/10.1039/C4CS00110A.

(78) Vreshch, V. D.; Yang, J.-H.; Zhang, H.; Filatov, A. S.; Dikarev, E. V. Monomeric Square-Planar Cobalt(II) Acetylacetonate: Mystery or Mistake? *Inorg. Chem.* **2010**, *49* (18), 8430–8434. https://doi.org/10.1021/ic100963r.

(79) Sokolow, J. D.; Trzop, E.; Chen, Y.; Tang, J.; Allen, L. J.; Crabtree, R. H.; Benedict, J. B.; Coppens, P. Binding Modes of Carboxylate- and Acetylacetonate-Linked Chromophores to Homodisperse Polyoxotitanate Nanoclusters. *J. Am. Chem. Soc.* **2012**, *134* (28), 11695–11700. https://doi.org/10.1021/ja303692r.

(80) Muñoz-García, A. B.; Sannino, F.; Vitiello, G.; Pirozzi, D.; Minieri, L.; Aronne, A.; Pernice, P.; Pavone, M.; D'Errico, G. Origin and Electronic Features of Reactive Oxygen Species at Hybrid Zirconia-Acetylacetonate Interfaces. *ACS Appl. Mater. Interfaces* **2015**, *7* (39), 21662–21667. https://doi.org/10.1021/acsami.5b06988.

(81) Seco, M. Acetylacetone: A Versatile Ligand. *J. Chem. Educ.* **1989**, *66* (9), 779. https://doi.org/10.1021/ed066p779.

(82) Allen, G.; Lewis, J.; Long, R. F.; Oldham, C. A Novel Form of Co-Ordination of Acetylacetone to Platinum(LI). *Nature* **1964**, *202*, 589–590. https://doi.org/10.1038/202589a0.

(83) Patra, S.; Mondal, B.; Sarkar, B.; Niemeyer, M.; Lahiri, G. K. First Example of μ_3-Sulfido Bridged Mixed-Valent Triruthenium Complex Triangle Ru$^{III}_2$ Ru^{II} (O , O -Acetylacetonate)$_3$ (μ - O , O ,γ- C -Acetylacetonate)$_3$ (μ_3 -S) (**1**) Incorporating Simultaneous O,O- and γ-C-Bonded Bridging Acetylacetonate Units. Synthesis, Crystal Structure, and Spectral and Redox Properties. *Inorg. Chem.* **2003**, *42* (4), 1322–1327. https://doi.org/10.1021/ic026221i.

(84) Zhu, D.; Budzelaar, P. H. M. N-Aryl β-Diiminate Complexes of the Platinum Metals. *Dalton Trans.* **2013**, *42* (32), 11343. https://doi.org/10.1039/c3dt50715g.

(85) Bernskoetter, W. H.; Lobkovsky, E.; Chirik, P. J. Ancillary Ligand Effects on C−H Bond Activation Reactions Promoted by β-Diiminate Iridium Complexes. *Organometallics* **2005**, *24* (25), 6250–6259. https://doi.org/10.1021/om050705f.

(86) Roesky, H. W. The Renaissance of Aluminum Chemistry. *Inorg. Chem.* **2004**, *43* (23), 7284–7293. https://doi.org/10.1021/ic0400641.

(87) Mears, K. L.; Stennett, C. R.; Taskinen, E. K.; Knapp, C. E.; Carmalt, C. J.; Tuononen, H. M.; Power, P. P. Molecular Complexes Featuring Unsupported Dispersion-Enhanced Aluminum–Copper and Gallium–Copper Bonds. *J. Am. Chem. Soc.* **2020**, *142* (47), 19874–19878. https://doi.org/10.1021/jacs.0c10099.

(88) Mondal, R.; Lozada, I. B.; Davis, R. L.; Williams, J. A. G.; Herbert, D. E. Exploiting Synergy between Ligand Design and Counterion Interactions to Boost Room Temperature Phosphorescence from Cu(I) Compounds. *J. Mater. Chem. C* **2019**, *7*, 3772–3778.

(89) Mandapati, P.; Braun, J. D.; Lozada, I. B.; Williams, J. A. G.; Herbert, D. E. Deep-Red Luminescence from Platinum(II) Complexes of N^N⁻^N-Amido Ligands with Benzannulated N-Heterocyclic Donor Arms. *Inorg. Chem.* **2020**, *59*, 12504–12517.

(90) Ortiz, R. J.; Braun, J. D.; Williams, J. A. G.; Herbert, D. E. Brightly Luminescent Platinum Complexes of *N^C⁻^N* Ligands Forming Six-Membered Chelate Rings: Offsetting Deleterious Ring Size Effects Using Site-Selective Benzannulation. *Inorg. Chem.* **2021**, *60*, 16881–16894.

(91) Lozada, I. B.; Huang, B.; Stilgenbauer, M.; Beach, T.; Qiu, Z.; Zheng, Y.; Herbert, D. E. Monofunctional Platinum(II) Anticancer Complexes Based on Multidentate Phenanthridine-Containing Ligand Frameworks. *Dalton Trans.* **2020**, *49*, 6557–6560.

(92) Myers, E. L.; Butts, C. P.; Aggarwal, V. K. BF3·OEt2 and TMSOTf: A Synergistic Combination of Lewis Acids. *Chem. Commun.* **2006**, No. 42, 4434–4436.

(93) Macedo, F. P.; Gwengo, C.; Lindeman, S. V.; Smith, M. D.; Gardinier, J. R. β-Diketonate, β-Ketoiminate, and β-Diiminate Complexes of Difluoroboron. *Eur. J. Inorg. Chem.* **2008**, *2008*, 3200–3211.

(94) Dohe, J.; Kossmann, J.; Mueller, T. J. J. Diversity-Oriented Four-Component Synthesis of Solid State Luminescent Difluoro Oxazaborinines. *Dyes Pigments* **2018**, *157*, 198–217.

(95) Köhling, J.; Kozel, V.; Jovanov, V.; Pajkert, R.; Tverdomed, S. N.; Gridenco, O.; Fugel, M.; Grabowsky, S.; Röschenthaler, G.-V.; Wagner, V. Synthesis and Characterization of Oxazaborinin Phosphonate for Blue OLED Emitter Applications. *ChemPhysChem* **2019**, *20*, 665–671.

(96) Mtiraoui, H.; Gharbi, R.; Msaddek, M.; Bretonnière, Y.; Andraud, C.; Renard, P.-Y.; Sabot, C. Solution and Solid-State Fluorescence of 2-(2′-Hydroxyphenyl)-1,5-Benzodiazepin-2-One (HBD) Borate Complexes. *RSC Adv.* **2016**, *6*, 86352–86360.

(97) Chęcińska, L.; Mebs, S.; Ośmiałowski, B.; Zakrzewska, A.; Ejsmont, K.; Kohout, M. Tuning the Electronic Properties of the Dative N−B Bond with Associated O−B Interaction: Electron Localizability Indicator from X-Ray Wavefunction Refinement. *ChemPhysChem* **2016**, *17*, 2395–2406.

(98) Itoh, K.; Okazaki, K.; Fujimoto, M. The Structure of 1,3-Enaminoketonatoboron Difluorides in Solution and in the Solid State. *Aust. J. Chem.* **2003**, *56*, 1209–1214.

(99) Grepioni, F.; Cojazzi, G.; Draper, S. M.; Scully, N.; Braga, D. Crystal Forms of Hexafluorophosphate Organometallic Salts and the Importance of Charge-Assisted C−H---F Hydrogen Bonds. *Organometallics* **1998**, *17*, 296–307.

(100) Mandapati, P.; Braun, J. D.; Killeen, C.; Davis, R. L.; Williams, J. A. G.; Herbert, D. E. Luminescent Platinum(II) Complexes of N^N⁻^N Amido Ligands with Benzannulated N-Heterocyclic Donor Arms: Quinolines Offer Unexpectedly Deeper Red Phosphorescence than Phenanthridines. *Inorg. Chem.* **2019**, *58*, 14808–14817.

(101) Lozada, I. B.; Williams, J. A. G.; Herbert, D. E. Platinum(II) Complexes of Benzannulated N^N⁻^O-Amido Ligands: Bright Orange Phosphors with Long-Lived Excited States. *Inorg. Chem. Front.* **2022**, *9*, 10–22.

(102) Donckt, E. V.; Dramaix, R.; Nasielski, J.; Vogels, C. Photochemistry of Aromatic Compounds. Part 1.—Acid-Base Properties of Singlet and Triplet Excited States of Pyrene Derivatives and Aza-Aromatic Compounds. *Trans. Faraday Soc.* **1969**, *65*, 3258–3262.

(103) Zander, M. The Significance of Donor-Acceptor Interactions in the External Heavy Atom Effect of Silver Nitrate on the Luminescence Behavior of Aza-Aromatic Systems and Carbazoles. *Z Naturforsch A* **1978**, *33*, 998–1000.

(104) Norek, M.; Dresner, J.; Prochorow, J. Spectroscopy and Photophysics of Monoazaphenanthrenes. I. Absorption and Fluorescence Spectra of Phenanthridine and 7,8-Benzoquinoline. *Acta Phys. Pol. A* **2003**, *104*, 425–439.

(105) Marzzacco, C. J.; Deckey, G.; Colarulli, R.; Siuzdak, G.; Halpern, A. M. Excited-State Protonation and Photophysical Properties of Azaphenanthrenes. *J. Phys. Chem.* **1989**, *93*, 2935–2939.

(106) Parker, D.; Senanayake, P. K.; Williams, J. A. G. Luminescent Sensors for PH, PO2, Halide and Hydroxide Ions Using Phenanthridine as a Photosensitiser in Macrocyclic Europium and Terbium Complexes. *J. Chem. Soc. Perkin Trans. 2* **1998**, 2129–2140.

(107) Norek, M.; Kozankiewicz, B.; Prochorow, J. Spectroscopy and Photophysics of Monoazaphenanthrenes. III. Luminescence of Phenanthridine and 7,8-Benzoquinoline in Crystalline State. *Acta Phys Pol A* **2004**, *106*, 77–94.

(108) Lozada, I. B.; Murray, T.; Herbert, D. E. Monomeric Zinc(II) Amide Complexes Supported by Bidentate, Benzannulated Phenanthridine Amido Ligands. *Polyhedron* **2019**, *161*, 261–267.

(109) Lozada, I. B.; Ortiz, R. J.; Braun, J. D.; Williams, J. A. G.; Herbert, D. E. Donor–Acceptor Boron-Ketoiminate Complexes with Pendent N-Heterocyclic Arms: Switched-on Luminescence through N-Heterocycle Methylation. *J. Org. Chem.* **2022**, *87*, 184–196.

(110) Bridgeman, A. J.; Cavigliasso, G.; Ireland, L. R.; Rothery, J. The Mayer Bond Order as a Tool in Inorganic Chemistry. *J. Chem. Soc. Dalton Trans.* **2001**, 2095–2108.

(111) Lu, T.; Chen, F. Atomic Dipole Moment Corrected Hirshfeld Population Method. *J. Theor. Comput. Chem.* **2012**, *11*, 163–183.

(112) Montalti, M.; Credi, A.; Prodi, L.; Gandolfi, M. *Handbook of Photochemistry. 3rd Ed.*; CRC Press: Boca Raton, 2006.

(113) Oyler, K. D.; Coughlin, F. J.; Bernhard, S. Controlling the Helicity of 2,2'-Bipyridyl Ruthenium(II) and Zinc(II) Hemicage Complexes. *J. Am. Chem. Soc.* **2007**, *129*, 210–217.

(114) Martinez, S.; Igoa, F.; Carrera, I.; Seoane, G.; Veiga, N.; De Camargo, A. S. S.; Kremer, C.; Torres, J. A Zn(II) Luminescent Complex with a Schiff Base Ligand: Solution, Computational and Solid State Studies. *J. Coord. Chem.* **2018**, *71*, 874–889.

(115) Mei, J.; Leung, N. L. C.; Kwok, R. T. K.; Lam, J. W. Y.; Tang, B. Z. Aggregation-Induced Emission: Together We Shine, United We Soar! *Chem. Rev.* **2015**, *115*, 11718–11940.

(116) Singh, K.; Siddiqui, I.; Sridharan, V.; Kumar Yadav, R. A.; Jou, J.-H.; Adhikari, D. Aggregation-Induced Enhanced Emission-Active Zinc(II) β-Diketiminate Complexes Enabling High-Performance Solution-Processable OLEDs. *Inorg. Chem.* **2021**, *60*, 19128–19135.

(117) Singh, K.; S., V.; Adhikari, D. Visible Light Photoredox by a (Ph,ArNacNac)2Zn Photocatalyst: Photophysical Properties and Mechanistic Understanding. *Inorg. Chem. Front.* **2021**, *8*, 2078–2087.

(118) Lozada, I. B.; Huang, B.; Stilgenbauer, M.; Beach, T.; Qiu, Z.; Zheng, Y.; Herbert, D. E. Monofunctional Platinum(II) Anticancer Complexes Based on Multidentate Phenanthridine-Containing Ligand Frameworks. *Dalton Trans.* **2020**, *49*, 6557–6560.

(119) Mandapati, P.; Giesbrecht, P. K.; Davis, R. L.; Herbert, D. E. Phenanthridine-Containing Pincer-like Amido Complexes of Nickel, Palladium, and Platinum. *Inorg. Chem.* **2017**, *56*, 3674–3685.

(120) Mandapati, P.; Braun, J. D.; Killeen, C.; Davis, R. L.; Williams, J. A. G.; Herbert, D. E. Luminescent Platinum(II) Complexes of N‸N-‸N Amido Ligands with Benzannulated N-Heterocyclic Donor Arms: Quinolines Offer Unexpectedly Deeper Red Phosphorescence than Phenanthridines. *Inorg Chem* **2019**, *58*, 14808–14817.

(121) Mandapati, P.; Braun, J. D.; Lozada, I. B.; Williams, J. A. G.; Herbert, D. E. Deep-Red Luminescence from Platinum(II) Complexes of N^N−^N-Amido Ligands with Benzannulated N-Heterocyclic Donor Arms. *Inorg. Chem.* **2020**, *59*, 12504–12517.

(122) Reineke, M. H.; Sampson, M. D.; Rheingold, A. L.; Kubiak, C. P. Synthesis and Structural Studies of Nickel(0) Tetracarbene Complexes with the Introduction of a New Four-Coordinate Geometric Index, Tδ. *Inorg. Chem.* **2015**, *54*, 3211–3217.

(123) Puttock, E. V.; Fradgley, J. D.; Yufit, D. S.; Williams, J. A. G. A Family of Readily Synthesised Phosphorescent Platinum(II) Complexes Based on Tridentate *N^N^O* -Coordinating Schiff-Base Ligands. *Dalton Trans.* **2019**, *48*, 15012–15028.

(124) Davidson, J. J.; DeMott, J. C.; Douvris, C.; Fafard, C. M.; Bhuvanesh, N.; Chen, C.-H.; Herbert, D. E.; Lee, C.-I.; McCulloch, B. J.; Foxman, B. M.; Ozerov, O. V. Comparison of the Electronic Properties of Diarylamido-Based PNZ Pincer Ligands: Redox Activity at the Ligand and Donor Ability Toward the Metal. *Inorg. Chem.* **2015**, *54*, 2916–2935.

(125) Giesbrecht, P. K.; Nemez, D. B.; Herbert, D. E. Electrochemical Hydrogenation of a Benzannulated Pyridine to a Dihydropyridine in Acidic Solution. *Chem. Commun.* **2018**, *54*, 338–341.

(126) Reichardt, C. Solvatochromic Dyes as Solvent Polarity Indicators. *Chem. Rev.* **1994**, *94*, 2319–2358.

(127) Catalán, J. Toward a Generalized Treatment of the Solvent Effect Based on Four Empirical Scales: Dipolarity (SdP, a New Scale), Polarizability (SP), Acidity (SA), and Basicity (SB) of the Medium. *J. Phys. Chem. B* **2009**, *113*, 5951–5960.

(128) Van der Zwan, G.; Hynes, J. T. Time-Dependent Fluorescence Solvent Shifts, Dielectric Friction, and Nonequilibrium Solvation in Polar Solvents. *J. Phys. Chem.* **1985**, *89*, 4181–4188.

(129) Caspar, J. V.; Meyer, T. J. Photochemistry of Tris(2,2'-Bipyridine)Ruthenium(2+) Ion $(Ru(Bpy)_3^{2+})$. Solvent Effects. *J. Am. Chem. Soc.* **1983**, *105*, 5583–5590.

(130) Kwok, C.-C.; Ngai, H. M. Y.; Chan, S.-C.; Sham, I. H. T.; Che, C.-M.; Zhu, N. [(O∧N∧N)PtX] Complexes as a New Class of Light-Emitting Materials for Electrophosphorescent Devices. *Inorg. Chem.* **2005**, *44*, 4442–4444.

(131) Garner, K. L.; Parkes, L. F.; Piper, J. D.; Williams, J. A. G. Luminescent Platinum Complexes with Terdentate Ligands Forming 6-Membered Chelate Rings: Advantageous and Deleterious Effects in N ^ N ^ N and N ^ C ^ N-Coordinated Complexes. *Inorg. Chem.* **2010**, *49*, 476–487.

(132) Williams, J. A. G. The Coordination Chemistry of Dipyridylbenzene: N-Deficient Terpyridine or Panacea for Brightly Luminescent Metal Complexes? *Chem. Soc. Rev.* **2009**, *38*, 1783–1801.

(133) Meech, S. R.; Phillips, D. Photophysics of Some Common Fluorescence Standards. *J. Photochem.* **1983**, *23*, 193–217.

(134) Suzuki, K.; Kobayashi, A.; Kaneko, S.; Takehira, K.; Yoshihara, T.; Ishida, H.; Shiina, Y.; Oishi, S.; Tobita, S. Reevaluation of Absolute Luminescence Quantum Yields of Standard Solutions Using a Spectrometer with an Integrating Sphere and a Back-Thinned CCD Detector. *Phys. Chem. Chem. Phys.* **2009**, *11*, 9850–9860.

(135) Murov, S. L.; Carmichael, I.; Hug, G. L. *Handbook of Photochemistry, 2nd Ed.*; Marcel Dekker: New York, 1993.

(136) Hohenberg, P.; Kohn, W. Inhomogeneous Electron Gas. *Phys. Rev.* **1964**, *136* (3B), B864–B871. https://doi.org/10.1103/PhysRev.136.B864.

(137) Kohn, W.; Sham, L. J. Self-Consistent Equations Including Exchange and Correlation Effects. *Phys. Rev.* **1965**, *140* (4A), A1133–A1138. https://doi.org/10.1103/PhysRev.140.A1133.

(138) Bühl, M.; Kabrede, H. Geometries of Transition-Metal Complexes from Density-Functional Theory. *J. Chem. Theory Comput.* **2006**, *2* (5), 1282–1290. https://doi.org/10.1021/ct6001187.

(139) Waller, M. P.; Braun, H.; Hojdis, N.; Bühl, M. Geometries of Second-Row Transition-Metal Complexes from Density-Functional Theory. *J. Chem. Theory Comput.* **2007**, *3* (6), 2234–2242. https://doi.org/10.1021/ct700178y.

(140) Bühl, M.; Reimann, C.; Pantazis, D. A.; Bredow, T.; Neese, F. Geometries of Third-Row Transition-Metal Complexes from Density-Functional Theory. *J. Chem. Theory Comput.* **2008**, *4* (9), 1449–1459. https://doi.org/10.1021/ct800172j.

(141) de Souza, B.; Farias, G.; Neese, F.; Izsák, R. Predicting Phosphorescence Rates of Light Organic Molecules Using Time-Dependent Density Functional Theory and the Path Integral Approach to Dynamics. *J. Chem. Theory Comput.* **2019**, *15* (3), 1896–1904. https://doi.org/10.1021/acs.jctc.8b00841.

(142) de Souza, B.; Neese, F.; Izsák, R. On the Theoretical Prediction of Fluorescence Rates from First Principles Using the Path Integral Approach. *J. Chem. Phys.* **2018**, *148* (3), 034104. https://doi.org/10.1063/1.5010895.

(143) Petrenko, T.; Neese, F. Analysis and Prediction of Absorption Band Shapes, Fluorescence Band Shapes, Resonance Raman Intensities, and Excitation Profiles Using the Time-Dependent Theory of Electronic Spectroscopy. *J. Chem. Phys.* **2007**, *127* (16), 164319. https://doi.org/10.1063/1.2770706.

(144) Wenger, O. S. Is Iron the New Ruthenium? *Chem. – Eur. J.* **2020**, *25*, 6043–6052.

(145) Baková, R.; Chergui, M.; Daniel, C.; Vlček Jr., A.; Záliš, S. Relativistic Effects in Spectroscopy and Photophysics of Heavy-Metal Complexes Illustrated by Spin–Orbit Calculations of [Re(Imidazole)(CO)3(Phen)]+. *Coord. Chem. Rev.* **2011**, *255* (7–8), 975–989. https://doi.org/10.1016/j.ccr.2010.12.027.

(146) Giesbrecht, P. K.; Nemez, D. B.; Herbert, D. E. Electrochemical Hydrogenation of a Benzannulated Pyridine to a Dihydropyridine in Acidic Solution. *Chem. Commun.* **2018**, *54* (4), 338–341. https://doi.org/10.1039/c7cc07907a.

(147) Mandapati, P.; Giesbrecht, P. K.; Davis, R. L.; Herbert, D. E. Phenanthridine-Containing Pincer-like Amido Complexes of Nickel, Palladium, and Platinum. *Inorg. Chem.* **2017**, *56* (6), 3674–3685. https://doi.org/10.1021/acs.inorgchem.7b00075.

(148) Mondal, R.; Lozada, I. B.; Davis, R. L.; Williams, J. A. G.; Herbert, D. E. Exploiting Synergy between Ligand Design and Counterion Interactions to Boost Room Temperature Phosphorescence from Cu(i) Compounds. *J. Mater. Chem. C* **2019**, *7* (13), 3772–3778. https://doi.org/10.1039/C9TC00040B.

(149) Mandapati, P.; Braun, J. D.; Killeen, C.; Davis, R. L.; Williams, J. A. G.; Herbert, D. E. Luminescent Platinum(II) Complexes of N^ N-^ N Amido Ligands with Benzannulated N-Heterocyclic Donor Arms: Quinolines Offer Unexpectedly Deeper Red Phosphorescence than Phenanthridines. *Inorg. Chem.* **2019**, *58* (21), 14808–14817. https://doi.org/10.1021/acs.inorgchem.9b02480.

(150) Lozada, I. B.; Murray, T.; Herbert, D. E. Monomeric Zinc(II) Amide Complexes Supported by Bidentate, Benzannulated Phenanthridine Amido Ligands. *Polyhedron* **2019**, *161*, 261–267. https://doi.org/10.1016/j.poly.2019.01.023.

(151) Braun, J. D.; Lozada, I. B.; Kolodziej, C.; Burda, C.; Newman, K. M. E.; van Lierop, J.; Davis, R. L.; Herbert, D. E. Iron(Ii) Coordination Complexes with Panchromatic Absorption and Nanosecond Charge-Transfer Excited State Lifetimes. *Nat. Chem.* **2019**, *11* (12), 1144–1150. https://doi.org/10.1038/s41557-019-0357-z.

(152) Mondal, R.; Lozada, I. B.; Davis, R. L.; Williams, J. A. G.; Herbert, D. E. Site-Selective Benzannulation of N-Heterocycles in Bidentate Ligands Leads to Blue-Shifted Emission from [(P^N)Cu]2(µ-X)2 Dimers. *Inorg. Chem.* **2018**, *57* (9), 4966–4978. https://doi.org/10.1021/acs.inorgchem.7b03223.

(153) Mondal, R.; Giesbrecht, P. K.; Herbert, D. E. Nickel(II), Copper(I) and Zinc(II) Complexes Supported by a (4-Diphenylphosphino)Phenanthridine Ligand. *Polyhedron* **2016**, *108*, 156–162. https://doi.org/10.1016/j.poly.2015.10.051.

(154) Stufkens, D. J.; Vlček, A. Ligand-Dependent Excited State Behaviour of Re(I) and Ru(II) Carbonyl-Diimine Complexes. *Coord. Chem. Rev.* **1998**, *177* (1), 127–179. https://doi.org/10.1016/s0010-8545(98)00132-5.

(155) Vlček, A. Ultrafast Excited-State Processes in Re(I) Carbonyl-Diimine Complexes: From Excitation to Photochemistry. *Top Organomet Chem* **2010**, *29* (May 2009), 73–114. https://doi.org/10.1007/3418.

(156) Mandapati, P.; Braun, J. D.; Killeen, C.; Davis, R. L.; Williams, J. A. G.; Herbert, D. E. Luminescent Platinum(II) Complexes of N^N-^N Amido Ligands with Benzannulated N-Heterocyclic Donor Arms: Quinolines Offer Unexpectedly Deeper Red Phosphorescence than Phenanthridines. *Inorg Chem* **2019**, *58*, 14808–14817.

(157) Dixon, I. M.; Khan, S.; Alary, F.; Boggio-Pasqua, M.; Heully, J.-L. Probing the Photophysical Capability of Mono and Bis(Cyclometallated) Fe(II) Polypyridine Complexes Using Inexpensive Ground State DFT. *Dalton Trans.* **2014**, *43*, 15898–15905.

(158) Zhang, K.; Ash, R.; Girolami, G. S.; Vura-Weis, J. Tracking the Metal-Centered Triplet in Photoinduced Spin Crossover of Fe(Phen)32+ with Tabletop Femtosecond M-Edge X-Ray Absorption Near-Edge Structure Spectroscopy. *J. Am. Chem. Soc.* **2019**, *141*, 17180–17188.

(159) Juban, E. A.; Smeigh, A. L.; Monat, J. E.; McCusker, J. K. Ultrafast Dynamics of Ligand-Field Excited States. *Coord Chem Rev* **2006**, *250*, 1783–1791.

(160) Gryn'ova, G.; Coote, M. L.; Corminboeuf, C. Theory and Practice of Uncommon Molecular Electronic Configurations. *WIREs Comput. Mol. Sci.* **2015**, *5* (6), 440–459. https://doi.org/10.1002/wcms.1233.

(161) Kaim, W. Manifestations of Noninnocent Ligand Behavior. *Inorg Chem* **2011**, *50* (20), 9752–9765.

(162) Bowman, D. N.; Jakubikova, E. Low-Spin versus High-Spin Ground State in Pseudo-Octahedral Iron Complexes. *Inorg. Chem.* **2012**, *51*, 6011–6019.

(163) Ashley, D. C.; Jakubikova, E. Ironing out the Photochemical and Spin-Crossover Behavior of Fe(II) Coordination Compounds with Computational Chemistry. *Coord. Chem. Rev.* **2017**, *337*, 97–111.

(164) Reiher, M.; Salomon, O.; Artur Hess, B. Reparameterization of Hybrid Functionals Based on Energy Differences of States of Different Multiplicity. *Theor. Chem. Acc.* **2001**, *107*, 48–55.

(165) Jakubikova, E.; Bowman, D. N. Fe(II)-Polypyridines as Chromophores in Dye-Sensitized Solar Cells: A Computational Perspective. *Acc. Chem. Res.* **2015**, *48*, 1441–1449.

(166) Nemykin, V. N.; Hadt, R. G. Influence of Hartree−Fock Exchange on the Calculated Mössbauer Isomer Shifts and Quadrupole Splittings in Ferrocene Derivatives Using Density Functional Theory. *Inorg. Chem.* **2006**, *45*, 8297–8307.

(167) Zhao, Y.; Truhlar, D. G. A New Local Density Functional for Main-Group Thermochemistry, Transition Metal Bonding, Thermochemical Kinetics, and Noncovalent Interactions. *J. Chem. Phys.* **2006**, *125*, 194101.

(168) Cohen, A. J.; Handy, N. C. Dynamic Correlation. *Mol. Phys.* **2001**, *99*, 607–615.

(169) Zhao, Y.; Truhlar, D. G. The M06 Suite of Density Functionals for Main Group Thermochemistry, Thermochemical Kinetics, Noncovalent Interactions, Excited States, and Transition Elements: Two New Functionals and Systematic Testing of Four M06-Class Functionals and 12 Other Functionals. *Theor. Chem. Acc.* **2008**, *120*, 215–241.

(170) Ditchfield, R.; Hehre, W. J.; Pople, J. A. Self-Consistent Molecular-Orbital Methods. IX. Extended Gaussian-Type Basis for Molecular-Orbital Studies of Organic Molecules. *J. Chem. Phys.* **1971**, *54*, 724–728. https://doi.org/10.1063/1.1674902.

(171) Hehre, W. J.; Ditchfield, R.; Pople, J. A. Self-Consistent Molecular Orbital Methods. XII. Further Extensions of Gaussian-Type Basis Sets for Use in Molecular Orbital Studies of Organic Molecules. *J. Chem. Phys.* **1972**, *56*, 2257–2261.

(172) Hariharan, P. C.; Pople, J. A. Influence of Polarization Functions on MO Hydrogenation Energies. *Theor. Chim. Acta* **1973**, *28*, 213–222.

(173) Clark, T.; Chandrasekhar, J.; Spitznagel, G. W.; Schleyer, P. v R. Efficient Diffuse Function-Augmented Basis Sets for Anion Calculations. III. The 3-21 + G Basis Set for First-Row Elements, Lithium to Fluorine. *J. Comput. Chem.* **1983**, *4*, 294–301.

(174) Rassolov, V. A.; Pople, J. A.; Ratner, M. A.; Windus, T. L. 6-31G* Basis Set for Atoms K through Zn. *J. Chem. Phys.* **1998**, *109*, 1223–1229.

(175) Zhao, Y.; Truhlar, D. G. A New Local Density Functional for Main-Group Thermochemistry, Transition Metal Bonding, Thermochemical Kinetics, and Noncovalent Interactions. *J. Chem. Phys.* **2006**, *125* (19), 194101. https://doi.org/10.1063/1.2370993.

(176) Krishnan, R.; Binkley, J. S.; Seeger, R.; Pople, J. A. Self-consistent Molecular Orbital Methods. XX. A Basis Set for Correlated Wave Functions. *J. Chem. Phys.* **1980**, *72* (1), 650–654. https://doi.org/10.1063/1.438955.

(177) Clark, T.; Chandrasekhar, J.; Spitznagel, G. W.; Schleyer, P. V. R. Efficient Diffuse Function-Augmented Basis Sets for Anion Calculations. III. The 3-21+G Basis Set for First-Row Elements, Li-F. *J. Comput. Chem.* **1983**, *4* (3), 294–301. https://doi.org/10.1002/jcc.540040303.

(178) Dennington, Roy; Keith, Todd A.; Millam, John M. *GaussView, Version 6*; Semichem Inc.: Shawnee Mission, KS, 2016.

(179) Soda, T.; Kitagawa, Y.; Onishi, T.; Takano, Y.; Shigeta, Y.; Nagao, H.; Yoshioka, Y.; Yamaguchi, K. Ab Initio Computations of Effective Exchange Integrals for H–H, H–He–H and Mn2O2 Complex: Comparison of Broken-Symmetry Approaches. *Chem. Phys. Lett.* **2000**, *319* (3–4), 223–230. https://doi.org/10.1016/S0009-2614(00)00166-4.

(180) Yamaguchi, K.; Takahara, Y.; Fueno, T. Ab-Initio Molecular Orbital Studies of Structure and Reactivity of Transition Metal-OXO Compounds. In *Applied Quantum Chemistry*;

Smith, V. H., Schaefer, H. F., Morokuma, K., Eds.; Springer Netherlands: Dordrecht, 1986; pp 155–184. https://doi.org/10.1007/978-94-009-4746-7_11.

(181) Heydová, R.; Gindensperger, E.; Romano, R.; Sýkora, J.; Vlček, A.; Záliš, S.; Daniel, C. Spin-Orbit Treatment of UV-Vis Absorption Spectra and Photophysics of Rhenium(I) Carbonyl-Bipyridine Complexes: MS-CASPT2 and TD-DFT Analysis. *J. Phys. Chem. A* **2012**, *116* (46), 11319–11329. https://doi.org/10.1021/jp305461z.

(182) Ronca, E.; De Angelis, F.; Fantacci, S. Time-Dependent Density Functional Theory Modeling of Spin-Orbit Coupling in Ruthenium and Osmium Solar Cell Sensitizers. *J. Phys. Chem. C* **2014**, *118* (30), 17067–17078. https://doi.org/10.1021/jp500869r.

(183) Mai, S.; Gattuso, H.; Fumanal, M.; Muñoz-Losa, A.; Monari, A.; Daniel, C.; González, L. Excited-States of a Rhenium Carbonyl Diimine Complex: Solvation Models, Spin-Orbit Coupling, and Vibrational Sampling Effects. *Phys. Chem. Chem. Phys.* **2017**, *19* (40), 27240–27250. https://doi.org/10.1039/c7cp05126c.

(184) Shi, L. L.; Liao, Y.; Zhao, L.; Su, Z. M.; Kan, Y. H.; Yang, G. C.; Yang, S. Y. Theoretical Studies on the Electronic Structure and Spectral Properties of Versatile Diarylethene-Containing 1,10-Phenanthroline Ligands and Their Rhenium(I) Complexes. *J. Organomet. Chem.* **2007**, *692* (24), 5368–5374. https://doi.org/10.1016/j.jorganchem.2007.08.031.

(185) Silva-Junior, M. R.; Schreiber, M.; Sauer, S. P. A.; Thiel, W. Benchmarks for Electronically Excited States: Time-Dependent Density Functional Theory and Density Functional Theory Based Multireference Configuration Interaction. *J. Chem. Phys.* **2008**, *129* (10). https://doi.org/10.1063/1.2973541.

(186) Jacquemin, D.; Perpète, E. A.; Ciofini, I.; Adamo, C. Assessment of Functionals for TD-DFT Calculations of Singlet-Triplet Transitions. *J. Chem. Theory Comput.* **2010**, *6* (5), 1532–1537. https://doi.org/10.1021/ct100005d.

(187) Santoro, F.; Lami, A.; Improta, R.; Barone, V. Effective Method to Compute Vibrationally Resolved Optical Spectra of Large Molecules at Finite Temperature in the Gas Phase and in Solution. *J. Chem. Phys.* **2007**, *126* (18). https://doi.org/10.1063/1.2721539.

(188) Tozer, D. J.; Handy, N. C. On the Determination of Excitation Energies Using Density Functional Theory. *Phys. Chem. Chem. Phys.* **2000**, *2* (10), 2117–2121. https://doi.org/10.1039/a910321j.

(189) Chibani, S.; Charaf-Eddin, A.; Le Guennic, B.; Jacquemin, D. Boranil and Related NBO Dyes: Insights From Theory. *J. Chem. Theory Comput.* **2013**, *9*, 3127–3135.

(190) Mondal, R.; Giesbrecht, P. K.; Herbert, D. E. Nickel(II), Copper(I) and Zinc(II) Complexes Supported by a (4-Diphenylphosphino)Phenanthridine Ligand. *Polyhedron* **2016**, *108*, 156–162.

(191) Mondal, R.; Lozada, I. B.; Davis, R. L.; Williams, J. A. G.; Herbert, D. E. Site-Selective Benzannulation of N-Heterocycles in Bidentate Ligands Leads to Blue-Shifted Emission from [(*P^N*)Cu]$_2$(μ-X)$_2$ Dimers. *Inorg Chem* **2018**, *57*, 4966–4978.

(192) Gaire, S.; Ortiz, R. J.; Schrage, B. R.; Lozada, I. B.; Mandapati, P.; Osinski, A. J.; Herbert, D. E.; Ziegler, C. J. (8-Amino)Quinoline and (4-Amino)Phenanthridine Complexes of Re(CO)3 Halides. *J. Organomet. Chem.* **2020**, *921*, 121338.

(193) Tomasi, J.; Mennucci, B.; Cammi, R. Quantum Mechanical Continuum Solvation Models. *Chem Rev* **2005**, *105*, 2999–3094.

(194) Melenbacher, A.; Dhindsa, J. S.; Gilroy, J. B.; Stillman, M. J. Unveiling the Hidden, Dark, and Short Life of a Vibronic State in a Boron Difluoride Formazanate Dye. *Angew. Chem. Int. Ed.* **2019**, *58* (43), 15339–15343.

(195) El-Sayed, M. A. Spin—Orbit Coupling and the Radiationless Processes in Nitrogen Heterocyclics. *J. Chem. Phys.* **1963**, *38* (12), 2834–2838.

(196) Braun, J. D.; Lozada, I. B.; Kolodziej, C.; Burda, C.; Newman, K. M. E.; van Lierop, J.; Davis, R. L.; Herbert, D. E. Iron(II) Coordination Complexes with Panchromatic Absorption and Nanosecond Charge-Transfer Excited State Lifetimes. *Nat. Chem.* **2019**, *11*, 1144–1150.

(197) Larsen, C. B.; Braun, J. D.; Lozada, I. B.; Kunnus, K.; Biasin, E.; Kolodziej, C.; Burda, C.; Cordones, A. A.; Gaffney, K. J.; Herbert, D. E. Reduction of Electron Repulsion in Highly Covalent Fe-Amido Complexes Counteracts the Impact of a Weak Ligand Field on Excited-State Ordering. *J. Am. Chem. Soc.* **2021**, *143*, 20645–20656.

(198) Das, S.; Thornbury, W. G.; Bartynski, A. N.; Thompson, M. E.; Bradforth, S. E. Manipulating Triplet Yield through Control of Symmetry-Breaking Charge Transfer. *J. Phys. Chem. Lett.* **2018**, *9*, 3264–3270.

(199) Trinh, C.; Kirlikovali, K.; Das, S.; Ener, M. E.; Gray, H. B.; Djurovich, P.; Bradforth, S. E.; Thompson, M. E. Symmetry-Breaking Charge Transfer of Visible Light Absorbing Systems: Zinc Dipyrrins. *J. Phys. Chem. C* **2014**, *118*, 21834–21845.

(200) Kellogg, M.; Akil, A.; Muthiah Ravinson, D. S.; Estergreen, L.; Bradforth, S. E.; Thompson, M. E. Symmetry Breaking Charge Transfer as a Means to Study Electron Transfer with No Driving Force. *Faraday Discuss.* **2019**, *216*, 379–394.

(201) Mahmood, Z.; Rehmat, N.; Ji, S.; Zhao, J.; Sun, S.; Di Donato, M.; Li, M.; Teddei, M.; Huo, Y. Tuning the Triplet Excited State of Bis(Dipyrrin) Zinc(II) Complexes: Symmetry Breaking Charge Transfer Architecture with Exceptionally Long Lived Triplet State for Upconversion. *Chem. – Eur. J.* **2020**, *26*, 14912–14918.

(202) Weller, A. Photoinduced Electron Transfer in Solution: Exciplex and Radical Ion Pair Formation Free Enthalpies and Their Solvent Dependence By. *Zeitshcrift Phys. Chem. N. F.* **1982**, *133*, 93–98.

(203) Rehm, D.; Weller, A. Kinetics of Fluorescence Quenching by Electron and H-Atom Transfer. *Isr. J. Chem.* **1970**, *8*, 259–271.

(204) Vauthey, E. Photoinduced Symmetry-Breaking Charge Separation. *ChemPhysChem* **2012**, *13*, 2001–2011.

(205) Smith, A. R. G.; Burn, P. L.; Powell, B. J. Spin–Orbit Coupling in Phosphorescent Iridium(III) Complexes. *ChemPhysChem* **2011**, *12*, 2429–2438.

(206) Ronca, E.; De Angelis, F.; Fantacci, S. Time-Dependent Density Functional Theory Modeling of Spin–Orbit Coupling in Ruthenium and Osmium Solar Cell Sensitizers. *J. Phys. Chem. C* **2014**, *118*, 17067–17078.

(207) Gourlaouen, C.; Daniel, C. Spin–Orbit Effects in Square-Planar Pt(II) Complexes with Bidentate and Terdentate Ligands: Theoretical Absorption/Emission Spectroscopy. *Dalton Trans* **2014**, *43*, 17806–17819.

(208) Braun, J. D.; Lozada, I. B.; Herbert, D. E. In Pursuit of Panchromatic Absorption in Metal Coordination Complexes: Experimental Delineation of the HOMO Inversion Model Using Pseudo-Octahedral Complexes of Diarylamido Ligands. *Inorg. Chem.* **2020**, *59*, 17746–17757.

(209) Hayashi, M.; Takahashi, Y.; Yoshida, Y.; Sugimoto, K.; Kitagawa, H. Role of D-Elements in a Proton–Electron Coupling of d–π Hybridized Electron Systems. *J. Am. Chem. Soc.* **2019**, *141*, 11686–11693.

(210) Spencer, M.; Santoro, A.; Freeman, G. R.; Díez, Á.; Murray, P. R.; Torroba, J.; Whitwood, A. C.; Yellowlees, L. J.; Williams, J. A. G.; Bruce, D. W. Phosphorescent, Liquid-Crystalline Complexes of Platinum(II): Influence of the β-Diketonate Co-Ligand on Mesomorphism and Emission Properties. *Dalton Trans.* **2012**, *41*, 14244–14256.

(211) Neese, F. The ORCA Program System. *WIREs Comput. Mol. Sci.* **2012**, *2*, 73–78.

(212) Neese, F. Software Update: The ORCA Program System, Version 4.0. *WIREs Comput. Mol. Sci.* **2018**, *8*, e1327.

(213) Frisch, M. J.; Trucks, G. W.; Schlegel, H. B.; Scuseria, G. E.; Robb, M. A.; Cheeseman, J. R.; Scalmani, G.; Barone, V.; Petersson, G. A.; Nakatsuji, H.; Li, X.; Caricato, M.; Marenich, A. V.; Bloino, J.; Janesko, B. G.; Gomperts, R.; Mennucci, B.; Hratchian, H. P.; Ortiz, J. V.; Izmaylov, A. F.; Sonnenberg, J. L.; Williams; Ding, F.; Lipparini, F.; Egidi, F.; Goings, J.; Peng, B.; Petrone, A.; Henderson, T.; Ranasinghe, D.; Zakrzewski, V. G.; Gao, J.; Rega, N.; Zheng, G.; Liang, W.; Hada, M.; Ehara, M.; Toyota, K.; Fukuda, R.; Hasegawa, J.; Ishida, M.; Nakajima, T.; Honda, Y.; Kitao, O.; Nakai, H.; Vreven, T.; Throssell, K.; Montgomery Jr., J. A.; Peralta, J. E.; Ogliaro, F.; Bearpark, M. J.; Heyd, J. J.; Brothers, E. N.; Kudin, K. N.; Staroverov, V. N.; Keith, T. A.; Kobayashi, R.; Normand, J.; Raghavachari, K.; Rendell, A. P.; Burant, J. C.; Iyengar, S. S.; Tomasi, J.; Cossi, M.; Millam, J. M.; Klene, M.; Adamo, C.; Cammi, R.; Ochterski, J. W.; Martin, R. L.; Morokuma, K.; Farkas, O.; Foresman, J. B.; Fox, D. J. *Gaussian 16 Rev. C.01*; Wallingford, CT, 2016.

(214) Marenich, A. V.; Cramer, C. J.; Truhlar, D. G. Universal Solvation Model Based on Solute Electron Density and on a Continuum Model of the Solvent Defined by the Bulk Dielectric Constant and Atomic Surface Tensions. *J Phys Chem B* **2009**, *113*, 6378–6396.

(215) Grimme, S.; Ehrlich, S.; Goerigk, L. Effect of the Damping Function in Dispersion Corrected Density Functional Theory. *J. Comput. Chem.* **2011**, *32*, 1456–1465.

(216) Becke, A. D. Density-Functional Thermochemistry. III. The Role of Exact Exchange. *J Chem Phys* **1993**, *98*, 5648–5652.

(217) Lee, C.; Yang, W.; Parr, R.G. Development of the Colle-Salvetti Correlation-Energy Formula into a Functional of the Electron Density. *Phys. Rev. B Condens. Matter* **1988**, *37*, 785–789.

(218) Vosko, S. H.; Wilk, L.; Nusair, M. Accurate Spin-Dependent Electron Liquid Correlation Energies for Local Spin Density Calculations: A Critical Analysis. *Can. J. Phys.* **1980**, *58*, 1200–1211.

(219) Stephens, P. J.; Devlin, F. J.; Chabalowski, C. F.; Frisch, M. J. Ab Initio Calculation of Vibrational Absorption and Circular Dichroism Spectra Using Density Functional Force Fields. *J Phys Chem* **1994**, *98*, 11623–11627.

(220) Weigend, F.; Ahlrichs, R. Balanced Basis Sets of Split Valence, Triple Zeta Valence and Quadruple Zeta Valence Quality for H to Rn: Design and Assessment of Accuracy. *Phys Chem Chem Phys* **2005**, *7*, 3297–3305.

(221) Tao, J.; Perdew, J. P.; Staroverov, V. N.; Scuseria, G. E. Climbing the Density Functional Ladder: Nonempirical Meta--Generalized Gradient Approximation Designed for Molecules and Solids. *Phys. Rev. Lett.* **2003**, *91*, 146401.

(222) Staroverov, V. N.; Scuseria, G. E.; Tao, J.; Perdew, J. P. Comparative Assessment of a New Nonempirical Density Functional: Molecules and Hydrogen-Bonded Complexes. *J. Chem. Phys.* **2003**, *119*, 12129–12137.

(223) O'Boyle, N. M.; Tenderholt, A. L.; Langner, K. M. Software News and Updates Cclib: A Library for Package-Independent Computational Chemistry Algorithms. *J Comput Chem* **2008**, *29*, 839–845.

(224) Lu, T.; Chen, F. Multiwfn: A Multifunctional Wavefunction Analyzer. *J Comput Chem* **2012**, *33*, 580–592.

(225) Xiao, M; Lu, T. Generalized Charge Decomposition Analysis (GCDA) Method. *J. Adv. Phys. Chem.* **2015**, *4*, 111–124.

(226) Frisch, M. J.; Trucks, G. W.; Schlegel, H. B.; Scuseria, G. E.; Robb, M. A.; Cheeseman, J. R.; Scalmani, G.; Barone, V.; Petersson, G. A.; Nakatsuji, H.; Li, X.; Caricato, M.; Marenich, A. V.; Bloino, J.; Janesko, B. G.; Gomperts, R.; Mennucci, B.; Hratchian, H. P.; Ortiz, J. V.; Izmaylov, A. F.; Sonnenberg, J. L.; Williams-Young, D.; Ding, F.; Lipparini, F.; Egidi, F.; Goings, J.; Peng, B.; Petrone, A.; Henderson, T.; Ranasinghe, D.; Zakrzewski, V. G.; Gao, J.; Rega, N.; Zheng, G.; Liang, W.; Hada, M.; Ehara, M.; Toyota, K.; Fukuda, R.; Hasegawa, J.; Ishida, M.; Nakajima, T.; Honda, Y.; Kitao, O.; Nakai, H.; Vreven, T.; Throssell, K.; Montgomery, J. A.; Peralta, J. E.; Ogliaro, F.; Bearpark, M. J.; Heyd, J. J.; Brothers, E. N.; Kudin, K. N.; Staroverov, V. N.; Keith, T. A.; Kobayashi, R.; Normand, J.; Raghavachari, K.; Rendell, A. P.; Burant, J. C.; Iyengar, S. S.; Tomasi, J.; Cossi, M.; Millam, J. M.; Klene, M.; Adamo, C.; Cammi, R.; Ochterski, J. W.; Martin, R. L.; Morokuma, K.; Farkas, O.; Foresman, J. B.; Fox, D. J. *Gaussian 16, Revision B.01*; Gaussian 16, Revision B.01, Gaussian, Inc., Wallingford CT; Gaussian, Inc.: Wallingford CT, 2016.

(227) Adamo, C.; Barone, V. Toward Reliable Density Functional Methods without Adjustable Parameters: The PBE0 Model. *J. Chem. Phys.* **1999**, *110* (13), 6158–6170.

(228) Andrae, D.; Huermann, U.; Dolg, M.; Stoll, H.; Preu, H. Energy-Adjustedab Initio Pseudopotentials for the Second and Third Row Transition Elements. *Theor. Chim. Acta* **1990**, *77*, 123–141.

(229) Yanai, T.; Tew, D. P.; Handy, N. C. A New Hybrid Exchange–Correlation Functional Using the Coulomb-Attenuating Method (CAM-B3LYP). *Chem. Phys. Lett.* **2004**, *393*, 51–57.

(230) Neese, F.; Wennmohs, F.; Hansen, A.; Becker, U. Efficient, Approximate and Parallel Hartree–Fock and Hybrid DFT Calculations. A 'Chain-of-Spheres' Algorithm for the Hartree–Fock Exchange. *Chem. Phys.* **2009**, *356*, 98–109.

(231) Lenthe, E. van; Baerends, E. J.; Snijders, J. G. Relativistic Regular Two-component Hamiltonians. *J. Chem. Phys.* **1993**, *99*, 4597–4610.

(232) Weigend, F. Accurate Coulomb-Fitting Basis Sets for H to Rn. *Phys. Chem. Chem. Phys.* **2006**, *8*, 1057.

(233) Pantazis, D. A.; Neese, F. All-Electron Scalar Relativistic Basis Sets for the Lanthanides. *J. Chem. Theory Comput.* **2009**, *5*, 2229–2238.

(234) Pantazis, D. A.; Neese, F. All-Electron Scalar Relativistic Basis Sets for the Actinides. *J. Chem. Theory Comput.* **2011**, *7*, 677–684.

(235) Pantazis, D. A.; Chen, X.-Y.; Landis, C. R.; Neese, F. All-Electron Scalar Relativistic Basis Sets for Third-Row Transition Metal Atoms. *J. Chem. Theory Comput.* **2008**, *4*, 908–919.

(236) Hirshfeld, F. L. Bonded-Atom Fragments for Describing Molecular Charge Densities. *Theor. Chim. Acta* **1977**, *44*, 129–138.

(237) Hanwell, M. D.; Curtis, D. E.; Lonie, D. C.; Vandermeersch, T.; Zurek, E.; Hutchison, G. R. Avogadro: An Advanced Semantic Chemical Editor, Visualization, and Analysis Platform. *J Cheminf* **2012**, *4*, 17.

(238) Frisch, M. J.; Trucks, G. W.; Schlegel, H. B.; Scuseria, G. E.; Robb, M. A.; Cheeseman, J. R.; Scalmani, G.; Barone, V.; Petersson, G. A.; Nakatsuji, H.; Li, X.; Caricato, M.; Marenich, A. V.; Bloino, J.; Janesko, B. G.; Gomperts, R.; Mennucci, B.; Hratchian, H. P.; Ortiz, J. V.; Izmaylov, A. F.; Sonnenberg, J. L.; Williams; Ding, F.; Lipparini, F.; Egidi, F.; Goings, J.; Peng, B.; Petrone, A.; Henderson, T.; Ranasinghe, D.; Zakrzewski, V. G.; Gao, J.; Rega, N.; Zheng, G.; Liang, W.; Hada, M.; Ehara, M.; Toyota, K.; Fukuda, R.; Hasegawa, J.; Ishida, M.; Nakajima, T.; Honda, Y.; Kitao, O.; Nakai, H.; Vreven, T.; Throssell, K.; Montgomery Jr., J. A.; Peralta, J. E.; Ogliaro, F.; Bearpark, M. J.; Heyd, J. J.; Brothers, E. N.; Kudin, K. N.; Staroverov, V. N.; Keith, T. A.; Kobayashi, R.; Normand, J.; Raghavachari, K.; Rendell, A. P.; Burant, J. C.; Iyengar, S. S.; Tomasi, J.; Cossi, M.; Millam, J. M.; Klene, M.; Adamo, C.; Cammi, R.; Ochterski, J. W.; Martin, R. L.; Morokuma, K.; Farkas, O.; Foresman, J. B.; Fox, D. J. Gaussian 16 Rev. C.01, 2016.

(239) Marenich, A. V.; Cramer, C. J.; Truhlar, D. G. Universal Solvation Model Based on Solute Electron Density and on a Continuum Model of the Solvent Defined by the Bulk Dielectric Constant and Atomic Surface Tensions. *J Phys Chem B* **2009**, *113*, 6378–6396.

(240) Dennington, Roy; Keith, Todd A.; Millam, John M. GaussView, Version 6, 2016.

(241) O'Boyle, N. M.; Tenderholt, A. L.; Langner, K. M. Software News and Updates Cclib: A Library for Package-Independent Computational Chemistry Algorithms. *J Comput Chem* **2008**, *29*, 839–845.

(242) Lu, T.; Chen, F. Multiwfn: A Multifunctional Wavefunction Analyzer. *J Comput Chem* **2012**, *33*, 580–592.

(243) Tian, L. U.; Fei-Wu, C. Calculation of Molecular Orbital Composition. *Acta Chim. Sin.* **2011**, *69*, 2393.

(244) Frisch, M. J.; Trucks, G. W.; Schlegel, H. B.; Scuseria, G. E.; Robb, M. A.; Cheeseman, J. R.; Scalmani, G.; Barone, V.; Petersson, G. A.; Nakatsuji, H.; Li, X.; Caricato, M.; Marenich, A. V.; Bloino, J.; Janesko, B. G.; Gomperts, R.; Mennucci, B.; Hratchian, H. P.; Ortiz, J. V.; Izmaylov, A. F.; Sonnenberg, J. L.; Williams-Young, D.; Ding, F.; Lipparini, F.; Egidi, F.; Goings, J.; Peng, B.; Petrone, A.; Henderson, T.; Ranasinghe, D.; Zakrzewski, V. G.; Gao, J.; Rega, N.; Zheng, G.; Liang, W.; Hada, M.; Ehara, M.; Toyota, K.; Fukuda, R.; Hasegawa, J.; Ishida, M.; Nakajima, T.; Honda, Y.; Kitao, O.; Nakai, H.; Vreven, T.; Throssell, K.; Montgomery Jr., J. A.; Peralta, J. E.; Ogliaro, F.; Bearpark, M. J.; Heyd, J. J.; Brothers, E. N.; Kudin, K. N.; Staroverov, V. N.; Keith, T. A.; Kobayashi, R.; Normand, J.; Raghavachari, K.; Rendell, A. P.; Burant, J. C.; Iyengar, S. S.; Tomasi, J.; Cossi, M.; Millam, J. M.; Klene, M.; Adamo, C.; Cammi, R.; Ochterski, J. W.; Martin, R. L.; Morokuma, K.; Farkas, O.; Foresman, J. B.; Fox, D. J. Gaussian 16 Rev. C.01, 2016.

(245) Marenich, A. V.; Cramer, C. J.; Truhlar, D. G. Universal Solvation Model Based on Solute Electron Density and on a Continuum Model of the Solvent Defined by the Bulk Dielectric Constant and Atomic Surface Tensions. *J Phys Chem B* **2009**, *113*, 6378–6396.

(246) Grimme, S.; Ehrlich, S.; Goerigk, L. Effect of the Damping Function in Dispersion Corrected Density Functional Theory. *J. Comput. Chem.* **2011**, *32*, 1456–1465.

(247) Weigend, F.; Ahlrichs, R. Balanced Basis Sets of Split Valence, Triple Zeta Valence and Quadruple Zeta Valence Quality for H to Rn: Design and Assessment of Accuracy. *Phys. Chem. Chem. Phys.* **2005**, *7*, 3297.

(248) Allouche, A.-R. Gabedit—A Graphical User Interface for Computational Chemistry Softwares. *J. Comput. Chem.* **2011**, *32*, 174–182.

(249) Liu, Z.; Lu, T.; Chen, Q. An Sp-Hybridized All-Carboatomic Ring, Cyclo[18]Carbon: Electronic Structure, Electronic Spectrum, and Optical Nonlinearity. *Carbon* **2020**, *165*, 461–467.

(250) Lu, T.; Chen, F. Multiwfn: A Multifunctional Wavefunction Analyzer. *J Comput Chem* **2012**, *33*, 580–592.

(251) Dennington, Roy; Keith, Todd A.; Millam, John M. GaussView, Version 6, 2016.

(252) Becke, A. D. Density-functional Thermochemistry. III. The Role of Exact Exchange. *J. Chem. Phys.* **1998**, *98*, 5648.

(253) Lee, C.; Yang, W.; Parr, R. G. Development of the Colle-Salvetti Correlation-Energy Formula into a Functional of the Electron Density. *Phys. Rev. B* **1988**, *37*, 785–789.

(254) Vosko, S. H.; Wilk, L.; Nusair, M. Accurate Spin-Dependent Electron Liquid Correlation Energies for Local Spin Density Calculations: A Critical Analysis. *Can. J. Phys.* **1980**, *58*, 1200–1211.

(255) Amin, E. A.; Truhlar, D. G. Zn Coordination Chemistry: Development of Benchmark Suites for Geometries, Dipole Moments, and Bond Dissociation Energies and Their Use To Test and Validate Density Functionals and Molecular Orbital Theory. *J. Chem. Theory Comput.* **2008**, *4*, 75–85.

(256) Otto, S.; Moll, J.; Förster, C.; Geißler, D.; Wang, C.; Resch-Genger, U.; Heinze, K. Three-in-One Crystal: The Coordination Diversity of Zinc Polypyridine Complexes. *Eur. J. Inorg. Chem.* **2017**, *2017*, 5033–5040.

(257) Grimme, S.; Antony, J.; Ehrlich, S.; Krieg, H. A Consistent and Accurate *Ab Initio* Parametrization of Density Functional Dispersion Correction (DFT-D) for the 94 Elements H-Pu. *J. Chem. Phys.* **2010**, *132*, 154104.

(258) Ernzerhof, M.; Scuseria, G. E. Assessment of the Perdew–Burke–Ernzerhof Exchange-Correlation Functional. *J. Chem. Phys.* **1999**, *110*, 5029–5036.

(259) Perdew, J. P.; Burke, K.; Ernzerhof, M. Generalized Gradient Approximation Made Simple. *Phys. Rev. Lett.* **1996**, *77*, 3865–3868.

(260) van Wüllen, C. Molecular Density Functional Calculations in the Regular Relativistic Approximation: Method, Application to Coinage Metal Diatomics, Hydrides, Fluorides and Chlorides, and Comparison with First-Order Relativistic Calculations. *J. Chem. Phys.* **1998**, *109* (2), 392–399.

(261) Rosenberg, B.; Van Camp, L.; Krigas, Thomas. Inhibition of Cell Division in Escherichia Coli by Electrolysis Products from a Platinum Electrode. *Nature* **1965**, *205* (4972), 698–699. https://doi.org/10.1038/205698a0.

(262) Wang, D.; Lippard, S. J. Cellular Processing of Platinum Anticancer Drugs. *Nat. Rev. Drug Discov.* **2005**, *4* (4), 307–320. https://doi.org/10.1038/nrd1691.

(263) Englinger, B.; Pirker, C.; Heffeter, P.; Terenzi, A.; Kowol, C. R.; Keppler, B. K.; Berger, W. Metal Drugs and the Anticancer Immune Response. *Chem. Rev.* **2019**, *119* (2), 1519–1624. https://doi.org/10.1021/acs.chemrev.8b00396.

(264) Wheate, N. Multi-Nuclear Platinum Complexes as Anti-Cancer Drugs. *Coord. Chem. Rev.* **2003**, *241* (1–2), 133–145. https://doi.org/10.1016/S0010-8545(03)00050-X.

(265) Johnstone, T. C.; Park, G. Y.; Lippard, S. J. Understanding and Improving Platinum Anticancer Drugs - Phenanthriplatin. *Anticancer Res.* **2014**, *34*, 471–476.

(266) Johnstone, T. C.; Wilson, J. J.; Lippard, S. J. Monofunctional and Higher-Valent Platinum Anticancer Agents. *Inorg. Chem.* **2013**, *52* (21), 12234–12249. https://doi.org/10.1021/ic400538c.

(267) Todd, R. C.; Lippard, S. J. Structure of Duplex DNA Containing the Cisplatin 1,2-{Pt(NH3)2}2+-d(GpG) Cross-Link at 1.77 Å Resolution. *J. Inorg. Biochem.* **2010**, *104*, 902–908.

(268) Park, G. Y.; Wilson, J. J.; Song, Y.; Lippard, S. J. Phenanthriplatin, a Monofunctional DNA-Binding Platinum Anticancer Drug Candidate with Unusual Potency and Cellular Activity Profile. *Proc Natl Acad Sci* **2012**, *109*, 11987–11992.

(269) Lovejoy, K. S.; Serova, M.; Bieche, I.; Emami, S.; D'Incalci, M.; Broggini, M.; Erba, E.; Gespach, C.; Cvitkovic, E.; Faivre, S.; Raymond, E.; Lippard, S. J. Spectrum of Cellular Responses to Pyriplatin, a Monofunctional Cationic Antineoplastic Platinum(II) Compound, in Human Cancer Cells. *Mol. Cancer Ther.* **2011**, *10* (9), 1709–1719. https://doi.org/10.1158/1535-7163.MCT-11-0250.

(270) Almaqwashi, A. A.; Zhou, W.; Naufer, M. N.; Riddell, I. A.; Yilmaz, Ö. H.; Lippard, S. J.; Williams, M. C. DNA Intercalation Facilitates Efficient DNA-Targeted Covalent Binding of Phenanthriplatin. *J. Am. Chem. Soc.* **2019**, *141* (4), 1537–1545. https://doi.org/10.1021/jacs.8b10252.

(271) Tullius, T. D.; Lippard, S. J. Ethidium Bromide Changes the Nuclease-Sensitive DNA Binding Sites of the Antitumor Drug Cis-Diamminedichloroplatinum(II). *Proc. Natl. Acad. Sci.* **1982**, *79* (11), 3489–3492. https://doi.org/10.1073/pnas.79.11.3489.

(272) Boulikas, T.; Vougiouka, M. Cisplatin and Platinum Drugs at the Molecular Level (Review). *Oncol. Rep.* **2003**. https://doi.org/10.3892/or.10.6.1663.

(273) Dasari, S.; Bernard Tchounwou, P. Cisplatin in Cancer Therapy: Molecular Mechanisms of Action. *Eur. J. Pharmacol.* **2014**, *740*, 364–378. https://doi.org/10.1016/j.ejphar.2014.07.025.

(274) Lozada, I. B.; Williams, J. A. G.; Herbert, D. E. Platinum(II) Complexes of Benzannulated N ^ N ¯^ O-Amido Ligands: Bright Orange Phosphors with Long-Lived Excited States. *Inorg. Chem. Front.* **2022**, *9* (1), 10–22. https://doi.org/10.1039/D1QI01120K.

(275) Che, C.-M.; Yang, M.; Wong, K.-H.; Chan, H.-L.; Lam, W. Platinum(II) Complexes of Dipyridophenazine as Metallointercalators for DNA and Potent Cytotoxic Agents against Carcinoma Cell Lines. *Chem. – Eur. J.* **1999**, *5*, 3350–3356.

(276) Kieltyka, R.; Fakhoury, J.; Moitessier, N.; Sleiman, H. F. Platinum Phenanthroimidazole Complexes as G-Quadruplex DNA Selective Binders. *Chem. – Eur. J.* **2008**, *14* (4), 1145–1154. https://doi.org/10.1002/chem.200700783.

(277) Cusumano, M.; Di Pietro, M. L.; Giannetto, A.; Nicolò, F.; Rotondo, E. Noncovalent Interactions of Platinum(II) Square Planar Complexes Containing Ligands Out-of-Plane with DNA. *Inorg. Chem.* **1998**, *37* (3), 563–568. https://doi.org/10.1021/ic9705406.

(278) Suntharalingam, K.; Mendoza, O.; Duarte, A. A.; Mann, D. J.; Vilar, R. A Platinum Complex That Binds Non-Covalently to DNA and Induces Cell Death via a Different

Mechanism than Cisplatin. *Metallomics* **2013**, *5* (5), 514. https://doi.org/10.1039/c3mt20252f.

(279) Luedtke, N. W.; Liu, Q.; Tor, Y. Synthesis, Photophysical Properties, and Nucleic Acid Binding of Phenanthridinium Derivatives Based on Ethidium. *Bioorg. Med. Chem.* **2003**, *11*, 5235–5247.

(280) Nandi, R.; Chaudhuri, K.; Maiti, M. EFFECTS OF IONIC STRENGTH and PH ON THE BINDING OF SANGUINARINE TO DEOXYRIBONUCLEIC ACID. *Photochem. Photobiol.* **1985**, *42* (5), 497–503. https://doi.org/10.1111/j.1751-1097.1985.tb01600.x.

(281) Howe-Grant, M.; Lippard, S. J. Binding of Platinum(II) Intercalation Reagents to Deoxyribonucleic Acid. Dependence on Base-Pair Composition, Nature of the Intercalator, and Ionic Strength. *Biochemistry* **1979**, *18* (26), 5762–5769. https://doi.org/10.1021/bi00593a003.

(282) Murphy, M. P. How Mitochondria Produce Reactive Oxygen Species. *Biochem. J.* **2009**, *417* (1), 1–13. https://doi.org/10.1042/BJ20081386.

(283) Ivashkevich, A.; Redon, C. E.; Nakamura, A. J.; Martin, R. F.; Martin, O. A. Use of the γ-H2AX Assay to Monitor DNA Damage and Repair in Translational Cancer Research. *Cancer Lett.* **2012**, *327* (1–2), 123–133. https://doi.org/10.1016/j.canlet.2011.12.025.

(284) Mah, L.-J.; El-Osta, A.; Karagiannis, T. C. ΓH2AX: A Sensitive Molecular Marker of DNA Damage and Repair. *Leukemia* **2010**, *24* (4), 679–686. https://doi.org/10.1038/leu.2010.6.

(285) Chargaff, E.; Lipshitz, R. Composition of Mammalian Desoxyribonucleic Acids [1]. *J. Am. Chem. Soc.* **1953**, *75* (15), 3658–3661. https://doi.org/10.1021/ja01111a016.

(286) Kaim, W.; Schwederski, B.; Klein, A. Manganese-Catalyzed Oxidation of Water to O2. In *Bioinorganic Chemistry: Inorganic Elements in the Chemistry of Life*; Wiley: Chichester, 2013; pp 67–74.

(287) Pan, D.; Schmieder, A. H.; Wickline, S. A.; Lanza, G. M. Manganese-Based MRI Contrast Agents: Past, Present, and Future. *Tetrahedron* **2011**, *67* (44), 8431–8444. https://doi.org/10.1016/j.tet.2011.07.076.

(288) East, N. R.; Förster, C.; Carrella, L. M.; Rentschler, E.; Heinze, K. The Full d^3–d^5 Redox Series of Mononuclear Manganese Complexes: Geometries and Electronic Structures of $[Mn(Dgpy)_2]^{n+}$. *Inorg. Chem.* **2022**, *61* (37), 14616–14625. https://doi.org/10.1021/acs.inorgchem.2c01680.

(289) Herr, P.; Kerzig, C.; Larsen, C. B.; Häussinger, D.; Wenger, O. S. Manganese(i) Complexes with Metal-to-Ligand Charge Transfer Luminescence and Photoreactivity. *Nat. Chem.* **2021**, *13* (10), 956–962. https://doi.org/10.1038/s41557-021-00744-9.

(290) Betley, T. A.; Qian, B. A.; Peters, J. C. Group VIII Coordination Chemistry of a Pincer-Type Bis(8-Quinolinyl)Amido Ligand. *Inorg. Chem.* **2008**, *47* (24), 11570–11582. https://doi.org/10.1021/ic801047s.

(291) Huynh, M. T.; Anson, C. W.; Cavell, A. C.; Stahl, S. S.; Hammes-Schiffer, S. Quinone 1 e⁻ and 2 e⁻/2 H⁺ Reduction Potentials: Identification and Analysis of Deviations from Systematic Scaling Relationships. *J. Am. Chem. Soc.* **2016**, *138* (49), 15903–15910. https://doi.org/10.1021/jacs.6b05797.

(292) Michaelis, L.; Hill, E. S. THE VIOLOGEN INDICATORS. *J. Gen. Physiol.* **1933**, *16* (6), 859–873. https://doi.org/10.1085/jgp.16.6.859.

(293) Woodhouse, M. D.; McCusker, J. K. Mechanistic Origin of Photoredox Catalysis Involving Iron(II) Polypyridyl Chromophores. *J. Am. Chem. Soc.* **2020**, *142* (38), 16229–16233. https://doi.org/10.1021/jacs.0c08389.

4 Computational Investigation of Benzannulated Complexes

4.1 Abstract

This chapter provides a quantum mechanical foundation to the discussed photophysical properties of the complexes discussed in Chapters 2 and 3. A few common themes emerge from these studies: (1) phenanthridine generally imbues lower-lying vacant π^*-MO and conspires with π-donor ligands to red-shift and widen the absorptive cross section of the complexes leading to panchromatic absorption in some complexes. (2) π-donor ligands can form π-bonds with metal complexes increasing the covalency of the M–L bond which lends additional ligand contribution to nominally MLCT transitions. Consequently, the absorption intensities are intensified which could prove advantageous for solar capture materials. (3) Emission in phenanthridine containing complexes is blue-shifted, and to some degree longer τ, compared with the quinoline derivatives thanks to the increased rigidity conferred by benzannulation. Additionally, some insights into the electronic structure of $3d$ transition metal complexes are presented and discussed. The role of Hartree-Fock exchange in modeling with DFT and TDDFT various properties of transition metal complexes is disclosed.

4.2 Introduction

4.2.1 General Implications of Benzannulation

As discussed in Chapter 1, benzannulation of conjugated, aromatic ligands is a widely used approach in influencing the optical properties of transition metal and main-group complexes. This strategy offers flexibility in designing new luminescent molecules and photosensitizers without extensive changes in the molecular shape. It is generally thought that benzannulation impacts the

optical and photophysical properties of molecular complexes by red-shifting their absorption and emission spectra. However, as discussed above, in a published series of (BPI)PtCl (BPI = *bis*(2-pyridylimino)isoindolate) complexes, red or blue shifts are both possible with increasing π-extension depending on (a) the site of benzannulation, and (b) how benzannulation influences the energies of the frontier orbitals (HOMO/LUMO).

In this context, our group has been interested in incorporating phenanthridine (3,4-benzoquinoline) in various multidentate ligand frameworks. In this chapter, I look into some peculiar impacts of phenanthridine on the optical and photophysical properties of various molecular complexes by employing state-of-the-art computational chemistry approaches. I first examine molecular complexes synthesized by in-group collaborators, establishing common trends in the electronic structures of molecular complexes. Furthermore, certain photophysical properties are calculated to provide some insights to the dynamics of the excited states. The concepts established from these systems are then extended to the molecular complexes I synthesized and characterized, which are presented in Chapter 3. Beyond the effects of benzannulation, I also examined how the metal centre perturbs the excited states of molecular complexes; in particular, the role of spin-orbit coupling in the excited state dynamics. Although DFT currently experiences some successes, this chapter also offers insights to its limitations and pitfalls in the hope that the reader will take some caution in drawing conclusions from this approach and appreciate the importance of being rigorous in modeling chemical phenomena that are in reality complex. This chapter draws in work from submitted and published manuscripts I have (co-)authored in various peer-reviewed journals as follows.

Section 4.3.1

Mondal, R.; Braun, J.D.; Lozada, I.B.; Nickel, R.; van Lierop, J.; Herbert, D.E. *New J. Chem.* **2021**, 45, 4427.

Gaire, S.; Ortiz, R.J.; Schrage, B.R.; Lozada, I.B.; Mandapati, P.; Osinski, A.J.; Herbert, D.E.; Ziegler, C. *J. Organomet. Chem.* **2020**, 121338.

Mandapati, P.; Braun, J.D.; Lozada, I.B.; Williams, J.A.G.; Herbert, D.E. *Inorg. Chem.* **2020**, 59, 12504.

Section 4.3.2

Larsen, C.B.[†]; Braun, J.D. [†]; Lozada, I.B. [†]; Kunnus, K.; Biasin, E.; Kolodziej, C.; Burda, C.; Cordones, A.; Gaffney, K.; Herbert, D.E. *J. Am. Chem. Soc.* **2021**, 143, 20645. †Contributed equally

Braun, J.D.; Lozada, I.B.; Shepit, M.; van Lierop, J.; Herbert, D.E. *RSC Adv.* **2021**, 11, 3547.

Braun, J.D.; Lozada, I.B.; Herbert, D.E. *Inorg. Chem.* **2020**, 59, 117746.

Braun, J.D.; Lozada, I.B.; Kolodziej, C.; Burda, C.; Newman, K.M.E.; van Lierop, J.; Davis, R.L.; Herbert, D.E. *Nat. Chem.* **2019**, 11, 1144.

Section 4.3.3

Lozada, I.B.; Ortiz, R.J.; Braun, J.D.; Williams, J.A.G.; Herbert, D.E. *J. Org. Chem.* **2022**, 87, 184.

Section 4.3.4

Lozada, I.B.; Braun, J.D.; Williams, J.A.G.; Herbert, D.E. *Inorg. Chem.* **2022**, *submitted*.

Section 4.3.5

Lozada, I.B.; Williams, J.A.G.; Herbert, D.E. *Inorg. Chem. Front.* **2022**, 9, 10.

4.2.2 The Electronic Structure Problem

Before elaborating the general approach and methodology employed in the computation of ground state and photophysical properties of phenanthridine-containing complexes, it is necessary to provide a concise description of the theories used. To compute and predict the properties of quantum mechanical systems, we need to go beyond classical mechanics. For this, quantum mechanics (QM) and the Schrödinger equation (SE) provide the necessary tools to describe the behaviour of quantum mechanical particles. In chemistry, SE attempts to describe the motion of the electrons—in atoms, ions and molecules—in the field of nuclear point charges. Fundamental to QM and SE is the wavefunction, Ψ, for which certain postulates impose constraints on what constitutes an acceptable wavefunction. The time-independent SE for a free particle in a one-dimensional system, eq. (4.1), is deceptively simple

$$\hat{H}\Psi(x) = \hat{T}\Psi(x) + \hat{V}\Psi(x) = E\Psi(x) \qquad (4.1)$$

where $\hat{H}$ is the Hamiltonian operator, $\hat{T}$ and $\hat{V}$ are the kinetic and potential energy operators, and $\Psi(x)$ is the one-dimensional antisymmetric wavefunction. For a two-body problem, such as in atomic hydrogen, the wavefunction will not only depend on the 3-dimensional spatial coordinates of the electron I but also the nuclei ($\mathbf{R}$), that is $\Psi(\mathbf{r},\mathbf{R})$. Generally, the coordinates $\mathbf{r}$ and $\mathbf{R}$ are expressed in spherical coordinates. It becomes evident from this that with increasing chemical complexity and accounting for every particle coordinate, solving the SE becomes cumbersome. It is for this reason that most systems of chemical interests are far too computationally demanding for wavefunction theory (WFT) limiting its general applicability. Invoking assumptions/approximations generally simplifies the problem enabling the computation and prediction of molecular properties. The Born-Oppenheimer approximation (BOA) is fundamental

175

to chemistry as it makes possible the separation of the motion of the nuclei from the electrons. BOA, or sometimes referred to as the adiabatic approximation in literature, exploits the disparity in the velocities of the nucleus and electron ($v_e \gg v_p$) as consequence of the greater mass of the nucleus. The electron is thus able to instantaneously adjust to any nuclear displacements, and the nuclei can be regarded as frozen in a single arrangement or molecular conformation. The electronic component of the SE can then be explicitly treated separately from the contributions of the nuclei to the total energy of the system. BOA has important implications that will be discussed later in this chapter.

The exact form of the molecular wavefunction is unknown. How, then, do we go about calculating molecular properties if the wavefunction is unknown? One solution is to extend the orbital concept, or one-electron wavefunction, to molecular systems enabling us to place electrons in different *molecular* orbitals (MO) and construct reference wavefunctions for different electronic configurations. We can then approximate the real molecular wavefunction (Ψ_T) as linear combinations of these different configurations (ψ_i) in a full configuration approach. This multiconfigurational character of the molecular wavefunction makes it cumbersome to compute molecular properties particularly for larger systems, thus further approximations must be introduced. For most systems without low-lying excited and near-degenerate states, a single reference or *ansatz* usually is a sufficient approximation. As will be seen in section 4.3.5, this single reference approximation breaks down in $3d$ metal complexes and in strongly-correlated systems.

Through linear combinations of atomic orbitals (LCAO), eq. (4.2), MOs (ϕ) are generated,

$$\phi = \sum_{i=1}^{N} a_i \varphi_i \qquad (4.2)$$

where the set of N functions φ_i is referred to as the 'basis set' (constitutes the atomic orbitals or AOs), and each has an associated coefficient a_i (related to the contributions of each atom to the MO). In practice, however, AOs are replaced with linear combination of Gaussian functions (Gaussian-type orbitals or GTOs) that mimic the behaviour of AOs. The analytical solutions available for GTOs allow for the relative ease in handling these functions computationally, while linear combinations of GTO enable flexibility in describing the electron density gradient and bonding. The variational principle can then be used to optimize the *ansatz* such that

$$\frac{\int \psi_{trial} \hat{H} \psi_{trial} d\mathbf{r}}{\int \psi_{trial}^2 d\mathbf{r}} \geq E_0 \qquad (4.3)$$

where E_0 corresponds to the real ground state energy. Overall, MO theory enjoys some successes in predicting and explaining chemical reactivity, interactions and other chemical phenomena.

A simplification to the many-body problem can be achieved through density functional theory (DFT), reducing the $3N$-dimensional complexity of the wavefunction in terms of the 3-dimensional electronic density of the system, $\rho(\mathbf{x,y,z})$. The electronic density is a physical observable, making DFT an attractive alternative to WFT methodologies. The relationship between the electronic wavefunction and the electronic density can be expressed in terms of the total number of electrons in the system (N),

$$N = \int \rho(\mathbf{r}) d\mathbf{r} \qquad (4.4)$$

While Hohenberg and Kohn[132] provided the rigorous theoretical foundations of modern DFT, its modern application is in the form introduced by Kohn and Sham (KS-DFT), including its spin-polarised extension.[133] KS-DFT is formulated by taking a *fictitious non-interacting* system of electrons as starting point that have the same ground-state density as the *real* system of interest

where the electrons interact. The total energy of the system, eq (4.4) can then be expressed as a sum of one-electron functionals

$$E[\rho(\boldsymbol{r})] = T_{ni}[\rho(\boldsymbol{r})] + V_{ne}[\rho(\boldsymbol{r})] + V_{ee}[\rho(\boldsymbol{r})] + \Delta T_{ni}[\rho(\boldsymbol{r})] + \Delta V_{ee}[\rho(\boldsymbol{r})] \qquad (4.4)$$

where T_{ni} is the kinetic energy of the non-interacting electrons, V_{ne} is the nuclear-electron interaction, V_{ee} is the classical electron-electron repulsion of the electron density with itself, ΔT_{ni} is the kinetic energy correction from the interacting nature of the electrons, and ΔV_{ee} encompasses all non-classical corrections to the electron-electron repulsion energy such as Coulomb and exchange repulsions. The last two terms are often lumped together, and this often called the exchange-correlation energy (E_{xc}). While this functional exists according to Hohenberg and Kohn, its exact form is unknown much like Ψ in WFT. Approximations to the E_{xc} are introduced that make DFT applicable to various chemical problems. Indeed, much of the effort in the past decades is dedicated to improving the E_{xc} approximations such that a plethora of different functional flavours can now be chosen or used. Perhaps, the most popular functionals are those that incorporate some Hartree-Fock exchange (HFX) or so-called hybrid functionals and are used extensively throughout the thesis. Thanks to the favourable scaling with system size and comparative accuracy to WFT, DFT has now become the preferred method for the calculation of the electronic structure of complex chemical systems. DFT can also be extended to account for time-dependent phenomena such as in light absorption and luminescence. Much of time-dependent DFT (TDDFT) simulations of molecular spectra are based on the linear-response formalism (LR-TDDFT) and can reasonably reproduce experimental molecular spectra. TDDFT also describes the photoexcitation more accurately compared with the HOMO-LUMO approximation. As will be

discussed later in the following section, the limitations of DFT and TDDFT become evident in highly correlated systems such as in $3d$ transition metal complexes.

4.3 Results and Discussion

4.3.1 General Approach

As discussed in section 4.2.2, the BOA allows for the calculation of electronic structures of different molecular conformations (minima, tautomers, and transition states for example). It is, therefore, possible to construct potential energy surfaces (PESs) for the ground and excited states by plotting the electronic energy as a function of the nuclear coordinates. The nuclear coordinates are generally defined as a specific molecular distortion such as M−L bond elongation, rotation about a single bond, etc. The usefulness of PESs in photophysics and photochemistry is exploited throughout this thesis, as it (a) provides a model through which specific photophysical parameters can be extracted and compared to experimentally determined values (pertinent parameters are shown in Figure 4.1), and (b) provides an in-depth understanding of the electronic structure and dynamic processes in molecular systems that are often beyond experimental reach.

As mentioned above, DFT and TDDFT are employed to model complex molecular systems thanks to the better balance between computational costs, efficiency, and accuracy these two approaches offer compared with WFT. The general approach relies on a simplified three-state model as shown in Figure 4.1. This model assumes that emission follows Kasha's rule, briefly defined as the propensity to emit from the lowest lying excited state (S_1 or T_1) following non-radiative relaxation (internal conversion, IC; or intersystem crossing, ISC) from the initial photoexcitation. This model is flexible in that depending on the photophysical problem at hand,

179

this can be reduced to the states of interest. For example, for most fluorescence processes, the lowest-lying triplet excited state can be ignored. Optimization of the ground state geometries of the ligands and complexes are first performed and compared with the coordinates obtained from single-crystal X-ray diffraction (SCXRD). For most of the complexes studied in this thesis, a good agreement between the bond distances and angles of the optimized ground state geometries and crystal structures are generally obtained. Optimizations are followed by frequency calculations to ensure the geometries are real minima. The choice of functional for optimization is largely reliant on benchmarking done previously for complexes containing the same metals as the ones presented here.[138–140] Similarly, the lowest-lying excited states are optimized at the same level of theory as the ground state. The excited states of interests are the S_1 and T_1 states, as often radiative deactivation occur from these states according to Kasha's rule.
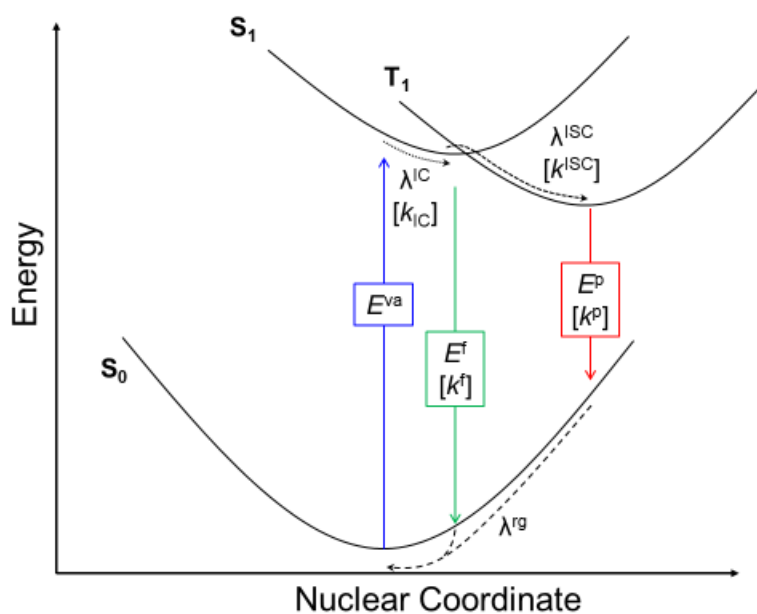
Figure 4.1. Three state model used to calculate relevant photophysical properties.

There are several information that can be extracted from Figure 4.1 and can be compared with experimental data. The E^f and E^p are energies associated with fluorescence and phosphorescence. In addition, the reorganization energies λ^{IC}, λ^{ISC} and λ^{rg} are associated with internal conversion, intersystem crossing, and ground state reorganization, respectively. Internal conversion is the nonradiative decay process from a higher energy to lower energy excited state of the same multiplicity ($S_n \rightarrow S_1$ or $T_n \rightarrow T_1$). In contrast, intersystem crossing involves the nonradiative deactivation from between two excited states of different multiplicities ($S_n \rightarrow T_n$). The ground state reorganization is a nonradiative process that pertains to the nuclear reorganization the molecule undertakes after relaxation from the geometry of the excited state on the ground state PES back to its ground state equilibrium geometry. These parameters are correlated with the Stokes shift and provide information on the molecular distortions that are associated with the nonradiative processes described above. These structural changes can then be leveraged for future ligand designs to reduce nonradiative losses.

Aside from these energies, it is also possible to estimate the coupling between the excited singlet and triplet state manifolds by calculating the spin-orbit coupling matrix elements (SOCMEs) between the excited states of interests. The SOCMEs are particularly useful in phosphorescent complexes or complexes that exhibit reverse intersystem crossing (RISC) as these provide potential trajectories of the initially generated excited state after photoexcitation. Moreover, SOCMEs allow the direct excitation from the ground state (often singlet) to a triplet excited state, which can manifest in complexes containing heavy elements. Neese and co-workers have recently incorporated an approach that solves the Fermi's Golden Rule-like equation using a

path integral approach.[141–143] Just like with the optimization, these calculations assume the Harmonic approximation is valid (as calculated Hessians from optimizations are used) and make use of the calculated SOCMEs.

4.3.2 Shedding Light on Some Unexpected Behaviours of Bezannulation

Presented in Section 2.3.2 of Chapter 2 were a few examples where bezannulation exhibit some unexpected results. The first example was the complexes **FP1** and **FP2**. There, benzannulation of the complexes led to a cathodic shift in the observed reduction events (**FP2**: $E_{1/2}$ = -1.61 V vs FcH$^{0/+}$; **FP1**: $E_{1/2}$ = -1.55 V vs FcH$^{0/+}$), and a hypsochromic shift in the energy of the MLCT absorption manifold ($\lambda_{max,abs}$: **FP2** 435 nm, **FP1** 449 nm). Single point calculations at the ground state equilibrium geometries were carried out to obtain the pertinent frontier molecular orbitals (FMOs) and are illustrated in Figure 4.2. In both complexes, the d-orbital splitting is consistent with a pseudo-octahedral ligand field; the HOMO, HOMO-1 and HOMO-2 molecular orbitals represent what would be the t_{2g} set and are comprised of the d_{xz}, d_{xy} and d_{yz} orbitals collectively (see Table 4.1 and 4.2 for population analysis). What would be the e_g set in a formally octahedral coordination environment, the $d_{x^2-y^2}$ and d_{z^2}, are accordingly destabilized and appear as the LUMO+3 and LUMO+4 (**FP1**) and LUMO+6 and LUMO+7 (**FP2**) with σ-anti-bonding character between Fe and the phosphines. The e_g-type orbitals lie at only slightly higher energies in **FP2** vs. **FP1**.
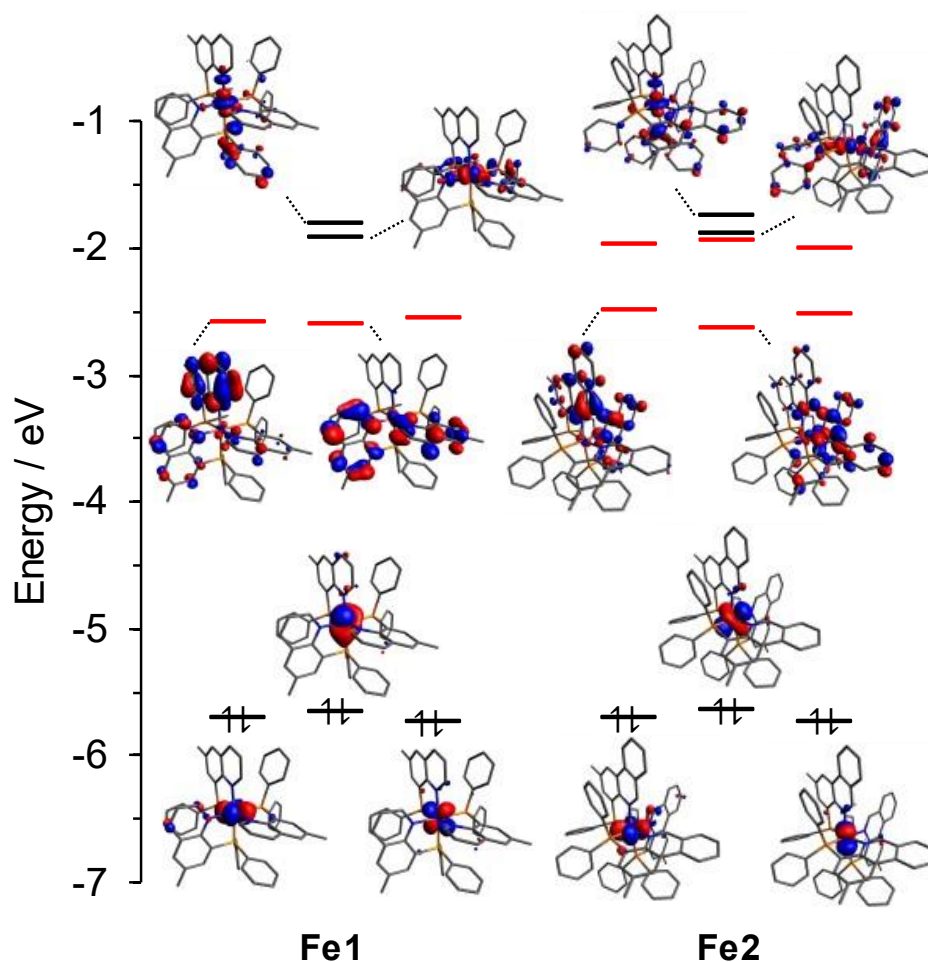
Figure 4.2. Selected ground state MO energy diagram and orbitals (isosurface = 0.04) for **FP1** and **FP2** (SMD-TPSSh/def2-SVP//SMD-B3LYP-D3(BJ)/def2-SVP). Vacant, acceptor ligand-based π* orbitals are highlighted in red. Fragment contributions to selected MOs are tabulated in Tables 4.1-4.2.

In **FP2**, the three lowest energy unoccupied MOs (the LUMO, LUMO+1 and LUMO+2) have considerable orbital density localized at the C=N sub-unit of the phenanthridinyl ligand (Table 4.2). The same three orbitals in **FP1** have analogous C=N (quinolinyl) character, but with a lower degree of localization. However, the more π-extended phenanthridinyl ligand provides

three additional, low-lying, vacant, ligand-based π^* orbitals (LUMO+3 through LUMO+5) compared with **FP1**. Population analysis (Table 4.1) indicates that these orbitals are localized on the phenanthridinyl π-system and are largely comprised of the phenanthridine aryl rings. To try to trace the origin of these orbitals to what can be thought of as the benzannulation of the quinolinyl moiety in **P1** to a phenanthridinyl unit in **P2**, we carried out charge decomposition analysis (CDA) on a **P2** ligand extracted from the optimized structure of **FP2**, splitting the **P2** ligand into its quinoline-congener and a *cis*-butadiene-type fragment. The relevant fragment orbital (FO) interactions are summarized in Figure 4.3. A relatively complex orbital interaction is observed to be in play between the quinolinyl and butadiene molecular fragments. Both the α- and β-orbitals indicate similar interactions, so only the α-manifold is discussed here focusing on those with FO composition $(\Theta_{m,i}) > 10\%$. Overall, the π^* orbital interactions between the quinolinyl α-LUMO (α-MO 87; $\Theta_{m,i} = 16$ %) and α-LUMO+1 (α-MO 88; $\Theta_{m,i} = 30$ %) and butadiene α-LUMO (α-MO 16; $\Theta_{m,i} = 33$ %) appear to be responsible for the three additional π^* orbitals found in **FP2**. Thus, the most significant interaction is a cooperative one between two vacant orbitals.
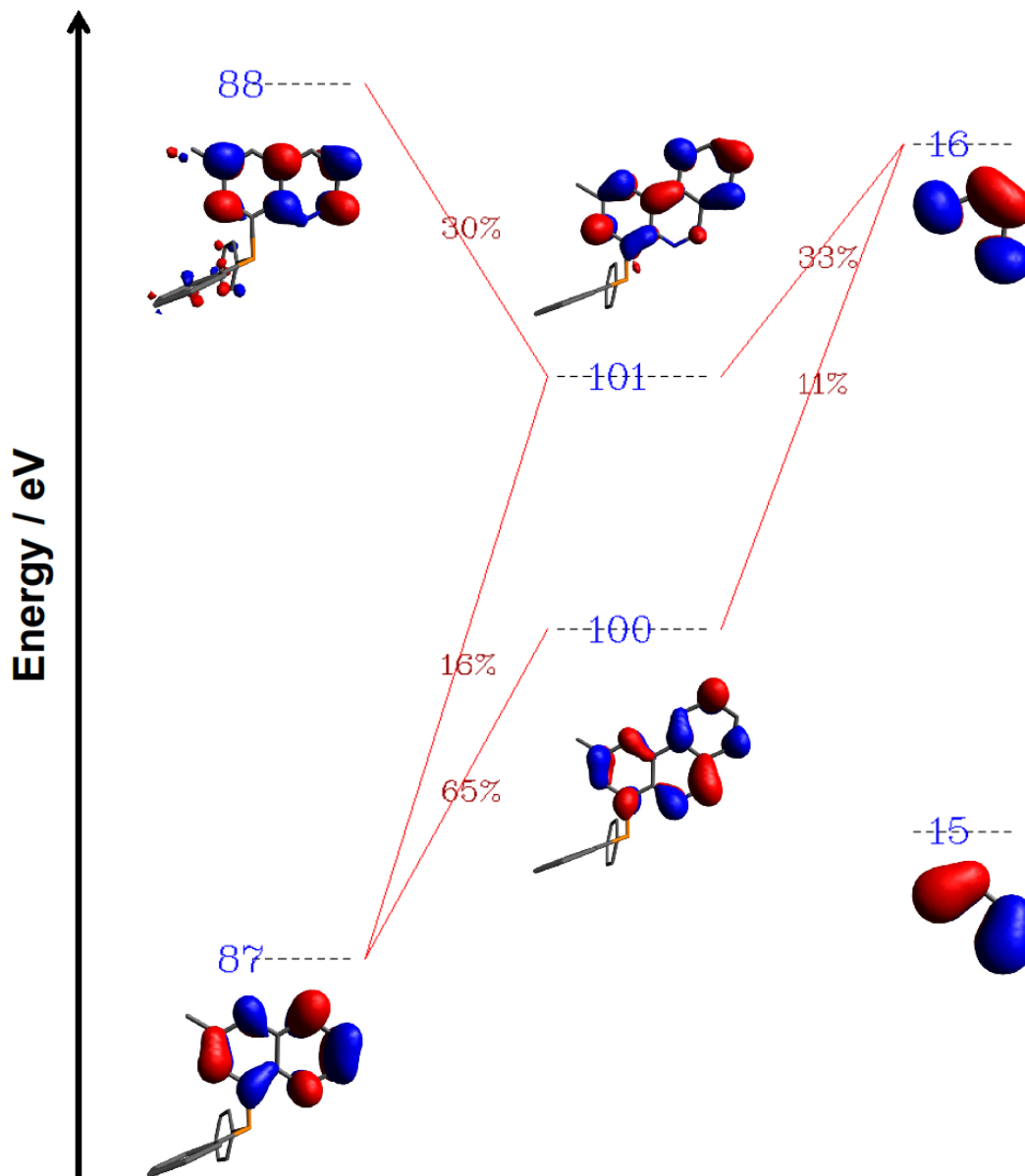
Figure 4.3. Orbital interaction diagram of relevant **P1** and s-*cis*-butadiene alpha-fragment orbitals, and fragment orbital contributions to the **P2** LUMO (MO 100) and LUMO+1 (MO 101). All isosurface values and fragment orbital contributions are set to 0.04 and >10%, respectively.

Table 4.1. Fragment contributions (%) to the ground state MOs of **FP1** using Hirshfeld atomic population method (SMD-rTPSSh/def2-SVP//SMD-rB3LYP-D3(BJ)/def2-SVP).

MO	Fe	C=N^{Quin}	Ar^{Quin}	PPh$_2$	Me
LUMO+4	42	6	7	45	0
LUMO+3	43	6	6	44	0
LUMO+2	2	23	66	7	1
LUMO+1	2	25	65	6	1
LUMO	2	28	63	6	1
HOMO	78	6	8	8	0
HOMO-1	77	5	8	9	0
HOMO-2	78	5	8	9	0

Table 4.2. Fragment contributions (%) to the ground state MOs of **FP2** using Hirshfeld atomic population method (SMD-rTPSSh/def2-SVP//SMD-rB3LYP-D3(BJ)/def2-SVP).

MOs	Fe	C=N^{Phen}	Ar^{Phen}	PPh$_2$	Me
LUMO+7	36	7	22	35	0
LUMO+6	28	5	35	32	0
LUMO+5	11	4	67	17	1
LUMO+4	11	4	68	17	1
LUMO+3	3	3	82	11	1
LUMO+2	3	32	58	6	1
LUMO+1	3	32	58	6	1
LUMO	2	37	55	4	1
HOMO	77	6	8	8	0
HOMO-1	75	6	9	9	0
HOMO-2	76	6	8	9	0

The above is reminiscent of the symmetry arguments made by Hanson *et al.*[67] in explaining the red-shift of both absorption and emission observed for a Pt(II) chloride complex of 1,3-*bis*(2-pyridylimino)benz(*e*)isoindolate compared with an analogous complex of 1,3-*bis*(2-

pyridylimino)isoindolate. In that case, however, the primary impact of benzannulation was on the frontier orbitals. Here, despite the expanded π-system in **FP2**, the calculated HOMO-LUMO gaps in **FP1** (3.06 eV) and **FP2** (3.02 eV) are not significantly different and indeed, in absolute terms, appear to contradict the cathodic and hypsochromic shifts observed for **FP2**. The additional vacant orbitals do have a significant impact on the observed absorption spectrum of **FP2**, however, as revealed by TDDFT. The electronic excitation with a dominant HOMO→LUMO contribution (State 4 in both **FP1** and **FP2**; Figures 4.4-4.5) is effectively turned-off in **FP1** ($f_{osc} = 0.004$; Table 4.3), but gains in intensity in **FP2** ($f_{osc} = 0.025$; Table 4.4). This contrasts with the behaviour of Group 10 metal complexes supported by *bis*(8-quinolinyl)amido, (8-quinolinyl)(4-phenanthridinyl)amido and *bis*(4-phenanthridinyl)amido ligands.[64] There, benzannulation has the opposite effect – the HOMO→LUMO transition has significant oscillator strength for the complex with the smallest π-system (*i.e.*, supported by the *bis*(8-quinolinyl)amido ligand) and is essentially dark for the complex of with the largest π-system (*i.e.*, supported by a *bis*(4-phenanthridinyl)amido scaffold).
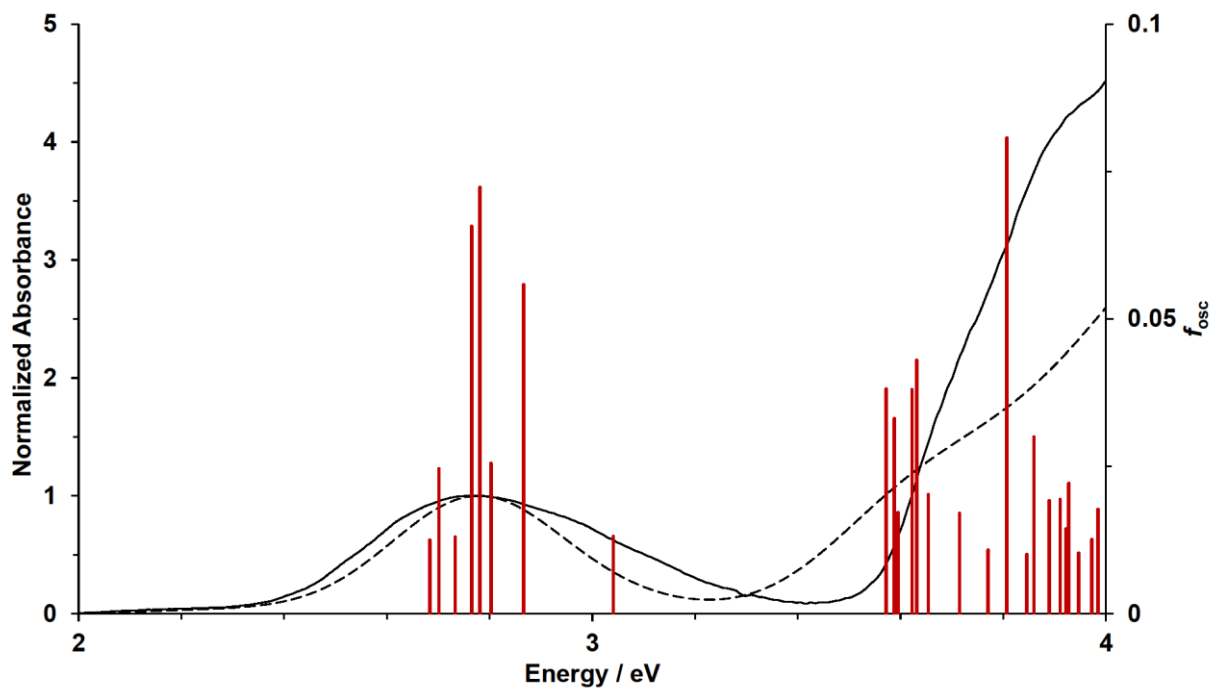
Figure 4.4. TD-DFT simulated spectrum (---) and calculated vertical excitation energies (red) superimposed on the experimental spectrum (−) of **FP1** in CH_3CN (SMD-rTPSSh/def2-SVP)//SMD-rB3LYP-D3(BJ)/def2-SVP); FWHM = 3000 cm-1 ; $f_{osc} > 0.01$).

Table 4.3. TD-DFT predicted vertical excitation energies, oscillator strengths ($f_{osc} > 0.01$) and MO contributions ($> 10\%$) for **FP1**.

No.	E / eV	f_{osc}	Major Contributions
4	2.66	0.004	HOMO→LUMO (75%)
5	2.68	0.013	H-1→LUMO (46%), H-1→L+1 (21%)
6	2.70	0.025	H-2→L+2 (15%), HOMO→L+1 (64%)
7	2.73	0.013	H-2→LUMO (19%), H-2→L+1 (12%), H-2→L+2 (11%), H-1→L+1 (16%), HOMO→L+1 (13%), HOMO→L+2 (10%)
9	2.76	0.066	H-2→LUMO (14%), H-1→LUMO (22%), HOMO→L+2 (42%)
10	2.78	0.072	H-2→LUMO (20%), H-2→L+1 (45%), H-1→LUMO (10%), HOMO→L+2 (10%)
11	2.80	0.026	H-2→L+2 (28%), H-1→L+2 (53%)
12	2.87	0.056	H-2→L+1 (11%), H-2→L+2 (26%), H-1→L+1 (14%), H-1→L+2 (25%)
13	3.04	0.013	H-2→L+3 (50%), HOMO→L+4 (14%)
16	3.57	0.038	H-3→LUMO (92%)
17	3.59	0.033	H-4→LUMO (28%), H-3→L+1 (64%)
18	3.59	0.017	H-4→LUMO (59%), H-3→L+1 (31%)
19	3.62	0.038	H-4→L+1 (88%)
20	3.63	0.043	H-3→L+2 (80%)
21	3.65	0.020	H-4→L+2 (80%)
23	3.71	0.017	H-5→LUMO (89%)
27	3.77	0.011	H-6→LUMO (76%)
29	3.81	0.081	H-5→L+1 (27%), H-5→L+2 (59%)
31	3.85	0.010	H-8→LUMO (25%), H-8→L+1 (12%), H-8→L+2 (14%), H-7→LUMO (22%)
33	3.86	0.030	H-7→L+1 (53%), HOMO→L+6 (13%)
35	3.89	0.019	H-10→LUMO (12%), H-9→LUMO (10%), H-8→L+1 (17%), H-7→LUMO (25%), H-7→L+2 (15%)
38	3.91	0.019	H-9→LUMO (13%), H-7→L+2 (42%), HOMO→L+7 (14%)
40	3.92	0.014	H-1→L+6 (71%)
41	3.93	0.022	H-9→LUMO (10%), H-9→L+1 (35%)
43	3.95	0.010	H-9→L+2 (16%), H-1→L+7 (14%), HOMO→L+8 (31%)
46	3.97	0.013	H-10→LUMO (18%), H-1→L+7 (29%), HOMO→L+8 (12%)
48	3.98	0.018	H-11→LUMO (14%), H-10→L+2 (16%), H-9→L+2 (20%), H-1→L+7 (16%), HOMO→L+8 (10%)
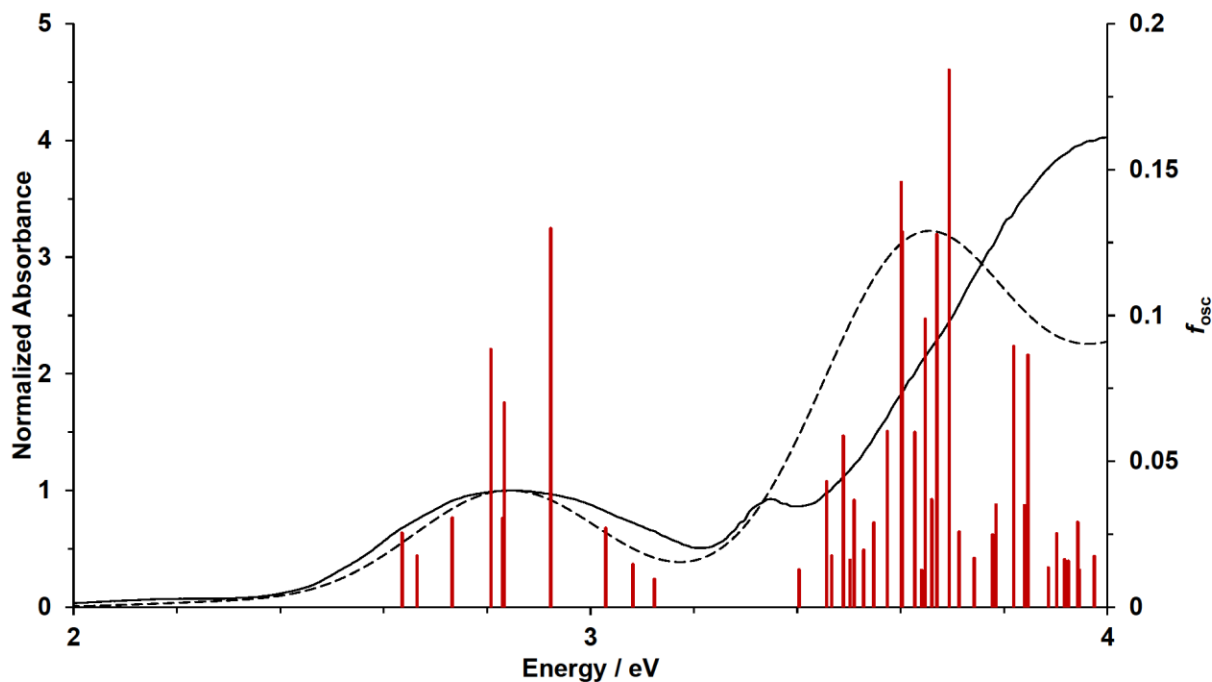
Figure 4.5. TD-DFT simulated spectrum (---) and calculated vertical excitation energies (red) superimposed on the experimental spectrum (−) of FP2 in CH_3CN (SMD-rTPSSh/def2-SVP)//SMD-rB3LYP-D3(BJ)/def2-SVP); FWHM = 3000 cm-1 ; $f_{osc} > 0.01$).

Table 4.4. TD-DFT predicted vertical excitation energies, oscillator strengths ($f_{osc} > 0.01$) and MO contributions (> 10%) for **FP2**.

No.	E / eV	f_{osc}	Major Contributions
4	2.64	0.025	HOMO→LUMO (81%)
5	2.66	0.018	H-1→LUMO (77%)
7	2.73	0.031	H-2→LUMO (29%), HOMO→L+1 (46%)
9	2.81	0.088	H-2→L+2 (10%), H-1→L+1 (25%), HOMO→L+1 (16%), HOMO→L+2 (27%)
10	2.83	0.030	H-2→L+1 (33%), H-1→L+2 (18%), HOMO→L+2 (28%)
11	2.83	0.070	H-1→L+2 (49%), HOMO→L+2 (27%)
12	2.92	0.130	H-2→L+2 (42%), H-1→L+1 (37%)
13	3.03	0.027	H-2→L+1 (10%), H-2→L+5 (11%), H-2→L+6 (24%)

190

14	3.08	0.015	H-2→L+2 (18%), H-2→L+7 (22%), HOMO→L+6 (11%)
15	3.12	0.010	H-1→L+4 (19%), H-1→L+7 (41%)
18	3.40	0.013	H-1→L+3 (36%), HOMO→L+4 (29%)
21	3.46	0.043	H-3→LUMO (48%), H-1→L+5 (14%)
22	3.47	0.018	H-3→LUMO (17%), H-1→L+4 (14%)
23	3.49	0.059	H-4→LUMO (24%), H-1→L+5 (27%)
24	3.50	0.016	H-5→LUMO (15%), H-4→LUMO (20%), H-2→L+5 (20%)
25	3.51	0.037	H-4→LUMO (22%), H-2→L+5 (26%), H-2→L+6 (10%), H-1→L+4 (13%)
26	3.53	0.020	H-6→LUMO (25%), H-5→LUMO (36%), H-1→L+4 (11%)
28	3.55	0.029	H-6→LUMO (50%), H-5→LUMO (35%)
29	3.57	0.060	H-3→L+1 (84%)
31	3.60	0.146	H-4→L+1 (33%), H-3→L+2 (38%)
32	3.60	0.129	H-4→L+1 (41%), H-3→L+2 (29%)
33	3.63	0.060	H-4→L+2 (83%)
34	3.64	0.013	H-6→L+1 (15%), H-5→L+1 (65%)
35	3.65	0.099	H-6→L+1 (70%), H-5→L+1 (10%)
36	3.66	0.037	H-8→LUMO (36%), H-5→L+2 (48%)
37	3.67	0.128	H-8→LUMO (12%), H-6→L+2 (68%)
38	3.69	0.184	H-8→LUMO (29%), H-6→L+2 (14%), H-5→L+2 (41%)
39	3.71	0.026	H-7→L+1 (84%)
40	3.74	0.017	H-7→L+2 (87%)
41	3.78	0.025	H-8→L+1 (78%)
42	3.78	0.035	H-9→LUMO (72%)
43	3.82	0.089	H-8→L+2 (86%)
44	3.84	0.035	H-11→LUMO (62%), H-10→LUMO (15%)
45	3.85	0.086	H-11→LUMO (20%), H-10→LUMO (60%)
47	3.89	0.013	H-13→LUMO (14%), H-12→LUMO (38%), H-10→LUMO (10%)
48	3.90	0.025	H-12→LUMO (10%), H-9→L+1 (58%), H-9→L+2 (17%)
49	3.92	0.016	H-13→LUMO (36%), H-12→LUMO (23%)
50	3.92	0.016	H-14→LUMO (44%), H-11→L+2 (17%)
51	3.94	0.029	H-10→L+1 (15%), H-9→L+2 (17%), H-1→L+8 (45%)
52	3.95	0.013	H-11→L+1 (27%), H-10→L+1 (23%), H-1→L+8 (35%)
55	3.97	0.017	H-13→LUMO (12%), HOMO→L+9 (51%)

TDDFT simulations of the electronic absorption spectra furthermore predict stronger vertical excitations ($f_{osc} > 0.05$) at lower energy (2.76-2.87 eV; see Table 4.3) for **FP1** compared with **FP2** (2.81-2.92 eV; see Table 4.4). This change in the strength of excitations at low energy appears to be one of the causes of the counterintuitive blue-shifted λ_{max} for the complex bearing the larger ligand π-system. Overall, in both systems, TDDFT assigned the lowest energy absorption manifold to have significant metal-to-ligand charge transfer character (MLCT; see Figures 4.6-4.7 for electron-hole density maps). The acceptor orbitals in both cases are ligand-centred with $\pi^*_{C=N}$ character (LUMO to LUMO+2) for both cations. Formally metal-centred (MC) excited states gain intensity ($f_{osc} > 0.01$) at slightly higher energy than the MLCT states. This suggests low-lying MC states could provide a non-radiative deactivation pathway for these complexes.[144]
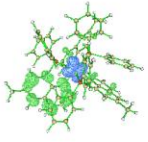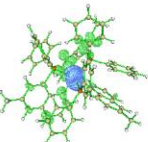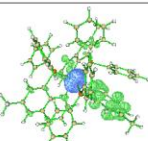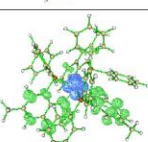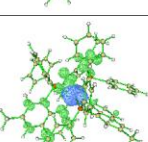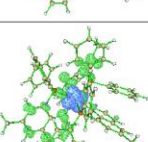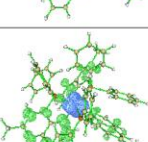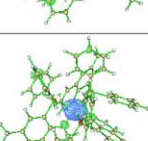
State	Electron-Hole Density Map	Character Assignment
5		MLCT
6		MLCT
7		MLCT
9		MLCT
10		MLCT
11		MLCT
12		MLCT
13		MC

Figure 4.6. Electron depletion (blue) and gain (green) density maps and assigned characters of the relevant electronic excitations (f_{osc} > 0.01; isosurface = 0.002) in the lowest energy absorption band of **FP1**.
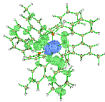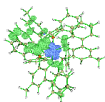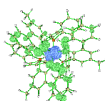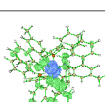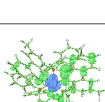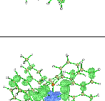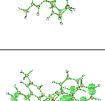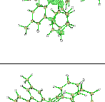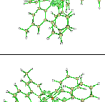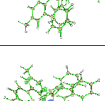
State	Electron-Hole Density Map	Character Assignment
4		MLCT
5		MLCT
7		MLCT
9		MLCT
10		MLCT
11		MLCT
12		MLCT
13		MC
14		MC
15		MC

Figure 4.7. Electron depletion (blue) and gain (green) density maps and assigned characters of the relevant electronic excitations ($f_{osc} > 0.01$; isosurface = 0.002) in the lowest energy absorption band of **FP2**.

The additional π^* orbitals of **FP2** discussed above lie below the formally e_g orbital set and are predicted to participate in excitations at higher energies (E > 3.2 eV; λ < 390 nm). These additional π^* orbitals have a considerable impact on the electronic transitions in this region of the spectrum. The formally MC states ($^1S_{13\text{-}15}$, Table 4.4) of **FP2** are higher in intensity than those of **FP1** ($^1S_{13}$, Table 4.3), as electron-hole pair contributions of MLCT character considerably mix with these states. The additional electron-hole pair contributions can be attributed to the 't_{2g}' donor and the additional π^* acceptor orbitals (LUMO+3 to LUMO+5). Additional MLCT states, with the three new π^* orbitals serving as acceptor orbitals, dominate the near-UV region of the spectrum. Consequently, absorbance in this region becomes more significant in **FP2**, consistent with the increased absorptive cross-section in the near-UV region. Increasing the molar absorptivity across the visible region of the electromagnetic spectrum is particularly important in the design of light harvesting dyes, for which expansion of the π-system of the ligand (**FP1** vs **FP2**) through benzannulation provides such a means.

It is also instructive to compare the observation of a blue-shifted λ_{max} for **FP2** compared with **FP1** with other transition metal complexes of pairs of phenanthridinyl and quinolinyl-containing ligands similarly related by ligand benzannulation. The counter-intuitive shift of the lowest energy absorption to higher energy for the complex comprised of a ligand with a larger π-system, **FP2**, stands in contrast to trends observed for Cu(I) complexes of related quinoline/phenanthridine-based $P{\wedge}N$ ligands.[63] There, a bathochromic shift of the lowest energy MLCT absorptions is observed for dimeric $(P{\wedge}N)_2Cu_2X_2$ complexes of **P2** compared with those of **P1**. In comparison, Group 10 complexes of pincer-like tridentate $N{\wedge}N{^-}{\wedge}N$ ligands bearing either quinolinyl or phenanthridinyl arms show nearly identical λ_{max} values that were invariant in the

195

face of increasing π-extension.[64] Isoenergetic lowest energy absorptions were also observed for pseudo-octahedral Re(CO)$_3$X (X = Br, Cl) complexes of bidentate (4-amino)phenanthridine and (8-amino)quinoline ligands.[65]

In each of these scenarios the different impacts of ligand benzannulation cannot be solely connected to the (de)stabilization of the frontier orbitals, as suggested by some other studies.[67–69] Rather, the particular benzannulation of quinoline to phenanthridine (3,4-benzoquinoline) can also strongly impact the oscillator strengths of the lowest energy transitions. This can have a less intuitive influence on the overall absorption profile. Changing from quinoline to phenanthridine in the aforementioned Group 11 (P^N)$_2$Cu$_2$X$_2$ series has a predictable (if small) effect – the lowest energy absorption tails to yet longer wavelengths.[63] In comparison, Group 10 complexes of tridentate phenanthridine/quinoline-containing ligands have nearly isoenergetic λ_{max} values.[64] There, while benzannulation does lower the energy of the LUMO, the HOMO-LUMO transition is effectively turned-off in phenanthridinyl-containing complexes in favor of higher energy HOMO-LUMO+1 transitions.

Similarly, the LUMO energies of both phenanthridinyl and quinolinyl supported (N^N)Re(CO)$_3$X complexes are calculated to lie at nearly identical energies.[65] In that case, the major difference observed was in the intensity of λ_{max}, attributed to a more purely MLCT-type excitation at lower energy for the phenanthridine-supported complex compared with the quinoline-ligated analog, similar to the findings reported **FP1** and **FP2**. With the Re(I) complexes, however, an additional factor contributes to the observed optical properties. As mentioned in Chapter 2, bezannulation can influence the S_n-T_n mixing in (N^N)Re(CO)$_3$X (**Re1** and **Re2** in Chapter 2) Within the framework of the spin-free approximation, the electronic states can be classified as

singlets ($S = 0$, $M = 1$) and triplets ($S = 1$, $M = 3$). Chemically relevant information can then be extracted, providing a molecular orbital character or the electron-hole pair distribution of the resulting SOC-excited states that form upon photoexcitation. Molecular orbital (MO) diagrams and orbital contour plots for the spin-free singlet ground states of **Re1** and **Re2** are shown in Figure 4.8. The three highest energy occupied MOs for both complexes (HOMO, HOMO-1 and HOMO-2) are predominantly localized on the d^6 rhenium centres, with some (d-π^*) back-bonding interactions with two of three carbonyl ligands evident for each MO. The HOMO and HOMO-1 additionally exhibit anti-bonding (d-p)π^* character with the chloride ligand, as befits a π-donor substituent. The mixing of the filled 't_{2g}-like' orbitals with ligand-based lone-pair and π^*-orbitals become significant in complexes containing π-donor ligands (*e.g.* halides, amides, alkoxides, *etc.*).[145]
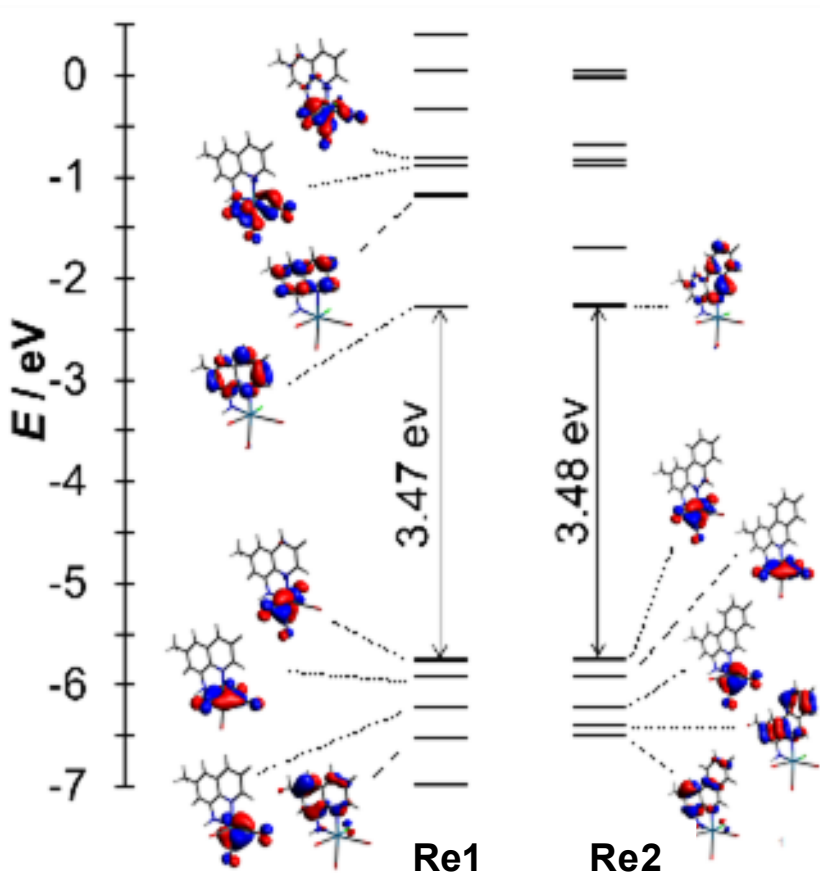
Figure 4.8. Molecular orbital diagrams of the spin free singlet ground states of **Re1** and **Re2** (RIJCOSX-ZORA-SMD-B3LYP*-D3(BJ)/def2-TZVP+SARC-ZORA-TZVP//SMD-PBE0-D3(BJ)/def2-SVP). Orbital contour plots (isosurface = 0.05) are shown for the orbitals most relevant to the transitions observed by UV-Vis absorption spectroscopy.

The highest occupied molecular orbitals of **Re1** and **Re2** (Figure 4.8) lie at similar energies due to their similar character; the identity of the nitrogenous chelate does not appear to significantly perturb the energies of the HOMO and HOMO-1. The HOMO-3 (and HOMO-4 for **5**) is comprised of the π system of the heterocyclic ligands and is higher in energy for the larger phenanthridinyl π-system. As expected, the LUMO is localized on the heterocyclic ligands, and

198

heavily at the C=N sub-unit of each heterocyclic ligand. Phenanthridines exhibit more localized 'imine-like' character at the 6-position C=N compared with closely related heterocycles, due to the position of benzannulation maximizing aromatic character within the two flanking six-carbon rings.[146] Previously reported phenanthridine-containing complexes of lighter transition metal complexes have been shown to exhibit similar character to the LUMO, which engender rich photophysical properties to the complexes.[147–153] Accordingly, the LUMO of **Re2** is more localized at the C=N of the heterocycle compared with the LUMO of **Re1** (28% vs. 36%; see Tables 4.3 and 4.4).

Despite the difference in LUMO character between **Re1** and **Re2**, the energies of the LUMO for both complexes are essentially the same (Figure 4.8) resulting in comparable HOMO-LUMO energy gaps. This is consistent with the experimental absorbance spectra of **Re1** and **Re2** which show similar spectral features and energies. A comparable effect was observed in Group 10 complexes of bis(quinolinyl)amides and their corresponding benzannulated, phenanthridine-containing congeners[147]. For the compounds here in particular, both spectra contain a weak absorbance band covering the entire visible region of the electromagnetic spectrum with maximum at 535 nm and 538 nm (~2.31 eV) for **Re1** and **Re2**, respectively. The effect of benzannulation seems to be more drastic with the energies of LUMO+1, where a significant stabilization of the energy of LUMO+1 in **Re2** compared to **Re1** (-1.7 eV for **Re2** vs -1.2 eV for **Re1**). In both cases, the LUMO+1 is largely of *N*-heterocycle anti-bonding character, delocalized largely in the aryl fragment of the *N*-heterocycle. The increased in delocalization with more bonding character to the LUMO+1 of **Re2** could be a reason for the observed stabilization with respect to **Re1**.

As discussed in Section 4.3.7, inclusion of spin-orbit coupling is necessary in simulating the spectra of **Re1** and **Re2**. This is also the case for other complexes that incorporates heavier transition metals. In the case of SOC-corrected TDDFT, the calculated energies of the dominant transition in the lowest energy absorption band for **Re1** (2.27 eV) and **Re2** (2.28 eV) is shifted by about 0.04 eV compared with their respective experimental spectra (2.31 eV for both complexes). Further analysis on the SOC-corrected spectra of **Re1** and **Re2** indicate that the broad peak at 2.31 eV is largely dominated by the SOC-state 2 for both **Re1** and **Re2**. Composition analysis reveals that triplet states contribute significantly to these SOC-states (**Re1**: $0.56T_2 + 0.40T_4$; **Re1** and **Re2**: $0.82T_2 + 0.14T_5$). Singlet state contribution to these SOC-states for **Re1** ($S_2 \sim 1\%$) and **Re2** ($S_1 \sim 1\%$) is minor resulting in the observed weak molar absorptivities ($\varepsilon < 250 \text{ M}^{-1} \text{ cm}^{-1}$). The molecular orbital characters of the contributing spin-free excited triplet states indicate that this SOC-state has mixed π-π^* and $ML_{quin}CT$ in **Re1** (Table 4.5), and purely $ML_{phen}CT$ in **Re2** (Table 4.6), indicating significant configurational interactions in **Re1** containing the smaller 6-methyl-(8-amino)quinoline ligand. The extent of the metal-to-ligand and intraligand (MLCT-IL) configurational interaction depends on the complex structure and the nature of the ligands.[154,155] This indicates that there is a larger redistribution of electron density upon excitation at 2.31 eV for **Re2** than in **Re1**, which could have significant effects in the excited state dynamics and reactivity of the complexes.[154]

Table 4.5. MO characters of the lowest energy main scalar and spin orbit transitions for **Re1**.

Scalar (Singlet-Singlet TDDFT)				
State	**E / eV**	f_{osc}	**Composition**	**Character**
1	3.03	0.032	H-1->L (16%), H->L (82%)	$^1ML_{quin}CT$
2	3.12	0.033	H-1->L (83%), H->L (15%)	$^1ML_{quin}CT$
4	4.02	0.011	H-3->L (23%), H->L+1 (49%), H->L+2 (16%)	$^1\pi\text{-}\pi^*, ^1ML_{quin}CT, ^1ML_{CO}CT$
5	4.04	0.039	H-3->L (53%), H->L+2 (31%)	$^1\pi\text{-}\pi^*, ^1ML_{CO}CT$
8	4.22	0.004	H-1->L+2 (37%), H-1->L+3 (40%), H->L+3 (11%)	$^1ML_{CO}CT$

Scalar (Singlet-Triplet TDDFT)				
State	**E / eV**	f_{osc}	**Composition**	**Character**
1	2.43	0.000	H-3->L (20%), H->L (73%)	$^3\pi\text{-}\pi^*, ^3ML_{quin}CT$
2	2.29	0.000	H-3->L (11%), H-1->L (73%), H->L (14%)	$^3\pi\text{-}\pi^*, ^3ML_{quin}CT$
3	2.82	0.000	H-3->L (57%), H-1->L (22%), H->L(12%)	$^3\pi\text{-}\pi^*, ^3ML_{quin}CT$
4	2.33	0.000	H-2->L (93%)	$^3ML_{quin}CT$
8	3.86	0.000	H-1->L+2 (35%), H-1->L+3 (35%), H->L+2 (16%)	$^3ML_{CO}CT$
9	3.98	0.000	H-2->L+2 (30%), H-1->L+2 (26%), H-1->L+3 (29%)	$^3ML_{CO}CT$
11	4.06	0.000	H-2->L+2 (50%), H-1->L+2 (13%), H-1->L+3 (22%)	$^3ML_{CO}CT$
28	4.03	0.000	H-3->L+2 (91%)	$L_{quin}L_{CO}CT$

Spin-Orbit Coupling (SOC-TDDFT)				
State	**E / eV**	f_{osc}	**Composition**	**Character**
2	2.27	0.002	S_2(1%), T_1(1%), T_2(56%), T_4(40%)	Mixed $ML_{quin}CT$, $\pi\text{-}\pi^*$
13	3.13	0.033	S_1(92%), T_3(5%)	Mixed $ML_{quin}CT$, $^3\pi\text{-}\pi^*$
14	3.21	0.028	S_2(97%)	$ML_{quin}CT$
43	4.09	0.015	S_4(46%), S_5(7%), T_9(1%), T_{28}(3 8%)	Mixed $ML_{CO}CT$, $\pi\text{-}\pi^*$, $L_{quin}L_{CO}CT$
47	4.11	0.030	S_4(5%), S_5(54%), S_8(2%), T_8(1%), T_9(5%), T_{11}(12%), T_{28}(14%)	$ML_{quin}CT$, $\pi\text{-}\pi^*$, Mixed $ML_{CO}C$, $L_{quin}L_{CO}CT$

Table 4.6. MO characters of the lowest energy main scalar and spin orbit transitions for **Re2**.

Scalar (Singlet-Singlet TDDFT)

State	E / eV	f_{osc}	Composition	Character
1	3.05	0.036	H-1→L (19%), H→L (78%)	^{1}ML$_{phen}$CT
2	3.16	0.057	H-1→L (80%), H→L (17%)	^{1}ML$_{phen}$CT
7	3.97	0.108	H-4→L (33%), H-3→L (41%)	$^1\pi$-π*

Scalar (Singlet-Triplet TDDFT)

State	E / eV	f_{osc}	Composition	Character
2	2.29	0.000	H-1→L (91%)	^{3}ML$_{phen}$CT
3	3.01	0.000	H-3→L (65%), H→L (16%)	$^3\pi$-π*, ^{3}ML$_{phen}$CT
4	3.17	0.000	H-4→L (58%), H-3→L (17%)	$^3\pi$-π*
5	2.48	0.000	H-2→L (89%)	^{3}ML$_{phen}$CT

Spin-Orbit Coupling (SOC-TDDFT)

State	E / eV	f_{osc}	Composition	Character
2	2.28	0.002	T$_2$ (82%), T$_5$ (14%), S$_1$ (1%)	ML$_{phen}$CT
19	3.11	0.035	S$_1$ (72%), T$_3$ (15%), T$_4$ (9%), S$_2$ (1%)	ML$_{phen}$CT,π-π*
20	3.21	0.013	T$_4$ (74%), S$_2$ (21%), T$_3$ (3%)	ML$_{phen}$CT,π-π*
22	3.22	0.011	T$_4$ (85%), S$_1$ (8%), S$_2$ (6%)	ML$_{phen}$CT,π-π*
23	3.23	0.026	S$_2$ (66%), T$_4$ (27%), S$_1$ (2%), T$_3$ (2%)	ML$_{phen}$CT,π-π*
59	4.02	0.104	S$_7$ (96%)	π-π*

The optical properties of Pt(II) complexes supported by diarylamido ligands **N1-3** are invariant with benzannulation, presenting another unusual behaviour with benzannulation. Here, the main contributor to the lowest energy absorption is from the HOMO→LUMO+1 transition.[38] Population analysis of both these orbitals revealed only small contributions of the carbon at the

site of substitution. For example, there is no orbital density present at the carbons directly bonded to the methyl groups, nor at the methyl groups themselves, in the HOMOs of **Pt1-3**. In yet another twist, quinoline to phenanthridine π-extension has a more pronounced impact on the phosphorescence from Pt(II) congeners of diarylamido ligands **Pt1-3**, which is blue-shifted in complexes of the benzannulated phenanthridinyl-based complexes, a phenomenon ascribed to the enhanced rigidity of the larger *N*-heterocyclic donor arms.[156] A similar effect has been observed in $(P^\wedge N)_2Cu_2X_2$ complexes of **P1** and **P2** with emission from **P2** blue-shifted compared with **P1**. The same enhanced rigidity in benzannulated analogues contributes to the hypsochromic shift. Collectively, these results reveal that ligand benzannulation can influence orbital energies, oscillator strengths of transitions and structural rigidity, with a range of consequences for photophysical properties of coordination complexes.

4.3.3 Counteracting Impact of Weak Ligand Field with Covalency

In section 2.3.3, Fe(II) complexes of asymmetric diarylamido ligands (neutral, **Fe1-3**; monocation, **Fe4-6**; see Figure 2.8, Chapter 2) display panchromatic absorption (Figure 4.9). To explain this observation, DFT and TDDFT were performed to investigate their electronic structure and excited states. Figure 2.7 in Chapter 2 illustrates the two factors that contribute to the observed properties of these complexes. This description of metal-ligand bonding is supported by DFT calculations which corroborate the mixed character of the occupied frontier orbitals of **Fe3**/**Fe6** and identify $d_{x^2-y^2}$ and d_{z^2} as the LUMO+10 and LUMO+11, respectively, for **Fe3** (Figure 4.7; see also Tables 4.7-4.10 and Figures 4.10-4.13 and Section 4.3.5 for a discussion of the choice of functional). In comparison, both the degenerate HOMO and HOMO-1 for **Ga1** have dominant N_{amido} character with no contribution from the metal.
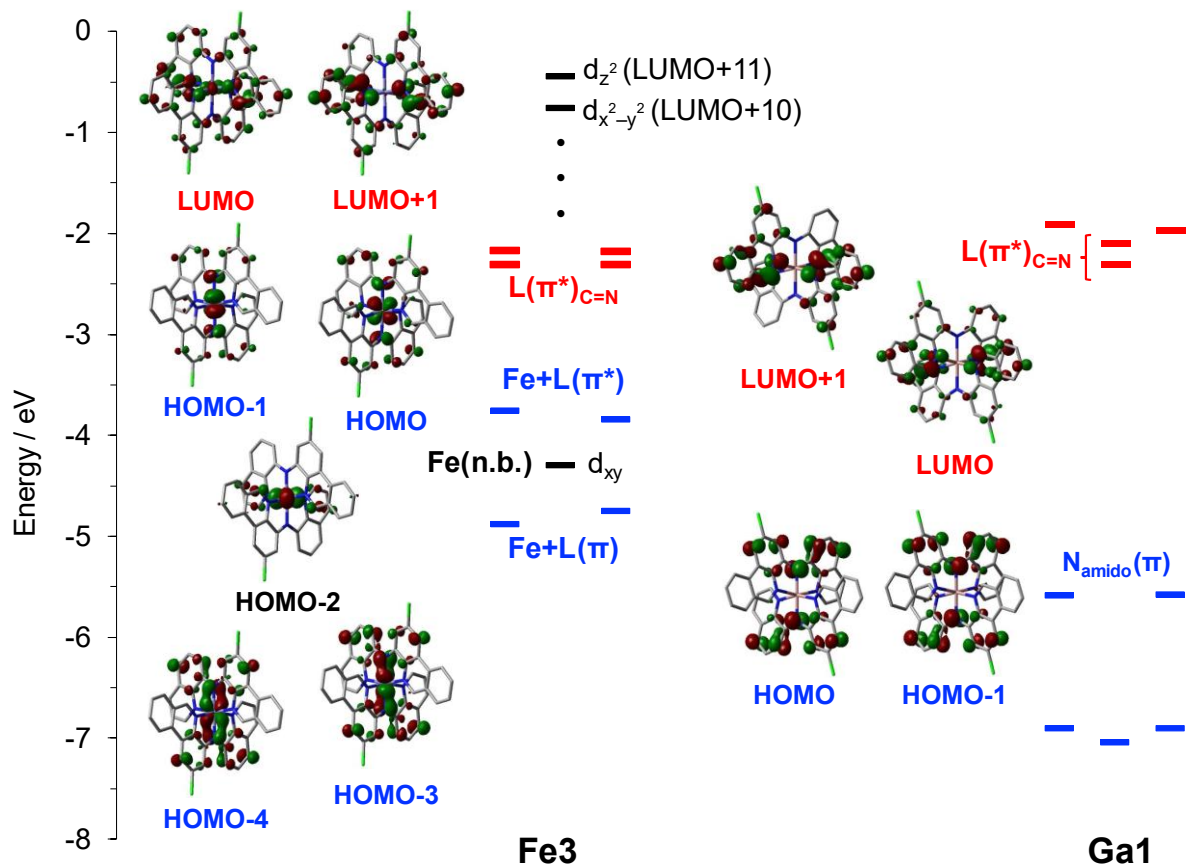
Figure 4.9. Selections from the ground-state MO diagrams of **Fe3** and **Ga1** comparing the relative energies of the metal d-orbitals, N_{amido} lone pairs, and ligand-based π^* orbitals (highlighted in red). MOs are shown with isosurface values of 0.04 and at the SMD-M06L/6-31+G(d,p)//SMD-O3LYP/6-31+G(d,p) level of theory.

Table 4.7. Fragment contributions (in %) to select ground state MOs of **Fe3** [SMD-rM06L/6-31+(d,p)//SMD-rO3LYP/6-31+G(d,p)].

MOs	Fe	N^{amide}	$HC=N^{phen}$	$HC=N^{quin}$	Ar^{phen}	Ar^{quin}	Cl
L+11	66	8	4	4	24	11	5
L+10	44	1	10	11	8	4	0
L+3	2	2	7	21	25	43	0
L+2	5	2	14	16	34	28	0
L+1	1	1	27	6	48	16	1
LUMO	12	1	18	9	34	25	1
HOMO	51	9	5	4	15	16	0
H-1	58	9	4	4	12	13	0
H-2	67	1	8	6	9	8	0
H-3	26	12	3	3	25	29	1
H-4	31	11	3	3	24	27	1

Table 4.8. Fragment contributions (in %) to select ground state MOs of **Ga1** [SMD-rPBE0/6-31+(d,p)//SMD-rO3LYP/6-31+G(d,p)].

MOs	Ga	N^{amide}	$HC=N^{phen}$	$HC=N^{quin}$	Ar^{phen}	Ar^{quin}	Cl
L+3	1	1	14	19	28	35	1
L+2	1	1	1	28	8	61	0
L+1	1	1	36	0	58	2	2
LUMO	1	1	23	11	37	26	1
HOMO	1	19	3	3	34	38	1
H-1	1	19	4	3	35	38	1
H-2	0	0	9	0	79	4	7
H-3	0	1	11	1	78	3	7
H-4	0	2	3	5	55	34	1

Table 4.9. Fragment contributions (in %) to select ground state α-MOs of **Fe6** [SMD-uM06L/6-31+G(d,p)//SMD-uO3LYP/6-31+G(d,p)].

α-MOs	Fe	N^{amide}	$HC=N^{phen}$	$HC=N^{quin}$	Ar^{phen}	Ar^{quin}	Cl
L+4	5	2	5	3	80	6	0
L+3	2	2	15	17	30	34	1
L+2	3	2	18	17	31	29	1
L+1[48]	2	1	21	11	37	27	1
LUMO	6	1	18	12	32	30	1
HOMO	15	17	4	3	29	31	0
H-1	21	18	4	3	26	29	0
H-2	64	1	8	6	11	10	0
H-3	63	4	3	3	12	13	1
H-4	6	0	7	0	78	1	7
H-7	51	3	3	2	32	8	2

Table 4.10. Fragment contributions (in %) to select ground state β-MOs of $[Fe(^{Cl}L)_2]^+$ [SMD-uM06L/6-31+G(d,p)//SMD-uO3LYP/6-31+G(d,p)].

β-MOs	Fe	N^{amide}	$HC=N^{phen}$	$HC=N^{quin}$	Ar^{phen}	Ar^{quin}	Cl
L+4	2	2	11	20	24	41	0
L+3	6	3	15	17	30	29	0
L+2	1	1	25	8	43	21	1
L+1	9	1	19	10	34	27	1
LUMO	43	11	5	4	18	19	0
HOMO	40	15	4	3	19	20	0
H-1	69	1	8	6	8	8	0
H-2	45	9	3	3	18	22	1
H-3	36	9	3	3	23	25	1
H-4	1	0	7	0	83	1	7
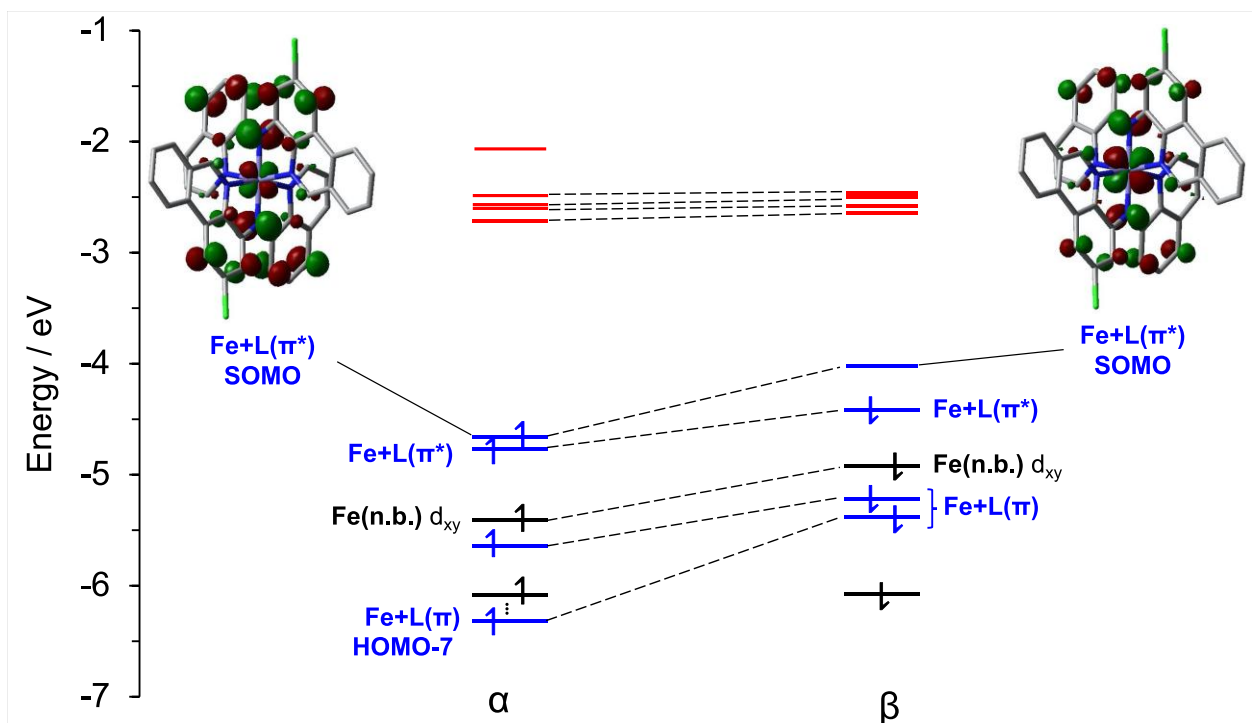
Figure 4.10. Select ground state MO energy and correlation (---) diagrams and α/β SOMO isosurfaces (isovalue = 0.04) for **Fe6** [SMD-uM06L/6-z31+G(d,p)//SMD-uO3LYP/6-31+G(d,p)].
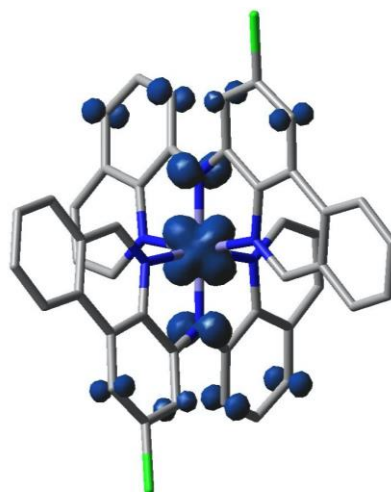
Spin Density	Fragment
Mulliken	**Fe** 0.59 **N**$_{amido}$ 0.14
Löwdin	**Fe** 0.59 **N**$_{amido}$ 0.16

Figure 4.11. Mulliken/Löwdin spin density (isosurface = 0.004) of **Fe6** [SMD-uM06L/6-31+G(d,p)//SMD-uO3LYP/6-31+G(d,p)].

LUMO+1   **LUMO**

**HOMO
(SOMO)**   **HOMO-1**   **HOMO-2**   **HOMO-3**

HOMO-4   **HOMO-5**   **HOMO-6**   **HOMO-7**
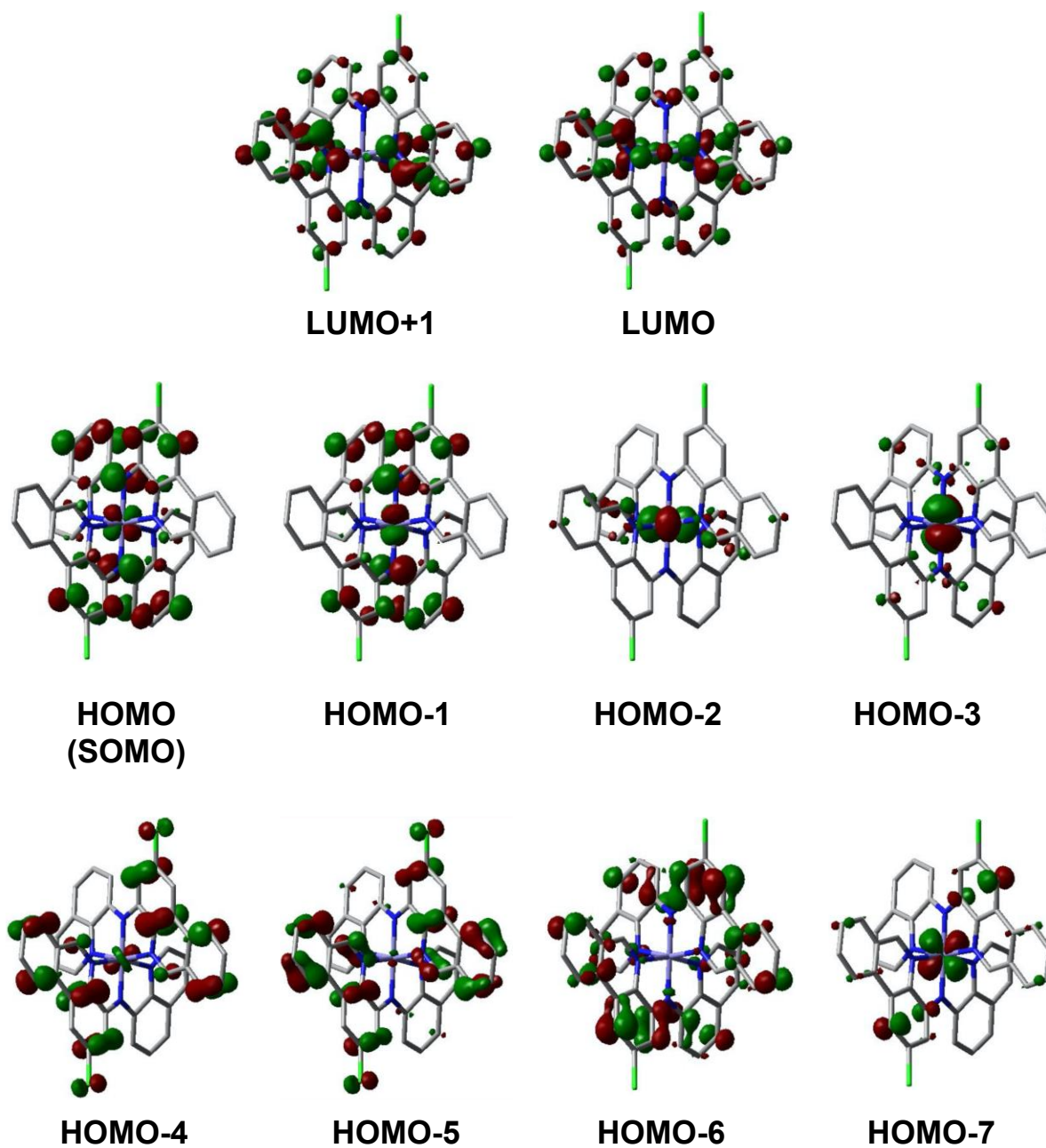
Figure 4.12. Ground-state α-MOs of **Fe6** (isosurface = 0.04; SMD-M06L/6-31+G(d,p)//SMD-

uO3LYP/6-31+G(d,p)).
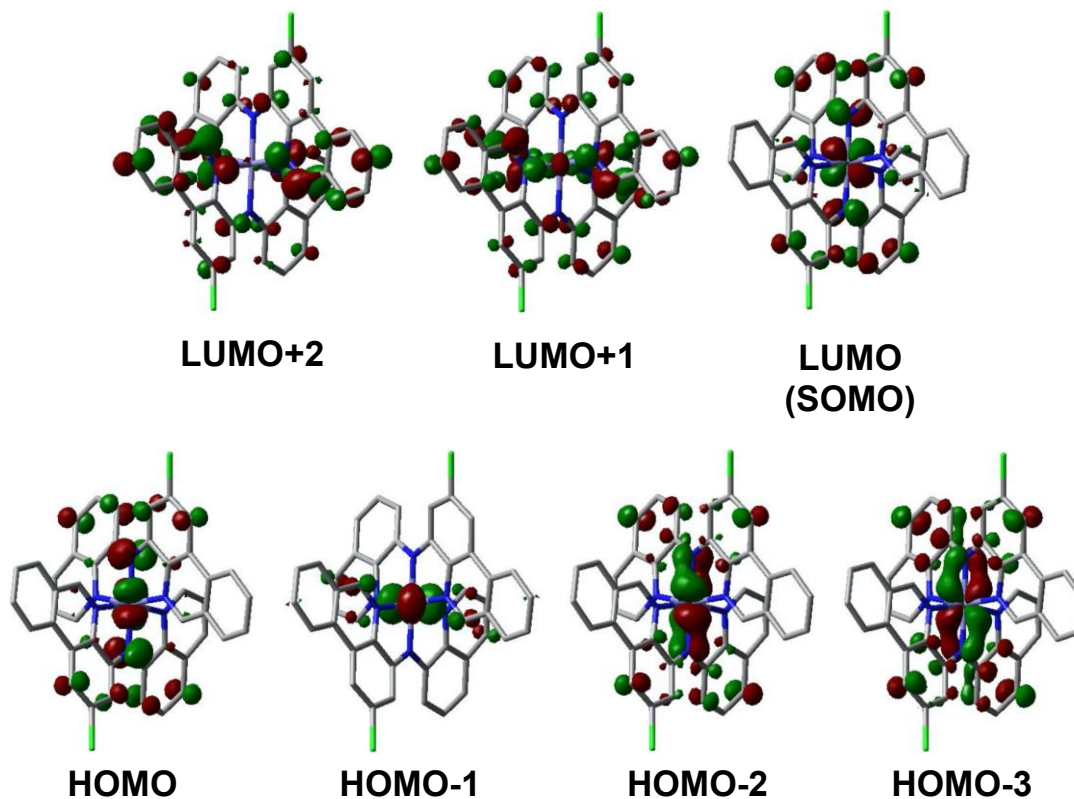
Figure 4.13. Ground-state β-MOs of **Fe6** (isosurface = 0.04; SMD-uM06L/6-31+G(d,p)//SMD-uO3LYP/6-31+G(d,p)).

Time-dependent DFT (TD-DFT) simulations (Figure 4.14) revealed the lowest-energy spectral manifold (650-900 nm) is dominated by six key transitions, in which electron density is relocated from occupied Fe+L(π*) anti-bonding orbitals (HOMO, HOMO-1) to *N*-heterocycle ligand-based π*-acceptor MOs (LUMO through to LUMO+3; Table 4.11) and can be described as '$\pi_{anti\text{-}bonding}$-to-ligand charge-transfer' (PALCT) in character.[157] In comparison, the prominent absorption bands in the visible region of the spectrum of **Ga1** are assigned to electronic excitations involving the degenerate HOMO and HOMO-1 (Figure 4.15, Table 4.12), which contain significant contributions from the N_{amido} lone pairs (19%; Table 4.10), and the π*-orbitals of the

phenanthridine arms (LUMO, LUMO+1). Thus, the low energy absorptions of **Ga1** have mixed intra/inter-ligand charge-transfer (ILCT) character.
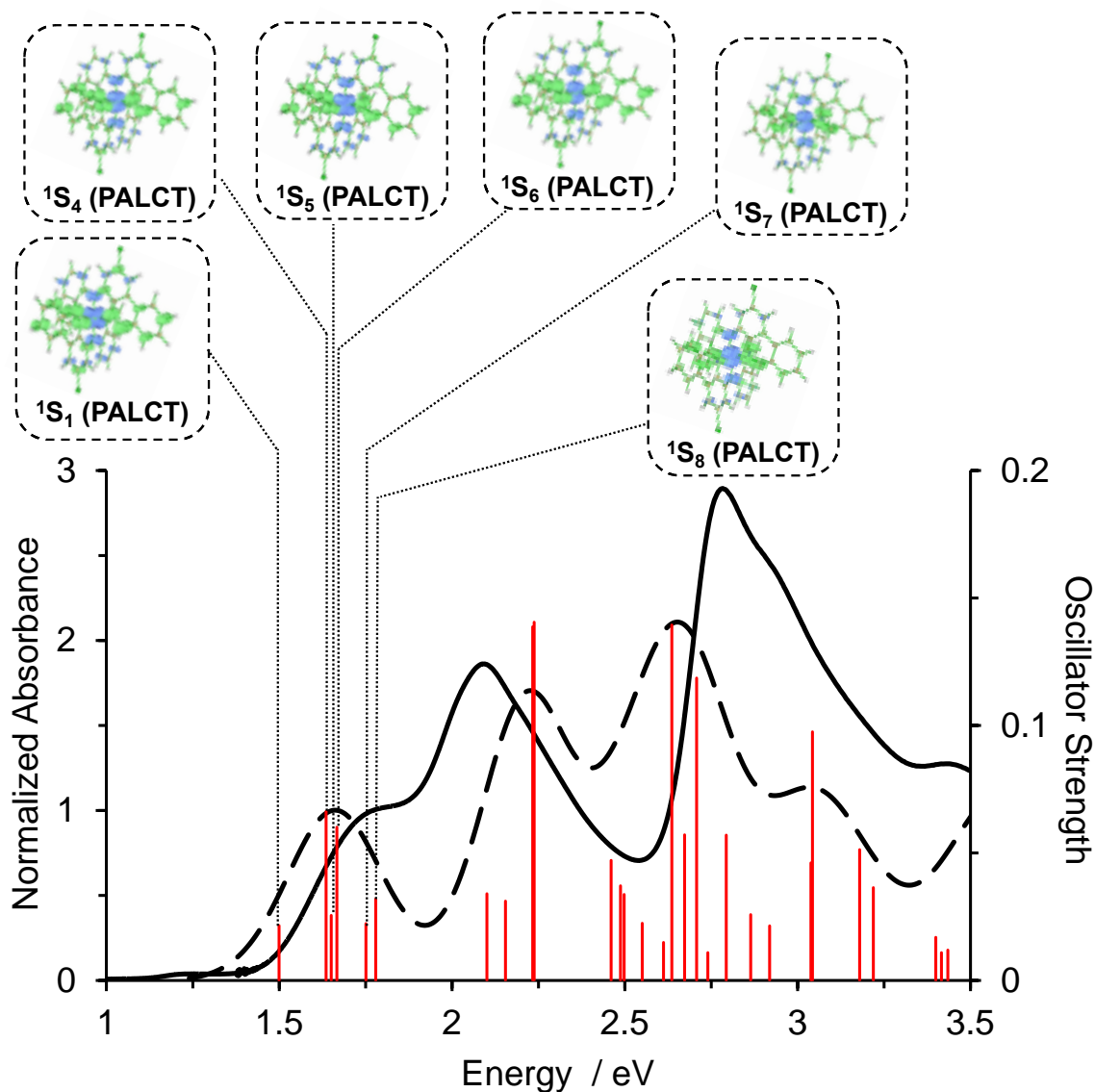
Figure 4.14. TD-DFT predicted vertical excitation energies (red) and simulated spectrum (---) superimposed on the experimental spectrum (−) of **Fe3** in CH_3CN (TD-SMD-rM06L/6-31+G(d,p)//SMD-rO3LYP/6-31+G(d,p); FWHM = 3000 cm^{-1}; $f_{osc} \geq 0.01$). Electron density gain (green) and depletion (blue) distribution maps (isosurface = 0.002) of the dominant π^*(Fe+N_{amido})-to-$(\pi_{L,C=N})^*$ charge transfer (PALCT) excitations are also shown.

Table 4.11. TD-DFT vertical excitation energies, oscillator strengths ($f_{osc} \geq 0.01$), and MO contributions (> 10%) for **Fe3** [TD-SMD-rM06L/6-31+G(d,p)//SMD-rO3LYP/6-31+G(d,p)]

No.	E / eV	f_{osc}	Major contributions
1	1.50	0.022	H-1→L (16%), H→L+1 (83%)
4	1.64	0.066	H-1→L+1 (41%), H-1→L+3 (16%), H→L (25%), H→L+2 (14%)
5	1.65	0.026	H-1→L+1 (16%), H-1→L+3 (17%), H→L (10%), H→L+2 (54%)
6	1.67	0.060	H-1→L (51%), H-1→L+2 (24%), H→L+1 (12%)
7	1.75	0.022	H-1→L+2 (62%), H→L+3 (26%)
8	1.78	0.032	H-1→L+3 (62%), H→L+2 (25%)
11	2.10	0.034	H-2→L+1 (82%), H-1→L+5 (10%)
13	2.15	0.031	H-1→L+5 (86%)
14	2.23	0.139	H-2→L+3 (88%)
15	2.24	0.141	H-2→L+2 (88%)
16	2.46	0.047	H-2→L (59%)
17	2.49	0.037	H-3→L+1 (83%)
18	2.50	0.034	H-4→L+1 (11%), H-3→L (77%)
20	2.55	0.022	H-2→L+4 (48%), H→L+6 (43%)
23	2.61	0.015	H-4→L+3 (14%), H-3→L+2 (83%)
25	2.64	0.139	H-4→L+1 (77%), H-3→L (12%)
26	2.67	0.057	H-4→L (35%), H-4→L+2 (12%), H-3→L+3 (13%), H→L+7 (22%)
27	2.71	0.119	H-4→L (15%), H-2→L+5 (14%), H-1→L+6 (13%), H→L+7 (26%)
28	2.74	0.011	H-1→L+7 (95%)
29	2.79	0.057	H-4→L+3 (79%), H-3→L+2 (11%)
32	2.86	0.026	H-4→L+2 (25%), H-1→L+9 (20%), H→L+8 (25%)
33	2.92	0.021	H→L+9 (59%), H→L+10 (26%)
36	3.04	0.046	H-1→L+8 (59%), H-1→L+11 (16%), H→L+10 (12%)
37	3.04	0.098	H-3→L+4 (34%), H-1→L+9 (39%)
41	3.18	0.051	H-4→L+4 (75%), H-3→L+5 (18%)
43	3.22	0.036	H-4→L+5 (88%)
44	3.40	0.017	H-1→L+10 (22%), H→L+11 (43%), H→L+13 (26%)
45	3.42	0.011	H-2→L+9 (21%), H-1→L+13 (10%), H→L+10 (10%), H→L+12 (45%)
46	3.43	0.012	H-2→L+9 (60%), HOMO→L+12 (29%)
51	3.54	0.026	H-6→L+1 (24%), H-5→LUMO (49%), H-1→L+13 (20%)
52	3.54	0.024	H-6→L+1 (23%), H-1→L+11 (10%), H-1→L+13 (53%)
53	3.55	0.022	H-6→LUMO (32%), H-5→L+1 (28%)
54	3.56	0.011	H-3→L+6 (46%), HOMO→L+14 (23%)
55	3.59	0.031	HOMO→L+14 (61%)
59	3.64	0.021	H-7→LUMO (30%), H-6→L+1 (10%), H-5→L+2 (50%)
64	3.73	0.027	H-4→L+6 (33%), H-3→L+7 (25%), H→L+15 (29%)
65	3.74	0.020	H-4→L+6 (14%), H-3→L+7 (11%), H→L+15 (69%)
67	3.76	0.034	H-8→L+3 (14%), H-7→L+2 (69%)
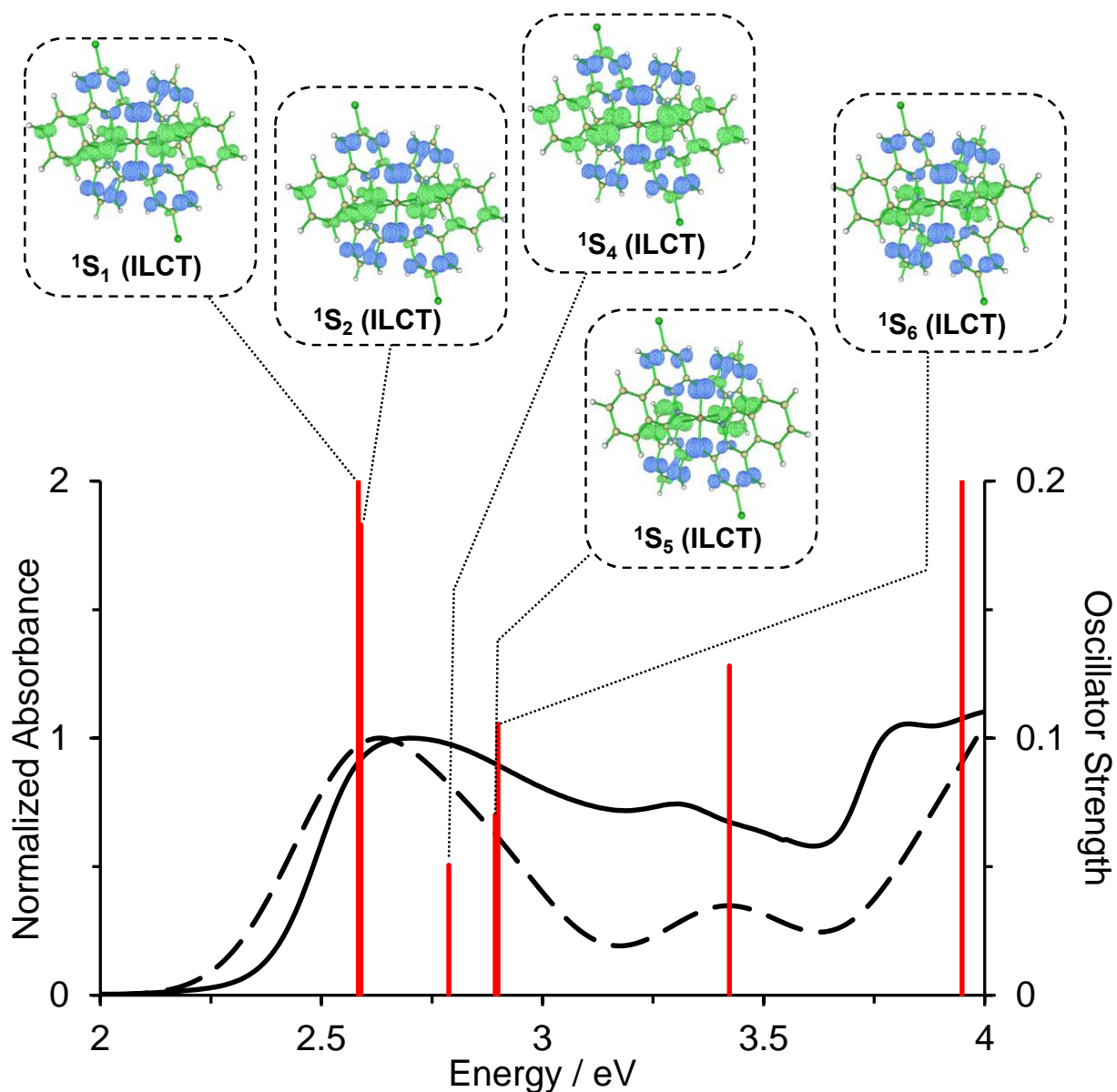
Figure 4.15. TD-DFT predicted vertical excitation energies (red) and simulated spectrum (---) superimposed on the experimental spectrum (−) of **Ga1** in CH₃CN (TD-SMD-rPBE0/6-31+G(d,p)//SMD-rO3LYP/6-31+G(d,p); FWHM = 3000 cm⁻¹; $f_{osc} \geq 0.05$). Electron density gain (green) and depletion (blue) distribution maps (isosurface = 0.002) of the dominant $(d\pi\text{-}n_{N,am}\pi)^*$-to-$(\pi_{L,C=N})^*$ charge transfer (¹ILCT) excitations are also shown.

212

Table 4.12. TD-DFT vertical excitation energies, oscillator strengths ($f_{osc} \geq 0.05$), and MO contributions (>10%) for **Ga1** [TD-SMD-rPBE0/6-31+G(d,p)//SMD-rO3LYP/6-31+G(d,p)].

No.	E / eV	f_{osc}	Major contributions
1	2.58	0.222	HOMO→LUMO (97%)
2	2.59	0.183	H-1→LUMO (96%)
4	2.79	0.051	H-1→L+1 (95%)
5	2.89	0.070	H-1→L+3 (20%), HOMO→L+2 (76%)
6	2.90	0.106	H-1→L+2 (67%), HOMO→L+3 (28%)
9	3.42	0.128	H-1→L+4 (46%), HOMO→L+5 (44%)
16	3.95	0.209	H-3→LUMO (67%), H-2→L+1 (10%)

For the one-electron oxidized **Fe6**, most of the absorptive cross-section between ~600-900 nm is attenuated, consistent with loss of the low energy PALCT transitions. Strong, broad CT transitions are evident at 410 and 495 nm (ε = 10-20 mM^{-1} cm^{-1}), while a low-energy absorption arises with a peak maximum at 1002 nm. This new feature falls in between that of **Fe4** (λ_{max} = 1024 nm) and **Fe5** (λ_{max} = 996 nm) and is assigned by TD-DFT (Figure 4.16, Table 4.13) to involve electron-transfer between the filled MO that retains π(d+p) Fe-N$_{amido}$ bonding character [HOMO-2(β)] and the singly-occupied π*(p+d) N$_{amido}$-Fe anti-bonding MO (here called the LUMO(β)). This transition can therefore be assigned as generating a locally excited (LE) state with $\pi_{bonding}$-to-$\pi_{anti\text{-}bonding}$ character (PB-PA LE) with limited electronic redistribution between the donor and acceptor orbitals.

Figure 4.16. TD-DFT simulated spectrum (---) and vertical excitation energies (red) superimposed on the experimental spectrum (−) of **Fe6** in CH_3CN (TD-SMD-uM06L/6-31+G(d,p)//SMD-uO3LYP/6-31+G(d,p); FWHM = 3000 cm^{-1}; $f_{osc} \geq 0.01$). Electron density gain (green) and depletion (blue) distribution maps (isosurface = 0.002) of the dominant transitions ($f_{osc} > 0.05$) are also shown [TD-SMD-uM06L/6-31+G(d,p)//SMD-uO3LYP/6-31+G(d,p)].

Table 4.13. TD-DFT predicted vertical excitation energies, oscillator strengths ($f \geq 0.01$), and MO contributions (> 10%) for **Fe6** [TD-SMD-uM06L/6-31+G(d,p)//SMD-uO3LYP/6-31+G(d,p)].

No.	E / eV	f_{osc}	Major contribs
1	0.31	0.010	HOMO(B)→LUMO(B) (98%)
3	1.17	0.055	H-2(B)→LUMO(B) (96%)
8	1.89	0.010	HOMO(A)→LUMO(A) (10%), HOMO(B)→L+2(B) (18%), HOMO(B)→L+4(B) (55%)
9	1.95	0.026	HOMO(A)→LUMO(A) (49%), HOMO(B)→L+4(B) (17%)
10	1.99	0.010	H-1(A)→LUMO(A) (21%), HOMO(A)→L+1(A) (25%), H-6(B)→LUMO(B) (19%), H-5(B)→LUMO(B) (15%), HOMO(B)→L+1(B) (10%)
13	2.05	0.017	H-1(A)→L+5(A) (10%), H-4(B)→LUMO(B) (51%), HOMO(B)→L+7(B) (17%)
18	2.15	0.020	HOMO(A)→L+3(A) (50%)
21	2.22	0.059	H-6(B)→LUMO(B) (49%)
22	2.28	0.029	H-1(A)→L+1(A) (10%), H-1(A)→L+3(A) (35%), H-7(B)→LUMO(B) (35%)
24	2.33	0.030	H-1(A)→L+3(A) (35%), H-7(B)→LUMO(B) (35%)
26	2.36	0.011	H-1(B)→L+2(B) (77%)
28	2.42	0.115	H-1(B)→L+3(B) (74%)
29	2.46	0.059	H-1(B)→L+4(B) (82%)
31	2.55	0.028	HOMO(A)→L+5(A) (26%), H-2(B)→L+1(B) (58%)
33	2.61	0.025	HOMO(A)→L+4(A) (75%), HOMO(B)→L+6(B) (10%)
37	2.69	0.016	H-2(A)→L+1(A) (11%), H-2(B)→L+3(B) (78%)
40	2.72	0.016	H-1(A)→L+4(A) (18%), HOMO(A)→L+7(A) (28%), H-3(B)→L+1(B) (32%)
45	2.81	0.014	H-2(A)→LUMO(A) (13%), H-2(A)→L+2(A) (14%), H-1(A)→L+5(A) (11%), H-3(B)→L+3(B) (19%), HOMO(B)→L+8(B) (18%)
48	2.86	0.117	H-2(A)→L+2(A) (45%), HOMO(B)→L+8(B) (10%)
53	2.92	0.072	H-2(A)→L+3(A) (39%), H-1(B)→L+5(B) (12%)
56	2.96	0.020	HOMO(A)→L+8(A) (11%), HOMO(B)→L+9(B) (22%), HOMO(B)→L+10(B) (39%)
57	2.98	0.010	H-10(B)→LUMO(B) (82%)
64	3.07	0.026	H-3(A)→L+2(A) (26%), H-12(B)→LUMO(B) (25%)
65	3.10	0.029	H-3(A)→L+1(A) (14%), H-13(B)→LUMO(B) (11%)
67	3.12	0.010	H-3(A)→L+2(A) (25%), HOMO(A)→L+8(A) (22%)
69	3.18	0.018	H-2(B)→L+5(B) (84%)

Excitation into the lowest energy manifold of **Fe3** should therefore populate low-lying excited states with PALCT character. DFT optimization of the structure of the lowest energy triplet state of **Fe3** starting from the ground-state equilibrium geometry converged to a structure with ^{3}PALCT character (Figure 4.17, Table 4.14), with a contraction of the Fe-N$_{amido}$ bonds by 0.041 Å nearly identical to that observed upon oxidation (Table 4.15); **Fe6** is therefore a structural proxy for the ^{3}PALCT excited state. In contrast, should rapid excited-state decay follow the usual pathway of Fe(II) coordination compounds and populate a metal-centreed state via a ^{3}MLCT→^{3}MC→^{5}MC cascade,[158] all metal-ligand bonds would be expected to elongate. Modeling the nominally ^{5}T$_{2g}$ MC state under octahedral symmetry accordingly shows a lengthening by 0.168 Å of the Fe-N$_{amido}$ bonds and 0.247 Å (average) for the Fe-N$_{quin}$ and Fe-N$_{phen}$ bonds. The structure of the lowest energy ^{3}MC (e.g., ^{3}T$_{1g}$) state similarly exhibited longer metal-ligand bonds – although to a lesser extent due to population of a single antibonding e_g* orbital as opposed to two in the ^{5}T$_{2g}$ state. Thus, compared to traditional Fe(II) polypyridyl complexes such as [Fe(bpy)$_3$]$^{2+}$ or [Fe(terpy)$_2$]$^{2+}$, in which the MLCT excited state exhibits very little structural distortion relative to the ground state,[159] DFT predicts far greater structural differences between CT and MC states in **Fe3**, imposing a larger inner-sphere reorganization energy cost for electron-transfer from CT to MC states.
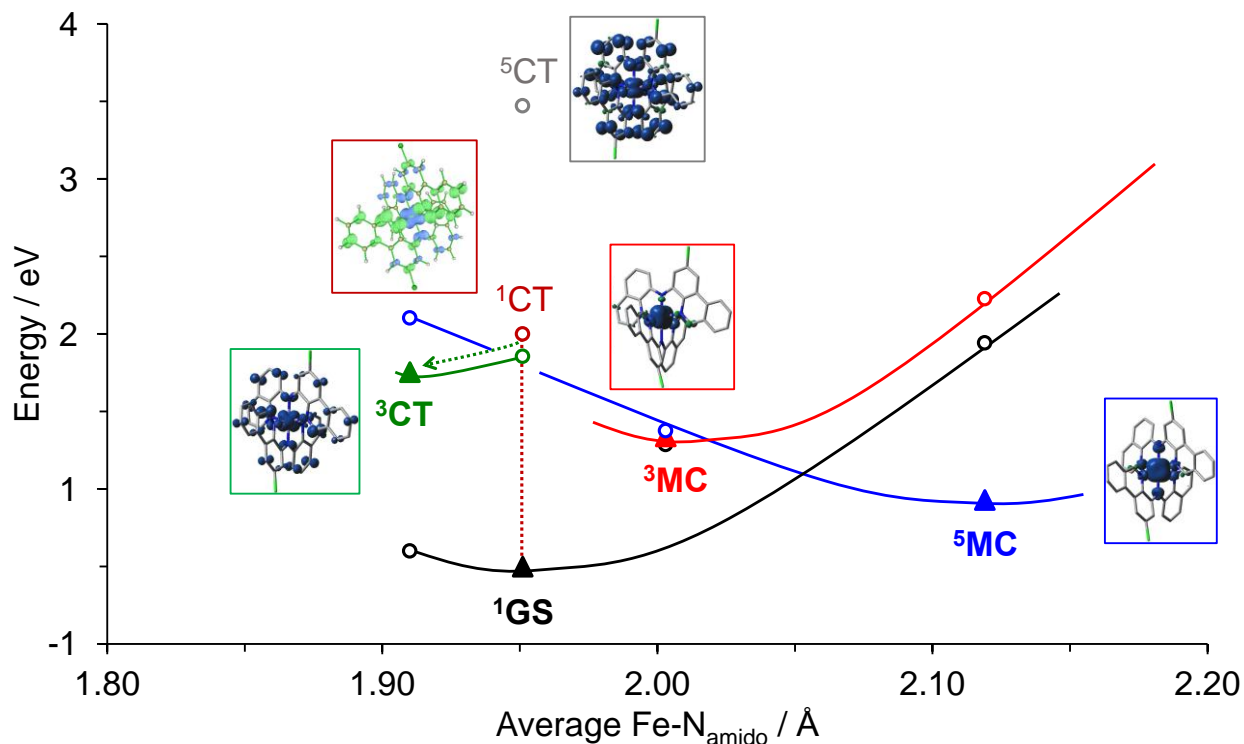
Figure 4.17. Energies and average Fe-N$_{amido}$ distances of relevant electronic states of **Fe3**. The filled triangles and bolded notation represent optimized geometries for **singlet**, **charge-transfer triplet**, **metal-centreed triplet** and **quintet** multiplicities. The open circles represent single-point calculations at the geometry of respective optimized structures in the same vertical position but changing the spin-state. Solid lines are included as a guide for the eye, and connect the optimized energy of each state (solid triangle) and the energies of the two other states (circles). Spin density (isosurface = 0.004; Table 4.14) and electron density gain (green) and depletion (blue) distribution maps (isosurface = 0.002) are also shown. The vertical red dashed-line (----) indicates the observed vertical excitation to the lowest-lying excited-state (^{1}CT). The green dashed-arrow (<----) indicates the proposed intersystem crossing (ISC) to lowest-lying excited ^{3}CT state [^{1}GS: SMD-rM06L/6-31+G(d,p); ^{1}CT: TD-SMD-rM06L/6-31+G(d,p); $^{3/5}$CT, $^{3/5}$MC: SMD-uM06L/6-31+G(d,p)].

Table 4.14. Calculated relative total energies (ΔE) in eV, average Fe-N^{amide} bond distances in Å (Avg. Fe-N), and Mulliken/Löwdin Spin Densities on iron (MD/LD (Fe)) for **Fe3**.

Equilibrium Geometry[a]	State[b]	ΔE / eV	MD/LD (Fe)	Avg. Fe-N^{amide} / Å
$^1GS_{eq}$	^{1}**GS**	0.00	-	
	^{3}**CT**	1.36	0.82/0.73	1.951
	^{5}**CT**	2.97	0.97/0.90	
$^3CT_{eq}$	^{1}**GS**	0.10	-	
	^{3}**CT**	1.25	0.76/0.73	1.910
	^{5}**MC**	1.60	3.82/3.80	
$^3MC_{eq}$	^{1}**GS**	0.79	-	
	^{3}**MC**	0.84	2.08/2.10	2.003
	^{5}**MC**	0.88	3.77/3.79	
$^5MC_{eq}$	^{1}**GS**	1.44	-	
	^{3}**MC**	1.73	2.37/2.18	2.119
	^{5}**MC**	0.43	4.18/3.79	

[a] Geometries calculated at: $^1GS_{eq}$, SMD-rO3LYP/6-31+G(d,p); $^3CT_{eq}$, $^3MC_{eq}$ and $^5MC_{eq}$, SMD-uO3LYP/6-31G(d,p).

[b] Single point energies calculated at: ^{1}GS, SMD-rM06L/6-31+G(d,p); $^{3/5}$CT and $^{3/5}$MC, SMD-uM06L/6-31+G(d,p)].

Table 4.15. Select optimized structural metrics for **Fe3**, **Fe6** and **Ga1** [SMD-xO3LYP/6-31+G(d,p)].[a]

			Fe(^{Cl}L)$_2$		[Fe(^{Cl}L)$_2$]$^+$	[Ga(^{Cl}L)$_2$]$^+$
Bond / Å	$^1GS_{eq}$	$^3CT_{eq}$	$^3MC_{eq}$	$^5MC_{eq}$	$^2GS_{,eq}$	$^1GS_{eq}$
Fe–N^{amide,1}	1.951	1.910	2.080	2.119	1.908	1.997
Fe–N^{amide,2}	1.951	1.910	1.926	2.119	1.908	1.997
Fe–N^{phen,1}	1.969	1.984	2.264	2.216	1.987	2.069
Fe–N^{phen,2}	1.969	1.984	1.974	2.216	1.987	2.069
Fe–N^{quin,1}	1.971	1.992	2.275	2.217	1.987	2.072
Fe–N^{quin2}	1.971	1.992	1.978	2.217	1.987	2.072
Angle / °	$^1GS_{eq}$	$^3CT_{eq}$	$^3MC_{eq}$	$^5MC_{eq}$	$^2GS_{,eq}$	$^1GS_{eq}$
N^{amide,1}–Fe–N^{amide,2}	179.9	179.3	179.8	179.9	180.0	179.6
N^{phen,1}–Fe–N^{phen,2}	90.9	88.2	91.2	93.8	89.4	92.0
N^{quin,1}–Fe–N^{quin,2}	90.8	88.8	91.7	94.2	89.3	91.4
trans-(N^{phen}–Fe–N^{quin})$_{avg}$	164.9	164.9	158.1	150.6	164.7	161.2

[a] x = r (restricted KS-DFT) for $^1GS_{eq}$; x = u (unrestricted KS-DFT) for $^3CT_{eq}$, $^3MC_{eq}$, $^5MC_{eq}$, $^2GS_{eq}$.

4.3.4 Delineating Impact of π-Donor Ligands: Effect of Metal Centre

From section 4.3.3, covalency conspired with low-lying vacant π*-MOs to achieve panchromatic absorption in Fe(II) diarylamido **Fe1-6** complexes. In contrast, the Co(III), Ni(II), Zn(II) and Ga(III) homoleptic complexes of the same diarylamido ligands display a totally different behaviour in their optical properties. To explain the stark difference in the electronic absorption spectra, density functional theory (DFT) modeling of **Co1**, **Ni1** and **Ga2** was undertaken in order to compare their electronic structures with that of **Fe4** (for a full discussion of the computational methodology, see the section 4.3.5). The Zn congener was omitted in favor of the isoelectronic, d^{10} Ga(III) complex for ease of comparison of the optimized structure with that experimentally determined by X-ray diffraction. The ground-state orbital energies and HOMO isosurfaces [SOMO for **Ni1**] are shown in Figure 4.18. In all the complexes, low-lying, vacant ligand-based π* orbitals are present, and in each case are comprised of significant contributions from the $(H)C=N_{phen}$ subunit of the phenanthridinyl arm of ^{tBu}L (Table 4.16). The strong electron density acceptor character of the benzannulated diarylamido ligand[48] attributed to the presence of the phenanthridine heterocyclic unit is thus retained across the series.
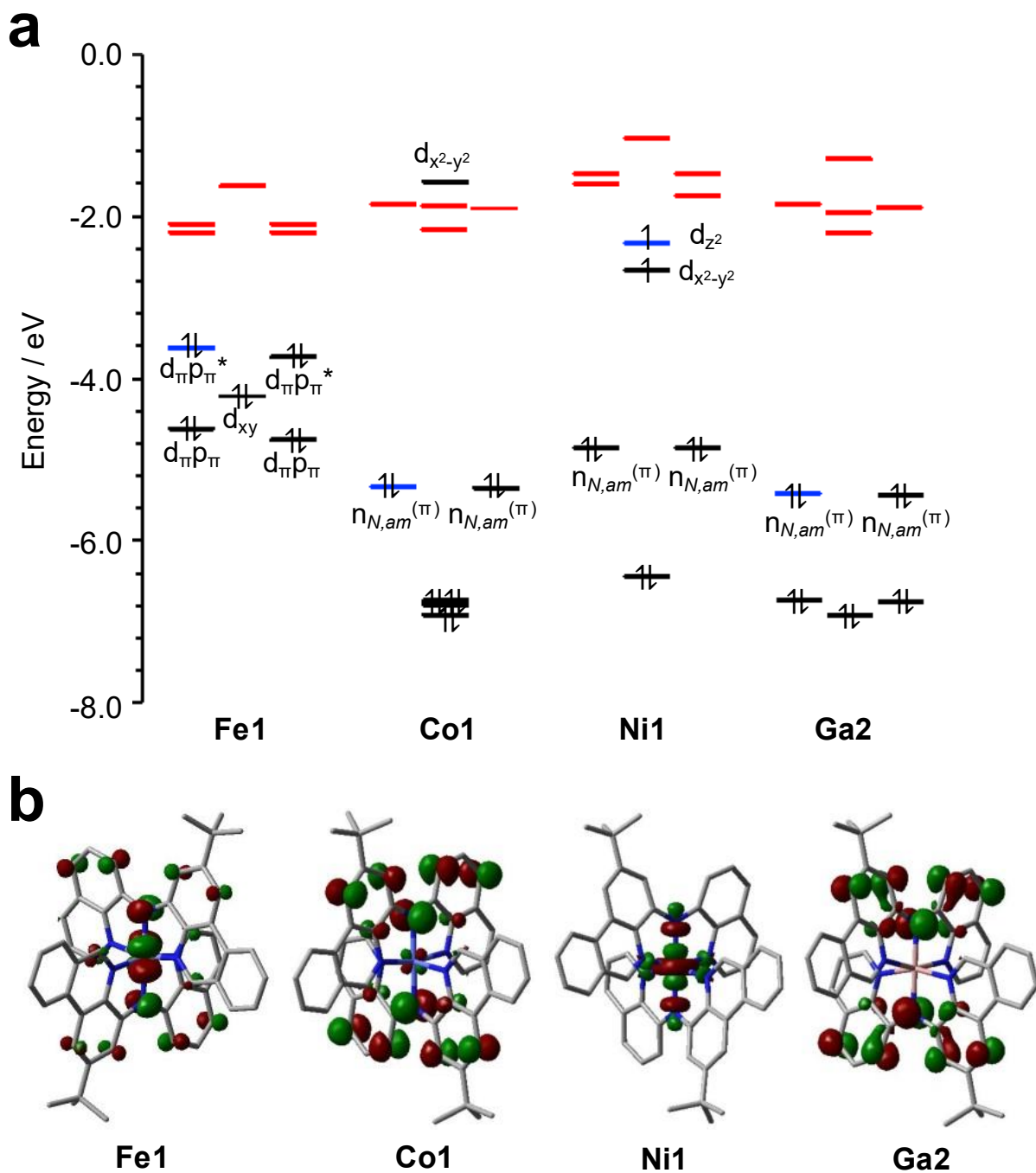
Figure 4.18. (a) Selections from the ground-state MO diagrams of **Fe1**, **Co1**, **Ni1** and **Ga2** comparing the relative energies of the metal d-orbitals, N_{amido} lone pairs, and ligand-based π^* orbitals (highlighted in red); (b) Isosurfaces of the highest energy occupied or partially occupied

MOs highlighted in (a) in blue. For M = Fe, SMD-rM06L/6-31+G(d,p) single point at the SMD-rO3LYP/6-31+G(d,p) optimized geometry; M = Co, Ga, SMD-rPBE0/6-31+G(d,p) single point at the SMD-rO3LYP/6-31+G(d,p) optimized geometry; M = Ni, SMD-uPBE0/6-31+G(d,p) single point at the SMD-uO3LYP/6-31+G(d,p) optimized geometry.

Table 4.16. Fragment contributions to the frontier molecular orbitals (MOs).

	MO	M	N_{amido}	$HC=N_{phen}$	$HC=N_{quin}$	Ar_{phen}	Ar_{quin}
Fe1 [151, a] $S = 0$	**LUMO+1**	11	1	19	9	33	22
	LUMO	3	1	28	6	49	14
	HOMO	48	10	4	4	15	18
	HOMO-1	56	10	4	4	12	14
Co1 [b] $S = 0$	**LUMO+1**	1	1	33	2	56	6
	LUMO	3	1	19	14	31	31
	HOMO	3	19	4	3	34	36
	HOMO-1	3	20	4	3	34	36
Ni1 [c] $S = 1$	**LUMO+1**	1	1	28	4	51	14
	LUMO	2	1	22	10	38	26
	SOMO 1	80	9	3	3	2	2
	SOMO 2	84	0	6	6	1	1
Ga2 [b] $S = 0$	**LUMO+1**	1	1	36	1	58	1
	LUMO	1	1	21	13	34	29
	HOMO	1	19	3	3	35	37
	HOMO-1	1	19	3	3	35	37

[a] SMD-rM06L/6-31+G(d,p) single point at the SMD-rO3LYP/6-31+G(d,p) optimized geometry.
[b] SMD-rPBE0/6-31+G(d,p) single point at the SMD-rO3LYP/6-31+G(d,p) optimized geometry.
[c] SMD-roPBE0/6-31+G(d,p) single point at the SMD-rO3LYP/6-31+G(d,p) optimized geometry.

In the ferrous complex **Fe1**, the two highest-energy occupied orbitals (HOMO, HOMO–1) represent π-anti-bonding overlap between filled orbitals at the metal centre and the amido lone pairs [(d+p)π*].[28] Population analysis reports 10% N_{amido} character in both the HOMO and HOMO-1 alongside significant metal contributions (~50%; Table 4.16). The HOMO–2 in contrast is localized at the iron (~67%) and has predominantly non-bonding character, while the HOMO-3 and HOMO-4 present the corresponding π-bonding overlap. Thus, $(^{tBu}L)_2Fe$ can be described as an intermediate case of the 'HOMO inversion' model, with significant mixing between the N(2p) and Fe(3d) orbitals of appropriate symmetry. This results in the *d*-orbital manifold covering a broader spread of energy levels, causing a considerable contraction of the HOMO-LUMO gap and additional transitions in the visible responsible for the observed broad, panchromatic absorption. In the isoelectronic $3d^6$ complex **Co1**, on the other hand, the lower energy d-orbitals of π symmetry do not mix as strongly with the N_{amido} p-type orbitals due to the greater disparity in energies. The HOMO and HOMO-1 of **Co1** are accordingly each comprised of only 3% metal character with stronger contributions from the two N_{amido} centres (~20%; Figure 4.18b), consistent with a ligand-based HOMO and HOMO-1 and a more complete case of 'HOMO inversion'. When the central metal is replaced with a $3d^{10}$ Ga(III) cation, the occupied *d*-orbitals of **Ga2** are now all stabilized to the extent where the highest occupied orbitals, the HOMO and HOMO-1, have even more negligible contributions from the metal centre (~1%) and are again largely comprised of N_{amido} lone pair character (19%) with significant contributions as well from the C_6 rings directly attached to the amido donors (~36% per ring). A similar electronic structure was reported for related pseudo-octahedral Ga(III) complexes of *bis*(pyrazolyl)amido ligands.[49]

While the fully occupied *d*-orbitals of **Ni1** are also lower in energy than the N_{amido} lone pairs, single point calculations at the optimized triplet ground-state geometry using the restricted

222

open-shell Kohn-Sham (ROKS) formalism reveal that the nearly degenerate $d_z{}^2$ (80%) and $d_x{}^2{}_{-y}{}^2$ (84%) in the d^8 Ni(II) structure contribute very strongly to the singly occupied molecular orbitals (SOMOs; Figures 4.18b and 4.19). Consistent with this, Evans' method measures a $\mu_{eff} = 2.90$ μ_B corresponding to two unpaired electrons and a triplet ground state. A calculated spin density map isolates the majority of this spin to the Ni metal centre (Figure 4.20). In comparison, square-planar Ni complexes of dithiolene ligands bearing protonated pyrazine moieties show strong $d\pi$-$p\pi$ hybridization, which only diminishes when the 3d metal is replaced by a heavier element such as Pt.[50] There, modulation of the HOMO energy level in the Ni(II) complex is sufficient to control proton-electron coupling in protonation reactions. Here, the energies of the filled π-type orbitals of diarylamido fragments do not closely enough match those of the appropriate symmetry within the Ni(II) ion's 3d manifold to engender substantial mixing.
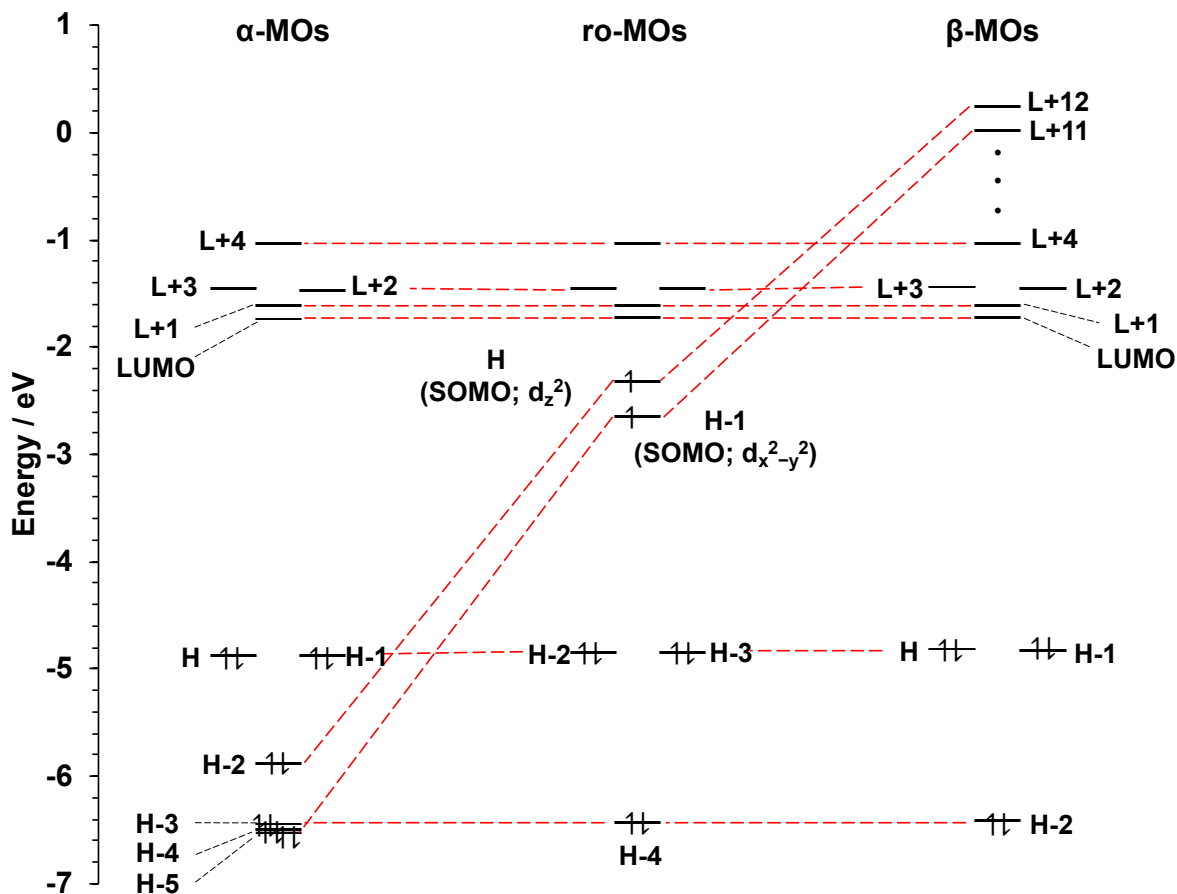
Figure 4.19. Molecular orbital diagrams for **Ni1** (S = 1) showing correlation between UKS (α-MOs, left; β-MOs, right; SMD-uPBE0/6-31+G(d,p) single point at theSMD-uO3LYP/6-31+G(d,p) optimized geometry) and ROKS (middle; roPBE0/6-31+G(d,p) single point at the uO3LYP/6-31+G(d,p) optimized geometry) solutions. The unpaired electrons are largely localized at Ni dz2 and dx2−y2 orbitals.

Fragment	Spin Density
Ni	1.74
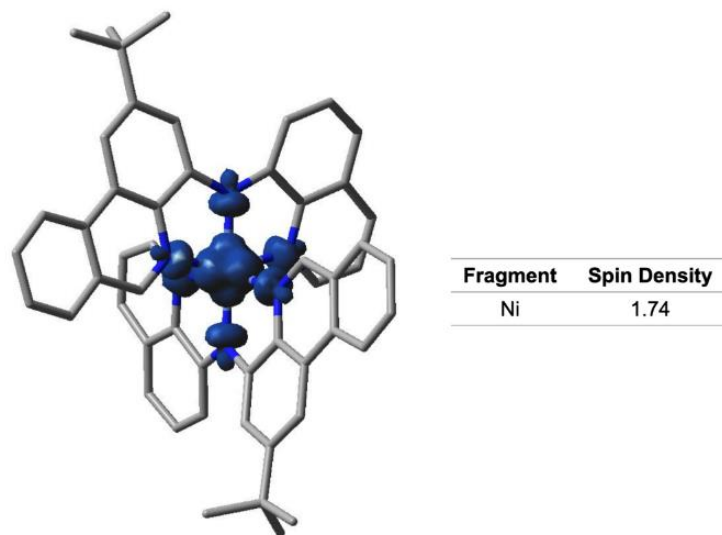
Figure 4.20. Spin density map of Ni1 (S = 1; SMD-uPBE0/6-31+G(d,p) single point at the SMD-uO3LYP/6-31+G(d,p) optimized geometry; isosurface = 0.004).

Simulations of the absorption spectra using time-dependent DFT (TD-DFT) for each compound were found to give good agreement with experimental data (Figures 4.21-4.28). For **Co1**, **Ni1** and **Ga2**, the prominent absorption bands in the visible region of the spectra can all be assigned to electronic excitations largely involving the degenerate HOMO and HOMO-1 (Tables 4.17-4.19). As noted, these MOs contain significant contributions from the N_{amido} lone pairs (**Co1** = 19%, **Ni1** = 20%, **Ga2** = 19%). In agreement with ground-state DFT calculations, the π^*-orbitals of the phenanthridine arms serve as the acceptor orbitals for transitions at lower energies ($\lambda > 460$ nm). Higher energy excitations ($\lambda < 460$ nm) populate orbitals that are largely localized on the quinoline arms of the ligand, consistent with phenanthridine offering more energetically accessible acceptor orbitals.[121] Altogether, the majority of absorptions observed in the visible region of the spectra of for **Co1**, **Ni1** and **Ga2**, are mainly comprised of ligand-to-ligand charge-transfer character (LLCT) consistent with the experimentally observed strong ε values.

225
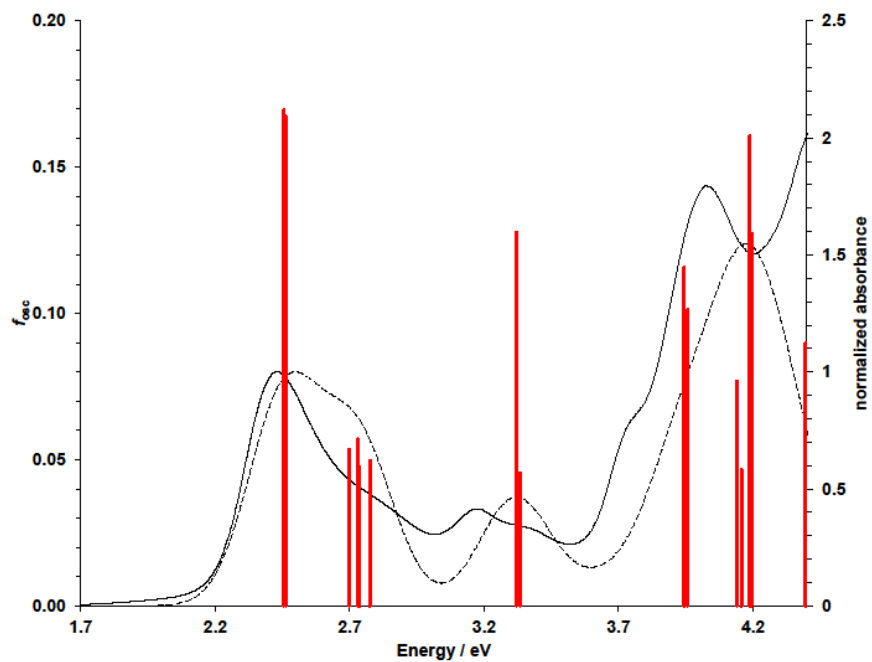
Figure 4.21. TD-DFT simulated spectrum (---) and vertical excitation energies (red) superimposed on the experimental spectrum (-) of **Co1** in CH_3CN ($S = 0$; TD-SMD-rPBE0/6-31+G(d,p) at the SMD-rO3LYP/6-31+G(d,p) optimized geometry; FWHM = 2500 cm^{-1}; $f > 0.05$).

Table 4.17. TDDFT predicted vertical excitation energies, oscillator strengths ($f_{osc} > 0.05$), and MO contributions (> 10%) **Co1** ($S = 0$; TD-SMD-rPBE0/6-31+G(d,p) at the SMD-rO3LYP/6-31+G(d,p) optimized geometry).

No.	E / eV	f_{osc}	Major MO contribs
3	2.45	0.17	HOMO→LUMO (98%)
4	2.46	0.17	H-1→LUMO (97%)
8	2.70	0.05	HOMO→L+1 (89%)
10	2.73	0.06	H-1→L+2 (58%), HOMO→L+3 (31%)
11	2.74	0.05	H-1→L+1 (10%), HOMO→L+2 (79%)
13	2.77	0.05	H-1→L+3 (87%), HOMO→L+2 (12%)
14	3.32	0.13	H-1→L+7 (30%), HOMO→L+5 (60%)
15	3.33	0.05	H-1→L+5 (54%), HOMO→L+7 (35%)
26	3.94	0.12	H-14→L+4 (10%), H-3→LUMO (38%)
28	3.96	0.10	H-14→L+4 (13%), H-3→LUMO (30%)
31	4.14	0.08	H-3->LUMO (16%), H-2->L+1 (65%)
32	4.16	0.05	H-4→LUMO (11%), H-3→L+1 (37%), H-2→L+2 (16%), HOMO→L+10 (14%)
33	4.19	0.16	H-1→L+10 (51%), HOMO→L+11 (29%)
34	4.19	0.13	H-3→L+1 (15%), H-1→L+11 (20%), HOMO→L+10 (47%)
44	4.39	0.09	H-5→L+2 (25%), H-4→L+3 (28%), H-2→L+3 (13%), HOMO→L+11 (13%)
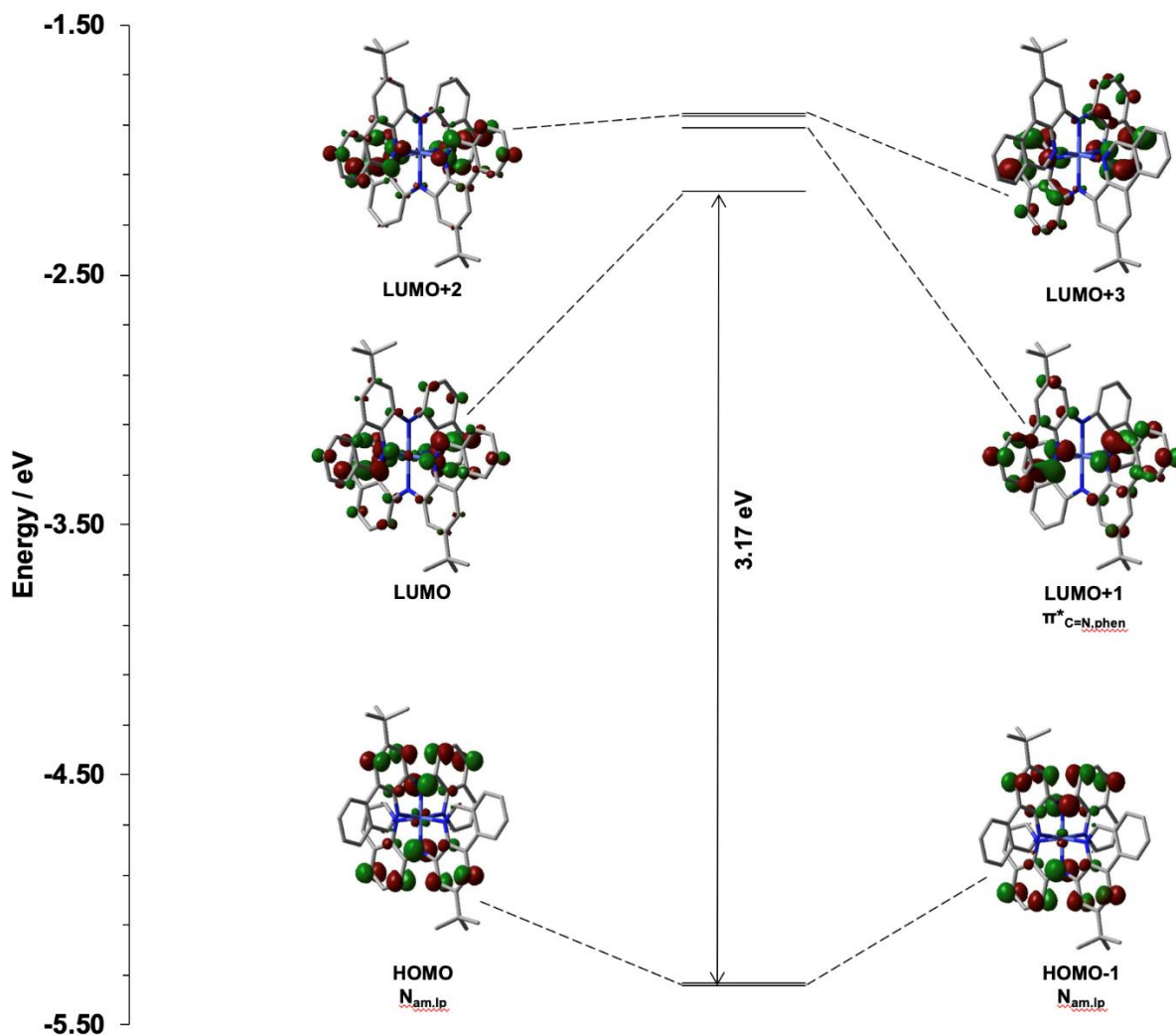
Figure 4.22. MO energies and diagrams dominating the visible region of the UV-Vis absorbance spectrum of **Co1** ($S = 0$; SMD-rPBE0/6-31+G(d,p) single point at the SMD-rO3LYP/6-31+G(d,p) optimized geometry; isosurface = 0.04).
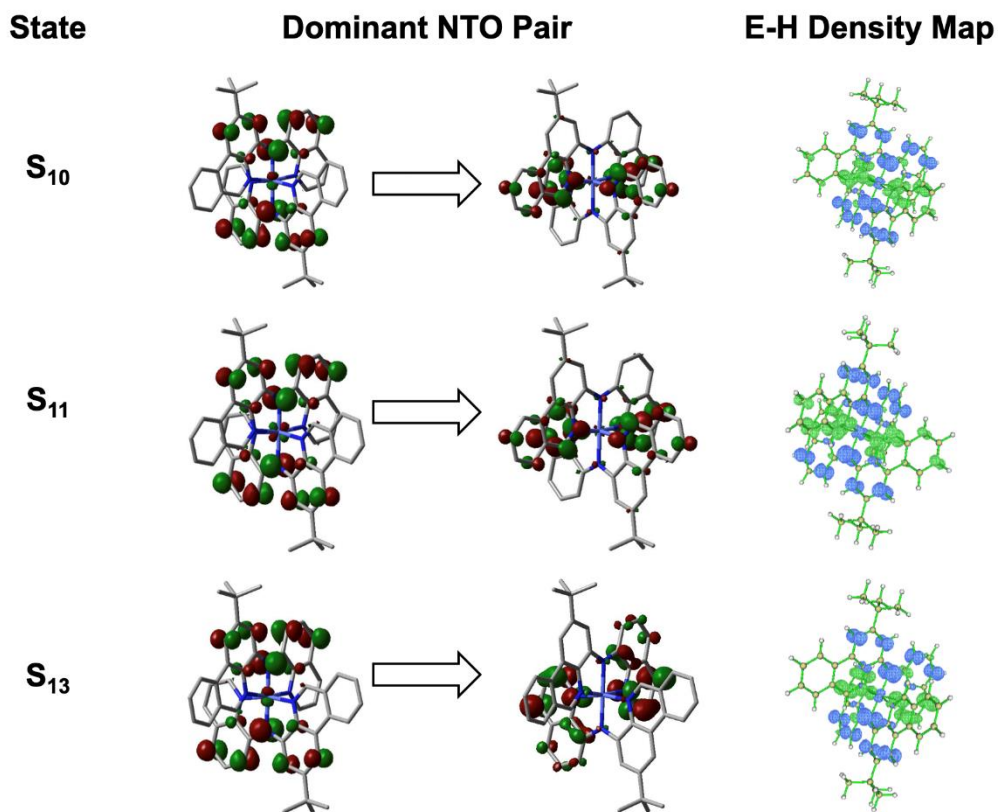
Figure 4.23. Natural transition orbitals (isosurface = 0.04) and TDDFT calculated electron density gain (green) and depletion (blue) maps (isosurface = 0.002) of the dominant excited states in the visible region of **Co1** (*S* = 0; TD-SMD-rPBE0/6-31+G(d,p) at the SMD-rO3LYP/6-31+G(d,p) optimized geometry). NTOs are calculated only for states with more than one MO pair contribution.
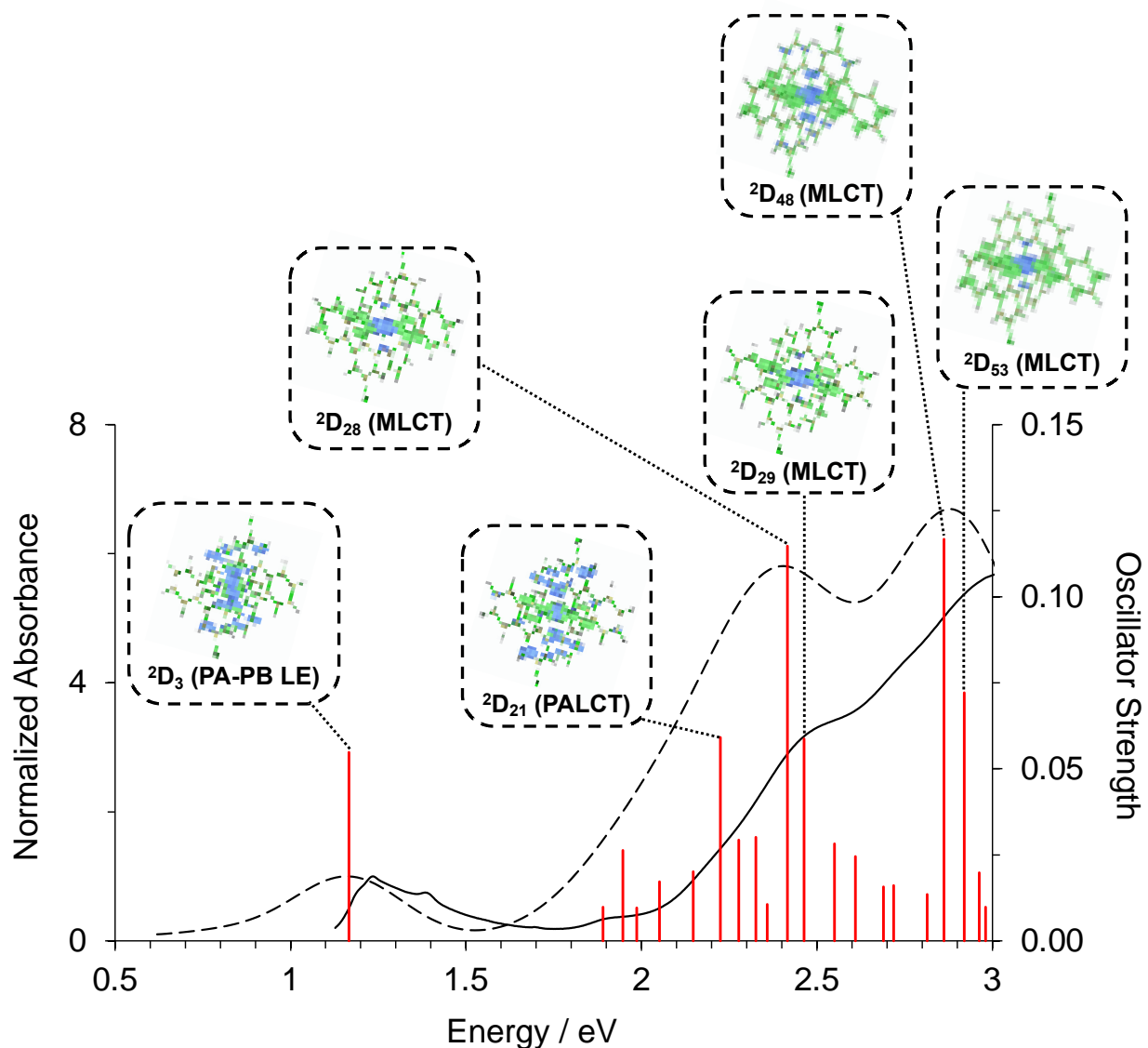
229
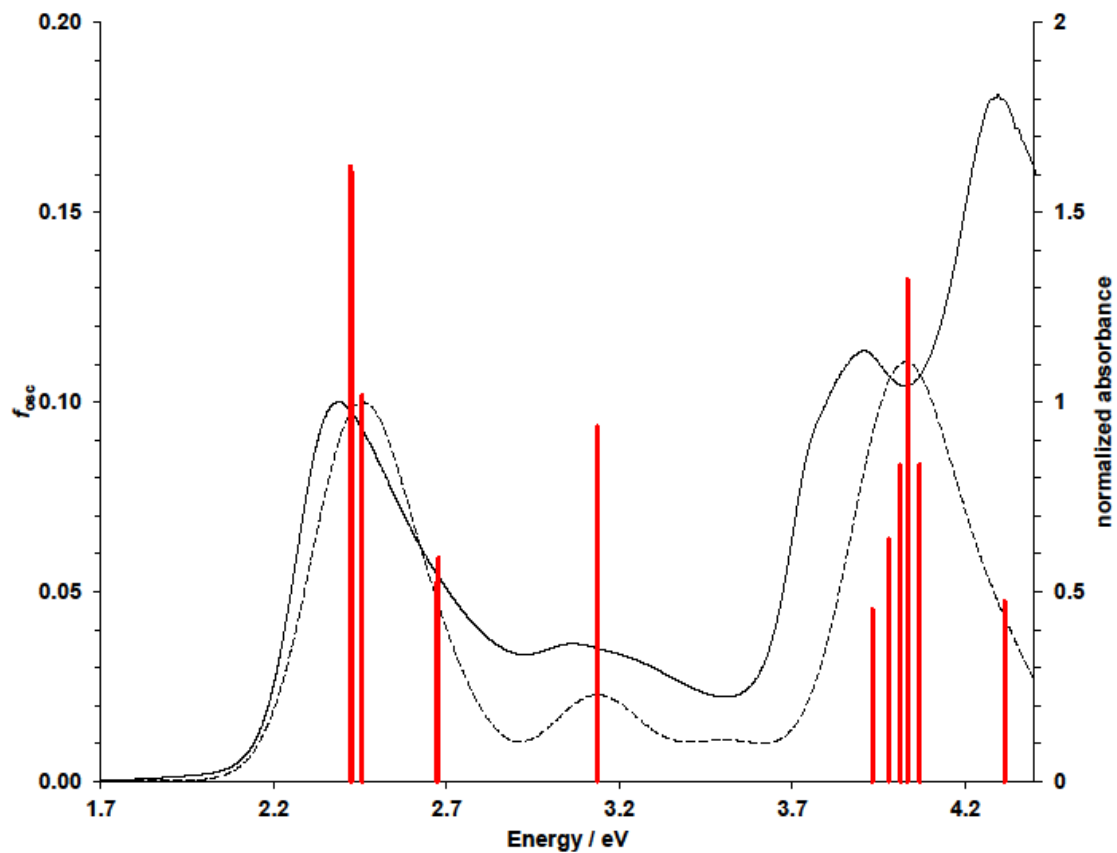
Figure 4.24. TD-DFT simulated spectrum (---) and vertical excitation energies (red) superimposed on the experimental spectrum (-) of **Ni1** in CH_3CN ($S = 1$; TD-SMD-uPBE0/6-31+G(d,p) at the SMD-uO3LYP/6-31+G(d,p) optimized geometry; FWHM = 2500 cm^{-1}; $f > 0.05$).

Table 4.18. TDDFT predicted vertical excitation energies, oscillator strengths ($f_{osc} > 0.05$), and MO contributions (> 10%) **Ni1** ($S = 1$; TD-SMD-uPBE0/6-31+G(d,p) at the SMD-uO3LYP/6-31+G(d,p) optimized geometry).

No.	E /eV	f_{osc}	Major MO contribs
8	2.42	0.16	H-1(A)→LUMO(A) (10%), HOMO(A)→LUMO(A) (19%), H-1(B)→LUMO(B) (14%), HOMO(B)→LUMO(B) (33%)
9	2.42	0.16	H-1(A)→LUMO(A) (17%), HOMO(A)→LUMO(A) (10%), H-1(B) →LUMO(B) (33%), HOMO(B) →LUMO(B) (14%)
10	2.46	0.09	H-1(A)→LUMO(A) (11%)
11	2.46	0.10	HOMO(A)→LUMO(A) (12%), H-9(B)→L+11(B) (10%)
18	2.67	0.05	HOMO(A)→L+2(A) (31%), HOMO(A)→L+3(A) (18%), HOMO(B)→L+2(B) (32%)
19	2.68	0.06	H-1(A) →L+2(A) (23%), H-1(A) →L+3(A) (27%), H-1(B) →L+2(B) (17%), H-1(B)→L+3(B) (21%)
29	3.14	0.09	H-1(A)→L+4(A) (17%), H-1(A)→L+5(A) (11%), HOMO(A)→L+4(A) (12%), HOMO(A)→L+5(A) (11%), H-1(B)→L+4(B) (15%), HOMO(B)→L+4(B) (10%)
58	3.93	0.05	HOMO(B)→L+9(B) (24%), HOMO(B)→L+11(B) (12%)
62	3.98	0.06	H-1(A)→L+8(A) (10%), H-1(B)→L+8(B) (18%), H-1(B) →L+9(B) (12%), H-1(B)→L+11(B) (21%)
65	4.01	0.08	H-3(A)→LUMO(A) (14%), H-2(B)→LUMO(B) (13%)
66	4.03	0.13	H-4(A)→LUMO(A) (13%), H-2(A)→L+5(A) (16%)
70	4.07	0.08	H-2(A)→L+5(A) (51%)
92	4.31	0.05	H-7(A)→LUMO(A) (16%), H-3(A)→L+3(A) (12%), H-4(B)→L+1(B) (15%), H-2(B)→L+3(B) (17%)
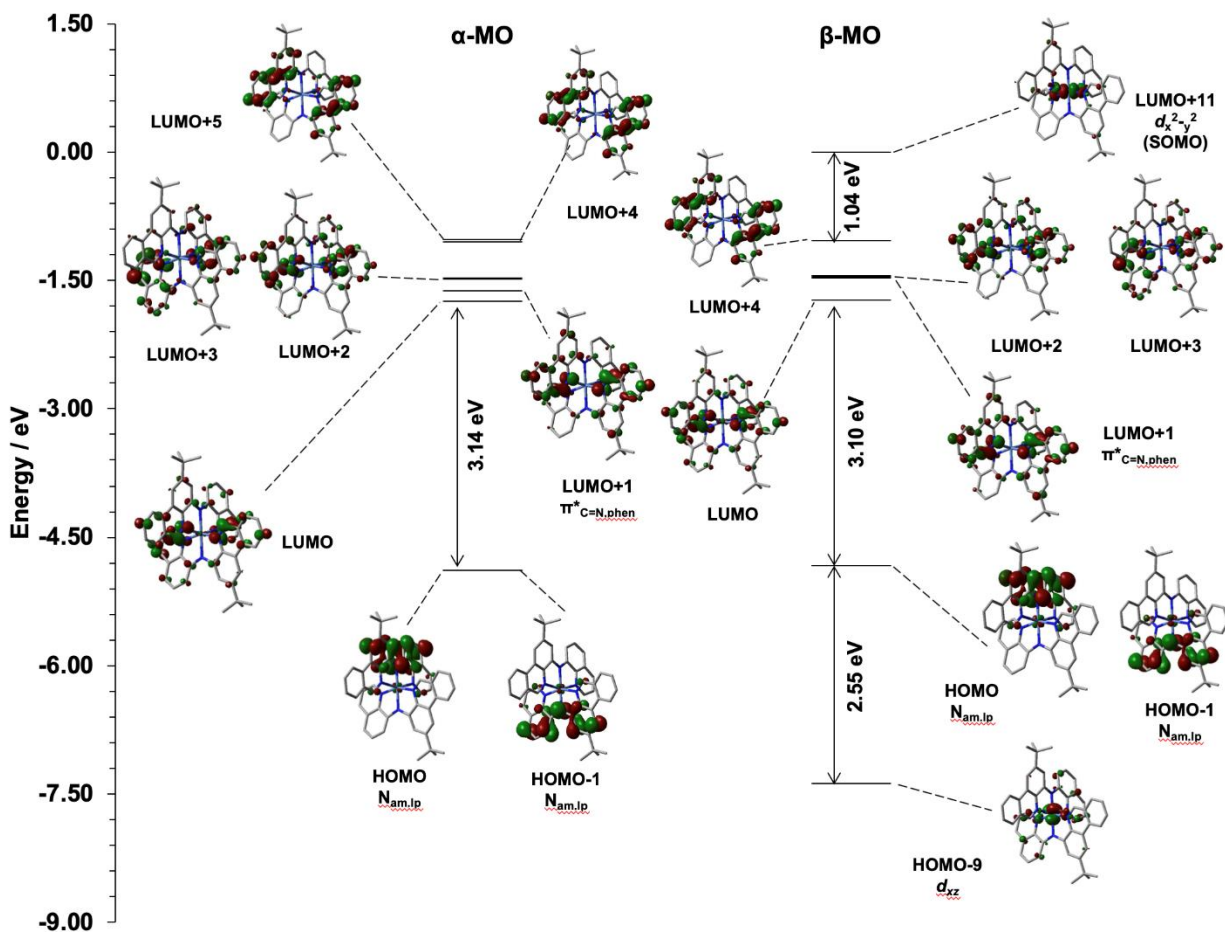
Figure 4.25. MO energies and diagrams dominating the visible region of the UV-Vis absorbance spectrum of **Ni1** ($S = 1$; TD-SMD-uPBE0/6-31+G(d,p) at the SMD-uO3LYP/6-31+G(d,p) optimized geometry; isosurface = 0.04).
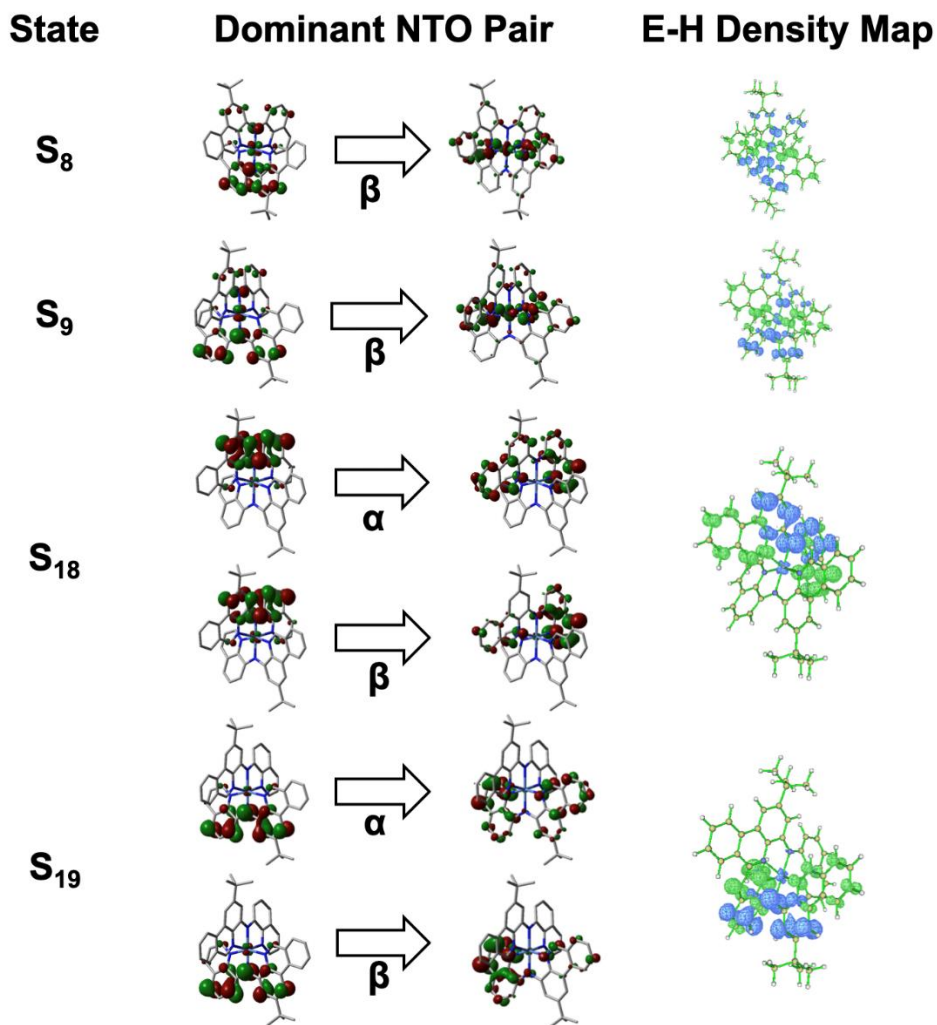
Figure 4.26. Natural transition orbitals (isosurface = 0.04) and TDDFT calculated electron density gain (green) and depletion (blue) maps (isosurface = 0.002) of the dominant excited states in the visible region of **Ni1** (S = 1; TD-SMD-uPBE0/6-31+G(d,p) at the SMD-uO3LYP/6-31+G(d,p) optimized geometry). NTOs are calculated only for states with more than one MO pair contribution.
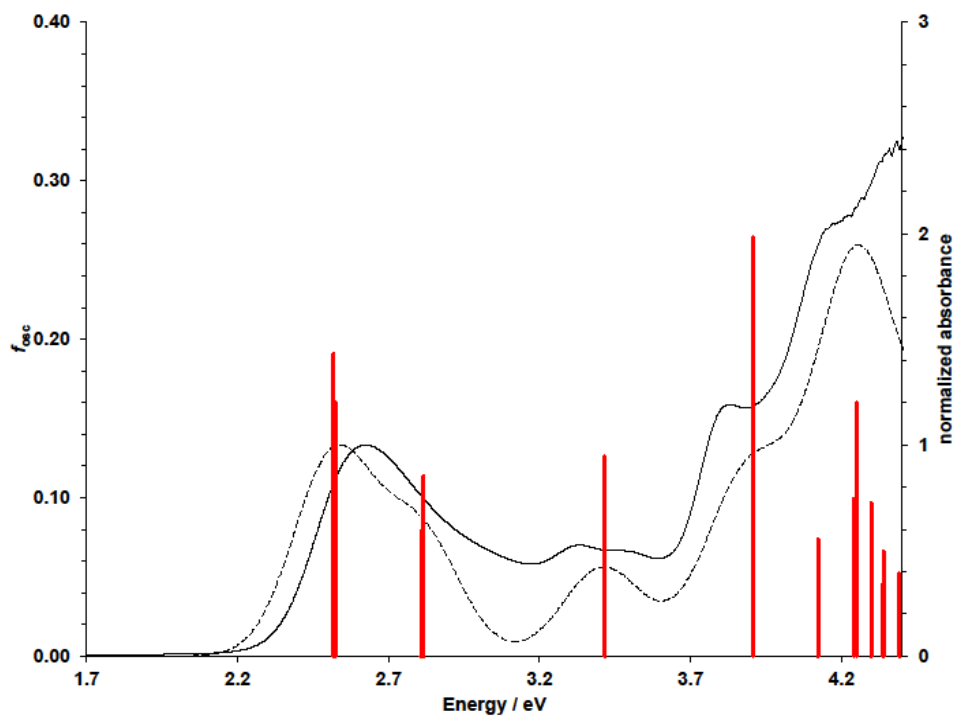
Figure 4.27. TD-DFT simulated spectrum (---) and vertical excitation energies (red) superimposed on the experimental spectrum (−) of **Ga2** in CH_3CN ($S = 0$; TD-SMD-rPBE0/6-31+G(d,p) at the SMD-rO3LYP/6-31+G(d,p) optimized geometry; FWHM = 2500 cm^{-1}; $f > 0.05$).

Table 4.19. TDDFT predicted vertical excitation energies, oscillator strengths ($f_{osc} > 0.05$), and MO contributions (> 10%) **Ga2** ($S = 0$; TD-SMD-rPBE0/6-31+G(d,p) single point at the SMD-rO3LYP/6-31+G(d,p) optimized geometry).

No.	E / eV	f_{osc}	Major MO contribs
1	2.52	0.19	HOMO→LUMO (97%)
2	2.52	0.16	H-1→LUMO (96%)
5	2.81	0.08	H-1→L+3 (13%), HOMO→L+2 (80%)
6	2.82	0.11	H-1→L+2 (71%), HOMO→L+3 (20%)
9	3.42	0.13	H-1→L+4 (44%), HOMO→L+5 (47%)
16	3.91	0.26	H-3→LUMO (70%)
21	4.12	0.07	H-3→LUMO (16%), H-2→L+1 (71%)
24	4.24	0.10	H-2→L+2 (48%), H-1→L+9 (11%), HOMO→L+8 (27%)
25	4.25	0.16	H-5→L+1 (26%), H-1→L+9 (11%), HOMO→L+8 (27%)
26	4.25	0.12	H-4→L+1 (11%), H-3→L+2 (38%), H-1→L+8 (27%), HOMO→L+9 (12%)
28	4.30	0.10	H-5→L+1 (25%), H-3→L+3 (48%)
29	4.34	0.05	H-5→L+1 (18%), H-3→L+3 (32%), H-2→L+2 (28%)
30	4.34	0.07	H-4→L+1 (15%), H-3→L+2 (34%), H-2→L+3 (26%)
32	4.39	0.05	H-5→L+2 (54%), H-4→L+3 (19%)
39	4.65	0.10	H-6→LUMO (60%)
40	4.67	0.27	H-7→LUMO (41%)
41	4.72	0.28	H-3→L+4 (27%), H-2→L+5 (24%)
42	4.74	0.30	H-7→LUMO (19%), H-3→L+5 (21%), H-2→L+4 (27%)
43	4.76	0.13	H-7→LUMO (10%), H-1→L+15 (14%), HOMO→L+12 (38%), HOMO→L+14 (12%)
49	4.90	0.08	H-7→LUMO (18%), H-7→L+3 (10%), H-6→L+2 (49%)
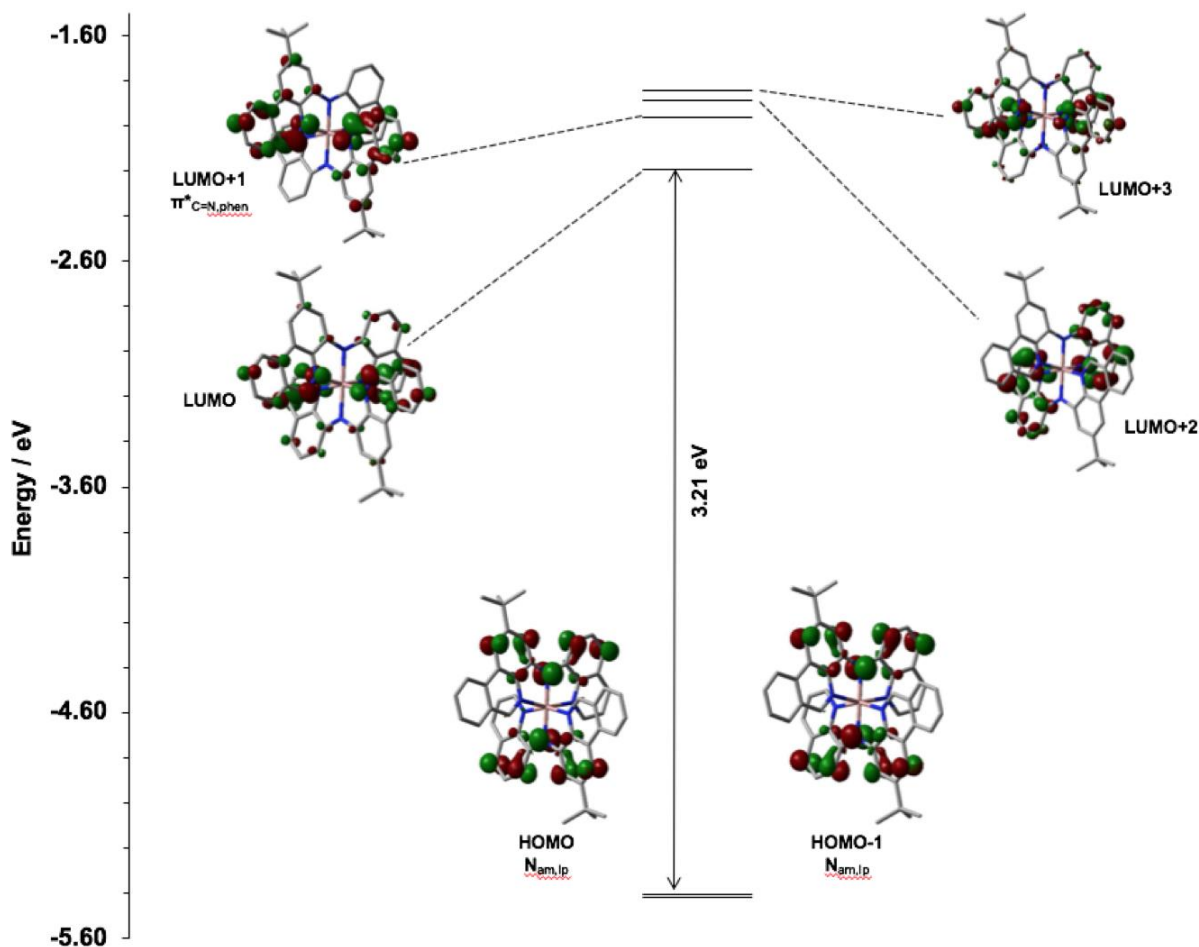
Figure 4.28. MO energies and diagrams dominating the visible region of the UV-Vis absorbance spectrum of **Ga2** ($S = 0$; SMD-rPBE0/6-31+G(d,p) single point at the SMD-rO3LYP/6-31+G(d,p) optimized geometry; isosurface = 0.04).

One way of explaining the similarities in both the absorption profile and redox behavior (*vide infra*) of **Ni1** compared to those of **Co1** and **Ga2** despite the presence of nearly degenerate metal-based SOMOs in **Ni1**, is to consider non-Aufbau behavior upon electromagnetic excitation or reduction/oxidation,[160] as has been described for vanadium complexes supported by porphyrinate and phthalocyanine ligands.[70] In such cases, a decrease in electron-electron repulsion

promotes both removal and excitation of an electron from a doubly occupied (ligand-based) orbital versus from the metal-based SOMOs, and charge transfer into fully vacant ligand-based orbitals before the metal-based SOMOs. Another possible description is that, electronically, the complex behaves as an isolated Ni(II) ion within a pseudo-octahedral NiN_6 coordination environment that only weakly interacts with the ligand π-system, as has been invoked for related Ni(II) complexes of diarylamido ligands with flanking pyrazolyl donors.[71]

As a result, **Co1**, **Ni1**, **Zn1** and **Ga2** all show similar anodic redox behavior, with two closely spaced quasi-reversible or irreversible oxidation events observed at ~ -0.05 V vs $FcH^{0/+}$ for the neutral parent species and between 0.3-0.6 V for the monocations. Metal-N_{amido} (d+p)π mixing stabilizes the radicals formed by these oxidations, and the events observed for **Co1** (and **Fe1**[151]) are the most reversible within the series, consistent with the smallest amount of 'naked' aminyl radical character.[161] For the Co(III) species, an electrochemically reversible reduction is observed at -1.30 V. Ligand-based reduction events are also observed for all complexes close to the edge of the solvent window (CH_3CN, ~ -2.5 V), consistent with the relatively similar calculated LUMO energies (Figure 4.18).

4.3.5 Insights from DFT and TDDFT

It is clear from the examples above that the rich electronic structure imbued by both the ligands and metal complexes can prove troublesome to both DFT and TDDFT. Practical aspects of DFT, such as the approximations to the E_{xc}, contribute to its deficiencies. These shortcomings become apparent from the examples in section 4.3.3 and 4.3.4. One of the challenges that became apparent in **Fe1-3** is modeling their panchromatic absorption and excited states. When modeling iron complexes in their ground and excited states, their spin-state energetics are generally challenging

for conventional DFT and TD-DFT, which can be traced back to the approximations used in the exchange-correlation functional.[162–165] Indeed, a strong dependence of the electronic structure of such systems on the amount of Hartree-Fock exchange (HFX) admixture has been previously highlighted, with low (high) HFX admixture favoring low (high) spin states.[162,164–166] Single point calculations were performed on the equilibrium ground state geometries of **Fe1-3** using three functionals with different HF admixtures, namely, M06L[167] (HF = 0), O3LYP[168] (HF = 12%), and M06[169] (HF = 26%), with 6-31+G(d,p) basis set on all atoms.[170–174] Consistent with previous reports on DFT modelling of the electronic structures of Fe(II) complexes[162,164] hybrid functionals (O3LYP and M06) were found to artificially stabilize the high spin quintet state, while the M06L functional (with zero HF admixture) predicted the same low spin singlet configuration for all complexes as was found experimentally.

For the same complexes **Fe1-3** modeling the dicationic species, two-electron oxidized complexes of **Fe1-3**, proved to be challenging as well. The two-electron oxidation of the complex removes one electron from each of the nominally $N_{amido}(\pi)$ leading to essentially a diradical complex. The dicationic **Fe1-3** could present either a triplet or an open-shell singlet multiplicity. These are often challenging for DFT owing to the construction of the KS wavefunction as single determinant. Broken-symmetry DFT (BS-DFT) calculations were therefore carried out in the gas phase. First, geometry optimization of **Fe1**$^{2+}$ in a high-spin (HS) triplet electronic configuration was performed using O3LYP/6-31+G(d,p). Single point gas-phase calculations (energies and wavefunction stability calculations) were conducted using M06L[175] in combination with different basis set sizes (*i.e.*, 6-31+G(d,p), 6-311G(d,p),[176] and 6-311+G(d,p);[176,177]) to evaluate basis set effects on the calculated single point energies at the optimized geometry of the triplet electronic configuration. A single point calculation on the open-shell singlet, at the optimized triplet

238

geometry, was similarly carried out using the fragment guess job feature available in Gaussview.[178] The unpaired electrons were each placed on a respective ligands, while the iron centre was left in the +2 oxidation state with all electrons paired. The gas phase magnetic coupling constant for the complex at the optimized triplet geometry was then estimated using the Yamaguchi formula (Table 4.20):[179,180]

$$J_{AB} = -\frac{(E_{HS} - E_{BS})}{\langle S^2 \rangle_{HS} - \langle S^2 \rangle_{BS}} \qquad (4.5)$$

In general, an increased in J_{AB} is observed with increasing basis-set size. The sign of J_{AB} implies that the triplet state, where both electrons have the same spin, in the dicationic complexes likely is the ground state electronic configuration.

Table 4.20. Basis set dependence of gas phase single-point energies and $\langle S^2 \rangle$ of triplet and broken-symmetry states at the gas phase optimized triplet geometry (uO3LYP/6-31+G(d,p)) and uM06L level of theory, and estimated gas phase magnetic coupling constant (J_{AB}) for **Fe1^{2+}**.

[Fe]$^{2+}$	6-31+G(d,p)	6-311G(d,p)	6-311+G(d,p)	$\langle S^2 \rangle$
E_{HS} / a.u.	-3599.73664020	- 3600.21424068	- 3600.23426220	2.0337
E_{BS} / a.u.	-3599.73479875	- 3600.21213016	- 3600.23233224	0.9336
$\Delta E_{HS\text{-}BS}$ / cm^{-1}	-404.2	-463.2	-423.6	
J_{AB} / cm^{-1}	367.3	420.6	385.5	

Similar functional dependence has also been observed in the one-electron oxidized complexes of **Co1**, **Ni1** and **Ga2**. This is indeed true when simulating the intervalence-charge transfer bands (IVCT) at ~0.6 eV. Full TDDFT treatment with the PBE0 functional severely underestimates the IVCT vertical excitation energy and intensity. We nevertheless were able to accurately simulate the absorption spectrum of the oxidized species **Co1**.

For the complexes containing heavier transition metal complexes, spin-orbit coupling manifests its effects in some of the optical spectra of Re(I) complexes **Re1-2** and [Pt(*N^*N*^O*)Cl] **8-11**. In these examples, spin-free TDDFT does not reproduce weak, low energy absorptions in the visible region of **Re1-2**. Explicit inclusion of spin-orbit coupling effects have been previously reported to drastically affect the excited state dynamics of complexes containing heavier elements.[181,182] Other recent work has concluded that SOC is not important to model the experimental absorption spectra of Re(I) carbonyl complexes, but does have an effect on the potential energy surface[183] and excitation energies.[184] For systems **Re1** and **Re2**, we found that the inclusion of SOC and using a functional with minimal HF-exchange (B3LYP*, HF = 15%) in TDDFT calculations allowed us to more accurately reproduce the experimental absorption spectra of **Re1** and **Re2** (Figures 4.29 and 4.30).
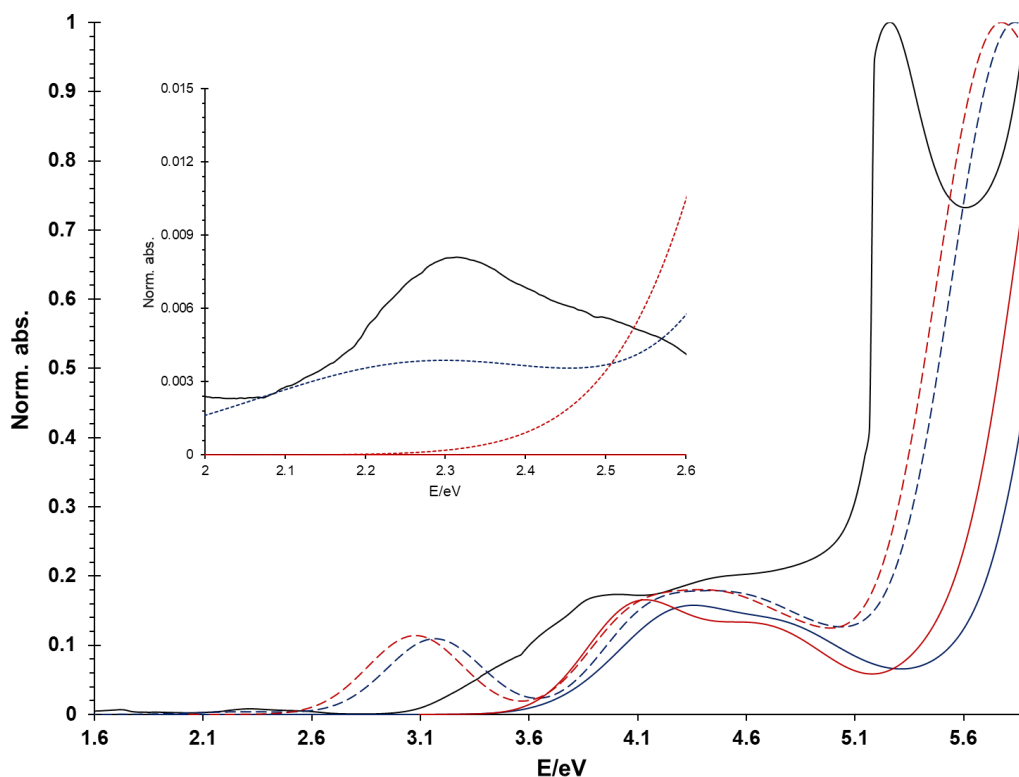
Figure 4.29. Comparison between the experimental spectrum (black solid line), and the computed relativistic spectra of **Re1** using different functionals in acetonitrile. Scalar spectra are shown for CAM-B3LYP (RIJCOSX-ZORA-SMD-CAM-B3LYP-D3(BJ)/def2-TZVP+SARC-TZVP) as red solid line and B3LYP* (RIJCOSX-ZORA-SMD-B3LYP*-D3(BJ)/def2-TZVP+SARC-TZVP) as red-dashed line; spin orbit corrected spectra are shown for CAM-B3LYP (SO-RIJCOSX-ZORA-SMD-CAM-B3LYP-D3(BJ)/def2-TZVP+SARC-TZVP) as blue solid line and B3LYP* (SO-RIJCOSX-ZORA-SMD-CAM-B3LYP-D3(BJ)/def2-TZVP+SARC-TZVP) as blue-dashed line.
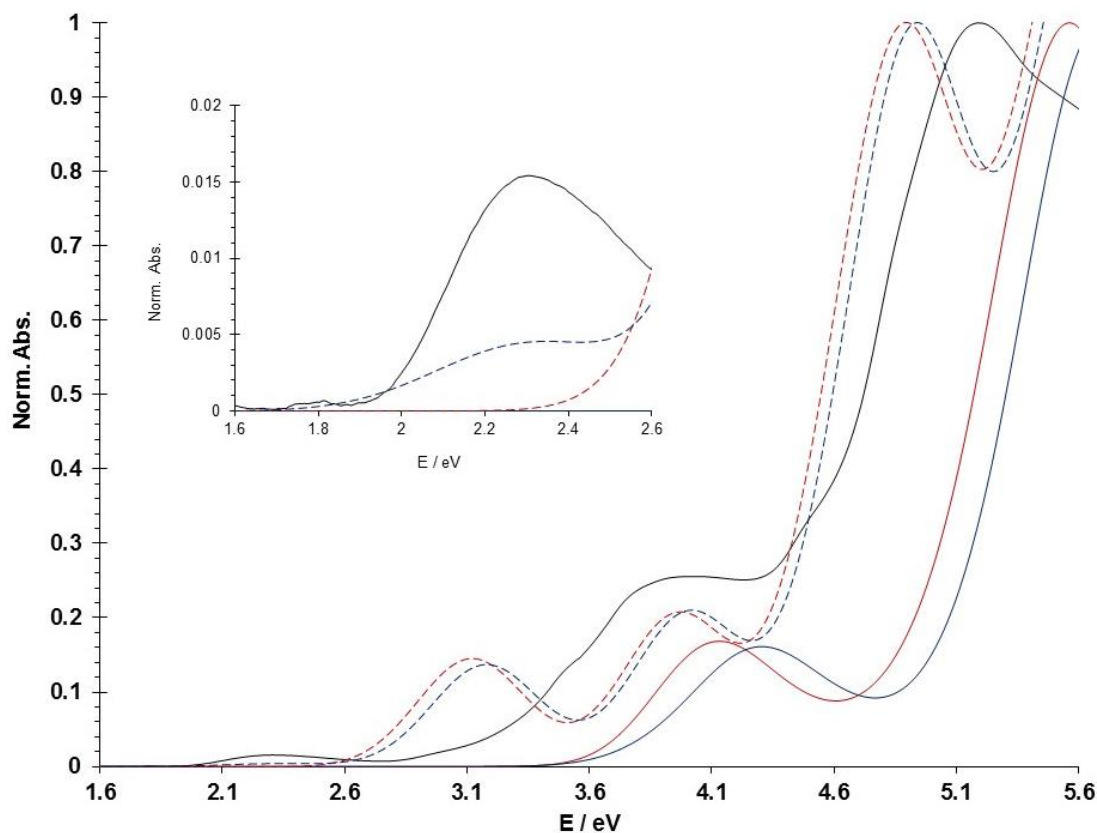
Figure 4.30. Comparison between the experimental spectrum (black solid line), and the computed relativistic spectra of **Re2** using different functionals in acetonitrile. Scalar spectra are shown for CAM-B3LYP (RIJCOSX-ZORA-SMD-CAM-B3LYP-D3(BJ)/def2-TZVP+SARC-TZVP) as red solid line and B3LYP* (RIJCOSX-ZORA-SMD-B3LYP*-D3(BJ)/def2-TZVP+SARC-TZVP) as red-dashed line; spin orbit corrected spectra are shown for CAM-B3LYP (SO-RIJCOSX-ZORA-SMD-CAM-B3LYP-D3(BJ)/def2-TZVP+SARC-TZVP) as blue solid line and B3LYP* (SO-RIJCOSX-ZORA-SMD-CAM-B3LYP-D3(BJ)/def2-TZVP+SARC-TZVP) as blue-dashed line.

By comparing the TDDFT calculated spectrum to the experimental spectrum of **Re1** and **Re2**, it can be seen that SOC is particularly important in modeling the low energy transitions of the spectrum. In both **Re1** and **Re2**, a weak absorption band at ~ 2.31 eV can be observed. In

242

comparison, spin-free spectra only show the higher energy absorption bands. In addition, the inclusion and the amount of HF-exchange have a profound effect in the energy of the lowest energy band. Within the spin-free approximation, modeling singlet-triplet excitations using global hybrid functionals with small amount of HF-exchange (HF < 30%) and GGA-functionals is typically less accurate.[185] This can be remedied using global hybrid functionals with increased HF-exchange or range separated hybrids[186] which highlights the difference in the electron-correlation requirement for triplet states.[187,188] Consistent with these findings, the energy of T_1 at the optimized ground state geometry is predicted to be higher in CAM-B3LYP compared to B3LYP*. In both cases, excitation to this low energy excited triplet state is forbidden ($f = 0$), consistent with the spin multiplicity conservation rule. The SOC-corrected TDDFT also shows a bathochromic shift in the absorbance spectra of **Re1** and **Re2** when using B3LYP* compared to CAM-B3LYP. However, only B3LYP* with SOC was able to reproduce the experimental spectra of both **Re1** and **Re2**. This suggests that the electron-correlation for SOC-states in these complexes may be similar to spin-free singlet states, preferring hybrid functionals with low amounts of HF admixture.

In the case of [Pt(*N^N^O*)Cl] **8-11**, focus is given on complex **11**. It can be seen from Figure 4.31 that the valley between 2.8 eV to 3.5 eV gains intensity with SOC correction. Analysis of the SOC-corrected spectrum of **11** (Figure 4.32) show one transition in this region, albeit low intensity, and that is absent without SOC. This increased participation of the triplet states in the form of direct $T_n \leftarrow S_0$ can have a profound impact in excited state dynamics of these complexes as discussed in section 4.3.8.
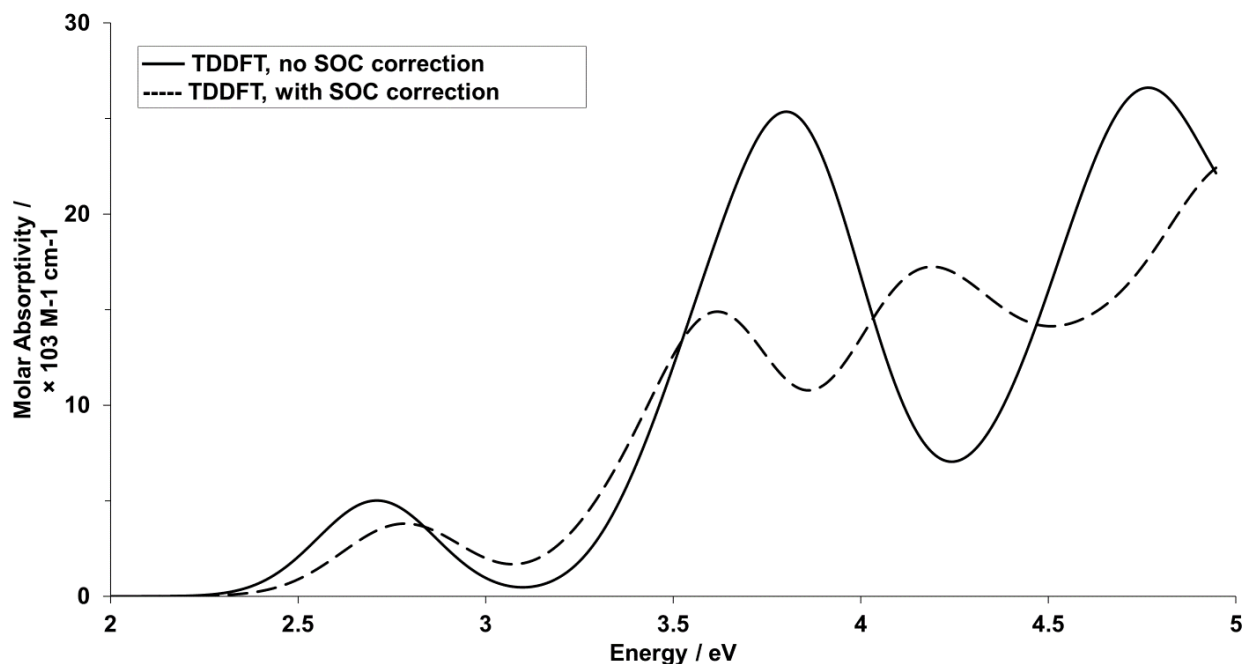
Figure 4.31. Effects of inclusion of spin-orbit coupling on the calculated UV-Vis absorption spectra of **11**.
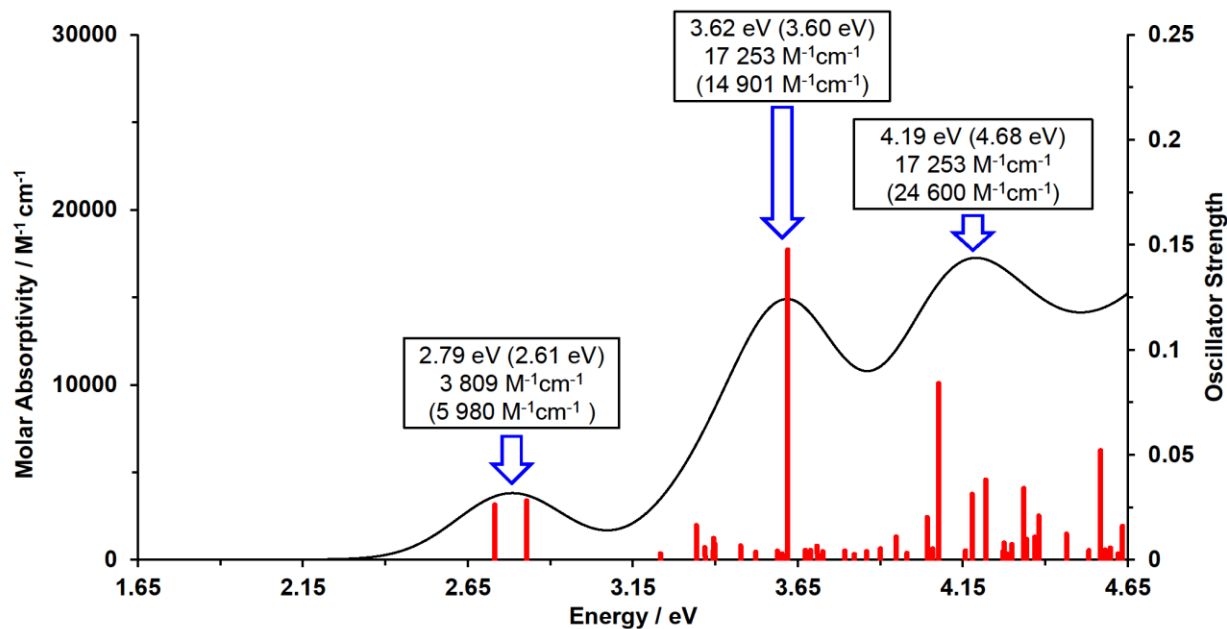
Figure 4.32. TDDFT simulated SOC-corrected spectrum (—), vertical excitations (—), and oscillator strengths of **11** in CH_2Cl_2. Calculated energies and molar absorptivities ($M^{-1}cm^{-1}$) at each peak maxima are shown with experimental (in parentheses).

244

4.3.6 Methylation Rigidifies Boron Ketoiminates

In section 3.3.2, boron ketoiminates **1**, **2** and **4** with pendent phenanthridine exhibit both phosphorescence and fluorescence likely due to some fluxionality of the pendent phenanthridine. Methylation, as in [**3**Me][OTf], minimizes nonradiative deactivation pathways such as ISC. To understand the dynamics in these compounds, DFT and TDDFT are both carried out. In addition, relaxed potential energy scans are carried to find potential pathways for ISC. In the excited state dynamics, more focus is given to **3** and [**3**Me][OTf]. Gas-phase optimizations of all compounds were first performed using the CAM-B3LYP functional which has been shown to model donor-acceptor complexes containing BF_2 in good agreement with experiment.[189] The structures of **3** and [**3**Me]$^+$ were also optimized using the solvation model based on density approach (SMD; CH_2Cl_2). The structural metrics so-obtained are in good agreement with the solid-state structures (Table 4.2.1), with the notable exception of the angle between the (N^O)B chelate plane and that of the phenanthridinyl subunit, which is larger in the solid state, likely due to packing effects. Better agreement is obtained for [**3**Me]$^+$ (gas phase DFT, 81.7°; SMD, 81.2°; X-ray, 88.7°).

Table 4.21. Ground-state optimized structural parameters for **1**-**4** and [**3**Me]$^+$.

Bond / Å	1	2	3	3	4	[3Me]$^+$	[3Me]$^+$
		Gas-phase		CH$_2$Cl$_2$ ^{a}		Gas-phase	CH$_2$Cl$_2$ ^{a}
B-O	1.481	1.481	1.480	1.468	1.480	1.477	1.468
B-N	1.576	1.576	1.575	1.555	1.576	1.576	1.558
B-F^1	1.382	1.382	1.384	1.394	1.380	1.369	1.387
B-F^2	1.366	1.366	1.366	1.383	1.366	1.377	1.385
Angle / °							
O-B-N	108.3	108.3	108.3	109.6	108.2	107.6	108.8
F1-B-F2	112.4	112.4	112.2	110.0	112.5	112.6	110.3
O-B-F1	109.0	109.0	109.0	109.0	109.2	110.2	109.5
N-B-F1	108.1	108.2	108.2	109.3	108.1	108.7	109.5
O-B-F2	109.5	109.5	109.6	109.1	109.6	109.4	109.1
N-B-F2	109.4	109.5	109.5	109.8	109.2	108.2	109.6
Interplanar angle^b / °	66.5	66.9	66.2	71.8	67.4	90.0	87.5
BF$_2$ "pucker"^{c} / °	7.0	6.8	7.0	4.4	6.5	12.5	11.9

^{a} Optimized at the SMD-CAM-B3LYP-D3(BJ)/def2-SVP.
^{b} Angle between calculated planes of phenanthridinyl and the (N^O)B chelate ring (see Figure S3a).
^{c} Angle between N2-C15-C16-C17-O1 and N2-B1-O1 planes (see Figure S3b).

Energies and isosurfaces of selected ground-state molecular orbitals (MOs) of **3** and [**3**Me]$^+$ are presented in Figure 4.33. For **1**-**4,** the three lowest energy vacant orbitals have both

246

phenanthridinyl (LUMO+2/LUMO+1/LUMO: **1**, 48/77/78; **2**, 50/79/68; **3**, 51/74/77; **4**, 37/77/88%) and oxazaborinine character (LUMO+2/LUMO+1/LUMO: **1**, 51/22/21; **2**, 48/17/28/; **3**, 49/24/21; **4**, 63/22/10%). The highly electron-withdrawing CF_3 substituent in **4** stabilizes the *N*-heterocyclic fragment, and the LUMO of **4** has the lowest oxazaborinine and highest phenanthridinyl character of the series. The phenanthridinyl substituents do not appear to impact the calculated HOMO-LUMO gaps, mirroring the similarity in $\lambda_{abs,max}$ for **1**-**4**, while the bathochromic shift to the lowest energy manifold of [**3**Me]$^+$ compared to **3** is reproduced by computation. As with coordination complexes of Lewis acidic metal ions supported by phenanthridine-based ligand scaffolds,[190–193] the LUMO has particularly localized orbital density at the C=N subunit of the phenanthridinyl, consistent with 'imine-bridged biphenyl' character to the tricyclic moiety. This is accentuated upon methylation of the phenanthridinyl nitrogen, such that the LUMO of **3** has 70% phenanthridine character, 21% of which is localized at the C=N sub-unit, while the comparable numbers for [**3**Me]$^+$ are 94% and 38%. The HOMO and HOMO-2 also show mixed phenanthridinyl (HOMO/HOMO-2: **1**, 63/41; **2**, 69/39; **3**, 62/40; **4**, 35/62) and oxazaborinine character (HOMO/HOMO-2: **1**, 34/57; **2**, 26/60; **3**, 36/59; **4**, 64/37). The HOMO-1, in comparison, has dominant phenanthridinyl character and only a small but non-negligible oxazaborinine contribution in **1**-**3** which drops to zero in **4**. Solvation has a minor impact on the energies of the MOs and a similar HOMO-LUMO gap is predicted for **3** in vacuum (6.52 eV) vs. CH_2Cl_2 (6.66 eV). The characters of the HOMO and HOMO-2, however, are quite different. The oxazaborinine contribution to the HOMO of **3** decreases from 36% in the gas phase to 6% in CH_2Cl_2, while a similar decrease in the phenanthridinyl contribution is observed for the HOMO-2 (vacuum: 40%; CH_2Cl_2: 28%).
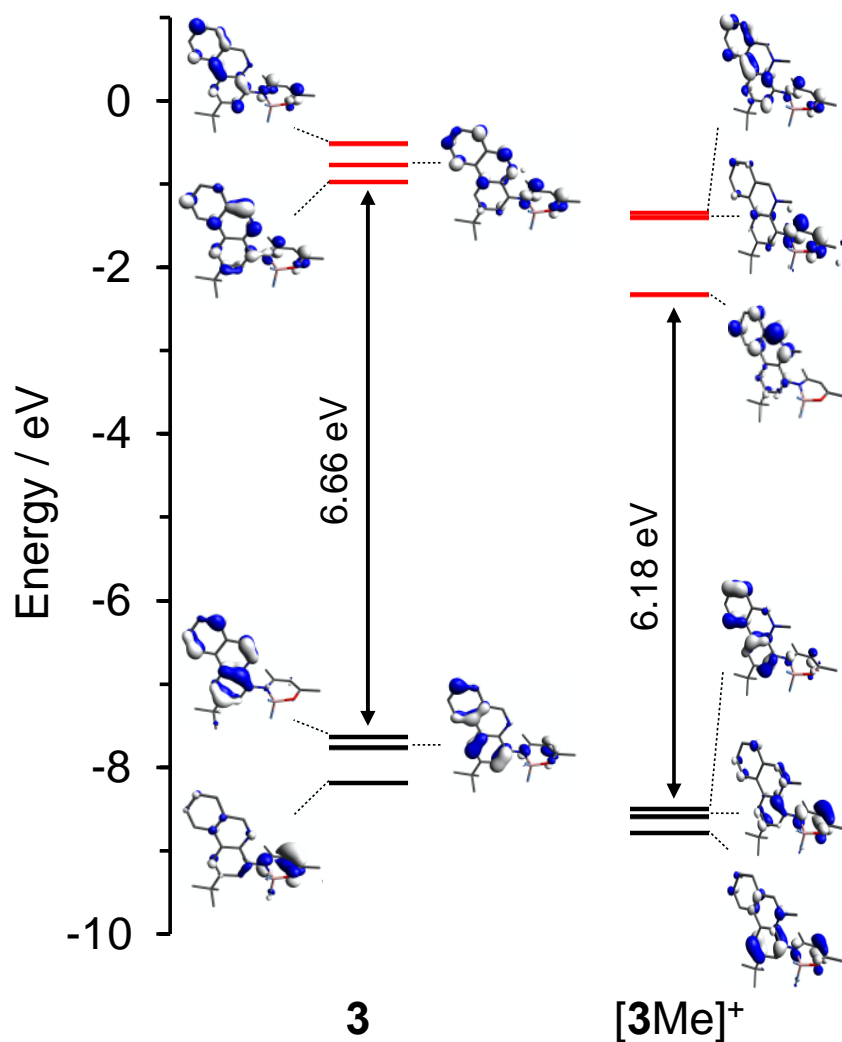
Figure 4.33. Selected molecular orbitals (SMD-RIJCOSX-rM06-2X/def2-TZVP(-f)+def2-J//SMD-rCAM-B3LYP-D3(BJ)/def2-SVP; solvent = CH_2Cl_2) of **3** and [**3**Me]$^+$ (isovalue = 0.04) and their relative energies.

Comparing **3** with its *N*-methylated congener [**3**Me]$^+$, the HOMO and LUMOs of the two complexes have somewhat inverted character. In **3**, the HOMO has dominant (89%) phenanthridinyl character, while the LUMO has mixed (70:29%) phenanthridinyl/(N^O)B character. In [**3**Me]$^+$, the LUMO has dominant (94%) phenanthridinyl character, while the HOMO

248

has more mixed 83:15 phenanthridinyl/(N^O)B chelate character. Overall, methylation enhances the phenanthridinium character to both frontier orbitals, which leads to the lowest energy transitions of this compound being of π-π* local excitation (LE) character, consistent with the lack of pronounced solvatochromism.

TDDFT simulations were then conducted for **3** and [**3**Me]$^+$ in CH_2Cl_2 (Figures 4.34 and 4.35). These calculations reveal that the major transitions responsible for the UV-Vis absorption spectrum of **3** present significant mixed character due to configuration interactions and cannot be fully attributed to HOMO-LUMO transitions. Electron-hole difference density maps (Figures 4.36 and 4.37) of the three dominant (f_{osc} > 0.01) transitions of **3** all indicate oxazaborinine→phenanthridine charge-transfer character. Accordingly, we calculate a significant change in the dipole moment relative to the ground-state for each of these excited-states ($\Delta\mu$ (CH_2Cl_2): S_1 9.5 D, S_2 10.2 D, S_4 9.8 D). In comparison, the lowest energy transitions calculated for [**3**Me]$^+$ have much more significant locally excited π-π* character originating from the redistribution of electron density within the phenanthridinyl moiety. The calculated change in dipole moment is accordingly smaller ($\Delta\mu$ (CH_2Cl_2): S_1 5.7 D, S_2 7.5 D).
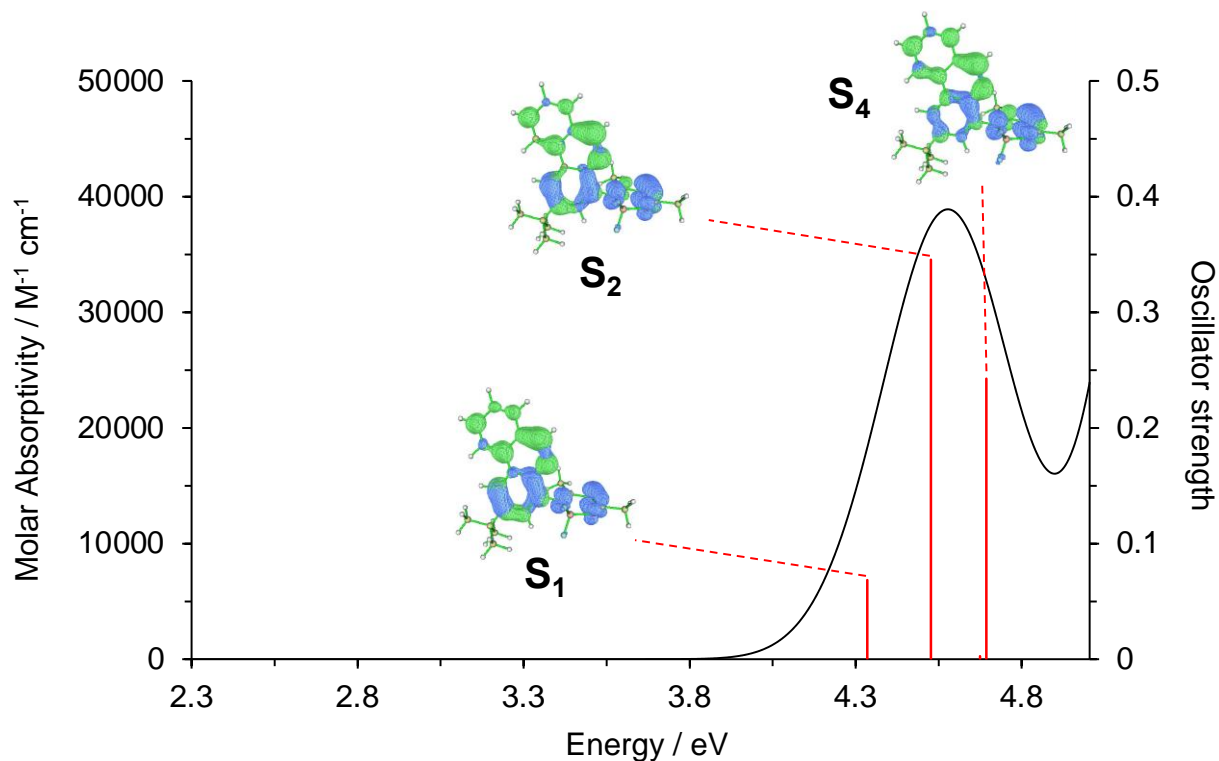
Figure 4. 34. TDDFT (SMD-TD-RIJCOSX-M06-2X/def2-TZVP(-f)+def2/J//SMD-CAM-B3LYP-D3(BJ)/def2-SVP) calculated UV-Vis spectrum (FWHM = 3000 cm^{-1}) and vertical excitation energies of **3** in CH$_2$Cl$_2$.

Table 4.22. TDDFT vertical excitation energies, oscillator strengths ($f_{osc} > 0.01$), and MO pair contributions (> 10%) of **3** in CH$_2$Cl$_2$ (TD-SMD-RIJCOSX-M06-2X/def2-TZVP(-f)+def2/J//SMD-CAM-B3LYP-D3(BJ)/def2-SVP).

No.	E / eV	f_{osc}	Major contributions
1	4.36	0.046	H-1→LUMO (17%), H-1→L+1 (20%), HOMO→LUMO (31%), HOMO→L+2 (18%)
2	4.62	0.299	H-1→LUMO (37%), HOMO→LUMO (32%)
4	4.85	0.438	H-2→LUMO (13%), H-1→L+2 (21%), HOMO→L+1 (42%)
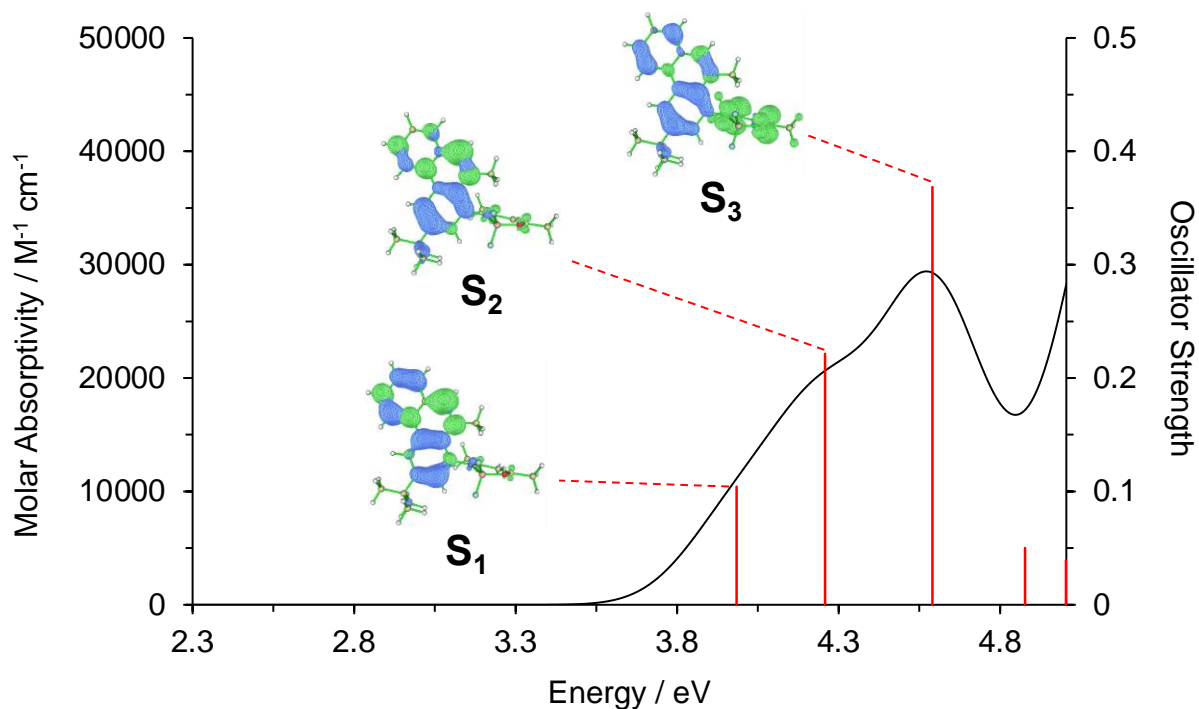
Figure 4.35. TDDFT (SMD-TD-RIJCOSX-M06-2X/def2-TZVP(-f)+def2/J//SMD-CAM-B3LYP-D3(BJ)/def2-SVP) calculated UV-Vis spectrum (FWHM = 3000 cm^{-1}) and vertical excitation energies ($f_{osc} > 0.01$) of [**3Me**]$^+$ in CH_2Cl_2.

Table 4.23. TDDFT vertical excitation energies, oscillator strengths ($f_{osc} > 0.01$), and MO pair contributions (> 10%) of [**3Me**]$^+$ in CH_2Cl_2 (TD-SMD-RIJCOSX-M06-2X/def2-TZVP(-f)+def2/J//SMD-CAM-B3LYP-D3(BJ)/def2-SVP).

No.	E / eV	f_{osc}	Major contributions
1	4.05	0.103	HOMO→LUMO (75%)
2	4.32	0.232	H-2→LUMO (36%), H-1→LUMO (46%)
3	4.74	0.219	H-2→LUMO (34%), H-1→LUMO (25%), H-1→L+1 (15%)
4	4.93	0.456	H-2→LUMO (12%), H-1→LUMO (11%), H-1→L+1 (31%), H-1→L+2 (11%), HOMO→L+2 (12%)

251
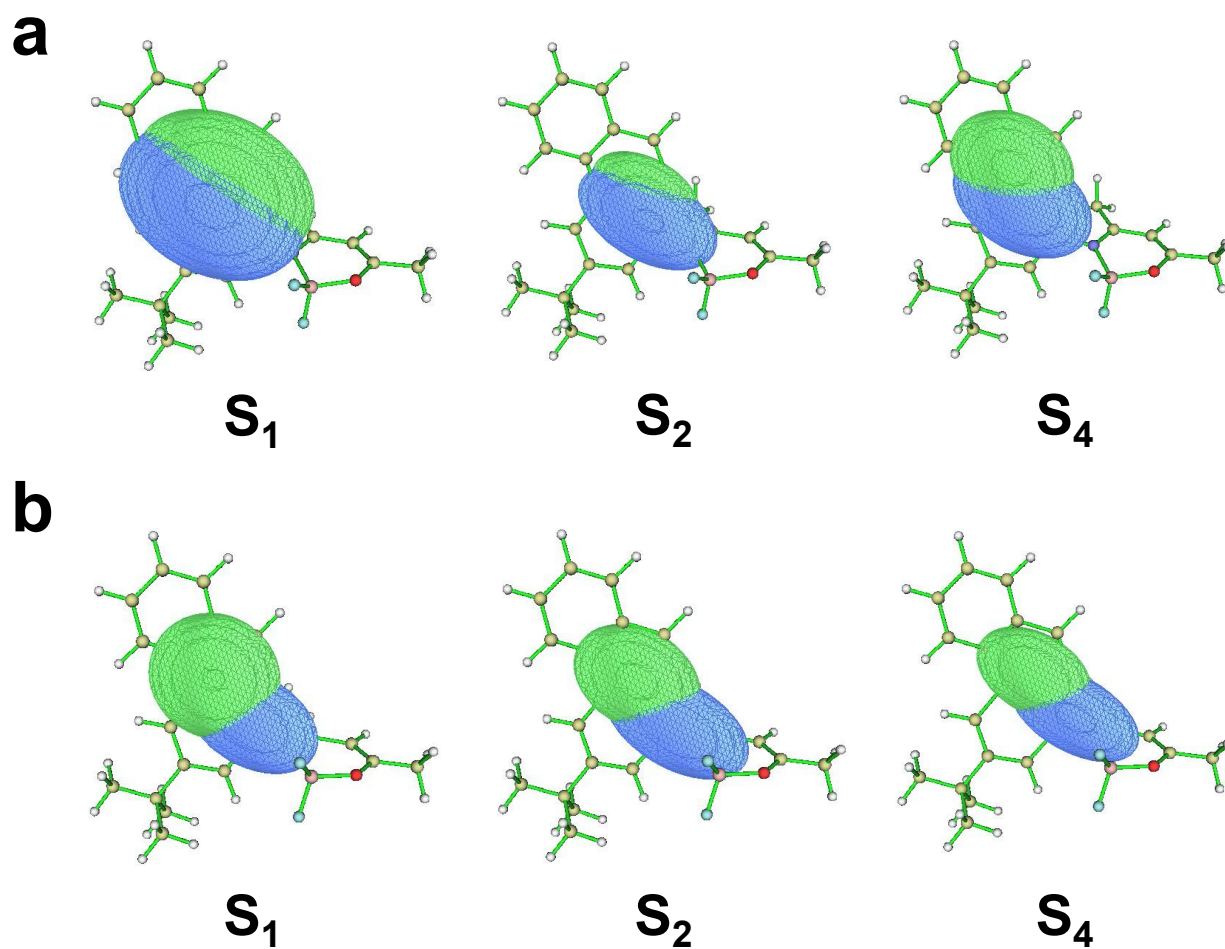
Figure 4.36. Electron-hole centroid overlap maps (isovalue = 0.0015) for the three lowest dominant transitions of **3** in (a) gas phase and (b) CH_2Cl_2.
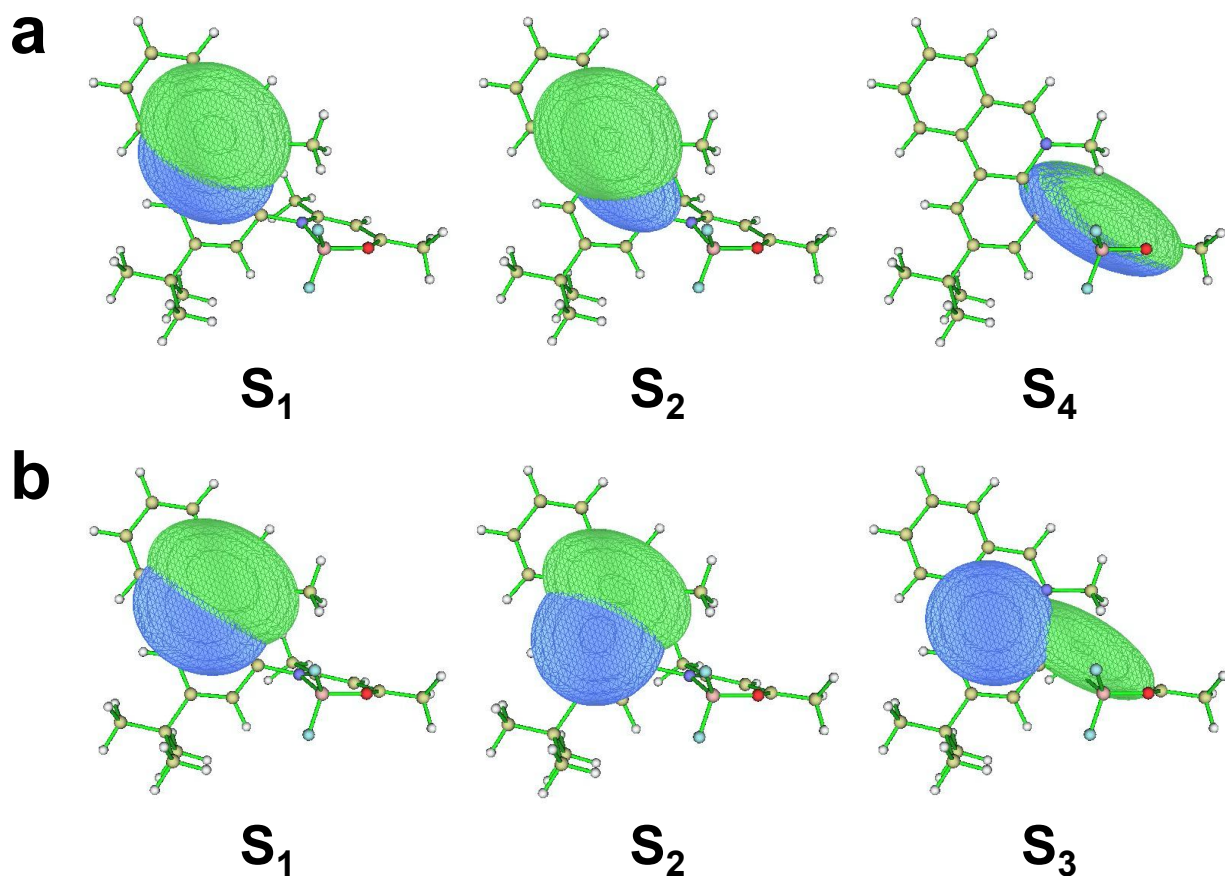
Figure 4.37. Electron-hole centroid overlap maps (isovalue = 0.0015) for the three lowest dominant transitions of $[\mathbf{3Me}]^+$ in (a) the gas phase and (b) CH_2Cl_2.

While the excitations associated with the lowest energy absorption of **3** and $[\mathbf{3Me}]^+$ are therefore clearly different, they are not so distinct as to explain the "switching-on" of emission in the methylated congener. We therefore proceeded to examine the potential energy surfaces (PES) of the ground state, the two lowest-lying excited singlet states (S_1 and S_2), and the lowest-lying excited triplet state (T_1) of **3** by scanning about the phenanthridinyl-oxazaborinine dihedral along the C-N bond adjoining these units and allowing for molecular relaxation after each rotation (Figure 4.37, CH_2Cl_2). Two minima are observed in the ground state with an associated transition energy of 1.4-1.7 eV. The rotation about the C-N bond connecting the phenanthridinyl and

253

oxazaborinine units involves a transition state where the phenanthridinyl and (N^O)B ring planes approach co-planarity, causing the geometry at the (N^O) nitrogen to become less planar in order to minimize unfavorable steric repulsion between the two fragments. The steep descent from the maxima indicates a discontinuity which may involve BF_2 dissociation from the ligand – this could provide a pathway for non-radiative decay.
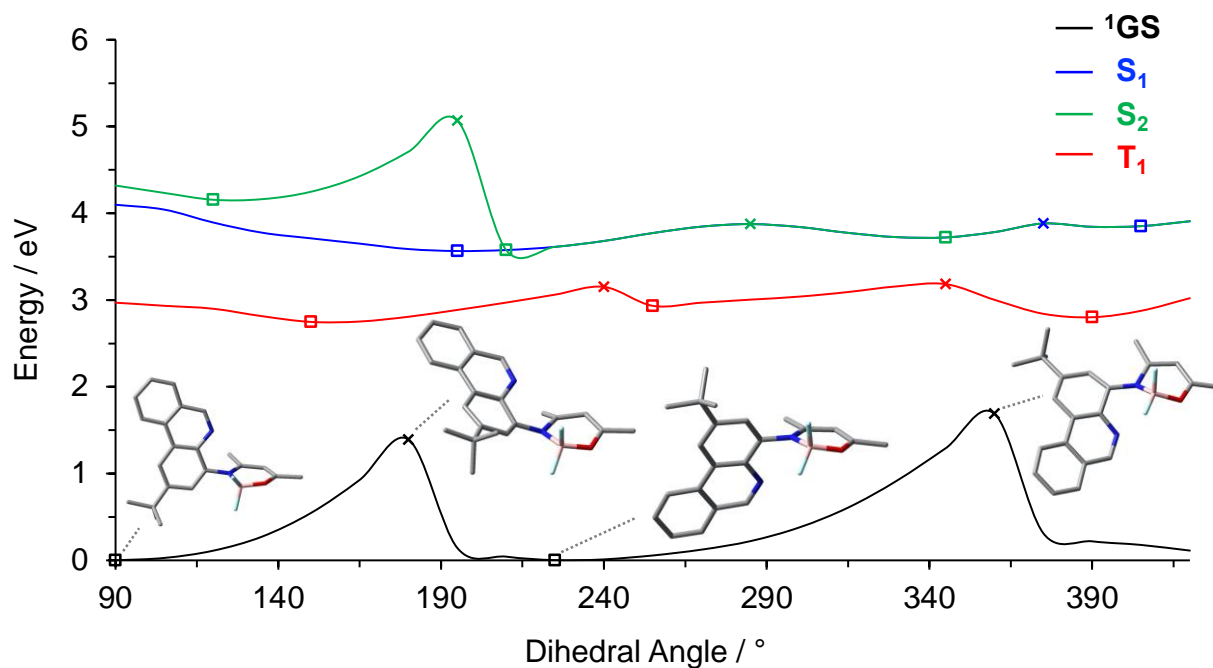
Figure 4.38. Relaxed PES of the ground state, two lowest-lying excited singlet states, and lowest-lying excited triplet state of **3** in the CH_2Cl_2 at the SMD-CAM-B3LYP-D3(BJ)/def2-SVP level of theory. Minima and maxima are denoted by open square and cross, respectively.

The excited singlet (S_1, S_2) and triplet (T_1) states show multiple shallow minima which more or less coincide with the maxima of the ground state PES of **3**. These minima are defined by reduced planarity at the (N^O) nitrogen atom, such that the phenanthridine and (N^O)BF_2 units hinge about this atom. Such 'butterfly modes' have been invoked in formazanate ligand BF_2 complexes to explain non-emissive excited states.[194] The PES of the excited singlet and triplet

254

states exhibit several energetically close structures which could facilitate rapid ISC to the low-lying excited triplet state through vibronic coupling and may explain the observed ratio of the integrated intensities of the fluorescence to phosphorescence bands in **3** (1:4). Methylation rigidifies [**3**Me]$^+$ compared to **3** and likely increases the barrier associated with the rotation about the phenanthridine-oxazaborinine connecting C-N bond. If ISC from S_1 to T_1 requires a change in geometry as described above, this rigidification may serve to inhibit ISC. Indeed, at 77 K, the fluorescence:phosphorescence ratio observed for [**3**Me]$^+$ is considerably larger (3.5:1) than for **3** (1:4). The similarity of the orbital characters of the S_1 and S_2 states ($^1\pi$-π^*) and the T_1 state ($^3\pi$-π^*) could similarly disfavor ISC. In comparison, in **3**, we find more pronounced difference in the characters of the low-lying excited singlet states compared with the triplet state. While the excited singlet states of **3** exhibit some CT character, the triplet state is predominantly phenanthridinyl π-π^* character (Figure 4.39). As per El-Sayed's rule,[195] differences in the orbital characters between the low-lying excited singlet and triplet states should enhance spin-orbit coupling between these states and facilitate efficient ISC. This could also contribute to the increased quantum yield in [**3**Me]OTf compared to **3** in fluid solution.

Furthermore, the anomalous excitation spectra of **1-4** with respect to their UV-Vis absorption spectra can be explained in light of the shallow PESs of the excited states. Closely related oxazaborinines exhibit extremely weak emission in solution but become emissive in the solid-state.[93,94] Restriction of such motions in the solid-state could explain the increased emission. Complexes **1**-**4** do not emit in the solid state, likely due to aggregation-induced quenching, but they are emissive in frozen glass at 77 K as discussed earlier. The spin density of the T_1 states of **3** and [**3**Me]$^+$ (Figures 4.39 and 4.40) indicates phenanthridinyl π-π^* character to both, in line with our earlier interpretation of phenanthridine-like fluorescence and phosphorescence.

255
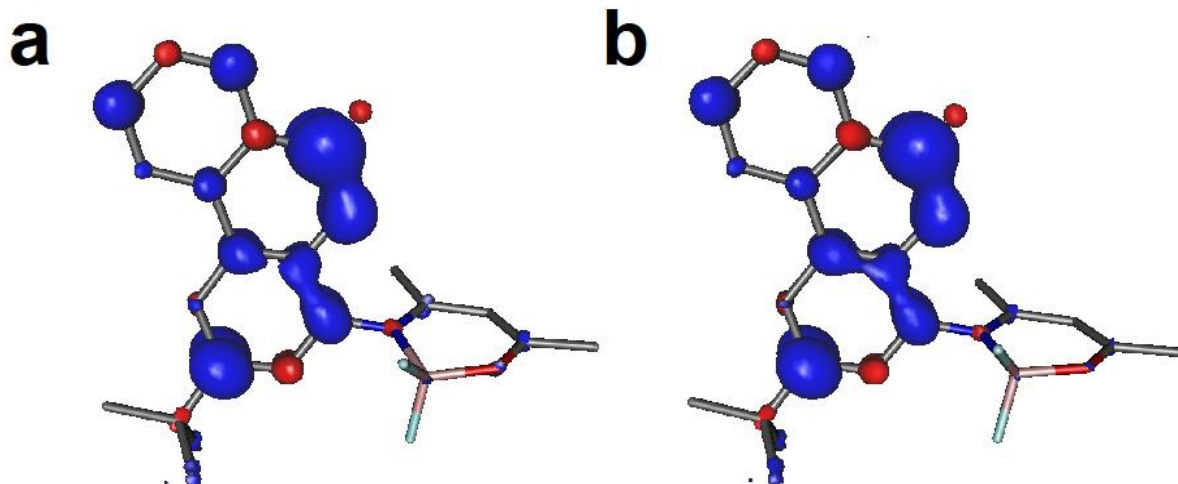
Figure 4.39. Spin density maps of the T_1 state for **3** in (a) the gas phase (RIJCOSX-uM06-2X/def2-TZVP(-f)+def2/J//uCAM-B3LYP-D3(BJ)/def2-SVP), and (b) in CH_2Cl_2 (SMD-RIJCOSX-uM06-2X/def2-TZVP(-f)+def2/J//SMD-uCAM-B3LYP-D3(BJ)/def2-SVP; isovalue = 0.004).
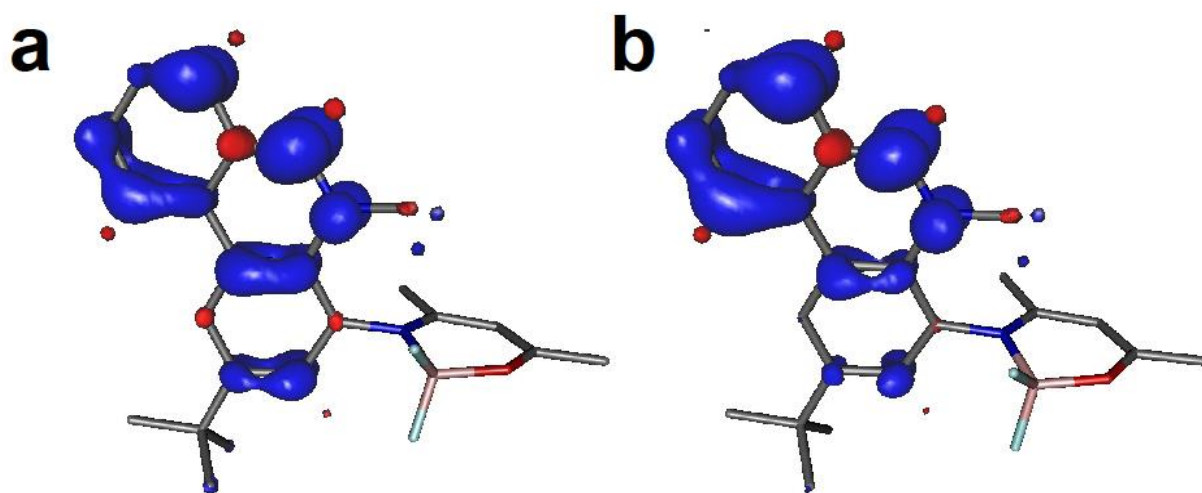
Figure 4.40. Spin density maps of of the T_1 state for [**3**Me]$^+$ in (a) the gas phase (RIJCOSX-uM06-2X/def2-TZVP(-f)+def2/J//uCAM-B3LYP-D3(BJ)/def2-SVP), and (b) in CH_2Cl_2 (SMD-RIJCOSX-uM06-2X/def2-TZVP(-f)+def2/J//SMD-uCAM-B3LYP-D3(BJ)/def2-SVP; isovalue = 0.004).

256

4.3.7 Phosphorescent Zinc(II) Complexes

Here, the origin of the unusual phosphorescence in zinc complexes (section 3.4.2) is presented through the lens of DFT and TDDFT. Single-point calculations with implicit solvation (SMD, CH_2Cl_2) were performed on the ground-state equilibrium geometries to model the frontier molecular orbitals (Figure 4.41; see Tables 4.24-4.26 for fragment contributions). The two highest filled MOs are largely comprised of the enolato-imine N^O moiety (~60%) and are nearly degenerate. The energy difference between the two highest filled MOs found by DFT ($\Delta E_{HOMO-HOMO-1} = 0.14$ eV) is in broad agreement with that estimated by cyclic voltammetry ($\Delta E_{HOMO-HOMO-1} = 0.30$-$0.37$ eV). The two lowest-lying, nearly degenerate vacant MOs ($\Delta E_{LUMO-LUMO+1} < 80$ meV) are largely phenanthridinyl-based (~90%) with significant density at the N=CH sub-unit (~30%). An electrochemical reduction can be clearly observed only for **7** (-2.21 V; -2.36 eV); cathodic events for **5/6** overlap with the solvent window. This shift to less negative potential for **7** is again in line with calculated LUMO values. Pseudo-square planar Pt(II) complexes of **L1-4** with a chloride co-ligand exhibit similar localization of the HOMO electron density at the N^O core, but with significant mixing between filled Pt(II) *d*-orbitals and a chloride lone-pair of the appropriate π-type symmetry.[101] In those complexes, the LUMO orbital density is similarly localized on the phenanthridinyl moiety. Interestingly, in **5-7** the HOMO and HOMO-1 show weak, but not completely negligible, p_π-d_π mixing (< 2%) of the N2 and O1 lone pairs with Zn(II) *d*-orbitals of appropriate symmetries. In combination with the diminished amido character of the ligand upon coordination to Zn(II), this p_π-d_π mixing could contribute to the enhanced stability of the present complexes to air and ambient moisture compared to homoleptic *N*-phenyl-phenanthridinylamidozinc(II) complexes.[108] Participation of metal *d*-orbitals in electronic

257

transitions should also promote both intersystem crossing (ISC) to low-lying excited triplet states and the subsequent radiative decay of the T_1 state to generate phosphorescence.
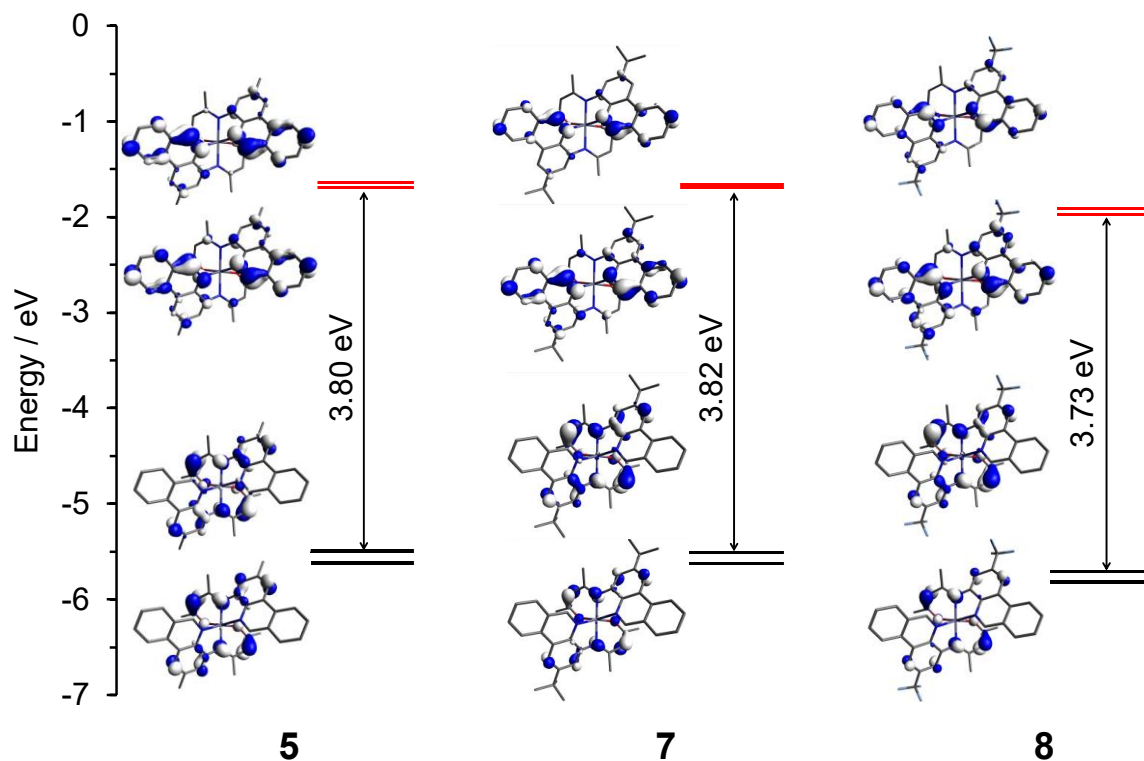
Figure 4. 41. Ground-state frontier molecular orbital energy level diagram (HOMO-1 to LUMO+1), HOMO-LUMO energy gaps and isosurfaces (isovalue = 0.04) for **5-7**.

Table 4.24. Fragment contributions to select ground-state MOs of **5**. Fragment contribution of the HC=N fragment of phenanthridinyl moiety is shown in parentheses.

MO	E / eV	Zn	Phenanthridinyl (HC=N)	N^O	Me
LUMO+1	-0.97	1	86 (28)	12	1
LUMO	-1.02	1	86 (28)	11	1
HOMO	-6.39	2	38	59	1
HOMO-1	-6.53	1	40	59	0

Table 4.25. Fragment contributions (in %) to select ground-state MOs of **6**. Fragment contribution of the HC=N fragment of phenanthridinyl moiety is shown in parentheses.

MO	E / eV	Zn	Phenanthridinyl (HC=N)	N^O	tBu
LUMO+1	-0.97	1	87 (29)	11	2
LUMO	-1.03	1	86 (29)	11	2
HOMO	-6.40	2	38	60	1
HOMO-1	-6.54	1	39	59	1

Table 4.26. Fragment contributions (in %) to select ground-state MOs of **7**. Fragment contribution of the HC=N fragment of phenanthridinyl moiety is shown in parentheses.

MO	E / eV	Zn	Phenanthridinyl (HC=N)	N^O	CF_3
LUMO+1	-1.24	1	86 (28)	11	2
LUMO	-1.32	1	86 (28)	11	2
HOMO	-6.61	2	34	64	1
HOMO-1	-6.74	1	36	63	0

Overall, the orbital characters of the frontier MOs imply that intraligand charge-transfer (ILCT) dominates the lowest energy absorption manifold (λ_{abs} > 375 nm) and contributes to the low energy tail observed in all complexes. To support this assignment, scalar relativistic TDDFT calculations on the gas-phase optimized ground-state geometries of the complexes were carried out in CH_2Cl_2 (Figures 4.42-4.44, Tables 4.27-4.29). These predict two electronic transitions with oscillator strengths > 0.1. The lowest energy predicted vertical excitations (S_1) are dominantly HOMO→LUMO in character (> 60%), with minor contribution from the HOMO-1→LUMO+1 (> 10%). The second lowest-lying excited singlet state largely consists of HOMO→LUMO+1 (~50%) and HOMO-1→LUMO excitations. Scalar TDDFT, therefore, supports ILCT character of the lowest energy absorption manifold of the complexes, with the low-energy tail associated with

259

the HOMO→LUMO excitation accounting for the intense yellow color of the complexes. This implies that exciton pairs generated from the two lowest-lying excited singlet states are highly delocalized between the two ligands.
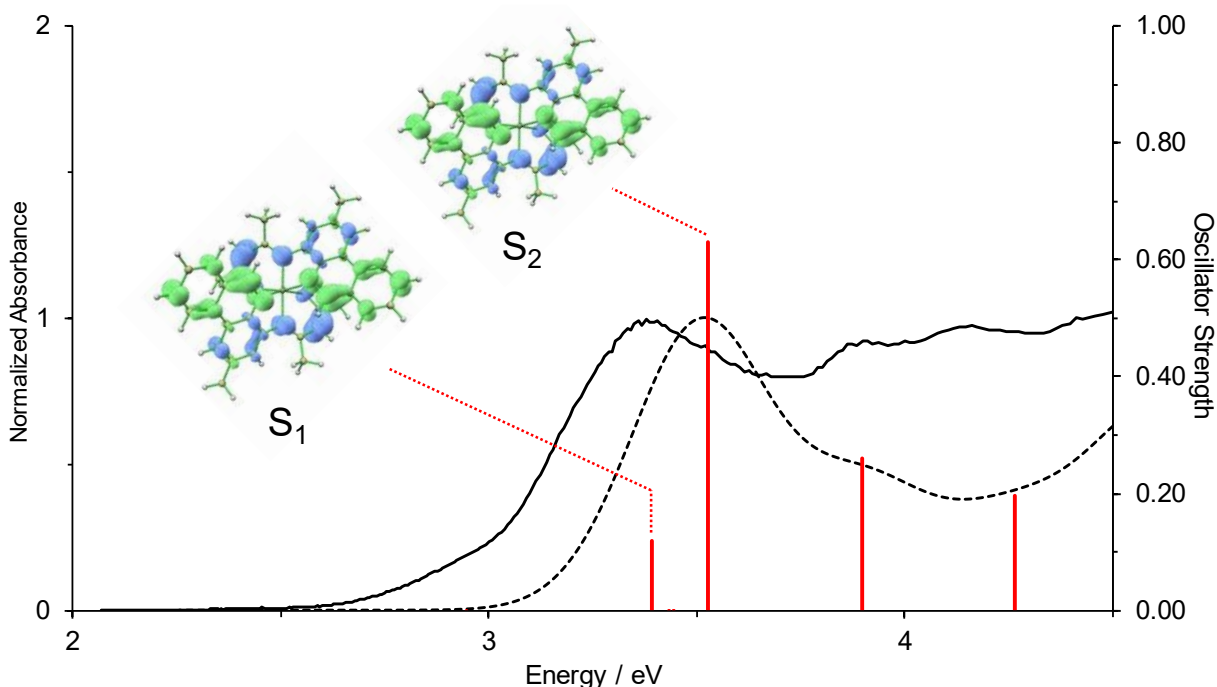
Figure 4.42. Normalized experimental UV-Vis absorption spectrum (─), normalized TDDFT simulated spectrum (---; FWHM = 0.372 eV), predicted singlet-singlet vertical excitation energies ($f_{osc} > 0.1$), and electron-hole density maps (isosurface value = 0.002) for the two lowest electronic transitions in the lowest energy absorption manifold of **5**.

Table 4.27. TDDFT predicted singlet-singlet vertical excitation energies, oscillator strengths ($f_{osc} > 0.1$), and MO pair contributions (>10%) for **6**.

No.	E /eV	f_{osc}	MO contributions
1	3.39	0.12	H L 67%, H -1→ L+1 13%
2	3.53	0.66	H → L+1 50%, H-1 → L 32%
5	3.90	0.26	H → L+2 42%, H → L+1 23%
10	4.27	0.20	H → L+4 28%, H-1 → L+5 16%, H-2 → L 12%
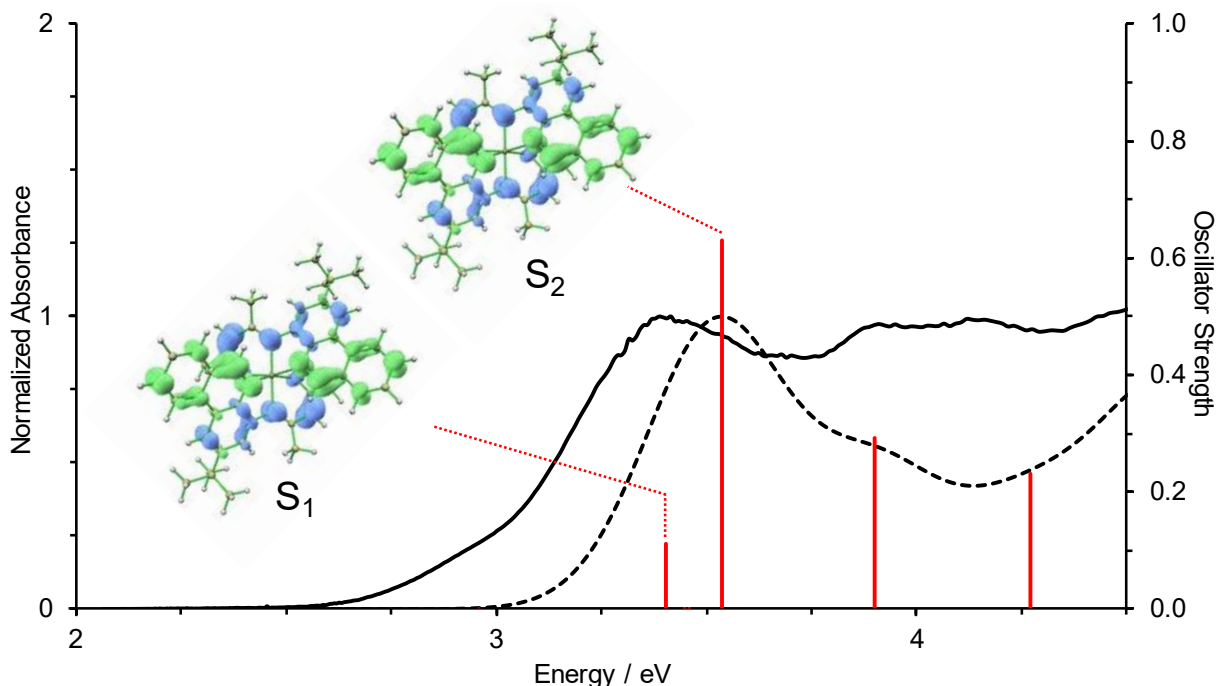
Figure 4.43. Normalized experimental UV-Vis absorption spectrum (─), normalized TDDFT simulated spectrum (---; FWHM = 0.372 eV), predicted singlet-singlet vertical excitation energies ($f_{osc} > 0.1$), and electron-hole density maps (isosurface value = 0.002) for the four lowest electronic transitions in the lowest energy absorption manifold of **6**.

Table 4.28. TDDFT predicted vertical excitation energies, oscillator strengths ($f_{osc} > 0.1$), and MO pair contributions (>10%) for **6**.

No.	E /eV	f_{osc}	MO contributions
1	3.41	0.11	H → L 67%, H-1 → L+1 12%
2	3.54	0.61	H → L+1 49%, H-1 → L 33%
3	3.9.	0.29	H → L+2 45%, H → L+1 19%, H-1 → L+3 11%
4	4.27	0.23	H → L+4 26%, H-1 → L+5 14%, H-2 → L 14%, H-3 → L+1 12%
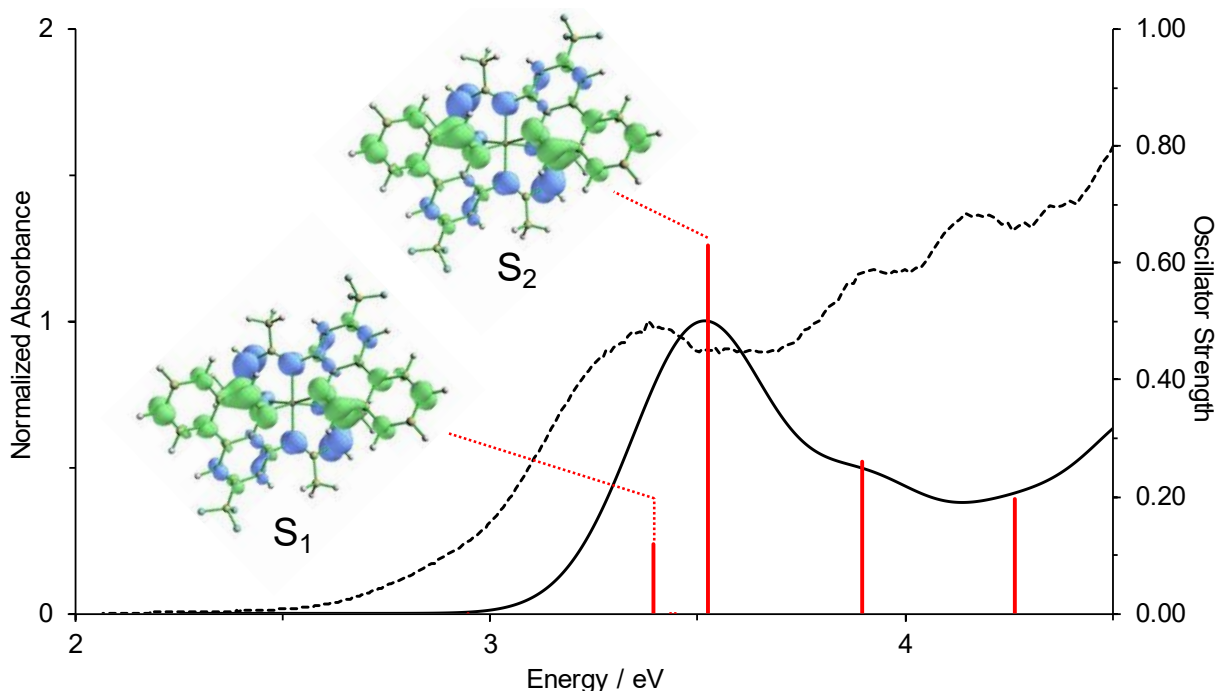
Figure 4.44. Normalized experimental UV-Vis absorption spectrum (─), normalized TDDFT simulated spectrum (---; FWHM = 0.372 eV), predicted singlet-singlet vertical excitation energies ($f_{osc} > 0.1$), and electron-hole density maps (isosurface value = 0.002) for the four lowest electronic transitions in the lowest energy absorption manifold of **7**.

Table 4.29. TDDFT predicted vertical excitation energies, oscillator strengths ($f_{osc} > 0.1$), and MO pair contributions (>10%) of **7**.

No.	E /eV	f_{osc}	MO contributions
1	3.33	0.11	H → L 72%, H-1 → L+1 11%
2	3.49	0.64	H → L+1 47%, H-1 → L 38%
5	3.88	0.23	H → L+2 52%, H-1 → L+3 15%
10	4.31	0.18	H → L+4 20%, H-4 → L 14%, H-1 → L+5 12%, H-3 → L+1 12%, H → L+2 11%

Electron-hole density maps are consistent with ILCT with electron transfer from the N^O chelate rings to the phenanthridinyl-acceptor moieties. While a CT assignment might imply a strong influence of the solvent dielectric, the complexes exhibit weak solvatochromism of the $\lambda_{max,abs}$; more prominent shifts are observed for the low-energy shoulder. Fe(II) complexes supported by 4-[*N*-(8-quinolinyl)]amidophenanthridines, also with approximate C_2 symmetry, exhibit CT excitations (pπ/dπ*-to-ligand CT or 'π-anti-bonding-to-ligand' PALCT) occurring between 600-800 nm and are similarly invariant to changes in solvent polarity,[196,197] as is the MLCT band of $[Ru(bpy)_3]^{2+}$, which shows only weak solvatochromism.[129] In each case, the complexes exhibit a more spherically symmetric redistribution of the electron density. As mentioned above, electron-hole density maps reveal a rather symmetric and delocalized redistribution of the exciton pair between ligands which may account for the weak solvatochromism.

The characteristics and trends in the emission of the complexes warrants further discussion. The millisecond (ms) lifetimes and the size of the apparent Stokes shift (1.2-1.3 eV) suggest that radiative decay occurs from a long-lived excited triplet state. To understand the decay process from the initially populated ^{1}ILCT states, the lowest energy excited triplet state was investigated computationally for all complexes. Firstly, the spin-orbit coupling (SOC) matrix elements (SOCMEs) in Tables 4.30-4.32 indicate weak but non-vanishing mixing between excited singlet and triplet states, which is commensurate with the efficiency of intersystem-crossing (ISC) from the initially populated ^{1}ILCT to the excited triplet state manifold and may explain the ms lifetimes observed for all complexes. The eight lowest triplet excited states at the ground-state geometry all exhibit coupling with the two lowest-lying excited singlet states such that ISC might occur (i) from ^{1}ILCT$_1$ or ^{1}ILCT$_2$ to any of these lower-lying excited triplet states before decaying to the emissive

triplet state; or (ii) via direct ISC to the emissive triplet state. Furthermore, these triplet excited states are also weakly coupled to the ground state, which may contribute to the low quantum yield.

Table 4.30. Spin-orbit coupling matrix elements for **5** between the eight lowest-lying excited triplet state with the ground state (S = 0), and two lowest-lying excited singlet states (S = 1, 2) calculated at the optimized ground state geometry.

Root		$<T|H_{SO}|S>$ (Re, Im) cm^{-1}		
T	S	Z	X	Y
1	0	(0.00 , -0.22)	(0.00 , 0.91)	(-0.00 , 1.08)
1	1	(0.00 , -0.03)	(0.00 , -0.20)	(-0.00 , -0.68)
1	2	(0.00 , 0.50)	(0.00 , 0.62)	(-0.00 , -0.60)
2	0	(0.00 , -1.37)	(0.00 , 0.54)	(-0.00 , -0.69)
2	1	(0.00 , -0.06)	(0.00 , 0.71)	(-0.00 , -0.28)
2	2	(0.00 , -0.13)	(0.00 , -0.43)	(-0.00 , -0.31)
3	0	(0.00 , -1.52)	(0.00 , 0.27)	(-0.00 , 0.03)
3	1	(0.00 , 1.07)	(0.00 , 1.88)	(-0.00 , -1.30)
4	0	(0.00 , 0.29)	(0.00 , 0.95)	(-0.00 , 1.36)
4	1	(0.00 , -0.08)	(0.00 , -0.00)	(-0.00 , 0.42)
4	2	(0.00 , 0.65)	(0.00 , 2.03)	(-0.00 , -1.48)
5	0	(0.00 , -0.23)	(0.00 , -0.75)	(-0.00 , 0.20)
5	1	(0.00 , -0.01)	(0.00 , 0.10)	(-0.00 , 1.05)
5	2	(0.00 , 0.43)	(0.00 , 1.88)	(-0.00 , -1.55)
6	0	(0.00 , -1.27)	(0.00 , -3.11)	(-0.00 , 2.20)
6	1	(0.00 , -0.26)	(0.00 , -1.92)	(-0.00 , 1.08)
6	2	(0.00 , -0.15)	(0.00 , -0.94)	(-0.00 , -0.33)
7	0	(0.00 , 0.20)	(0.00 , 0.21)	(-0.00 , 0.78)
7	1	(0.00 , -0.22)	(0.00 , -0.38)	(-0.00 , 0.03)
7	2	(0.00 , -0.16)	(0.00 , 0.72)	(-0.00 , -0.44)
8	0	(0.00 , 0.39)	(0.00 , -1.19)	(-0.00 , 0.50)
8	1	(0.00 , -0.72)	(0.00 , -0.86)	(-0.00 , 0.71)
8	2	(0.00 , 0.04)	(0.00 , -0.15)	(-0.00 , 0.25)

Table 4.31. Spin-orbit coupling matrix elements for **6** between the eight lowest-lying excited triplet state with the ground state (S = 0), and two lowest-lying excited singlet states (S = 1, 2) calculated at the optimized ground state geometry.

Root		$<T|H_{SO}|S>$ (Re, Im) cm^{-1}		
T	S	Z	X	Y
1	0	(0.00 , -0.20)	(0.00 , 0.88)	(-0.00 , 1.14)
1	1	(0.00 , 0.04)	(0.00 , 0.20)	(-0.00 , 0.67)
1	2	(0.00 , -0.48)	(0.00 , -0.71)	(-0.00 , 0.64)
2	0	(0.00 , 1.35)	(0.00 , -0.37)	(-0.00 , 0.60)
2	1	(0.00 , -0.07)	(0.00 , 0.74)	(-0.00 , -0.30)
2	2	(0.00 , -0.11)	(0.00 , -0.43)	(-0.00 , -0.31)
3	0	(0.00 , 1.51)	(0.00 , -0.23)	(-0.00 , -0.10)
3	1	(0.00 , 1.04)	(0.00 , 1.87)	(-0.00 , -1.27)
3	2	(0.00 , 0.12)	(0.00 , 0.55)	(-0.00 , 0.22)
4	0	(0.00 , 0.31)	(0.00 , 0.84)	(-0.00 , 1.27)
4	1	(0.00 , 0.11)	(0.00 , 0.06)	(-0.00 , -0.48)
4	2	(0.00 , -0.59)	(0.00 , -2.00)	(-0.00 , 1.47)
5	0	(0.00 , 0.24)	(0.00 , 0.89)	(-0.00 , -0.22)
5	1	(0.00 , -0.01)	(0.00 , 0.07)	(-0.00 , 1.07)
5	2	(0.00 , 0.43)	(0.00 , 1.89)	(-0.00 , -1.55)
6	0	(0.00 , 1.20)	(0.00 , 3.30)	(-0.00 , -2.34)
6	1	(0.00 , -0.27)	(0.00 , -1.92)	(-0.00 , 1.06)
6	2	(0.00 , -0.14)	(0.00 , -0.94)	(-0.00 , -0.30)
7	0	(0.00 , -0.18)	(0.00 , -0.23)	(-0.00 , -0.88)
7	1	(0.00 , -0.22)	(0.00 , -0.37)	(-0.00 , 0.06)
7	2	(0.00 , -0.14)	(0.00 , 0.79)	(-0.00 , -0.49)
8	0	(0.00 , -0.35)	(0.00 , 1.25)	(-0.00 , -0.51)
8	1	(0.00 , -0.77)	(0.00 , -0.96)	(-0.00 , 0.75)
8	2	(0.00 , 0.02)	(0.00 , -0.15)	(-0.00 , 0.26)

Table 4.32. Spin-orbit coupling matrix elements for **7** between the eight lowest-lying excited triplet state with the ground state (S = 0), and two lowest-lying excited singlet states (S = 1, 2) calculated at the optimized ground state geometry.

Root		$<T|H_{SO}|S>$ (Re, Im) cm^{-1}		
T	S	Z	X	Y
1	0	(0.00 , 0.04)	(0.00 , 0.03)	(-0.00 , -1.66)
1	1	(0.00 , 0.01)	(0.00 , 0.02)	(-0.00 , 0.62)
1	2	(0.00 , -0.49)	(0.00 , 0.89)	(-0.00 , 0.01)
2	0	(0.00 , -1.26)	(0.00 , -1.02)	(-0.00 , -0.05)
2	1	(0.00 , -0.23)	(0.00 , -0.49)	(-0.00 , 0.02)
2	2	(0.00 , -0.01)	(0.00 , 0.03)	(-0.00 , -0.45)
3	0	(0.00 , -1.78)	(0.00 , -0.99)	(-0.00 , 0.02)
3	1	(0.00 , 1.09)	(0.00 , -2.35)	(-0.00 , 0.01)
3	2	(0.00 , 0.01)	(0.00 , -0.04)	(-0.00 , 0.42)
4	0	(0.00 , 0.03)	(0.00 , 0.02)	(-0.00 , 1.24)
4	1	(0.00 , -0.02)	(0.00 , 0.03)	(-0.00 , 0.43)
4	2	(0.00 , 0.56)	(0.00 , -2.62)	(-0.00 , -0.01)
5	0	(0.00 , 0.01)	(0.00 , -0.00)	(-0.00 , -0.78)
5	1	(0.00 , -0.00)	(0.00 , -0.01)	(-0.00 , 0.45)
5	2	(0.00 , 0.66)	(0.00 , -2.06)	(-0.00 , 0.00)
6	0	(0.00 , 1.03)	(0.00 , -2.27)	(-0.00 , 0.00)
6	1	(0.00 , -0.11)	(0.00 , -0.81)	(-0.00 , -0.01)
6	2	(0.00 , -0.01)	(0.00 , 0.03)	(-0.00 , 0.24)
7	0	(0.00 , -0.04)	(0.00 , 0.24)	(-0.00 , -0.59)
7	1	(0.00 , -0.03)	(0.00 , 0.12)	(-0.00 , -0.43)
7	2	(0.00 , -0.10)	(0.00 , 2.06)	(-0.00 , -0.02)
8	0	(0.00 , 0.67)	(0.00 , -4.97)	(-0.00 , -0.03)
8	1	(0.00 , 0.65)	(0.00 , -2.34)	(-0.00 , -0.02)
8	2	(0.00 , -0.00)	(0.00 , 0.10)	(-0.00 , 0.37)

It is also worth noting that relaxation of the S_1 and S_n states (from the Franck-Condon region) to the T_1 breaks the symmetry of the electron distribution such that both unpaired electrons are localized in one ligand (Figure 4.45-4.47). The spin densities of the excited T_1 states of the

266

complexes on the ground state geometries also exhibit this symmetry breaking. This calculated character is invariant to the degree of Hartree-Fock admixture introduced. Such symmetry-broken charge transfer (SBCT) states have been observed in bis(dipyrrin)zinc(II) and are thought to promote efficient ISC to low-lying triplet manifolds either through radical pair ISC (RP-ISC) or spin-orbit, charge transfer ISC (SOCT-ISC).[198–201] However, to our knowledge, bis(dipyrrin)zinc(II) do not exhibit detectable phosphorescence either in solution or the solid state, unlike **5-7**. The driving force for charge-separation, ΔG_{CS},[202,203] in **7** was estimated (neglecting Coulombic interactions between the electron-hole pair, E_c) to have upper and lower limits of -0.78 and -0.44 eV in CH_2Cl_2, respectively using Equation (4.5) where $E_{ox/red}$ are the oxidation and reduction potentials observed for **7** and E^* (the energy of the excited state) is estimated from λ_{max}(absorption).[204] These values agree with the calculated energy gap between the excited S_1 and T_1 states in the ground-state equilibrium geometry.

$$\Delta G_{CS} = e[E_{ox}(D) - E_{red}(A)] - E^* - E_c \qquad (4.6)$$
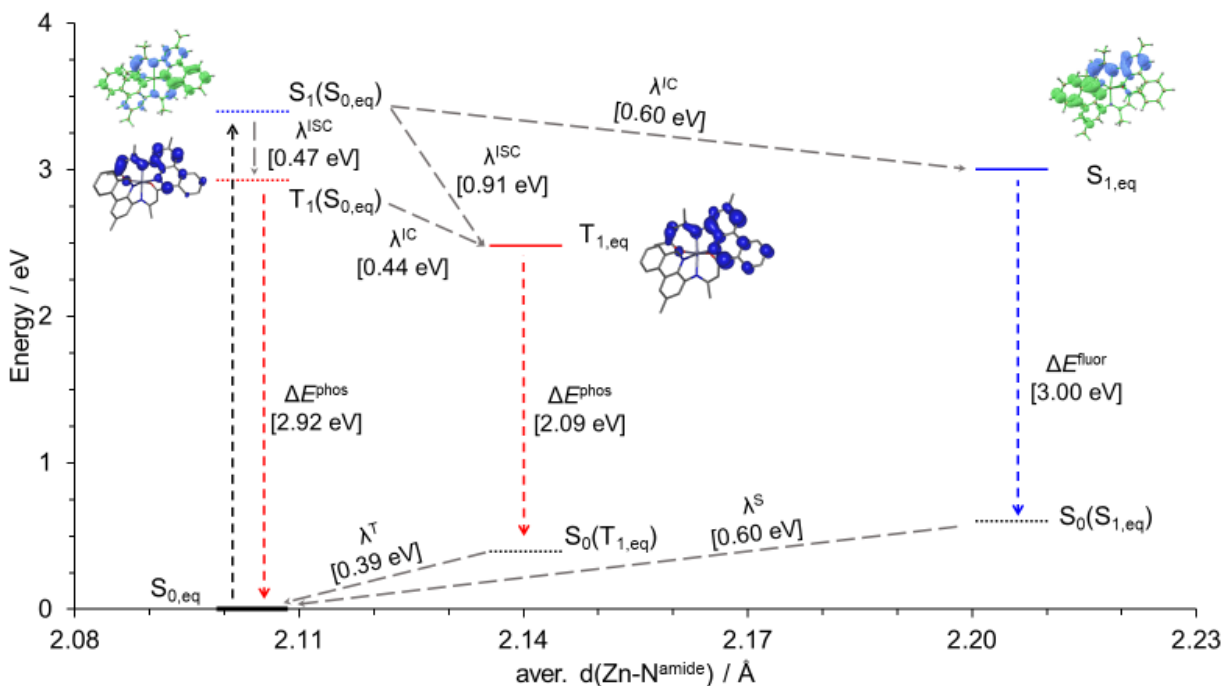
Figure 4.45. Simplified Jablonksi diagram of **5** with calculated photophysical properties ΔE^{phos}, ΔE^{fluor}, λ^{ISC}, λ^{IC}, λ_T, and λ^S. Horizontal solid lines represent minima of a given electronic state. Isosurface values for the spin density [$T_1(S_{0,eq})$ and $T_{1,eq}$] and electron-hole density maps [$S_1(S_{0,eq})$ and $S_{1,eq}$] are set to 0.004 and 0.002, respectively. The vertical, black dashed arrow indicates the initial vertical excitation from the ground state equilibrium geometry, while the vertical blue/red and gray dashed arrows indicate radiative and nonradiative decay pathways, respectively.

Figure 4.46. Simplified Jablonksi diagram of **6** with calculated photophysical properties ΔE^{phos}, λ^{ISC}, λ^{IC}, and λ_{T}. The S_1 equilibrium geometry could not be successfully optimized. Horizontal solid lines represent minima of a given electronic state. Isosurface values for the spin density [$T_1(S_{0,eq})$ and $T_{1,eq}$] and electron-hole density maps [$S_1(S_{0,eq})$] are set to 0.004 and 0.002, respectively. The vertical, black dashed arrow indicates the initial vertical excitation from the ground state equilibrium geometry, while the vertical blue/red and gray dashed arrows indicate radiative and nonradiative decay pathways, respectively.
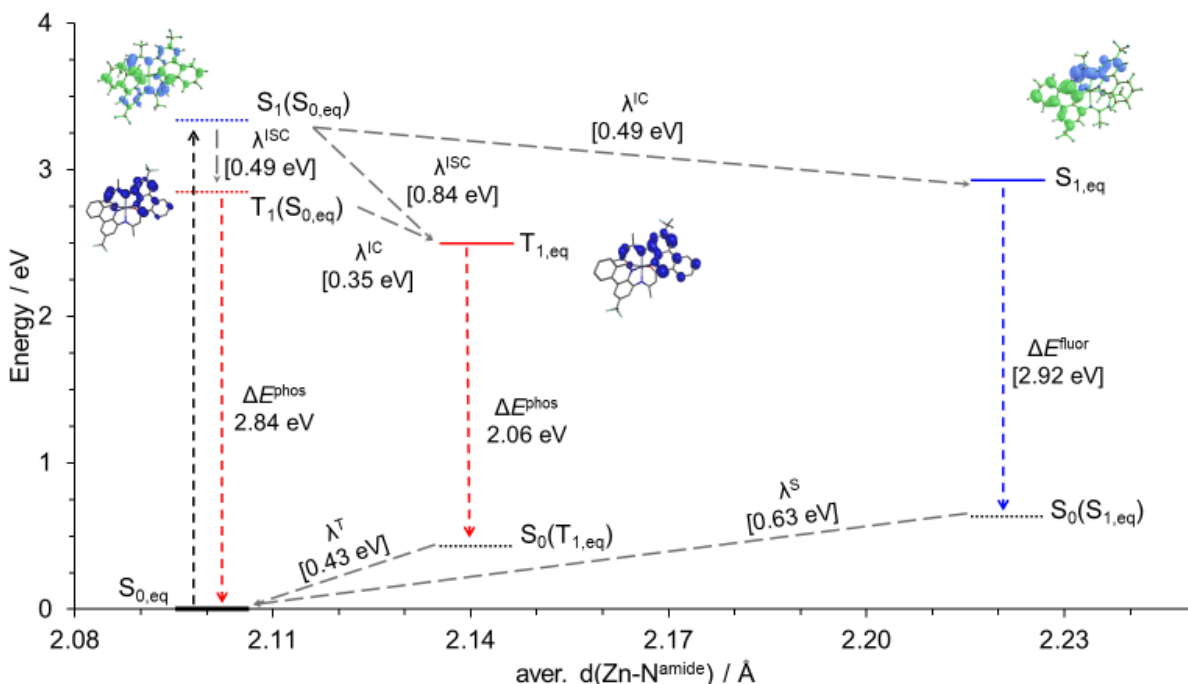
Figure 4.47. Simplified Jablonksi diagram of **7** with calculated photophysical properties ΔE^{phos}, ΔE^{fluor}, λ^{ISC}, λ^{IC}, λ_T, and λ^S. Horizontal solid lines represent minima of a given electronic state. Isosurface values for the spin density [$T_1(S_{0,eq})$ and $T_{1,eq}$] and electron-hole density maps [$S_1(S_{0,eq})$ and $S_{1,eq}$] are set to 0.004 and 0.002, respectively. The vertical, black dashed arrow indicates the initial vertical excitation from the ground state equilibrium geometry, while the vertical blue/red and gray dashed arrows indicate radiative and nonradiative decay pathways, respectively.

The calculated phosphorescence energies are in agreement with the experimental $\lambda_{max,em}$ in CH_2Cl_2 at room temperature [**5**: 2.09 eV *cf.* 2.11 eV (experimental); **6**: 1.81 eV *cf.* 2.09 eV (experimental); **7**: 2.06 eV *cf.* 2.23 eV (experimental); see Figures 4.45-4.47]. The observed Stokes shift can be accounted for by the energy loss from ISC calculated from the energy difference between the $S_1(S_{0,eq})$ and $T_{1,eq}$ with values ranging between 0.7 and 0.9 eV. Structural comparisons

between the ground state and $T_{1,eq}$ reveal an asymmetric elongation of the ligands (Figure 4.48). In addition, the O1-Zn-O2 bond angle decreases upon relaxation to the T_1 minima by 9°, while the N1-Zn-N1'/N1-Zn-N3 bond angle opens by 8°. Such molecular distortions should be attenuated in frozen glass at 77 K and in the solid state, consistent with the observed blue-shift in emission compared with in fluid solution. The energy of the lowest-lying triplet state at the ground state geometry, calculated using the energy difference between the energies of $T_1(S_{0,eq})$ and $S_{0,eq}$, mirrors this hypsochromic effect. A better agreement can be obtained when configuration interactions are accounted for in the electronic excitations through TDDFT. In contrast, *bis*[phenanthridinyl-4-(*N*-phenyl)amidozinc(II)] complexes do not exhibit any appreciable luminescence upon excitation of the ^{1}ILCT band (~500 nm) and excitation at higher energies shows emission that strongly overlaps with the ILCT absorption manifold.[108] The observation of phosphorescence from **5-7** may thus be attributed to the SBCT phenomena described above, particularly the Coulombic interaction in the generated exciton pair. The results presented here suggest that emission can be 'turned on' in Zn(II) complexes supported by N^N^O amido-type frameworks, through increased delocalization of the nitrogen lone pair and enhanced rigidity through saturating the coordination environment of the metal.
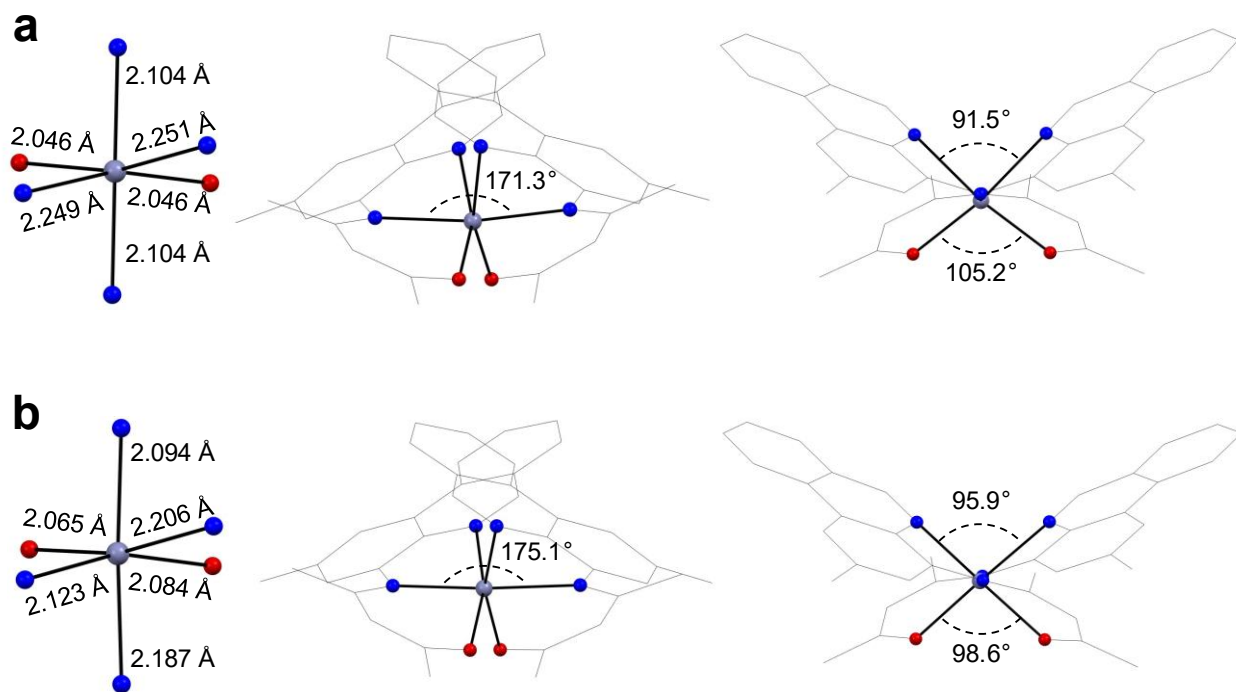
Figure 4.48. Select structural parameters for the gas-phase optimized geometries of (a) ground and (b) lowest-lying excited triplet states for **5**.

4.3.8 Phosphorescent Platinum Complexes

To better understand the trends in absorption, emission and electrochemistry, density functional theory (DFT) modelling of **8-10** was carried out. Molecular orbital energies from ground-state optimized geometries (Figure 4.49; Tables 4.33-4.36) corroborate the trends in the HOMO-LUMO gaps gleaned from electrochemistry and electronic absorption spectroscopy(see Table 3.3). In particular, the HOMO energies are slightly stabilized upon deprotonation/metal coordination and mirror the ordering discussed above. In each case, the HOMO has significant contributions from platinum (~20%), the N^O donor chelate (~45%) and the chloride (~10%), with

Pt-N$_{amido}$/O/Cl π-antibonding character evident in the MO isosurfaces. The LUMO, on the other hand, is largely comprised of the phenanthridinyl π* manifold, with significant contribution from the C=N fragment (**8** 28, **9** 31, **10** 29, **11** 28%), minor delocalization into the N^O chelate (~15%) and negligible metal (2%) and halide (0%) contributions. As noted in section 3.5.2, comparing the electrochemical data of **L1**-**L4** and **8**-**11** reveals a more pronounced shift to the potentials associated with reductions of **8**-**11** vs **L1**-**L4** compared to their respective oxidations. The localization of the LUMO at the C=N sub-unit apparently amplifies the stabilizing effect of coordination to Pt(II) on the vacant, low-lying orbitals.
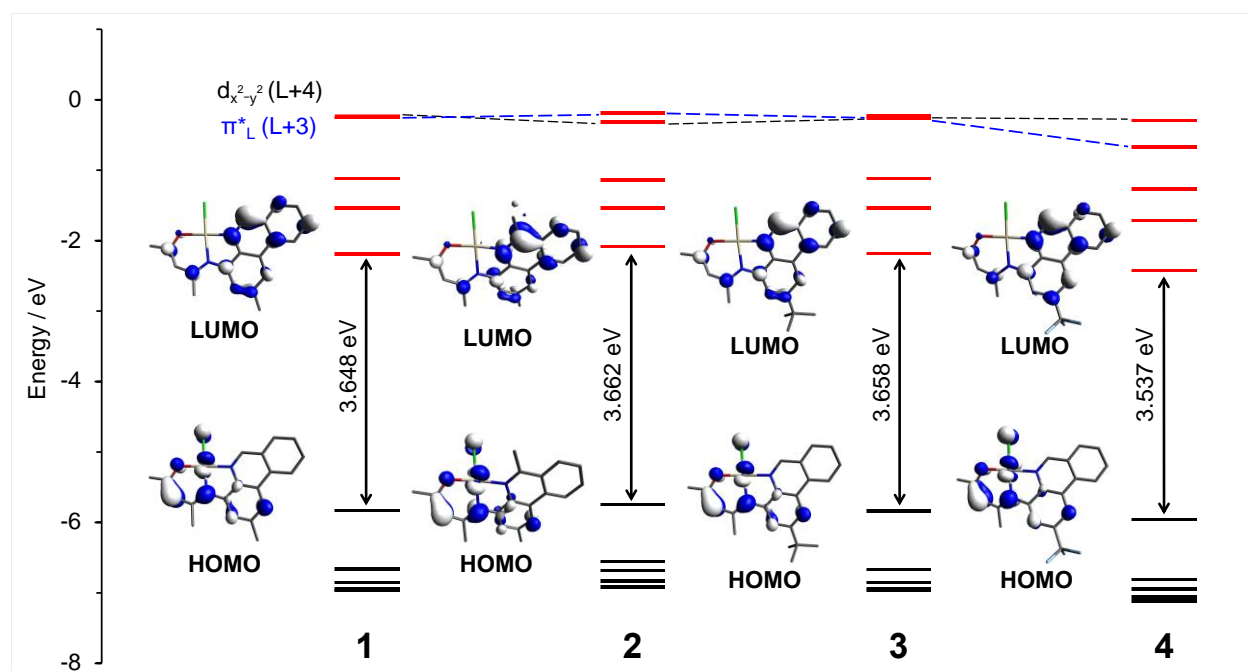
Figure 4.49. Molecular orbital energy level diagrams, HOMO-LUMO gaps and isosurfaces (isovalue = 0.04) for **1**-**4**.

Table 4.33. Fragment contributions (in %) to the ground state MOs of **8**.

MOs	E/eV	Pt	Cl	HC=N	Ar^{phen}	NAcAc	CH$_3$
L+4	-0.228	43	13	8	19	17	1
L+3	-0.254	10	3	7	62	15	4
L+2	-1.118	4	0	6	52	37	0
L+1	-1.534	3	0	7	69	20	1
L	-2.186	2	0	28	51	17	1
H	-5.834	18	9	1	23	48	0
H-1	-6.663	32	0	15	39	11	2
H-2	-6.851	39	32	1	14	13	1
H-3	-6.945	19	0	3	70	7	1
H-4	-6.966	59	21	2	10	7	0

Table 4.34. Fragment contributions (in %) to the ground state MOs of **9**.

MOs	E/eV	Pt	Cl	(CH$_3$)C=N	Ar^{phen}	NAcAc	CH$_3$
L+4	-0.191	9	2	8	68	9	4
L+3	-0.32	40	11	7	13	29	1
L+2	-1.141	6	1	6	57	30	0
L+1	-1.536	4	0	7	62	25	1
L	-2.081	2	0	31	50	15	1
H	-5.743	20	8	2	23	46	0
H-1	-6.553	38	12	14	21	14	1
H-2	-6.683	40	32	2	13	12	1
H-3	-6.83	12	10	5	68	3	2
H-4	-6.918	80	3	3	8	6	0

Table 4.35. Fragment contributions (in %) to the ground state MOs of **10**.

MOs	E/eV	Pt	Cl	HC=N	Ar^{phen}	NAcAc	tBu
L+4	-0.227	44	13	8	16	13	1
L+3	-0.259	8	2	7	65	12	4
L+2	-1.116	4	0	6	52	32	1
L+1	-1.535	3	0	6	68	18	2
L	-2.18	2	0	29	50	15	1
H	-5.838	19	9	1	23	41	0
H-1	-6.669	34	0	15	37	8	2
H-2	-6.855	39	32	1	16	11	1
H-3	-6.936	13	0	4	74	5	2
H-4	-6.965	65	20	2	6	3	0

Table S8. Fragment contributions (in %) to the ground state MOs of **11**.

MOs	E/eV	Pt	Cl	HC=N	Ar^{phen}	NAcAc	CF$_3$
L+4	-0.293	50	15	8	6	21	0
L+3	-0.671	2	0	3	70	20	6
L+2	-1.27	5	1	8	51	35	1
L+1	-1.712	2	0	6	73	17	1
L	-2.421	2	0	28	52	16	2
H	-5.958	21	10	1	20	47	0
H-1	-6.808	46	4	11	21	18	0
H-2	-6.947	38	35	2	13	12	0
H-3	-7.057	78	7	2	4	7	0
H-4	-7.115	40	39	4	9	7	0

The nature of the frontier orbitals is in line with previously studied transition metal complexes supported by ligand frameworks containing phenanthridinyl moieties, with mixed (metal + n_N) HOMO and π_{phen}* LUMO frontier orbitals.[108,196] It is notable in the HOMOs that there

is no orbital density at the 2-position of the phenanthridinyl ring. The slight perturbation in the HOMO energies thus appears to originate from the weak inductive effect of the substituent, through the orbital density at the 1- and 3- positions. The CH_3 substituent at the 6-position did not have any notable effect on the energy of the HOMO of **2** as there is no significant orbital density at the attached carbon or the adjacent nitrogen. In comparison, the LUMOs present orbital density at carbon atoms in both the 6- (*C*=N) and 2-positions; thus, the CF_3 substituent in **11** stabilizes the vacant MO and enhances the electron-accepting character of the LUMO, while the LUMO of **2** is destabilized compared to **8** as a result of hyperconjugation of the CH_3 σ_{C-H} to the phenanthridinyl $\pi^*_{HC=N}$ orbital.

TDDFT simulations were also carried out. Given the presence of the third-row transition metal ion, as discussed in section 4.3.5 spin-orbit coupling (SOC) is necessary to accurately simulate the UV-Vis spectra of a representative complex (**11**). The scalar simulated TDDFT spectrum of **11** shows only one particle-hole pair involved in the lowest energy manifold of HOMO→LUMO character (97%; Table 4.36) consistent with a mixed (M+L)LCT assignment. A notable absence of transitions is observed in the valley region between the lowest energy (~460 nm) and mid-energy (~353 nm) absorption manifolds within the spin-only approximation. Inclusion of SOC (SOC-TDDFT) leads to an increase in the spectral intensity of this region. Previous computational modelling on the UV-Vis absorption spectra of Re(I) carbonyl complexes supported by 8-aminophenanthridines and 4-aminoquinolines indicated that SOC is necessary in accounting for weak, low-energy transitions in the 450-650 nm range of such complexes.[192] In addition, an increasing body of literature supports the necessity of SOC to properly model the absorption spectra of complexes containing heavy elements, providing a mechanism to account for the direct population of low-lying excited triplet states.[192,205–207]

Table 4.36. Spin-only and SOC-corrected TDDFT predicted singlet-singlet, singlet-triplet, and singlet-SOC vertical excitation energies ($f > 0.003$), MO contributions (>10%), singlet/triplet contributions (>5 %) for **11**. Entries in red reflect SOC calculated transitions which appear in valley regions of the absorption spectrum.

^1S_n	E/eV	f_{osc}	MO contributions (> 10%)
1	2.71	0.069	H->L (97%)
2	3.46	0.026	H->L+1 (67%), H-1->L (17%)
3	3.55	0.066	H-1->L (53%), H->L+1 (16%), H-2->L (16%), H-3->L (11%)
4	3.59	0.002	H-3->L (52%), H-2->L (45%)
5	3.67	0.080	H-4->L (30%), H-2->L (24%), H-3->L (18%), H-1->L (11%)
6	3.76	0.010	H->L+2 (46%), H-4->L (28%), H->L+4 (12%)
7	3.82	0.196	H-4->L (37%), H-3->L (13%), H-2->L (12%), H->L+2 (11%)
8	3.91	0.067	H-5->L (55%), H-1->L+1 (10%)
9	4.06	0.058	H->L+4 (55%), H->L+2 (24%)
^3T_n	E/eV	f_{osc}	MO contributions (> 10%)
1	2.17	0.000	H->L (69%)
2	2.68	0.000	H-1->L (55%)
3	2.99	0.000	H->L+1 (51%), H->L (22%)
4	3.2	0.000	H-5->L (32%), H->L+2 (23%)
5	3.32	0.000	H->L+4 (36%), H-5->L (26%)
6	3.4	0.000	H->L+2 (24%), H-5->L+1 (16%), H-2->L (14%), H-5->L (13%)
7	3.42	0.000	H-2->L (24%), H-1->L (18%)
8	3.52	0.000	H-3->L (49%)
9	3.59	0.000	H-3->L (34%), H-5->L (13%)
10	3.62	0.000	H-4->L (48%), H-2->L (24%)
11	3.71	0.000	H-1->L+2 (23%), H-4->L (17%), H-5->L+1 (17%)
12	3.86	0.000	H-1->L+4 (33%), H-3->L+4 (26%)
13	3.91	0.000	H-3->L+4 (35%), H-1->L+4 (20%)
14	3.99	0.000	H-1->L+1 (37%)
15	4.04	0.000	H-4->L+4 (34%), H-2->L+4 (22%)
16	4.09	0.000	H-2->L+1 (22%)

SOC	E/eV	f_{osc}	Singlet contributions (> 5%)	Triplet contributions (> 5%)
4	2.73	0.026	1 (41%)	2 (53%)
7	2.83	0.028	1 (49%)	2 (40%), 8 (6%)
13	3.24	0.003		4 (41%), 5 (30%)
14	3.34	0.016	2 (15%), 3 (21%)	6 (7%), 7 (15%), 8 (17%), 10 (5%)
16	3.37	0.006	2 (5%), 5 (5%)	7 (47%), 8 (14%), 9 (6%), 10 (5%)
18	3.40	0.004	-	4 (44%), 5 (37%), 7 (8%)
19	3.40	0.010	-	4 (28%), 5 (38%), 7 (13%)
20	3.40	0.008	-	4 (38%), 5 (35%)
23	3.48	0.007	-	6 (62%), 7 (9%), 8 (5%)
24	3.53	0.004	2 (22%), 3 (18%), 6 (8%)	6 (8%), 8 (13%), 10 (5%)
25	3.59	0.004	-	9 (8%), 11 (16%), 12 (25%), 13 (22%), 15 (9%)
26	3.60	0.003	2 (6%)	9 (9%), 11 (19%), 12 (22%) 13 (18%)
27	3.62	0.148	2 (18%), 4 (7%), 5 (11%), 7 (10%)	8 (10%), 9 (9%), 10 (6%)

SOC-TDDFT simulated spectra for all four complexes calculated using a polarizable continuum of CH_2Cl_2 are in excellent agreement with the experimental UV-Vis absorption spectra. In general, our simulations suggest that two important transitions are responsible for the lowest energy manifold of the experimental UV-Vis spectra. For **8**-**10**, one weaker, lower-energy (SOC4, $f_{osc} > 0.005$) and a stronger, higher-energy transition (SOC7, $f_{osc} > 0.049$) are prominent, while the weaker SOC4 gains intensity in **11** due to increased participation of S_1 (**8-10** < 11%, **11** ~ 40%). Both transitions have largely S_1 excited singlet state contributions, while T_2 states dominate the excited triplet state. The S_1 state is largely HOMO→LUMO; that is, (M+L)LCT, in character. The T_2 excited state, on the other hand, has significant contribution from the HOMO-1→LUMO

transition, which comprises a similar (M+L)LCT character but with increased contribution from Pt (%Pt, HOMO-1: **8** 32, **9** 38, **10** 34, **11** 46) and reduced Cl (%Cl, HOMO-1: **8** 0, **9** 12, **10** 0, **11** 4) contribution. This would suggest that the lowest energy absorption manifold can be reasonably attributed to HOMO→LUMO transitions, which enables us to estimate the E_g from the λ_{max} of this band. This also explains the excellent agreement between the experimental $\Delta E_{HOMO-LUMO}$ from electrochemistry and E_g estimated by optical spectroscopy. Thus, the spectral shifts observed between the Pt(II) complexes can be largely attributed to the electronic perturbations identified in the frontier MOs. In either case, relaxation to the lowest-lying triplet state (T_1) is expected prior to radiative decay.

The optimized geometries of the T_1 state, in each case, show a general contraction of the Pt-N$_{amido}$ (Pt1−N2) and Pt−Cl bond distances. This is consistent with depopulation of an orbital (HOMO) with Pt-N$_{amido}$/Pt-Cl antibonding character. The increase in bond order reflects the charge-transfer (CT) character of T_1, as metal-centreed (MC) states would be expected to result in longer metal-ligand bonds thanks to population of metal-ligand anti-bonding orbitals. Similar π-mixing between ligand π-orbitals and metal d-orbitals of appropriate symmetry has been observed in Fe(II) complexes of diarylamido ligands, but not for other metals.[208] In the former, depopulation of a highly covalent HOMO with metal-N$_{amido}$ (dπ-pπ)* anti-bonding character is similarly thought to induce a metal-ligand bond contraction in the CT state, with consequences for CT/MC excited state ordering. In comparison, square planar Pt complexes of dithiolene ligands bearing protonated pyrazine units show diminished dπ-pπ hybridization compared to complexes of lighter elements such as Ni.[209] Of the four complexes, **9** exhibits the most distortion both in its solid-state structure, and in its optimized ground-state and lowest-lying excited triplet state geometries. This is clear from the calculated $\tau_4{}^\delta$ parameter (0.16) which indicates a distorted square planar geometry (Figure

279

4.50). The anomalously weak emission from **9** can thus be attributed to competitive non-radiative decay pathways made possible by excited state distortions.[210]
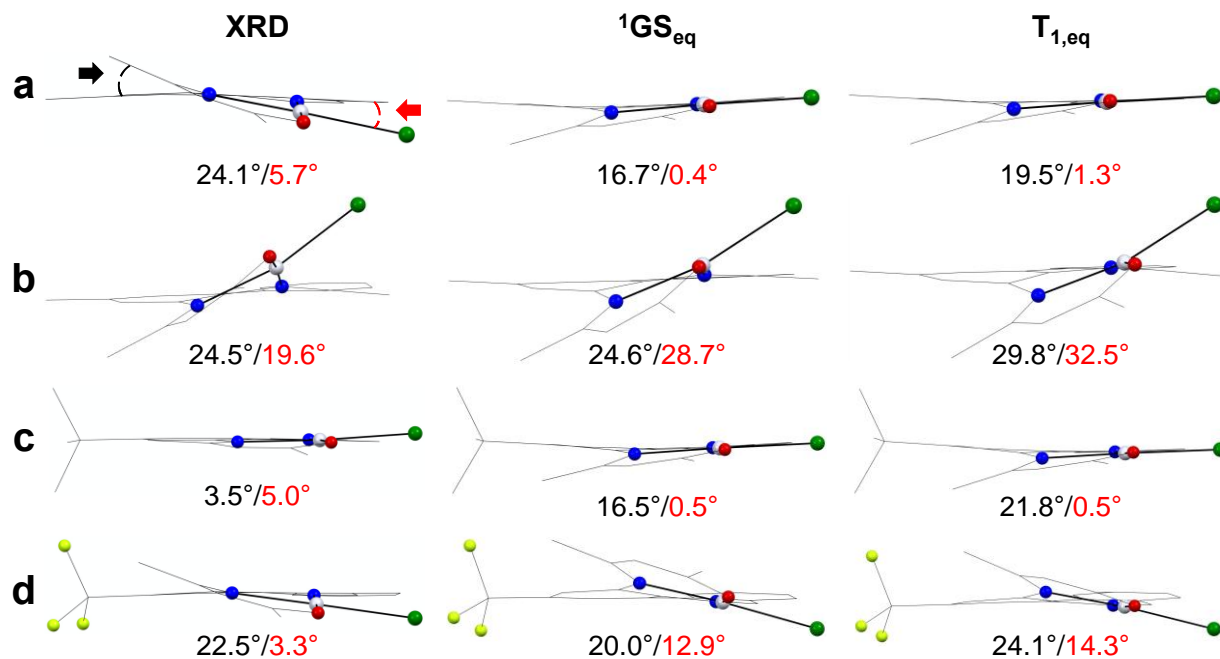
Figure 4.50. Torsional parameters (θphen-NAcac and θphen-PtNNOCl) of the solid-state, optimized 1GSeq, and T1,eq structures of (a) **8**, (b) **9**, (c) **10** and (d) **11**. Ground and triplet state geometries are optimized at the RIJCOSX-xPBE0-D3(BJ)/def2-TZVP+def2/J (x = r, 1GSeq; u, T1,eq) level of theory.

Finally, for the brightest emitter (**11**), we probed the excited state dynamics (ESD) via the ESD module implemented in the ORCA software suite,[211,212] using the optimized geometries of the ground-state ($^1GS_{eq}$) and lowest-lying triplet excited state (T_1). We first estimated the rate of intersystem crossing (k_{ISC}) of the scalar S_1 (the dominant transition in the visible region) and S_7 (the dominant transition contributing to the band at 360 nm) states at the ^1GS geometry to the lowest-lying excited triplet state at its equilibrium geometry. Rapid and efficient population of the

280

triplet state is calculated with average k_{ISC} of 8.870×10^{12} s^{-1} (S$_1$→T$_1$) and 1.020×10^{13} s^{-1} (S$_7$→T$_1$). This suggests strong coupling between these states and the presumably emissive T$_1$ state, consistent with the strong mixing between the singlet and triplet states through the influence of SOC evident in the UV-Vis absorption spectra, as discussed above. SOC-TDDFT simulations also predict strong mixing between S$_1$ and T$_2$, both of which contribute significantly to the predicted strong, low-energy absorptions in the calculated SOC-TDDFT spectrum, and which both exhibit (M+L)LCT character. This suggests that T$_2$ is also populated, which likely undergoes rapid internal conversion to T$_1$.

We also simulated the phosphorescence spectra and decay parameters for **11** (Tables 4.37-4.38). In general, the simulated spectra of **11** at room temperature (Figure 4.51) and 77 K (Figure 4.52) faithfully reproduce the respective experimental spectra, with errors of < 0.2 eV. The vibrational progression observed experimentally at 77 K that appears as a low-energy shoulder at 295 K is reproduced in both calculated spectra, indicating the molecule retains rigidity in solution at 295 K with only minimal distortion, as shown by similar values for $\tau_4{}^{\delta}$ for both ^{1}GS$_{eq}$ and T$_{1,eq}$. In contrast, the emission spectrum of **9** is broad and weak at 295 K, but resembles those of **8**, **10** and **11** at 77 K. This implies that significant distortions occur at elevated temperature, in line with the weakness of the emission. Spin density maps reveal a similar (M+L)LCT character of the emissive triplet state of all four complexes (Figure 4.53).

Table 4.37. Calculated rate of intersystem crossing from $^1S_1(^1GS_{eq})$ and $^1S_7(^1GS_{eq})$ to the three substates of $^3T_{1,eq}$ ($M_S = -1, 0, +1$) for **11** at 298 K and 77 K in CH_2Cl_2.

Temp / K	k_1 / s^{-1} $M_S = -1$	k_2 / s^{-1} $M_S = 0$	k_3 / s^{-1} $M_S = +1$	$k_{aver.}$ / s^{-1}
$S_1(^1GSeq) \rightarrow T_{1,Ms}(T_{1,eq})$	3.845×10^{12}	0	2.317×10^{13}	8.870×10^{12}
$S_7(^1GSeq) \rightarrow T_{1,Ms}(T_{1,eq})$	2.928×10^{13}	0	0	1.020×10^{13}

Table 4.38. Calculated phosphorescence parameters for **11** at 298 K and 77 K in CH_2Cl_2.

Temp / K	k_1 / s^{-1}	k_2 / s^{-1}	k_3 / s^{-1}	$k_{aver.}$ / s^{-1}
298	36 631	57 303	77 508	56 777
77	29 492	52 137	72 632	49 973
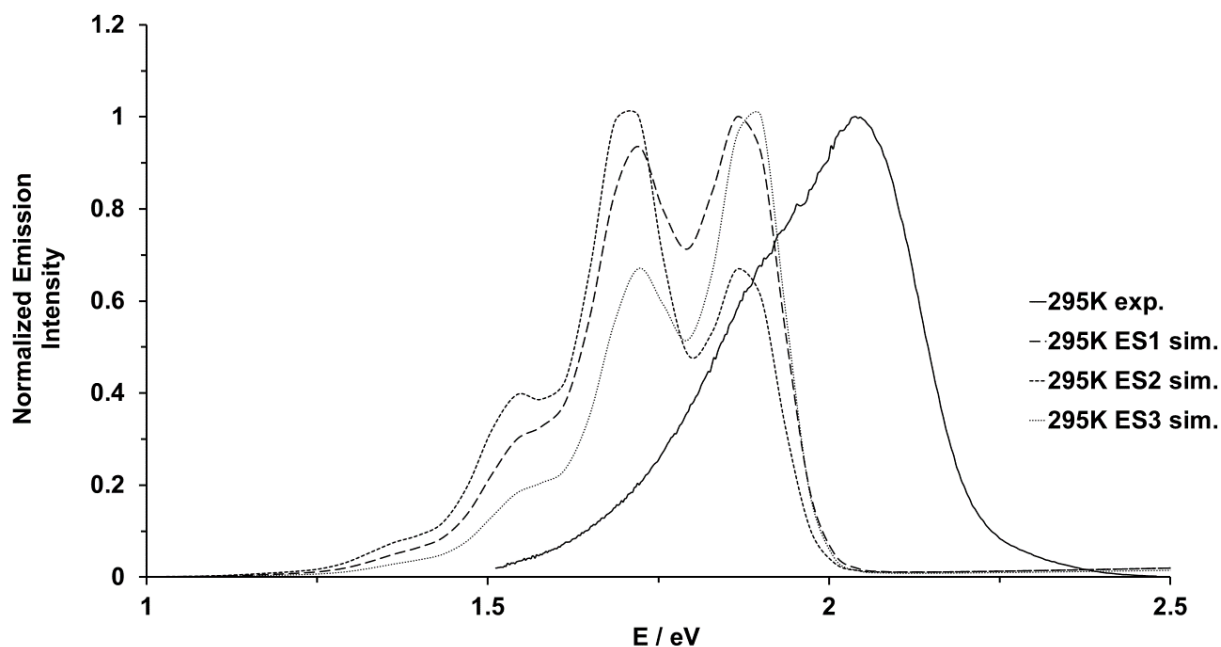
Figure 4.51. TDDFT simulated (FWHM = 3000 cm^{-1}, T = 298 K) and experimental (T = 295 K) phosphorescence spectra of **11** in CH_2Cl_2. The three substates ($M_S = -1, 0, +1$) of the lowest excited triplet state are considered.
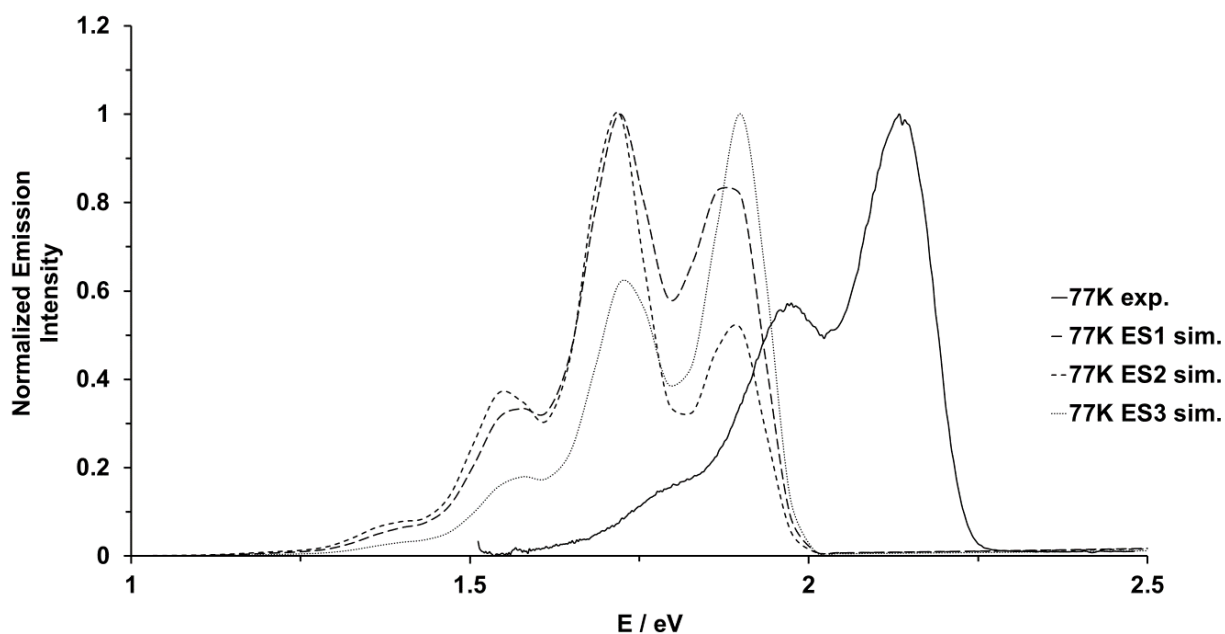
Figure 4.52. TDDFT simulated (FWHM = 3000 cm^{-1}, CH$_2$Cl$_2$) and experimental phosphorescence spectra of **11** at 77 K. The three substates (M_S = -1, 0, +1) of the lowest excited triplet state are considered.

1
[0.09/0.07]

2
[0.11/0.10]

3
[0.10/0.09]

4
[0.13/0.12]
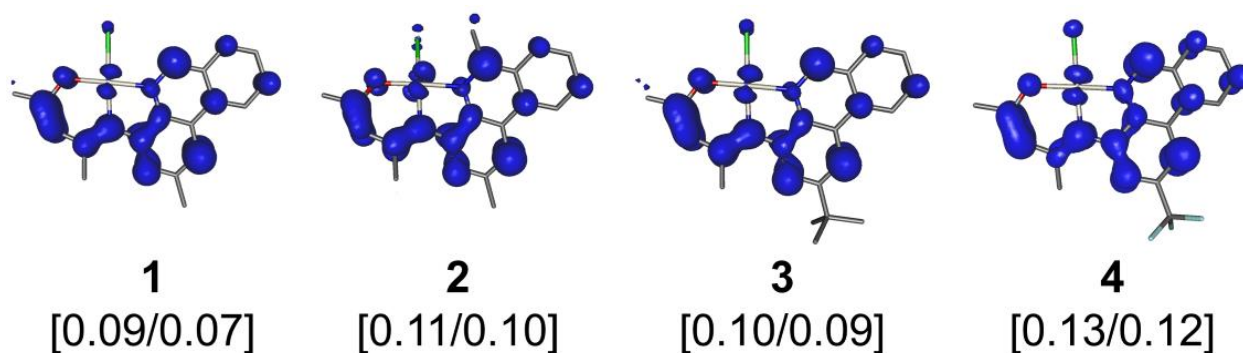
Figure 4.53. Spin density maps (isovalue = 0.004) of **8-11** at the equilibrium geometries of the lowest-lying excited triplet state. Shown in square brackets are the Löwdin/Mulliken spin densities on Pt.

4.4 Computational Details

4.4.1 Complexes FP1 and FP2

Calculations were performed using Gaussian 16, Rev. C.01[213], and at the density functional level of theory with the restricted Kohn-Sham formalism. Cartesian coordinates from solid-state structures were used as starting input, and solvent effects were accounted implicitly using the solvation model based on density (SMD[214]; solvent = CH_3CN). Singlet ground-state geometry optimizations for **FP1** and **FP2** were carried out with the dispersion corrected (D3-BJ[215]) B3LYP[216–219] functional and def2-SVP[220] basis sets on all atoms [*i.e.* SMD-rB3LYP-D3(BJ)/def2-SVP]. The absence of imaginary frequencies confirm that all optimized geometries were at minima. Time-dependent DFT (TDDFT) single point calculations at the optimized singlet ground state geometries were subsequently performed to simulate the UV-Vis spectra of the complexes in acetonitrile. A total of 100 excited singlet states were considered to cover the visible and a portion of the UV regions of the electromagnetic spectrum. All single point calculations, including TDDFT, were conducted using the meta-hybrid GGA functional TPSSh[221,222] (HF = 10%) and the def2-SVP[220] basis sets on all atoms. Relevant ground state molecular orbitals (MOs) were generated using Avogadro. Simulated UV-Vis spectra from TDDFT calculated vertical excitation energies were generated with the GaussSum package.[223] Electron-hole density maps of relevant excited states, and population analysis on all presented MOs were generated using Multiwfn.[224]

To further understand the effect of benzannulation to the electronic structure of the complexes, we performed charge decomposition analysis (CDA)[225] on the optimized geometry of **FP2** again using Multiwfn.[224] To simplify the analysis, only a single **P2** ligand was considered using coordinates from the optimized complex geometry. Two fragments were considered (a) **P1**

and (b) butadiene in the *cis* configuration. Since these fragments are bound covalently, the interaction between the fragments was treated as an open-shell case, as described in the Multiwfn manual.[224] Single point calculations were done on these fragments at the SMD-TPSSh/def2-SVP level of theory, both with multiplicity of 3 ($S = 1$). A single point calculation was also conducted on the **P2** ligand at the same level of theory with multiplicity of 1 ($S = 0$). CDA was subsequently carried out on **P2** and the two fragments (**P1**, *cis*-butadiene) using Multiwfn and an orbital interaction diagram printed out.

4.4.2 Complexes Re1 and Re2

ORCA version 4.1.2[211,212] was used for single point and TD-DFT calculations, to explicitly account for both scalar relativistic effects and spin-orbit coupling (SOC). It has been previously shown that SOC can have a significant effect in the observed optical spectra of Re(I) carbonyl complexes of N-heterocyclic ligands. Simulating SOC-corrected spectrum within the TDDFT framework can be approximately accounted for by allowing the single-triplet transitions to borrow intensity from singlet-singlet transitions. This can be expressed as a linear combination of scalar singlet-singlet and singlet triplet excitations, with the oscillator strength of the spin corrected spectrum expressed as in Equation (4.7)[206].

$$f_{soc} = \frac{<\Psi_S|\hat{h}_{soc}|\Psi_T>}{E_T - E_S} f_S \qquad\qquad (4.7)$$

where the numerator is the SOC matrix element, the denominator is the difference in energy of the coupled triplet and singlet state, $\hat{h}_{SOC}$ is the SOC Hamiltonian, and f_S is the oscillator strength of the singlet state. Solvent and dispersion effects were accounted for using the solvation model

based on density (SMD; solvent = CH_3CN)[214] and Grimme's D3 dispersion correction with the Becke-Johnson damping (D3BJ).[215] The ground state geometries of the complexes were optimized using Gaussian 16, Rev. B.01.[226] employing the PBE0[227] functional and def2-SVP[220,228] basis set on non-metal atoms and the corresponding ECP basis set for Re (SMD-PBE0-D3(BJ)/def2-SVP). Crystal structure coordinates were used as input coordinates and frequency calculations were performed to confirm all optimized structures were at a minimum. To probe the effects of HF exchange we employed two functionals: the modified global hybrid B3LYP* (HFX = 15%)[164] and the range-separated hybrid CAM-B3LYP (HFX = 19-65%)[216,229]. The 'resolution of identity with chain-of-sphere' approximation was used in all single point and TD-DFT calculations (RIJCOSX[230]; intaccx: 4.01, 4.01, 4.34; gridx 1,1,2). Scalar relativistic and SOC effects were included using the two-component zeroth order regular approximation (ZORA)[231] as implemented in ORCA. The ZORA all-electron relativistic basis sets, def2-TZVP was used for all non-metal elements (H, C, N, O and Cl) while the SARC-TZVP was used for the heavy element Re[220] with their corresponding auxiliary basis sets[232–235]. SCF convergence and grid criteria were set to TightSCF and grid5, respectively, while the grid criteria for the final energy evaluation was set to FinalGrid6. The first 50 excited singlet and triplet-excited states were considered, which produced 200 SOC-states. Scalar and SOC-corrected spectra were simulated using Multiwfn version 3.6 software and fragment contribution to the MOs were generated using the same program[224] using the Hirshfeld partition method[236]. All structures and MOs were generated using Avagadro[237].

4.4.3 Complexes Fe1-6, Co1-2, Ni1-2 and Ga1-2

Unless otherwise noted, (TD-)DFT calculations were performed using Gaussian 16 Rev. B01[238] and restricted or unrestricted Kohn-Sham density functional theory (KS-DFT) formalisms

for closed-shell ($^1GS_{eq}$) and open-shell ($^3CT_{eq}/^3CT$, $^3MC_{eq}/^3MC$, $^5MC_{eq}/^5MC$, $[^2GS_{eq}]^+/[^2GS]^+$) species, respectively. No symmetry constraints were applied. Geometries were optimized in a polarizable continuum solvation (SMD[239], solvent = CH_3CN) using the O3LYP[168] hybrid functional and 6-31+G(d,p) basis sets[171–174] on all atoms. Coordinates obtained from the solid-state structures were used as starting input for the ground state geometries. For the optimization of the $^3CT_{eq}$ and $^5MC_{eq}$ states, the optimized $^1GS_{eq}$ were used as starting input, while the optimized coordinates of the $^3MC_{eq}$ was obtained using the optimized $^5MC_{eq}$ as starting input. The absence of imaginary frequencies confirmed all optimized geometries are at minima. For **Fe1-6** the M06L[167] *meta*-GGA functional, in combination with the 6-31+G(d,p) basis sets for all atoms and SMD, was used for single-point calculations including time-dependent DFT (TD-DFT). The first 100 electronic excitations for both complexes were considered to cover a significant portion of the UV-visible-NIR regions of the electromagnetic spectrum. The PBE0[9] functional, 6-31+G(d,p) basis sets on all atoms and SMD were used for $[Ga(^{Cl}L)_2]^+$ single-point calculations including TD-DFT. The first 50 singlet-singlet excitations were considered. All MO and spin density isosurfaces were generated using Gaussview.[240] UV-Vis spectra were simulated by applying Gaussian broadening (FWHM: 3000 cm^{-1}, σ: 0.2) to the TD-DFT predicted vertical excitation energies using the GaussSum software[241].

Fragment contributions to the relevant MOs were determined using the Hirshfeld method[236] and electron-hole density maps were generated using Multiwfn 3.6.[242,243] The molecular orbital compositions were partitioned into different fragment contributions (*i.e.*, metal and ligand fragments) included in Tables 4.16 in order to describe the bonding and electronic structure of the complexes presented here. The ligand units were further sub-divided into N^{amide}, HC=N^{phen}, Ar^{phen},

287

HC=N^{quin}, Ar^{quin}, and Cl fragments to highlight the individual contributions of these moieties to each MO.

4.4.4 Complexes 1-4

Optimizations and PES scans were performed using Gaussian 16 Rev.C01[244], while single points were carried out using Orca ver. 4.2.1.[212] Restricted and unrestricted Kohn-Sham density functional theory (DFT) were carried out on close-shell ($^1S_{0,eq}$) and open-shell species ($^3T_{1,eq}$), respectively. The ground state and lowest excited triplet state geometries of **1-4** and [**3**Me]$^+$ were carried out both in gas and solution phases (SMD[245] = CH$_2$Cl$_2$) using the CAM-B3LYP functional[229] in combination with Grimme's dispersion correction with Becke-Johnson damping (D3BJ)[246] and Ahlrichs double-ζ basis with polarization on non-hydrogen atoms, def2-SV(P)[247]. The absence of imaginary frequencies confirmed that the optimized geometries were at minima. The potential energy surface of **3** in gas and solution phases (SMD = CH$_2$Cl$_2$) were scanned along the oxazaborinine-phenanthridinyl dihedral allowing nuclear relaxation after each rotation employing CAM-B3LYP-D3(BJ)/def2-SV(P). Single point calculations including time-dependent DFT (TDDFT) were carried out using M062X[169] with Ahlrichs triple-ζ basis with reduced polarization on hydrogen atom, def2-TZVP(-f)[247]. The resolution of identity with chains of spheres approximation and def2/J[232] auxiliary basis sets were implemented to speed up single-point and TDDFT calculations. DFT integration grids were set to Grid5 and Finalgrid6, while the COSX integration grids were set to intaccx: 4.34, 4.34, 4.67 and gridx 2,2,2. SCF and energy convergence criteria were set to tightscf. Molecular orbital isosurfaces were generated using Avogadro,[237] while spin densities of the lowest-lying excited triplet states were generated using Gabedit.[248] Orbital

and electronic excitation[249] analyses were carried out using Multiwfn v.3.7.[250] PESs were generated using Gaussview 6.[251]

4.4.5 Complexes 5-7

All computations were performed using ORCA v.4.2.1.[211,212] The zeroth order regular approximation (ZORA) was used in all calculations to account for scalar relativistic effects. No symmetry constraints were imposed on all calculations. Both restricted and unrestricted Kohn-Sham Density Functional Theory (KS-DFT) were employed for closed-shell and open-shell systems, respectively. Optimizations were performed in the gas phase with the B3LYP[252–254] functional augmented with Grimme's D3 dipsersion correction with Becke-Johnson damping[246] (B3LYP-D3(BJ)) in combination with the recontracted Ahlrichs split-valence double-ζ basis set with polarization only on non-hydrogen atoms ZORA-def2-SV(P)[247]. B3LYP has been shown to accurately reproduce ground state geometries of Zn(II) coordination complexes.[255,256,114] Crystal structure coordinates for **6** and **7** were used as starting input for ground state optimization ($S_{0,eq}$), while modified coordinates from **6** were used for **5**, using Avogadro.[237] Coordinates from the ground-state equilibrium geometries were then used to optimize the lowest-lying excited triplet-state geometry ($T_{1,eq}$). DFT integration grids, optimization and SCF convergence criteria were set to grid5/finalgrid7, tightopt, and tightscf, respectively. Additional radial integration grid (specialgridatom, 30; specialgridintacc, 7, 7, 7) were implemented for Zn. "No resolution-of-identity" (nori) was employed for all optimizations. The absence of imaginary frequencies confirm that all optimized geometries are real minima. Single-point calculations including TDDFT were performed using the M06-2X[169] functional in combination with the recontracted Ahlrichs split-valence triple-ζ basis set with polarization on all atoms, ZORA-def2-TZVP[247]. We employed the

RIJCOSX approximation as implemented on Orca, in addition to the SARC/J auxiliary basis set[232], to speed up all single-point and TDDFT calculations. DFT and COSX integration grids, and SCF convergence criteria were set to Grid6/finalgrid7, specialgridintacc (7, 7, 7), intaccx(4.34, 4.34, 4.67)/gridx(2, 2, 2), and tightscf. Both scalar and spin-orbit coupling corrected TDDFT were performed in all complexes to determine the extent of SOC between S_n and T_n states. The first 30 S_n and T_n states were considered to cover the relevant region of the UV-Vis spectrum. TDDFT predicted spectra for all complexes were simulated using Multiwfn version 3.8, applying Gaussian broadening scheme with FWHM of 0.372 eV. Ground-state molecular orbital isosurfaces and electron-hole density maps for the relevant excited states were generated from Multiwfn with isosurface values of 0.04 and 0.002, respectively. Spin density maps for all relevant triplet states were simulated using Orca_plot module and Gabedit with isosurface value of 0.004.

4.4.6 Complexes 8-11

Modeling of complexes **8-11** was carried out using ORCA version 4.2.1.[211,212] The resolution-of-identity with chain-of-spheres approximation (RIJCOSX[230]) was used to speed up all calculations. Geometry optimizations were performed in the gas phase with the dispersion corrected (D3BJ[246,257]) PBE0[227,258,259] functional and the def2-TZVP(-f)[228,247] on all atoms and the corresponding ECP basis set on Pt; def2/J auxiliary basis sets were used on all atoms in the density fitting. The $^1GS_{eq}$ and $T_{1,eq}$ geometries were optimized for all four complexes to understand the deactivation mechanisms in the Pt(II) complexes. The starting input for ground state ($^1GS_{eq}$) geometries was obtained from the coordinates of each solid-state structure. The following SCF and geometry convergence criteria, DFT grids, COSX grids were used for the optimizations:

tightscf, tightopt, grid5, finalgrid6, intaccx (4.34,4.34,4.67), and gridx (2,2,2). Frequency calculations were carried to confirm that all geometries are at a minimum.

Single point calculations were conducted using the same dispersion corrected PBE0 functional and inclusion of implicit solvation using the solvation model based on density (SMD[239], solvent = CH_2Cl_2) on gas-phase optimized geometries. However, to best account for scalar relativistic effects, we employed the zeroth order regular approximation (ZORA[260]), ZORA-optimized all-electron relativistic (ZORA-def2-TZVP[247] on H, C, N, O, F, and Cl; SARC-ZORA-TZVP on Pt) and the appropriate auxiliary basis sets (SARC/J[232,235]). We used the same SCF convergence criteria and COS-X grid for all single points (tightscf; intaccx 4.34, 4.34, 4.67; gridx 2,2,2), while the DFT integration grids were increased to grid6 and finalgrid7. We also increased the grid around Pt (specialgridintacc 9). Time-dependent DFT (TDDFT) was used to predict the first 50 $S_{n,FC} \leftarrow {}^1GS_{eq}$ and $T_{n,FC} \leftarrow {}^1GS_{eq}$ excitations (FC implies electronic excitations within the Franck-Condon approximation) to simulate the UV-Vis spectra of the complexes without spin-orbit correction. In addition, we also predicted the extent of SOC effects by allowing mixing of S_n and T_n states as implemented in ORCA.

The excited dynamics of **11** was probed using the ESD module implemented in ORCA.[211,212] The phosphorescence spectrum was simulated and phosphorescence rate constants (k_{phos}, and intersystem crossing rate (k_{ISC}) were calculated. The three substates ($M_S = -1, 0, +1$) of the lowest excited triplet state were considered in estimating k_{phos} and k_{ISC} at 298 K and 77 K. For k_{ISC}, we considered the ground state optimized geometry as the geometry of the populated excited singlet states initially populated upon light excitation. This was performed for both $S_1({}^1GS_{eq})$ and $S_7({}^1GS_{eq})$, as these have the strongest oscillator strengths in the absorbance bands at 475 and 360

291

nm, respectively. The final geometry is of the lowest-lying excited triplet state. For the k_{phos}, initial and final geometries are of the lowest-lying excited triplet state and ground state, respectively.

Conclusions

Metal complexes supported by phenanthridine-based ligands exhibit rich electronic structures and photophysical properties. While in general phenanthridine-based ligands provide metal complexes with low-lying vacant acceptor orbitals, the nature of electronic states can be complicated by configuration interactions. For example, modeling ground and excited states of $3d$ transition metal complexes is often complicated by low-lying excited states. By combining the phenanthridine acceptors with π-donor ligands panchromatic absorption can be achieved. Moreover, the extension of the π-system in quinoline as in 3,4-benzoquinoline rigidifies molecular complexes and enhances noncovalent π-stacking leading to enhancement of the photophysical properties of molecular complexes.

References

(1)   Faraday, M. On New Compounds of Carbon and Hydrogen, and on Certain Other Products Obtained during the Decomposition of Oil by Heatrstl.1825.Pdf. *Philos. Trans. R. Soc.* **1825**, *115*, 440–466.
(2)   Heo, I.; Lee, J. C.; Özer, B. R.; Schultz, T. Mass-Correlated High-Resolution Spectra and the Structure of Benzene. *J. Phys. Chem. Lett.* **2022**, *13* (35), 8278–8283. https://doi.org/10.1021/acs.jpclett.2c02035.
(3)   Kunishige, S.; Katori, T.; Baba, M.; Nakajima, M.; Endo, Y. Spectroscopic Study on Deuterated Benzenes. I. Microwave Spectra and Molecular Structure in the Ground State. *J. Chem. Phys.* **2015**, *143* (24), 244302. https://doi.org/10.1063/1.4937949.
(4)   Watson, M. D.; Fechtenkötter, A.; Müllen, K. Big Is Beautiful−"Aromaticity" Revisited from the Viewpoint of Macromolecular and Supramolecular Benzene Chemistry. *Chem. Rev.* **2001**, *101* (5), 1267–1300. https://doi.org/10.1021/cr990322p.
(5)   Vij, V.; Bhalla, V.; Kumar, M. Hexaarylbenzene: Evolution of Properties and Applications of Multitalented Scaffold. *Chem. Rev.* **2016**, *116* (16), 9565–9627. https://doi.org/10.1021/acs.chemrev.6b00144.
(6)   Price, C. C. Substitution and Orientation in the Benzene Ring. *Chem. Rev.* **1941**, *29* (1), 37–67. https://doi.org/10.1021/cr60092a002.

(7)   Papadakis, R.; Ottosson, H. The Excited State Antiaromatic Benzene Ring: A Molecular Mr Hyde? *Chem. Soc. Rev.* **2015**, *44* (18), 6472–6493. https://doi.org/10.1039/C5CS00057B.

(8)   Swami, B.; Yadav, D.; Menon, R. S. Benzannulation Reactions: A Case for Perspective Change From Arene Decoration to Arene Construction. *Chem. Rec.* **2022**, *22* (1), e202100249. https://doi.org/10.1002/tcr.202100249.

(9)   Hart-Davis, A. J.; White, C.; Mawby, F. J. Reactions Of-WIndeny Complexes of Transition Metals. III.' Kinetics and Mechanisms of Substitution Reactions of Tricarbonyl-Mindenylhalomolybdenum(II) Complexes. 6.

(10)   Rerek, M. E.; Basolo, F. Kinetics and Mechanism of Substitution Reactions of .Eta.5-Cyclopentadienyldicarbonylrhodium(I) Derivatives. Rate Enhancement of Associative Substitution in Cyclopentadienylmetal Compounds. *J. Am. Chem. Soc.* **1984**, *106* (20), 5908–5912. https://doi.org/10.1021/ja00332a026.

(11)   Rerek, M. E.; Ji, L.-N.; Basolo, F. The Lndenyl Ligand Effect on the Rate of Substitution Reactions of Rh(Rl-C9H7)C(O), and Mn(Rl -CgH7)C(O)a. 2.

(12)   Okada, Y.; Miyamoto, N.; Hishimoto, M.; Hayashi, T. Studies on Ferrocene Derivatives. Part XIII. Ligand Exchange Reactions of Benzoferrocenes. *Transit. Met Chem* **1999**, 5.

(13)   Treichel, P. M.; Johnson, J. W.; Wagner, K. P. OXIDATIONS OF VARIOUS INDENYL-IRON. 4.

(14)   Crossley, N. S.; Green, J. C.; Nagy, A.; Stringer, G. Electronic Structure of Transition-Metal Lndenyl Compounds: A He I and He I I Photoelectron Spectroscopic Study of [Mn(Q5-C,H7)(CO),], [Fe(Q5-CgH7),]. Ru(Q5-C9H7)21 and Ru(T5-C9H7)(q-C5Me5) I t. *J CHEM SOC DALTON TRANS* **1989**, 9.

(15)   Brady, E. D.; Overby, J. S.; Meredith, M. B.; Mussman, A. B.; Cohn, M. A.; Hanusa, T. P.; Yee, G. T.; Pink, M. Spin-State Alteration from Sterically Enforced Ligand Rotation in Bis(Indenyl)Chromium(II) Complexes [1]. *J. Am. Chem. Soc.* **2002**, *124* (32), 9556–9566. https://doi.org/10.1021/ja012390a.

(16)   Shimizu, A.; Ishizaki, Y.; Horiuchi, S.; Hirose, T.; Matsuda, K.; Sato, H.; Yoshida, J. HOMO–LUMO Energy-Gap Tuning of π-Conjugated Zwitterions Composed of Electron-Donating Anion and Electron-Accepting Cation. *J. Org. Chem.* **2021**, *86* (1), 770–781. https://doi.org/10.1021/acs.joc.0c02343.

(17)   Hanson, K.; Roskop, L.; Djurovich, P. I.; Zahariev, F.; Gordon, M. S.; Thompson, M. E. A Paradigm for Blue- or Red-Shifted Absorption of Small Molecules Depending on the Site of π-Extension. *J. Am. Chem. Soc.* **2010**, *132* (45), 16247–16255. https://doi.org/10.1021/ja1075162.

(18)   Liu, B.; Lystrom, L.; Kilina, S.; Sun, W. Effects of Varying the Benzannulation Site and π Conjugation of the Cyclometalating Ligand on the Photophysics and Reverse Saturable Absorption of Monocationic Iridium(III) Complexes. *Inorg. Chem.* **2019**, *58* (1), 476–488. https://doi.org/10.1021/acs.inorgchem.8b02714.

(19)   Liu, B.; Lystrom, L.; Brown, S. L.; Hobbie, E. K.; Kilina, S.; Sun, W. Impact of Benzannulation Site at the Diimine (N^N) Ligand on the Excited-State Properties and Reverse Saturable Absorption of Biscyclometallated Iridium(III) Complexes. *Inorg. Chem.* **2019**, *58* (9), 5483–5493. https://doi.org/10.1021/acs.inorgchem.8b03162.

(20)   Wang, L.; Yin, H.; Jabed, M. A.; Hetu, M.; Wang, C.; Monro, S.; Zhu, X.; Kilina, S.; McFarland, S. A.; Sun, W. π-Expansive Heteroleptic Ruthenium(II) Complexes as Reverse

Saturable Absorbers and Photosensitizers for Photodynamic Therapy. *Inorg. Chem.* **2017**, *56* (6), 3245–3259. https://doi.org/10.1021/acs.inorgchem.6b02624.

(21) Chen, T.; Li, M.; Liu, J. π–π Stacking Interaction: A Nondestructive and Facile Means in Material Engineering for Bioapplications. *Cryst. Growth Des.* **2018**, *18* (5), 2765–2783. https://doi.org/10.1021/acs.cgd.7b01503.

(22) Sinnokrot, M. O.; Valeev, E. F.; Sherrill, C. D. Estimates of the Ab Initio Limit for Π−π Interactions: The Benzene Dimer. *J. Am. Chem. Soc.* **2002**, *124* (36), 10887–10893. https://doi.org/10.1021/ja025896h.

(23) Cai, M.; Song, X.; Zhang, D.; Qiao, J.; Duan, L. π–π Stacking: A Strategy to Improve the Electron Mobilities of Bipolar Hosts for TADF and Phosphorescent Devices with Low Efficiency Roll-Off. *J. Mater. Chem. C* **2017**, *5* (13), 3372–3381. https://doi.org/10.1039/C7TC00733G.

(24) Hong, Y.; Lam, J. W. Y.; Tang, B. Z. Aggregation-Induced Emission: Phenomenon, Mechanism and Applications. *Chem. Commun.* **2009**, No. 29, 4332. https://doi.org/10.1039/b904665h.

(25) McGaughey, G. B.; Gagné, M.; Rappé, A. K. π-Stacking Interactions. *J. Biol. Chem.* **1998**, *273* (25), 15458–15463. https://doi.org/10.1074/jbc.273.25.15458.

(26) Babine, R. E.; Bender, S. L. Molecular Recognition of Protein−Ligand Complexes: Applications to Drug Design. *Chem. Rev.* **1997**, *97* (5), 1359–1472. https://doi.org/10.1021/cr960370z.

(27) Pages, B. J.; Garbutcheon-Singh, K. B.; Aldrich-Wright, J. R. Platinum Intercalators of DNA as Anticancer Agents. *Eur. J. Inorg. Chem.* **2017**, *2017* (12), 1613–1624. https://doi.org/10.1002/ejic.201601204.

(28) Hayashi, K.; Nakatani, M.; Hayashi, A.; Takano, M.; Okazaki, M.; Toyota, K.; Yoshifuji, M.; Ozawa, F. Synthesis and Structures of Platinum(0) Alkyne Complexes with Extended π-Conjugated Systems. *Organometallics* **2008**, *27* (9), 1970–1972. https://doi.org/10.1021/om800163p.

(29) Flamigni, L.; Encinas, S.; Barigelletti, F.; MacDonnell, F. M.; Kim, K.-J.; Puntoriero, F.; Campagna, S. Excited-State Interconversion between Emissive MLCT Levels in a Dinuclear Ru(Ii) Complex Containing a Bridging Ligand with an Extended π System. *Chem. Commun.* **2000**, No. 13, 1185–1186. https://doi.org/10.1039/b004109m.

(30) Roznyatovskiy, V. V.; Lee, C.-H.; Sessler, J. L. π-Extended Isomeric and Expanded Porphyrins. *Chem Soc Rev* **2013**, *42* (5), 1921–1933. https://doi.org/10.1039/C2CS35418G.

(31) Barbon, S. M.; Staroverov, V. N.; Gilroy, J. B. Effect of Extended π Conjugation on the Spectroscopic and Electrochemical Properties of Boron Difluoride Formazanate Complexes. *J. Org. Chem.* **2015**, *80* (10), 5226–5235. https://doi.org/10.1021/acs.joc.5b00620.

(32) Kappaun, S.; Rentenberger, S.; Pogantsch, A.; Zojer, E.; Mereiter, K.; Trimmel, G.; Saf, R.; Möller, K. C.; Stelzer, F.; Slugovc, C. Organoboron Quinolinolates with Extended Conjugated Chromophores: Synthesis, Structure, and Electronic and Electroluminescent Properties. *Chem. Mater.* **2006**, *18* (15), 3539–3547. https://doi.org/10.1021/cm060720q.

(33) Kiprof, P.; Carlson, J. C.; Anderson, D. R.; Nemykin, V. N. Systematic Color Tuning of a Family of Luminescent Azole-Based Organoboron Compounds Suitable for OLED Applications. *Dalton Trans.* **2013**, *42* (42), 15120. https://doi.org/10.1039/c3dt51853a.

(34) Bossi, A.; Rausch, A. F.; Leitl, M. J.; Czerwieniec, R.; Whited, M. T.; Djurovich, P. I.; Yersin, H.; Thompson, M. E. Photophysical Properties of Cyclometallated Pt(II) Complexes: Counterintuitive Blue Shift in Emission with an Expanded Ligand π System. *Inorg. Chem.* **2013**, *52* (21), 12403–12415. https://doi.org/10.1021/ic4011532.

(35) Gunanathan, C.; Gnanaprakasam, B.; Iron, M. A.; Shimon, L. J. W.; Milstein, D. "Long-Range" Metal−Ligand Cooperation in H $_2$ Activation and Ammonia-Promoted Hydride Transfer with a Ruthenium−Acridine Pincer Complex. *J. Am. Chem. Soc.* **2010**, *132* (42), 14763–14765. https://doi.org/10.1021/ja107770y.

(36) Neufeldt, S. R.; Sanford, M. S. Controlling Site Selectivity in Palladium-Catalyzed C–H Bond Functionalization. *Acc. Chem. Res.* **2012**, *45* (6), 936–946. https://doi.org/10.1021/ar300014f.

(37) Krichevsky, O.; Bonnet, Gregoire. Fluorescence Correlation Spectroscopy: The Technique and Its Applications. *Rep. Prog. Phys.* **2002**, *65* (2), 251–297. https://doi.org/10.1088/0034-4885/65/2/203.

(38) Tumir, L.-M.; Stojkovic, M. R.; Piantanida, I. Come-Back of Phenanthridine and Phenanthridinium Derivatives in the 21st Century. *Beilstein J Org Chem* **2014**, *10*, 2930–2954.

(39) Park, G. Y.; Wilson, J. J.; Song, Y.; Lippard, S. J. Phenanthriplatin, a Monofunctional DNA-Binding Platinum Anticancer Drug Candidate with Unusual Potency and Cellular Activity Profile. *Proc Natl Acad Sci* **2012**, *109*, 11987–11992.

(40) Lu, L.-Q.; Li, Y.; Junge, K.; Beller, Matthias. Iron-Catalyzed Hydrogenation for the In Situ Regeneration of an NAD(P)H Model: Biomimetic Reduction of α-Keto-/α-Iminoesters. *Angew. Chem. Int. Ed.* **2013**, *52* (32), 8382–8386. https://doi.org/10.1002/anie.201301972.

(41) Chen, Q.-A.; Gao, K.; Duan, Y.; Ye, Z.-S.; Shi, L.; Yang, Y.; Zhou, Y.-Gui. Dihydrophenanthridine: A New and Easily Regenerable NAD(P)H Model for Biomimetic Asymmetric Hydrogenation. *J. Am. Chem. Soc.* **2012**, *134* (4), 2442–2448. https://doi.org/10.1021/ja211684v.

(42) Jensen, K. A.; Nielsen, P. Halfdan. Chelates with Heterocyclic Ligands. I. Chelates Derived from e N,N'-Bis(8-Quinolyl)Ethylenediamine and Analogous Compounds. *Acta Chem. Scand. 1947-1973* **1964**, *18* (1), 1–10. https://doi.org/10.3891/acta.chem.scand.18-0001.

(43) Puzas, J. P.; Nakon, R.; Petersen, J. L. Direct Evidence for an SN1CB Mechanism. 4. Crystal and Molecular Structure of Chloro(Bis(8-Quinolinyl)Amido-N1,N2,N3)Copper(II), a Metal Chelate Containing an Sp2-Hybridized Deprotonated Amine. *Inorg. Chem.* **1986**, *25* (21), 3837–3840. https://doi.org/10.1021/ic00241a026.

(44) Peters, J. C.; Harkins, S. B.; Brown, S. D.; Day, M. W. Pincer-like Amido Complexes of Platinum, Palladium, and Nickel. *Inorg. Chem.* **2001**, *40* (20), 5083–5091. https://doi.org/10.1021/ic010336p.

(45) Maiti, D.; Paul, H.; Chanda, N.; Chakraborty, S.; Mondal, B.; Puranik, V. G.; Lahiri, G. Kumar. Synthesis, Structure, Spectral and Electron-Transfer Properties of Octahedral-[CoIII(L)2]+/[ZnII(L)2] and Square Planar-[CuII(L){OC(=O)CH3}] Complexes Incorporating Anionic Form of Tridentate Bis(8-Quinolinyl)Amine [N1C9H6-N2-C9H6N3, L-] Ligand. *Polyhedron* **2004**, *23* (5), 831–840. https://doi.org/10.1016/j.poly.2003.11.053.

(46) Valk, J.-M.; Claridge, T. D. W.; Brown, J. M.; Hibbs, D.; Hursthouse, M. B. Synthesis and Chemistry of a New P-N Chelating Ligand; (R)- and (S)-6-(2'-Diphenylphosphino-1'-

Naphthyl)Phenanthridine. *Tetrahedron Asymmetry* **1995**, *6* (Copyright (C) 2017 American Chemical Society (ACS). All Rights Reserved.), 2597–2610. https://doi.org/10.1016/0957-4166(95)00341-L.

(47) Raszeja, L.; Maghnouj, A.; Hahn, S.; Metzler-Nolte, Nils. A Novel Organometallic ReI Complex with Favourable Properties for Bioimaging and Applicability in Solid-Phase Peptide Synthesis. *ChemBioChem* **2011**, *12* (3), 371–376. https://doi.org/10.1002/cbic.201000576.

(48) Sicilia, V.; Fuertes, S.; Martin, A.; Palacios, Adrian. N-Assisted CPh-H Activation in 3,8-Dinitro-6-Phenylphenanthridine. New C,N-Cyclometallated Compounds of Platinum(II): Synthesis, Structure, and Luminescence Studies. *Organometallics* **2013**, *32* (15), 4092–4102. https://doi.org/10.1021/om400159g.

(49) Jiang, B.; Gu, Y.; Qin, J.; Ning, X.; Gong, S.; Xie, G.; Yang, Chuluo. Deep-Red Iridium(III) Complexes Cyclometallated by Phenanthridine Derivatives for Highly Efficient Solution-Processed Organic Light-Emitting Diodes. *J. Mater. Chem. C Mater. Opt. Electron. Devices* **2016**, *4* (16), 3492–3498. https://doi.org/10.1039/C6TC00148C.

(50) Theobald, R. S.; Schofield, K. The Chemistry of Phenanthridine and Its Derivatives. *Chem. Rev.* **1950**, *46* (1), 170–189. https://doi.org/10.1021/cr60143a004.

(51) Crystal and molecular structure of phenanthridine. Roychowdhury1973.Pdf. *Acta. Cryst., Sect. B* **1973**, *29*, 1362–1364.

(52) Brett, W. A.; Rademacher, P.; Boese, R. Redetermination of the Structure of Phenanthridine. *Acta Crystallogr. C* **1993**, *49* (9), 1564–1566. https://doi.org/10.1107/S0108270193005062.

(53) Katritzky, A. R. *Handbook of Heterocyclic Chemistry*, 3rd ed.; Elsevier, 2010.

(54) Benmachiche, A.; Zendaoui, S.-M.; Bouaoud, S.-E.; Zouchoune, B. Electronic Structure and Coordination Chemistry of Phenanthridine Ligand in First-Row Transition Metal Complexes: A DFT Study. *Int. J. Quantum Chem.* **2013**, *113* (7), 985–996. https://doi.org/10.1002/qua.24071.

(55) Giesbrecht, P. K.; Nemez, D. B.; Herbert, D. E. Electrochemical Hydrogenation of a Benzannulated Pyridine to a Dihydropyridine in Acidic Solution. *Chem. Commun.* **2018**, *54* (4), 338–341. https://doi.org/10.1039/C7CC07907A.

(56) Mondal, R.; Giesbrecht, P. K.; Herbert, D. E. Nickel(II), Copper(I) and Zinc(II) Complexes Supported by a (4-Diphenylphosphino)Phenanthridine Ligand. *Polyhedron* **2016**, *108*, 156–162.

(57) Mandapati, P.; Giesbrecht, P. K.; Davis, R. L.; Herbert, D. E. Phenanthridine-Containing Pincer-like Amido Complexes of Nickel, Palladium, and Platinum. *Inorg Chem* **2017**, *56*, 3674–3685.

(58) Mandapati, P.; Braun, J. D.; Killeen, C.; Davis, R. L.; Williams, J. A. G.; Herbert, D. E. Luminescent Platinum(II) Complexes of N^N⁻^N Amido Ligands with Benzannulated N-Heterocyclic Donor Arms: Quinolines Offer Unexpectedly Deeper Red Phosphorescence than Phenanthridines. *Inorg Chem* **2019**, *58*, 14808–14817.

(59) Mandapati, P.; Braun, J. D.; Lozada, I. B.; Williams, J. A. G.; Herbert, D. E. Deep-Red Luminescence from Platinum(II) Complexes of N^N⁻^N-Amido Ligands with Benzannulated N-Heterocyclic Donor Arms. *Inorg. Chem.* **2020**, *59*, 12504–12517.

(60) Mondal, R.; Lozada, I. B.; Davis, R. L.; Williams, J. A. G.; Herbert, D. E. Site-Selective Benzannulation of N-Heterocycles in Bidentate Ligands Leads to Blue-Shifted Emission from [(P^N)Cu]$_2$(μ-X)$_2$ Dimers. *Inorg Chem* **2018**, *57*, 4966–4978.

(61) Mondal, R.; Lozada, I. B.; Davis, R. L.; Williams, J. A. G.; Herbert, D. E. Exploiting Synergy between Ligand Design and Counterion Interactions to Boost Room Temperature Phosphorescence from Cu(I) Compounds. *J. Mater. Chem. C* **2019**, *7*, 3772–3778.

(62) Lozada, I. B.; Murray, T.; Herbert, D. E. Monomeric Zinc(II) Amide Complexes Supported by Bidentate, Benzannulated Phenanthridine Amido Ligands. *Polyhedron* **2019**, *161*, 261–267.

(63) Mondal, R.; Lozada, I. B.; Davis, R. L.; Williams, J. A. G.; Herbert, D. E. Site-Selective Benzannulation of N-Heterocycles in Bidentate Ligands Leads to Blue-Shifted Emission from [(P^N)Cu]2(μ-X)2 Dimers. *Inorg Chem* **2018**, *57*, 4966–4978.

(64) Mandapati, P.; Giesbrecht, P. K.; Davis, R. L.; Herbert, D. E. Phenanthridine-Containing Pincer-like Amido Complexes of Nickel, Palladium, and Platinum. *Inorg Chem* **2017**, *56*, 3674–3685.

(65) Gaire, S.; Ortiz, R. J.; Schrage, B. R.; Lozada, I. B.; Mandapati, P.; Osinski, A. J.; Herbert, D. E.; Ziegler, C. J. (8-Amino)Quinoline and (4-Amino)Phenanthridine Complexes of Re(CO)3 Halides. *J. Organomet. Chem.* **2020**, *921*, 121338.

(66) Nemez, D. B.; Lozada, I. B.; Braun, J. D.; Williams, J. A. G.; Herbert, D. E. Synthesis and Coordination Chemistry of a Benzannulated Bipyridine: 6,6′-Biphenanthridine. *Inorg. Chem.* **2022**, *61* (34), 13386–13398. https://doi.org/10.1021/acs.inorgchem.2c01514.

(67) Hanson, K.; Roskop, L.; Djurovich, P. I.; Zahariev, F.; Gordon, M. S.; Thompson, M. E. A Paradigm for Blue- or Red-Shifted Absorption of Small Molecules Depending on the Site of π-Extension. *J. Am. Chem. Soc.* **2010**, *132*, 16247–16255.

(68) Barbon, S. M.; Staroverov, V. N.; Gilroy, J. B. Effect of Extended π Conjugation on the Spectroscopic and Electrochemical Properties of Boron Difluoride Formazanate Complexes. *J. Org. Chem.* **2015**, *80*, 5226–5235.

(69) Liu, B.; Lystrom, L.; Kilina, S.; Sun, W. Tuning the Ground State and Excited State Properties of Monocationic Iridium(III) Complexes by Varying the Site of Benzannulation on Diimine Ligand. *Inorg. Chem.* **2017**, *56*, 5361–5370.

(70) Westcott, B. L.; Gruhn, N. E.; Michelsen, L. J.; Lichtenberger, D. L. Experimental Observation of Non-Aufbau Behavior: Photoelectron Spectra of Vanadyloctaethylporphyrinate and Vanadylphthalocyanine. *J. Am. Chem. Soc.* **2000**, *122*, 8083–8084.

(71) Hewage, J. S.; Wanniarachchi, S.; Morin, T. J.; Liddle, B. J.; Banaszynski, M.; Lindeman, S. V.; Bennett, B.; Gardinier, J. R. Homoleptic Nickel(II) Complexes of Redox-Tunable Pincer-Type Ligands. *Inorg. Chem.* **2014**, *53* (19), 10070–10084. https://doi.org/10.1021/ic500657e.

(72) Lozada, I. B.; Ortiz, R. J.; Braun, J. D.; Williams, J. A. G.; Herbert, D. E. Donor–Acceptor Boron-Ketoiminate Complexes with Pendent *N*-Heterocyclic Arms: Switched-on Luminescence through *N*-Heterocycle Methylation. *J. Org. Chem.* **2022**, *87* (1), 184–196. https://doi.org/10.1021/acs.joc.1c02138.

(73) Braun, J. D.; Lozada, I. B.; Kolodziej, C.; Burda, C.; Newman, K. M. E.; van Lierop, J.; Davis, R. L.; Herbert, D. E. Iron(II) Coordination Complexes with Panchromatic Absorption

and Nanosecond Charge-Transfer Excited State Lifetimes. *Nat. Chem.* **2019**, *11*, 1144–1150.

(74) Bruker-AXS. APEX3 V2016.1-0, 2016.

(75) Dolomanov, O. V.; Bourhis, L. J.; Gildea, R. J.; Howard, J. A. K.; Puschmann, H. OLEX2: A Complete Structure Solution, Refinement and Analysis Program. *J. Appl. Crystallogr.* **2009**, *42*, 339–341.

(76) Spek, A. L. Structure Validation in Chemical Crystallography. *Acta Cryst* **2009**, *D65*, 148–155.

(77) Fan, C.; Yang, C. Yellow/Orange Emissive Heavy-Metal Complexes as Phosphors in Monochromatic and White Organic Light-Emitting Devices. *Chem Soc Rev* **2014**, *43* (17), 6439–6469. https://doi.org/10.1039/C4CS00110A.

(78) Vreshch, V. D.; Yang, J.-H.; Zhang, H.; Filatov, A. S.; Dikarev, E. V. Monomeric Square-Planar Cobalt(II) Acetylacetonate: Mystery or Mistake? *Inorg. Chem.* **2010**, *49* (18), 8430–8434. https://doi.org/10.1021/ic100963r.

(79) Sokolow, J. D.; Trzop, E.; Chen, Y.; Tang, J.; Allen, L. J.; Crabtree, R. H.; Benedict, J. B.; Coppens, P. Binding Modes of Carboxylate- and Acetylacetonate-Linked Chromophores to Homodisperse Polyoxotitanate Nanoclusters. *J. Am. Chem. Soc.* **2012**, *134* (28), 11695–11700. https://doi.org/10.1021/ja303692r.

(80) Muñoz-García, A. B.; Sannino, F.; Vitiello, G.; Pirozzi, D.; Minieri, L.; Aronne, A.; Pernice, P.; Pavone, M.; D'Errico, G. Origin and Electronic Features of Reactive Oxygen Species at Hybrid Zirconia-Acetylacetonate Interfaces. *ACS Appl. Mater. Interfaces* **2015**, *7* (39), 21662–21667. https://doi.org/10.1021/acsami.5b06988.

(81) Seco, M. Acetylacetone: A Versatile Ligand. *J. Chem. Educ.* **1989**, *66* (9), 779. https://doi.org/10.1021/ed066p779.

(82) Allen, G.; Lewis, J.; Long, R. F.; Oldham, C. A Novel Form of Co-Ordination of Acetylacetone to Platinum(LI). *Nature* **1964**, *202*, 589–590. https://doi.org/10.1038/202589a0.

(83) Patra, S.; Mondal, B.; Sarkar, B.; Niemeyer, M.; Lahiri, G. K. First Example of μ $_3$ -Sulfido Bridged Mixed-Valent Triruthenium Complex Triangle Ru ^{III} $_2$ Ru ^{II} (*O* , *O* -Acetylacetonate) $_3$ (*μ* - *O* , *O* ,γ- *C* -Acetylacetonate) $_3$ (μ $_3$ -S) (**1**) Incorporating Simultaneous O,O- and γ-C-Bonded Bridging Acetylacetonate Units. Synthesis, Crystal Structure, and Spectral and Redox Properties. *Inorg. Chem.* **2003**, *42* (4), 1322–1327. https://doi.org/10.1021/ic026221i.

(84) Zhu, D.; Budzelaar, P. H. M. N-Aryl β-Diiminate Complexes of the Platinum Metals. *Dalton Trans.* **2013**, *42* (32), 11343. https://doi.org/10.1039/c3dt50715g.

(85) Bernskoetter, W. H.; Lobkovsky, E.; Chirik, P. J. Ancillary Ligand Effects on C−H Bond Activation Reactions Promoted by β-Diiminate Iridium Complexes. *Organometallics* **2005**, *24* (25), 6250–6259. https://doi.org/10.1021/om050705f.

(86) Roesky, H. W. The Renaissance of Aluminum Chemistry. *Inorg. Chem.* **2004**, *43* (23), 7284–7293. https://doi.org/10.1021/ic0400641.

(87) Mears, K. L.; Stennett, C. R.; Taskinen, E. K.; Knapp, C. E.; Carmalt, C. J.; Tuononen, H. M.; Power, P. P. Molecular Complexes Featuring Unsupported Dispersion-Enhanced Aluminum–Copper and Gallium–Copper Bonds. *J. Am. Chem. Soc.* **2020**, *142* (47), 19874–19878. https://doi.org/10.1021/jacs.0c10099.

(88) Mondal, R.; Lozada, I. B.; Davis, R. L.; Williams, J. A. G.; Herbert, D. E. Exploiting Synergy between Ligand Design and Counterion Interactions to Boost Room Temperature Phosphorescence from Cu(I) Compounds. *J. Mater. Chem. C* **2019**, *7*, 3772–3778.

(89) Mandapati, P.; Braun, J. D.; Lozada, I. B.; Williams, J. A. G.; Herbert, D. E. Deep-Red Luminescence from Platinum(II) Complexes of N^N⁻^N-Amido Ligands with Benzannulated N-Heterocyclic Donor Arms. *Inorg. Chem.* **2020**, *59*, 12504–12517.

(90) Ortiz, R. J.; Braun, J. D.; Williams, J. A. G.; Herbert, D. E. Brightly Luminescent Platinum Complexes of *N^C⁻^N* Ligands Forming Six-Membered Chelate Rings: Offsetting Deleterious Ring Size Effects Using Site-Selective Benzannulation. *Inorg. Chem.* **2021**, *60*, 16881–16894.

(91) Lozada, I. B.; Huang, B.; Stilgenbauer, M.; Beach, T.; Qiu, Z.; Zheng, Y.; Herbert, D. E. Monofunctional Platinum(II) Anticancer Complexes Based on Multidentate Phenanthridine-Containing Ligand Frameworks. *Dalton Trans.* **2020**, *49*, 6557–6560.

(92) Myers, E. L.; Butts, C. P.; Aggarwal, V. K. BF3·OEt2 and TMSOTf: A Synergistic Combination of Lewis Acids. *Chem. Commun.* **2006**, No. 42, 4434–4436.

(93) Macedo, F. P.; Gwengo, C.; Lindeman, S. V.; Smith, M. D.; Gardinier, J. R. β-Diketonate, β-Ketoiminate, and β-Diiminate Complexes of Difluoroboron. *Eur. J. Inorg. Chem.* **2008**, *2008*, 3200–3211.

(94) Dohe, J.; Kossmann, J.; Mueller, T. J. J. Diversity-Oriented Four-Component Synthesis of Solid State Luminescent Difluoro Oxazaborinines. *Dyes Pigments* **2018**, *157*, 198–217.

(95) Köhling, J.; Kozel, V.; Jovanov, V.; Pajkert, R.; Tverdomed, S. N.; Gridenco, O.; Fugel, M.; Grabowsky, S.; Röschenthaler, G.-V.; Wagner, V. Synthesis and Characterization of Oxazaborinin Phosphonate for Blue OLED Emitter Applications. *ChemPhysChem* **2019**, *20*, 665–671.

(96) Mtiraoui, H.; Gharbi, R.; Msaddek, M.; Bretonnière, Y.; Andraud, C.; Renard, P.-Y.; Sabot, C. Solution and Solid-State Fluorescence of 2-(2′-Hydroxyphenyl)-1,5-Benzodiazepin-2-One (HBD) Borate Complexes. *RSC Adv.* **2016**, *6*, 86352–86360.

(97) Chęcińska, L.; Mebs, S.; Ośmiałowski, B.; Zakrzewska, A.; Ejsmont, K.; Kohout, M. Tuning the Electronic Properties of the Dative N−B Bond with Associated O−B Interaction: Electron Localizability Indicator from X-Ray Wavefunction Refinement. *ChemPhysChem* **2016**, *17*, 2395–2406.

(98) Itoh, K.; Okazaki, K.; Fujimoto, M. The Structure of 1,3-Enaminoketonatoboron Difluorides in Solution and in the Solid State. *Aust. J. Chem.* **2003**, *56*, 1209–1214.

(99) Grepioni, F.; Cojazzi, G.; Draper, S. M.; Scully, N.; Braga, D. Crystal Forms of Hexafluorophosphate Organometallic Salts and the Importance of Charge-Assisted C−H---F Hydrogen Bonds. *Organometallics* **1998**, *17*, 296–307.

(100) Mandapati, P.; Braun, J. D.; Killeen, C.; Davis, R. L.; Williams, J. A. G.; Herbert, D. E. Luminescent Platinum(II) Complexes of N^N⁻^N Amido Ligands with Benzannulated N-Heterocyclic Donor Arms: Quinolines Offer Unexpectedly Deeper Red Phosphorescence than Phenanthridines. *Inorg. Chem.* **2019**, *58*, 14808–14817.

(101) Lozada, I. B.; Williams, J. A. G.; Herbert, D. E. Platinum(II) Complexes of Benzannulated N^N⁻^O-Amido Ligands: Bright Orange Phosphors with Long-Lived Excited States. *Inorg. Chem. Front.* **2022**, *9*, 10–22.

(102) Donckt, E. V.; Dramaix, R.; Nasielski, J.; Vogels, C. Photochemistry of Aromatic Compounds. Part 1.—Acid-Base Properties of Singlet and Triplet Excited States of Pyrene Derivatives and Aza-Aromatic Compounds. *Trans. Faraday Soc.* **1969**, *65*, 3258–3262.

(103) Zander, M. The Significance of Donor-Acceptor Interactions in the External Heavy Atom Effect of Silver Nitrate on the Luminescence Behavior of Aza-Aromatic Systems and Carbazoles. *Z Naturforsch A* **1978**, *33*, 998–1000.

(104) Norek, M.; Dresner, J.; Prochorow, J. Spectroscopy and Photophysics of Monoazaphenanthrenes. I. Absorption and Fluorescence Spectra of Phenanthridine and 7,8-Benzoquinoline. *Acta Phys. Pol. A* **2003**, *104*, 425–439.

(105) Marzzacco, C. J.; Deckey, G.; Colarulli, R.; Siuzdak, G.; Halpern, A. M. Excited-State Protonation and Photophysical Properties of Azaphenanthrenes. *J. Phys. Chem.* **1989**, *93*, 2935–2939.

(106) Parker, D.; Senanayake, P. K.; Williams, J. A. G. Luminescent Sensors for PH, PO2, Halide and Hydroxide Ions Using Phenanthridine as a Photosensitiser in Macrocyclic Europium and Terbium Complexes. *J. Chem. Soc. Perkin Trans. 2* **1998**, 2129–2140.

(107) Norek, M.; Kozankiewicz, B.; Prochorow, J. Spectroscopy and Photophysics of Monoazaphenanthrenes. III. Luminescence of Phenanthridine and 7,8-Benzoquinoline in Crystalline State. *Acta Phys Pol A* **2004**, *106*, 77–94.

(108) Lozada, I. B.; Murray, T.; Herbert, D. E. Monomeric Zinc(II) Amide Complexes Supported by Bidentate, Benzannulated Phenanthridine Amido Ligands. *Polyhedron* **2019**, *161*, 261–267.

(109) Lozada, I. B.; Ortiz, R. J.; Braun, J. D.; Williams, J. A. G.; Herbert, D. E. Donor–Acceptor Boron-Ketoiminate Complexes with Pendent N-Heterocyclic Arms: Switched-on Luminescence through N-Heterocycle Methylation. *J. Org. Chem.* **2022**, *87*, 184–196.

(110) Bridgeman, A. J.; Cavigliasso, G.; Ireland, L. R.; Rothery, J. The Mayer Bond Order as a Tool in Inorganic Chemistry. *J. Chem. Soc. Dalton Trans.* **2001**, 2095–2108.

(111) Lu, T.; Chen, F. Atomic Dipole Moment Corrected Hirshfeld Population Method. *J. Theor. Comput. Chem.* **2012**, *11*, 163–183.

(112) Montalti, M.; Credi, A.; Prodi, L.; Gandolfi, M. *Handbook of Photochemistry. 3rd Ed.*; CRC Press: Boca Raton, 2006.

(113) Oyler, K. D.; Coughlin, F. J.; Bernhard, S. Controlling the Helicity of 2,2'-Bipyridyl Ruthenium(II) and Zinc(II) Hemicage Complexes. *J. Am. Chem. Soc.* **2007**, *129*, 210–217.

(114) Martinez, S.; Igoa, F.; Carrera, I.; Seoane, G.; Veiga, N.; De Camargo, A. S. S.; Kremer, C.; Torres, J. A Zn(II) Luminescent Complex with a Schiff Base Ligand: Solution, Computational and Solid State Studies. *J. Coord. Chem.* **2018**, *71*, 874–889.

(115) Mei, J.; Leung, N. L. C.; Kwok, R. T. K.; Lam, J. W. Y.; Tang, B. Z. Aggregation-Induced Emission: Together We Shine, United We Soar! *Chem. Rev.* **2015**, *115*, 11718–11940.

(116) Singh, K.; Siddiqui, I.; Sridharan, V.; Kumar Yadav, R. A.; Jou, J.-H.; Adhikari, D. Aggregation-Induced Enhanced Emission-Active Zinc(II) β-Diketiminate Complexes Enabling High-Performance Solution-Processable OLEDs. *Inorg. Chem.* **2021**, *60*, 19128–19135.

(117) Singh, K.; S., V.; Adhikari, D. Visible Light Photoredox by a (Ph,ArNacNac)2Zn Photocatalyst: Photophysical Properties and Mechanistic Understanding. *Inorg. Chem. Front.* **2021**, *8*, 2078–2087.

(118) Lozada, I. B.; Huang, B.; Stilgenbauer, M.; Beach, T.; Qiu, Z.; Zheng, Y.; Herbert, D. E. Monofunctional Platinum(II) Anticancer Complexes Based on Multidentate Phenanthridine-Containing Ligand Frameworks. *Dalton Trans.* **2020**, *49*, 6557–6560.

(119) Mandapati, P.; Giesbrecht, P. K.; Davis, R. L.; Herbert, D. E. Phenanthridine-Containing Pincer-like Amido Complexes of Nickel, Palladium, and Platinum. *Inorg. Chem.* **2017**, *56*, 3674–3685.

(120) Mandapati, P.; Braun, J. D.; Killeen, C.; Davis, R. L.; Williams, J. A. G.; Herbert, D. E. Luminescent Platinum(II) Complexes of N′N-′N Amido Ligands with Benzannulated N-Heterocyclic Donor Arms: Quinolines Offer Unexpectedly Deeper Red Phosphorescence than Phenanthridines. *Inorg Chem* **2019**, *58*, 14808–14817.

(121) Mandapati, P.; Braun, J. D.; Lozada, I. B.; Williams, J. A. G.; Herbert, D. E. Deep-Red Luminescence from Platinum(II) Complexes of N^N−^N-Amido Ligands with Benzannulated N-Heterocyclic Donor Arms. *Inorg. Chem.* **2020**, *59*, 12504–12517.

(122) Reineke, M. H.; Sampson, M. D.; Rheingold, A. L.; Kubiak, C. P. Synthesis and Structural Studies of Nickel(0) Tetracarbene Complexes with the Introduction of a New Four-Coordinate Geometric Index, Tδ. *Inorg. Chem.* **2015**, *54*, 3211–3217.

(123) Puttock, E. V.; Fradgley, J. D.; Yufit, D. S.; Williams, J. A. G. A Family of Readily Synthesised Phosphorescent Platinum(II) Complexes Based on Tridentate *N^N^O* -Coordinating Schiff-Base Ligands. *Dalton Trans.* **2019**, *48*, 15012–15028.

(124) Davidson, J. J.; DeMott, J. C.; Douvris, C.; Fafard, C. M.; Bhuvanesh, N.; Chen, C.-H.; Herbert, D. E.; Lee, C.-I.; McCulloch, B. J.; Foxman, B. M.; Ozerov, O. V. Comparison of the Electronic Properties of Diarylamido-Based PNZ Pincer Ligands: Redox Activity at the Ligand and Donor Ability Toward the Metal. *Inorg. Chem.* **2015**, *54*, 2916–2935.

(125) Giesbrecht, P. K.; Nemez, D. B.; Herbert, D. E. Electrochemical Hydrogenation of a Benzannulated Pyridine to a Dihydropyridine in Acidic Solution. *Chem. Commun.* **2018**, *54*, 338–341.

(126) Reichardt, C. Solvatochromic Dyes as Solvent Polarity Indicators. *Chem. Rev.* **1994**, *94*, 2319–2358.

(127) Catalán, J. Toward a Generalized Treatment of the Solvent Effect Based on Four Empirical Scales: Dipolarity (SdP, a New Scale), Polarizability (SP), Acidity (SA), and Basicity (SB) of the Medium. *J. Phys. Chem. B* **2009**, *113*, 5951–5960.

(128) Van der Zwan, G.; Hynes, J. T. Time-Dependent Fluorescence Solvent Shifts, Dielectric Friction, and Nonequilibrium Solvation in Polar Solvents. *J. Phys. Chem.* **1985**, *89*, 4181–4188.

(129) Caspar, J. V.; Meyer, T. J. Photochemistry of Tris(2,2'-Bipyridine)Ruthenium(2+) Ion (Ru(Bpy)$_3^{2+}$). Solvent Effects. *J. Am. Chem. Soc.* **1983**, *105*, 5583–5590.

(130) Kwok, C.-C.; Ngai, H. M. Y.; Chan, S.-C.; Sham, I. H. T.; Che, C.-M.; Zhu, N. [(O∧N∧N)PtX] Complexes as a New Class of Light-Emitting Materials for Electrophosphorescent Devices. *Inorg. Chem.* **2005**, *44*, 4442–4444.

(131) Garner, K. L.; Parkes, L. F.; Piper, J. D.; Williams, J. A. G. Luminescent Platinum Complexes with Terdentate Ligands Forming 6-Membered Chelate Rings: Advantageous and Deleterious Effects in N ^ N ^ N and N ^ C ^ N-Coordinated Complexes. *Inorg. Chem.* **2010**, *49*, 476–487.

(132) Williams, J. A. G. The Coordination Chemistry of Dipyridylbenzene: N-Deficient Terpyridine or Panacea for Brightly Luminescent Metal Complexes? *Chem. Soc. Rev.* **2009**, *38*, 1783–1801.

(133) Meech, S. R.; Phillips, D. Photophysics of Some Common Fluorescence Standards. *J. Photochem.* **1983**, *23*, 193–217.

(134) Suzuki, K.; Kobayashi, A.; Kaneko, S.; Takehira, K.; Yoshihara, T.; Ishida, H.; Shiina, Y.; Oishi, S.; Tobita, S. Reevaluation of Absolute Luminescence Quantum Yields of Standard Solutions Using a Spectrometer with an Integrating Sphere and a Back-Thinned CCD Detector. *Phys. Chem. Chem. Phys.* **2009**, *11*, 9850–9860.

(135) Murov, S. L.; Carmichael, I.; Hug, G. L. *Handbook of Photochemistry, 2ⁿᵈ Ed.*; Marcel Dekker: New York, 1993.

(136) Hohenberg, P.; Kohn, W. Inhomogeneous Electron Gas. *Phys. Rev.* **1964**, *136* (3B), B864–B871. https://doi.org/10.1103/PhysRev.136.B864.

(137) Kohn, W.; Sham, L. J. Self-Consistent Equations Including Exchange and Correlation Effects. *Phys. Rev.* **1965**, *140* (4A), A1133–A1138. https://doi.org/10.1103/PhysRev.140.A1133.

(138) Bühl, M.; Kabrede, H. Geometries of Transition-Metal Complexes from Density-Functional Theory. *J. Chem. Theory Comput.* **2006**, *2* (5), 1282–1290. https://doi.org/10.1021/ct6001187.

(139) Waller, M. P.; Braun, H.; Hojdis, N.; Bühl, M. Geometries of Second-Row Transition-Metal Complexes from Density-Functional Theory. *J. Chem. Theory Comput.* **2007**, *3* (6), 2234–2242. https://doi.org/10.1021/ct700178y.

(140) Bühl, M.; Reimann, C.; Pantazis, D. A.; Bredow, T.; Neese, F. Geometries of Third-Row Transition-Metal Complexes from Density-Functional Theory. *J. Chem. Theory Comput.* **2008**, *4* (9), 1449–1459. https://doi.org/10.1021/ct800172j.

(141) de Souza, B.; Farias, G.; Neese, F.; Izsák, R. Predicting Phosphorescence Rates of Light Organic Molecules Using Time-Dependent Density Functional Theory and the Path Integral Approach to Dynamics. *J. Chem. Theory Comput.* **2019**, *15* (3), 1896–1904. https://doi.org/10.1021/acs.jctc.8b00841.

(142) de Souza, B.; Neese, F.; Izsák, R. On the Theoretical Prediction of Fluorescence Rates from First Principles Using the Path Integral Approach. *J. Chem. Phys.* **2018**, *148* (3), 034104. https://doi.org/10.1063/1.5010895.

(143) Petrenko, T.; Neese, F. Analysis and Prediction of Absorption Band Shapes, Fluorescence Band Shapes, Resonance Raman Intensities, and Excitation Profiles Using the Time-Dependent Theory of Electronic Spectroscopy. *J. Chem. Phys.* **2007**, *127* (16), 164319. https://doi.org/10.1063/1.2770706.

(144) Wenger, O. S. Is Iron the New Ruthenium? *Chem. – Eur. J.* **2020**, *25*, 6043–6052.

(145) Baková, R.; Chergui, M.; Daniel, C.; Vlček Jr., A.; Záliš, S. Relativistic Effects in Spectroscopy and Photophysics of Heavy-Metal Complexes Illustrated by Spin–Orbit Calculations of [Re(Imidazole)(CO)3(Phen)]+. *Coord. Chem. Rev.* **2011**, *255* (7–8), 975–989. https://doi.org/10.1016/j.ccr.2010.12.027.

(146) Giesbrecht, P. K.; Nemez, D. B.; Herbert, D. E. Electrochemical Hydrogenation of a Benzannulated Pyridine to a Dihydropyridine in Acidic Solution. *Chem. Commun.* **2018**, *54* (4), 338–341. https://doi.org/10.1039/c7cc07907a.

(147) Mandapati, P.; Giesbrecht, P. K.; Davis, R. L.; Herbert, D. E. Phenanthridine-Containing Pincer-like Amido Complexes of Nickel, Palladium, and Platinum. *Inorg. Chem.* **2017**, *56* (6), 3674–3685. https://doi.org/10.1021/acs.inorgchem.7b00075.

(148) Mondal, R.; Lozada, I. B.; Davis, R. L.; Williams, J. A. G.; Herbert, D. E. Exploiting Synergy between Ligand Design and Counterion Interactions to Boost Room Temperature Phosphorescence from Cu(i) Compounds. *J. Mater. Chem. C* **2019**, *7* (13), 3772–3778. https://doi.org/10.1039/C9TC00040B.

(149) Mandapati, P.; Braun, J. D.; Killeen, C.; Davis, R. L.; Williams, J. A. G.; Herbert, D. E. Luminescent Platinum(II) Complexes of N^ N-^ N Amido Ligands with Benzannulated N-Heterocyclic Donor Arms: Quinolines Offer Unexpectedly Deeper Red Phosphorescence than Phenanthridines. *Inorg. Chem.* **2019**, *58* (21), 14808–14817. https://doi.org/10.1021/acs.inorgchem.9b02480.

(150) Lozada, I. B.; Murray, T.; Herbert, D. E. Monomeric Zinc(II) Amide Complexes Supported by Bidentate, Benzannulated Phenanthridine Amido Ligands. *Polyhedron* **2019**, *161*, 261–267. https://doi.org/10.1016/j.poly.2019.01.023.

(151) Braun, J. D.; Lozada, I. B.; Kolodziej, C.; Burda, C.; Newman, K. M. E.; van Lierop, J.; Davis, R. L.; Herbert, D. E. Iron(Ii) Coordination Complexes with Panchromatic Absorption and Nanosecond Charge-Transfer Excited State Lifetimes. *Nat. Chem.* **2019**, *11* (12), 1144–1150. https://doi.org/10.1038/s41557-019-0357-z.

(152) Mondal, R.; Lozada, I. B.; Davis, R. L.; Williams, J. A. G.; Herbert, D. E. Site-Selective Benzannulation of N-Heterocycles in Bidentate Ligands Leads to Blue-Shifted Emission from [(P^N)Cu]2(μ-X)2 Dimers. *Inorg. Chem.* **2018**, *57* (9), 4966–4978. https://doi.org/10.1021/acs.inorgchem.7b03223.

(153) Mondal, R.; Giesbrecht, P. K.; Herbert, D. E. Nickel(II), Copper(I) and Zinc(II) Complexes Supported by a (4-Diphenylphosphino)Phenanthridine Ligand. *Polyhedron* **2016**, *108*, 156–162. https://doi.org/10.1016/j.poly.2015.10.051.

(154) Stufkens, D. J.; Vlček, A. Ligand-Dependent Excited State Behaviour of Re(I) and Ru(II) Carbonyl-Diimine Complexes. *Coord. Chem. Rev.* **1998**, *177* (1), 127–179. https://doi.org/10.1016/s0010-8545(98)00132-5.

(155) Vlček, A. Ultrafast Excited-State Processes in Re(I) Carbonyl-Diimine Complexes: From Excitation to Photochemistry. *Top Organomet Chem* **2010**, *29* (May 2009), 73–114. https://doi.org/10.1007/3418.

(156) Mandapati, P.; Braun, J. D.; Killeen, C.; Davis, R. L.; Williams, J. A. G.; Herbert, D. E. Luminescent Platinum(II) Complexes of N´N-´N Amido Ligands with Benzannulated N-Heterocyclic Donor Arms: Quinolines Offer Unexpectedly Deeper Red Phosphorescence than Phenanthridines. *Inorg Chem* **2019**, *58*, 14808–14817.

(157) Dixon, I. M.; Khan, S.; Alary, F.; Boggio-Pasqua, M.; Heully, J.-L. Probing the Photophysical Capability of Mono and Bis(Cyclometallated) Fe(II) Polypyridine Complexes Using Inexpensive Ground State DFT. *Dalton Trans.* **2014**, *43*, 15898–15905.

(158) Zhang, K.; Ash, R.; Girolami, G. S.; Vura-Weis, J. Tracking the Metal-Centered Triplet in Photoinduced Spin Crossover of Fe(Phen)32+ with Tabletop Femtosecond M-Edge X-Ray Absorption Near-Edge Structure Spectroscopy. *J. Am. Chem. Soc.* **2019**, *141*, 17180–17188.

(159) Juban, E. A.; Smeigh, A. L.; Monat, J. E.; McCusker, J. K. Ultrafast Dynamics of Ligand-Field Excited States. *Coord Chem Rev* **2006**, *250*, 1783–1791.

(160) Gryn'ova, G.; Coote, M. L.; Corminboeuf, C. Theory and Practice of Uncommon Molecular Electronic Configurations. *WIREs Comput. Mol. Sci.* **2015**, *5* (6), 440–459. https://doi.org/10.1002/wcms.1233.

(161) Kaim, W. Manifestations of Noninnocent Ligand Behavior. *Inorg Chem* **2011**, *50* (20), 9752–9765.

(162) Bowman, D. N.; Jakubikova, E. Low-Spin versus High-Spin Ground State in Pseudo-Octahedral Iron Complexes. *Inorg. Chem.* **2012**, *51*, 6011–6019.

(163) Ashley, D. C.; Jakubikova, E. Ironing out the Photochemical and Spin-Crossover Behavior of Fe(II) Coordination Compounds with Computational Chemistry. *Coord. Chem. Rev.* **2017**, *337*, 97–111.

(164) Reiher, M.; Salomon, O.; Artur Hess, B. Reparameterization of Hybrid Functionals Based on Energy Differences of States of Different Multiplicity. *Theor. Chem. Acc.* **2001**, *107*, 48–55.

(165) Jakubikova, E.; Bowman, D. N. Fe(II)-Polypyridines as Chromophores in Dye-Sensitized Solar Cells: A Computational Perspective. *Acc. Chem. Res.* **2015**, *48*, 1441–1449.

(166) Nemykin, V. N.; Hadt, R. G. Influence of Hartree−Fock Exchange on the Calculated Mössbauer Isomer Shifts and Quadrupole Splittings in Ferrocene Derivatives Using Density Functional Theory. *Inorg. Chem.* **2006**, *45*, 8297–8307.

(167) Zhao, Y.; Truhlar, D. G. A New Local Density Functional for Main-Group Thermochemistry, Transition Metal Bonding, Thermochemical Kinetics, and Noncovalent Interactions. *J. Chem. Phys.* **2006**, *125*, 194101.

(168) Cohen, A. J.; Handy, N. C. Dynamic Correlation. *Mol. Phys.* **2001**, *99*, 607–615.

(169) Zhao, Y.; Truhlar, D. G. The M06 Suite of Density Functionals for Main Group Thermochemistry, Thermochemical Kinetics, Noncovalent Interactions, Excited States, and Transition Elements: Two New Functionals and Systematic Testing of Four M06-Class Functionals and 12 Other Functionals. *Theor. Chem. Acc.* **2008**, *120*, 215–241.

(170) Ditchfield, R.; Hehre, W. J.; Pople, J. A. Self-Consistent Molecular-Orbital Methods. IX. Extended Gaussian-Type Basis for Molecular-Orbital Studies of Organic Molecules. *J. Chem. Phys.* **1971**, *54*, 724–728. https://doi.org/10.1063/1.1674902.

(171) Hehre, W. J.; Ditchfield, R.; Pople, J. A. Self-Consistent Molecular Orbital Methods. XII. Further Extensions of Gaussian-Type Basis Sets for Use in Molecular Orbital Studies of Organic Molecules. *J. Chem. Phys.* **1972**, *56*, 2257–2261.

(172) Hariharan, P. C.; Pople, J. A. Influence of Polarization Functions on MO Hydrogenation Energies. *Theor. Chim. Acta* **1973**, *28*, 213–222.

(173) Clark, T.; Chandrasekhar, J.; Spitznagel, G. W.; Schleyer, P. v R. Efficient Diffuse Function-Augmented Basis Sets for Anion Calculations. III. The 3-21 + G Basis Set for First-Row Elements, Lithium to Fluorine. *J. Comput. Chem.* **1983**, *4*, 294–301.

(174) Rassolov, V. A.; Pople, J. A.; Ratner, M. A.; Windus, T. L. 6-31G* Basis Set for Atoms K through Zn. *J. Chem. Phys.* **1998**, *109*, 1223–1229.

(175) Zhao, Y.; Truhlar, D. G. A New Local Density Functional for Main-Group Thermochemistry, Transition Metal Bonding, Thermochemical Kinetics, and Noncovalent Interactions. *J. Chem. Phys.* **2006**, *125* (19), 194101. https://doi.org/10.1063/1.2370993.

(176) Krishnan, R.; Binkley, J. S.; Seeger, R.; Pople, J. A. Self-consistent Molecular Orbital Methods. XX. A Basis Set for Correlated Wave Functions. *J. Chem. Phys.* **1980**, *72* (1), 650–654. https://doi.org/10.1063/1.438955.

(177) Clark, T.; Chandrasekhar, J.; Spitznagel, G. W.; Schleyer, P. V. R. Efficient Diffuse Function-Augmented Basis Sets for Anion Calculations. III. The 3-21+G Basis Set for First-Row Elements, Li-F. *J. Comput. Chem.* **1983**, *4* (3), 294–301. https://doi.org/10.1002/jcc.540040303.

(178) Dennington, Roy; Keith, Todd A.; Millam, John M. *GaussView, Version 6*; Semichem Inc.: Shawnee Mission, KS, 2016.

(179) Soda, T.; Kitagawa, Y.; Onishi, T.; Takano, Y.; Shigeta, Y.; Nagao, H.; Yoshioka, Y.; Yamaguchi, K. Ab Initio Computations of Effective Exchange Integrals for H–H, H–He–H and Mn2O2 Complex: Comparison of Broken-Symmetry Approaches. *Chem. Phys. Lett.* **2000**, *319* (3–4), 223–230. https://doi.org/10.1016/S0009-2614(00)00166-4.

(180) Yamaguchi, K.; Takahara, Y.; Fueno, T. Ab-Initio Molecular Orbital Studies of Structure and Reactivity of Transition Metal-OXO Compounds. In *Applied Quantum Chemistry*; Smith, V. H., Schaefer, H. F., Morokuma, K., Eds.; Springer Netherlands: Dordrecht, 1986; pp 155–184. https://doi.org/10.1007/978-94-009-4746-7_11.

(181) Heydová, R.; Gindensperger, E.; Romano, R.; Sýkora, J.; Vlček, A.; Záliš, S.; Daniel, C. Spin-Orbit Treatment of UV-Vis Absorption Spectra and Photophysics of Rhenium(I) Carbonyl-Bipyridine Complexes: MS-CASPT2 and TD-DFT Analysis. *J. Phys. Chem. A* **2012**, *116* (46), 11319–11329. https://doi.org/10.1021/jp305461z.

(182) Ronca, E.; De Angelis, F.; Fantacci, S. Time-Dependent Density Functional Theory Modeling of Spin-Orbit Coupling in Ruthenium and Osmium Solar Cell Sensitizers. *J. Phys. Chem. C* **2014**, *118* (30), 17067–17078. https://doi.org/10.1021/jp500869r.

(183) Mai, S.; Gattuso, H.; Fumanal, M.; Muñoz-Losa, A.; Monari, A.; Daniel, C.; González, L. Excited-States of a Rhenium Carbonyl Diimine Complex: Solvation Models, Spin-Orbit Coupling, and Vibrational Sampling Effects. *Phys. Chem. Chem. Phys.* **2017**, *19* (40), 27240–27250. https://doi.org/10.1039/c7cp05126c.

(184) Shi, L. L.; Liao, Y.; Zhao, L.; Su, Z. M.; Kan, Y. H.; Yang, G. C.; Yang, S. Y. Theoretical Studies on the Electronic Structure and Spectral Properties of Versatile Diarylethene-Containing 1,10-Phenanthroline Ligands and Their Rhenium(I) Complexes. *J. Organomet. Chem.* **2007**, *692* (24), 5368–5374. https://doi.org/10.1016/j.jorganchem.2007.08.031.

(185) Silva-Junior, M. R.; Schreiber, M.; Sauer, S. P. A.; Thiel, W. Benchmarks for Electronically Excited States: Time-Dependent Density Functional Theory and Density Functional Theory Based Multireference Configuration Interaction. *J. Chem. Phys.* **2008**, *129* (10). https://doi.org/10.1063/1.2973541.

(186) Jacquemin, D.; Perpète, E. A.; Ciofini, I.; Adamo, C. Assessment of Functionals for TD-DFT Calculations of Singlet-Triplet Transitions. *J. Chem. Theory Comput.* **2010**, *6* (5), 1532–1537. https://doi.org/10.1021/ct100005d.

(187) Santoro, F.; Lami, A.; Improta, R.; Barone, V. Effective Method to Compute Vibrationally Resolved Optical Spectra of Large Molecules at Finite Temperature in the Gas Phase and in Solution. *J. Chem. Phys.* **2007**, *126* (18). https://doi.org/10.1063/1.2721539.

(188) Tozer, D. J.; Handy, N. C. On the Determination of Excitation Energies Using Density Functional Theory. *Phys. Chem. Chem. Phys.* **2000**, *2* (10), 2117–2121. https://doi.org/10.1039/a910321j.

(189) Chibani, S.; Charaf-Eddin, A.; Le Guennic, B.; Jacquemin, D. Boranil and Related NBO Dyes: Insights From Theory. *J. Chem. Theory Comput.* **2013**, *9*, 3127–3135.

(190) Mondal, R.; Giesbrecht, P. K.; Herbert, D. E. Nickel(II), Copper(I) and Zinc(II) Complexes Supported by a (4-Diphenylphosphino)Phenanthridine Ligand. *Polyhedron* **2016**, *108*, 156–162.

(191) Mondal, R.; Lozada, I. B.; Davis, R. L.; Williams, J. A. G.; Herbert, D. E. Site-Selective Benzannulation of N-Heterocycles in Bidentate Ligands Leads to Blue-Shifted Emission from [(*P^N*)Cu]2(μ-X)2 Dimers. *Inorg Chem* **2018**, *57*, 4966–4978.

(192) Gaire, S.; Ortiz, R. J.; Schrage, B. R.; Lozada, I. B.; Mandapati, P.; Osinski, A. J.; Herbert, D. E.; Ziegler, C. J. (8-Amino)Quinoline and (4-Amino)Phenanthridine Complexes of Re(CO)3 Halides. *J. Organomet. Chem.* **2020**, *921*, 121338.

(193) Tomasi, J.; Mennucci, B.; Cammi, R. Quantum Mechanical Continuum Solvation Models. *Chem Rev* **2005**, *105*, 2999–3094.

(194) Melenbacher, A.; Dhindsa, J. S.; Gilroy, J. B.; Stillman, M. J. Unveiling the Hidden, Dark, and Short Life of a Vibronic State in a Boron Difluoride Formazanate Dye. *Angew. Chem. Int. Ed.* **2019**, *58* (43), 15339–15343.

(195) El-Sayed, M. A. Spin—Orbit Coupling and the Radiationless Processes in Nitrogen Heterocyclics. *J. Chem. Phys.* **1963**, *38* (12), 2834–2838.

(196) Braun, J. D.; Lozada, I. B.; Kolodziej, C.; Burda, C.; Newman, K. M. E.; van Lierop, J.; Davis, R. L.; Herbert, D. E. Iron(II) Coordination Complexes with Panchromatic Absorption and Nanosecond Charge-Transfer Excited State Lifetimes. *Nat. Chem.* **2019**, *11*, 1144–1150.

(197) Larsen, C. B.; Braun, J. D.; Lozada, I. B.; Kunnus, K.; Biasin, E.; Kolodziej, C.; Burda, C.; Cordones, A. A.; Gaffney, K. J.; Herbert, D. E. Reduction of Electron Repulsion in Highly Covalent Fe-Amido Complexes Counteracts the Impact of a Weak Ligand Field on Excited-State Ordering. *J. Am. Chem. Soc.* **2021**, *143*, 20645–20656.

(198) Das, S.; Thornbury, W. G.; Bartynski, A. N.; Thompson, M. E.; Bradforth, S. E. Manipulating Triplet Yield through Control of Symmetry-Breaking Charge Transfer. *J. Phys. Chem. Lett.* **2018**, *9*, 3264–3270.

(199) Trinh, C.; Kirlikovali, K.; Das, S.; Ener, M. E.; Gray, H. B.; Djurovich, P.; Bradforth, S. E.; Thompson, M. E. Symmetry-Breaking Charge Transfer of Visible Light Absorbing Systems: Zinc Dipyrrins. *J. Phys. Chem. C* **2014**, *118*, 21834–21845.

(200) Kellogg, M.; Akil, A.; Muthiah Ravinson, D. S.; Estergreen, L.; Bradforth, S. E.; Thompson, M. E. Symmetry Breaking Charge Transfer as a Means to Study Electron Transfer with No Driving Force. *Faraday Discuss.* **2019**, *216*, 379–394.

(201) Mahmood, Z.; Rehmat, N.; Ji, S.; Zhao, J.; Sun, S.; Di Donato, M.; Li, M.; Teddei, M.; Huo, Y. Tuning the Triplet Excited State of Bis(Dipyrrin) Zinc(II) Complexes: Symmetry Breaking Charge Transfer Architecture with Exceptionally Long Lived Triplet State for Upconversion. *Chem. – Eur. J.* **2020**, *26*, 14912–14918.

(202) Weller, A. Photoinduced Electron Transfer in Solution: Exciplex and Radical Ion Pair Formation Free Enthalpies and Their Solvent Dependence By. *Zeitshcrift Phys. Chem. N. F.* **1982**, *133*, 93–98.

(203) Rehm, D.; Weller, A. Kinetics of Fluorescence Quenching by Electron and H-Atom Transfer. *Isr. J. Chem.* **1970**, *8*, 259–271.

(204) Vauthey, E. Photoinduced Symmetry-Breaking Charge Separation. *ChemPhysChem* **2012**, *13*, 2001–2011.

(205) Smith, A. R. G.; Burn, P. L.; Powell, B. J. Spin–Orbit Coupling in Phosphorescent Iridium(III) Complexes. *ChemPhysChem* **2011**, *12*, 2429–2438.

(206) Ronca, E.; De Angelis, F.; Fantacci, S. Time-Dependent Density Functional Theory Modeling of Spin–Orbit Coupling in Ruthenium and Osmium Solar Cell Sensitizers. *J. Phys. Chem. C* **2014**, *118*, 17067–17078.

(207) Gourlaouen, C.; Daniel, C. Spin–Orbit Effects in Square-Planar Pt(II) Complexes with Bidentate and Terdentate Ligands: Theoretical Absorption/Emission Spectroscopy. *Dalton Trans* **2014**, *43*, 17806–17819.

(208) Braun, J. D.; Lozada, I. B.; Herbert, D. E. In Pursuit of Panchromatic Absorption in Metal Coordination Complexes: Experimental Delineation of the HOMO Inversion Model Using Pseudo-Octahedral Complexes of Diarylamido Ligands. *Inorg. Chem.* **2020**, *59*, 17746–17757.

(209) Hayashi, M.; Takahashi, Y.; Yoshida, Y.; Sugimoto, K.; Kitagawa, H. Role of D-Elements in a Proton–Electron Coupling of d–π Hybridized Electron Systems. *J. Am. Chem. Soc.* **2019**, *141*, 11686–11693.

(210) Spencer, M.; Santoro, A.; Freeman, G. R.; Díez, Á.; Murray, P. R.; Torroba, J.; Whitwood, A. C.; Yellowlees, L. J.; Williams, J. A. G.; Bruce, D. W. Phosphorescent, Liquid-Crystalline Complexes of Platinum(II): Influence of the β-Diketonate Co-Ligand on Mesomorphism and Emission Properties. *Dalton Trans.* **2012**, *41*, 14244–14256.

(211) Neese, F. The ORCA Program System. *WIREs Comput. Mol. Sci.* **2012**, *2*, 73–78.

(212) Neese, F. Software Update: The ORCA Program System, Version 4.0. *WIREs Comput. Mol. Sci.* **2018**, *8*, e1327.

(213) Frisch, M. J.; Trucks, G. W.; Schlegel, H. B.; Scuseria, G. E.; Robb, M. A.; Cheeseman, J. R.; Scalmani, G.; Barone, V.; Petersson, G. A.; Nakatsuji, H.; Li, X.; Caricato, M.; Marenich, A. V.; Bloino, J.; Janesko, B. G.; Gomperts, R.; Mennucci, B.; Hratchian, H. P.; Ortiz, J. V.; Izmaylov, A. F.; Sonnenberg, J. L.; Williams; Ding, F.; Lipparini, F.; Egidi, F.; Goings, J.; Peng, B.; Petrone, A.; Henderson, T.; Ranasinghe, D.; Zakrzewski, V. G.; Gao, J.; Rega, N.; Zheng, G.; Liang, W.; Hada, M.; Ehara, M.; Toyota, K.; Fukuda, R.; Hasegawa, J.; Ishida, M.; Nakajima, T.; Honda, Y.; Kitao, O.; Nakai, H.; Vreven, T.; Throssell, K.; Montgomery Jr., J. A.; Peralta, J. E.; Ogliaro, F.; Bearpark, M. J.; Heyd, J. J.; Brothers, E. N.; Kudin, K. N.; Staroverov, V. N.; Keith, T. A.; Kobayashi, R.; Normand, J.; Raghavachari, K.; Rendell, A. P.; Burant, J. C.; Iyengar, S. S.; Tomasi, J.; Cossi, M.; Millam, J. M.; Klene, M.; Adamo, C.; Cammi, R.; Ochterski, J. W.; Martin, R. L.; Morokuma, K.; Farkas, O.; Foresman, J. B.; Fox, D. J. *Gaussian 16 Rev. C.01*; Wallingford, CT, 2016.

(214) Marenich, A. V.; Cramer, C. J.; Truhlar, D. G. Universal Solvation Model Based on Solute Electron Density and on a Continuum Model of the Solvent Defined by the Bulk Dielectric Constant and Atomic Surface Tensions. *J Phys Chem B* **2009**, *113*, 6378–6396.

(215) Grimme, S.; Ehrlich, S.; Goerigk, L. Effect of the Damping Function in Dispersion Corrected Density Functional Theory. *J. Comput. Chem.* **2011**, *32*, 1456–1465.

(216) Becke, A. D. Density-Functional Thermochemistry. III. The Role of Exact Exchange. *J Chem Phys* **1993**, *98*, 5648–5652.

(217) Lee, C.; Yang, W.; Parr, R.G. Development of the Colle-Salvetti Correlation-Energy Formula into a Functional of the Electron Density. *Phys. Rev. B Condens. Matter* **1988**, *37*, 785–789.

(218) Vosko, S. H.; Wilk, L.; Nusair, M. Accurate Spin-Dependent Electron Liquid Correlation Energies for Local Spin Density Calculations: A Critical Analysis. *Can. J. Phys.* **1980**, *58*, 1200–1211.

(219) Stephens, P. J.; Devlin, F. J.; Chabalowski, C. F.; Frisch, M. J. Ab Initio Calculation of Vibrational Absorption and Circular Dichroism Spectra Using Density Functional Force Fields. *J Phys Chem* **1994**, *98*, 11623–11627.

(220) Weigend, F.; Ahlrichs, R. Balanced Basis Sets of Split Valence, Triple Zeta Valence and Quadruple Zeta Valence Quality for H to Rn: Design and Assessment of Accuracy. *Phys Chem Chem Phys* **2005**, *7*, 3297–3305.

(221) Tao, J.; Perdew, J. P.; Staroverov, V. N.; Scuseria, G. E. Climbing the Density Functional Ladder: Nonempirical Meta--Generalized Gradient Approximation Designed for Molecules and Solids. *Phys. Rev. Lett.* **2003**, *91*, 146401.

(222) Staroverov, V. N.; Scuseria, G. E.; Tao, J.; Perdew, J. P. Comparative Assessment of a New Nonempirical Density Functional: Molecules and Hydrogen-Bonded Complexes. *J. Chem. Phys.* **2003**, *119*, 12129–12137.

(223) O'Boyle, N. M.; Tenderholt, A. L.; Langner, K. M. Software News and Updates Cclib: A Library for Package-Independent Computational Chemistry Algorithms. *J Comput Chem* **2008**, *29*, 839–845.

(224) Lu, T.; Chen, F. Multiwfn: A Multifunctional Wavefunction Analyzer. *J Comput Chem* **2012**, *33*, 580–592.

(225) Xiao, M; Lu, T. Generalized Charge Decomposition Analysis (GCDA) Method. *J. Adv. Phys. Chem.* **2015**, *4*, 111–124.

(226) Frisch, M. J.; Trucks, G. W.; Schlegel, H. B.; Scuseria, G. E.; Robb, M. A.; Cheeseman, J. R.; Scalmani, G.; Barone, V.; Petersson, G. A.; Nakatsuji, H.; Li, X.; Caricato, M.; Marenich, A. V.; Bloino, J.; Janesko, B. G.; Gomperts, R.; Mennucci, B.; Hratchian, H. P.; Ortiz, J. V.; Izmaylov, A. F.; Sonnenberg, J. L.; Williams-Young, D.; Ding, F.; Lipparini, F.; Egidi, F.; Goings, J.; Peng, B.; Petrone, A.; Henderson, T.; Ranasinghe, D.; Zakrzewski, V. G.; Gao, J.; Rega, N.; Zheng, G.; Liang, W.; Hada, M.; Ehara, M.; Toyota, K.; Fukuda, R.; Hasegawa, J.; Ishida, M.; Nakajima, T.; Honda, Y.; Kitao, O.; Nakai, H.; Vreven, T.; Throssell, K.; Montgomery, J. A.; Peralta, J. E.; Ogliaro, F.; Bearpark, M. J.; Heyd, J. J.; Brothers, E. N.; Kudin, K. N.; Staroverov, V. N.; Keith, T. A.; Kobayashi, R.; Normand, J.; Raghavachari, K.; Rendell, A. P.; Burant, J. C.; Iyengar, S. S.; Tomasi, J.; Cossi, M.; Millam, J. M.; Klene, M.; Adamo, C.; Cammi, R.; Ochterski, J. W.; Martin, R. L.; Morokuma, K.; Farkas, O.; Foresman, J. B.; Fox, D. J. *Gaussian 16, Revision B.01*; Gaussian 16, Revision B.01, Gaussian, Inc., Wallingford CT; Gaussian, Inc.: Wallingford CT, 2016.

(227) Adamo, C.; Barone, V. Toward Reliable Density Functional Methods without Adjustable Parameters: The PBE0 Model. *J. Chem. Phys.* **1999**, *110* (13), 6158–6170.

(228) Andrae, D.; Huermann, U.; Dolg, M.; Stoll, H.; Preu, H. Energy-Adjustedab Initio Pseudopotentials for the Second and Third Row Transition Elements. *Theor. Chim. Acta* **1990**, *77*, 123–141.

(229) Yanai, T.; Tew, D. P.; Handy, N. C. A New Hybrid Exchange–Correlation Functional Using the Coulomb-Attenuating Method (CAM-B3LYP). *Chem. Phys. Lett.* **2004**, *393*, 51–57.

(230) Neese, F.; Wennmohs, F.; Hansen, A.; Becker, U. Efficient, Approximate and Parallel Hartree–Fock and Hybrid DFT Calculations. A 'Chain-of-Spheres' Algorithm for the Hartree–Fock Exchange. *Chem. Phys.* **2009**, *356*, 98–109.

(231) Lenthe, E. van; Baerends, E. J.; Snijders, J. G. Relativistic Regular Two-component Hamiltonians. *J. Chem. Phys.* **1993**, *99*, 4597–4610.

(232) Weigend, F. Accurate Coulomb-Fitting Basis Sets for H to Rn. *Phys. Chem. Chem. Phys.* **2006**, *8*, 1057.

(233) Pantazis, D. A.; Neese, F. All-Electron Scalar Relativistic Basis Sets for the Lanthanides. *J. Chem. Theory Comput.* **2009**, *5*, 2229–2238.

(234) Pantazis, D. A.; Neese, F. All-Electron Scalar Relativistic Basis Sets for the Actinides. *J. Chem. Theory Comput.* **2011**, *7*, 677–684.

(235) Pantazis, D. A.; Chen, X.-Y.; Landis, C. R.; Neese, F. All-Electron Scalar Relativistic Basis Sets for Third-Row Transition Metal Atoms. *J. Chem. Theory Comput.* **2008**, *4*, 908–919.

(236) Hirshfeld, F. L. Bonded-Atom Fragments for Describing Molecular Charge Densities. *Theor. Chim. Acta* **1977**, *44*, 129–138.

(237) Hanwell, M. D.; Curtis, D. E.; Lonie, D. C.; Vandermeersch, T.; Zurek, E.; Hutchison, G. R. Avogadro: An Advanced Semantic Chemical Editor, Visualization, and Analysis Platform. *J Cheminf* **2012**, *4*, 17.

(238) Frisch, M. J.; Trucks, G. W.; Schlegel, H. B.; Scuseria, G. E.; Robb, M. A.; Cheeseman, J. R.; Scalmani, G.; Barone, V.; Petersson, G. A.; Nakatsuji, H.; Li, X.; Caricato, M.; Marenich, A. V.; Bloino, J.; Janesko, B. G.; Gomperts, R.; Mennucci, B.; Hratchian, H. P.; Ortiz, J. V.; Izmaylov, A. F.; Sonnenberg, J. L.; Williams; Ding, F.; Lipparini, F.; Egidi, F.; Goings, J.; Peng, B.; Petrone, A.; Henderson, T.; Ranasinghe, D.; Zakrzewski, V. G.; Gao, J.; Rega, N.; Zheng, G.; Liang, W.; Hada, M.; Ehara, M.; Toyota, K.; Fukuda, R.; Hasegawa, J.; Ishida, M.; Nakajima, T.; Honda, Y.; Kitao, O.; Nakai, H.; Vreven, T.; Throssell, K.; Montgomery Jr., J. A.; Peralta, J. E.; Ogliaro, F.; Bearpark, M. J.; Heyd, J. J.; Brothers, E. N.; Kudin, K. N.; Staroverov, V. N.; Keith, T. A.; Kobayashi, R.; Normand, J.; Raghavachari, K.; Rendell, A. P.; Burant, J. C.; Iyengar, S. S.; Tomasi, J.; Cossi, M.; Millam, J. M.; Klene, M.; Adamo, C.; Cammi, R.; Ochterski, J. W.; Martin, R. L.; Morokuma, K.; Farkas, O.; Foresman, J. B.; Fox, D. J. Gaussian 16 Rev. C.01, 2016.

(239) Marenich, A. V.; Cramer, C. J.; Truhlar, D. G. Universal Solvation Model Based on Solute Electron Density and on a Continuum Model of the Solvent Defined by the Bulk Dielectric Constant and Atomic Surface Tensions. *J Phys Chem B* **2009**, *113*, 6378–6396.

(240) Dennington, Roy; Keith, Todd A.; Millam, John M. GaussView, Version 6, 2016.

(241) O'Boyle, N. M.; Tenderholt, A. L.; Langner, K. M. Software News and Updates Cclib: A Library for Package-Independent Computational Chemistry Algorithms. *J Comput Chem* **2008**, *29*, 839–845.

(242) Lu, T.; Chen, F. Multiwfn: A Multifunctional Wavefunction Analyzer. *J Comput Chem* **2012**, *33*, 580–592.

(243) Tian, L. U.; Fei-Wu, C. Calculation of Molecular Orbital Composition. *Acta Chim. Sin.* **2011**, *69*, 2393.

(244) Frisch, M. J.; Trucks, G. W.; Schlegel, H. B.; Scuseria, G. E.; Robb, M. A.; Cheeseman, J. R.; Scalmani, G.; Barone, V.; Petersson, G. A.; Nakatsuji, H.; Li, X.; Caricato, M.; Marenich, A. V.; Bloino, J.; Janesko, B. G.; Gomperts, R.; Mennucci, B.; Hratchian, H. P.; Ortiz, J. V.; Izmaylov, A. F.; Sonnenberg, J. L.; Williams-Young, D.; Ding, F.; Lipparini,

F.; Egidi, F.; Goings, J.; Peng, B.; Petrone, A.; Henderson, T.; Ranasinghe, D.; Zakrzewski, V. G.; Gao, J.; Rega, N.; Zheng, G.; Liang, W.; Hada, M.; Ehara, M.; Toyota, K.; Fukuda, R.; Hasegawa, J.; Ishida, M.; Nakajima, T.; Honda, Y.; Kitao, O.; Nakai, H.; Vreven, T.; Throssell, K.; Montgomery Jr., J. A.; Peralta, J. E.; Ogliaro, F.; Bearpark, M. J.; Heyd, J. J.; Brothers, E. N.; Kudin, K. N.; Staroverov, V. N.; Keith, T. A.; Kobayashi, R.; Normand, J.; Raghavachari, K.; Rendell, A. P.; Burant, J. C.; Iyengar, S. S.; Tomasi, J.; Cossi, M.; Millam, J. M.; Klene, M.; Adamo, C.; Cammi, R.; Ochterski, J. W.; Martin, R. L.; Morokuma, K.; Farkas, O.; Foresman, J. B.; Fox, D. J. Gaussian 16 Rev. C.01, 2016.

(245) Marenich, A. V.; Cramer, C. J.; Truhlar, D. G. Universal Solvation Model Based on Solute Electron Density and on a Continuum Model of the Solvent Defined by the Bulk Dielectric Constant and Atomic Surface Tensions. *J Phys Chem B* **2009**, *113*, 6378–6396.

(246) Grimme, S.; Ehrlich, S.; Goerigk, L. Effect of the Damping Function in Dispersion Corrected Density Functional Theory. *J. Comput. Chem.* **2011**, *32*, 1456–1465.

(247) Weigend, F.; Ahlrichs, R. Balanced Basis Sets of Split Valence, Triple Zeta Valence and Quadruple Zeta Valence Quality for H to Rn: Design and Assessment of Accuracy. *Phys. Chem. Chem. Phys.* **2005**, *7*, 3297.

(248) Allouche, A.-R. Gabedit—A Graphical User Interface for Computational Chemistry Softwares. *J. Comput. Chem.* **2011**, *32*, 174–182.

(249) Liu, Z.; Lu, T.; Chen, Q. An Sp-Hybridized All-Carboatomic Ring, Cyclo[18]Carbon: Electronic Structure, Electronic Spectrum, and Optical Nonlinearity. *Carbon* **2020**, *165*, 461–467.

(250) Lu, T.; Chen, F. Multiwfn: A Multifunctional Wavefunction Analyzer. *J Comput Chem* **2012**, *33*, 580–592.

(251) Dennington, Roy; Keith, Todd A.; Millam, John M. GaussView, Version 6, 2016.

(252) Becke, A. D. Density-functional Thermochemistry. III. The Role of Exact Exchange. *J. Chem. Phys.* **1998**, *98*, 5648.

(253) Lee, C.; Yang, W.; Parr, R. G. Development of the Colle-Salvetti Correlation-Energy Formula into a Functional of the Electron Density. *Phys. Rev. B* **1988**, *37*, 785–789.

(254) Vosko, S. H.; Wilk, L.; Nusair, M. Accurate Spin-Dependent Electron Liquid Correlation Energies for Local Spin Density Calculations: A Critical Analysis. *Can. J. Phys.* **1980**, *58*, 1200–1211.

(255) Amin, E. A.; Truhlar, D. G. Zn Coordination Chemistry: Development of Benchmark Suites for Geometries, Dipole Moments, and Bond Dissociation Energies and Their Use To Test and Validate Density Functionals and Molecular Orbital Theory. *J. Chem. Theory Comput.* **2008**, *4*, 75–85.

(256) Otto, S.; Moll, J.; Förster, C.; Geißler, D.; Wang, C.; Resch-Genger, U.; Heinze, K. Three-in-One Crystal: The Coordination Diversity of Zinc Polypyridine Complexes. *Eur. J. Inorg. Chem.* **2017**, *2017*, 5033–5040.

(257) Grimme, S.; Antony, J.; Ehrlich, S.; Krieg, H. A Consistent and Accurate *Ab Initio* Parametrization of Density Functional Dispersion Correction (DFT-D) for the 94 Elements H-Pu. *J. Chem. Phys.* **2010**, *132*, 154104.

(258) Ernzerhof, M.; Scuseria, G. E. Assessment of the Perdew–Burke–Ernzerhof Exchange-Correlation Functional. *J. Chem. Phys.* **1999**, *110*, 5029–5036.

(259) Perdew, J. P.; Burke, K.; Ernzerhof, M. Generalized Gradient Approximation Made Simple. *Phys. Rev. Lett.* **1996**, *77*, 3865–3868.

(260) van Wüllen, C. Molecular Density Functional Calculations in the Regular Relativistic Approximation: Method, Application to Coinage Metal Diatomics, Hydrides, Fluorides and Chlorides, and Comparison with First-Order Relativistic Calculations. *J. Chem. Phys.* **1998**, *109* (2), 392–399.

(261) Rosenberg, B.; Van Camp, L.; Krigas, Thomas. Inhibition of Cell Division in Escherichia Coli by Electrolysis Products from a Platinum Electrode. *Nature* **1965**, *205* (4972), 698–699. https://doi.org/10.1038/205698a0.

(262) Wang, D.; Lippard, S. J. Cellular Processing of Platinum Anticancer Drugs. *Nat. Rev. Drug Discov.* **2005**, *4* (4), 307–320. https://doi.org/10.1038/nrd1691.

(263) Englinger, B.; Pirker, C.; Heffeter, P.; Terenzi, A.; Kowol, C. R.; Keppler, B. K.; Berger, W. Metal Drugs and the Anticancer Immune Response. *Chem. Rev.* **2019**, *119* (2), 1519–1624. https://doi.org/10.1021/acs.chemrev.8b00396.

(264) Wheate, N. Multi-Nuclear Platinum Complexes as Anti-Cancer Drugs. *Coord. Chem. Rev.* **2003**, *241* (1–2), 133–145. https://doi.org/10.1016/S0010-8545(03)00050-X.

(265) Johnstone, T. C.; Park, G. Y.; Lippard, S. J. Understanding and Improving Platinum Anticancer Drugs - Phenanthriplatin. *Anticancer Res.* **2014**, *34*, 471–476.

(266) Johnstone, T. C.; Wilson, J. J.; Lippard, S. J. Monofunctional and Higher-Valent Platinum Anticancer Agents. *Inorg. Chem.* **2013**, *52* (21), 12234–12249. https://doi.org/10.1021/ic400538c.

(267) Todd, R. C.; Lippard, S. J. Structure of Duplex DNA Containing the Cisplatin 1,2-{Pt(NH3)2}2+-d(GpG) Cross-Link at 1.77 Å Resolution. *J. Inorg. Biochem.* **2010**, *104*, 902–908.

(268) Park, G. Y.; Wilson, J. J.; Song, Y.; Lippard, S. J. Phenanthriplatin, a Monofunctional DNA-Binding Platinum Anticancer Drug Candidate with Unusual Potency and Cellular Activity Profile. *Proc Natl Acad Sci* **2012**, *109*, 11987–11992.

(269) Lovejoy, K. S.; Serova, M.; Bieche, I.; Emami, S.; D'Incalci, M.; Broggini, M.; Erba, E.; Gespach, C.; Cvitkovic, E.; Faivre, S.; Raymond, E.; Lippard, S. J. Spectrum of Cellular Responses to Pyriplatin, a Monofunctional Cationic Antineoplastic Platinum(II) Compound, in Human Cancer Cells. *Mol. Cancer Ther.* **2011**, *10* (9), 1709–1719. https://doi.org/10.1158/1535-7163.MCT-11-0250.

(270) Almaqwashi, A. A.; Zhou, W.; Naufer, M. N.; Riddell, I. A.; Yilmaz, Ö. H.; Lippard, S. J.; Williams, M. C. DNA Intercalation Facilitates Efficient DNA-Targeted Covalent Binding of Phenanthriplatin. *J. Am. Chem. Soc.* **2019**, *141* (4), 1537–1545. https://doi.org/10.1021/jacs.8b10252.

(271) Tullius, T. D.; Lippard, S. J. Ethidium Bromide Changes the Nuclease-Sensitive DNA Binding Sites of the Antitumor Drug Cis-Diamminedichloroplatinum(II). *Proc. Natl. Acad. Sci.* **1982**, *79* (11), 3489–3492. https://doi.org/10.1073/pnas.79.11.3489.

(272) Boulikas, T.; Vougiouka, M. Cisplatin and Platinum Drugs at the Molecular Level (Review). *Oncol. Rep.* **2003**. https://doi.org/10.3892/or.10.6.1663.

(273) Dasari, S.; Bernard Tchounwou, P. Cisplatin in Cancer Therapy: Molecular Mechanisms of Action. *Eur. J. Pharmacol.* **2014**, *740*, 364–378. https://doi.org/10.1016/j.ejphar.2014.07.025.

(274) Lozada, I. B.; Williams, J. A. G.; Herbert, D. E. Platinum(II) Complexes of Benzannulated N ^ N ¯^ O-Amido Ligands: Bright Orange Phosphors with Long-Lived Excited States. *Inorg. Chem. Front.* **2022**, *9* (1), 10–22. https://doi.org/10.1039/D1QI01120K.

(275) Che, C.-M.; Yang, M.; Wong, K.-H.; Chan, H.-L.; Lam, W. Platinum(II) Complexes of Dipyridophenazine as Metallointercalators for DNA and Potent Cytotoxic Agents against Carcinoma Cell Lines. *Chem. – Eur. J.* **1999**, *5*, 3350–3356.

(276) Kieltyka, R.; Fakhoury, J.; Moitessier, N.; Sleiman, H. F. Platinum Phenanthroimidazole Complexes as G-Quadruplex DNA Selective Binders. *Chem. – Eur. J.* **2008**, *14* (4), 1145–1154. https://doi.org/10.1002/chem.200700783.

(277) Cusumano, M.; Di Pietro, M. L.; Giannetto, A.; Nicolò, F.; Rotondo, E. Noncovalent Interactions of Platinum(II) Square Planar Complexes Containing Ligands Out-of-Plane with DNA. *Inorg. Chem.* **1998**, *37* (3), 563–568. https://doi.org/10.1021/ic9705406.

(278) Suntharalingam, K.; Mendoza, O.; Duarte, A. A.; Mann, D. J.; Vilar, R. A Platinum Complex That Binds Non-Covalently to DNA and Induces Cell Death via a Different Mechanism than Cisplatin. *Metallomics* **2013**, *5* (5), 514. https://doi.org/10.1039/c3mt20252f.

(279) Luedtke, N. W.; Liu, Q.; Tor, Y. Synthesis, Photophysical Properties, and Nucleic Acid Binding of Phenanthridinium Derivatives Based on Ethidium. *Bioorg. Med. Chem.* **2003**, *11*, 5235–5247.

(280) Nandi, R.; Chaudhuri, K.; Maiti, M. EFFECTS OF IONIC STRENGTH and PH ON THE BINDING OF SANGUINARINE TO DEOXYRIBONUCLEIC ACID. *Photochem. Photobiol.* **1985**, *42* (5), 497–503. https://doi.org/10.1111/j.1751-1097.1985.tb01600.x.

(281) Howe-Grant, M.; Lippard, S. J. Binding of Platinum(II) Intercalation Reagents to Deoxyribonucleic Acid. Dependence on Base-Pair Composition, Nature of the Intercalator, and Ionic Strength. *Biochemistry* **1979**, *18* (26), 5762–5769. https://doi.org/10.1021/bi00593a003.

(282) Murphy, M. P. How Mitochondria Produce Reactive Oxygen Species. *Biochem. J.* **2009**, *417* (1), 1–13. https://doi.org/10.1042/BJ20081386.

(283) Ivashkevich, A.; Redon, C. E.; Nakamura, A. J.; Martin, R. F.; Martin, O. A. Use of the γ-H2AX Assay to Monitor DNA Damage and Repair in Translational Cancer Research. *Cancer Lett.* **2012**, *327* (1–2), 123–133. https://doi.org/10.1016/j.canlet.2011.12.025.

(284) Mah, L.-J.; El-Osta, A.; Karagiannis, T. C. ΓH2AX: A Sensitive Molecular Marker of DNA Damage and Repair. *Leukemia* **2010**, *24* (4), 679–686. https://doi.org/10.1038/leu.2010.6.

(285) Chargaff, E.; Lipshitz, R. Composition of Mammalian Desoxyribonucleic Acids [1]. *J. Am. Chem. Soc.* **1953**, *75* (15), 3658–3661. https://doi.org/10.1021/ja01111a016.

(286) Kaim, W.; Schwederski, B.; Klein, A. Manganese-Catalyzed Oxidation of Water to O2. In *Bioinorganic Chemistry: Inorganic Elements in the Chemistry of Life*; Wiley: Chichester, 2013; pp 67–74.

(287) Pan, D.; Schmieder, A. H.; Wickline, S. A.; Lanza, G. M. Manganese-Based MRI Contrast Agents: Past, Present, and Future. *Tetrahedron* **2011**, *67* (44), 8431–8444. https://doi.org/10.1016/j.tet.2011.07.076.

(288) East, N. R.; Förster, C.; Carrella, L. M.; Rentschler, E.; Heinze, K. The Full d^3–d^5 Redox Series of Mononuclear Manganese Complexes: Geometries and Electronic Structures of $[Mn(Dgpy)_2]^{n+}$. *Inorg. Chem.* **2022**, *61* (37), 14616–14625. https://doi.org/10.1021/acs.inorgchem.2c01680.

(289) Herr, P.; Kerzig, C.; Larsen, C. B.; Häussinger, D.; Wenger, O. S. Manganese(i) Complexes with Metal-to-Ligand Charge Transfer Luminescence and Photoreactivity. *Nat. Chem.* **2021**, *13* (10), 956–962. https://doi.org/10.1038/s41557-021-00744-9.

(290) Betley, T. A.; Qian, B. A.; Peters, J. C. Group VIII Coordination Chemistry of a Pincer-Type Bis(8-Quinolinyl)Amido Ligand. *Inorg. Chem.* **2008**, *47* (24), 11570–11582. https://doi.org/10.1021/ic801047s.

(291) Huynh, M. T.; Anson, C. W.; Cavell, A. C.; Stahl, S. S.; Hammes-Schiffer, S. Quinone 1 e$^-$ and 2 e$^-$/2 H$^+$ Reduction Potentials: Identification and Analysis of Deviations from Systematic Scaling Relationships. *J. Am. Chem. Soc.* **2016**, *138* (49), 15903–15910. https://doi.org/10.1021/jacs.6b05797.

(292) Michaelis, L.; Hill, E. S. THE VIOLOGEN INDICATORS. *J. Gen. Physiol.* **1933**, *16* (6), 859–873. https://doi.org/10.1085/jgp.16.6.859.

(293) Woodhouse, M. D.; McCusker, J. K. Mechanistic Origin of Photoredox Catalysis Involving Iron(II) Polypyridyl Chromophores. *J. Am. Chem. Soc.* **2020**, *142* (38), 16229–16233. https://doi.org/10.1021/jacs.0c08389.

5 Antineoplastic Activity of Cisplatin-Like Compounds Supported by Benzannulated $N \char94 N^- \char94 O$ Ligands

5.1 Abstract

Phenanthriplatin, *cis*-[Pt(NH$_3$)$_2$(phenanthridine)Cl]NO$_3$, is a leading preclinical anticancer Pt(II) complex with significantly greater efficacy and a distinct spectrum of activity compared to clinically approved drugs such as cisplatin (*cis*-diamminedichloroplatinum). The distinguishing feature of phenanthriplatin is the presence of a benzannulated *N*-heterocyclic ligand, phenanthridine (3,4-benzoquinoline), which binds perpendicular to the coordination plane of the Pt(II) centre and facilitates DNA-targeted covalent binding via intercalation. To examine the impact of restricting the geometry of the *N*-heterocycle to be coplanar with the four platinum-ligand bonds on anticancer activity, planar *mer*-binding phenanthridine-based *N^N^O* ligand frameworks were designed and used to construct flat Pt(II) complexes (**10** and **11**). In this chapter these geometrically restricted, planar phenanthridine-containing monofunctional platinum compounds exhibit key differences in their anticancer activity and toxicity compared with cisplatin and phenanthriplatin, leading to a superior therapeutic index *in vitro*. In addition, complex **11** exhibits 'turn-on' emission in the presence of DNA which provided preliminary exploration of the complex's interaction with DNA suggesting intercalation is operative. As shown in Chapter 3, these Pt(II) complexes emit from the T$_1$ state which can be harnessed to enhance the cytotoxicity of **11** likely through the generation of reactive-oxygen species. These results suggest that Pt(II) complexes supported by benzannulated *N^N$^-$^O* ligands have the potential to be photodynamic therapy and bioimaging agents.

5.2 Introduction

Cisplatin[261] and related platinum(II) drugs are key tools in modern cancer treatment.[262,263] Notwithstanding its history of transformative clinical implementation, Pt chemotherapy can be limited by severe side effects caused by off-target activity and reduced efficacy due to acquired or intrinsic resistance in certain types of cancers.[264] One strategy for increasing potency and expanding the spectrum of activity of a class of compounds while mitigating side effects is to search out analogues that operate by novel mechanisms of action.[265] In this respect, monofunctional platinum anticancer complexes, a class of platin drug candidates containing only a single labile ligand first studied in earnest in the late 1980s, are attracting renewed interest.[266] Compared with bifunctional anticancer complexes such as cisplatin which deform DNA strands via formation of inter- and intrastrand crosslinks,[267] monofunctional Pt(II) complexes can only bind to DNA through a single coordination site opened up by the one vacating chloride. The antineoplastic activity of monofunctional complexes such as phenanthriplatin ([*cis*-Pt(NH$_3$)$_2$(phenanthridine)Cl][NO$_3$])[268] thus arises from different biochemical interactions compared to compounds like cisplatin (*cis*-Pt(NH$_3$)$_2$Cl$_2$), with a distinct spectrum of action and potential for altered resistance/side-effect profiles.

While phenanthriplatin shows heightened activity,[268] pyriplatin, in which phenanthridine is replaced with the parent *N*-heterocycle pyridine, is ten-fold *less* potent.[269] Single-molecule DNA-stretching experiments revealed a two-step binding process for phenanthriplatin, where rapid unwinding of DNA triggered by intercalation of the phenanthridine unit is followed by slower covalent modification. The smaller pyridine does not associate as effectively with duplex DNA prior to covalent binding, lowering efficacy. The disposition of the *N*-heterocycle to the

labile ligand is also important; DNA intercalation of the stereoisomer of phenanthriplatin with the heterocycle *trans* disposed to the chloride ([*trans*-Pt(NH$_3$)$_2$(phenanthridine)Cl][NO$_3$]) competes with - rather than enhancing - covalent binding, reducing the number of Pt-DNA adducts formed.[270] *Trans*-phenanthriplatin is nevertheless still an effective anticancer agent, with quite different activity compared to phenanthriplatin.[270] This is not true of *trans*platin. Covalent binding of phenanthridine to platinum to form a true monofunctional drug in phenanthriplatin also has superior activity compared with the simple combination of an intercalator such as ethidium bromide and cisplatin, which do not form a stable adduct in solution.[271]

We have recently developed synthetic mechanisms for incorporating phenanthridine into multidentate ligand architectures to explore their coordination chemistry with late transition metals. By appending additional donors, the heterocycle can be forced *cis* to the labile chloride and exhibits a diminished tendency to dissociate irreversibly from the metal thanks to the chelate effect. As the attenuation of chemical reactivity and possible side effects of bifunctional platin drugs such as carboplatin and oxaliplatin are attributed in part to the stabilizing impact of chelating ligand structures, we pursued the synthesis and characterization of multidentate phenanthridine-based ligands (**L1**, **L3** and **L4**) and their platinum complexes to evaluate the potential of Pt(II) derivatives of chelating phenanthridine-based ligands as monofunctional chemotherapeutics. We find these chelate-supported phenanthriplatin analogs show a superior therapeutic index compared to cisplatin and phenanthriplatin *in vitro*.

5.3   Results and Discussion

5.3.1 *In vitro* Activity of [Pt(*N^N^O*)Cl]

To assess the biological activity of planar phenanthridine-containing monofunctional Pt(II) compounds **10** and **11** (see Scheme 3.3 and Figure 3.18 for structures), *in vitro* cytotoxicities were evaluated using MTT assays (MTT = [3-(4,5-dimethylthiazol-2-yl)-2,5-diphenyltetrazolium bromide]; see Experimental Section). Table 5.1 reports IC_{50} (50% growth inhibition concentrations) for two separate ovarian cancer cell lines. The results revealed promising activity for both **10** and **11** compared with cisplatin, as well as a dependence on substituent structure. For example, **11** (R = CF_3) showed much higher *in vitro* efficacy as compared to cisplatin, as well as less resistance than cisplatin (IC_{50} of A2780cis/IC50 of A2780) against both A2780 (cisplatin sensitive) and A2780cis (cisplatin resistant) ovarian cancer cell lines. The higher efficacy for **11** (R = CF_3) vs **10** (R = *t*Bu) highlights the opportunity to fine-tune biological activity via ligand backbone substitution. In addition, neither the proligand **L4** or precursors 4-amino-(2-*tert*-butyl)phenanthridine or 4-amino-(2-trifluoromethyl)phenanthridine - which may be generated upon hydrolysis of **L4** - were found to be effective in the absence of Pt(II). The differing profile compared to cisplatin (i.e., higher *in vitro* efficacy and lower cross-resistance) implies a different mechanism of operation from cisplatin, which, considering the planar structure of **10** and **11** compared to phenanthriplatin[8] likely involves a more prominent role for intercalation. As noted above, intercalation enhances covalent binding and ultimately boosts the number of complex-DNA adducts observed for phenanthriplatin, but only when these two processes are concurrent.[10] The lack of activity in the absence of Pt(II) highlights a key role for the metal centre in the cytotoxicity of **10** and **11**. In addition, phenanthridines in general are anticipated to interact with DNA via an

317

intercalation mechanism, similar to the mechanism of operation of the DNA stain ethidium bromide, of which phenanthridine forms the molecular core.[22] The poor activity of the parent aminophenanthridines rules out demetallation or hydrolysis of the proligands as the source of the anticancer activity.

Table 5.1. MTT cytotoxicity assay data A2780 and A2780cis cell lines.

Compound	A2780 IC$_{50}$ (µM)	A2780cis IC$_{50}$ (µM)
cisplatin	1.41 ± 0.54	32.94 ± 8.82
10	2.81±0.168	4.57±1.41
10	0.48 ± 0.17	0.55 ± 0.22
L4	7.22±2.07	20.1±7.17
4-amino-(2-*tert*-butyl)phenanthridine	8.38±2.83	20.5±6.07
4-amino-(2-trifluoromethyl)phenanthridine	19.3±12.1	>100 µM

With these results in hand, complex **11** was selected for further screening against additional human cancer and non-cancerous cell lines, including the non-small cell lung cancer cell line A549, ovarian cancer cell line A2780, and cisplatin-resistant ovarian cancer cell line A2780cis, ovarian cancer cell line SKOV-3, triple-negative breast cancer cell line MDA-MB-231, non-cancerous mesothelial cell line MET-5A and non-cancerous kidney cell line HEK293. Cisplatin and phenanthriplatin were used as controls. Cancerous and normal cells were treated for 72 h and cell viability was assessed. The IC$_{50}$ values represent compound concentrations required to inhibit cell growth by 50%, and these data are tabulated in Figure 5.1a. Compared with cisplatin, **11** exhibits much lower IC$_{50}$ values among all tested cell lines. For example, in A2780cis cisplatin-resistant ovarian cancer cell line, the IC$_{50}$ (**11**) = 0.55±0.22 µM is nearly 60 times lower than that of cisplatin (IC$_{50}$ = 32.94±8.82 µM).

a

IC$_{50}$ (μM)	A2780 Cisplatin-Sensitive Ovarian Cancer	A2780cis Cisplatin-Resistant Ovarian Cancer	SKOV-3 Ovarian Cancer	MDA-MB-231 Breast Cancer	A549 Lung Cancer	MET5A Mesothelial Cells	HEK-293 Human Embryonic Kidney Cells
cisplatin	1.41 ±0.54	32.94 ±8.82	28.60± 4.79	25.89± 20.8	34.86± 1.42	3.49± 0.86	4.99± 0.87
phenanthriplatin	0.17± 0.06	0.46 ±0.11	1.09± 0.29	1.09± 0.22	0.137± 0.11	0.41± 0.25	4.41± 2.22
11	0.48 ±0.17	0.55± 0.22	1.23± 0.06	1.11± 0.19	12.94± 3.55	1.97± 0.37	8.25± 2.18

b

Figure 5.1. Cytotoxicity profiles of cisplatin, phenanthriplatin, and **11** against a panel of human cancer and normal cell lines: (a) table of IC$_{50}$ values, and (b) killing curves of cisplatin, phenanthriplatin, and **11** against A2780 and A2780cis ovarian cancer cells highlighting the lower resistance factor (RF) of **11**.

Complex **11** also has comparable efficacy to phenanthriplatin across a range of cancer cell lines under the conditions tested. Importantly, however, **11** proved less toxic to normal cells (MET-5A and HEK293) compared with phenanthriplatin and displays a lower resistance factor (RF = IC$_{50(A2780cis)}$/IC$_{50(A2780)}$ = 1.1) in ovarian cancer cell lines than cisplatin (RF = 23) or phenanthriplatin (RF = 2.7; Figure 5.1b). The MTT results collectively support that the planar, monofunctional phenanthridine-based platinum compound **11** shows a superior therapeutic index compared with cisplatin and phenanthriplatin *in vitro*.

We next investigated the cellular uptake and cellular responses of **11** in order to better understand its cellular behaviour. First, uptake was evaluated using graphite furnace atomic absorption spectroscopy (GFAAS), with cisplatin and phenanthriplatin again employed as

controls. In the experiment, SKOV3 cells were incubated for 24 h with 2 μM concentrations of each of the three different platinum compounds. The treated cells were then harvested and digested for GFAAS analysis. Complex **11** exhibits higher cellular uptake (4.09 ± 0.138 pmol Pt per million cells) compared with cisplatin (2.12±0.129 pmol Pt per million cells) or phenanthriplatin (2.88±0.023 pmol Pt per million cells; Figure 5.2a). Similar to cisplatin,[22] phenanthriplatin uptake has been shown to be mediated by organic cation transporters (OCT); phenanthriplatin is considered a high affinity substrate for OCT2, while showing a lower apparent affinity for the multi-drug and toxin extrusion proteins (MATE) responsible for excretion of platinum into the urine.[23] Though not a cation itself, a similar affinity for transport and extrusion proteins might be plausibly expected for the chemically related **11**, as also has been observed for initially neutral platins such as cisplatin and oxaliplatin.[24] The enhanced uptake of **11** compared with phenanthriplatin does not clearly correlate with decreased cell viability for SKOV3 cells. This effect plausibly also features in the lower toxicity observed *in vitro* towards non-cancer cell lines.

With respect to cellular responses, a dual staining Annexin V/PI flow cytometry assay was used to probe the occurrence of apoptosis. In particular, SKOV3 ovarian cancer cells were treated with and without **11**. The results in Figure 5.2b clearly indicate that **11** induced apoptosis, stimulating the SKOV3 cells to undergo early (0.87%) and late (11.82%) stage apoptosis after 72 h of incubation, the populations of which were much higher than those of control. The evidence compiled from the cell-based studies suggest that planar phenanthridine-ligated Pt(II) complexes such as **11** can readily enter cancer cells and trigger apoptosis to kill cancer cells.
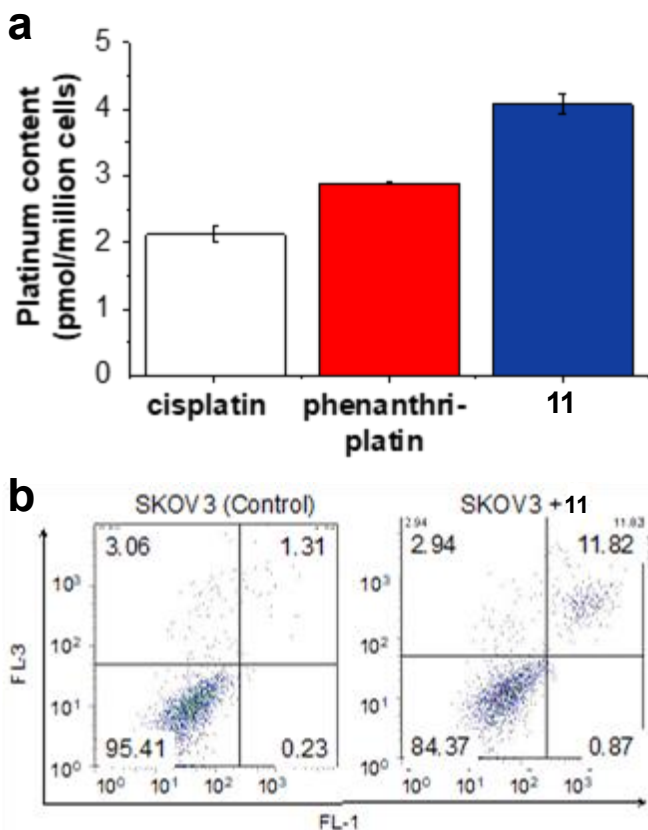
Figure 5.2. (a) Cellular uptake of cisplatin, phenanthriplatin, and **11** in SKOV3 ovarian cancer cells ([Pt] = 2 μM, 24 h at 37 °C, 5% CO_2); (b) Annexin V/PI flow cytometric analysis of the apoptotic events of SKOV3 cells with or without the treatment of **11** ([Pt] = 1 μM, 72 h at 37 °C, 5% CO_2).

Monofunctional phenanthriplatin-type complexes based on chelating tridentate *N*-heterocycle-containing ligands thus show promising *in vitro* anticancer activity, highlighting the potential of this new class of anticancer agents. The high activity towards cisplatin-resistant cancer cells is a critical finding, as tumors resistant to cisplatin often show cross-resistance to a diverse range of unrelated antitumour drugs.[25] The activation of independent pathways by the molecular

structure of phenanthridine-based Pt(II) complexes similar to what is observed with phenanthriplatin[8] is likely responsible for the increased sensitivity of resistant cells to **10** and **11**.[26]

In addition, a distinguishing feature of both *cis*-phenanthriplatin and *trans*-phenanthriplatin is the orientation of the phenanthridine ligand with respect to the coordination plane of platinum. The heterocycle is nearly orthogonal in the *cis* isomer (dihedral angle ~ 89°)[8] and slightly less so in *trans*-phenanthriplatin (~ 67°).[11] Coupled with the asymmetry of phenanthridine with respect to the position of benzannulation relative to the nitrogen atom, phenanthriplatin is chiral.[27] While racemization upon rotation about the Pt-N(phenanthridine) bond is rapid enough to preclude requiring administration of a single enantiomer, there is a preference for diastereomer formation upon binding to DNA.[27] Forcing the phenanthridinyl unit coplanar with the metal coordination plane obviates this chirality and raises the interesting question of why **10** and **11** show enhanced anticancer efficacy compared with phenanthriplatin *in vitro*. Identification of the molecular targets of **10** and **11** and investigation of potential intercalation-based mechanisms[28] therefore represent the next steps in this line of inquiry.

5.3.2 'Turn-on' Emission Behaviour of [Pt($N{\wedge}N{\wedge}O$)Cl] with DNA

As discussed in **5.3.1** the antineoplastic properties of **11** compared with cisplatin and phenanthriplatin in dark conditions, that is without prolonged light exposure of the assays, are markedly improved. In addition, complex **11** proved to be less toxic to normal cancer cell lines compared with cisplatin and even to phenanthriplatin. The mechanism of action represents the next step in the investigation of this new class of monofunctional Pt(II) complex. Historically, Pt(II) complexes exert antineoplastic activity by disrupting the cell's ability to replicate and repair DNA.[272,273] It is generally thought that the chloride ligands of cisplatin are displaced by water

molecules in the cytoplasm forming the more reactive mono- or diaquo complexes (will be collectively called as aquo complexes from here on). It is the aquo complex that is believed to form covalent adducts with DNA, particularly to the N7 atom of purine residues (Figure 5.3), introducing kinks to the DNA double helix. This arrests the replication and repair of DNA leading to apoptosis and proliferation. The affinity of platin-based drugs and monofunctional analogues represents the first step in understanding the antineoplastic activity of [Pt(*N^N^O*)Cl] complexes.
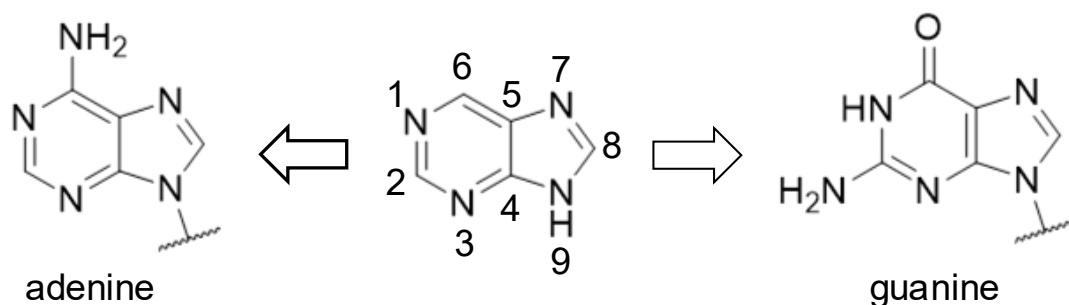
Figure 5.3. Molecular structures of purine residues. At the centre is the structure of purine and IUPAC numbering scheme.

We initially carried out our studies with calf-thymus DNA (ct-DNA) and **11** and collected the UV-Vis absorbance spectra of the complex after treating with ct-DNA (Figure 5.4). The spectrum of the complex in the absence of ct-DNA reveals a broad, structureless absorption band centred at ~475 nm that is blue-shifted relative to the spectra of the complex in CH_2Cl_2 ($\lambda_{max,abs}$, 484 nm). Previous studies[274] (see sections 3.5 and 4.3.8) on the photophysical behavior of **11** and other related complexes indicate that the lowest energy manifold is of mixed MLCT and ILCT character thanks to the π-bonding between the *N^O* donor fragment of the ligand scaffold and the Pt(II) $5d$ orbitals of appropriate energy and symmetry. Moreover, solvent analyses indicate that both solvent-analyte dipole interactions and hydrogen bonding (with the chloride and/or the

oxygen lone pairs as the likely hydrogen bond acceptors) preferentially stabilize the ground state electronic structure of the complex. The previous observations imply that the hypochromic shift in buffered aqueous solutions in the absence of ct-DNA can be attributed to these solvent-analyte interactions. Notably, there is no evidence of exciplex formation in the UV-Vis absorbance spectra. Surprisingly, the spectral features and absorbance intensities of the complex remain the same regardless of the ct-DNA concentration (when compared to the spectrum without ct-DNA) suggesting that the complex experiences a similar environment when interacting with ct-DNA. In addition, this invariability suggests that weak, noncovalent interactions may be at play in the mode of action of **11**. Several examples of Pt(II) complexes ligated by fused aromatic, *N*-heterocyclic ligands exhibit nonclassic interaction with DNA,[275–278] in stark contrast to cisplatin and derivatives that form covalent adducts with DNA nucleobases. Instead, these complexes interact with DNA through intercalation enabled by π-stacking in between DNA bases. Generally, however, intercalation is characterized by hypochromicity, the decrease in the intensity of absorbance spectrum intensity, that is not observed in solutions of **11** with ct-DNA.
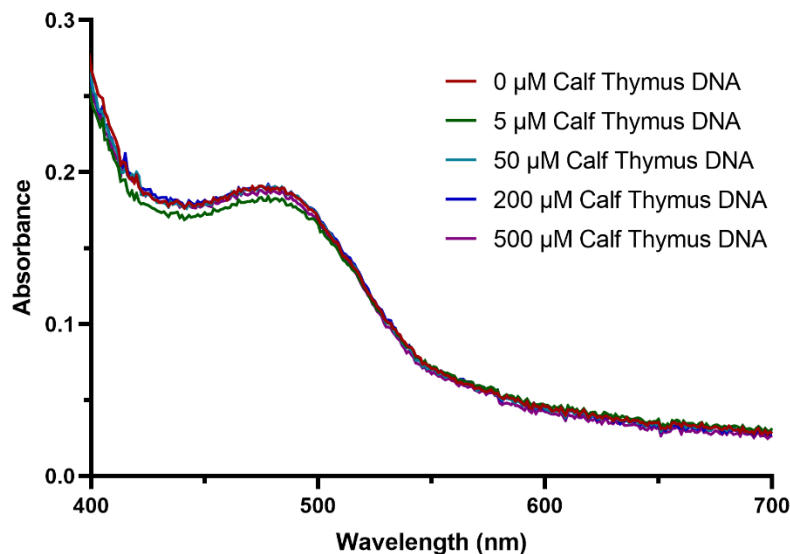
Figure 5.4. UV-Vis spectra of **11** with increasing ct-DNA concentration.

Chapter 3 discusses the photophysical behaviour of complex **11** in deoxygenated solution ($\Phi_P = 16\%$ in CH_2Cl_2) with the emission maxima centred at 608 nm and microsecond excited state lifetime (τ, 23 μs). This indicates phosphorescence is operative in the deactivation process which is enabled by the heavy Pt(II) centre. Consequently, a significant decrease in τ and emission intensity are observed when a solution of **11** in CH_2Cl_2 is saturated with O_2, but the emission remained detectable even in O_2-saturated conditions. A modest degree of self-quenching is also observed in concentrated solutions and no evidence of excimer emission to lower energy at elevated concentrations. This suggests that some degree of aggregation-induced quenching is operative at elevated concentrations. We hypothesized if DNA might be able to solubilize **11** and turn-on phosphorescence in aqueous media. This allows for the direct investigation of the complex's interaction with DNA through titration experiments. Indeed, phosphorescence is observed in solutions containing ct-DNA (Figure 5.5), with the band maximum centred at ~585 nm. This is relatively blue shifted compared with the emission of the complex in CH_2Cl_2 ($\lambda_{max,em}$

325

608 nm). No evidence of phosphorescence is observed in **11** without ct-DNA, indicating that the

turn-on phosphorescence phenomenon arises likely due to two factors (i) hydrophobic effect and

(ii) disintegration of aggregates. The hydrophobic effect is invoked in ethidium bromide (**EthBr**),

a commonly used probe in displacement assays to estimate the binding affinity of intercalators

with DNA. The significant overlap with the emission band of **EthBr** ($\lambda_{max,em}$ 608 nm) precludes

the use of this probe to estimate the affinity of **11** with DNA. This highlights the potential of

complex **11** and likely similar complexes as potential bioimaging agents.
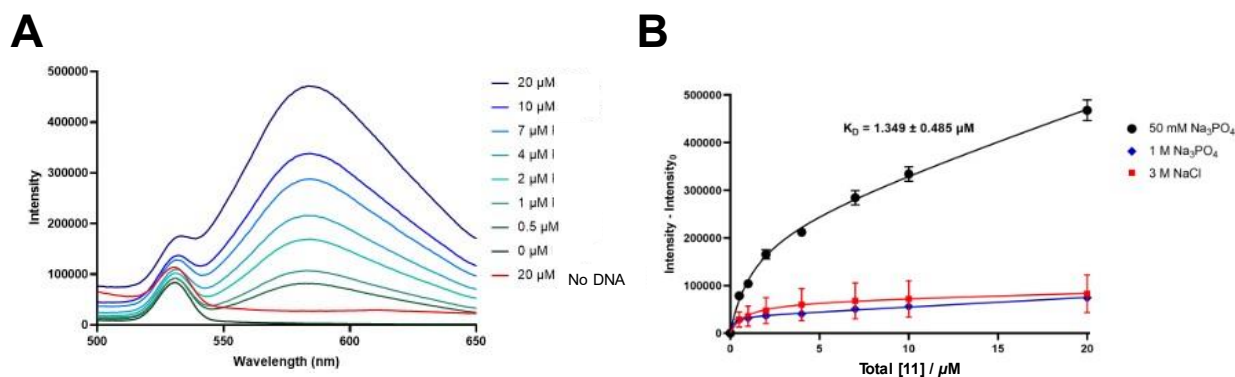
Figure 5.5. (a) Turn-on phosphorescence with varying concertation of **11** with and without ct-DNA and (b) K_D with ct-DNA at various ionic strengths.

Remarkably, the emission intensity increases with increasing **11** concentration (Figure 5.5)

and can be fit to a one site−total and nonspecific binding saturation model with a binding

dissociation constant (K_D) of 1.3 ± 0.5 μM, which is comparable to the K_D of EthBr (2.3 μM[279]).

This indicates that **11** strongly intercalates with ct-DNA. In contrast, phenanthriplatin exhibits an

order of magnitude weaker affinity to DNA ($K_D > 10$ μM)[270] owing to the near-orthogonal

orientation of phenanthridine with respect to the Pt–L coordination plane preventing full

326

intercalation of phenanthriplatin to DNA. Structurally, **11** shows coplanarity between the phenanthridinyl moiety and the Pt–L coordination planes enforced by the pincer-like nature of the ligand. An apparent decrease in the emission intensity and K_D are observed in samples with increased ionic strength (Figure 5.5b) and are independent of the charge and identity of the anion. This dependence on the ionic strength of the medium is generally observed in cationic intercalators[277,280,281] but is unusual for the neutral **11**. Nevertheless, this suggests that some degree of electrostatic interaction may also be operative in the interaction of **11** with ct-DNA. Intercalation of cationic intercalators may be a multistep process that involves an external binding mode with an electrostatic attraction between the charged molecule and the negatively charged phosphate group.

The interaction of **11** with other biomacromolecules was also examined with bovine serum albumin (BSA) and a helical <u>RNA</u> Helicase associated with <u>AU</u>-rich element (RHAU) protein. It is thought that formation of Pt−S covalent adducts with sulfur-containing amino acid monomers and oligomers, such as glutathione, deactivates the Pt(II)-complex and leads to its excretion from the cell. This experiment may provide insight to other possible interactions of **11** in the cell as deactivation pathways. Interestingly, turn-on phosphorescence was not observed in all samples with BSA and RHAU which suggests that the complex either does not interact with proteins completely or may interact in completely different manner that leads to quenching of phosphorescence.

The specificity of **11** binding to DNA was examined by performing titrations with hairpin single stranded DNA (ss-DNA) as shown in Figure 5.6 and Figure 5.7. All samples exhibit turn-on phosphorescence with apparent K_D of 0.7 ± 0.4 µM, 1.5 ± 0.6 µM and 6.3 ± 4.8 µM with ss-

DNA containing GG, TT, and TG, respectively. This suggests a preferential interaction with guanine-rich regions of DNA. This is further supported by titration with various ss-5mers, and only samples titrated with 5'-GGGGG showed turn-on phosphorescence and a comparable K_D (0.50 ± 0.18 μM) to that found in GG-rich ss-DNA. The increased dipole moment and number of hydrogen bonds in G-C base pair, compared with A-T pair, contributes to its greater polarity and polarizability. Consequently, intercalators generally show greater G-C specificity in DNA binding.[281]
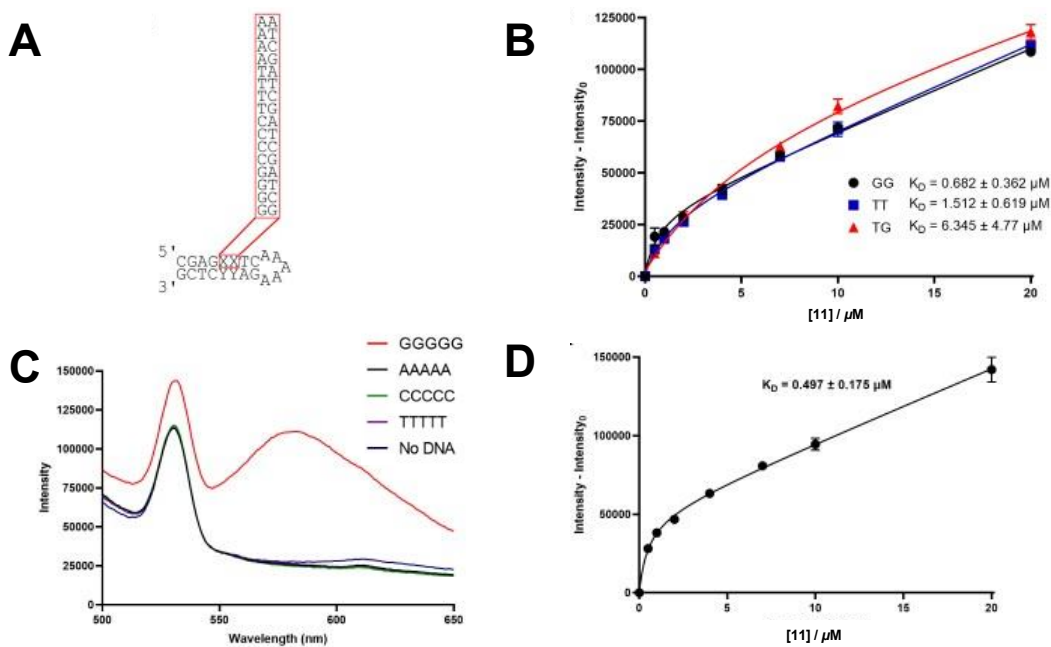
Figure 5.6. (a) Coding for ss-DNA hairpins illustrating sites of modification, (b) K_D with single ss-DNA (c) selective turn-on phosphorescence with 5G-mers and (d) K_D of **11** with 5G-mers.
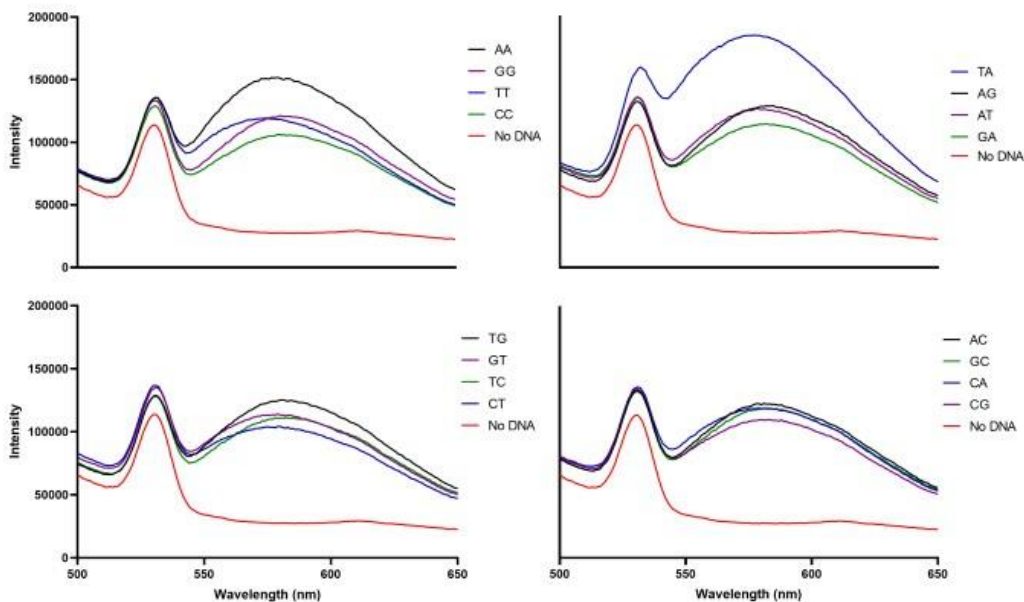
Figure 5.7. Turn-on phosphorescence with other ss-DNA hairpins.

5.3.3 [Pt(*N^N^O*)Cl] as a Potential Photodynamic Therapeutic Agent

With the encouraging results in section 5.3.2, we further hypothesized that the emissive triplet state can be leveraged to increase the cytotoxicity of complex **11**. Table 5.2 summarizes the results from this experiment. Consistent with the results from Table 5.1, Complex **11** is demonstrably more efficacious than cisplatin in all cancerous-cell lines. Incubation of the cell assays (5 h) under irradiation (15 min) with a lamp (480 nm) leads to a further decrease in the IC_{50} values for the cell lines treated with **11** compared with those incubated in the dark. In contrast,

there is no appreciable decrease in the IC_{50} observed in cisplatin-treated cell lines that have been incubated with irradiation compared with those that were left in the dark. This strongly suggests that a long-live emissive triplet state induces the cytotoxicity enhancement in **11**.

To better understand the mode of action of the complex we further investigated the cellular uptake and cellular responses of **11** beyond our previous studies in Table 5.1. Consistent with Figure 5.2b, there is greater cellular concentration of Pt in **11** compared with cisplatin (Figure 5.8). The distribution within the cell is also investigated as shown in Figure 5.8. Unsurprisingly, both **11** and cisplatin are found in the nucleus with **11** exhibiting significantly more than cisplatin. This likely contributes to the enhanced efficacy of **11** compared with cisplatin. Astonishingly, a small portion of **11** reaches the mitochondria. Mitochondria are an important source of reactive oxygen species (ROS) which contributes to mitochondrial damage leading to a range of pathologies.[282] This suggests that mitochondria may also be targeted by **11** besides from DNA. Overall, generation of ROSs is hypothesized to be operational in the increased cytotoxicity of **11** with light. The rest of **11** is distributed in the cytosol, albeit in smaller amounts, but could lead to fewer encounters with proteins and other biomacromolecules that could lead to the deactivation of the complex. This may explain the better performance of **11** with cisplatin-resistant cell lines (Figure 5.1 and Figure 5.2).

Table 5.2. Cytotoxicity of complex **11** and cisplatin in dark and with exposure to light (λ_{lamp} 480 nm).[a]

IC$_{50}$ (μM)	A2780cis		SKOV3		A549		MDA MB 231		HeLa	
	Platinum-resistant ovarian cancer		Ovarian cancer		Lung cancer		Breast Cancer		Cervical Cancer	
	Dark	Light	Dark	Light	Dark	Light	Dark	Light	Dark	Light
Cisplatin	125.0 ± 4.2	102.3 ± 0.68	141.5 ± 24.0	179.0 ± 12.6	246.5 ± 21	231.1 ± 3.7	201.4 ± 14.3	198.2 ± 3.9	166.3 ± 26.8	133.2 ± 43.1
11	7.23 ± 2.3	1.20 ± 0.94	7.54 ± 4.7	4.40 ± 0.1	44.0 ± 16.1	13.7 ± 1.6	10.90 ± 0.52	2.05 ± 1.90	17.1 ± 2.8	2.26 ± 0.99

[a] Conditions: 5 h incubation time; 15 min irradiation with λ_{lamp} 480 nm; changed medium after irradiation, 24 h MTT.
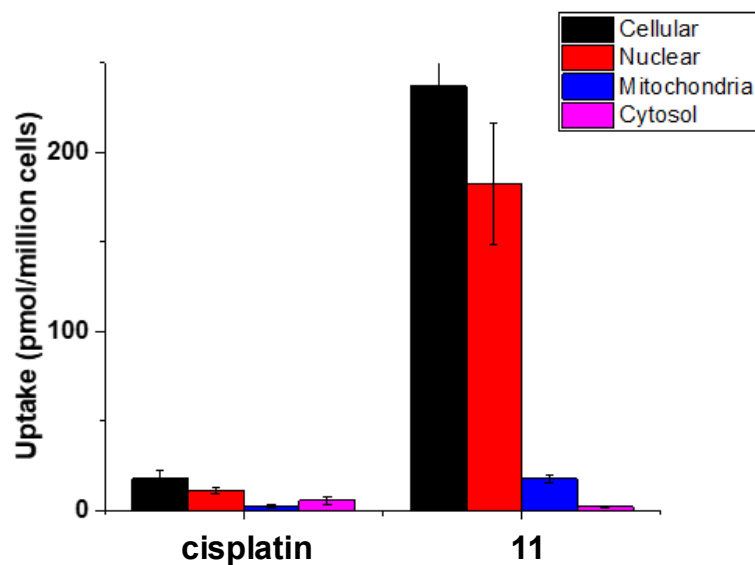
Figure 5.8. Pt content and localization in cell of complex cisplatin and **11**.

To support the ROS hypothesis two assays were performed (Figure 5.9 and 5.10). The γ-H2AX assay is conducted to monitor DNA stress/damage.[283,284] In Figure 5.9, assays incubated in the dark (**As1-As5**) do not exhibit a broad tail compared with assay **As6** (indicated by red arrow).This indicates a significant DNA stress/damage likely through the generation of ROS introducing double-stranded breaks. We also performed mitoSOX assays (Figure 5.10) on cisplatin and **11** to determine the implication of platinum distribution in the mitochondria. Similar to the behaviour of **11** in Figure 5.9, only assay **A12** exhibit a broad tail indicating the mitochondria is under oxidative stress under these conditions. Overall, these results indicate that **11** induces additional stress to both DNA and mitochondria through the generation of ROSs, and highlights the potential of [Pt(*N^N^O*)Cl] as photodynamic therapy agents.
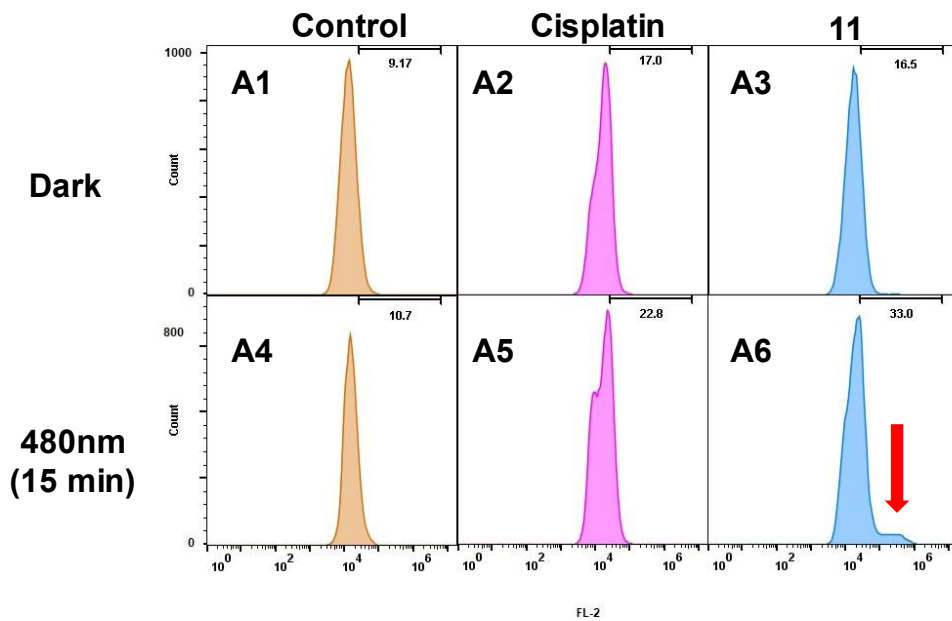
Figure 5.9. γ-H2AX assays to test for DNA damages.
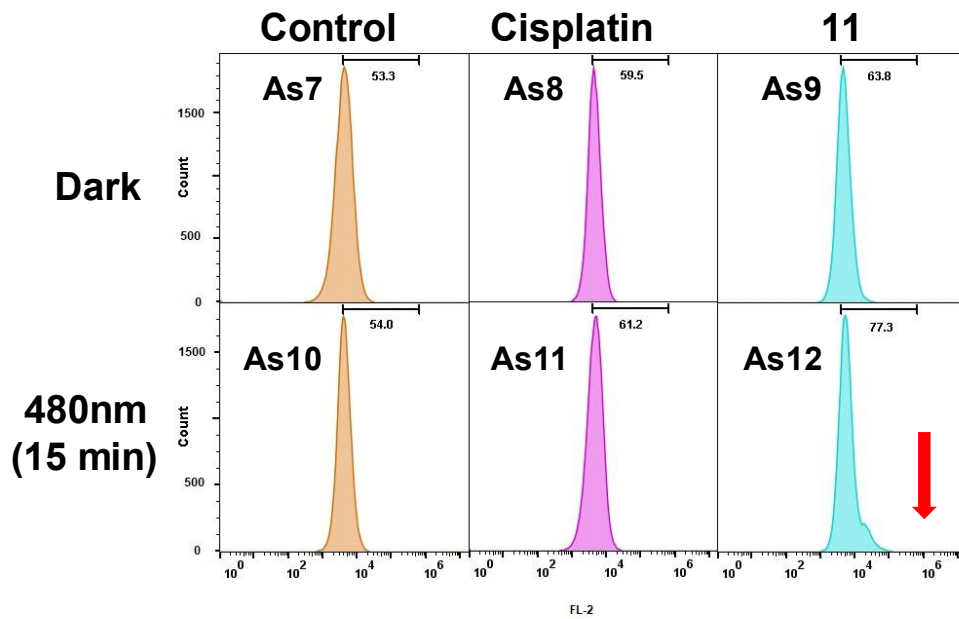
Figure 5.10. MitoSOX assays to test for mitochondrial damages.

5.4   Experimental Details

5.4.1 Cytotoxicity Assays

Unless mentioned otherwise, these experiments were conducted by the Zheng group (Prof. Yaorong Zheng, Kent State University).

Cell Cultures: A2780 and A2780cis cell lines were cultured in RPMI 1640 with L-glutamine supplemented with 10% FBS and 1% PS. SKOV-3, MDA-MB-231, A549, and HEK293 cell line were cultured in DMEM 1g/L glucose, with L-glutamine & sodium pyruvate supplemented with 10% FBS and 1% PS. MET5A cell line was cultured in M199 supplemented with 10% FBS, 1% PS, insulin, 0.1% Trace Elements B, 4 mM Hydrocortisone, and 4 ng/mL EGF. All cell lines were incubated at 37°C under an atmosphere containing 5% CO_2. Cells were passaged by trypsinization and split in a 1:5 ratio.

Cytotoxicity Assays: MTT assays were completed to determine the cytotoxicity of compounds. 100 μL of cell solution containing 2 x 10^4 cells/ mL was seeded in a 96-well plate. The plate was incubated for at 37 °C under an atmosphere containing 5% CO_2 for 24 hr to allow for adherence of cells. 50 μL of cell medium with varying concentrations of compounds was added, and the cells were incubated for 72 hr. After 72 hr, 30 μL of 5.0 mg/mL MTT in PBS was added to the cell medium. After 2-4 h, the medium was aspirated, and 200 μL of DMSO was added to each well. The plate was shaken for 10 minutes at room temperature. The absorbance of purple formazan was recorded at 562 nm with a BioTek ELx800 plate reader. IC_{50} values were determined using Origin software. All experiments were performed in triplicate.

Uptake: SKOV-3 cells were plated in a 6-well and at 37 °C under an atmosphere containing 5% CO_2 for 24 hr. Cells were then treated with 2 μM Pt compound for 24 hr. After incubation with Pt, cells were collected by trypsinization and washed with 1 mL PBS. Cells were counted, recollected, and resuspended in 200 μL 65% nitric acid. Samples were stored shaking at room temperature overnight. After the cell pellet was dissolved, the solutions were diluted with water and analyzed by GFAAS. All experiments were performed in triplicate.

Apoptosis: SKOV-3 cells were seeded in a 6-well plate at a concentration of 4 x 10^5 cells/well. Cells were then incubated at 37°C under an atmosphere containing 5% CO_2 for 24 hr. Cells were treated with compound for 72 hr (15 μM cisplatin, 1 μM phenanthriplatin, 1 μM **11**). Cells were harvested, the supernatant was then discarded, and cells were resuspended in 1 mL PBS. Cells were resuspended in 1X binding buffer using the FITC Annexin V Apoptosis Detection Kit 1 (BD Biosciences, Franklin Lakes, NJ, USA) reaching a concentration of 10^6 cells/ mL. 100 μL of this cell solution was transferred to a 5 mL culture tube. Then, 5 μL of Annexin V-FITC and 10 μL propidium iodide (PI) solutions were added to cells. Cells were incubated for 15 min at RT in the dark and then brought to a final volume of 400 μL with 1X binding buffer. Cells were then analyzed with FITC and PerCP-Cy5-5 channels on FACSAria™II (BD Biosciences, Franklin Lakes, NJ, USA) and data was processed using FlowJo software.

MTT assays of cisplatin and 11 against A2780cis, SKOV3, A549, MDA MB 231 and Hela cells with and without 15-min irradiation by 480 nm LED. The cells were seeded in 96-well microplates (two plates from each cell line) in 100 μL cell suspensions (6×10^4 cells per mL) per well to begin and were incubated for 24 h at 37 ℃, 5% CO_2. Next, 50 μL volume of RPMI or DMEM with various concentrations of Pt compounds was added to each well of the microplates.

The cells were then incubated for an additional 5 h at 37 °C, 5% CO_2. Next, one plate was kept in the dark and other plate was irradiated with 480 nm LED for 15 minutes. After the irradiation, medium in both plates were aspirated out and filled with 150 µL of fresh medium followed by one time washing with 200 µL fresh medium. The plates were then incubated for 24 h at 37 °C, 5% CO_2. Next, a volume of 30 µL MTT (Alfa Aesar) (5 mg mL^{-1} in PBS) was added to the cells and then the cells were incubated for an additional 2-4 h at 37 °C, 5% CO_2. The solutions were then aspirated, leaving behind insoluble purple formazan. A volume of 200 µL DMSO was added to the wells and the plates were shaken for 10 min. Next, the microplates were analyzed for absorbance at 562 nm with an ELx800 absorbance reader (BioTek, Winooski, VT, USA). Finally, the data were analyzed using Origin software to produce dose-response curves and to determine IC_{50} values. All experiments were performed in triplicate.

Measurements of cellular Pt contents. A2780cis cells were seeded in a 6-well plate at a concentration of 2×10^5 cells/mL per well and incubated at 37 °C, 5% CO_2 overnight. These cells were treated with Cisplatin or **11** ([Pt] = 20 µM) for 5 h at 37 °C, 5% CO_2. The remaining alive cells were harvested by trypsinization and counted. The cells were then digested in 200 µL 65% HNO_3 and were shaken at 400 rpm on an Eppendorf ThermoMixer™ F1.5 at R.T. overnight. The Pt contents in the cells were analyzed by GFAAS (graphite furnace atomic absorption spectroscopy) after diluting the fractions 10x in water. All experiments were performed in triplicate.

Measurements of Cytosolic/Mitochondrial Pt contents. A2780cis cells were seeded on a 6-well microplate (2×10^5 cells/mL) and incubated at 37 °C 5% CO_2 overnight. The cells were then treated with either 20 µM cisplatin or **11** and incubate for 5 h. The remaining alive cells were harvested by trypsinization and counted. Cytosolic and mitochondrial fractions were isolated using the Thermo Scientific™ Mitochondria Isolation Kit for Mammalian Cells. The mitochondrial fraction was then dissolved in 100 µL 65% nitric acid and were shaken at 400 rpm on an Eppendorf ThermoMixer™ F1.5 at R.T. overnight while the cytosolic fraction was maintained at -20 °C. Next, the fractions were diluted 10x in water and the platinum content was analysed using GFAAS. All experiments were performed in triplicate.

Measurements of Nuclear Pt contents. A2780cis cells were seeded on a 6-well microplate (2×10^5 cells/mL) and incubated at 37 °C 5% CO_2 overnight. The cells were then treated with cisplatin (20 µM) or **11** (20 µM) and incubate for 5 h. The remaining alive cells were harvested by trypsinization and counted. Next, the cells were suspended in 1 mL solution of PBS with 0.1% NP-40 followed by centrifugation to dissociate the cell membrane. This step was duplicated. The isolated nuclei were digested in 200 µL 65% HNO_3 on an Eppendorf ThermoMixer™ F1.5 at R.T. overnight. The platinum content was analyzed by GFAAS. All experiments were performed in triplicate.

Florescence imaging experiments for HeLa cells treated with 11 and Mitotracker Red. HeLa cells were seeded in an imaging disk (MatTek) at a concentration of 5 x 10^4 cells with 2 mL of complete medium and incubated for 24 h at 37 °C. The cells were then treated with IBML 4 182

337

(10 µM) and incubated for 2h at 37 °C, 5% CO_2. Next, MitoTracker Red FM (Invitrogen) was added to the dish and incubated for another 30 minutes. The medium was aspirated out and washed 3 times with 1 mL of PBS. 1 mL PBS with 0.5% BSA was added into the dish and images were acquired using an Olympus IX70 inverted epifluorescence microscope equipped with a digital CCD camera (QImaging). Images were processed and intensities were quantified with ImageJ software (NIH).

Live/Dead cells viability assay. HeLa cells (5×10^4 cells per mL) were cultured on two 35 mm sterile glass bottom culture dishes (MATTEK Corporation) for 24 h at 37 °C. The cells were then treated with 10 µM [11] for 5 h at 37 °C. Next, one dish was irradiated with 480 nm LED for 15 minutes while the other was kept in the dark. Both dishes were washed and replaced with regular DMEM medium and incubate at 37 °C overnight. Before the assay, the cells were washed with 1 mL PBS. A 100 µL volume of LIVE/DEAD working solution (formed by mixing 1 mL of calcein AM and 5 µL ethidium homodimer-1) was carefully added to the disks, which were then incubated at r.t. for 15 min. 1 mL PBS was added into each disk and images were acquired using an Olympus IX70 inverted epifluorescence microscope equipped with a digital CCD camera (QImaging). Images were processed and intensities were quantified with ImageJ software (NIH).

MitoSOX™ (mitochondrial ROS production) analysis. A2780Cis cells were seeded in two 6-well plates at a concentration of 2×10^5 cells per mL and incubated for 24 h at 37 °C under an atmosphere containing 5% CO_2. Next, the cells were treated with cisplatin (10 µM) or [11] (10 µM) while one well was kept as a control and incubated 37 °C for 5h. One plate was irradiated with

338

480nm for 15 minutes while the other was kept in the dark. Both plates were washed with the medium and incubated overnight. MitoSOX Red Mitochondrial Superoxide Indicator (Thermo Scientific, Rochester, NY, USA) was then added to the cells to reach a concentration of 5 µM and incubated at 37 °C for 30 minutes. The cells were then collected, washed with PBS, and resuspended in PBS containing 0.5% BSA. The cell solutions were analyzed using the FL-2 channel on a BD Accuri C6™ flow cytometer.

Flow cytometric analysis of phosphorylation of H2AX (γH2AX). A2780Cis cells were seeded in two 6-well plates at a concentration of 2×10^5 cells per mL and incubated for 24 h at 37 °C under an atmosphere containing 5% CO_2. Next, the cells were treated with cisplatin (10 µM) or [11] (10 µM) while one well was kept as a control and incubated 37 °C for 5h. One plate was irradiated with 480nm for 15 minutes while the other was kept in the dark. Both plates were washed with the medium and incubated overnight. Cells were harvested from adherent cultures by trypsinization. Following centrifugation at 1500 rpm for 5 min, cells were washed with PBS. All samples were resuspended in BD fixation/Permeabilization solution (250 µL) for 20 minutes at 4 ℃. Then the supernatant was removed, the samples were resuspended with BD Perm/Wash Buffer (1 mL) and centrifuged. About 50 µL of buffer was left in the tube and 5 µL of BD Alexa 488-anti γH2AX antibody solution was added followed by 60 minutes incubation in the dark at room temperature. The cells were resuspended in PBS and analyzed using the FL-1 channel on a BD Accuri C6™ flow cytometer.

Flow cytometric apoptosis assay. A2780cis cells were seeded in two 6-well plates at a concentration of 2×10^5 cells per well and incubated for 24 h at 37 °C. Next day, the cells were treated with [11] or cisplatin (10 µM), while one well was kept as a control and incubated 37 °C for 5h. One plate was irradiated with 480nm for 15 minutes while the other was kept in the dark. Both

plates were washed with the medium and incubated for 24 h at 37 °C. The medium was collected in clean 15 mL falcon tubes along with washed PBS solution. 1 mL trypsin was added to the wells. After 5 min, the cell suspensions were transferred to the falcon tubes that contained the media and PBS, and centrifuged at 1400 rpm at 4 °C for 5 min. The cell pellet was re-suspended in 1 mL PBS and the cells were counted. The cell pellet was collected again and an appropriate amount of $1\times$ binding buffer was added to reach a concentration of 10^6 cells per mL. 100 μL cell suspensions were added to new 2 mL Eppendorf tubes and 5 μL Annexin V-FITC and 5 μL PI solution was added. The cells were gently vortexed and incubated at r.t. for 15 min in the dark. 400 μL $1\times$ binding buffer was added to each Eppendorf tube and the cell suspensions were transferred to flow cytometry tubes. Flow cytometry analysis was done using FL-1 and FL-3 channels on a BD Accuri C6™ flow cytometer at 10,000 events.

5.4.2. DNA Binding Studies

Unless mentioned otherwise, these experiments were conducted by I with Danny Gusakovsky as a collaborative effort with the McKenna group (Prof. Sean McKenna, University of Manitoba).

DNA binding studies. For the titration studies, 10 mm × 10 mm, 0.7 mL nominal volume Spectrosil Quartz cuvettes equipped with PTFE stopper (Starna Cells) were used. UV-Vis absorbance spectra were collected using a Helios Zeta UV-Vis spectrophotometer (Thermo-Fisher), while the emission and excitation spectra were measured in a Fluorolog-3 spectrofluorometer (Horiba Scientific, Kyoto, Japan) exciting at 450 nm, and using 5 nm entrance/exit slit widths. All samples were present in 50 mM, pH 7.0 Na_3PO_4 aqueous solution, unless stated otherwise, and incubated with 500 μM calf thymus DNA (CT-DNA) for 16 hours at room temperature in the dark. The concentrations of CT-DNA samples (Thermo-Fisher Scientific,

Ottawa, Canada) were determined by taking the absorbances at 260 nm with a NanoDrop 2000 spectrophotometer (Therfo-Fisher) and using the $\varepsilon = 6\ 600\ M^{-1}cm^{-1}$ as the molar absorption coefficient.[285] A 5 mM stock solution of **11** in DMSO was prepared prior to dilutions in aqueous solution. Emission spectra were collected for biological triplicates of $0 - 20\ \mu M$ **11** with CT-DNA, with final DMSO concentrations of ≤ 0.4 % v/v. UV-Vis absorbance and excitation spectra were also collected for the 20 μM **11** with CT-DNA sample (0.4% V/V DMSO final concentration). To investigate the effect of ionic strength, two sets of biological triplicates of 0-20 μM **11** were prepared in 1 M Na_3PO_4 and 3 M NaCl, pH 7.0 aqueous solutions. The emission spectrum of a 20 μM sample without CT- DNA was also collected to serve as control. The binding affinity of the complex was explored using double stranded hairpin DNA oligonucleotides (Integrated DNA Technologies, Coralville, IA, USA) with the following sequences 5' – GTGGTGTGCAGCGAGAATAG, 5' – CTCCTCTCCACCCACAATAC, 5' – AAAAA, 5' – GGGGG, 5' – CCCCC, 5' – TTTTT, and 5' – AAGAA; which were prepared in a similar manner as described for CT- DNA samples. Emission spectra were collected for samples containing $0 -$ 20 μM **11** in the presence of 5 μM double stranded hairpin DNA oligonucleotides. Samples of the shorter 5-mer oligonucleotides were prepared by preparing triplicate solutions of 10 μM 5' – AAAAA, 5' – GGGGG, 5' – CCCCC, 5' – TTTTT, or 5' – AAGAA containing 20 μM **11**. The data were fitted to a one site−total and nonspecific binding saturation model, using (1) on a GraphPad Prism 9.

$$y = \frac{(B_{max})(x)}{x+K_D} + NS * x + BG \hspace{3cm} (1)$$

where B_{max} is the maximum specific binding ($B_{max} = 1$, for 1:1 DNA-Pt binding), K_D is the equilibrium dissociation constant, NS is the slope of the nonspecific binding, and BG is the amount of nonspecific binding.

Binding Studies with other biomacromolecules. Additional emission spectra were also collected for $0 - 20$ μM **11** in the presence of 20 μM bovine serum albumin, and 20 μM of a truncation of the protein RHAU including amino acids 53-105 purified.

Conclusions

In conclusion, planar analogs of monofunctional phenanthriplatin-type prodrugs with altered binding geometry of the *N*-heterocycle show promising anticancer activity, with a superior *in vitro* therapeutic index compared with cisplatin and phenanthriplatin. The activity of monofunctional **10** and **11** towards cisplatin-resistant cancer cells is a critical finding, as tumors resistant to cisplatin often show cross-resistance to a diverse range of unrelated antitumour drugs. The activation of independent pathways by the molecular structure of planar phenanthridine-based Pt(II) complexes is likely responsible for the increased sensitivity of resistant cells to these compounds. Equally important, the diminished toxicity of planar phenanthridine-ligated Pt(II) complexes presented here compared with phenanthriplatin further highlights how the disposition of the benzannulated *N*-heterocyclic ligand with respect to the coordination plane of the metal centre can influence activity. In addition, the *in vitro* cytotoxicity of **11** is further improved through the irradiation of treated assays. The generation of ROSs likely induces the additional damages/ stresses not only with DNA but also in the mitochondria. As substitution of the phenanthridinyl ring modulates anti-neoplastic behaviour, this therefore represents our target for second-generation analogs.

References

(1)   Faraday, M. On New Compounds of Carbon and Hydrogen, and on Certain Other Products Obtained during the Decomposition of Oil by Heatrstl.1825.Pdf. *Philos. Trans. R. Soc.* **1825**, *115*, 440–466.

(2)   Heo, I.; Lee, J. C.; Özer, B. R.; Schultz, T. Mass-Correlated High-Resolution Spectra and the Structure of Benzene. *J. Phys. Chem. Lett.* **2022**, *13* (35), 8278–8283. https://doi.org/10.1021/acs.jpclett.2c02035.

(3)   Kunishige, S.; Katori, T.; Baba, M.; Nakajima, M.; Endo, Y. Spectroscopic Study on Deuterated Benzenes. I. Microwave Spectra and Molecular Structure in the Ground State. *J. Chem. Phys.* **2015**, *143* (24), 244302. https://doi.org/10.1063/1.4937949.

(4)   Watson, M. D.; Fechtenkötter, A.; Müllen, K. Big Is Beautiful−"Aromaticity" Revisited from the Viewpoint of Macromolecular and Supramolecular Benzene Chemistry. *Chem. Rev.* **2001**, *101* (5), 1267–1300. https://doi.org/10.1021/cr990322p.

(5)   Vij, V.; Bhalla, V.; Kumar, M. Hexaarylbenzene: Evolution of Properties and Applications of Multitalented Scaffold. *Chem. Rev.* **2016**, *116* (16), 9565–9627. https://doi.org/10.1021/acs.chemrev.6b00144.

(6)   Price, C. C. Substitution and Orientation in the Benzene Ring. *Chem. Rev.* **1941**, *29* (1), 37–67. https://doi.org/10.1021/cr60092a002.

(7)   Papadakis, R.; Ottosson, H. The Excited State Antiaromatic Benzene Ring: A Molecular Mr Hyde? *Chem. Soc. Rev.* **2015**, *44* (18), 6472–6493. https://doi.org/10.1039/C5CS00057B.

(8)   Swami, B.; Yadav, D.; Menon, R. S. Benzannulation Reactions: A Case for Perspective Change From Arene Decoration to Arene Construction. *Chem. Rec.* **2022**, *22* (1), e202100249. https://doi.org/10.1002/tcr.202100249.

(9)   Hart-Davis, A. J.; White, C.; Mawby, F. J. Reactions Of-WIndeny Complexes of Transition Metals. III.' Kinetics and Mechanisms of Substitution Reactions of Tricarbonyl-Mindenylhalomolybdenum(II) Complexes. 6.

(10) Rerek, M. E.; Basolo, F. Kinetics and Mechanism of Substitution Reactions of .Eta.5-Cyclopentadienyldicarbonylrhodium(I) Derivatives. Rate Enhancement of Associative Substitution in Cyclopentadienylmetal Compounds. *J. Am. Chem. Soc.* **1984**, *106* (20), 5908–5912. https://doi.org/10.1021/ja00332a026.

(11) Rerek, M. E.; Ji, L.-N.; Basolo, F. The Lndenyl Ligand Effect on the Rate of Substitution Reactions of Rh(Rl-C9H7)C(O), and Mn(Rl -CgH7)C(O)a. 2.

(12) Okada, Y.; Miyamoto, N.; Hishimoto, M.; Hayashi, T. Studies on Ferrocene Derivatives. Part XIII. Ligand Exchange Reactions of Benzoferrocenes. *Transit. Met Chem* **1999**, 5.

(13) Treichel, P. M.; Johnson, J. W.; Wagner, K. P. OXIDATIONS OF VARIOUS INDENYL-IRON. 4.

(14) Crossley, N. S.; Green, J. C.; Nagy, A.; Stringer, G. Electronic Structure of Transition-Metal Lndenyl Compounds: A He I and He I I Photoelectron Spectroscopic Study of [Mn(Q5-C,H7)(CO),], [Fe(Q5-CgH7),]. Ru(Q5-C9H7)21 and Ru(T5-C9H7)(q-C5Me5) I t. *J CHEM SOC DALTON TRANS* **1989**, 9.

(15) Brady, E. D.; Overby, J. S.; Meredith, M. B.; Mussman, A. B.; Cohn, M. A.; Hanusa, T. P.; Yee, G. T.; Pink, M. Spin-State Alteration from Sterically Enforced Ligand Rotation in

Bis(Indenyl)Chromium(II) Complexes [1]. *J. Am. Chem. Soc.* **2002**, *124* (32), 9556–9566. https://doi.org/10.1021/ja012390a.

(16) Shimizu, A.; Ishizaki, Y.; Horiuchi, S.; Hirose, T.; Matsuda, K.; Sato, H.; Yoshida, J. HOMO–LUMO Energy-Gap Tuning of π-Conjugated Zwitterions Composed of Electron-Donating Anion and Electron-Accepting Cation. *J. Org. Chem.* **2021**, *86* (1), 770–781. https://doi.org/10.1021/acs.joc.0c02343.

(17) Hanson, K.; Roskop, L.; Djurovich, P. I.; Zahariev, F.; Gordon, M. S.; Thompson, M. E. A Paradigm for Blue- or Red-Shifted Absorption of Small Molecules Depending on the Site of π-Extension. *J. Am. Chem. Soc.* **2010**, *132* (45), 16247–16255. https://doi.org/10.1021/ja1075162.

(18) Liu, B.; Lystrom, L.; Kilina, S.; Sun, W. Effects of Varying the Benzannulation Site and π Conjugation of the Cyclometalating Ligand on the Photophysics and Reverse Saturable Absorption of Monocationic Iridium(III) Complexes. *Inorg. Chem.* **2019**, *58* (1), 476–488. https://doi.org/10.1021/acs.inorgchem.8b02714.

(19) Liu, B.; Lystrom, L.; Brown, S. L.; Hobbie, E. K.; Kilina, S.; Sun, W. Impact of Benzannulation Site at the Diimine (N^N) Ligand on the Excited-State Properties and Reverse Saturable Absorption of Biscyclometallated Iridium(III) Complexes. *Inorg. Chem.* **2019**, *58* (9), 5483–5493. https://doi.org/10.1021/acs.inorgchem.8b03162.

(20) Wang, L.; Yin, H.; Jabed, M. A.; Hetu, M.; Wang, C.; Monro, S.; Zhu, X.; Kilina, S.; McFarland, S. A.; Sun, W. π-Expansive Heteroleptic Ruthenium(II) Complexes as Reverse Saturable Absorbers and Photosensitizers for Photodynamic Therapy. *Inorg. Chem.* **2017**, *56* (6), 3245–3259. https://doi.org/10.1021/acs.inorgchem.6b02624.

(21) Chen, T.; Li, M.; Liu, J. π–π Stacking Interaction: A Nondestructive and Facile Means in Material Engineering for Bioapplications. *Cryst. Growth Des.* **2018**, *18* (5), 2765–2783. https://doi.org/10.1021/acs.cgd.7b01503.

(22) Sinnokrot, M. O.; Valeev, E. F.; Sherrill, C. D. Estimates of the Ab Initio Limit for Π−π Interactions: The Benzene Dimer. *J. Am. Chem. Soc.* **2002**, *124* (36), 10887–10893. https://doi.org/10.1021/ja025896h.

(23) Cai, M.; Song, X.; Zhang, D.; Qiao, J.; Duan, L. π–π Stacking: A Strategy to Improve the Electron Mobilities of Bipolar Hosts for TADF and Phosphorescent Devices with Low Efficiency Roll-Off. *J. Mater. Chem. C* **2017**, *5* (13), 3372–3381. https://doi.org/10.1039/C7TC00733G.

(24) Hong, Y.; Lam, J. W. Y.; Tang, B. Z. Aggregation-Induced Emission: Phenomenon, Mechanism and Applications. *Chem. Commun.* **2009**, No. 29, 4332. https://doi.org/10.1039/b904665h.

(25) McGaughey, G. B.; Gagné, M.; Rappé, A. K. π-Stacking Interactions. *J. Biol. Chem.* **1998**, *273* (25), 15458–15463. https://doi.org/10.1074/jbc.273.25.15458.

(26) Babine, R. E.; Bender, S. L. Molecular Recognition of Protein−Ligand Complexes: Applications to Drug Design. *Chem. Rev.* **1997**, *97* (5), 1359–1472. https://doi.org/10.1021/cr960370z.

(27) Pages, B. J.; Garbutcheon-Singh, K. B.; Aldrich-Wright, J. R. Platinum Intercalators of DNA as Anticancer Agents. *Eur. J. Inorg. Chem.* **2017**, *2017* (12), 1613–1624. https://doi.org/10.1002/ejic.201601204.

(28) Hayashi, K.; Nakatani, M.; Hayashi, A.; Takano, M.; Okazaki, M.; Toyota, K.; Yoshifuji, M.; Ozawa, F. Synthesis and Structures of Platinum(0) Alkyne Complexes with Extended

π-Conjugated Systems. *Organometallics* **2008**, *27* (9), 1970–1972. https://doi.org/10.1021/om800163p.

(29) Flamigni, L.; Encinas, S.; Barigelletti, F.; MacDonnell, F. M.; Kim, K.-J.; Puntoriero, F.; Campagna, S. Excited-State Interconversion between Emissive MLCT Levels in a Dinuclear Ru(Ii) Complex Containing a Bridging Ligand with an Extended π System. *Chem. Commun.* **2000**, No. 13, 1185–1186. https://doi.org/10.1039/b004109m.

(30) Roznyatovskiy, V. V.; Lee, C.-H.; Sessler, J. L. π-Extended Isomeric and Expanded Porphyrins. *Chem Soc Rev* **2013**, *42* (5), 1921–1933. https://doi.org/10.1039/C2CS35418G.

(31) Barbon, S. M.; Staroverov, V. N.; Gilroy, J. B. Effect of Extended π Conjugation on the Spectroscopic and Electrochemical Properties of Boron Difluoride Formazanate Complexes. *J. Org. Chem.* **2015**, *80* (10), 5226–5235. https://doi.org/10.1021/acs.joc.5b00620.

(32) Kappaun, S.; Rentenberger, S.; Pogantsch, A.; Zojer, E.; Mereiter, K.; Trimmel, G.; Saf, R.; Möller, K. C.; Stelzer, F.; Slugovc, C. Organoboron Quinolinolates with Extended Conjugated Chromophores: Synthesis, Structure, and Electronic and Electroluminescent Properties. *Chem. Mater.* **2006**, *18* (15), 3539–3547. https://doi.org/10.1021/cm060720q.

(33) Kiprof, P.; Carlson, J. C.; Anderson, D. R.; Nemykin, V. N. Systematic Color Tuning of a Family of Luminescent Azole-Based Organoboron Compounds Suitable for OLED Applications. *Dalton Trans.* **2013**, *42* (42), 15120. https://doi.org/10.1039/c3dt51853a.

(34) Bossi, A.; Rausch, A. F.; Leitl, M. J.; Czerwieniec, R.; Whited, M. T.; Djurovich, P. I.; Yersin, H.; Thompson, M. E. Photophysical Properties of Cyclometallated Pt(II) Complexes: Counterintuitive Blue Shift in Emission with an Expanded Ligand π System. *Inorg. Chem.* **2013**, *52* (21), 12403–12415. https://doi.org/10.1021/ic4011532.

(35) Gunanathan, C.; Gnanaprakasam, B.; Iron, M. A.; Shimon, L. J. W.; Milstein, D. "Long-Range" Metal−Ligand Cooperation in H $_2$ Activation and Ammonia-Promoted Hydride Transfer with a Ruthenium−Acridine Pincer Complex. *J. Am. Chem. Soc.* **2010**, *132* (42), 14763–14765. https://doi.org/10.1021/ja107770y.

(36) Neufeldt, S. R.; Sanford, M. S. Controlling Site Selectivity in Palladium-Catalyzed C–H Bond Functionalization. *Acc. Chem. Res.* **2012**, *45* (6), 936–946. https://doi.org/10.1021/ar300014f.

(37) Krichevsky, O.; Bonnet, Gregoire. Fluorescence Correlation Spectroscopy: The Technique and Its Applications. *Rep. Prog. Phys.* **2002**, *65* (2), 251–297. https://doi.org/10.1088/0034-4885/65/2/203.

(38) Tumir, L.-M.; Stojkovic, M. R.; Piantanida, I. Come-Back of Phenanthridine and Phenanthridinium Derivatives in the 21st Century. *Beilstein J Org Chem* **2014**, *10*, 2930–2954.

(39) Park, G. Y.; Wilson, J. J.; Song, Y.; Lippard, S. J. Phenanthriplatin, a Monofunctional DNA-Binding Platinum Anticancer Drug Candidate with Unusual Potency and Cellular Activity Profile. *Proc Natl Acad Sci* **2012**, *109*, 11987–11992.

(40) Lu, L.-Q.; Li, Y.; Junge, K.; Beller, Matthias. Iron-Catalyzed Hydrogenation for the In Situ Regeneration of an NAD(P)H Model: Biomimetic Reduction of α-Keto-/α-Iminoesters. *Angew. Chem. Int. Ed.* **2013**, *52* (32), 8382–8386. https://doi.org/10.1002/anie.201301972.

(41) Chen, Q.-A.; Gao, K.; Duan, Y.; Ye, Z.-S.; Shi, L.; Yang, Y.; Zhou, Y.-Gui. Dihydrophenanthridine: A New and Easily Regenerable NAD(P)H Model for Biomimetic

Asymmetric Hydrogenation. *J. Am. Chem. Soc.* **2012**, *134* (4), 2442–2448. https://doi.org/10.1021/ja211684v.

(42) Jensen, K. A.; Nielsen, P. Halfdan. Chelates with Heterocyclic Ligands. I. Chelates Derived from e N,N'-Bis(8-Quinolyl)Ethylenediamine and Analogous Compounds. *Acta Chem. Scand. 1947-1973* **1964**, *18* (1), 1–10. https://doi.org/10.3891/acta.chem.scand.18-0001.

(43) Puzas, J. P.; Nakon, R.; Petersen, J. L. Direct Evidence for an SN1CB Mechanism. 4. Crystal and Molecular Structure of Chloro(Bis(8-Quinolinyl)Amido-N1,N2,N3)Copper(II), a Metal Chelate Containing an Sp2-Hybridized Deprotonated Amine. *Inorg. Chem.* **1986**, *25* (21), 3837–3840. https://doi.org/10.1021/ic00241a026.

(44) Peters, J. C.; Harkins, S. B.; Brown, S. D.; Day, M. W. Pincer-like Amido Complexes of Platinum, Palladium, and Nickel. *Inorg. Chem.* **2001**, *40* (20), 5083–5091. https://doi.org/10.1021/ic010336p.

(45) Maiti, D.; Paul, H.; Chanda, N.; Chakraborty, S.; Mondal, B.; Puranik, V. G.; Lahiri, G. Kumar. Synthesis, Structure, Spectral and Electron-Transfer Properties of Octahedral-[CoIII(L)2]+/[ZnII(L)2] and Square Planar-[CuII(L){OC(=O)CH3}] Complexes Incorporating Anionic Form of Tridentate Bis(8-Quinolinyl)Amine [N1C9H6-N2-C9H6N3, L-] Ligand. *Polyhedron* **2004**, *23* (5), 831–840. https://doi.org/10.1016/j.poly.2003.11.053.

(46) Valk, J.-M.; Claridge, T. D. W.; Brown, J. M.; Hibbs, D.; Hursthouse, M. B. Synthesis and Chemistry of a New P-N Chelating Ligand; (R)- and (S)-6-(2'-Diphenylphosphino-1'-Naphthyl)Phenanthridine. *Tetrahedron Asymmetry* **1995**, *6* (Copyright (C) 2017 American Chemical Society (ACS). All Rights Reserved.), 2597–2610. https://doi.org/10.1016/0957-4166(95)00341-L.

(47) Raszeja, L.; Maghnouj, A.; Hahn, S.; Metzler-Nolte, Nils. A Novel Organometallic ReI Complex with Favourable Properties for Bioimaging and Applicability in Solid-Phase Peptide Synthesis. *ChemBioChem* **2011**, *12* (3), 371–376. https://doi.org/10.1002/cbic.201000576.

(48) Sicilia, V.; Fuertes, S.; Martin, A.; Palacios, Adrian. N-Assisted CPh-H Activation in 3,8-Dinitro-6-Phenylphenanthridine. New C,N-Cyclometallated Compounds of Platinum(II): Synthesis, Structure, and Luminescence Studies. *Organometallics* **2013**, *32* (15), 4092–4102. https://doi.org/10.1021/om400159g.

(49) Jiang, B.; Gu, Y.; Qin, J.; Ning, X.; Gong, S.; Xie, G.; Yang, Chuluo. Deep-Red Iridium(III) Complexes Cyclometallated by Phenanthridine Derivatives for Highly Efficient Solution-Processed Organic Light-Emitting Diodes. *J. Mater. Chem. C Mater. Opt. Electron. Devices* **2016**, *4* (16), 3492–3498. https://doi.org/10.1039/C6TC00148C.

(50) Theobald, R. S.; Schofield, K. The Chemistry of Phenanthridine and Its Derivatives. *Chem. Rev.* **1950**, *46* (1), 170–189. https://doi.org/10.1021/cr60143a004.

(51) Crystal and molecular structure of phenanthridine. Roychowdhury1973.Pdf. *Acta. Cryst., Sect. B* **1973**, *29*, 1362–1364.

(52) Brett, W. A.; Rademacher, P.; Boese, R. Redetermination of the Structure of Phenanthridine. *Acta Crystallogr. C* **1993**, *49* (9), 1564–1566. https://doi.org/10.1107/S0108270193005062.

(53) Katritzky, A. R. *Handbook of Heterocyclic Chemistry*, 3rd ed.; Elsevier, 2010.

(54) Benmachiche, A.; Zendaoui, S.-M.; Bouaoud, S.-E.; Zouchoune, B. Electronic Structure and Coordination Chemistry of Phenanthridine Ligand in First-Row Transition Metal

Complexes: A DFT Study. *Int. J. Quantum Chem.* **2013**, *113* (7), 985–996. https://doi.org/10.1002/qua.24071.

(55) Giesbrecht, P. K.; Nemez, D. B.; Herbert, D. E. Electrochemical Hydrogenation of a Benzannulated Pyridine to a Dihydropyridine in Acidic Solution. *Chem. Commun.* **2018**, *54* (4), 338–341. https://doi.org/10.1039/C7CC07907A.

(56) Mondal, R.; Giesbrecht, P. K.; Herbert, D. E. Nickel(II), Copper(I) and Zinc(II) Complexes Supported by a (4-Diphenylphosphino)Phenanthridine Ligand. *Polyhedron* **2016**, *108*, 156–162.

(57) Mandapati, P.; Giesbrecht, P. K.; Davis, R. L.; Herbert, D. E. Phenanthridine-Containing Pincer-like Amido Complexes of Nickel, Palladium, and Platinum. *Inorg Chem* **2017**, *56*, 3674–3685.

(58) Mandapati, P.; Braun, J. D.; Killeen, C.; Davis, R. L.; Williams, J. A. G.; Herbert, D. E. Luminescent Platinum(II) Complexes of N^N⁻^N Amido Ligands with Benzannulated N-Heterocyclic Donor Arms: Quinolines Offer Unexpectedly Deeper Red Phosphorescence than Phenanthridines. *Inorg Chem* **2019**, *58*, 14808–14817.

(59) Mandapati, P.; Braun, J. D.; Lozada, I. B.; Williams, J. A. G.; Herbert, D. E. Deep-Red Luminescence from Platinum(II) Complexes of N^N⁻^N-Amido Ligands with Benzannulated N-Heterocyclic Donor Arms. *Inorg. Chem.* **2020**, *59*, 12504–12517.

(60) Mondal, R.; Lozada, I. B.; Davis, R. L.; Williams, J. A. G.; Herbert, D. E. Site-Selective Benzannulation of N-Heterocycles in Bidentate Ligands Leads to Blue-Shifted Emission from [(P^N)Cu]₂(μ-X)₂ Dimers. *Inorg Chem* **2018**, *57*, 4966–4978.

(61) Mondal, R.; Lozada, I. B.; Davis, R. L.; Williams, J. A. G.; Herbert, D. E. Exploiting Synergy between Ligand Design and Counterion Interactions to Boost Room Temperature Phosphorescence from Cu(I) Compounds. *J. Mater. Chem. C* **2019**, *7*, 3772–3778.

(62) Lozada, I. B.; Murray, T.; Herbert, D. E. Monomeric Zinc(II) Amide Complexes Supported by Bidentate, Benzannulated Phenanthridine Amido Ligands. *Polyhedron* **2019**, *161*, 261–267.

(63) Mondal, R.; Lozada, I. B.; Davis, R. L.; Williams, J. A. G.; Herbert, D. E. Site-Selective Benzannulation of N-Heterocycles in Bidentate Ligands Leads to Blue-Shifted Emission from [(P^N)Cu]2(μ-X)2 Dimers. *Inorg Chem* **2018**, *57*, 4966–4978.

(64) Mandapati, P.; Giesbrecht, P. K.; Davis, R. L.; Herbert, D. E. Phenanthridine-Containing Pincer-like Amido Complexes of Nickel, Palladium, and Platinum. *Inorg Chem* **2017**, *56*, 3674–3685.

(65) Gaire, S.; Ortiz, R. J.; Schrage, B. R.; Lozada, I. B.; Mandapati, P.; Osinski, A. J.; Herbert, D. E.; Ziegler, C. J. (8-Amino)Quinoline and (4-Amino)Phenanthridine Complexes of Re(CO)3 Halides. *J. Organomet. Chem.* **2020**, *921*, 121338.

(66) Nemez, D. B.; Lozada, I. B.; Braun, J. D.; Williams, J. A. G.; Herbert, D. E. Synthesis and Coordination Chemistry of a Benzannulated Bipyridine: 6,6′-Biphenanthridine. *Inorg. Chem.* **2022**, *61* (34), 13386–13398. https://doi.org/10.1021/acs.inorgchem.2c01514.

(67) Hanson, K.; Roskop, L.; Djurovich, P. I.; Zahariev, F.; Gordon, M. S.; Thompson, M. E. A Paradigm for Blue- or Red-Shifted Absorption of Small Molecules Depending on the Site of π-Extension. *J. Am. Chem. Soc.* **2010**, *132*, 16247–16255.

(68) Barbon, S. M.; Staroverov, V. N.; Gilroy, J. B. Effect of Extended π Conjugation on the Spectroscopic and Electrochemical Properties of Boron Difluoride Formazanate Complexes. *J. Org. Chem.* **2015**, *80*, 5226–5235.

347

(69) Liu, B.; Lystrom, L.; Kilina, S.; Sun, W. Tuning the Ground State and Excited State Properties of Monocationic Iridium(III) Complexes by Varying the Site of Benzannulation on Diimine Ligand. *Inorg. Chem.* **2017**, *56*, 5361–5370.

(70) Westcott, B. L.; Gruhn, N. E.; Michelsen, L. J.; Lichtenberger, D. L. Experimental Observation of Non-Aufbau Behavior: Photoelectron Spectra of Vanadyloctaethylporphyrinate and Vanadylphthalocyanine. *J. Am. Chem. Soc.* **2000**, *122*, 8083–8084.

(71) Hewage, J. S.; Wanniarachchi, S.; Morin, T. J.; Liddle, B. J.; Banaszynski, M.; Lindeman, S. V.; Bennett, B.; Gardinier, J. R. Homoleptic Nickel(II) Complexes of Redox-Tunable Pincer-Type Ligands. *Inorg. Chem.* **2014**, *53* (19), 10070–10084. https://doi.org/10.1021/ic500657e.

(72) Lozada, I. B.; Ortiz, R. J.; Braun, J. D.; Williams, J. A. G.; Herbert, D. E. Donor–Acceptor Boron-Ketoiminate Complexes with Pendent *N*-Heterocyclic Arms: Switched-on Luminescence through *N*-Heterocycle Methylation. *J. Org. Chem.* **2022**, *87* (1), 184–196. https://doi.org/10.1021/acs.joc.1c02138.

(73) Braun, J. D.; Lozada, I. B.; Kolodziej, C.; Burda, C.; Newman, K. M. E.; van Lierop, J.; Davis, R. L.; Herbert, D. E. Iron(II) Coordination Complexes with Panchromatic Absorption and Nanosecond Charge-Transfer Excited State Lifetimes. *Nat. Chem.* **2019**, *11*, 1144–1150.

(74) Bruker-AXS. APEX3 V2016.1-0, 2016.

(75) Dolomanov, O. V.; Bourhis, L. J.; Gildea, R. J.; Howard, J. A. K.; Puschmann, H. OLEX2: A Complete Structure Solution, Refinement and Analysis Program. *J. Appl. Crystallogr.* **2009**, *42*, 339–341.

(76) Spek, A. L. Structure Validation in Chemical Crystallography. *Acta Cryst* **2009**, *D65*, 148–155.

(77) Fan, C.; Yang, C. Yellow/Orange Emissive Heavy-Metal Complexes as Phosphors in Monochromatic and White Organic Light-Emitting Devices. *Chem Soc Rev* **2014**, *43* (17), 6439–6469. https://doi.org/10.1039/C4CS00110A.

(78) Vreshch, V. D.; Yang, J.-H.; Zhang, H.; Filatov, A. S.; Dikarev, E. V. Monomeric Square-Planar Cobalt(II) Acetylacetonate: Mystery or Mistake? *Inorg. Chem.* **2010**, *49* (18), 8430–8434. https://doi.org/10.1021/ic100963r.

(79) Sokolow, J. D.; Trzop, E.; Chen, Y.; Tang, J.; Allen, L. J.; Crabtree, R. H.; Benedict, J. B.; Coppens, P. Binding Modes of Carboxylate- and Acetylacetonate-Linked Chromophores to Homodisperse Polyoxotitanate Nanoclusters. *J. Am. Chem. Soc.* **2012**, *134* (28), 11695–11700. https://doi.org/10.1021/ja303692r.

(80) Muñoz-García, A. B.; Sannino, F.; Vitiello, G.; Pirozzi, D.; Minieri, L.; Aronne, A.; Pernice, P.; Pavone, M.; D'Errico, G. Origin and Electronic Features of Reactive Oxygen Species at Hybrid Zirconia-Acetylacetonate Interfaces. *ACS Appl. Mater. Interfaces* **2015**, *7* (39), 21662–21667. https://doi.org/10.1021/acsami.5b06988.

(81) Seco, M. Acetylacetone: A Versatile Ligand. *J. Chem. Educ.* **1989**, *66* (9), 779. https://doi.org/10.1021/ed066p779.

(82) Allen, G.; Lewis, J.; Long, R. F.; Oldham, C. A Novel Form of Co-Ordination of Acetylacetone to Platinum(LI). *Nature* **1964**, *202*, 589–590. https://doi.org/10.1038/202589a0.

(83) Patra, S.; Mondal, B.; Sarkar, B.; Niemeyer, M.; Lahiri, G. K. First Example of μ$_3$-Sulfido Bridged Mixed-Valent Triruthenium Complex Triangle Ru^{III}$_2$ Ru^{II} (*O* , *O* -Acetylacetonate) $_3$ (*μ* - *O* , *O* ,γ- *C* -Acetylacetonate) $_3$ (μ$_3$-S) (**1**) Incorporating Simultaneous O,O- and γ-C-Bonded Bridging Acetylacetonate Units. Synthesis, Crystal Structure, and Spectral and Redox Properties. *Inorg. Chem.* **2003**, *42* (4), 1322–1327. https://doi.org/10.1021/ic026221i.

(84) Zhu, D.; Budzelaar, P. H. M. N-Aryl β-Diiminate Complexes of the Platinum Metals. *Dalton Trans.* **2013**, *42* (32), 11343. https://doi.org/10.1039/c3dt50715g.

(85) Bernskoetter, W. H.; Lobkovsky, E.; Chirik, P. J. Ancillary Ligand Effects on C−H Bond Activation Reactions Promoted by β-Diiminate Iridium Complexes. *Organometallics* **2005**, *24* (25), 6250–6259. https://doi.org/10.1021/om050705f.

(86) Roesky, H. W. The Renaissance of Aluminum Chemistry. *Inorg. Chem.* **2004**, *43* (23), 7284–7293. https://doi.org/10.1021/ic0400641.

(87) Mears, K. L.; Stennett, C. R.; Taskinen, E. K.; Knapp, C. E.; Carmalt, C. J.; Tuononen, H. M.; Power, P. P. Molecular Complexes Featuring Unsupported Dispersion-Enhanced Aluminum–Copper and Gallium–Copper Bonds. *J. Am. Chem. Soc.* **2020**, *142* (47), 19874–19878. https://doi.org/10.1021/jacs.0c10099.

(88) Mondal, R.; Lozada, I. B.; Davis, R. L.; Williams, J. A. G.; Herbert, D. E. Exploiting Synergy between Ligand Design and Counterion Interactions to Boost Room Temperature Phosphorescence from Cu(I) Compounds. *J. Mater. Chem. C* **2019**, *7*, 3772–3778.

(89) Mandapati, P.; Braun, J. D.; Lozada, I. B.; Williams, J. A. G.; Herbert, D. E. Deep-Red Luminescence from Platinum(II) Complexes of N^N⁻^N-Amido Ligands with Benzannulated N-Heterocyclic Donor Arms. *Inorg. Chem.* **2020**, *59*, 12504–12517.

(90) Ortiz, R. J.; Braun, J. D.; Williams, J. A. G.; Herbert, D. E. Brightly Luminescent Platinum Complexes of *N^C⁻^N* Ligands Forming Six-Membered Chelate Rings: Offsetting Deleterious Ring Size Effects Using Site-Selective Benzannulation. *Inorg. Chem.* **2021**, *60*, 16881–16894.

(91) Lozada, I. B.; Huang, B.; Stilgenbauer, M.; Beach, T.; Qiu, Z.; Zheng, Y.; Herbert, D. E. Monofunctional Platinum(II) Anticancer Complexes Based on Multidentate Phenanthridine-Containing Ligand Frameworks. *Dalton Trans.* **2020**, *49*, 6557–6560.

(92) Myers, E. L.; Butts, C. P.; Aggarwal, V. K. BF3·OEt2 and TMSOTf: A Synergistic Combination of Lewis Acids. *Chem. Commun.* **2006**, No. 42, 4434–4436.

(93) Macedo, F. P.; Gwengo, C.; Lindeman, S. V.; Smith, M. D.; Gardinier, J. R. β-Diketonate, β-Ketoiminate, and β-Diiminate Complexes of Difluoroboron. *Eur. J. Inorg. Chem.* **2008**, *2008*, 3200–3211.

(94) Dohe, J.; Kossmann, J.; Mueller, T. J. J. Diversity-Oriented Four-Component Synthesis of Solid State Luminescent Difluoro Oxazaborinines. *Dyes Pigments* **2018**, *157*, 198–217.

(95) Köhling, J.; Kozel, V.; Jovanov, V.; Pajkert, R.; Tverdomed, S. N.; Gridenco, O.; Fugel, M.; Grabowsky, S.; Röschenthaler, G.-V.; Wagner, V. Synthesis and Characterization of Oxazaborinin Phosphonate for Blue OLED Emitter Applications. *ChemPhysChem* **2019**, *20*, 665–671.

(96) Mtiraoui, H.; Gharbi, R.; Msaddek, M.; Bretonnière, Y.; Andraud, C.; Renard, P.-Y.; Sabot, C. Solution and Solid-State Fluorescence of 2-(2′-Hydroxyphenyl)-1,5-Benzodiazepin-2-One (HBD) Borate Complexes. *RSC Adv.* **2016**, *6*, 86352–86360.

(97) Chęcińska, L.; Mebs, S.; Ośmiałowski, B.; Zakrzewska, A.; Ejsmont, K.; Kohout, M. Tuning the Electronic Properties of the Dative N−B Bond with Associated O−B Interaction: Electron Localizability Indicator from X-Ray Wavefunction Refinement. *ChemPhysChem* **2016**, *17*, 2395–2406.

(98) Itoh, K.; Okazaki, K.; Fujimoto, M. The Structure of 1,3-Enaminoketonatoboron Difluorides in Solution and in the Solid State. *Aust. J. Chem.* **2003**, *56*, 1209–1214.

(99) Grepioni, F.; Cojazzi, G.; Draper, S. M.; Scully, N.; Braga, D. Crystal Forms of Hexafluorophosphate Organometallic Salts and the Importance of Charge-Assisted C−H--- F Hydrogen Bonds. *Organometallics* **1998**, *17*, 296–307.

(100) Mandapati, P.; Braun, J. D.; Killeen, C.; Davis, R. L.; Williams, J. A. G.; Herbert, D. E. Luminescent Platinum(II) Complexes of N^N⁻^N Amido Ligands with Benzannulated N-Heterocyclic Donor Arms: Quinolines Offer Unexpectedly Deeper Red Phosphorescence than Phenanthridines. *Inorg. Chem.* **2019**, *58*, 14808–14817.

(101) Lozada, I. B.; Williams, J. A. G.; Herbert, D. E. Platinum(II) Complexes of Benzannulated N^N⁻^O-Amido Ligands: Bright Orange Phosphors with Long-Lived Excited States. *Inorg. Chem. Front.* **2022**, *9*, 10–22.

(102) Donckt, E. V.; Dramaix, R.; Nasielski, J.; Vogels, C. Photochemistry of Aromatic Compounds. Part 1.—Acid-Base Properties of Singlet and Triplet Excited States of Pyrene Derivatives and Aza-Aromatic Compounds. *Trans. Faraday Soc.* **1969**, *65*, 3258–3262.

(103) Zander, M. The Significance of Donor-Acceptor Interactions in the External Heavy Atom Effect of Silver Nitrate on the Luminescence Behavior of Aza-Aromatic Systems and Carbazoles. *Z Naturforsch A* **1978**, *33*, 998–1000.

(104) Norek, M.; Dresner, J.; Prochorow, J. Spectroscopy and Photophysics of Monoazaphenanthrenes. I. Absorption and Fluorescence Spectra of Phenanthridine and 7,8-Benzoquinoline. *Acta Phys. Pol. A* **2003**, *104*, 425–439.

(105) Marzzacco, C. J.; Deckey, G.; Colarulli, R.; Siuzdak, G.; Halpern, A. M. Excited-State Protonation and Photophysical Properties of Azaphenanthrenes. *J. Phys. Chem.* **1989**, *93*, 2935–2939.

(106) Parker, D.; Senanayake, P. K.; Williams, J. A. G. Luminescent Sensors for PH, PO2, Halide and Hydroxide Ions Using Phenanthridine as a Photosensitiser in Macrocyclic Europium and Terbium Complexes. *J. Chem. Soc. Perkin Trans. 2* **1998**, 2129–2140.

(107) Norek, M.; Kozankiewicz, B.; Prochorow, J. Spectroscopy and Photophysics of Monoazaphenanthrenes. III. Luminescence of Phenanthridine and 7,8-Benzoquinoline in Crystalline State. *Acta Phys Pol A* **2004**, *106*, 77–94.

(108) Lozada, I. B.; Murray, T.; Herbert, D. E. Monomeric Zinc(II) Amide Complexes Supported by Bidentate, Benzannulated Phenanthridine Amido Ligands. *Polyhedron* **2019**, *161*, 261–267.

(109) Lozada, I. B.; Ortiz, R. J.; Braun, J. D.; Williams, J. A. G.; Herbert, D. E. Donor–Acceptor Boron-Ketoiminate Complexes with Pendent N-Heterocyclic Arms: Switched-on Luminescence through N-Heterocycle Methylation. *J. Org. Chem.* **2022**, *87*, 184–196.

(110) Bridgeman, A. J.; Cavigliasso, G.; Ireland, L. R.; Rothery, J. The Mayer Bond Order as a Tool in Inorganic Chemistry. *J. Chem. Soc. Dalton Trans.* **2001**, 2095–2108.

(111) Lu, T.; Chen, F. Atomic Dipole Moment Corrected Hirshfeld Population Method. *J. Theor. Comput. Chem.* **2012**, *11*, 163–183.

(112) Montalti, M.; Credi, A.; Prodi, L.; Gandolfi, M. *Handbook of Photochemistry. 3rd Ed.*; CRC Press: Boca Raton, 2006.

(113) Oyler, K. D.; Coughlin, F. J.; Bernhard, S. Controlling the Helicity of 2,2'-Bipyridyl Ruthenium(II) and Zinc(II) Hemicage Complexes. *J. Am. Chem. Soc.* **2007**, *129*, 210–217.

(114) Martinez, S.; Igoa, F.; Carrera, I.; Seoane, G.; Veiga, N.; De Camargo, A. S. S.; Kremer, C.; Torres, J. A Zn(II) Luminescent Complex with a Schiff Base Ligand: Solution, Computational and Solid State Studies. *J. Coord. Chem.* **2018**, *71*, 874–889.

(115) Mei, J.; Leung, N. L. C.; Kwok, R. T. K.; Lam, J. W. Y.; Tang, B. Z. Aggregation-Induced Emission: Together We Shine, United We Soar! *Chem. Rev.* **2015**, *115*, 11718–11940.

(116) Singh, K.; Siddiqui, I.; Sridharan, V.; Kumar Yadav, R. A.; Jou, J.-H.; Adhikari, D. Aggregation-Induced Enhanced Emission-Active Zinc(II) β-Diketiminate Complexes Enabling High-Performance Solution-Processable OLEDs. *Inorg. Chem.* **2021**, *60*, 19128–19135.

(117) Singh, K.; S., V.; Adhikari, D. Visible Light Photoredox by a (Ph,ArNacNac)2Zn Photocatalyst: Photophysical Properties and Mechanistic Understanding. *Inorg. Chem. Front.* **2021**, *8*, 2078–2087.

(118) Lozada, I. B.; Huang, B.; Stilgenbauer, M.; Beach, T.; Qiu, Z.; Zheng, Y.; Herbert, D. E. Monofunctional Platinum(II) Anticancer Complexes Based on Multidentate Phenanthridine-Containing Ligand Frameworks. *Dalton Trans.* **2020**, *49*, 6557–6560.

(119) Mandapati, P.; Giesbrecht, P. K.; Davis, R. L.; Herbert, D. E. Phenanthridine-Containing Pincer-like Amido Complexes of Nickel, Palladium, and Platinum. *Inorg. Chem.* **2017**, *56*, 3674–3685.

(120) Mandapati, P.; Braun, J. D.; Killeen, C.; Davis, R. L.; Williams, J. A. G.; Herbert, D. E. Luminescent Platinum(II) Complexes of N´N-´N Amido Ligands with Benzannulated N-Heterocyclic Donor Arms: Quinolines Offer Unexpectedly Deeper Red Phosphorescence than Phenanthridines. *Inorg Chem* **2019**, *58*, 14808–14817.

(121) Mandapati, P.; Braun, J. D.; Lozada, I. B.; Williams, J. A. G.; Herbert, D. E. Deep-Red Luminescence from Platinum(II) Complexes of N^N−^N-Amido Ligands with Benzannulated N-Heterocyclic Donor Arms. *Inorg. Chem.* **2020**, *59*, 12504–12517.

(122) Reineke, M. H.; Sampson, M. D.; Rheingold, A. L.; Kubiak, C. P. Synthesis and Structural Studies of Nickel(0) Tetracarbene Complexes with the Introduction of a New Four-Coordinate Geometric Index, Τδ. *Inorg. Chem.* **2015**, *54*, 3211–3217.

(123) Puttock, E. V.; Fradgley, J. D.; Yufit, D. S.; Williams, J. A. G. A Family of Readily Synthesised Phosphorescent Platinum(II) Complexes Based on Tridentate *N^N^O* - Coordinating Schiff-Base Ligands. *Dalton Trans.* **2019**, *48*, 15012–15028.

(124) Davidson, J. J.; DeMott, J. C.; Douvris, C.; Fafard, C. M.; Bhuvanesh, N.; Chen, C.-H.; Herbert, D. E.; Lee, C.-I.; McCulloch, B. J.; Foxman, B. M.; Ozerov, O. V. Comparison of the Electronic Properties of Diarylamido-Based PNZ Pincer Ligands: Redox Activity at the Ligand and Donor Ability Toward the Metal. *Inorg. Chem.* **2015**, *54*, 2916–2935.

(125) Giesbrecht, P. K.; Nemez, D. B.; Herbert, D. E. Electrochemical Hydrogenation of a Benzannulated Pyridine to a Dihydropyridine in Acidic Solution. *Chem. Commun.* **2018**, *54*, 338–341.

(126) Reichardt, C. Solvatochromic Dyes as Solvent Polarity Indicators. *Chem. Rev.* **1994**, *94*, 2319–2358.

(127) Catalán, J. Toward a Generalized Treatment of the Solvent Effect Based on Four Empirical Scales: Dipolarity (SdP, a New Scale), Polarizability (SP), Acidity (SA), and Basicity (SB) of the Medium. *J. Phys. Chem. B* **2009**, *113*, 5951–5960.

(128) Van der Zwan, G.; Hynes, J. T. Time-Dependent Fluorescence Solvent Shifts, Dielectric Friction, and Nonequilibrium Solvation in Polar Solvents. *J. Phys. Chem.* **1985**, *89*, 4181–4188.

(129) Caspar, J. V.; Meyer, T. J. Photochemistry of Tris(2,2'-Bipyridine)Ruthenium(2+) Ion ($Ru(Bpy)_3^{2+}$). Solvent Effects. *J. Am. Chem. Soc.* **1983**, *105*, 5583–5590.

(130) Kwok, C.-C.; Ngai, H. M. Y.; Chan, S.-C.; Sham, I. H. T.; Che, C.-M.; Zhu, N. [(OΛNΛN)PtX] Complexes as a New Class of Light-Emitting Materials for Electrophosphorescent Devices. *Inorg. Chem.* **2005**, *44*, 4442–4444.

(131) Garner, K. L.; Parkes, L. F.; Piper, J. D.; Williams, J. A. G. Luminescent Platinum Complexes with Terdentate Ligands Forming 6-Membered Chelate Rings: Advantageous and Deleterious Effects in N ^ N ^ N and N ^ C ^ N-Coordinated Complexes. *Inorg. Chem.* **2010**, *49*, 476–487.

(132) Williams, J. A. G. The Coordination Chemistry of Dipyridylbenzene: N-Deficient Terpyridine or Panacea for Brightly Luminescent Metal Complexes? *Chem. Soc. Rev.* **2009**, *38*, 1783–1801.

(133) Meech, S. R.; Phillips, D. Photophysics of Some Common Fluorescence Standards. *J. Photochem.* **1983**, *23*, 193–217.

(134) Suzuki, K.; Kobayashi, A.; Kaneko, S.; Takehira, K.; Yoshihara, T.; Ishida, H.; Shiina, Y.; Oishi, S.; Tobita, S. Reevaluation of Absolute Luminescence Quantum Yields of Standard Solutions Using a Spectrometer with an Integrating Sphere and a Back-Thinned CCD Detector. *Phys. Chem. Chem. Phys.* **2009**, *11*, 9850–9860.

(135) Murov, S. L.; Carmichael, I.; Hug, G. L. *Handbook of Photochemistry, 2nd Ed.*; Marcel Dekker: New York, 1993.

(136) Hohenberg, P.; Kohn, W. Inhomogeneous Electron Gas. *Phys. Rev.* **1964**, *136* (3B), B864–B871. https://doi.org/10.1103/PhysRev.136.B864.

(137) Kohn, W.; Sham, L. J. Self-Consistent Equations Including Exchange and Correlation Effects. *Phys. Rev.* **1965**, *140* (4A), A1133–A1138. https://doi.org/10.1103/PhysRev.140.A1133.

(138) Bühl, M.; Kabrede, H. Geometries of Transition-Metal Complexes from Density-Functional Theory. *J. Chem. Theory Comput.* **2006**, *2* (5), 1282–1290. https://doi.org/10.1021/ct6001187.

(139) Waller, M. P.; Braun, H.; Hojdis, N.; Bühl, M. Geometries of Second-Row Transition-Metal Complexes from Density-Functional Theory. *J. Chem. Theory Comput.* **2007**, *3* (6), 2234–2242. https://doi.org/10.1021/ct700178y.

(140) Bühl, M.; Reimann, C.; Pantazis, D. A.; Bredow, T.; Neese, F. Geometries of Third-Row Transition-Metal Complexes from Density-Functional Theory. *J. Chem. Theory Comput.* **2008**, *4* (9), 1449–1459. https://doi.org/10.1021/ct800172j.

(141) de Souza, B.; Farias, G.; Neese, F.; Izsák, R. Predicting Phosphorescence Rates of Light Organic Molecules Using Time-Dependent Density Functional Theory and the Path Integral Approach to Dynamics. *J. Chem. Theory Comput.* **2019**, *15* (3), 1896–1904. https://doi.org/10.1021/acs.jctc.8b00841.

(142) de Souza, B.; Neese, F.; Izsák, R. On the Theoretical Prediction of Fluorescence Rates from First Principles Using the Path Integral Approach. *J. Chem. Phys.* **2018**, *148* (3), 034104. https://doi.org/10.1063/1.5010895.

(143) Petrenko, T.; Neese, F. Analysis and Prediction of Absorption Band Shapes, Fluorescence Band Shapes, Resonance Raman Intensities, and Excitation Profiles Using the Time-Dependent Theory of Electronic Spectroscopy. *J. Chem. Phys.* **2007**, *127* (16), 164319. https://doi.org/10.1063/1.2770706.

(144) Wenger, O. S. Is Iron the New Ruthenium? *Chem. – Eur. J.* **2020**, *25*, 6043–6052.

(145) Baková, R.; Chergui, M.; Daniel, C.; Vlček Jr., A.; Záliš, S. Relativistic Effects in Spectroscopy and Photophysics of Heavy-Metal Complexes Illustrated by Spin–Orbit Calculations of [Re(Imidazole)(CO)3(Phen)]+. *Coord. Chem. Rev.* **2011**, *255* (7–8), 975–989. https://doi.org/10.1016/j.ccr.2010.12.027.

(146) Giesbrecht, P. K.; Nemez, D. B.; Herbert, D. E. Electrochemical Hydrogenation of a Benzannulated Pyridine to a Dihydropyridine in Acidic Solution. *Chem. Commun.* **2018**, *54* (4), 338–341. https://doi.org/10.1039/c7cc07907a.

(147) Mandapati, P.; Giesbrecht, P. K.; Davis, R. L.; Herbert, D. E. Phenanthridine-Containing Pincer-like Amido Complexes of Nickel, Palladium, and Platinum. *Inorg. Chem.* **2017**, *56* (6), 3674–3685. https://doi.org/10.1021/acs.inorgchem.7b00075.

(148) Mondal, R.; Lozada, I. B.; Davis, R. L.; Williams, J. A. G.; Herbert, D. E. Exploiting Synergy between Ligand Design and Counterion Interactions to Boost Room Temperature Phosphorescence from Cu(i) Compounds. *J. Mater. Chem. C* **2019**, *7* (13), 3772–3778. https://doi.org/10.1039/C9TC00040B.

(149) Mandapati, P.; Braun, J. D.; Killeen, C.; Davis, R. L.; Williams, J. A. G.; Herbert, D. E. Luminescent Platinum(II) Complexes of N^ N-^ N Amido Ligands with Benzannulated N-Heterocyclic Donor Arms: Quinolines Offer Unexpectedly Deeper Red Phosphorescence than Phenanthridines. *Inorg. Chem.* **2019**, *58* (21), 14808–14817. https://doi.org/10.1021/acs.inorgchem.9b02480.

(150) Lozada, I. B.; Murray, T.; Herbert, D. E. Monomeric Zinc(II) Amide Complexes Supported by Bidentate, Benzannulated Phenanthridine Amido Ligands. *Polyhedron* **2019**, *161*, 261–267. https://doi.org/10.1016/j.poly.2019.01.023.

(151) Braun, J. D.; Lozada, I. B.; Kolodziej, C.; Burda, C.; Newman, K. M. E.; van Lierop, J.; Davis, R. L.; Herbert, D. E. Iron(Ii) Coordination Complexes with Panchromatic Absorption and Nanosecond Charge-Transfer Excited State Lifetimes. *Nat. Chem.* **2019**, *11* (12), 1144–1150. https://doi.org/10.1038/s41557-019-0357-z.

(152) Mondal, R.; Lozada, I. B.; Davis, R. L.; Williams, J. A. G.; Herbert, D. E. Site-Selective Benzannulation of N-Heterocycles in Bidentate Ligands Leads to Blue-Shifted Emission from [(P^N)Cu]2(μ-X)2 Dimers. *Inorg. Chem.* **2018**, *57* (9), 4966–4978. https://doi.org/10.1021/acs.inorgchem.7b03223.

(153) Mondal, R.; Giesbrecht, P. K.; Herbert, D. E. Nickel(II), Copper(I) and Zinc(II) Complexes Supported by a (4-Diphenylphosphino)Phenanthridine Ligand. *Polyhedron* **2016**, *108*, 156–162. https://doi.org/10.1016/j.poly.2015.10.051.

(154) Stufkens, D. J.; Vlček, A. Ligand-Dependent Excited State Behaviour of Re(I) and Ru(II) Carbonyl-Diimine Complexes. *Coord. Chem. Rev.* **1998**, *177* (1), 127–179. https://doi.org/10.1016/s0010-8545(98)00132-5.

(155) Vlček, A. Ultrafast Excited-State Processes in Re(I) Carbonyl-Diimine Complexes: From Excitation to Photochemistry. *Top Organomet Chem* **2010**, *29* (May 2009), 73–114. https://doi.org/10.1007/3418.

(156) Mandapati, P.; Braun, J. D.; Killeen, C.; Davis, R. L.; Williams, J. A. G.; Herbert, D. E. Luminescent Platinum(II) Complexes of N⌃N-⌃N Amido Ligands with Benzannulated N-Heterocyclic Donor Arms: Quinolines Offer Unexpectedly Deeper Red Phosphorescence than Phenanthridines. *Inorg Chem* **2019**, *58*, 14808–14817.

(157) Dixon, I. M.; Khan, S.; Alary, F.; Boggio-Pasqua, M.; Heully, J.-L. Probing the Photophysical Capability of Mono and Bis(Cyclometallated) Fe(II) Polypyridine Complexes Using Inexpensive Ground State DFT. *Dalton Trans.* **2014**, *43*, 15898–15905.

(158) Zhang, K.; Ash, R.; Girolami, G. S.; Vura-Weis, J. Tracking the Metal-Centered Triplet in Photoinduced Spin Crossover of Fe(Phen)32+ with Tabletop Femtosecond M-Edge X-Ray Absorption Near-Edge Structure Spectroscopy. *J. Am. Chem. Soc.* **2019**, *141*, 17180–17188.

(159) Juban, E. A.; Smeigh, A. L.; Monat, J. E.; McCusker, J. K. Ultrafast Dynamics of Ligand-Field Excited States. *Coord Chem Rev* **2006**, *250*, 1783–1791.

(160) Gryn'ova, G.; Coote, M. L.; Corminboeuf, C. Theory and Practice of Uncommon Molecular Electronic Configurations. *WIREs Comput. Mol. Sci.* **2015**, *5* (6), 440–459. https://doi.org/10.1002/wcms.1233.

(161) Kaim, W. Manifestations of Noninnocent Ligand Behavior. *Inorg Chem* **2011**, *50* (20), 9752–9765.

(162) Bowman, D. N.; Jakubikova, E. Low-Spin versus High-Spin Ground State in Pseudo-Octahedral Iron Complexes. *Inorg. Chem.* **2012**, *51*, 6011–6019.

(163) Ashley, D. C.; Jakubikova, E. Ironing out the Photochemical and Spin-Crossover Behavior of Fe(II) Coordination Compounds with Computational Chemistry. *Coord. Chem. Rev.* **2017**, *337*, 97–111.

(164) Reiher, M.; Salomon, O.; Artur Hess, B. Reparameterization of Hybrid Functionals Based on Energy Differences of States of Different Multiplicity. *Theor. Chem. Acc.* **2001**, *107*, 48–55.

(165) Jakubikova, E.; Bowman, D. N. Fe(II)-Polypyridines as Chromophores in Dye-Sensitized Solar Cells: A Computational Perspective. *Acc. Chem. Res.* **2015**, *48*, 1441–1449.

(166) Nemykin, V. N.; Hadt, R. G. Influence of Hartree−Fock Exchange on the Calculated Mössbauer Isomer Shifts and Quadrupole Splittings in Ferrocene Derivatives Using Density Functional Theory. *Inorg. Chem.* **2006**, *45*, 8297–8307.

(167) Zhao, Y.; Truhlar, D. G. A New Local Density Functional for Main-Group Thermochemistry, Transition Metal Bonding, Thermochemical Kinetics, and Noncovalent Interactions. *J. Chem. Phys.* **2006**, *125*, 194101.

(168) Cohen, A. J.; Handy, N. C. Dynamic Correlation. *Mol. Phys.* **2001**, *99*, 607–615.

(169) Zhao, Y.; Truhlar, D. G. The M06 Suite of Density Functionals for Main Group Thermochemistry, Thermochemical Kinetics, Noncovalent Interactions, Excited States, and Transition Elements: Two New Functionals and Systematic Testing of Four M06-Class Functionals and 12 Other Functionals. *Theor. Chem. Acc.* **2008**, *120*, 215–241.

(170) Ditchfield, R.; Hehre, W. J.; Pople, J. A. Self-Consistent Molecular-Orbital Methods. IX. Extended Gaussian-Type Basis for Molecular-Orbital Studies of Organic Molecules. *J. Chem. Phys.* **1971**, *54*, 724–728. https://doi.org/10.1063/1.1674902.

(171) Hehre, W. J.; Ditchfield, R.; Pople, J. A. Self-Consistent Molecular Orbital Methods. XII. Further Extensions of Gaussian-Type Basis Sets for Use in Molecular Orbital Studies of Organic Molecules. *J. Chem. Phys.* **1972**, *56*, 2257–2261.

(172) Hariharan, P. C.; Pople, J. A. Influence of Polarization Functions on MO Hydrogenation Energies. *Theor. Chim. Acta* **1973**, *28*, 213–222.

(173) Clark, T.; Chandrasekhar, J.; Spitznagel, G. W.; Schleyer, P. v R. Efficient Diffuse Function-Augmented Basis Sets for Anion Calculations. III. The 3-21 + G Basis Set for First-Row Elements, Lithium to Fluorine. *J. Comput. Chem.* **1983**, *4*, 294–301.

(174) Rassolov, V. A.; Pople, J. A.; Ratner, M. A.; Windus, T. L. 6-31G* Basis Set for Atoms K through Zn. *J. Chem. Phys.* **1998**, *109*, 1223–1229.

(175) Zhao, Y.; Truhlar, D. G. A New Local Density Functional for Main-Group Thermochemistry, Transition Metal Bonding, Thermochemical Kinetics, and Noncovalent Interactions. *J. Chem. Phys.* **2006**, *125* (19), 194101. https://doi.org/10.1063/1.2370993.

(176) Krishnan, R.; Binkley, J. S.; Seeger, R.; Pople, J. A. Self-consistent Molecular Orbital Methods. XX. A Basis Set for Correlated Wave Functions. *J. Chem. Phys.* **1980**, *72* (1), 650–654. https://doi.org/10.1063/1.438955.

(177) Clark, T.; Chandrasekhar, J.; Spitznagel, G. W.; Schleyer, P. V. R. Efficient Diffuse Function-Augmented Basis Sets for Anion Calculations. III. The 3-21+G Basis Set for First-Row Elements, Li-F. *J. Comput. Chem.* **1983**, *4* (3), 294–301. https://doi.org/10.1002/jcc.540040303.

(178) Dennington, Roy; Keith, Todd A.; Millam, John M. *GaussView, Version 6*; Semichem Inc.: Shawnee Mission, KS, 2016.

(179) Soda, T.; Kitagawa, Y.; Onishi, T.; Takano, Y.; Shigeta, Y.; Nagao, H.; Yoshioka, Y.; Yamaguchi, K. Ab Initio Computations of Effective Exchange Integrals for H–H, H–He–H and Mn2O2 Complex: Comparison of Broken-Symmetry Approaches. *Chem. Phys. Lett.* **2000**, *319* (3–4), 223–230. https://doi.org/10.1016/S0009-2614(00)00166-4.

(180) Yamaguchi, K.; Takahara, Y.; Fueno, T. Ab-Initio Molecular Orbital Studies of Structure and Reactivity of Transition Metal-OXO Compounds. In *Applied Quantum Chemistry*; Smith, V. H., Schaefer, H. F., Morokuma, K., Eds.; Springer Netherlands: Dordrecht, 1986; pp 155–184. https://doi.org/10.1007/978-94-009-4746-7_11.

(181) Heydová, R.; Gindensperger, E.; Romano, R.; Sýkora, J.; Vlček, A.; Záliš, S.; Daniel, C. Spin-Orbit Treatment of UV-Vis Absorption Spectra and Photophysics of Rhenium(I) Carbonyl-Bipyridine Complexes: MS-CASPT2 and TD-DFT Analysis. *J. Phys. Chem. A* **2012**, *116* (46), 11319–11329. https://doi.org/10.1021/jp305461z.

(182) Ronca, E.; De Angelis, F.; Fantacci, S. Time-Dependent Density Functional Theory Modeling of Spin-Orbit Coupling in Ruthenium and Osmium Solar Cell Sensitizers. *J. Phys. Chem. C* **2014**, *118* (30), 17067–17078. https://doi.org/10.1021/jp500869r.

(183) Mai, S.; Gattuso, H.; Fumanal, M.; Muñoz-Losa, A.; Monari, A.; Daniel, C.; González, L. Excited-States of a Rhenium Carbonyl Diimine Complex: Solvation Models, Spin-Orbit Coupling, and Vibrational Sampling Effects. *Phys. Chem. Chem. Phys.* **2017**, *19* (40), 27240–27250. https://doi.org/10.1039/c7cp05126c.

(184) Shi, L. L.; Liao, Y.; Zhao, L.; Su, Z. M.; Kan, Y. H.; Yang, G. C.; Yang, S. Y. Theoretical Studies on the Electronic Structure and Spectral Properties of Versatile Diarylethene-Containing 1,10-Phenanthroline Ligands and Their Rhenium(I) Complexes. *J. Organomet. Chem.* **2007**, *692* (24), 5368–5374. https://doi.org/10.1016/j.jorganchem.2007.08.031.

(185) Silva-Junior, M. R.; Schreiber, M.; Sauer, S. P. A.; Thiel, W. Benchmarks for Electronically Excited States: Time-Dependent Density Functional Theory and Density Functional Theory Based Multireference Configuration Interaction. *J. Chem. Phys.* **2008**, *129* (10). https://doi.org/10.1063/1.2973541.

(186) Jacquemin, D.; Perpète, E. A.; Ciofini, I.; Adamo, C. Assessment of Functionals for TD-DFT Calculations of Singlet-Triplet Transitions. *J. Chem. Theory Comput.* **2010**, *6* (5), 1532–1537. https://doi.org/10.1021/ct100005d.

(187) Santoro, F.; Lami, A.; Improta, R.; Barone, V. Effective Method to Compute Vibrationally Resolved Optical Spectra of Large Molecules at Finite Temperature in the Gas Phase and in Solution. *J. Chem. Phys.* **2007**, *126* (18). https://doi.org/10.1063/1.2721539.

(188) Tozer, D. J.; Handy, N. C. On the Determination of Excitation Energies Using Density Functional Theory. *Phys. Chem. Chem. Phys.* **2000**, *2* (10), 2117–2121. https://doi.org/10.1039/a910321j.

(189) Chibani, S.; Charaf-Eddin, A.; Le Guennic, B.; Jacquemin, D. Boranil and Related NBO Dyes: Insights From Theory. *J. Chem. Theory Comput.* **2013**, *9*, 3127–3135.

(190) Mondal, R.; Giesbrecht, P. K.; Herbert, D. E. Nickel(II), Copper(I) and Zinc(II) Complexes Supported by a (4-Diphenylphosphino)Phenanthridine Ligand. *Polyhedron* **2016**, *108*, 156–162.

(191) Mondal, R.; Lozada, I. B.; Davis, R. L.; Williams, J. A. G.; Herbert, D. E. Site-Selective Benzannulation of N-Heterocycles in Bidentate Ligands Leads to Blue-Shifted Emission from [(*P^N*)Cu]$_2$(μ-X)$_2$ Dimers. *Inorg Chem* **2018**, *57*, 4966–4978.

(192) Gaire, S.; Ortiz, R. J.; Schrage, B. R.; Lozada, I. B.; Mandapati, P.; Osinski, A. J.; Herbert, D. E.; Ziegler, C. J. (8-Amino)Quinoline and (4-Amino)Phenanthridine Complexes of Re(CO)3 Halides. *J. Organomet. Chem.* **2020**, *921*, 121338.

(193) Tomasi, J.; Mennucci, B.; Cammi, R. Quantum Mechanical Continuum Solvation Models. *Chem Rev* **2005**, *105*, 2999–3094.

(194) Melenbacher, A.; Dhindsa, J. S.; Gilroy, J. B.; Stillman, M. J. Unveiling the Hidden, Dark, and Short Life of a Vibronic State in a Boron Difluoride Formazanate Dye. *Angew. Chem. Int. Ed.* **2019**, *58* (43), 15339–15343.

(195) El-Sayed, M. A. Spin—Orbit Coupling and the Radiationless Processes in Nitrogen Heterocyclics. *J. Chem. Phys.* **1963**, *38* (12), 2834–2838.

(196) Braun, J. D.; Lozada, I. B.; Kolodziej, C.; Burda, C.; Newman, K. M. E.; van Lierop, J.; Davis, R. L.; Herbert, D. E. Iron(II) Coordination Complexes with Panchromatic Absorption and Nanosecond Charge-Transfer Excited State Lifetimes. *Nat. Chem.* **2019**, *11*, 1144–1150.

(197) Larsen, C. B.; Braun, J. D.; Lozada, I. B.; Kunnus, K.; Biasin, E.; Kolodziej, C.; Burda, C.; Cordones, A. A.; Gaffney, K. J.; Herbert, D. E. Reduction of Electron Repulsion in Highly Covalent Fe-Amido Complexes Counteracts the Impact of a Weak Ligand Field on Excited-State Ordering. *J. Am. Chem. Soc.* **2021**, *143*, 20645–20656.

(198) Das, S.; Thornbury, W. G.; Bartynski, A. N.; Thompson, M. E.; Bradforth, S. E. Manipulating Triplet Yield through Control of Symmetry-Breaking Charge Transfer. *J. Phys. Chem. Lett.* **2018**, *9*, 3264–3270.

(199) Trinh, C.; Kirlikovali, K.; Das, S.; Ener, M. E.; Gray, H. B.; Djurovich, P.; Bradforth, S. E.; Thompson, M. E. Symmetry-Breaking Charge Transfer of Visible Light Absorbing Systems: Zinc Dipyrrins. *J. Phys. Chem. C* **2014**, *118*, 21834–21845.

356

(200) Kellogg, M.; Akil, A.; Muthiah Ravinson, D. S.; Estergreen, L.; Bradforth, S. E.; Thompson, M. E. Symmetry Breaking Charge Transfer as a Means to Study Electron Transfer with No Driving Force. *Faraday Discuss.* **2019**, *216*, 379–394.

(201) Mahmood, Z.; Rehmat, N.; Ji, S.; Zhao, J.; Sun, S.; Di Donato, M.; Li, M.; Teddei, M.; Huo, Y. Tuning the Triplet Excited State of Bis(Dipyrrin) Zinc(II) Complexes: Symmetry Breaking Charge Transfer Architecture with Exceptionally Long Lived Triplet State for Upconversion. *Chem. – Eur. J.* **2020**, *26*, 14912–14918.

(202) Weller, A. Photoinduced Electron Transfer in Solution: Exciplex and Radical Ion Pair Formation Free Enthalpies and Their Solvent Dependence By. *Zeitshcrift Phys. Chem. N. F.* **1982**, *133*, 93–98.

(203) Rehm, D.; Weller, A. Kinetics of Fluorescence Quenching by Electron and H-Atom Transfer. *Isr. J. Chem.* **1970**, *8*, 259–271.

(204) Vauthey, E. Photoinduced Symmetry-Breaking Charge Separation. *ChemPhysChem* **2012**, *13*, 2001–2011.

(205) Smith, A. R. G.; Burn, P. L.; Powell, B. J. Spin–Orbit Coupling in Phosphorescent Iridium(III) Complexes. *ChemPhysChem* **2011**, *12*, 2429–2438.

(206) Ronca, E.; De Angelis, F.; Fantacci, S. Time-Dependent Density Functional Theory Modeling of Spin–Orbit Coupling in Ruthenium and Osmium Solar Cell Sensitizers. *J. Phys. Chem. C* **2014**, *118*, 17067–17078.

(207) Gourlaouen, C.; Daniel, C. Spin–Orbit Effects in Square-Planar Pt(II) Complexes with Bidentate and Terdentate Ligands: Theoretical Absorption/Emission Spectroscopy. *Dalton Trans* **2014**, *43*, 17806–17819.

(208) Braun, J. D.; Lozada, I. B.; Herbert, D. E. In Pursuit of Panchromatic Absorption in Metal Coordination Complexes: Experimental Delineation of the HOMO Inversion Model Using Pseudo-Octahedral Complexes of Diarylamido Ligands. *Inorg. Chem.* **2020**, *59*, 17746–17757.

(209) Hayashi, M.; Takahashi, Y.; Yoshida, Y.; Sugimoto, K.; Kitagawa, H. Role of D-Elements in a Proton–Electron Coupling of d–π Hybridized Electron Systems. *J. Am. Chem. Soc.* **2019**, *141*, 11686–11693.

(210) Spencer, M.; Santoro, A.; Freeman, G. R.; Díez, Á.; Murray, P. R.; Torroba, J.; Whitwood, A. C.; Yellowlees, L. J.; Williams, J. A. G.; Bruce, D. W. Phosphorescent, Liquid-Crystalline Complexes of Platinum(II): Influence of the β-Diketonate Co-Ligand on Mesomorphism and Emission Properties. *Dalton Trans.* **2012**, *41*, 14244–14256.

(211) Neese, F. The ORCA Program System. *WIREs Comput. Mol. Sci.* **2012**, *2*, 73–78.

(212) Neese, F. Software Update: The ORCA Program System, Version 4.0. *WIREs Comput. Mol. Sci.* **2018**, *8*, e1327.

(213) Frisch, M. J.; Trucks, G. W.; Schlegel, H. B.; Scuseria, G. E.; Robb, M. A.; Cheeseman, J. R.; Scalmani, G.; Barone, V.; Petersson, G. A.; Nakatsuji, H.; Li, X.; Caricato, M.; Marenich, A. V.; Bloino, J.; Janesko, B. G.; Gomperts, R.; Mennucci, B.; Hratchian, H. P.; Ortiz, J. V.; Izmaylov, A. F.; Sonnenberg, J. L.; Williams; Ding, F.; Lipparini, F.; Egidi, F.; Goings, J.; Peng, B.; Petrone, A.; Henderson, T.; Ranasinghe, D.; Zakrzewski, V. G.; Gao, J.; Rega, N.; Zheng, G.; Liang, W.; Hada, M.; Ehara, M.; Toyota, K.; Fukuda, R.; Hasegawa, J.; Ishida, M.; Nakajima, T.; Honda, Y.; Kitao, O.; Nakai, H.; Vreven, T.; Throssell, K.; Montgomery Jr., J. A.; Peralta, J. E.; Ogliaro, F.; Bearpark, M. J.; Heyd, J. J.; Brothers, E. N.; Kudin, K. N.; Staroverov, V. N.; Keith, T. A.; Kobayashi, R.; Normand, J.;

Raghavachari, K.; Rendell, A. P.; Burant, J. C.; Iyengar, S. S.; Tomasi, J.; Cossi, M.; Millam, J. M.; Klene, M.; Adamo, C.; Cammi, R.; Ochterski, J. W.; Martin, R. L.; Morokuma, K.; Farkas, O.; Foresman, J. B.; Fox, D. J. *Gaussian 16 Rev. C.01*; Wallingford, CT, 2016.

(214) Marenich, A. V.; Cramer, C. J.; Truhlar, D. G. Universal Solvation Model Based on Solute Electron Density and on a Continuum Model of the Solvent Defined by the Bulk Dielectric Constant and Atomic Surface Tensions. *J Phys Chem B* **2009**, *113*, 6378–6396.

(215) Grimme, S.; Ehrlich, S.; Goerigk, L. Effect of the Damping Function in Dispersion Corrected Density Functional Theory. *J. Comput. Chem.* **2011**, *32*, 1456–1465.

(216) Becke, A. D. Density-Functional Thermochemistry. III. The Role of Exact Exchange. *J Chem Phys* **1993**, *98*, 5648–5652.

(217) Lee, C.; Yang, W.; Parr, R.G. Development of the Colle-Salvetti Correlation-Energy Formula into a Functional of the Electron Density. *Phys. Rev. B Condens. Matter* **1988**, *37*, 785–789.

(218) Vosko, S. H.; Wilk, L.; Nusair, M. Accurate Spin-Dependent Electron Liquid Correlation Energies for Local Spin Density Calculations: A Critical Analysis. *Can. J. Phys.* **1980**, *58*, 1200–1211.

(219) Stephens, P. J.; Devlin, F. J.; Chabalowski, C. F.; Frisch, M. J. Ab Initio Calculation of Vibrational Absorption and Circular Dichroism Spectra Using Density Functional Force Fields. *J Phys Chem* **1994**, *98*, 11623–11627.

(220) Weigend, F.; Ahlrichs, R. Balanced Basis Sets of Split Valence, Triple Zeta Valence and Quadruple Zeta Valence Quality for H to Rn: Design and Assessment of Accuracy. *Phys Chem Chem Phys* **2005**, *7*, 3297–3305.

(221) Tao, J.; Perdew, J. P.; Staroverov, V. N.; Scuseria, G. E. Climbing the Density Functional Ladder: Nonempirical Meta--Generalized Gradient Approximation Designed for Molecules and Solids. *Phys. Rev. Lett.* **2003**, *91*, 146401.

(222) Staroverov, V. N.; Scuseria, G. E.; Tao, J.; Perdew, J. P. Comparative Assessment of a New Nonempirical Density Functional: Molecules and Hydrogen-Bonded Complexes. *J. Chem. Phys.* **2003**, *119*, 12129–12137.

(223) O'Boyle, N. M.; Tenderholt, A. L.; Langner, K. M. Software News and Updates Cclib: A Library for Package-Independent Computational Chemistry Algorithms. *J Comput Chem* **2008**, *29*, 839–845.

(224) Lu, T.; Chen, F. Multiwfn: A Multifunctional Wavefunction Analyzer. *J Comput Chem* **2012**, *33*, 580–592.

(225) Xiao, M; Lu, T. Generalized Charge Decomposition Analysis (GCDA) Method. *J. Adv. Phys. Chem.* **2015**, *4*, 111–124.

(226) Frisch, M. J.; Trucks, G. W.; Schlegel, H. B.; Scuseria, G. E.; Robb, M. A.; Cheeseman, J. R.; Scalmani, G.; Barone, V.; Petersson, G. A.; Nakatsuji, H.; Li, X.; Caricato, M.; Marenich, A. V.; Bloino, J.; Janesko, B. G.; Gomperts, R.; Mennucci, B.; Hratchian, H. P.; Ortiz, J. V.; Izmaylov, A. F.; Sonnenberg, J. L.; Williams-Young, D.; Ding, F.; Lipparini, F.; Egidi, F.; Goings, J.; Peng, B.; Petrone, A.; Henderson, T.; Ranasinghe, D.; Zakrzewski, V. G.; Gao, J.; Rega, N.; Zheng, G.; Liang, W.; Hada, M.; Ehara, M.; Toyota, K.; Fukuda, R.; Hasegawa, J.; Ishida, M.; Nakajima, T.; Honda, Y.; Kitao, O.; Nakai, H.; Vreven, T.; Throssell, K.; Montgomery, J. A.; Peralta, J. E.; Ogliaro, F.; Bearpark, M. J.; Heyd, J. J.; Brothers, E. N.; Kudin, K. N.; Staroverov, V. N.; Keith, T. A.; Kobayashi, R.; Normand, J.;

Raghavachari, K.; Rendell, A. P.; Burant, J. C.; Iyengar, S. S.; Tomasi, J.; Cossi, M.; Millam, J. M.; Klene, M.; Adamo, C.; Cammi, R.; Ochterski, J. W.; Martin, R. L.; Morokuma, K.; Farkas, O.; Foresman, J. B.; Fox, D. J. *Gaussian 16, Revision B.01*; Gaussian 16, Revision B.01, Gaussian, Inc., Wallingford CT; Gaussian, Inc.: Wallingford CT, 2016.

(227) Adamo, C.; Barone, V. Toward Reliable Density Functional Methods without Adjustable Parameters: The PBE0 Model. *J. Chem. Phys.* **1999**, *110* (13), 6158–6170.

(228) Andrae, D.; Huermann, U.; Dolg, M.; Stoll, H.; Preu, H. Energy-Adjustedab Initio Pseudopotentials for the Second and Third Row Transition Elements. *Theor. Chim. Acta* **1990**, *77*, 123–141.

(229) Yanai, T.; Tew, D. P.; Handy, N. C. A New Hybrid Exchange–Correlation Functional Using the Coulomb-Attenuating Method (CAM-B3LYP). *Chem. Phys. Lett.* **2004**, *393*, 51–57.

(230) Neese, F.; Wennmohs, F.; Hansen, A.; Becker, U. Efficient, Approximate and Parallel Hartree–Fock and Hybrid DFT Calculations. A 'Chain-of-Spheres' Algorithm for the Hartree–Fock Exchange. *Chem. Phys.* **2009**, *356*, 98–109.

(231) Lenthe, E. van; Baerends, E. J.; Snijders, J. G. Relativistic Regular Two-component Hamiltonians. *J. Chem. Phys.* **1993**, *99*, 4597–4610.

(232) Weigend, F. Accurate Coulomb-Fitting Basis Sets for H to Rn. *Phys. Chem. Chem. Phys.* **2006**, *8*, 1057.

(233) Pantazis, D. A.; Neese, F. All-Electron Scalar Relativistic Basis Sets for the Lanthanides. *J. Chem. Theory Comput.* **2009**, *5*, 2229–2238.

(234) Pantazis, D. A.; Neese, F. All-Electron Scalar Relativistic Basis Sets for the Actinides. *J. Chem. Theory Comput.* **2011**, *7*, 677–684.

(235) Pantazis, D. A.; Chen, X.-Y.; Landis, C. R.; Neese, F. All-Electron Scalar Relativistic Basis Sets for Third-Row Transition Metal Atoms. *J. Chem. Theory Comput.* **2008**, *4*, 908–919.

(236) Hirshfeld, F. L. Bonded-Atom Fragments for Describing Molecular Charge Densities. *Theor. Chim. Acta* **1977**, *44*, 129–138.

(237) Hanwell, M. D.; Curtis, D. E.; Lonie, D. C.; Vandermeersch, T.; Zurek, E.; Hutchison, G. R. Avogadro: An Advanced Semantic Chemical Editor, Visualization, and Analysis Platform. *J Cheminf* **2012**, *4*, 17.

(238) Frisch, M. J.; Trucks, G. W.; Schlegel, H. B.; Scuseria, G. E.; Robb, M. A.; Cheeseman, J. R.; Scalmani, G.; Barone, V.; Petersson, G. A.; Nakatsuji, H.; Li, X.; Caricato, M.; Marenich, A. V.; Bloino, J.; Janesko, B. G.; Gomperts, R.; Mennucci, B.; Hratchian, H. P.; Ortiz, J. V.; Izmaylov, A. F.; Sonnenberg, J. L.; Williams; Ding, F.; Lipparini, F.; Egidi, F.; Goings, J.; Peng, B.; Petrone, A.; Henderson, T.; Ranasinghe, D.; Zakrzewski, V. G.; Gao, J.; Rega, N.; Zheng, G.; Liang, W.; Hada, M.; Ehara, M.; Toyota, K.; Fukuda, R.; Hasegawa, J.; Ishida, M.; Nakajima, T.; Honda, Y.; Kitao, O.; Nakai, H.; Vreven, T.; Throssell, K.; Montgomery Jr., J. A.; Peralta, J. E.; Ogliaro, F.; Bearpark, M. J.; Heyd, J. J.; Brothers, E. N.; Kudin, K. N.; Staroverov, V. N.; Keith, T. A.; Kobayashi, R.; Normand, J.; Raghavachari, K.; Rendell, A. P.; Burant, J. C.; Iyengar, S. S.; Tomasi, J.; Cossi, M.; Millam, J. M.; Klene, M.; Adamo, C.; Cammi, R.; Ochterski, J. W.; Martin, R. L.; Morokuma, K.; Farkas, O.; Foresman, J. B.; Fox, D. J. Gaussian 16 Rev. C.01, 2016.

(239) Marenich, A. V.; Cramer, C. J.; Truhlar, D. G. Universal Solvation Model Based on Solute Electron Density and on a Continuum Model of the Solvent Defined by the Bulk Dielectric Constant and Atomic Surface Tensions. *J Phys Chem B* **2009**, *113*, 6378–6396.

(240) Dennington, Roy; Keith, Todd A.; Millam, John M. GaussView, Version 6, 2016.

(241) O'Boyle, N. M.; Tenderholt, A. L.; Langner, K. M. Software News and Updates Cclib: A Library for Package-Independent Computational Chemistry Algorithms. *J Comput Chem* **2008**, *29*, 839–845.

(242) Lu, T.; Chen, F. Multiwfn: A Multifunctional Wavefunction Analyzer. *J Comput Chem* **2012**, *33*, 580–592.

(243) Tian, L. U.; Fei-Wu, C. Calculation of Molecular Orbital Composition. *Acta Chim. Sin.* **2011**, *69*, 2393.

(244) Frisch, M. J.; Trucks, G. W.; Schlegel, H. B.; Scuseria, G. E.; Robb, M. A.; Cheeseman, J. R.; Scalmani, G.; Barone, V.; Petersson, G. A.; Nakatsuji, H.; Li, X.; Caricato, M.; Marenich, A. V.; Bloino, J.; Janesko, B. G.; Gomperts, R.; Mennucci, B.; Hratchian, H. P.; Ortiz, J. V.; Izmaylov, A. F.; Sonnenberg, J. L.; Williams-Young, D.; Ding, F.; Lipparini, F.; Egidi, F.; Goings, J.; Peng, B.; Petrone, A.; Henderson, T.; Ranasinghe, D.; Zakrzewski, V. G.; Gao, J.; Rega, N.; Zheng, G.; Liang, W.; Hada, M.; Ehara, M.; Toyota, K.; Fukuda, R.; Hasegawa, J.; Ishida, M.; Nakajima, T.; Honda, Y.; Kitao, O.; Nakai, H.; Vreven, T.; Throssell, K.; Montgomery Jr., J. A.; Peralta, J. E.; Ogliaro, F.; Bearpark, M. J.; Heyd, J. J.; Brothers, E. N.; Kudin, K. N.; Staroverov, V. N.; Keith, T. A.; Kobayashi, R.; Normand, J.; Raghavachari, K.; Rendell, A. P.; Burant, J. C.; Iyengar, S. S.; Tomasi, J.; Cossi, M.; Millam, J. M.; Klene, M.; Adamo, C.; Cammi, R.; Ochterski, J. W.; Martin, R. L.; Morokuma, K.; Farkas, O.; Foresman, J. B.; Fox, D. J. Gaussian 16 Rev. C.01, 2016.

(245) Marenich, A. V.; Cramer, C. J.; Truhlar, D. G. Universal Solvation Model Based on Solute Electron Density and on a Continuum Model of the Solvent Defined by the Bulk Dielectric Constant and Atomic Surface Tensions. *J Phys Chem B* **2009**, *113*, 6378–6396.

(246) Grimme, S.; Ehrlich, S.; Goerigk, L. Effect of the Damping Function in Dispersion Corrected Density Functional Theory. *J. Comput. Chem.* **2011**, *32*, 1456–1465.

(247) Weigend, F.; Ahlrichs, R. Balanced Basis Sets of Split Valence, Triple Zeta Valence and Quadruple Zeta Valence Quality for H to Rn: Design and Assessment of Accuracy. *Phys. Chem. Chem. Phys.* **2005**, *7*, 3297.

(248) Allouche, A.-R. Gabedit—A Graphical User Interface for Computational Chemistry Softwares. *J. Comput. Chem.* **2011**, *32*, 174–182.

(249) Liu, Z.; Lu, T.; Chen, Q. An Sp-Hybridized All-Carboatomic Ring, Cyclo[18]Carbon: Electronic Structure, Electronic Spectrum, and Optical Nonlinearity. *Carbon* **2020**, *165*, 461–467.

(250) Lu, T.; Chen, F. Multiwfn: A Multifunctional Wavefunction Analyzer. *J Comput Chem* **2012**, *33*, 580–592.

(251) Dennington, Roy; Keith, Todd A.; Millam, John M. GaussView, Version 6, 2016.

(252) Becke, A. D. Density-functional Thermochemistry. III. The Role of Exact Exchange. *J. Chem. Phys.* **1998**, *98*, 5648.

(253) Lee, C.; Yang, W.; Parr, R. G. Development of the Colle-Salvetti Correlation-Energy Formula into a Functional of the Electron Density. *Phys. Rev. B* **1988**, *37*, 785–789.

(254) Vosko, S. H.; Wilk, L.; Nusair, M. Accurate Spin-Dependent Electron Liquid Correlation Energies for Local Spin Density Calculations: A Critical Analysis. *Can. J. Phys.* **1980**, *58*, 1200–1211.

(255) Amin, E. A.; Truhlar, D. G. Zn Coordination Chemistry: Development of Benchmark Suites for Geometries, Dipole Moments, and Bond Dissociation Energies and Their Use To Test

and Validate Density Functionals and Molecular Orbital Theory. *J. Chem. Theory Comput.* **2008**, *4*, 75–85.

(256) Otto, S.; Moll, J.; Förster, C.; Geißler, D.; Wang, C.; Resch-Genger, U.; Heinze, K. Three-in-One Crystal: The Coordination Diversity of Zinc Polypyridine Complexes. *Eur. J. Inorg. Chem.* **2017**, *2017*, 5033–5040.

(257) Grimme, S.; Antony, J.; Ehrlich, S.; Krieg, H. A Consistent and Accurate *Ab Initio* Parametrization of Density Functional Dispersion Correction (DFT-D) for the 94 Elements H-Pu. *J. Chem. Phys.* **2010**, *132*, 154104.

(258) Ernzerhof, M.; Scuseria, G. E. Assessment of the Perdew–Burke–Ernzerhof Exchange-Correlation Functional. *J. Chem. Phys.* **1999**, *110*, 5029–5036.

(259) Perdew, J. P.; Burke, K.; Ernzerhof, M. Generalized Gradient Approximation Made Simple. *Phys. Rev. Lett.* **1996**, *77*, 3865–3868.

(260) van Wüllen, C. Molecular Density Functional Calculations in the Regular Relativistic Approximation: Method, Application to Coinage Metal Diatomics, Hydrides, Fluorides and Chlorides, and Comparison with First-Order Relativistic Calculations. *J. Chem. Phys.* **1998**, *109* (2), 392–399.

(261) Rosenberg, B.; Van Camp, L.; Krigas, Thomas. Inhibition of Cell Division in Escherichia Coli by Electrolysis Products from a Platinum Electrode. *Nature* **1965**, *205* (4972), 698–699. https://doi.org/10.1038/205698a0.

(262) Wang, D.; Lippard, S. J. Cellular Processing of Platinum Anticancer Drugs. *Nat. Rev. Drug Discov.* **2005**, *4* (4), 307–320. https://doi.org/10.1038/nrd1691.

(263) Englinger, B.; Pirker, C.; Heffeter, P.; Terenzi, A.; Kowol, C. R.; Keppler, B. K.; Berger, W. Metal Drugs and the Anticancer Immune Response. *Chem. Rev.* **2019**, *119* (2), 1519–1624. https://doi.org/10.1021/acs.chemrev.8b00396.

(264) Wheate, N. Multi-Nuclear Platinum Complexes as Anti-Cancer Drugs. *Coord. Chem. Rev.* **2003**, *241* (1–2), 133–145. https://doi.org/10.1016/S0010-8545(03)00050-X.

(265) Johnstone, T. C.; Park, G. Y.; Lippard, S. J. Understanding and Improving Platinum Anticancer Drugs - Phenanthriplatin. *Anticancer Res.* **2014**, *34*, 471–476.

(266) Johnstone, T. C.; Wilson, J. J.; Lippard, S. J. Monofunctional and Higher-Valent Platinum Anticancer Agents. *Inorg. Chem.* **2013**, *52* (21), 12234–12249. https://doi.org/10.1021/ic400538c.

(267) Todd, R. C.; Lippard, S. J. Structure of Duplex DNA Containing the Cisplatin 1,2-{Pt(NH3)2}2+-d(GpG) Cross-Link at 1.77 Å Resolution. *J. Inorg. Biochem.* **2010**, *104*, 902–908.

(268) Park, G. Y.; Wilson, J. J.; Song, Y.; Lippard, S. J. Phenanthriplatin, a Monofunctional DNA-Binding Platinum Anticancer Drug Candidate with Unusual Potency and Cellular Activity Profile. *Proc Natl Acad Sci* **2012**, *109*, 11987–11992.

(269) Lovejoy, K. S.; Serova, M.; Bieche, I.; Emami, S.; D'Incalci, M.; Broggini, M.; Erba, E.; Gespach, C.; Cvitkovic, E.; Faivre, S.; Raymond, E.; Lippard, S. J. Spectrum of Cellular Responses to Pyriplatin, a Monofunctional Cationic Antineoplastic Platinum(II) Compound, in Human Cancer Cells. *Mol. Cancer Ther.* **2011**, *10* (9), 1709–1719. https://doi.org/10.1158/1535-7163.MCT-11-0250.

(270) Almaqwashi, A. A.; Zhou, W.; Naufer, M. N.; Riddell, I. A.; Yilmaz, Ö. H.; Lippard, S. J.; Williams, M. C. DNA Intercalation Facilitates Efficient DNA-Targeted Covalent Binding

of Phenanthriplatin. *J. Am. Chem. Soc.* **2019**, *141* (4), 1537–1545. https://doi.org/10.1021/jacs.8b10252.

(271) Tullius, T. D.; Lippard, S. J. Ethidium Bromide Changes the Nuclease-Sensitive DNA Binding Sites of the Antitumor Drug Cis-Diamminedichloroplatinum(II). *Proc. Natl. Acad. Sci.* **1982**, *79* (11), 3489–3492. https://doi.org/10.1073/pnas.79.11.3489.

(272) Boulikas, T.; Vougiouka, M. Cisplatin and Platinum Drugs at the Molecular Level (Review). *Oncol. Rep.* **2003**. https://doi.org/10.3892/or.10.6.1663.

(273) Dasari, S.; Bernard Tchounwou, P. Cisplatin in Cancer Therapy: Molecular Mechanisms of Action. *Eur. J. Pharmacol.* **2014**, *740*, 364–378. https://doi.org/10.1016/j.ejphar.2014.07.025.

(274) Lozada, I. B.; Williams, J. A. G.; Herbert, D. E. Platinum(II) Complexes of Benzannulated N ^ N ⁻^ O-Amido Ligands: Bright Orange Phosphors with Long-Lived Excited States. *Inorg. Chem. Front.* **2022**, *9* (1), 10–22. https://doi.org/10.1039/D1QI01120K.

(275) Che, C.-M.; Yang, M.; Wong, K.-H.; Chan, H.-L.; Lam, W. Platinum(II) Complexes of Dipyridophenazine as Metallointercalators for DNA and Potent Cytotoxic Agents against Carcinoma Cell Lines. *Chem. – Eur. J.* **1999**, *5*, 3350–3356.

(276) Kieltyka, R.; Fakhoury, J.; Moitessier, N.; Sleiman, H. F. Platinum Phenanthroimidazole Complexes as G-Quadruplex DNA Selective Binders. *Chem. – Eur. J.* **2008**, *14* (4), 1145–1154. https://doi.org/10.1002/chem.200700783.

(277) Cusumano, M.; Di Pietro, M. L.; Giannetto, A.; Nicolò, F.; Rotondo, E. Noncovalent Interactions of Platinum(II) Square Planar Complexes Containing Ligands Out-of-Plane with DNA. *Inorg. Chem.* **1998**, *37* (3), 563–568. https://doi.org/10.1021/ic9705406.

(278) Suntharalingam, K.; Mendoza, O.; Duarte, A. A.; Mann, D. J.; Vilar, R. A Platinum Complex That Binds Non-Covalently to DNA and Induces Cell Death via a Different Mechanism than Cisplatin. *Metallomics* **2013**, *5* (5), 514. https://doi.org/10.1039/c3mt20252f.

(279) Luedtke, N. W.; Liu, Q.; Tor, Y. Synthesis, Photophysical Properties, and Nucleic Acid Binding of Phenanthridinium Derivatives Based on Ethidium. *Bioorg. Med. Chem.* **2003**, *11*, 5235–5247.

(280) Nandi, R.; Chaudhuri, K.; Maiti, M. EFFECTS OF IONIC STRENGTH and PH ON THE BINDING OF SANGUINARINE TO DEOXYRIBONUCLEIC ACID. *Photochem. Photobiol.* **1985**, *42* (5), 497–503. https://doi.org/10.1111/j.1751-1097.1985.tb01600.x.

(281) Howe-Grant, M.; Lippard, S. J. Binding of Platinum(II) Intercalation Reagents to Deoxyribonucleic Acid. Dependence on Base-Pair Composition, Nature of the Intercalator, and Ionic Strength. *Biochemistry* **1979**, *18* (26), 5762–5769. https://doi.org/10.1021/bi00593a003.

(282) Murphy, M. P. How Mitochondria Produce Reactive Oxygen Species. *Biochem. J.* **2009**, *417* (1), 1–13. https://doi.org/10.1042/BJ20081386.

(283) Ivashkevich, A.; Redon, C. E.; Nakamura, A. J.; Martin, R. F.; Martin, O. A. Use of the γ-H2AX Assay to Monitor DNA Damage and Repair in Translational Cancer Research. *Cancer Lett.* **2012**, *327* (1–2), 123–133. https://doi.org/10.1016/j.canlet.2011.12.025.

(284) Mah, L.-J.; El-Osta, A.; Karagiannis, T. C. ΓH2AX: A Sensitive Molecular Marker of DNA Damage and Repair. *Leukemia* **2010**, *24* (4), 679–686. https://doi.org/10.1038/leu.2010.6.

(285) Chargaff, E.; Lipshitz, R. Composition of Mammalian Desoxyribonucleic Acids [1]. *J. Am. Chem. Soc.* **1953**, *75* (15), 3658–3661. https://doi.org/10.1021/ja01111a016.

(286) Kaim, W.; Schwederski, B.; Klein, A. Manganese-Catalyzed Oxidation of Water to O2. In *Bioinorganic Chemistry: Inorganic Elements in the Chemistry of Life*; Wiley: Chichester, 2013; pp 67–74.

(287) Pan, D.; Schmieder, A. H.; Wickline, S. A.; Lanza, G. M. Manganese-Based MRI Contrast Agents: Past, Present, and Future. *Tetrahedron* **2011**, *67* (44), 8431–8444. https://doi.org/10.1016/j.tet.2011.07.076.

(288) East, N. R.; Förster, C.; Carrella, L. M.; Rentschler, E.; Heinze, K. The Full d ^{3} –d ^{5} Redox Series of Mononuclear Manganese Complexes: Geometries and Electronic Structures of [Mn(Dgpy) $_2$] $^{n+}$. *Inorg. Chem.* **2022**, *61* (37), 14616–14625. https://doi.org/10.1021/acs.inorgchem.2c01680.

(289) Herr, P.; Kerzig, C.; Larsen, C. B.; Häussinger, D.; Wenger, O. S. Manganese(i) Complexes with Metal-to-Ligand Charge Transfer Luminescence and Photoreactivity. *Nat. Chem.* **2021**, *13* (10), 956–962. https://doi.org/10.1038/s41557-021-00744-9.

(290) Betley, T. A.; Qian, B. A.; Peters, J. C. Group VIII Coordination Chemistry of a Pincer-Type Bis(8-Quinolinyl)Amido Ligand. *Inorg. Chem.* **2008**, *47* (24), 11570–11582. https://doi.org/10.1021/ic801047s.

(291) Huynh, M. T.; Anson, C. W.; Cavell, A. C.; Stahl, S. S.; Hammes-Schiffer, S. Quinone 1 e $^-$ and 2 e $^-$ /2 H $^+$ Reduction Potentials: Identification and Analysis of Deviations from Systematic Scaling Relationships. *J. Am. Chem. Soc.* **2016**, *138* (49), 15903–15910. https://doi.org/10.1021/jacs.6b05797.

(292) Michaelis, L.; Hill, E. S. THE VIOLOGEN INDICATORS. *J. Gen. Physiol.* **1933**, *16* (6), 859–873. https://doi.org/10.1085/jgp.16.6.859.

(293) Woodhouse, M. D.; McCusker, J. K. Mechanistic Origin of Photoredox Catalysis Involving Iron(II) Polypyridyl Chromophores. *J. Am. Chem. Soc.* **2020**, *142* (38), 16229–16233. https://doi.org/10.1021/jacs.0c08389.

6 Conclusions and Outlook

6.1 Summary

This thesis describes benzannulation and its impact on the photophysical properties of molecular complexes.

Chapter 2: This chapter dives into the incorporation of benzannulated *N*-heterocyclic PAHs to ligand scaffolds. Firstly, it demonstrates how benzannulation impacts the optical properties of some complexes by comparing quinolinyl and phenanthridinyl (3,4-benzoquinoline) containing ligands. It then introduces how other photophysical properties such as luminescence is also

affected, and by combining low-lying vacant π*-MO of phenanthridine and amido π-donors panchromatic absorption can be achieved. Taking design principles from these examples a new ligands based on β-ketoimines [*N^N*H*^O*] are presented incorporating oxygen π-donors. It details the synthesis and characterization of the new ligands..

Chapter 3: The synthesis and photophysical properties of transition metal complexes supported by of phenanthridine-based tridentate *N^N*H*^O* ligands are presented and described. These complexes are studied and characterized with a full suite of experimental characterization tools including X-ray crystallography, IR, multinuclear NMR, UV-Vis absorption and luminescence spectroscopies, and electrochemistry (CV and DPV). Interestingly, these complexes exhibit long-lived excited states with zinc and platinum radiatively decaying from an emissive triplet state.

Chapter 4: This chapter delves deep into the electronic structures of a variety of complexes supported by benzannulated ligands using DFT and TDDFT. These calculations reveal the impact of benzannulation on the observed photophysical properties, providing a quantum mechanical foundation to experimental findings. Furthermore, the excited state dynamics and potential energy hypersurface of some complexes are explored to rationalize the behaviour of the molecules in their excited state. Lastly, the synergism between phenanthridine acceptors and amido π-donors in stabilizing MLCT states are revealed.

Chapter 5: The antineoplastic activity of some [Pt(NNO)Cl] complexes described in Chapter 3 are investigated. The studies show that the new complexes have improved *in vitro* efficacy compared with cisplatin and comparable to phenanthriplatin, a monofunctional phenanthridine ligated cisplatin analogue, in a range of cancerous cell lines including cisplatin resistant cells. Compared with phenanthriplatin the new complexes are less toxic to normal cell lines, an

advantage in the development of more selective and efficacious Pt(II) based anticancer drugs. Studies reveal the increased uptake of the complexes compared with cisplatin and may contribute to its enhanced antineoplastic activity. Furthermore, utilizing the photophysical properties of the Pt(NNO)Cl complex described in Chapter 3 and 4, we attempt to unravel its preferred interaction with DNA by monitoring the 'turn-on' phosphorescence with DNA. The results are suggestive of intercalation with some electrostatic component. We also show that the cytotoxicity of the complexes can be improved further with light irradiation of cell lines irradiated with light. Extensive studies indicate the generation of ROSs induced by the long-lived, emissive triplet state leading to DNA and mitochondrial oxidative stress. These results indicate the potential for the [Pt(NNO)Cl] complexes as imaging and PDT agents.

6.2 Conclusions

Several conclusions can be summarized from this thesis:

(i)   Expansion of ligand π-system through benzannulation introduces lower-lying vacant π*-MO and can be utilized to stabilize CT states. These CT states can be further stabilized by incorporating amido or oxo π-donors, achieving broader (and in some examples panchromatic) absorptive cross-sections. In addition, mixing of metal and ligand orbitals (covalency) enhances the transition intensities of CT states, which can be advantageous in DSSCs as it implies more photons are taken-up and used, and energy stored.

(ii)   While benzannulation generally leads to a red-shift in the optical and photophysical properties of most compounds, here in this thesis it is demonstrated that benzannulation of quinoline to phenanthridine (3,4-benzoquinoline) leads to a counterintuitive blue-

365

shift in the emission, and to some degree elongation of excited state lifetimes, of some Pt(II) complexes. I show, through computational analyses of the ground and excited state equilibrium geometries, that the blue-shift in emission is due to the enhanced rigidity in phenanthridine-containing complexes thanks to benzannulation.

(iii)   As discussed in Chapter 1, benzannulation enhances noncovalent intermolecular π-stacking interactions. By incorporating benzannulated phenanthridine (3,4-benzoquinoline), phosphorescence is enhanced in powdered samples of zinc complexes, compared with in fluid solutions, by extensive π-stacking in solid state.

(iv)   The enhanced noncovalent interaction proves to be advantageous in the improved antineoplastic activity of some [Pt(*N^N^*O)Cl] complexes. Benzannulation facilitates intercalative interaction between the complexes and DNA.

These conclusions point overall to benzannulation as a ligand design strategy in modifying the properties of molecular complexes with minimal structural changes from the parent compound. These encouraging and exciting results expand the chemical space and possibilities for new and exciting complexes with tailored properties for specific applications. Benzannulation, therefore, shows promise as a strategy in green energy, photochemistry, emissive materials, and biological applications.

6.3 Outlook

With the development of innovative synthetic methodologies, it is possible to fuse benzene rings not just in purely organic applications but also in coordination chemistry through ligand synthesis. Several outlooks are identified for different aspects that emerged from this thesis.

6.3.1 Expanding the Chemical Space of Asymmetric Diarylamido [*N*^*N*⁻^*N*] Ligands

In Chapter 2, a series of metal complexes were presented and discussed. However, these only incorporate metal complexes on the right of iron. To understand fully the role of the metal-centre and the extent of pπ-dπ mixing, it is necessary to investigate the elements to the left of iron and other group 8 elements. Of interests are manganese, chromium, vanadium, ruthenium and osmium (Figure 6.1). There are several motivations for this proposal. Manganese for example, particularly Mn(II), has been used as magnetic resonance imaging (MRI) contrast agent. This element is of biological importance owing to its role as cofactor in enzyme and receptors.[286] The intrinsic high spin number of Mn(II), d^5 electron count, and long electronic relaxation time enables the shortening of the spin-lattice relaxation time (T1) of water protons. This increases the T1w magnetic resonance signal intensity.[287] In addition to its magnetic properties, manganese has also shown promise in photochemistry. Recently, Heinze and co-workers[288] have demonstrated the isolation of three oxidation states (OS: +2, +3, and +4) of manganese supported by neutral, tridentate 2,6-diguanidylpyridine ligands. The isolation of highly oxidizing Mn(IV), d^3 electron count, could prove useful in the oxidation of organic substrates that are not amenable to typical oxidants. Emissive pseudo-octahedral Mn(I) complexes,[289] d^6 electron count, supported by neutral, multidentate thiophenyl-bridged aryl-isonitriles have also been isolated. These are some of the first examples of emissive $3d^6$ pseudo-octahedral complexes and a step forward towards the development of emissive $3d$ analogues of [Ru(bpy)$_3$]$^{2+}$. Moreover, while heteroleptic Ru(II) complexes supported by bis(8-quinolinyl)amide are known,[290] the impact of the increasing covalency through pπ-dπ mixing on the photophysics of heavier group 8 analogues is not known.

The $[Ru(tpy)_2]^{2+}$ *complex* is a non-emissive congener of $[Ru(bpy)_3]^{2+}$, it would thus be an endeavour worth pursuing the transferability of the covalency principle and its implications to the excited state dynamics to the complexes of $4d$ and $5d$ transition metals. It can be envisaged that the degree of covalency or pπ-dπ mixing of the nominally t_{2g} orbital set with the amido π-donors can be tuned by modifying the t_{2g} orbital energies through the metal centre. It is seen from the examples presented in this thesis that this mixing decreases to the right of iron, and a full HOMO inversion (amido lone pair) is fully realized with zinc and gallium. I strongly believe that covalency will have a strong impact on the magnetic and photophysical properties of the proposed complexes and will be crucial in the development of complexes for various applications.
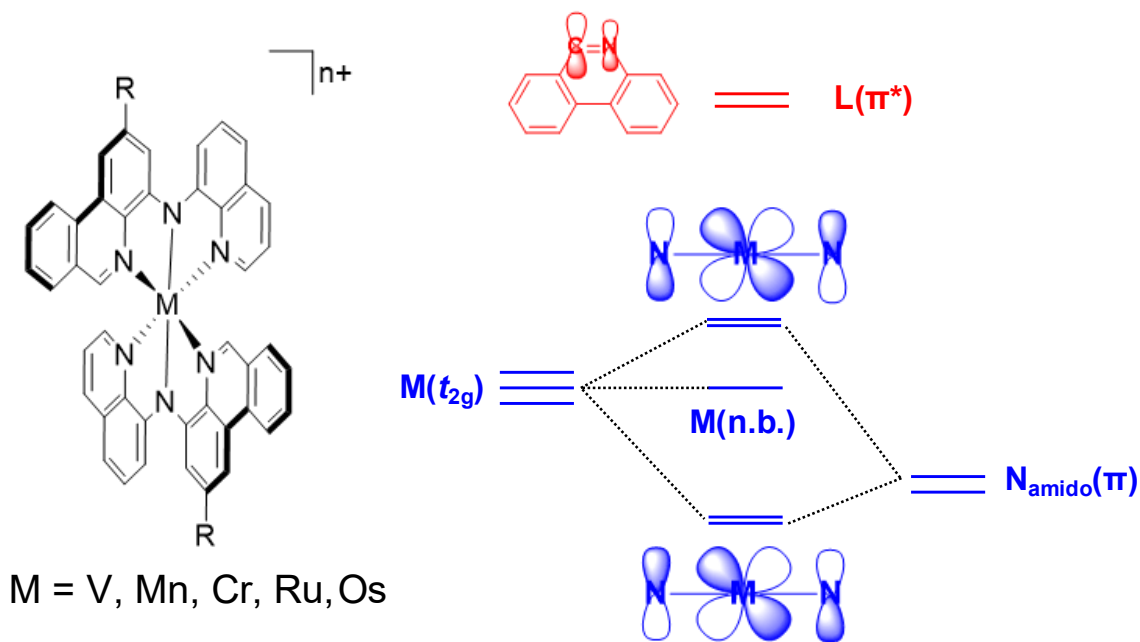
Figure 6.1. Controlling pπ-dπ mixing and covalency in homoleptic diarylamido transition metal complexes.

6.3.2 Anchoring Iron Complexes with Panchromatic Absorption to Surfaces

It is discussed in Chapter 2 that panchromatic absorption can be achieved through a combined strategy of lowering vacant ligand π^*-MO and amido π-donors. The next step to this long-term project is the applicability of the complex to solar energy capture. For this, new phenanthridine-based precursors are necessary that incorporates nitrogen- and oxygen-containing functional groups such as carboxylate and hydroxamate, and nitrile. Future endeavours will be given to the isolation and characterization of Fe(II) complexes (Figure 6.2) and testing their applicability in DSSCs through collaboration. In addition to this, these new complexes containing IR-active functionalities will be exploited to further study the structural dynamics of their excited states in the hopes of identifying pertinent structural distortions that can be attenuated through ligand design leading to the selective population of emissive ^{3}CT states upon relaxation.
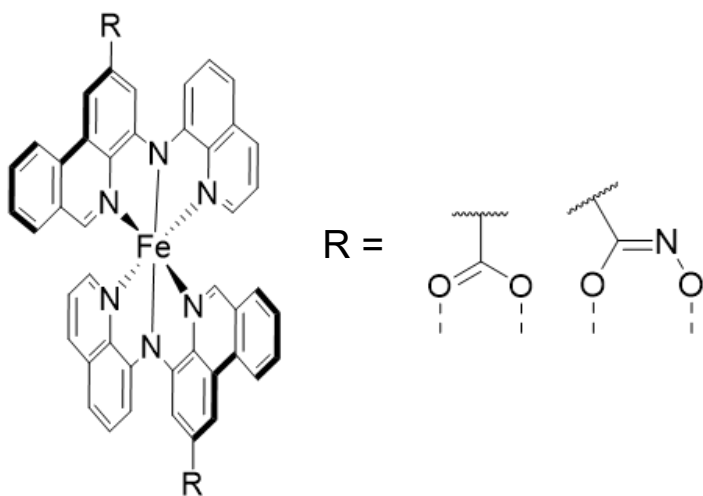
Figure 6.2. Target anchoring groups suitable for tethering to metal oxide surface.

6.3.3 Photochemical Investigation of Iron Complexes

As an extension to section 6.3.2, the photochemistry of the iron complexes will also be investigated. For this, I proposes some key experiments that will provide insight to the photochemistry of the iron complexes. Energy and electron transfer are the two most common mechanisms in photochemically active transition metal complexes. To examine if the CT excited states of the iron complexes can participate in electron transfer processes, the complexes will be exposed to various electron acceptors (Scheme 6.1a) with known ground state redox potentials[291,292]. In collaboration with field experts, time-resolved transient absorption experiments will be carried out with and without electron acceptors. By determining changes in the excited state lifetimes and detecting changes in the transient spectra of the complexes,[293] the excited state redox potentials of the complexes can be established and be compared with known photoredox catalysts such as $[Ru(bpy)_3]^{2+}$. In addition to the photoinduced electron transfer mechanisms, these complexes might also be expected to undergo energy transfer. For this inquiry, innovative approaches are necessary due to the strong panchromatic absorption of the complexes. Scheme 6.1b shows 1,3-isobenzofuran and 1-[(1*E*)-2-methoxyethenyl)]pyrene as singlet oxygen ($^1O_2$) scavengers and fluoresces as a by-product of their reaction with $^1O_2$. Similarly, delayed fluorescence, originating from triplet-triplet annihilation, from anthracene can also be utilized to establish energy transfer mechanisms in the iron complexes.
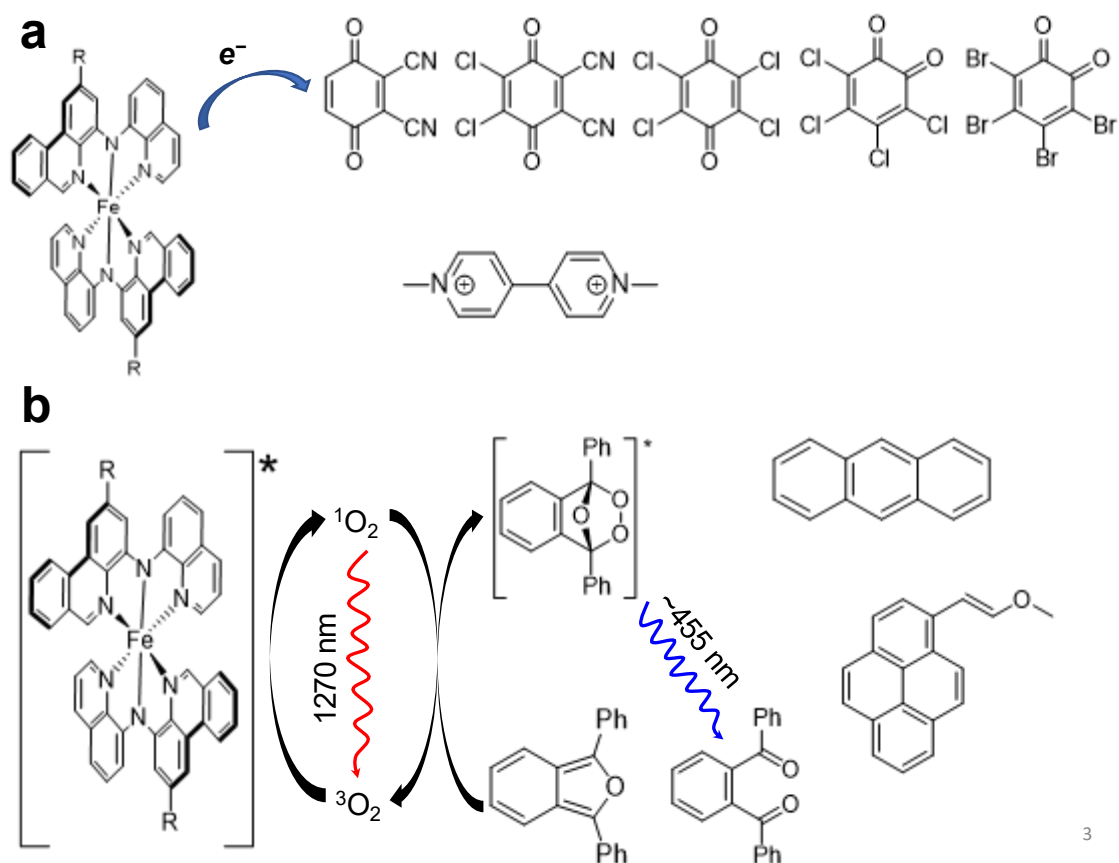
Scheme 6.1. Proposed experiments for asymmetric diarylamido Fe(II) homoleptic complexes to probe their photochemical potential.

6.3.4 Controlling Antineoplastic Activity of [Pt(*N^N^O*)Cl] Through Hydrophilic and Lipophilic Functional Groups

Finally, one of the significant challenges in the biological studies of the [Pt(*N^N^O*)Cl] is the inherent insolubility of the complexes in aqueous media. While the complexes can be solubilized, it requires initial dissolution in DMSO before diluting in buffered aqueous solutions. Functional groups such as carboxylate and hydroxamate are appended on phenanthridine to increase water solubility. In addition, studies presented in Chapter 5 suggest that the CF$_3$ functional

group plays a critical role in the activity of **11**. CF$_3$ groups likely modify the lipophilicity of the complex and may facilitate the passive diffusion of **11** into the cell thereby increasing the intracellular concentration of the complex. In addition, replacement of one of the methyl groups in the *N^O* fragment of the *N^N*H*^O* ligand with CF$_3$ is anticipated to increase the lipophilicity of the complexes. With these new series (Figure 6.3), the role of CF$_3$ in the biological activity of the complexes can be unraveled.
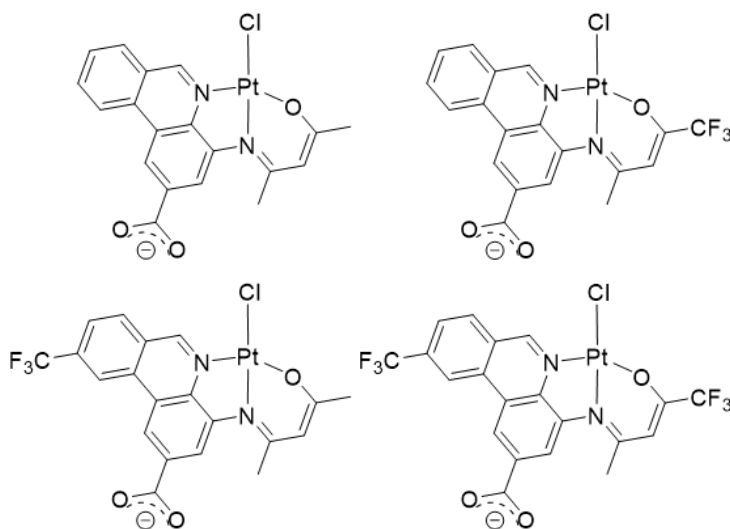
Figure 6.3. [Pt(*N^N^O*)Cl] complexes with lipophilic CF$_3$ and hydrophilic carboxylate functional groups.

References

(1)   Faraday, M. On New Compounds of Carbon and Hydrogen, and on Certain Other Products Obtained during the Decomposition of Oil by Heatrstl.1825.Pdf. *Philos. Trans. R. Soc.* **1825**, *115*, 440–466.
(2)   Heo, I.; Lee, J. C.; Özer, B. R.; Schultz, T. Mass-Correlated High-Resolution Spectra and the Structure of Benzene. *J. Phys. Chem. Lett.* **2022**, *13* (35), 8278–8283. https://doi.org/10.1021/acs.jpclett.2c02035.
(3)   Kunishige, S.; Katori, T.; Baba, M.; Nakajima, M.; Endo, Y. Spectroscopic Study on Deuterated Benzenes. I. Microwave Spectra and Molecular Structure in the Ground State. *J. Chem. Phys.* **2015**, *143* (24), 244302. https://doi.org/10.1063/1.4937949.

(4)   Watson, M. D.; Fechtenkötter, A.; Müllen, K. Big Is Beautiful−"Aromaticity" Revisited from the Viewpoint of Macromolecular and Supramolecular Benzene Chemistry. *Chem. Rev.* **2001**, *101* (5), 1267–1300. https://doi.org/10.1021/cr990322p.

(5)   Vij, V.; Bhalla, V.; Kumar, M. Hexaarylbenzene: Evolution of Properties and Applications of Multitalented Scaffold. *Chem. Rev.* **2016**, *116* (16), 9565–9627. https://doi.org/10.1021/acs.chemrev.6b00144.

(6)   Price, C. C. Substitution and Orientation in the Benzene Ring. *Chem. Rev.* **1941**, *29* (1), 37–67. https://doi.org/10.1021/cr60092a002.

(7)   Papadakis, R.; Ottosson, H. The Excited State Antiaromatic Benzene Ring: A Molecular Mr Hyde? *Chem. Soc. Rev.* **2015**, *44* (18), 6472–6493. https://doi.org/10.1039/C5CS00057B.

(8)   Swami, B.; Yadav, D.; Menon, R. S. Benzannulation Reactions: A Case for Perspective Change From Arene Decoration to Arene Construction. *Chem. Rec.* **2022**, *22* (1), e202100249. https://doi.org/10.1002/tcr.202100249.

(9)   Hart-Davis, A. J.; White, C.; Mawby, F. J. Reactions Of-WIndeny Complexes of Transition Metals. III.' Kinetics and Mechanisms of Substitution Reactions of Tricarbonyl-Mindenylhalomolybdenum(II) Complexes. 6.

(10)   Rerek, M. E.; Basolo, F. Kinetics and Mechanism of Substitution Reactions of .Eta.5-Cyclopentadienyldicarbonylrhodium(I) Derivatives. Rate Enhancement of Associative Substitution in Cyclopentadienylmetal Compounds. *J. Am. Chem. Soc.* **1984**, *106* (20), 5908–5912. https://doi.org/10.1021/ja00332a026.

(11)   Rerek, M. E.; Ji, L.-N.; Basolo, F. The Lndenyl Ligand Effect on the Rate of Substitution Reactions of Rh(Rl-C9H7)C(O), and Mn(Rl -CgH7)C(O)a. 2.

(12)   Okada, Y.; Miyamoto, N.; Hishimoto, M.; Hayashi, T. Studies on Ferrocene Derivatives. Part XIII. Ligand Exchange Reactions of Benzoferrocenes. *Transit. Met Chem* **1999**, 5.

(13)   Treichel, P. M.; Johnson, J. W.; Wagner, K. P. OXIDATIONS OF VARIOUS INDENYL-IRON. 4.

(14)   Crossley, N. S.; Green, J. C.; Nagy, A.; Stringer, G. Electronic Structure of Transition-Metal Lndenyl Compounds: A He I and He I I Photoelectron Spectroscopic Study of [Mn(Q5-C,H7)(CO),], [Fe(Q5-CgH7),]. Ru(Q5-C9H7)21 and Ru(T5-C9H7)(q-C5Me5) I t. *J CHEM SOC DALTON TRANS* **1989**, 9.

(15)   Brady, E. D.; Overby, J. S.; Meredith, M. B.; Mussman, A. B.; Cohn, M. A.; Hanusa, T. P.; Yee, G. T.; Pink, M. Spin-State Alteration from Sterically Enforced Ligand Rotation in Bis(Indenyl)Chromium(II) Complexes [1]. *J. Am. Chem. Soc.* **2002**, *124* (32), 9556–9566. https://doi.org/10.1021/ja012390a.

(16)   Shimizu, A.; Ishizaki, Y.; Horiuchi, S.; Hirose, T.; Matsuda, K.; Sato, H.; Yoshida, J. HOMO–LUMO Energy-Gap Tuning of π-Conjugated Zwitterions Composed of Electron-Donating Anion and Electron-Accepting Cation. *J. Org. Chem.* **2021**, *86* (1), 770–781. https://doi.org/10.1021/acs.joc.0c02343.

(17)   Hanson, K.; Roskop, L.; Djurovich, P. I.; Zahariev, F.; Gordon, M. S.; Thompson, M. E. A Paradigm for Blue- or Red-Shifted Absorption of Small Molecules Depending on the Site of π-Extension. *J. Am. Chem. Soc.* **2010**, *132* (45), 16247–16255. https://doi.org/10.1021/ja1075162.

(18)   Liu, B.; Lystrom, L.; Kilina, S.; Sun, W. Effects of Varying the Benzannulation Site and π Conjugation of the Cyclometalating Ligand on the Photophysics and Reverse Saturable

Absorption of Monocationic Iridium(III) Complexes. *Inorg. Chem.* **2019**, *58* (1), 476–488. https://doi.org/10.1021/acs.inorgchem.8b02714.

(19)   Liu, B.; Lystrom, L.; Brown, S. L.; Hobbie, E. K.; Kilina, S.; Sun, W. Impact of Benzannulation Site at the Diimine (N^N) Ligand on the Excited-State Properties and Reverse Saturable Absorption of Biscyclometallated Iridium(III) Complexes. *Inorg. Chem.* **2019**, *58* (9), 5483–5493. https://doi.org/10.1021/acs.inorgchem.8b03162.

(20)   Wang, L.; Yin, H.; Jabed, M. A.; Hetu, M.; Wang, C.; Monro, S.; Zhu, X.; Kilina, S.; McFarland, S. A.; Sun, W. π-Expansive Heteroleptic Ruthenium(II) Complexes as Reverse Saturable Absorbers and Photosensitizers for Photodynamic Therapy. *Inorg. Chem.* **2017**, *56* (6), 3245–3259. https://doi.org/10.1021/acs.inorgchem.6b02624.

(21)   Chen, T.; Li, M.; Liu, J. π–π Stacking Interaction: A Nondestructive and Facile Means in Material Engineering for Bioapplications. *Cryst. Growth Des.* **2018**, *18* (5), 2765–2783. https://doi.org/10.1021/acs.cgd.7b01503.

(22)   Sinnokrot, M. O.; Valeev, E. F.; Sherrill, C. D. Estimates of the Ab Initio Limit for Π−π Interactions: The Benzene Dimer. *J. Am. Chem. Soc.* **2002**, *124* (36), 10887–10893. https://doi.org/10.1021/ja025896h.

(23)   Cai, M.; Song, X.; Zhang, D.; Qiao, J.; Duan, L. π–π Stacking: A Strategy to Improve the Electron Mobilities of Bipolar Hosts for TADF and Phosphorescent Devices with Low Efficiency Roll-Off. *J. Mater. Chem. C* **2017**, *5* (13), 3372–3381. https://doi.org/10.1039/C7TC00733G.

(24)   Hong, Y.; Lam, J. W. Y.; Tang, B. Z. Aggregation-Induced Emission: Phenomenon, Mechanism and Applications. *Chem. Commun.* **2009**, No. 29, 4332. https://doi.org/10.1039/b904665h.

(25)   McGaughey, G. B.; Gagné, M.; Rappé, A. K. π-Stacking Interactions. *J. Biol. Chem.* **1998**, *273* (25), 15458–15463. https://doi.org/10.1074/jbc.273.25.15458.

(26)   Babine, R. E.; Bender, S. L. Molecular Recognition of Protein−Ligand Complexes: Applications to Drug Design. *Chem. Rev.* **1997**, *97* (5), 1359–1472. https://doi.org/10.1021/cr960370z.

(27)   Pages, B. J.; Garbutcheon-Singh, K. B.; Aldrich-Wright, J. R. Platinum Intercalators of DNA as Anticancer Agents. *Eur. J. Inorg. Chem.* **2017**, *2017* (12), 1613–1624. https://doi.org/10.1002/ejic.201601204.

(28)   Hayashi, K.; Nakatani, M.; Hayashi, A.; Takano, M.; Okazaki, M.; Toyota, K.; Yoshifuji, M.; Ozawa, F. Synthesis and Structures of Platinum(0) Alkyne Complexes with Extended π-Conjugated Systems. *Organometallics* **2008**, *27* (9), 1970–1972. https://doi.org/10.1021/om800163p.

(29)   Flamigni, L.; Encinas, S.; Barigelletti, F.; MacDonnell, F. M.; Kim, K.-J.; Puntoriero, F.; Campagna, S. Excited-State Interconversion between Emissive MLCT Levels in a Dinuclear Ru(Ii) Complex Containing a Bridging Ligand with an Extended π System. *Chem. Commun.* **2000**, No. 13, 1185–1186. https://doi.org/10.1039/b004109m.

(30)   Roznyatovskiy, V. V.; Lee, C.-H.; Sessler, J. L. π-Extended Isomeric and Expanded Porphyrins. *Chem Soc Rev* **2013**, *42* (5), 1921–1933. https://doi.org/10.1039/C2CS35418G.

(31)   Barbon, S. M.; Staroverov, V. N.; Gilroy, J. B. Effect of Extended π Conjugation on the Spectroscopic and Electrochemical Properties of Boron Difluoride Formazanate Complexes. *J. Org. Chem.* **2015**, *80* (10), 5226–5235. https://doi.org/10.1021/acs.joc.5b00620.

(32) Kappaun, S.; Rentenberger, S.; Pogantsch, A.; Zojer, E.; Mereiter, K.; Trimmel, G.; Saf, R.; Möller, K. C.; Stelzer, F.; Slugovc, C. Organoboron Quinolinolates with Extended Conjugated Chromophores: Synthesis, Structure, and Electronic and Electroluminescent Properties. *Chem. Mater.* **2006**, *18* (15), 3539–3547. https://doi.org/10.1021/cm060720q.

(33) Kiprof, P.; Carlson, J. C.; Anderson, D. R.; Nemykin, V. N. Systematic Color Tuning of a Family of Luminescent Azole-Based Organoboron Compounds Suitable for OLED Applications. *Dalton Trans.* **2013**, *42* (42), 15120. https://doi.org/10.1039/c3dt51853a.

(34) Bossi, A.; Rausch, A. F.; Leitl, M. J.; Czerwieniec, R.; Whited, M. T.; Djurovich, P. I.; Yersin, H.; Thompson, M. E. Photophysical Properties of Cyclometallated Pt(II) Complexes: Counterintuitive Blue Shift in Emission with an Expanded Ligand π System. *Inorg. Chem.* **2013**, *52* (21), 12403–12415. https://doi.org/10.1021/ic4011532.

(35) Gunanathan, C.; Gnanaprakasam, B.; Iron, M. A.; Shimon, L. J. W.; Milstein, D. "Long-Range" Metal−Ligand Cooperation in H $_2$ Activation and Ammonia-Promoted Hydride Transfer with a Ruthenium−Acridine Pincer Complex. *J. Am. Chem. Soc.* **2010**, *132* (42), 14763–14765. https://doi.org/10.1021/ja107770y.

(36) Neufeldt, S. R.; Sanford, M. S. Controlling Site Selectivity in Palladium-Catalyzed C–H Bond Functionalization. *Acc. Chem. Res.* **2012**, *45* (6), 936–946. https://doi.org/10.1021/ar300014f.

(37) Krichevsky, O.; Bonnet, Gregoire. Fluorescence Correlation Spectroscopy: The Technique and Its Applications. *Rep. Prog. Phys.* **2002**, *65* (2), 251–297. https://doi.org/10.1088/0034-4885/65/2/203.

(38) Tumir, L.-M.; Stojkovic, M. R.; Piantanida, I. Come-Back of Phenanthridine and Phenanthridinium Derivatives in the 21st Century. *Beilstein J Org Chem* **2014**, *10*, 2930–2954.

(39) Park, G. Y.; Wilson, J. J.; Song, Y.; Lippard, S. J. Phenanthriplatin, a Monofunctional DNA-Binding Platinum Anticancer Drug Candidate with Unusual Potency and Cellular Activity Profile. *Proc Natl Acad Sci* **2012**, *109*, 11987–11992.

(40) Lu, L.-Q.; Li, Y.; Junge, K.; Beller, Matthias. Iron-Catalyzed Hydrogenation for the In Situ Regeneration of an NAD(P)H Model: Biomimetic Reduction of α-Keto-/α-Iminoesters. *Angew. Chem. Int. Ed.* **2013**, *52* (32), 8382–8386. https://doi.org/10.1002/anie.201301972.

(41) Chen, Q.-A.; Gao, K.; Duan, Y.; Ye, Z.-S.; Shi, L.; Yang, Y.; Zhou, Y.-Gui. Dihydrophenanthridine: A New and Easily Regenerable NAD(P)H Model for Biomimetic Asymmetric Hydrogenation. *J. Am. Chem. Soc.* **2012**, *134* (4), 2442–2448. https://doi.org/10.1021/ja211684v.

(42) Jensen, K. A.; Nielsen, P. Halfdan. Chelates with Heterocyclic Ligands. I. Chelates Derived from e N,N'-Bis(8-Quinolyl)Ethylenediamine and Analogous Compounds. *Acta Chem. Scand. 1947-1973* **1964**, *18* (1), 1–10. https://doi.org/10.3891/acta.chem.scand.18-0001.

(43) Puzas, J. P.; Nakon, R.; Petersen, J. L. Direct Evidence for an SN1CB Mechanism. 4. Crystal and Molecular Structure of Chloro(Bis(8-Quinolinyl)Amido-N1,N2,N3)Copper(II), a Metal Chelate Containing an Sp2-Hybridized Deprotonated Amine. *Inorg. Chem.* **1986**, *25* (21), 3837–3840. https://doi.org/10.1021/ic00241a026.

(44) Peters, J. C.; Harkins, S. B.; Brown, S. D.; Day, M. W. Pincer-like Amido Complexes of Platinum, Palladium, and Nickel. *Inorg. Chem.* **2001**, *40* (20), 5083–5091. https://doi.org/10.1021/ic010336p.

(45) Maiti, D.; Paul, H.; Chanda, N.; Chakraborty, S.; Mondal, B.; Puranik, V. G.; Lahiri, G. Kumar. Synthesis, Structure, Spectral and Electron-Transfer Properties of Octahedral-[CoIII(L)2]+/[ZnII(L)2] and Square Planar-[CuII(L){OC(=O)CH3}] Complexes Incorporating Anionic Form of Tridentate Bis(8-Quinolinyl)Amine [N1C9H6-N2-C9H6N3, L-] Ligand. *Polyhedron* **2004**, *23* (5), 831–840. https://doi.org/10.1016/j.poly.2003.11.053.

(46) Valk, J.-M.; Claridge, T. D. W.; Brown, J. M.; Hibbs, D.; Hursthouse, M. B. Synthesis and Chemistry of a New P-N Chelating Ligand; (R)- and (S)-6-(2'-Diphenylphosphino-1'-Naphthyl)Phenanthridine. *Tetrahedron Asymmetry* **1995**, *6* (Copyright (C) 2017 American Chemical Society (ACS). All Rights Reserved.), 2597–2610. https://doi.org/10.1016/0957-4166(95)00341-L.

(47) Raszeja, L.; Maghnouj, A.; Hahn, S.; Metzler-Nolte, Nils. A Novel Organometallic ReI Complex with Favourable Properties for Bioimaging and Applicability in Solid-Phase Peptide Synthesis. *ChemBioChem* **2011**, *12* (3), 371–376. https://doi.org/10.1002/cbic.201000576.

(48) Sicilia, V.; Fuertes, S.; Martin, A.; Palacios, Adrian. N-Assisted CPh-H Activation in 3,8-Dinitro-6-Phenylphenanthridine. New C,N-Cyclometallated Compounds of Platinum(II): Synthesis, Structure, and Luminescence Studies. *Organometallics* **2013**, *32* (15), 4092–4102. https://doi.org/10.1021/om400159g.

(49) Jiang, B.; Gu, Y.; Qin, J.; Ning, X.; Gong, S.; Xie, G.; Yang, Chuluo. Deep-Red Iridium(III) Complexes Cyclometallated by Phenanthridine Derivatives for Highly Efficient Solution-Processed Organic Light-Emitting Diodes. *J. Mater. Chem. C Mater. Opt. Electron. Devices* **2016**, *4* (16), 3492–3498. https://doi.org/10.1039/C6TC00148C.

(50) Theobald, R. S.; Schofield, K. The Chemistry of Phenanthridine and Its Derivatives. *Chem. Rev.* **1950**, *46* (1), 170–189. https://doi.org/10.1021/cr60143a004.

(51) Crystal and molecular structure of phenanthridine. Roychowdhury1973.Pdf. *Acta. Cryst., Sect. B* **1973**, *29*, 1362–1364.

(52) Brett, W. A.; Rademacher, P.; Boese, R. Redetermination of the Structure of Phenanthridine. *Acta Crystallogr. C* **1993**, *49* (9), 1564–1566. https://doi.org/10.1107/S0108270193005062.

(53) Katritzky, A. R. *Handbook of Heterocyclic Chemistry*, 3rd ed.; Elsevier, 2010.

(54) Benmachiche, A.; Zendaoui, S.-M.; Bouaoud, S.-E.; Zouchoune, B. Electronic Structure and Coordination Chemistry of Phenanthridine Ligand in First-Row Transition Metal Complexes: A DFT Study. *Int. J. Quantum Chem.* **2013**, *113* (7), 985–996. https://doi.org/10.1002/qua.24071.

(55) Giesbrecht, P. K.; Nemez, D. B.; Herbert, D. E. Electrochemical Hydrogenation of a Benzannulated Pyridine to a Dihydropyridine in Acidic Solution. *Chem. Commun.* **2018**, *54* (4), 338–341. https://doi.org/10.1039/C7CC07907A.

(56) Mondal, R.; Giesbrecht, P. K.; Herbert, D. E. Nickel(II), Copper(I) and Zinc(II) Complexes Supported by a (4-Diphenylphosphino)Phenanthridine Ligand. *Polyhedron* **2016**, *108*, 156–162.

(57) Mandapati, P.; Giesbrecht, P. K.; Davis, R. L.; Herbert, D. E. Phenanthridine-Containing Pincer-like Amido Complexes of Nickel, Palladium, and Platinum. *Inorg Chem* **2017**, *56*, 3674–3685.

(58) Mandapati, P.; Braun, J. D.; Killeen, C.; Davis, R. L.; Williams, J. A. G.; Herbert, D. E. Luminescent Platinum(II) Complexes of N^N$^-$^N Amido Ligands with Benzannulated N-Heterocyclic Donor Arms: Quinolines Offer Unexpectedly Deeper Red Phosphorescence than Phenanthridines. *Inorg Chem* **2019**, *58*, 14808–14817.

(59) Mandapati, P.; Braun, J. D.; Lozada, I. B.; Williams, J. A. G.; Herbert, D. E. Deep-Red Luminescence from Platinum(II) Complexes of N^N$^-$^N-Amido Ligands with Benzannulated N-Heterocyclic Donor Arms. *Inorg. Chem.* **2020**, *59*, 12504–12517.

(60) Mondal, R.; Lozada, I. B.; Davis, R. L.; Williams, J. A. G.; Herbert, D. E. Site-Selective Benzannulation of N-Heterocycles in Bidentate Ligands Leads to Blue-Shifted Emission from [(P^N)Cu]$_2$(μ-X)$_2$ Dimers. *Inorg Chem* **2018**, *57*, 4966–4978.

(61) Mondal, R.; Lozada, I. B.; Davis, R. L.; Williams, J. A. G.; Herbert, D. E. Exploiting Synergy between Ligand Design and Counterion Interactions to Boost Room Temperature Phosphorescence from Cu(I) Compounds. *J. Mater. Chem. C* **2019**, *7*, 3772–3778.

(62) Lozada, I. B.; Murray, T.; Herbert, D. E. Monomeric Zinc(II) Amide Complexes Supported by Bidentate, Benzannulated Phenanthridine Amido Ligands. *Polyhedron* **2019**, *161*, 261–267.

(63) Mondal, R.; Lozada, I. B.; Davis, R. L.; Williams, J. A. G.; Herbert, D. E. Site-Selective Benzannulation of N-Heterocycles in Bidentate Ligands Leads to Blue-Shifted Emission from [(P^N)Cu]2(μ-X)2 Dimers. *Inorg Chem* **2018**, *57*, 4966–4978.

(64) Mandapati, P.; Giesbrecht, P. K.; Davis, R. L.; Herbert, D. E. Phenanthridine-Containing Pincer-like Amido Complexes of Nickel, Palladium, and Platinum. *Inorg Chem* **2017**, *56*, 3674–3685.

(65) Gaire, S.; Ortiz, R. J.; Schrage, B. R.; Lozada, I. B.; Mandapati, P.; Osinski, A. J.; Herbert, D. E.; Ziegler, C. J. (8-Amino)Quinoline and (4-Amino)Phenanthridine Complexes of Re(CO)3 Halides. *J. Organomet. Chem.* **2020**, *921*, 121338.

(66) Nemez, D. B.; Lozada, I. B.; Braun, J. D.; Williams, J. A. G.; Herbert, D. E. Synthesis and Coordination Chemistry of a Benzannulated Bipyridine: 6,6′-Biphenanthridine. *Inorg. Chem.* **2022**, *61* (34), 13386–13398. https://doi.org/10.1021/acs.inorgchem.2c01514.

(67) Hanson, K.; Roskop, L.; Djurovich, P. I.; Zahariev, F.; Gordon, M. S.; Thompson, M. E. A Paradigm for Blue- or Red-Shifted Absorption of Small Molecules Depending on the Site of π-Extension. *J. Am. Chem. Soc.* **2010**, *132*, 16247–16255.

(68) Barbon, S. M.; Staroverov, V. N.; Gilroy, J. B. Effect of Extended π Conjugation on the Spectroscopic and Electrochemical Properties of Boron Difluoride Formazanate Complexes. *J. Org. Chem.* **2015**, *80*, 5226–5235.

(69) Liu, B.; Lystrom, L.; Kilina, S.; Sun, W. Tuning the Ground State and Excited State Properties of Monocationic Iridium(III) Complexes by Varying the Site of Benzannulation on Diimine Ligand. *Inorg. Chem.* **2017**, *56*, 5361–5370.

(70) Westcott, B. L.; Gruhn, N. E.; Michelsen, L. J.; Lichtenberger, D. L. Experimental Observation of Non-Aufbau Behavior: Photoelectron Spectra of Vanadyloctaethylporphyrinate and Vanadylphthalocyanine. *J. Am. Chem. Soc.* **2000**, *122*, 8083–8084.

(71) Hewage, J. S.; Wanniarachchi, S.; Morin, T. J.; Liddle, B. J.; Banaszynski, M.; Lindeman, S. V.; Bennett, B.; Gardinier, J. R. Homoleptic Nickel(II) Complexes of Redox-Tunable Pincer-Type Ligands. *Inorg. Chem.* **2014**, *53* (19), 10070–10084. https://doi.org/10.1021/ic500657e.

(72) Lozada, I. B.; Ortiz, R. J.; Braun, J. D.; Williams, J. A. G.; Herbert, D. E. Donor–Acceptor Boron-Ketoiminate Complexes with Pendent *N* -Heterocyclic Arms: Switched-on Luminescence through *N* -Heterocycle Methylation. *J. Org. Chem.* **2022**, *87* (1), 184–196. https://doi.org/10.1021/acs.joc.1c02138.

(73) Braun, J. D.; Lozada, I. B.; Kolodziej, C.; Burda, C.; Newman, K. M. E.; van Lierop, J.; Davis, R. L.; Herbert, D. E. Iron(II) Coordination Complexes with Panchromatic Absorption and Nanosecond Charge-Transfer Excited State Lifetimes. *Nat. Chem.* **2019**, *11*, 1144–1150.

(74) Bruker-AXS. APEX3 V2016.1-0, 2016.

(75) Dolomanov, O. V.; Bourhis, L. J.; Gildea, R. J.; Howard, J. A. K.; Puschmann, H. OLEX2: A Complete Structure Solution, Refinement and Analysis Program. *J. Appl. Crystallogr.* **2009**, *42*, 339–341.

(76) Spek, A. L. Structure Validation in Chemical Crystallography. *Acta Cryst* **2009**, *D65*, 148–155.

(77) Fan, C.; Yang, C. Yellow/Orange Emissive Heavy-Metal Complexes as Phosphors in Monochromatic and White Organic Light-Emitting Devices. *Chem Soc Rev* **2014**, *43* (17), 6439–6469. https://doi.org/10.1039/C4CS00110A.

(78) Vreshch, V. D.; Yang, J.-H.; Zhang, H.; Filatov, A. S.; Dikarev, E. V. Monomeric Square-Planar Cobalt(II) Acetylacetonate: Mystery or Mistake? *Inorg. Chem.* **2010**, *49* (18), 8430–8434. https://doi.org/10.1021/ic100963r.

(79) Sokolow, J. D.; Trzop, E.; Chen, Y.; Tang, J.; Allen, L. J.; Crabtree, R. H.; Benedict, J. B.; Coppens, P. Binding Modes of Carboxylate- and Acetylacetonate-Linked Chromophores to Homodisperse Polyoxotitanate Nanoclusters. *J. Am. Chem. Soc.* **2012**, *134* (28), 11695–11700. https://doi.org/10.1021/ja303692r.

(80) Muñoz-García, A. B.; Sannino, F.; Vitiello, G.; Pirozzi, D.; Minieri, L.; Aronne, A.; Pernice, P.; Pavone, M.; D'Errico, G. Origin and Electronic Features of Reactive Oxygen Species at Hybrid Zirconia-Acetylacetonate Interfaces. *ACS Appl. Mater. Interfaces* **2015**, *7* (39), 21662–21667. https://doi.org/10.1021/acsami.5b06988.

(81) Seco, M. Acetylacetone: A Versatile Ligand. *J. Chem. Educ.* **1989**, *66* (9), 779. https://doi.org/10.1021/ed066p779.

(82) Allen, G.; Lewis, J.; Long, R. F.; Oldham, C. A Novel Form of Co-Ordination of Acetylacetone to Platinum(LI). *Nature* **1964**, *202*, 589–590. https://doi.org/10.1038/202589a0.

(83) Patra, S.; Mondal, B.; Sarkar, B.; Niemeyer, M.; Lahiri, G. K. First Example of μ $_3$ -Sulfido Bridged Mixed-Valent Triruthenium Complex Triangle Ru ^{III} $_2$ Ru ^{II} (*O* , *O* -Acetylacetonate) $_3$ (*μ - O* , *O* ,γ- *C* -Acetylacetonate) $_3$ (μ $_3$ -S) (**1**) Incorporating Simultaneous O,O- and γ-C-Bonded Bridging Acetylacetonate Units. Synthesis, Crystal Structure, and Spectral and Redox Properties. *Inorg. Chem.* **2003**, *42* (4), 1322–1327. https://doi.org/10.1021/ic026221i.

(84) Zhu, D.; Budzelaar, P. H. M. N-Aryl β-Diiminate Complexes of the Platinum Metals. *Dalton Trans.* **2013**, *42* (32), 11343. https://doi.org/10.1039/c3dt50715g.

(85) Bernskoetter, W. H.; Lobkovsky, E.; Chirik, P. J. Ancillary Ligand Effects on C−H Bond Activation Reactions Promoted by β-Diiminate Iridium Complexes. *Organometallics* **2005**, *24* (25), 6250–6259. https://doi.org/10.1021/om050705f.

(86) Roesky, H. W. The Renaissance of Aluminum Chemistry. *Inorg. Chem.* **2004**, *43* (23), 7284–7293. https://doi.org/10.1021/ic0400641.

(87) Mears, K. L.; Stennett, C. R.; Taskinen, E. K.; Knapp, C. E.; Carmalt, C. J.; Tuononen, H. M.; Power, P. P. Molecular Complexes Featuring Unsupported Dispersion-Enhanced Aluminum–Copper and Gallium–Copper Bonds. *J. Am. Chem. Soc.* **2020**, *142* (47), 19874–19878. https://doi.org/10.1021/jacs.0c10099.

(88) Mondal, R.; Lozada, I. B.; Davis, R. L.; Williams, J. A. G.; Herbert, D. E. Exploiting Synergy between Ligand Design and Counterion Interactions to Boost Room Temperature Phosphorescence from Cu(I) Compounds. *J. Mater. Chem. C* **2019**, *7*, 3772–3778.

(89) Mandapati, P.; Braun, J. D.; Lozada, I. B.; Williams, J. A. G.; Herbert, D. E. Deep-Red Luminescence from Platinum(II) Complexes of N^N⁻^N-Amido Ligands with Benzannulated N-Heterocyclic Donor Arms. *Inorg. Chem.* **2020**, *59*, 12504–12517.

(90) Ortiz, R. J.; Braun, J. D.; Williams, J. A. G.; Herbert, D. E. Brightly Luminescent Platinum Complexes of *N^C⁻^N* Ligands Forming Six-Membered Chelate Rings: Offsetting Deleterious Ring Size Effects Using Site-Selective Benzannulation. *Inorg. Chem.* **2021**, *60*, 16881–16894.

(91) Lozada, I. B.; Huang, B.; Stilgenbauer, M.; Beach, T.; Qiu, Z.; Zheng, Y.; Herbert, D. E. Monofunctional Platinum(II) Anticancer Complexes Based on Multidentate Phenanthridine-Containing Ligand Frameworks. *Dalton Trans.* **2020**, *49*, 6557–6560.

(92) Myers, E. L.; Butts, C. P.; Aggarwal, V. K. BF3·OEt2 and TMSOTf: A Synergistic Combination of Lewis Acids. *Chem. Commun.* **2006**, No. 42, 4434–4436.

(93) Macedo, F. P.; Gwengo, C.; Lindeman, S. V.; Smith, M. D.; Gardinier, J. R. β-Diketonate, β-Ketoiminate, and β-Diiminate Complexes of Difluoroboron. *Eur. J. Inorg. Chem.* **2008**, *2008*, 3200–3211.

(94) Dohe, J.; Kossmann, J.; Mueller, T. J. J. Diversity-Oriented Four-Component Synthesis of Solid State Luminescent Difluoro Oxazaborinines. *Dyes Pigments* **2018**, *157*, 198–217.

(95) Köhling, J.; Kozel, V.; Jovanov, V.; Pajkert, R.; Tverdomed, S. N.; Gridenco, O.; Fugel, M.; Grabowsky, S.; Röschenthaler, G.-V.; Wagner, V. Synthesis and Characterization of Oxazaborinin Phosphonate for Blue OLED Emitter Applications. *ChemPhysChem* **2019**, *20*, 665–671.

(96) Mtiraoui, H.; Gharbi, R.; Msaddek, M.; Bretonnière, Y.; Andraud, C.; Renard, P.-Y.; Sabot, C. Solution and Solid-State Fluorescence of 2-(2′-Hydroxyphenyl)-1,5-Benzodiazepin-2-One (HBD) Borate Complexes. *RSC Adv.* **2016**, *6*, 86352–86360.

(97) Chęcińska, L.; Mebs, S.; Ośmiałowski, B.; Zakrzewska, A.; Ejsmont, K.; Kohout, M. Tuning the Electronic Properties of the Dative N−B Bond with Associated O−B Interaction: Electron Localizability Indicator from X-Ray Wavefunction Refinement. *ChemPhysChem* **2016**, *17*, 2395–2406.

(98) Itoh, K.; Okazaki, K.; Fujimoto, M. The Structure of 1,3-Enaminoketonatoboron Difluorides in Solution and in the Solid State. *Aust. J. Chem.* **2003**, *56*, 1209–1214.

(99) Grepioni, F.; Cojazzi, G.; Draper, S. M.; Scully, N.; Braga, D. Crystal Forms of Hexafluorophosphate Organometallic Salts and the Importance of Charge-Assisted C−H---F Hydrogen Bonds. *Organometallics* **1998**, *17*, 296–307.

(100) Mandapati, P.; Braun, J. D.; Killeen, C.; Davis, R. L.; Williams, J. A. G.; Herbert, D. E. Luminescent Platinum(II) Complexes of N^N⁻^N Amido Ligands with Benzannulated N-

Heterocyclic Donor Arms: Quinolines Offer Unexpectedly Deeper Red Phosphorescence than Phenanthridines. *Inorg. Chem.* **2019**, *58*, 14808–14817.

(101) Lozada, I. B.; Williams, J. A. G.; Herbert, D. E. Platinum(II) Complexes of Benzannulated N^N⁻^O-Amido Ligands: Bright Orange Phosphors with Long-Lived Excited States. *Inorg. Chem. Front.* **2022**, *9*, 10–22.

(102) Donckt, E. V.; Dramaix, R.; Nasielski, J.; Vogels, C. Photochemistry of Aromatic Compounds. Part 1.—Acid-Base Properties of Singlet and Triplet Excited States of Pyrene Derivatives and Aza-Aromatic Compounds. *Trans. Faraday Soc.* **1969**, *65*, 3258–3262.

(103) Zander, M. The Significance of Donor-Acceptor Interactions in the External Heavy Atom Effect of Silver Nitrate on the Luminescence Behavior of Aza-Aromatic Systems and Carbazoles. *Z Naturforsch A* **1978**, *33*, 998–1000.

(104) Norek, M.; Dresner, J.; Prochorow, J. Spectroscopy and Photophysics of Monoazaphenanthrenes. I. Absorption and Fluorescence Spectra of Phenanthridine and 7,8-Benzoquinoline. *Acta Phys. Pol. A* **2003**, *104*, 425–439.

(105) Marzzacco, C. J.; Deckey, G.; Colarulli, R.; Siuzdak, G.; Halpern, A. M. Excited-State Protonation and Photophysical Properties of Azaphenanthrenes. *J. Phys. Chem.* **1989**, *93*, 2935–2939.

(106) Parker, D.; Senanayake, P. K.; Williams, J. A. G. Luminescent Sensors for PH, PO2, Halide and Hydroxide Ions Using Phenanthridine as a Photosensitiser in Macrocyclic Europium and Terbium Complexes. *J. Chem. Soc. Perkin Trans. 2* **1998**, 2129–2140.

(107) Norek, M.; Kozankiewicz, B.; Prochorow, J. Spectroscopy and Photophysics of Monoazaphenanthrenes. III. Luminescence of Phenanthridine and 7,8-Benzoquinoline in Crystalline State. *Acta Phys Pol A* **2004**, *106*, 77–94.

(108) Lozada, I. B.; Murray, T.; Herbert, D. E. Monomeric Zinc(II) Amide Complexes Supported by Bidentate, Benzannulated Phenanthridine Amido Ligands. *Polyhedron* **2019**, *161*, 261–267.

(109) Lozada, I. B.; Ortiz, R. J.; Braun, J. D.; Williams, J. A. G.; Herbert, D. E. Donor–Acceptor Boron-Ketoiminate Complexes with Pendent N-Heterocyclic Arms: Switched-on Luminescence through N-Heterocycle Methylation. *J. Org. Chem.* **2022**, *87*, 184–196.

(110) Bridgeman, A. J.; Cavigliasso, G.; Ireland, L. R.; Rothery, J. The Mayer Bond Order as a Tool in Inorganic Chemistry. *J. Chem. Soc. Dalton Trans.* **2001**, 2095–2108.

(111) Lu, T.; Chen, F. Atomic Dipole Moment Corrected Hirshfeld Population Method. *J. Theor. Comput. Chem.* **2012**, *11*, 163–183.

(112) Montalti, M.; Credi, A.; Prodi, L.; Gandolfi, M. *Handbook of Photochemistry. 3rd Ed.*; CRC Press: Boca Raton, 2006.

(113) Oyler, K. D.; Coughlin, F. J.; Bernhard, S. Controlling the Helicity of 2,2'-Bipyridyl Ruthenium(II) and Zinc(II) Hemicage Complexes. *J. Am. Chem. Soc.* **2007**, *129*, 210–217.

(114) Martinez, S.; Igoa, F.; Carrera, I.; Seoane, G.; Veiga, N.; De Camargo, A. S. S.; Kremer, C.; Torres, J. A Zn(II) Luminescent Complex with a Schiff Base Ligand: Solution, Computational and Solid State Studies. *J. Coord. Chem.* **2018**, *71*, 874–889.

(115) Mei, J.; Leung, N. L. C.; Kwok, R. T. K.; Lam, J. W. Y.; Tang, B. Z. Aggregation-Induced Emission: Together We Shine, United We Soar! *Chem. Rev.* **2015**, *115*, 11718–11940.

(116) Singh, K.; Siddiqui, I.; Sridharan, V.; Kumar Yadav, R. A.; Jou, J.-H.; Adhikari, D. Aggregation-Induced Enhanced Emission-Active Zinc(II) β-Diketiminate Complexes

Enabling High-Performance Solution-Processable OLEDs. *Inorg. Chem.* **2021**, *60*, 19128–19135.

(117) Singh, K.; S., V.; Adhikari, D. Visible Light Photoredox by a (Ph,ArNacNac)2Zn Photocatalyst: Photophysical Properties and Mechanistic Understanding. *Inorg. Chem. Front.* **2021**, *8*, 2078–2087.

(118) Lozada, I. B.; Huang, B.; Stilgenbauer, M.; Beach, T.; Qiu, Z.; Zheng, Y.; Herbert, D. E. Monofunctional Platinum(II) Anticancer Complexes Based on Multidentate Phenanthridine-Containing Ligand Frameworks. *Dalton Trans.* **2020**, *49*, 6557–6560.

(119) Mandapati, P.; Giesbrecht, P. K.; Davis, R. L.; Herbert, D. E. Phenanthridine-Containing Pincer-like Amido Complexes of Nickel, Palladium, and Platinum. *Inorg. Chem.* **2017**, *56*, 3674–3685.

(120) Mandapati, P.; Braun, J. D.; Killeen, C.; Davis, R. L.; Williams, J. A. G.; Herbert, D. E. Luminescent Platinum(II) Complexes of N⏜N-⏜N Amido Ligands with Benzannulated N-Heterocyclic Donor Arms: Quinolines Offer Unexpectedly Deeper Red Phosphorescence than Phenanthridines. *Inorg Chem* **2019**, *58*, 14808–14817.

(121) Mandapati, P.; Braun, J. D.; Lozada, I. B.; Williams, J. A. G.; Herbert, D. E. Deep-Red Luminescence from Platinum(II) Complexes of N^N−^N-Amido Ligands with Benzannulated N-Heterocyclic Donor Arms. *Inorg. Chem.* **2020**, *59*, 12504–12517.

(122) Reineke, M. H.; Sampson, M. D.; Rheingold, A. L.; Kubiak, C. P. Synthesis and Structural Studies of Nickel(0) Tetracarbene Complexes with the Introduction of a New Four-Coordinate Geometric Index, Tδ. *Inorg. Chem.* **2015**, *54*, 3211–3217.

(123) Puttock, E. V.; Fradgley, J. D.; Yufit, D. S.; Williams, J. A. G. A Family of Readily Synthesised Phosphorescent Platinum(II) Complexes Based on Tridentate *N^N^O* -Coordinating Schiff-Base Ligands. *Dalton Trans.* **2019**, *48*, 15012–15028.

(124) Davidson, J. J.; DeMott, J. C.; Douvris, C.; Fafard, C. M.; Bhuvanesh, N.; Chen, C.-H.; Herbert, D. E.; Lee, C.-I.; McCulloch, B. J.; Foxman, B. M.; Ozerov, O. V. Comparison of the Electronic Properties of Diarylamido-Based PNZ Pincer Ligands: Redox Activity at the Ligand and Donor Ability Toward the Metal. *Inorg. Chem.* **2015**, *54*, 2916–2935.

(125) Giesbrecht, P. K.; Nemez, D. B.; Herbert, D. E. Electrochemical Hydrogenation of a Benzannulated Pyridine to a Dihydropyridine in Acidic Solution. *Chem. Commun.* **2018**, *54*, 338–341.

(126) Reichardt, C. Solvatochromic Dyes as Solvent Polarity Indicators. *Chem. Rev.* **1994**, *94*, 2319–2358.

(127) Catalán, J. Toward a Generalized Treatment of the Solvent Effect Based on Four Empirical Scales: Dipolarity (SdP, a New Scale), Polarizability (SP), Acidity (SA), and Basicity (SB) of the Medium. *J. Phys. Chem. B* **2009**, *113*, 5951–5960.

(128) Van der Zwan, G.; Hynes, J. T. Time-Dependent Fluorescence Solvent Shifts, Dielectric Friction, and Nonequilibrium Solvation in Polar Solvents. *J. Phys. Chem.* **1985**, *89*, 4181–4188.

(129) Caspar, J. V.; Meyer, T. J. Photochemistry of Tris(2,2'-Bipyridine)Ruthenium(2+) Ion (Ru(Bpy)$_3^{2+}$). Solvent Effects. *J. Am. Chem. Soc.* **1983**, *105*, 5583–5590.

(130) Kwok, C.-C.; Ngai, H. M. Y.; Chan, S.-C.; Sham, I. H. T.; Che, C.-M.; Zhu, N. [(O⋀N⋀N)PtX] Complexes as a New Class of Light-Emitting Materials for Electrophosphorescent Devices. *Inorg. Chem.* **2005**, *44*, 4442–4444.

(131) Garner, K. L.; Parkes, L. F.; Piper, J. D.; Williams, J. A. G. Luminescent Platinum Complexes with Terdentate Ligands Forming 6-Membered Chelate Rings: Advantageous and Deleterious Effects in N ^ N ^ N and N ^ C ^ N-Coordinated Complexes. *Inorg. Chem.* **2010**, *49*, 476–487.

(132) Williams, J. A. G. The Coordination Chemistry of Dipyridylbenzene: N-Deficient Terpyridine or Panacea for Brightly Luminescent Metal Complexes? *Chem. Soc. Rev.* **2009**, *38*, 1783–1801.

(133) Meech, S. R.; Phillips, D. Photophysics of Some Common Fluorescence Standards. *J. Photochem.* **1983**, *23*, 193–217.

(134) Suzuki, K.; Kobayashi, A.; Kaneko, S.; Takehira, K.; Yoshihara, T.; Ishida, H.; Shiina, Y.; Oishi, S.; Tobita, S. Reevaluation of Absolute Luminescence Quantum Yields of Standard Solutions Using a Spectrometer with an Integrating Sphere and a Back-Thinned CCD Detector. *Phys. Chem. Chem. Phys.* **2009**, *11*, 9850–9860.

(135) Murov, S. L.; Carmichael, I.; Hug, G. L. *Handbook of Photochemistry, 2nd Ed.*; Marcel Dekker: New York, 1993.

(136) Hohenberg, P.; Kohn, W. Inhomogeneous Electron Gas. *Phys. Rev.* **1964**, *136* (3B), B864–B871. https://doi.org/10.1103/PhysRev.136.B864.

(137) Kohn, W.; Sham, L. J. Self-Consistent Equations Including Exchange and Correlation Effects. *Phys. Rev.* **1965**, *140* (4A), A1133–A1138. https://doi.org/10.1103/PhysRev.140.A1133.

(138) Bühl, M.; Kabrede, H. Geometries of Transition-Metal Complexes from Density-Functional Theory. *J. Chem. Theory Comput.* **2006**, *2* (5), 1282–1290. https://doi.org/10.1021/ct6001187.

(139) Waller, M. P.; Braun, H.; Hojdis, N.; Bühl, M. Geometries of Second-Row Transition-Metal Complexes from Density-Functional Theory. *J. Chem. Theory Comput.* **2007**, *3* (6), 2234–2242. https://doi.org/10.1021/ct700178y.

(140) Bühl, M.; Reimann, C.; Pantazis, D. A.; Bredow, T.; Neese, F. Geometries of Third-Row Transition-Metal Complexes from Density-Functional Theory. *J. Chem. Theory Comput.* **2008**, *4* (9), 1449–1459. https://doi.org/10.1021/ct800172j.

(141) de Souza, B.; Farias, G.; Neese, F.; Izsák, R. Predicting Phosphorescence Rates of Light Organic Molecules Using Time-Dependent Density Functional Theory and the Path Integral Approach to Dynamics. *J. Chem. Theory Comput.* **2019**, *15* (3), 1896–1904. https://doi.org/10.1021/acs.jctc.8b00841.

(142) de Souza, B.; Neese, F.; Izsák, R. On the Theoretical Prediction of Fluorescence Rates from First Principles Using the Path Integral Approach. *J. Chem. Phys.* **2018**, *148* (3), 034104. https://doi.org/10.1063/1.5010895.

(143) Petrenko, T.; Neese, F. Analysis and Prediction of Absorption Band Shapes, Fluorescence Band Shapes, Resonance Raman Intensities, and Excitation Profiles Using the Time-Dependent Theory of Electronic Spectroscopy. *J. Chem. Phys.* **2007**, *127* (16), 164319. https://doi.org/10.1063/1.2770706.

(144) Wenger, O. S. Is Iron the New Ruthenium? *Chem. – Eur. J.* **2020**, *25*, 6043–6052.

(145) Baková, R.; Chergui, M.; Daniel, C.; Vlček Jr., A.; Záliš, S. Relativistic Effects in Spectroscopy and Photophysics of Heavy-Metal Complexes Illustrated by Spin–Orbit Calculations of [Re(Imidazole)(CO)3(Phen)]+. *Coord. Chem. Rev.* **2011**, *255* (7–8), 975–989. https://doi.org/10.1016/j.ccr.2010.12.027.

(146) Giesbrecht, P. K.; Nemez, D. B.; Herbert, D. E. Electrochemical Hydrogenation of a Benzannulated Pyridine to a Dihydropyridine in Acidic Solution. *Chem. Commun.* **2018**, *54* (4), 338–341. https://doi.org/10.1039/c7cc07907a.

(147) Mandapati, P.; Giesbrecht, P. K.; Davis, R. L.; Herbert, D. E. Phenanthridine-Containing Pincer-like Amido Complexes of Nickel, Palladium, and Platinum. *Inorg. Chem.* **2017**, *56* (6), 3674–3685. https://doi.org/10.1021/acs.inorgchem.7b00075.

(148) Mondal, R.; Lozada, I. B.; Davis, R. L.; Williams, J. A. G.; Herbert, D. E. Exploiting Synergy between Ligand Design and Counterion Interactions to Boost Room Temperature Phosphorescence from Cu(i) Compounds. *J. Mater. Chem. C* **2019**, *7* (13), 3772–3778. https://doi.org/10.1039/C9TC00040B.

(149) Mandapati, P.; Braun, J. D.; Killeen, C.; Davis, R. L.; Williams, J. A. G.; Herbert, D. E. Luminescent Platinum(II) Complexes of N^ N-^ N Amido Ligands with Benzannulated N-Heterocyclic Donor Arms: Quinolines Offer Unexpectedly Deeper Red Phosphorescence than Phenanthridines. *Inorg. Chem.* **2019**, *58* (21), 14808–14817. https://doi.org/10.1021/acs.inorgchem.9b02480.

(150) Lozada, I. B.; Murray, T.; Herbert, D. E. Monomeric Zinc(II) Amide Complexes Supported by Bidentate, Benzannulated Phenanthridine Amido Ligands. *Polyhedron* **2019**, *161*, 261–267. https://doi.org/10.1016/j.poly.2019.01.023.

(151) Braun, J. D.; Lozada, I. B.; Kolodziej, C.; Burda, C.; Newman, K. M. E.; van Lierop, J.; Davis, R. L.; Herbert, D. E. Iron(Ii) Coordination Complexes with Panchromatic Absorption and Nanosecond Charge-Transfer Excited State Lifetimes. *Nat. Chem.* **2019**, *11* (12), 1144–1150. https://doi.org/10.1038/s41557-019-0357-z.

(152) Mondal, R.; Lozada, I. B.; Davis, R. L.; Williams, J. A. G.; Herbert, D. E. Site-Selective Benzannulation of N-Heterocycles in Bidentate Ligands Leads to Blue-Shifted Emission from [(P^N)Cu]2(μ-X)2 Dimers. *Inorg. Chem.* **2018**, *57* (9), 4966–4978. https://doi.org/10.1021/acs.inorgchem.7b03223.

(153) Mondal, R.; Giesbrecht, P. K.; Herbert, D. E. Nickel(II), Copper(I) and Zinc(II) Complexes Supported by a (4-Diphenylphosphino)Phenanthridine Ligand. *Polyhedron* **2016**, *108*, 156–162. https://doi.org/10.1016/j.poly.2015.10.051.

(154) Stufkens, D. J.; Vlček, A. Ligand-Dependent Excited State Behaviour of Re(I) and Ru(II) Carbonyl-Diimine Complexes. *Coord. Chem. Rev.* **1998**, *177* (1), 127–179. https://doi.org/10.1016/s0010-8545(98)00132-5.

(155) Vlček, A. Ultrafast Excited-State Processes in Re(I) Carbonyl-Diimine Complexes: From Excitation to Photochemistry. *Top Organomet Chem* **2010**, *29* (May 2009), 73–114. https://doi.org/10.1007/3418.

(156) Mandapati, P.; Braun, J. D.; Killeen, C.; Davis, R. L.; Williams, J. A. G.; Herbert, D. E. Luminescent Platinum(II) Complexes of N ̂N- ̂N Amido Ligands with Benzannulated N-Heterocyclic Donor Arms: Quinolines Offer Unexpectedly Deeper Red Phosphorescence than Phenanthridines. *Inorg Chem* **2019**, *58*, 14808–14817.

(157) Dixon, I. M.; Khan, S.; Alary, F.; Boggio-Pasqua, M.; Heully, J.-L. Probing the Photophysical Capability of Mono and Bis(Cyclometallated) Fe(II) Polypyridine Complexes Using Inexpensive Ground State DFT. *Dalton Trans.* **2014**, *43*, 15898–15905.

(158) Zhang, K.; Ash, R.; Girolami, G. S.; Vura-Weis, J. Tracking the Metal-Centered Triplet in Photoinduced Spin Crossover of Fe(Phen)32+ with Tabletop Femtosecond M-Edge X-Ray Absorption Near-Edge Structure Spectroscopy. *J. Am. Chem. Soc.* **2019**, *141*, 17180–17188.

(159) Juban, E. A.; Smeigh, A. L.; Monat, J. E.; McCusker, J. K. Ultrafast Dynamics of Ligand-Field Excited States. *Coord Chem Rev* **2006**, *250*, 1783–1791.

(160) Gryn'ova, G.; Coote, M. L.; Corminboeuf, C. Theory and Practice of Uncommon Molecular Electronic Configurations. *WIREs Comput. Mol. Sci.* **2015**, *5* (6), 440–459. https://doi.org/10.1002/wcms.1233.

(161) Kaim, W. Manifestations of Noninnocent Ligand Behavior. *Inorg Chem* **2011**, *50* (20), 9752–9765.

(162) Bowman, D. N.; Jakubikova, E. Low-Spin versus High-Spin Ground State in Pseudo-Octahedral Iron Complexes. *Inorg. Chem.* **2012**, *51*, 6011–6019.

(163) Ashley, D. C.; Jakubikova, E. Ironing out the Photochemical and Spin-Crossover Behavior of Fe(II) Coordination Compounds with Computational Chemistry. *Coord. Chem. Rev.* **2017**, *337*, 97–111.

(164) Reiher, M.; Salomon, O.; Artur Hess, B. Reparameterization of Hybrid Functionals Based on Energy Differences of States of Different Multiplicity. *Theor. Chem. Acc.* **2001**, *107*, 48–55.

(165) Jakubikova, E.; Bowman, D. N. Fe(II)-Polypyridines as Chromophores in Dye-Sensitized Solar Cells: A Computational Perspective. *Acc. Chem. Res.* **2015**, *48*, 1441–1449.

(166) Nemykin, V. N.; Hadt, R. G. Influence of Hartree−Fock Exchange on the Calculated Mössbauer Isomer Shifts and Quadrupole Splittings in Ferrocene Derivatives Using Density Functional Theory. *Inorg. Chem.* **2006**, *45*, 8297–8307.

(167) Zhao, Y.; Truhlar, D. G. A New Local Density Functional for Main-Group Thermochemistry, Transition Metal Bonding, Thermochemical Kinetics, and Noncovalent Interactions. *J. Chem. Phys.* **2006**, *125*, 194101.

(168) Cohen, A. J.; Handy, N. C. Dynamic Correlation. *Mol. Phys.* **2001**, *99*, 607–615.

(169) Zhao, Y.; Truhlar, D. G. The M06 Suite of Density Functionals for Main Group Thermochemistry, Thermochemical Kinetics, Noncovalent Interactions, Excited States, and Transition Elements: Two New Functionals and Systematic Testing of Four M06-Class Functionals and 12 Other Functionals. *Theor. Chem. Acc.* **2008**, *120*, 215–241.

(170) Ditchfield, R.; Hehre, W. J.; Pople, J. A. Self-Consistent Molecular-Orbital Methods. IX. Extended Gaussian-Type Basis for Molecular-Orbital Studies of Organic Molecules. *J. Chem. Phys.* **1971**, *54*, 724–728. https://doi.org/10.1063/1.1674902.

(171) Hehre, W. J.; Ditchfield, R.; Pople, J. A. Self-Consistent Molecular Orbital Methods. XII. Further Extensions of Gaussian-Type Basis Sets for Use in Molecular Orbital Studies of Organic Molecules. *J. Chem. Phys.* **1972**, *56*, 2257–2261.

(172) Hariharan, P. C.; Pople, J. A. Influence of Polarization Functions on MO Hydrogenation Energies. *Theor. Chim. Acta* **1973**, *28*, 213–222.

(173) Clark, T.; Chandrasekhar, J.; Spitznagel, G. W.; Schleyer, P. v R. Efficient Diffuse Function-Augmented Basis Sets for Anion Calculations. III. The 3-21 + G Basis Set for First-Row Elements, Lithium to Fluorine. *J. Comput. Chem.* **1983**, *4*, 294–301.

(174) Rassolov, V. A.; Pople, J. A.; Ratner, M. A.; Windus, T. L. 6-31G* Basis Set for Atoms K through Zn. *J. Chem. Phys.* **1998**, *109*, 1223–1229.

(175) Zhao, Y.; Truhlar, D. G. A New Local Density Functional for Main-Group Thermochemistry, Transition Metal Bonding, Thermochemical Kinetics, and Noncovalent Interactions. *J. Chem. Phys.* **2006**, *125* (19), 194101. https://doi.org/10.1063/1.2370993.

(176) Krishnan, R.; Binkley, J. S.; Seeger, R.; Pople, J. A. Self-consistent Molecular Orbital Methods. XX. A Basis Set for Correlated Wave Functions. *J. Chem. Phys.* **1980**, *72* (1), 650–654. https://doi.org/10.1063/1.438955.

(177) Clark, T.; Chandrasekhar, J.; Spitznagel, G. W.; Schleyer, P. V. R. Efficient Diffuse Function-Augmented Basis Sets for Anion Calculations. III. The 3-21+G Basis Set for First-Row Elements, Li-F. *J. Comput. Chem.* **1983**, *4* (3), 294–301. https://doi.org/10.1002/jcc.540040303.

(178) Dennington, Roy; Keith, Todd A.; Millam, John M. *GaussView, Version 6*; Semichem Inc.: Shawnee Mission, KS, 2016.

(179) Soda, T.; Kitagawa, Y.; Onishi, T.; Takano, Y.; Shigeta, Y.; Nagao, H.; Yoshioka, Y.; Yamaguchi, K. Ab Initio Computations of Effective Exchange Integrals for H–H, H–He–H and Mn2O2 Complex: Comparison of Broken-Symmetry Approaches. *Chem. Phys. Lett.* **2000**, *319* (3–4), 223–230. https://doi.org/10.1016/S0009-2614(00)00166-4.

(180) Yamaguchi, K.; Takahara, Y.; Fueno, T. Ab-Initio Molecular Orbital Studies of Structure and Reactivity of Transition Metal-OXO Compounds. In *Applied Quantum Chemistry*; Smith, V. H., Schaefer, H. F., Morokuma, K., Eds.; Springer Netherlands: Dordrecht, 1986; pp 155–184. https://doi.org/10.1007/978-94-009-4746-7_11.

(181) Heydová, R.; Gindensperger, E.; Romano, R.; Sýkora, J.; Vlček, A.; Záliš, S.; Daniel, C. Spin-Orbit Treatment of UV-Vis Absorption Spectra and Photophysics of Rhenium(I) Carbonyl-Bipyridine Complexes: MS-CASPT2 and TD-DFT Analysis. *J. Phys. Chem. A* **2012**, *116* (46), 11319–11329. https://doi.org/10.1021/jp305461z.

(182) Ronca, E.; De Angelis, F.; Fantacci, S. Time-Dependent Density Functional Theory Modeling of Spin-Orbit Coupling in Ruthenium and Osmium Solar Cell Sensitizers. *J. Phys. Chem. C* **2014**, *118* (30), 17067–17078. https://doi.org/10.1021/jp500869r.

(183) Mai, S.; Gattuso, H.; Fumanal, M.; Muñoz-Losa, A.; Monari, A.; Daniel, C.; González, L. Excited-States of a Rhenium Carbonyl Diimine Complex: Solvation Models, Spin-Orbit Coupling, and Vibrational Sampling Effects. *Phys. Chem. Chem. Phys.* **2017**, *19* (40), 27240–27250. https://doi.org/10.1039/c7cp05126c.

(184) Shi, L. L.; Liao, Y.; Zhao, L.; Su, Z. M.; Kan, Y. H.; Yang, G. C.; Yang, S. Y. Theoretical Studies on the Electronic Structure and Spectral Properties of Versatile Diarylethene-Containing 1,10-Phenanthroline Ligands and Their Rhenium(I) Complexes. *J. Organomet. Chem.* **2007**, *692* (24), 5368–5374. https://doi.org/10.1016/j.jorganchem.2007.08.031.

(185) Silva-Junior, M. R.; Schreiber, M.; Sauer, S. P. A.; Thiel, W. Benchmarks for Electronically Excited States: Time-Dependent Density Functional Theory and Density Functional Theory Based Multireference Configuration Interaction. *J. Chem. Phys.* **2008**, *129* (10). https://doi.org/10.1063/1.2973541.

(186) Jacquemin, D.; Perpète, E. A.; Ciofini, I.; Adamo, C. Assessment of Functionals for TD-DFT Calculations of Singlet-Triplet Transitions. *J. Chem. Theory Comput.* **2010**, *6* (5), 1532–1537. https://doi.org/10.1021/ct100005d.

(187) Santoro, F.; Lami, A.; Improta, R.; Barone, V. Effective Method to Compute Vibrationally Resolved Optical Spectra of Large Molecules at Finite Temperature in the Gas Phase and in Solution. *J. Chem. Phys.* **2007**, *126* (18). https://doi.org/10.1063/1.2721539.

(188) Tozer, D. J.; Handy, N. C. On the Determination of Excitation Energies Using Density Functional Theory. *Phys. Chem. Chem. Phys.* **2000**, *2* (10), 2117–2121. https://doi.org/10.1039/a910321j.

(189) Chibani, S.; Charaf-Eddin, A.; Le Guennic, B.; Jacquemin, D. Boranil and Related NBO Dyes: Insights From Theory. *J. Chem. Theory Comput.* **2013**, *9*, 3127–3135.

(190) Mondal, R.; Giesbrecht, P. K.; Herbert, D. E. Nickel(II), Copper(I) and Zinc(II) Complexes Supported by a (4-Diphenylphosphino)Phenanthridine Ligand. *Polyhedron* **2016**, *108*, 156–162.

(191) Mondal, R.; Lozada, I. B.; Davis, R. L.; Williams, J. A. G.; Herbert, D. E. Site-Selective Benzannulation of N-Heterocycles in Bidentate Ligands Leads to Blue-Shifted Emission from [(*P^N*)Cu]$_2$(μ-X)$_2$ Dimers. *Inorg Chem* **2018**, *57*, 4966–4978.

(192) Gaire, S.; Ortiz, R. J.; Schrage, B. R.; Lozada, I. B.; Mandapati, P.; Osinski, A. J.; Herbert, D. E.; Ziegler, C. J. (8-Amino)Quinoline and (4-Amino)Phenanthridine Complexes of Re(CO)3 Halides. *J. Organomet. Chem.* **2020**, *921*, 121338.

(193) Tomasi, J.; Mennucci, B.; Cammi, R. Quantum Mechanical Continuum Solvation Models. *Chem Rev* **2005**, *105*, 2999–3094.

(194) Melenbacher, A.; Dhindsa, J. S.; Gilroy, J. B.; Stillman, M. J. Unveiling the Hidden, Dark, and Short Life of a Vibronic State in a Boron Difluoride Formazanate Dye. *Angew. Chem. Int. Ed.* **2019**, *58* (43), 15339–15343.

(195) El-Sayed, M. A. Spin—Orbit Coupling and the Radiationless Processes in Nitrogen Heterocyclics. *J. Chem. Phys.* **1963**, *38* (12), 2834–2838.

(196) Braun, J. D.; Lozada, I. B.; Kolodziej, C.; Burda, C.; Newman, K. M. E.; van Lierop, J.; Davis, R. L.; Herbert, D. E. Iron(II) Coordination Complexes with Panchromatic Absorption and Nanosecond Charge-Transfer Excited State Lifetimes. *Nat. Chem.* **2019**, *11*, 1144–1150.

(197) Larsen, C. B.; Braun, J. D.; Lozada, I. B.; Kunnus, K.; Biasin, E.; Kolodziej, C.; Burda, C.; Cordones, A. A.; Gaffney, K. J.; Herbert, D. E. Reduction of Electron Repulsion in Highly Covalent Fe-Amido Complexes Counteracts the Impact of a Weak Ligand Field on Excited-State Ordering. *J. Am. Chem. Soc.* **2021**, *143*, 20645–20656.

(198) Das, S.; Thornbury, W. G.; Bartynski, A. N.; Thompson, M. E.; Bradforth, S. E. Manipulating Triplet Yield through Control of Symmetry-Breaking Charge Transfer. *J. Phys. Chem. Lett.* **2018**, *9*, 3264–3270.

(199) Trinh, C.; Kirlikovali, K.; Das, S.; Ener, M. E.; Gray, H. B.; Djurovich, P.; Bradforth, S. E.; Thompson, M. E. Symmetry-Breaking Charge Transfer of Visible Light Absorbing Systems: Zinc Dipyrrins. *J. Phys. Chem. C* **2014**, *118*, 21834–21845.

(200) Kellogg, M.; Akil, A.; Muthiah Ravinson, D. S.; Estergreen, L.; Bradforth, S. E.; Thompson, M. E. Symmetry Breaking Charge Transfer as a Means to Study Electron Transfer with No Driving Force. *Faraday Discuss.* **2019**, *216*, 379–394.

(201) Mahmood, Z.; Rehmat, N.; Ji, S.; Zhao, J.; Sun, S.; Di Donato, M.; Li, M.; Teddei, M.; Huo, Y. Tuning the Triplet Excited State of Bis(Dipyrrin) Zinc(II) Complexes: Symmetry Breaking Charge Transfer Architecture with Exceptionally Long Lived Triplet State for Upconversion. *Chem. – Eur. J.* **2020**, *26*, 14912–14918.

(202) Weller, A. Photoinduced Electron Transfer in Solution: Exciplex and Radical Ion Pair Formation Free Enthalpies and Their Solvent Dependence By. *Zeitshcrift Phys. Chem. N. F.* **1982**, *133*, 93–98.

(203) Rehm, D.; Weller, A. Kinetics of Fluorescence Quenching by Electron and H-Atom Transfer. *Isr. J. Chem.* **1970**, *8*, 259–271.

(204) Vauthey, E. Photoinduced Symmetry-Breaking Charge Separation. *ChemPhysChem* **2012**, *13*, 2001–2011.

(205) Smith, A. R. G.; Burn, P. L.; Powell, B. J. Spin–Orbit Coupling in Phosphorescent Iridium(III) Complexes. *ChemPhysChem* **2011**, *12*, 2429–2438.

(206) Ronca, E.; De Angelis, F.; Fantacci, S. Time-Dependent Density Functional Theory Modeling of Spin–Orbit Coupling in Ruthenium and Osmium Solar Cell Sensitizers. *J. Phys. Chem. C* **2014**, *118*, 17067–17078.

(207) Gourlaouen, C.; Daniel, C. Spin–Orbit Effects in Square-Planar Pt(II) Complexes with Bidentate and Terdentate Ligands: Theoretical Absorption/Emission Spectroscopy. *Dalton Trans* **2014**, *43*, 17806–17819.

(208) Braun, J. D.; Lozada, I. B.; Herbert, D. E. In Pursuit of Panchromatic Absorption in Metal Coordination Complexes: Experimental Delineation of the HOMO Inversion Model Using Pseudo-Octahedral Complexes of Diarylamido Ligands. *Inorg. Chem.* **2020**, *59*, 17746–17757.

(209) Hayashi, M.; Takahashi, Y.; Yoshida, Y.; Sugimoto, K.; Kitagawa, H. Role of D-Elements in a Proton–Electron Coupling of d–π Hybridized Electron Systems. *J. Am. Chem. Soc.* **2019**, *141*, 11686–11693.

(210) Spencer, M.; Santoro, A.; Freeman, G. R.; Díez, Á.; Murray, P. R.; Torroba, J.; Whitwood, A. C.; Yellowlees, L. J.; Williams, J. A. G.; Bruce, D. W. Phosphorescent, Liquid-Crystalline Complexes of Platinum(II): Influence of the β-Diketonate Co-Ligand on Mesomorphism and Emission Properties. *Dalton Trans.* **2012**, *41*, 14244–14256.

(211) Neese, F. The ORCA Program System. *WIREs Comput. Mol. Sci.* **2012**, *2*, 73–78.

(212) Neese, F. Software Update: The ORCA Program System, Version 4.0. *WIREs Comput. Mol. Sci.* **2018**, *8*, e1327.

(213) Frisch, M. J.; Trucks, G. W.; Schlegel, H. B.; Scuseria, G. E.; Robb, M. A.; Cheeseman, J. R.; Scalmani, G.; Barone, V.; Petersson, G. A.; Nakatsuji, H.; Li, X.; Caricato, M.; Marenich, A. V.; Bloino, J.; Janesko, B. G.; Gomperts, R.; Mennucci, B.; Hratchian, H. P.; Ortiz, J. V.; Izmaylov, A. F.; Sonnenberg, J. L.; Williams; Ding, F.; Lipparini, F.; Egidi, F.; Goings, J.; Peng, B.; Petrone, A.; Henderson, T.; Ranasinghe, D.; Zakrzewski, V. G.; Gao, J.; Rega, N.; Zheng, G.; Liang, W.; Hada, M.; Ehara, M.; Toyota, K.; Fukuda, R.; Hasegawa, J.; Ishida, M.; Nakajima, T.; Honda, Y.; Kitao, O.; Nakai, H.; Vreven, T.; Throssell, K.; Montgomery Jr., J. A.; Peralta, J. E.; Ogliaro, F.; Bearpark, M. J.; Heyd, J. J.; Brothers, E. N.; Kudin, K. N.; Staroverov, V. N.; Keith, T. A.; Kobayashi, R.; Normand, J.; Raghavachari, K.; Rendell, A. P.; Burant, J. C.; Iyengar, S. S.; Tomasi, J.; Cossi, M.; Millam, J. M.; Klene, M.; Adamo, C.; Cammi, R.; Ochterski, J. W.; Martin, R. L.; Morokuma, K.; Farkas, O.; Foresman, J. B.; Fox, D. J. *Gaussian 16 Rev. C.01*; Wallingford, CT, 2016.

(214) Marenich, A. V.; Cramer, C. J.; Truhlar, D. G. Universal Solvation Model Based on Solute Electron Density and on a Continuum Model of the Solvent Defined by the Bulk Dielectric Constant and Atomic Surface Tensions. *J Phys Chem B* **2009**, *113*, 6378–6396.

(215) Grimme, S.; Ehrlich, S.; Goerigk, L. Effect of the Damping Function in Dispersion Corrected Density Functional Theory. *J. Comput. Chem.* **2011**, *32*, 1456–1465.

(216) Becke, A. D. Density-Functional Thermochemistry. III. The Role of Exact Exchange. *J Chem Phys* **1993**, *98*, 5648–5652.

(217) Lee, C.; Yang, W.; Parr, R.G. Development of the Colle-Salvetti Correlation-Energy Formula into a Functional of the Electron Density. *Phys. Rev. B Condens. Matter* **1988**, *37*, 785–789.

(218) Vosko, S. H.; Wilk, L.; Nusair, M. Accurate Spin-Dependent Electron Liquid Correlation Energies for Local Spin Density Calculations: A Critical Analysis. *Can. J. Phys.* **1980**, *58*, 1200–1211.

(219) Stephens, P. J.; Devlin, F. J.; Chabalowski, C. F.; Frisch, M. J. Ab Initio Calculation of Vibrational Absorption and Circular Dichroism Spectra Using Density Functional Force Fields. *J Phys Chem* **1994**, *98*, 11623–11627.

(220) Weigend, F.; Ahlrichs, R. Balanced Basis Sets of Split Valence, Triple Zeta Valence and Quadruple Zeta Valence Quality for H to Rn: Design and Assessment of Accuracy. *Phys Chem Chem Phys* **2005**, *7*, 3297–3305.

(221) Tao, J.; Perdew, J. P.; Staroverov, V. N.; Scuseria, G. E. Climbing the Density Functional Ladder: Nonempirical Meta--Generalized Gradient Approximation Designed for Molecules and Solids. *Phys. Rev. Lett.* **2003**, *91*, 146401.

(222) Staroverov, V. N.; Scuseria, G. E.; Tao, J.; Perdew, J. P. Comparative Assessment of a New Nonempirical Density Functional: Molecules and Hydrogen-Bonded Complexes. *J. Chem. Phys.* **2003**, *119*, 12129–12137.

(223) O'Boyle, N. M.; Tenderholt, A. L.; Langner, K. M. Software News and Updates Cclib: A Library for Package-Independent Computational Chemistry Algorithms. *J Comput Chem* **2008**, *29*, 839–845.

(224) Lu, T.; Chen, F. Multiwfn: A Multifunctional Wavefunction Analyzer. *J Comput Chem* **2012**, *33*, 580–592.

(225) Xiao, M; Lu, T. Generalized Charge Decomposition Analysis (GCDA) Method. *J. Adv. Phys. Chem.* **2015**, *4*, 111–124.

(226) Frisch, M. J.; Trucks, G. W.; Schlegel, H. B.; Scuseria, G. E.; Robb, M. A.; Cheeseman, J. R.; Scalmani, G.; Barone, V.; Petersson, G. A.; Nakatsuji, H.; Li, X.; Caricato, M.; Marenich, A. V.; Bloino, J.; Janesko, B. G.; Gomperts, R.; Mennucci, B.; Hratchian, H. P.; Ortiz, J. V.; Izmaylov, A. F.; Sonnenberg, J. L.; Williams-Young, D.; Ding, F.; Lipparini, F.; Egidi, F.; Goings, J.; Peng, B.; Petrone, A.; Henderson, T.; Ranasinghe, D.; Zakrzewski, V. G.; Gao, J.; Rega, N.; Zheng, G.; Liang, W.; Hada, M.; Ehara, M.; Toyota, K.; Fukuda, R.; Hasegawa, J.; Ishida, M.; Nakajima, T.; Honda, Y.; Kitao, O.; Nakai, H.; Vreven, T.; Throssell, K.; Montgomery, J. A.; Peralta, J. E.; Ogliaro, F.; Bearpark, M. J.; Heyd, J. J.; Brothers, E. N.; Kudin, K. N.; Staroverov, V. N.; Keith, T. A.; Kobayashi, R.; Normand, J.; Raghavachari, K.; Rendell, A. P.; Burant, J. C.; Iyengar, S. S.; Tomasi, J.; Cossi, M.; Millam, J. M.; Klene, M.; Adamo, C.; Cammi, R.; Ochterski, J. W.; Martin, R. L.; Morokuma, K.; Farkas, O.; Foresman, J. B.; Fox, D. J. *Gaussian 16, Revision B.01*; Gaussian 16, Revision B.01, Gaussian, Inc., Wallingford CT; Gaussian, Inc.: Wallingford CT, 2016.

(227) Adamo, C.; Barone, V. Toward Reliable Density Functional Methods without Adjustable Parameters: The PBE0 Model. *J. Chem. Phys.* **1999**, *110* (13), 6158–6170.

(228) Andrae, D.; Huermann, U.; Dolg, M.; Stoll, H.; Preu, H. Energy-Adjustedab Initio Pseudopotentials for the Second and Third Row Transition Elements. *Theor. Chim. Acta* **1990**, *77*, 123–141.

(229) Yanai, T.; Tew, D. P.; Handy, N. C. A New Hybrid Exchange–Correlation Functional Using the Coulomb-Attenuating Method (CAM-B3LYP). *Chem. Phys. Lett.* **2004**, *393*, 51–57.

(230) Neese, F.; Wennmohs, F.; Hansen, A.; Becker, U. Efficient, Approximate and Parallel Hartree–Fock and Hybrid DFT Calculations. A 'Chain-of-Spheres' Algorithm for the Hartree–Fock Exchange. *Chem. Phys.* **2009**, *356*, 98–109.

(231) Lenthe, E. van; Baerends, E. J.; Snijders, J. G. Relativistic Regular Two-component Hamiltonians. *J. Chem. Phys.* **1993**, *99*, 4597–4610.

(232) Weigend, F. Accurate Coulomb-Fitting Basis Sets for H to Rn. *Phys. Chem. Chem. Phys.* **2006**, *8*, 1057.

(233) Pantazis, D. A.; Neese, F. All-Electron Scalar Relativistic Basis Sets for the Lanthanides. *J. Chem. Theory Comput.* **2009**, *5*, 2229–2238.

(234) Pantazis, D. A.; Neese, F. All-Electron Scalar Relativistic Basis Sets for the Actinides. *J. Chem. Theory Comput.* **2011**, *7*, 677–684.

(235) Pantazis, D. A.; Chen, X.-Y.; Landis, C. R.; Neese, F. All-Electron Scalar Relativistic Basis Sets for Third-Row Transition Metal Atoms. *J. Chem. Theory Comput.* **2008**, *4*, 908–919.

(236) Hirshfeld, F. L. Bonded-Atom Fragments for Describing Molecular Charge Densities. *Theor. Chim. Acta* **1977**, *44*, 129–138.

(237) Hanwell, M. D.; Curtis, D. E.; Lonie, D. C.; Vandermeersch, T.; Zurek, E.; Hutchison, G. R. Avogadro: An Advanced Semantic Chemical Editor, Visualization, and Analysis Platform. *J Cheminf* **2012**, *4*, 17.

(238) Frisch, M. J.; Trucks, G. W.; Schlegel, H. B.; Scuseria, G. E.; Robb, M. A.; Cheeseman, J. R.; Scalmani, G.; Barone, V.; Petersson, G. A.; Nakatsuji, H.; Li, X.; Caricato, M.; Marenich, A. V.; Bloino, J.; Janesko, B. G.; Gomperts, R.; Mennucci, B.; Hratchian, H. P.; Ortiz, J. V.; Izmaylov, A. F.; Sonnenberg, J. L.; Williams; Ding, F.; Lipparini, F.; Egidi, F.; Goings, J.; Peng, B.; Petrone, A.; Henderson, T.; Ranasinghe, D.; Zakrzewski, V. G.; Gao, J.; Rega, N.; Zheng, G.; Liang, W.; Hada, M.; Ehara, M.; Toyota, K.; Fukuda, R.; Hasegawa, J.; Ishida, M.; Nakajima, T.; Honda, Y.; Kitao, O.; Nakai, H.; Vreven, T.; Throssell, K.; Montgomery Jr., J. A.; Peralta, J. E.; Ogliaro, F.; Bearpark, M. J.; Heyd, J. J.; Brothers, E. N.; Kudin, K. N.; Staroverov, V. N.; Keith, T. A.; Kobayashi, R.; Normand, J.; Raghavachari, K.; Rendell, A. P.; Burant, J. C.; Iyengar, S. S.; Tomasi, J.; Cossi, M.; Millam, J. M.; Klene, M.; Adamo, C.; Cammi, R.; Ochterski, J. W.; Martin, R. L.; Morokuma, K.; Farkas, O.; Foresman, J. B.; Fox, D. J. Gaussian 16 Rev. C.01, 2016.

(239) Marenich, A. V.; Cramer, C. J.; Truhlar, D. G. Universal Solvation Model Based on Solute Electron Density and on a Continuum Model of the Solvent Defined by the Bulk Dielectric Constant and Atomic Surface Tensions. *J Phys Chem B* **2009**, *113*, 6378–6396.

(240) Dennington, Roy; Keith, Todd A.; Millam, John M. GaussView, Version 6, 2016.

(241) O'Boyle, N. M.; Tenderholt, A. L.; Langner, K. M. Software News and Updates Cclib: A Library for Package-Independent Computational Chemistry Algorithms. *J Comput Chem* **2008**, *29*, 839–845.

(242) Lu, T.; Chen, F. Multiwfn: A Multifunctional Wavefunction Analyzer. *J Comput Chem* **2012**, *33*, 580–592.

(243) Tian, L. U.; Fei-Wu, C. Calculation of Molecular Orbital Composition. *Acta Chim. Sin.* **2011**, *69*, 2393.

(244) Frisch, M. J.; Trucks, G. W.; Schlegel, H. B.; Scuseria, G. E.; Robb, M. A.; Cheeseman, J. R.; Scalmani, G.; Barone, V.; Petersson, G. A.; Nakatsuji, H.; Li, X.; Caricato, M.;

Marenich, A. V.; Bloino, J.; Janesko, B. G.; Gomperts, R.; Mennucci, B.; Hratchian, H. P.; Ortiz, J. V.; Izmaylov, A. F.; Sonnenberg, J. L.; Williams-Young, D.; Ding, F.; Lipparini, F.; Egidi, F.; Goings, J.; Peng, B.; Petrone, A.; Henderson, T.; Ranasinghe, D.; Zakrzewski, V. G.; Gao, J.; Rega, N.; Zheng, G.; Liang, W.; Hada, M.; Ehara, M.; Toyota, K.; Fukuda, R.; Hasegawa, J.; Ishida, M.; Nakajima, T.; Honda, Y.; Kitao, O.; Nakai, H.; Vreven, T.; Throssell, K.; Montgomery Jr., J. A.; Peralta, J. E.; Ogliaro, F.; Bearpark, M. J.; Heyd, J. J.; Brothers, E. N.; Kudin, K. N.; Staroverov, V. N.; Keith, T. A.; Kobayashi, R.; Normand, J.; Raghavachari, K.; Rendell, A. P.; Burant, J. C.; Iyengar, S. S.; Tomasi, J.; Cossi, M.; Millam, J. M.; Klene, M.; Adamo, C.; Cammi, R.; Ochterski, J. W.; Martin, R. L.; Morokuma, K.; Farkas, O.; Foresman, J. B.; Fox, D. J. Gaussian 16 Rev. C.01, 2016.

(245) Marenich, A. V.; Cramer, C. J.; Truhlar, D. G. Universal Solvation Model Based on Solute Electron Density and on a Continuum Model of the Solvent Defined by the Bulk Dielectric Constant and Atomic Surface Tensions. *J Phys Chem B* **2009**, *113*, 6378–6396.

(246) Grimme, S.; Ehrlich, S.; Goerigk, L. Effect of the Damping Function in Dispersion Corrected Density Functional Theory. *J. Comput. Chem.* **2011**, *32*, 1456–1465.

(247) Weigend, F.; Ahlrichs, R. Balanced Basis Sets of Split Valence, Triple Zeta Valence and Quadruple Zeta Valence Quality for H to Rn: Design and Assessment of Accuracy. *Phys. Chem. Chem. Phys.* **2005**, *7*, 3297.

(248) Allouche, A.-R. Gabedit—A Graphical User Interface for Computational Chemistry Softwares. *J. Comput. Chem.* **2011**, *32*, 174–182.

(249) Liu, Z.; Lu, T.; Chen, Q. An Sp-Hybridized All-Carboatomic Ring, Cyclo[18]Carbon: Electronic Structure, Electronic Spectrum, and Optical Nonlinearity. *Carbon* **2020**, *165*, 461–467.

(250) Lu, T.; Chen, F. Multiwfn: A Multifunctional Wavefunction Analyzer. *J Comput Chem* **2012**, *33*, 580–592.

(251) Dennington, Roy; Keith, Todd A.; Millam, John M. GaussView, Version 6, 2016.

(252) Becke, A. D. Density-functional Thermochemistry. III. The Role of Exact Exchange. *J. Chem. Phys.* **1998**, *98*, 5648.

(253) Lee, C.; Yang, W.; Parr, R. G. Development of the Colle-Salvetti Correlation-Energy Formula into a Functional of the Electron Density. *Phys. Rev. B* **1988**, *37*, 785–789.

(254) Vosko, S. H.; Wilk, L.; Nusair, M. Accurate Spin-Dependent Electron Liquid Correlation Energies for Local Spin Density Calculations: A Critical Analysis. *Can. J. Phys.* **1980**, *58*, 1200–1211.

(255) Amin, E. A.; Truhlar, D. G. Zn Coordination Chemistry: Development of Benchmark Suites for Geometries, Dipole Moments, and Bond Dissociation Energies and Their Use To Test and Validate Density Functionals and Molecular Orbital Theory. *J. Chem. Theory Comput.* **2008**, *4*, 75–85.

(256) Otto, S.; Moll, J.; Förster, C.; Geißler, D.; Wang, C.; Resch-Genger, U.; Heinze, K. Three-in-One Crystal: The Coordination Diversity of Zinc Polypyridine Complexes. *Eur. J. Inorg. Chem.* **2017**, *2017*, 5033–5040.

(257) Grimme, S.; Antony, J.; Ehrlich, S.; Krieg, H. A Consistent and Accurate *Ab Initio* Parametrization of Density Functional Dispersion Correction (DFT-D) for the 94 Elements H-Pu. *J. Chem. Phys.* **2010**, *132*, 154104.

(258) Ernzerhof, M.; Scuseria, G. E. Assessment of the Perdew–Burke–Ernzerhof Exchange-Correlation Functional. *J. Chem. Phys.* **1999**, *110*, 5029–5036.

(259) Perdew, J. P.; Burke, K.; Ernzerhof, M. Generalized Gradient Approximation Made Simple. *Phys. Rev. Lett.* **1996**, *77*, 3865–3868.

(260) van Wüllen, C. Molecular Density Functional Calculations in the Regular Relativistic Approximation: Method, Application to Coinage Metal Diatomics, Hydrides, Fluorides and Chlorides, and Comparison with First-Order Relativistic Calculations. *J. Chem. Phys.* **1998**, *109* (2), 392–399.

(261) Rosenberg, B.; Van Camp, L.; Krigas, Thomas. Inhibition of Cell Division in Escherichia Coli by Electrolysis Products from a Platinum Electrode. *Nature* **1965**, *205* (4972), 698–699. https://doi.org/10.1038/205698a0.

(262) Wang, D.; Lippard, S. J. Cellular Processing of Platinum Anticancer Drugs. *Nat. Rev. Drug Discov.* **2005**, *4* (4), 307–320. https://doi.org/10.1038/nrd1691.

(263) Englinger, B.; Pirker, C.; Heffeter, P.; Terenzi, A.; Kowol, C. R.; Keppler, B. K.; Berger, W. Metal Drugs and the Anticancer Immune Response. *Chem. Rev.* **2019**, *119* (2), 1519–1624. https://doi.org/10.1021/acs.chemrev.8b00396.

(264) Wheate, N. Multi-Nuclear Platinum Complexes as Anti-Cancer Drugs. *Coord. Chem. Rev.* **2003**, *241* (1–2), 133–145. https://doi.org/10.1016/S0010-8545(03)00050-X.

(265) Johnstone, T. C.; Park, G. Y.; Lippard, S. J. Understanding and Improving Platinum Anticancer Drugs - Phenanthriplatin. *Anticancer Res.* **2014**, *34*, 471–476.

(266) Johnstone, T. C.; Wilson, J. J.; Lippard, S. J. Monofunctional and Higher-Valent Platinum Anticancer Agents. *Inorg. Chem.* **2013**, *52* (21), 12234–12249. https://doi.org/10.1021/ic400538c.

(267) Todd, R. C.; Lippard, S. J. Structure of Duplex DNA Containing the Cisplatin 1,2-{Pt(NH3)2}2+-d(GpG) Cross-Link at 1.77 Å Resolution. *J. Inorg. Biochem.* **2010**, *104*, 902–908.

(268) Park, G. Y.; Wilson, J. J.; Song, Y.; Lippard, S. J. Phenanthriplatin, a Monofunctional DNA-Binding Platinum Anticancer Drug Candidate with Unusual Potency and Cellular Activity Profile. *Proc Natl Acad Sci* **2012**, *109*, 11987–11992.

(269) Lovejoy, K. S.; Serova, M.; Bieche, I.; Emami, S.; D'Incalci, M.; Broggini, M.; Erba, E.; Gespach, C.; Cvitkovic, E.; Faivre, S.; Raymond, E.; Lippard, S. J. Spectrum of Cellular Responses to Pyriplatin, a Monofunctional Cationic Antineoplastic Platinum(II) Compound, in Human Cancer Cells. *Mol. Cancer Ther.* **2011**, *10* (9), 1709–1719. https://doi.org/10.1158/1535-7163.MCT-11-0250.

(270) Almaqwashi, A. A.; Zhou, W.; Naufer, M. N.; Riddell, I. A.; Yilmaz, Ö. H.; Lippard, S. J.; Williams, M. C. DNA Intercalation Facilitates Efficient DNA-Targeted Covalent Binding of Phenanthriplatin. *J. Am. Chem. Soc.* **2019**, *141* (4), 1537–1545. https://doi.org/10.1021/jacs.8b10252.

(271) Tullius, T. D.; Lippard, S. J. Ethidium Bromide Changes the Nuclease-Sensitive DNA Binding Sites of the Antitumor Drug Cis-Diamminedichloroplatinum(II). *Proc. Natl. Acad. Sci.* **1982**, *79* (11), 3489–3492. https://doi.org/10.1073/pnas.79.11.3489.

(272) Boulikas, T.; Vougiouka, M. Cisplatin and Platinum Drugs at the Molecular Level (Review). *Oncol. Rep.* **2003**. https://doi.org/10.3892/or.10.6.1663.

(273) Dasari, S.; Bernard Tchounwou, P. Cisplatin in Cancer Therapy: Molecular Mechanisms of Action. *Eur. J. Pharmacol.* **2014**, *740*, 364–378. https://doi.org/10.1016/j.ejphar.2014.07.025.

(274) Lozada, I. B.; Williams, J. A. G.; Herbert, D. E. Platinum(II) Complexes of Benzannulated N ^ N ⁻^ O-Amido Ligands: Bright Orange Phosphors with Long-Lived Excited States. *Inorg. Chem. Front.* **2022**, *9* (1), 10–22. https://doi.org/10.1039/D1QI01120K.

(275) Che, C.-M.; Yang, M.; Wong, K.-H.; Chan, H.-L.; Lam, W. Platinum(II) Complexes of Dipyridophenazine as Metallointercalators for DNA and Potent Cytotoxic Agents against Carcinoma Cell Lines. *Chem. – Eur. J.* **1999**, *5*, 3350–3356.

(276) Kieltyka, R.; Fakhoury, J.; Moitessier, N.; Sleiman, H. F. Platinum Phenanthroimidazole Complexes as G-Quadruplex DNA Selective Binders. *Chem. – Eur. J.* **2008**, *14* (4), 1145–1154. https://doi.org/10.1002/chem.200700783.

(277) Cusumano, M.; Di Pietro, M. L.; Giannetto, A.; Nicolò, F.; Rotondo, E. Noncovalent Interactions of Platinum(II) Square Planar Complexes Containing Ligands Out-of-Plane with DNA. *Inorg. Chem.* **1998**, *37* (3), 563–568. https://doi.org/10.1021/ic9705406.

(278) Suntharalingam, K.; Mendoza, O.; Duarte, A. A.; Mann, D. J.; Vilar, R. A Platinum Complex That Binds Non-Covalently to DNA and Induces Cell Death via a Different Mechanism than Cisplatin. *Metallomics* **2013**, *5* (5), 514. https://doi.org/10.1039/c3mt20252f.

(279) Luedtke, N. W.; Liu, Q.; Tor, Y. Synthesis, Photophysical Properties, and Nucleic Acid Binding of Phenanthridinium Derivatives Based on Ethidium. *Bioorg. Med. Chem.* **2003**, *11*, 5235–5247.

(280) Nandi, R.; Chaudhuri, K.; Maiti, M. EFFECTS OF IONIC STRENGTH and PH ON THE BINDING OF SANGUINARINE TO DEOXYRIBONUCLEIC ACID. *Photochem. Photobiol.* **1985**, *42* (5), 497–503. https://doi.org/10.1111/j.1751-1097.1985.tb01600.x.

(281) Howe-Grant, M.; Lippard, S. J. Binding of Platinum(II) Intercalation Reagents to Deoxyribonucleic Acid. Dependence on Base-Pair Composition, Nature of the Intercalator, and Ionic Strength. *Biochemistry* **1979**, *18* (26), 5762–5769. https://doi.org/10.1021/bi00593a003.

(282) Murphy, M. P. How Mitochondria Produce Reactive Oxygen Species. *Biochem. J.* **2009**, *417* (1), 1–13. https://doi.org/10.1042/BJ20081386.

(283) Ivashkevich, A.; Redon, C. E.; Nakamura, A. J.; Martin, R. F.; Martin, O. A. Use of the γ-H2AX Assay to Monitor DNA Damage and Repair in Translational Cancer Research. *Cancer Lett.* **2012**, *327* (1–2), 123–133. https://doi.org/10.1016/j.canlet.2011.12.025.

(284) Mah, L.-J.; El-Osta, A.; Karagiannis, T. C. ΓH2AX: A Sensitive Molecular Marker of DNA Damage and Repair. *Leukemia* **2010**, *24* (4), 679–686. https://doi.org/10.1038/leu.2010.6.

(285) Chargaff, E.; Lipshitz, R. Composition of Mammalian Desoxyribonucleic Acids [1]. *J. Am. Chem. Soc.* **1953**, *75* (15), 3658–3661. https://doi.org/10.1021/ja01111a016.

(286) Kaim, W.; Schwederski, B.; Klein, A. Manganese-Catalyzed Oxidation of Water to O2. In *Bioinorganic Chemistry: Inorganic Elements in the Chemistry of Life*; Wiley: Chichester, 2013; pp 67–74.

(287) Pan, D.; Schmieder, A. H.; Wickline, S. A.; Lanza, G. M. Manganese-Based MRI Contrast Agents: Past, Present, and Future. *Tetrahedron* **2011**, *67* (44), 8431–8444. https://doi.org/10.1016/j.tet.2011.07.076.

(288) East, N. R.; Förster, C.; Carrella, L. M.; Rentschler, E.; Heinze, K. The Full d^3–d^5 Redox Series of Mononuclear Manganese Complexes: Geometries and Electronic Structures of $[Mn(Dgpy)_2]^{n+}$. *Inorg. Chem.* **2022**, *61* (37), 14616–14625. https://doi.org/10.1021/acs.inorgchem.2c01680.

(289) Herr, P.; Kerzig, C.; Larsen, C. B.; Häussinger, D.; Wenger, O. S. Manganese(i) Complexes with Metal-to-Ligand Charge Transfer Luminescence and Photoreactivity. *Nat. Chem.* **2021**, *13* (10), 956–962. https://doi.org/10.1038/s41557-021-00744-9.

(290) Betley, T. A.; Qian, B. A.; Peters, J. C. Group VIII Coordination Chemistry of a Pincer-Type Bis(8-Quinolinyl)Amido Ligand. *Inorg. Chem.* **2008**, *47* (24), 11570–11582. https://doi.org/10.1021/ic801047s.

(291) Huynh, M. T.; Anson, C. W.; Cavell, A. C.; Stahl, S. S.; Hammes-Schiffer, S. Quinone 1 e$^-$ and 2 e$^-$/2 H$^+$ Reduction Potentials: Identification and Analysis of Deviations from Systematic Scaling Relationships. *J. Am. Chem. Soc.* **2016**, *138* (49), 15903–15910. https://doi.org/10.1021/jacs.6b05797.

(292) Michaelis, L.; Hill, E. S. THE VIOLOGEN INDICATORS. *J. Gen. Physiol.* **1933**, *16* (6), 859–873. https://doi.org/10.1085/jgp.16.6.859.

(293) Woodhouse, M. D.; McCusker, J. K. Mechanistic Origin of Photoredox Catalysis Involving Iron(II) Polypyridyl Chromophores. *J. Am. Chem. Soc.* **2020**, *142* (38), 16229–16233. https://doi.org/10.1021/jacs.0c08389.